



HAL
open science

Dynamique des structures cohérentes de méso et sousméso-échelle en mer d'Arabie

Charly de Marez

► **To cite this version:**

Charly de Marez. Dynamique des structures cohérentes de méso et sousméso-échelle en mer d'Arabie. Océanographie. Université de Bretagne occidentale - Brest, 2021. Français. NNT : 2021BRES0064 . tel-03658650

HAL Id: tel-03658650

<https://theses.hal.science/tel-03658650>

Submitted on 4 May 2022

HAL is a multi-disciplinary open access archive for the deposit and dissemination of scientific research documents, whether they are published or not. The documents may come from teaching and research institutions in France or abroad, or from public or private research centers.

L'archive ouverte pluridisciplinaire **HAL**, est destinée au dépôt et à la diffusion de documents scientifiques de niveau recherche, publiés ou non, émanant des établissements d'enseignement et de recherche français ou étrangers, des laboratoires publics ou privés.

THESE DE DOCTORAT

L'UNIVERSITE
DE BRETAGNE OCCIDENTALE

ECOLE DOCTORALE N° 598

Sciences de la Mer et du littoral

Spécialité : Océanographie physique et environnement

Par

Charly DE MAREZ

**Dynamique des structures cohérentes de méso
et sousméso-échelle en mer d'Arabie**

Thèse présentée et soutenue à Plouzané le 03/09/2021

Unité de recherche : Laboratoire d'Océanographie Physique et Spatiale (UMR 6223)

Rapportrices avant soutenance : Composition du Jury :

Sabrina SPEICH
(Professeure, ENS, IPSL, Paris)

Chantal STAQUET
(Professeure, LEGI, Grenoble)

Présidente :
Anne-Marie TREGUIER

(Directrice de recherche CNRS, LOPS, Brest)

Examinatrices :
Sabrina SPEICH
Chantal STAQUET
Anne PETRENKO
Rosemary MORROW
Claire MENESGUEN

(Professeure, ENS, IPSL, Paris)
(Professeure, LEGI, Grenoble)
(Maître de conférences, MIO, Marseille)
(Physicienne CNAP, LEGOS, Toulouse)
(Chercheure IFREMER, LOPS, Brest)

Directeur de thèse :
Xavier CARTON

Professeur, LOPS, UBO, Brest)

Invités :
Thomas MEUNIER
Jonathan GULA
Alexandre STEGNER
Pierre L'HÉGARET
Isabelle GUILLOTON-CHAINTREUIL

(Research associate, WHOI, Woods Hole)
(Maître de conférences, LOPS, UBO, Brest)
(Chercheur CNRS, LMD, École Polytechnique, Paris)
(Chercheur contractuel, LMD, ENS, Paris)
(DGA, Paris)

REMERCIEMENTS

En premier lieu, j'aimerais remercier l'ensemble des membres du jury pour leur participation et pour le temps qu'elles ont apporté à la relecture de ce travail. Il convient également de remercier l'Université de Bretagne Occidentale ainsi que la Direction Générale de l'Armement d'avoir soutenu mes travaux financièrement et matériellement.

Ensuite, parmi tous les gens que j'ai côtoyés depuis les débuts de ma scolarité jusqu'à mon arrivée à Brest, de nombreuses personnes seraient à remercier. Ces personnes, je ne les remercierai pas toutes parce qu'elles savent à quel point elles m'ont aidé, au travail comme dans la vie. A toutes ces personnes je dis merci du fond du cœur. Les deux seules personnes que je nommerai et remercierai ici sont celles sans qui rien de tout ce travail de thèse, même une infime partie, n'aurait été possible.

Xavier, merci pour tout. Dans la vie il est peu d'instant où l'on rencontre des personnes sur lesquelles aucun doute n'est possible. Ici il n'y en a aucun. Pas besoin d'un hommage de trente pages pour dire simplement que je suis très chanceux d'avoir rencontré, collaboré et eu le mal de mer aux côtés d'une personne aussi sage, brillante et gentille que toi. Peut-être que sur Terre il existe d'autres gens de la même espèce. J'ai hâte de les rencontrer.

Thomas, les trois-quarts du travail présenté dans ce manuscrit, les idées, les techniques et les interprétations n'auraient pas existé si tu n'avais pas fumé encore plus de clopes que moi en bas du bâtiment D. Les discussions scientifiques et humaines que nous avons eues ont énormément dirigé ma réflexion pendant ces trois ans. Si dans vingt ans Les Quatre Vents est ouvert, j'espère que l'on pourra discuter de l'échec de nos vies professionnelles en terrasse sous la pluie.

Ces travaux de thèse, mais aussi les précédents et tous les suivants sont dédiés à Andrée et Annick.

*Et j'ai plein d'questions pour mon Créateur,
En attendant j'traîne, j'fais plein d'erreurs.*

Autre monde

INTRODUCTION GÉNÉRALE

L'océan est un système complexe dans lequel un fluide, l'eau de mer, est mis en mouvement par des forçages extérieurs, et se meut dans un très large spectre de distances. D'un côté, les échelles climatiques, avec des évolutions des courants sur des milliers de kilomètres et des milliers d'années; de l'autre, des courants évoluant très rapidement, sur des échelles de l'ordre du mètre. Au carrefour de ces échelles, les *tourbillons océaniques*, de part leur omniprésence dans tous les bassins, constituent une part significative de la circulation océanique. Du fait de leur dynamique complexe et fortement non-linéaire, ces structures sont intensément étudiées depuis plusieurs décennies. Ces études ont entre autres montré que (1) les importantes vitesses de rotation des tourbillons permettent l'advection de traceurs biogéochimiques et sont ainsi déterminantes pour la répartition géographique des composant essentielles aux activités biologiques, et (2) la structure cohérente des tourbillons permet le transport de masses d'eaux à travers l'océan sur (parfois) des milliers de kilomètres. Ainsi, le transport zonal de masse induit par les tourbillons océaniques est du même ordre de grandeur que celui induit par les vents de grande échelle et la circulation thermohaline.

Dans des régions particulières du globe, les tourbillons ont un impact plus grand sur la circulation que la circulation grande échelle elle-même. C'est le cas en *mer d'Arabie*, où le transport des propriétés de la colonne d'eau est dominé par le transport induit par les tourbillons. Les tourbillons impactent ainsi fortement la production primaire et les activités biologiques dans cette région où la pêche est primordiale pour les quelque 120 millions de personnes vivant sur les côtes.

Comprendre *la dynamique des tourbillons en mer d'Arabie* est donc d'une importance primordiale, car leur cycle de vie et leurs interactions avec l'environnement sont déterminants pour leur impact sur l'écosystème marin. Ce manuscrit de thèse s'attache à donner de nouvelles clefs à la compréhension de la dynamique des tourbillons, avec une attention plus particulière sur la mer d'Arabie. Cette problématique étant très vaste, nous ne donnons pas ici une réponse à une question précise. Nous utilisons les outils actuels, observationnels et numériques, pour améliorer notre connaissance des tourbillons océaniques dans la lignée des études menées depuis plus de cinquante ans.

Cette courte introduction est complétée par une présentation de la dynamique des fluides géophysiques, de la problématique des tourbillons en mer d'Arabie, et des méthodes utilisées dans les sections 1, 2 et 3 respectivement. Les différentes études menées durant cette thèse sont ensuite présentées sous la forme d'articles publiés dans des journaux à comité de lecture dans les sections 4, 5 et 6. Après une

brève conclusion sur le travail mené concernant la dynamique des tourbillons en mer d'Arabie, nous présentons également en annexe plusieurs études menées ou terminées au cours de ces trois ans, en parallèle à la problématique principale.

TABLE DES MATIÈRES

Introduction	7
1 L'océan, un système physique décrit par la mécanique des fluides	13
1.1 Sur le mouvement d'un fluide	14
1.2 Le cas particulier de l'océan	17
1.2.1 L'océan, un système sphérique en rotation	17
1.2.2 La stratification de la colonne d'eau	19
1.2.3 L'océan, un système couplé à son environnement	21
1.2.4 Quid de la viscosité?	21
1.3 L'échelle des courants océaniques	23
1.4 Des modèles simplifiés pour décrire la dynamique océanique	28
1.4.1 Les équations primitives hydrostatiques	28
1.4.2 Le modèle quasi-géostrophique 2 couches	29
1.5 Résumé	32
2 Les tourbillons océaniques et la mer d'Arabie	33
2.1 Les tourbillons océaniques	34
2.1.1 La stabilité des tourbillons	37
2.1.2 Un cas d'interaction tourbillon-tourbillon : la fusion	42
2.1.3 L'interaction des tourbillons avec les bords ouest	45
2.1.4 Par delà la méso-échelle : les tourbillons de sousméso-échelle	48
2.2 La mer d'Arabie : un lieu dominé par la dynamique tourbillonnaire	50
2.2.1 Généralités	51
2.2.2 La dynamique tourbillonnaire en mer d'Arabie	54
2.2.3 Plus généralement, en mer d'Arabie...	59
2.3 Les questions posées dans ce manuscrit	61
3 Observer et étudier la mer d'Arabie	63
3.1 Les moyens observationnels	64

3.1.1	Altimétrie	64
3.1.2	Plateformes autonomes	65
3.1.3	La campagne océanographique PHYSINDIEN 2019	66
3.2	Les moyens numériques	68
3.2.1	CROCO	68
3.2.2	Ré-analyse HYCOM 1/12°	70
3.2.3	Modèle QG 2 couches	71
4	La structure des tourbillons de méso-échelle en mer d'Arabie	73
4.1	Article publié dans <i>Deep Sea Research Part I</i>	73
4.2	Supplément sur la signature de PGW dans le tourbillon composite	90
4.3	Conclusion sur la structure 3D des tourbillons en mer d'Arabie	92
5	Le cycle de vie des tourbillons isolés en mer d'Arabie	93
5.1	Stabilité	94
5.1.1	La stabilité du cyclone composite : Article publié dans <i>Ocean Modelling</i>	94
5.1.2	Supplément sur l'asymétrie cyclone/anticyclone	113
5.1.3	Supplément sur l'impact de l'effet- β pour la stabilité du cyclone composite	115
5.2	Interaction sur le bord ouest	117
5.2.1	L'interaction du tourbillon composite avec un bord ouest	118
5.2.2	Le problème général tourbillon-mur sur le plan- β : Article publié dans <i>Geophysical and Astrophysical Fluid Dynamics</i>	119
5.3	Observation d'un tourbillon cyclonique profond de sousmésos-échelle	139
5.3.1	L'observation : Article publié dans <i>Geophysical Research Letters</i>	139
5.3.2	Supplément sur la possibilité de génération de ce tourbillon par interaction tourbillon-ondes de Kelvin sur le bord ouest	150
5.4	Conclusion sur la dynamique des tourbillons isolés	151
6	Les interactions entre tourbillons en mer d'Arabie	153
6.1	La fusion de tourbillons en mer d'Arabie	154
6.2	Les mécanismes de la fusion dans l'océan ouvert	155
6.2.1	De la mer d'Arabie à l'océan global	155
6.2.2	Est ce que la fusion de tourbillons peut être considérée comme isolée? Article publié dans <i>Scientific Reports</i>	155
6.3	L'impact d'une marche topographique sur la fusion de tourbillons	166

6.3.1	Article publié dans <i>Fluids</i>	166
6.4	Conclusion sur la fusion de tourbillons	191
Conclusion		193
Annexes		197
A Sur l'impact acoustique des structures tourbillonnaires		197
B Informations supplémentaires pour la section 6.2.2		205
C La sphéricité de la Terre et son impact sur la dynamique océanique		217
D Étude de l'interaction tourbillon-upwelling		231
E Étude idéalisée du cycle de vie d'un tourbillon semi-permanent		251
F Ondes de sillage dans le Gulf Stream		265
Bibliographie		277

L'OCÉAN, UN SYSTÈME PHYSIQUE DÉCRIT PAR LA MÉCANIQUE DES FLUIDES

Cette partie introductive présente succinctement les équations et concepts fondamentaux utilisés dans ce manuscrit. Elle ne vise pas à présenter l'océanographie physique dans son intégralité, et ne discute pas tous les phénomènes océaniques en détails. En partant d'un cadre général, nous dérivons les modèles mathématiques considérés ensuite, *i.e.* les équations primitives hydrostatiques, et le modèle quasi géostrophique. Ainsi, cette partie permettra aux physiciens de tous horizons, de comprendre les choix, et modèles mathématiques utilisés dans ce manuscrit.

1.1 Sur le mouvement d’un fluide



FIGURE 1.1 – Études d’eau turbulente, ou la description du mouvement des fluides par Léonard de Vinci (Kemp, 2019). Crédit : Léonard de Vinci, Études sur les eaux turbulentes, Royal Collection Trust.

L’étude du mouvement des fluides remonte à l’antiquité Grecque, Archimède étudiait alors le principe de flottabilité des corps plongés dans un liquide, dans ses ouvrages *Des Corps Flottants I & II* (250 av. J.C.). Quinze siècles plus tard, de Vinci, Torricelli, Newton, Pascal et Bernoulli participèrent à l’avancée rapide de la compréhension du mouvement des fluides, par le biais d’observations expérimentales, et des premières formalisations mathématiques des principes de la statique des fluides. C’est avec le développement des outils mathématiques modernes que les équations fondatrices de la mécanique des fluides virent le jour. Notamment, Claude-Louis Navier et George Gabriel Stokes présentèrent les équations de Navier–Stokes, au cours du XIX^{ème} siècle. Elles formalisent la dynamique des fluides de manière mathématique, et restent aujourd’hui la manière générale de décrire le mouvement des fluides (Guyon et al., 1991).

Cette formulation repose sur les lois Newtoniennes de conservation de la quantité de mouvement. Le principe fondamental de la dynamique appliqué à une particule fluide de densité ρ , de vitesse $\mathbf{u} = (u, v, w)$, et de volume $V(t)$, à l’instant t , s’écrit

$$\iiint_{V(t)} \rho \frac{d}{dt} \mathbf{u} dV = \sum \vec{\mathcal{F}}, \quad (1.1)$$

où $\frac{d}{dt} = \partial_t + u\partial_x + v\partial_y + w\partial_z$ est la dérivée matérielle, et $\sum \vec{\mathcal{F}}$ la somme des forces appliquées sur la

particule fluide. La particule fluide considérée est soumise à des actions à distance \mathbf{f} (*e.g.* la pesanteur), et des actions de contact (les actions qu'exercent les particules fluides les unes sur les autres, *e.g.* la friction, la pression...). Ces dernières sont définies par le biais du tenseur des contraintes $[\sigma]$, de composantes σ_{ij} , décrivant le fluide considéré. Pour chaque composante du mouvement u_i , l'eq. (1.1) devient alors

$$\iiint_{V(t)} \rho \frac{d}{dt} u_i dV = \iiint_{V(t)} f_i dV + \iint_{\partial V(t)} \sigma_{ij} n_j dS, \quad (1.2)$$

où nous avons utilisé la notation d'Einstein sur la sommation des indices, et où n_j sont les composantes du vecteur normal à la surface de la particule fluide $\partial V(t)$. En appliquant le théorème de Stokes à l'intégrale surfacique, l'eq. (1.2) devient

$$\iiint_{V(t)} \rho \frac{d}{dt} u_i dV = \iiint_{V(t)} f_i dV + \iiint_{V(t)} \partial_j \sigma_{ij} dV, \quad (1.3)$$

et on a alors l'identité locale

$$\rho \frac{d}{dt} u_i = f_i + \sigma_{ij} n_j. \quad (1.4)$$

Dans le cadre d'un fluide Newtonien, tel que l'eau de mer, le tenseur des contraintes est défini comme

$$\sigma_{ij} = -P\delta_{ij} + \eta(\partial_i u_j + \partial_j u_i) + \xi(\partial_k u_k)\delta_{ij}, \quad (1.5)$$

où δ_{ij} est le symbole de Kronecker, P est la pression au sein du fluide, η la viscosité dynamique et ξ la viscosité de compression; η et ξ sont des constantes propres au fluide. On obtient alors les équations de Navier-Stokes sous leur forme la plus générale, pour un fluide Newtonien :

$$\rho \frac{d}{dt} u_i = -\partial_i P + \eta\Delta u_i + (\eta + \xi)\partial_i(\partial_j u_j) - f_i, \quad (1.6)$$

où Δ est l'opérateur Laplacien. Ces équations permettent de décrire le mouvement des fluides de l'échelle centimétrique à l'échelle atmosphérique. Dans le cas de l'océan, la seule force qui s'exerce sur le fluide est la pesanteur, telle que $\mathbf{f} = \rho\mathbf{g}$. Également, pour décrire les courants océaniques, le fluide est considéré incompressible (cette hypothèse à des limites, notamment à très grandes profondeurs $z < -2000$ m), ce qui implique par conservation de la masse que $\partial_j u_j = 0$. Les équations de Navier-Stokes pour un fluide Newtonien incompressible, soumis à l'action de la pesanteur sont alors :

$$\rho \frac{d\mathbf{u}}{dt} = -\nabla P + \eta\Delta\mathbf{u} + \rho\mathbf{g}, \quad (1.7)$$

Ces équations sont valables dans n'importe quel repère inertiel. Elles décrivent le mouvement du fluide

de manière Eulérienne, c’est à dire sans considérer une particule fluide en particulier. L’objet de la mécanique des fluides, et par extension de l’océanographie physique, est de décrire les propriétés du champ de vitesse \mathbf{u} et du champ de pression P du fluide, dans des conditions données, de la même manière que le faisait Léonard de Vinci, il y a 500 ans (Fig. 1.1).

1.2 Le cas particulier de l'océan

L'océan est un système fluide classique, pouvant être décrit par les équations présentées plus haut. Néanmoins, il convient de mettre en avant les différentes particularités de l'océan, qui font de lui un système unique. Ce caractère remarquable transparaît dans les courants, pouvant déplacer des tonnes de plastique tout autour du globe, et les ondes de surface, telles des raz de marée, capables de submerger des kilomètres de terre.

1.2.1 L'océan, un système sphérique en rotation

L'océan se trouve sur un corps céleste en rotation. Pour décrire les mouvements océaniques dans le référentiel tournant, associé à la Terre, il convient de modifier les équations dérivées précédemment. L'accélération d'un fluide dans un référentiel tournant peut être exprimé dans un référentiel inertiel comme

$$\frac{d\mathbf{u}_i}{dt} = \frac{d\mathbf{u}_r}{dt} + \underbrace{2\boldsymbol{\Omega} \times \mathbf{u}_r}_{\text{Terme de Coriolis}} + \overbrace{\boldsymbol{\Omega} \times (\boldsymbol{\Omega} \times \mathbf{x}_i)}^{\text{Terme axifuge}}, \quad (1.8)$$

où \mathbf{u}_i est la vitesse du fluide exprimé dans un repère inertiel, \mathbf{u}_r , la vitesse du fluide exprimée dans le repère tournant, \mathbf{x}_i la position du fluide dans le référentiel inertiel, et $\boldsymbol{\Omega}$ le vecteur rotation du repère tournant. Pour l'étude de l'océan, le référentiel tournant choisi est un plan tangent à la surface terrestre (Fig. 1.2). On appelle direction zonale la direction suivant l'axe \mathbf{e}_x , direction méridienne selon l'axe \mathbf{e}_y , et verticale selon l'axe \mathbf{e}_z .

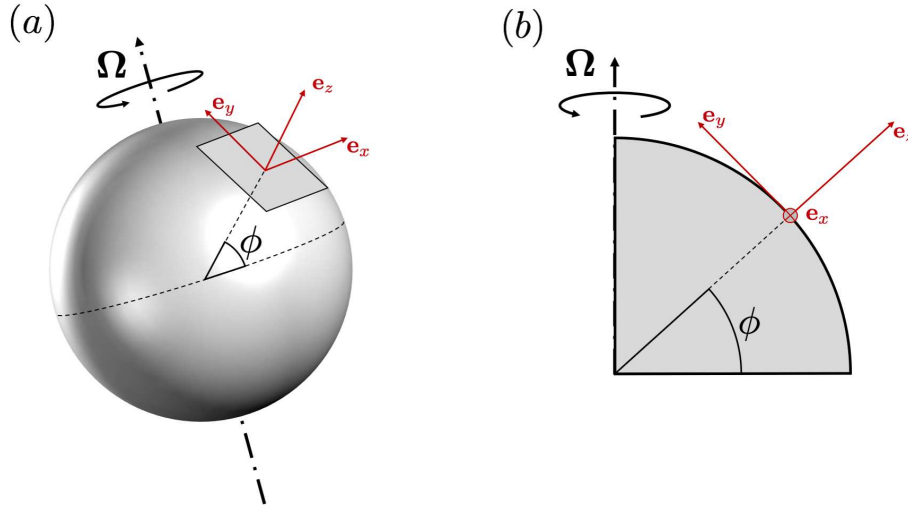


FIGURE 1.2 – (a) Vue 3D et (b) vue 2D du repère tangent, considéré pour décrire la dynamique des fluides océaniques.

Le terme axifuge peut être négligé, car il représente une faible déviation $O(1)\%$ de la force de pesanteur (Vallis, 2017). En substituant eq. (1.8) dans eq. (1.7), et en abandonnant les indices correspondant au repère tournant par simplicité de notation, on obtient les équations de Navier-Stokes en repère tournant :

$$\rho \frac{d\mathbf{u}}{dt} + 2\boldsymbol{\Omega} \times \mathbf{u} = -\nabla P + \mu \Delta \mathbf{u} + \rho \mathbf{g}, \quad (1.9)$$

où \mathbf{u} et $\boldsymbol{\Omega}$ sont exprimés dans le repère tangent $(\mathbf{e}_x, \mathbf{e}_y, \mathbf{e}_z)$. On obtient alors pour les trois composants du mouvement :

$$\begin{cases} \frac{d}{dt}u - fv + f^*w = -\frac{1}{\rho}\partial_x P + \nu\Delta u \\ \frac{d}{dt}v + fu = -\frac{1}{\rho}\partial_y P + \nu\Delta v \\ \frac{d}{dt}w - f^*u = -\frac{1}{\rho}\partial_z P + \nu\Delta w - g, \end{cases} \quad (1.10)$$

avec $\nu = \eta/\rho$ la viscosité cinématique du fluide, et $f = 2\Omega \sin \phi$ et $f^* = 2\Omega \cos \phi$, les composantes traditionnelle et non traditionnelle de Coriolis. Elles représentent la projection de $\boldsymbol{\Omega}$ dans la direction verticale et méridienne au plan local. Comme nous ne nous intéresserons pas aux dynamiques équatoriales, la composante non traditionnelle sera négligée.

La Terre étant sphérique (voir l'annexe C pour une discussion sur ce point), f varie avec la latitude. Cette variation induit de nombreux phénomènes, incluant la propagation des ondes de Rossby

planétaire et le déplacement vers l'ouest des structures cohérentes (voir Cushman-Roisin et al. (1990); Chelton & Schlax (1996) et section 1.2.1 de Vic (2015) pour une discussion sur la distinction entre ces deux phénomènes qui peut mener à des ambiguïtés). Pour simplifier les équations, il peut être utile de faire un développement limité de f autour d'une latitude moyenne ϕ_0 :

$$f(\phi) = f(\phi_0) + (\phi - \phi_0) \frac{df}{d\phi}(\phi_0) + \dots \quad (1.11)$$

$$= 2\Omega \sin \phi_0 + (\phi - \phi_0) R_t \frac{2\Omega \cos \phi_0}{R_t} + \dots \quad (1.12)$$

$$= f_0 + \beta y + \dots, \quad (1.13)$$

où R_t est le rayon de la terre, et β le paramètre de Rossby. On parle d'approximation du plan- f lorsque $f \approx f_0$, et d'approximation du plan- β lorsque $f \approx f_0 + \beta y$. L'approximation du plan- f convient à l'étude des processus de petite échelle, pour lesquels les termes en β sont négligeables devant les termes en f_0 . L'approximation du plan- β permet de considérer les processus induits par la sphéricité de la terre (l'effet- β), comme les ondes de Rossby, tout en gardant une expression linéaire de f .

1.2.2 La stratification de la colonne d'eau

L'eau de mer est une solution complexe, composée de nombreux sels et gaz dissous, dont la concentration dépend du lieu et de la position dans la colonne d'eau. La thermodynamique nous apprend que les propriétés de l'eau de mer peuvent être résumées dans une équation d'état

$$\rho = \rho(P, T, S), \quad (1.14)$$

où T et S sont la température et la salinité, respectivement. De manière générale, à une position géographique donnée, on retrouve des eaux plus chaudes en surface qu'en profondeur. Il y a des exceptions à cette règle, telles les eaux issues des mers marginales. Ces dernières produisent un maximum relatif de température sous la surface. Ce sera en particulier le cas dans cette thèse. La salinité de la colonne d'eau quant à elle est déterminé par des flux surfaciques (*e.g.* la balance évaporation/précipitation), ou latéraux (*e.g.* la décharge d'eau douce des fleuves ou d'eaux issues de mers marginales) faisant varier la salinité autour d'une salinité moyenne. Ainsi, l'océan est un fluide stratifié, dont la densité varie avec (1) la profondeur et (2) la position autour du globe.

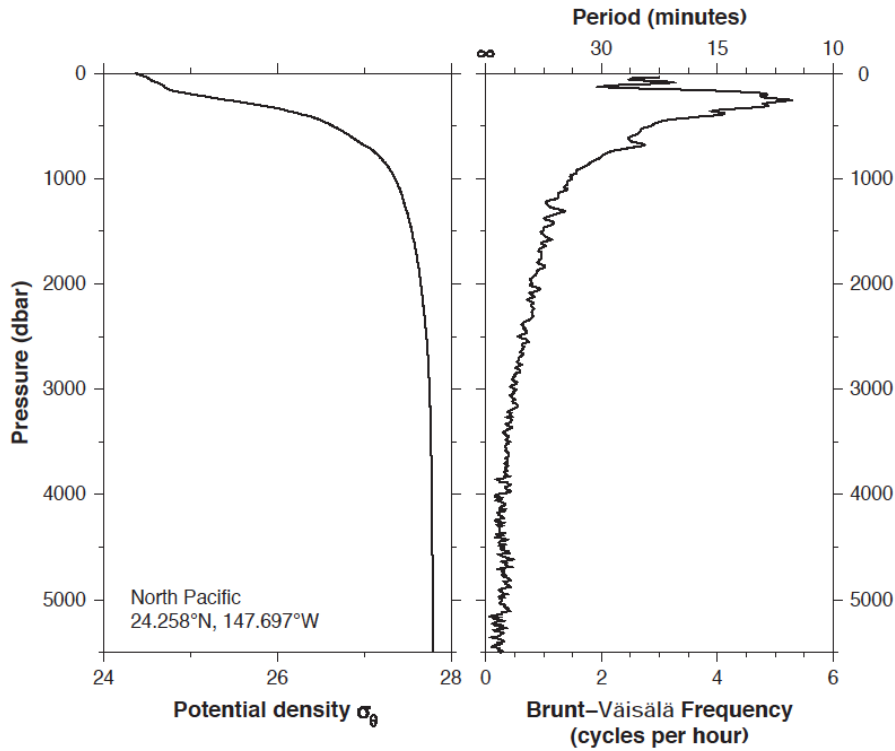


FIGURE 1.3 – Exemple de profil de densité potentielle (gauche) et de fréquence de Brunt-Väisälä N associé (droite) dans le pacifique Nord, d’après Talley (2011). On peut voir la stratification typique de la colonne d’eau océanique : une couche de surface assez homogène (N constant), puis une forte variation de densité (pycnocline ou thermocline si S constant), et une couche profonde épaisse et homogène.

Afin de décrire la dynamique océanique, il faut alors ajouter aux eq. (1.10), une équation d’état (McDougall & Barker, 2011), et une stratification moyenne $\bar{\rho}(z)$, représentant les variations de densité avec la profondeur. Cette stratification moyenne est très variable selon le lieu considéré. Un exemple typique de stratification (Fig. 1.3), montre l’eau "légère" et chaude en surface, et "lourde" et froide au fond. Cette stratification est d’une importance toute particulière, car elle induit une asymétrie entre les coordonnées verticales et horizontales, et permet la propagation d’ondes internes (Garrett & Munk, 1979). Pour décrire la stratification, on introduit la fréquence de Brunt-Väisälä

$$N^2 = \frac{-g}{\rho_0} \frac{\partial \sigma_0}{\partial z}, \quad (1.15)$$

où ρ_0 est une valeur de densité moyenne, et σ_0 est la densité potentielle (la densité de la particule fluide, lorsque ramenée adiabatiquement à la surface). De fortes (resp. faibles) valeurs de N correspondent à

un fluide très (resp. peu) stratifié. Lorsque $N^2 < 0$, le fluide est statiquement instable, avec de l'eau plus légère se trouvant en dessous d'eau plus lourde.

1.2.3 L'océan, un système couplé à son environnement

L'océan est un système dynamique couplé, hautement non-linéaire, dont les frontières (solides et fluides) forcent la dynamique.

Premièrement, le fond marin et la côte, constituent les frontières solides inférieure et latérale au système océan. Ces dernières contraignent les mouvements à grande échelle, et imposent des variations bathymétriques pouvant atteindre $\mathcal{O}(1000)$ m sur quelques kilomètres de distance. Elles sont, par exemple, responsables en partie du décrochement du Gulf Stream à Cape Hatteras (Chassignet & Marshall, 2008). À plus petite échelle, en contraignant la vitesse du fluide au fond, et par le biais d'interactions visqueuses, les variations bathymétriques génèrent des processus de petite échelle, *e.g.* des ondes internes (Cusack et al., 2017) et des tourbillons (D'Asaro, 1988). Pour décrire la dynamique océanique, il faut donc considérer les eq. (1.10) ainsi que les conditions limites adaptées au problème.

Deuxièmement, à la surface, l'océan est contraint par l'atmosphère. Le rayonnement solaire incident et les vents impactent les couches océaniques superficielles. Ces mouvements se répercutent ensuite sur toute la colonne d'eau, et forcent la dynamique à l'échelle des bassins (Stommel, 1948) et à petite échelle en surface (Callies et al., 2015). Les eq. (1.10) peuvent donc être modifiées en y ajoutant des termes de forçages \mathbf{F} , représentant par exemple la tension de vent en surface.

$$\begin{cases} \frac{d}{dt}u - fv = -\frac{1}{\rho}\partial_x P + \nu\Delta u + F_x \\ \frac{d}{dt}v + fu = -\frac{1}{\rho}\partial_y P + \nu\Delta v + F_y \\ \frac{d}{dt}w = -\frac{1}{\rho}\partial_z P + \nu\Delta w - g, \end{cases} \quad (1.16)$$

Les traceurs sont également décrit par des équations adéquates, prenant en compte *e.g.* le flux de chaleur en surface pour la température, et l'équilibre précipitation-évaporation pour la salinité.

1.2.4 Quid de la viscosité?

L'océan, de par les échelles des courants y prenant place, peut *a priori* être considéré comme un fluide non visqueux. En effet, si on introduit une échelle des vitesses horizontales des courants océaniques $U \sim 1 \text{ m s}^{-1}$, une extension horizontale de ces courants $L \sim 10^5 \text{ m}$, et la viscosité cinématique

de l’eau de mer $\nu \sim 10^{-6} \text{ m}^2 \text{ s}^{-1}$, le nombre de Reynolds des courants océaniques

$$Re = \frac{UL}{\nu} = \mathcal{O}(10^{11}), \quad (1.17)$$

est très grand. Le régime est turbulent, et les effets inertiels sont dominants devant les effets visqueux. On obtient alors un système d’équation de *type Euler tournant* :

$$\begin{cases} \frac{d}{dt}u - fv = -\frac{1}{\rho}\partial_x P + F_x & \text{(a)} \\ \frac{d}{dt}v + fu = -\frac{1}{\rho}\partial_y P + F_y & \text{(b)} \\ \frac{d}{dt}w = -\frac{1}{\rho}\partial_z P - g. & \text{(c)} \end{cases} \quad (1.18)$$

Cette simplification provient du fait que la différence d’échelle entre les effets visqueux (moléculaires) et les effets advectifs (kilométriques) est importante. Nous considérerons ces équations pour développer les modèles mathématiques utilisés plus loin.

Dans les eq. (1.18), l’énergie n’est plus dissipée. Ceci signifie que l’on a exclu les processus dissipatifs à l’échelle moléculaire pour la description des phénomènes. Or, l’océan est continuellement accéléré par les forçages extérieurs. Cet apport d’énergie doit aboutir aux échelles dissipatives (Ferrari & Wunsch, 2009). En effet, plusieurs siècles d’observations montrent l’océan à l’équilibre énergétique. Pour que l’énergie océanique aboutisse, un chemin vers la dissipation visqueuse des courants océaniques est nécessaire. La compréhension de ce chemin est un sujet d’étude actuel, mais n’est pas l’objet du travail présenté ici. Notons cependant que pour refermer le budget énergétique, dans le cadre d’études numériques, des paramétrisations de mélange vertical, et de dissipation horizontale turbulente sont ajoutés.

1.3 L'échelle des courants océaniques

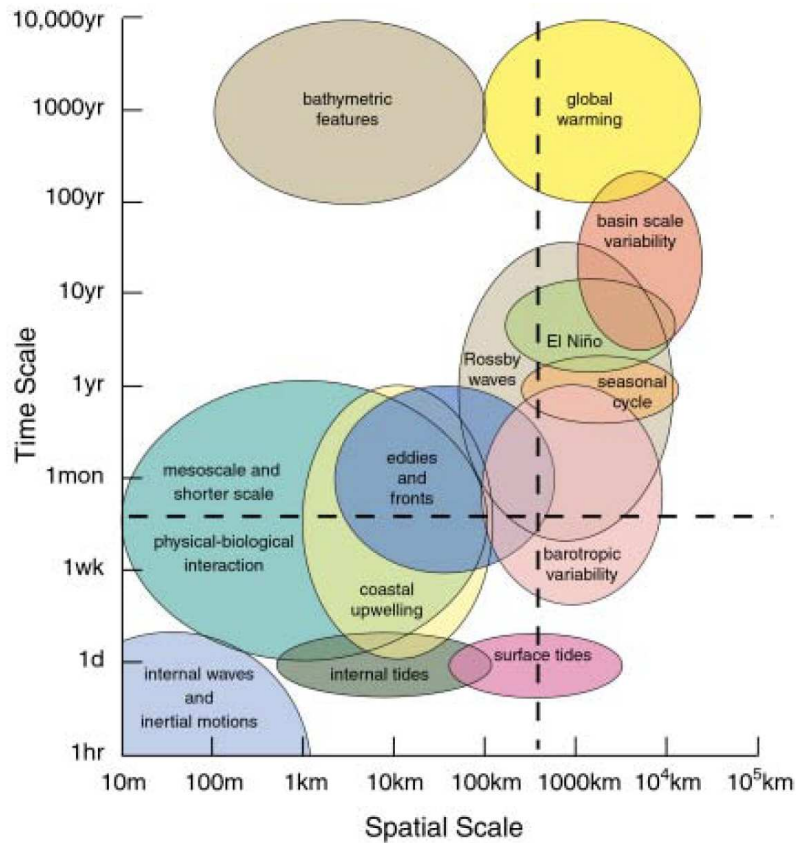


FIGURE 1.4 – Échelles spatiales et temporelles des phénomènes océaniques, d'après Chelton (2001). Voir aussi historiquement Fig. 1 de Stommel (1963) et Fig. 1 de Dickey (1991). La zone bleue, "eddies and fronts", recouvre la méso-échelle et la sousméso-échelle, les échelles typiques des phénomènes étudiés dans ce manuscrit.

Du fait des nombreuses échelles auxquelles les phénomènes océaniques agissent, l'océan est un système complexe, et très riche. D'un côté, les échelles climatiques, avec les courants thermohalins évoluant sur des milliers de kilomètres et des milliers d'années; de l'autre, les vagues se brisant sur des échelles de l'ordre du mètre. Ce manuscrit traite de l'étude des tourbillons océaniques, dont les échelles temporelles et spatiales sont situés au carrefour de ces échelles (Fig. 1.4). Cette partie décrit les régimes d'écoulement dans lesquels les courants étudiés ici peuvent être classés, d'après leurs échelles temporelle et spatiale.

L'océan a la particularité d'être un système "très plat". Les courants océaniques, ont en effet géné-

ralement une extension horizontale $L \sim 100$ km, beaucoup plus grande que leur extension verticale $H \sim 1000$ m; ainsi le rapport d’aspect des mouvements océaniques est

$$\delta = \frac{H}{L} \ll 1. \quad (1.19)$$

Connaissant l’échelle de vitesse des courants, et la stratification typique de la colonne d’eau $N \sim 10^{-2} \text{ s}^{-1}$, il en résulte que le nombre de Froude est petit

$$Fr = \frac{U}{NH} \ll 1. \quad (1.20)$$

D’après la conservation de la masse, et la non divergence de la vitesse, la quantité $Fr^2\delta^2$ représente l’importance de l’accélération verticale devant le gradient vertical de pression, dans l’eq. (1.18c). Ainsi, comme

$$Fr^2\delta^2 \ll 1, \quad (1.21)$$

l’accélération verticale des courants océaniques peut être négligée devant le gradient de pression, c’est l’hypothèse *hydrostatique*. On a alors

$$\begin{cases} \frac{d}{dt}u - fv = -\frac{1}{\rho}\partial_x P + F_x & \text{(a)} \\ \frac{d}{dt}v + fu = -\frac{1}{\rho}\partial_y P + F_y & \text{(b)} \\ \partial_z P = -\rho g. & \text{(c)} \end{cases} \quad (1.22)$$

Sur l’horizontale, de nombreuses échelles coexistent, et s’influencent mutuellement (Fig. 1.4). Une grandeur de référence, pour discuter des échelles horizontales dans l’océan est le rayon de déformation de Rossby (Chelton et al., 1998). Il est défini pour une latitude et une stratification données comme

$$R_{D,n} = \frac{NH}{n\pi f_0}, \quad (1.23)$$

où n est un entier positif. Le premier rayon de déformation de Rossby $R_{D,1} = R_D$, représente l’échelle typique des tourbillons océaniques. Aux basses latitudes (proche de l’équateur) $R_D > 200$ km, alors qu’à moyennes latitudes, $R_D \sim 50$ km (Fig. 1.5). En mer d’Arabie, la proximité avec l’équateur induit un rayon de déformation de Rossby relativement grand, $R_D \sim 50-100$ km. On appellera *méso-échelle* les processus ayant une extension horizontale L de l’ordre du rayon de Rossby ou un peu supérieur, ainsi $R_D^2/L^2 \leq 1$. La *sousméso-échelle* réfèrera aux processus d’extension horizontale inférieure au rayon de déformation de Rossby, tel que $R_D^2/L^2 > 1$. En mer d’Arabie par exemple, les tourbillons de méso-échelle ont typiquement des extensions horizontales $\mathcal{O}(100)$ km, et les tourbillon de sousméso-

échelle des extensions horizontales $\mathcal{O}(10)$ km. Le rapport

$$Bu = \frac{R_D^2}{L^2} \quad (1.24)$$

est le nombre de Burger. Il représente le ratio entre l'importance des effets de la stratification et de la rotation terrestre : à sous-méso-échelle, les effets dûs à la stratification jouent un rôle important devant les effets liés à la rotation terrestre.

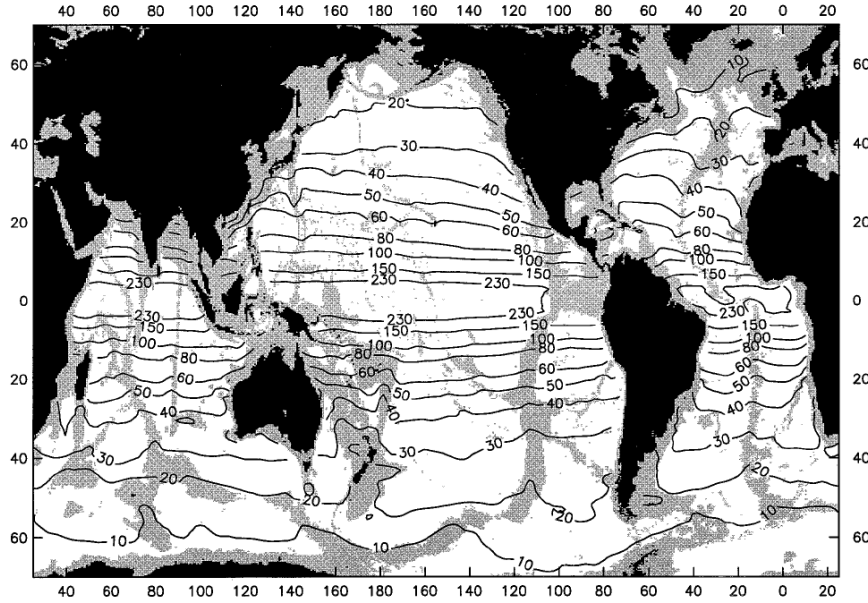


FIGURE 1.5 – Valeur du premier rayon de déformation de Rossby R_D dans l'océan global, d'après Chelton et al. (1998). En mer d'Arabie par exemple, $50 \text{ km} < R_D < 100 \text{ km}$.

Le travail présenté dans ce manuscrit porte sur la dynamique océanique de méso-échelle et de sous-méso-échelle. A ces échelles spatiales, les mouvements évoluent sur des temps longs, avec une échelle temporelle $T \geq 1$ jour. D'après les ordres de grandeurs définis plus haut, les différents termes du membre de gauche des eq. (1.22a,b) sont de l'ordre de

$$\begin{aligned} \frac{d}{dt} \begin{vmatrix} u \\ v \end{vmatrix} &\sim \frac{U}{T} + \frac{U^2}{L} \\ f \begin{vmatrix} u \\ v \end{vmatrix} &\sim f_0 U. \end{aligned} \quad (1.25)$$

L'importance relative des termes inertiels par rapport aux termes de rotation peut donc s'exprimer sous

la forme du nombre de Rossby temporel

$$Ro_T = \frac{1}{f_0 T}, \quad (1.26)$$

et du nombre de Rossby spatial (ensuite simplement appelé nombre de Rossby)

$$Ro = \frac{U}{f_0 L}. \quad (1.27)$$

À méso-échelle et à moyenne latitude, pour des courants de vitesse $U \sim 1 \text{ m s}^{-1}$ et de taille $L \sim 100 \text{ km}$, on a $Ro_T \ll 1$, et $Ro \ll 1$. Les eq. (1.22a,b), dans lesquelles nous oublions volontairement les termes de forçage par simplicité, se réduisent alors à un équilibre entre les termes de rotation et les gradients de pression horizontaux, l’équilibre géostrophique :

$$\begin{cases} -fv = -\frac{1}{\rho} \partial_x P \\ +fu = -\frac{1}{\rho} \partial_y P. \end{cases} \quad (1.28)$$

Ces équations, purement diagnostiques, permettent de déterminer le champ de vitesse associé à une anomalie de pression donnée. En utilisant l’hydrostatisme (eq. (1.9c)), le champ de vitesse peut être calculé à partir du champ de densité; ce sont les équations du *vent thermique*. Dans l’hémisphère Nord, une anomalie de densité positive est associée à un tourbillon cyclonique. Cette anomalie se reflétera dans un creux de la surface de la mer (on note SSH la hauteur de la surface océanique, et on a alors $\delta\text{SSH} < 0$ pour un tourbillon cyclonique).

Pour des courants de plus petite échelle, où ayant des vitesses importantes, cet équilibre n’est plus valable, et la courbure de l’écoulement doit être pris en compte (Penven et al., 2014). On parle alors d’équilibre du gradient de vent ou d’équilibre cyclo-géostrophique dont la forme générale est

$$2\mathcal{J}(u, v) + f(\partial_x v - \partial_y u) = \frac{1}{\rho} \Delta P, \quad (1.29)$$

où $\mathcal{J}(u, v) = \partial_x u \partial_y v - \partial_y u \partial_x v$ est l’opérateur Jacobien. Dans le cas d’un courant axisymétrique (un tourbillon), on peut se placer en coordonnées polaires (r, θ) référencées au centre du tourbillon, et eq. (1.29) devient

$$\frac{v_\theta^2}{r} + f v_\theta = \frac{1}{\rho} \partial_r P, \quad (1.30)$$

où v_θ est la vitesse azimutale du tourbillon. Cet équilibre induit une asymétrie entre les tourbillons cycloniques (sens anti-horaire dans l’hémisphère Nord) et anticycloniques (sens horaire dans l’hémi-

sphère Nord). Ainsi, dans l'océan, deux tourbillons ayant des anomalies de pression égales mais de signes opposés auront des vitesses de rotation non égales en module. Pour une anomalie de pression donnée, un cyclone aura une vitesse de rotation inférieure à un anticyclone (Stegner & Dritschel, 2000).

1.4 Des modèles simplifiés pour décrire la dynamique océanique

Numériquement et analytiquement, il est difficile de traiter avec les équations de Navier-Stokes telles que présentées plus haut, *e.g.* eq. (1.22). Il convient alors de faire de nouvelles approximations, qui permettront une description plus aisée des phénomènes océaniques, mais également une résolution numérique efficace.

1.4.1 Les équations primitives hydrostatiques

Partant des eq. (1.22), on considère que les variations de densité ρ sont négligeables, excepté dans le terme de pesanteur (eq. (1.22c)) : c’est l’approximation de Boussinesq. Cette approximation est raisonnable sachant que, généralement, $\rho \in [1020, 1050] \text{ kg m}^{-3}$. Les variations de densité ne modifient donc que très peu les valeurs du gradient horizontal de pression. Ainsi, en considérant une valeur de densité moyenne dans eq. (1.22a,b), on obtient le système des *équations primitives hydrostatiques* :

$$\begin{cases} \frac{d}{dt}u - fv = -\frac{1}{\rho_0}\partial_x P & \text{(a)} \\ \frac{d}{dt}v + fu = -\frac{1}{\rho_0}\partial_y P & \text{(b)} \\ \partial_z P = -\rho g, & \text{(c)} \end{cases} \quad (1.31)$$

où nous négligeons volontairement les termes de forçage par simplicité. Ces équations sont celles résolues numériquement par le modèle CROCO, décrit dans la section 3.2.1.

Ce système d’équation a la propriété de conserver une grandeur appelée *vorticité potentielle d’Ertel* Q . Cette dernière est une quantité scalaire, conservée pour une particule fluide le long des isopycnes (*i.e.* à ρ constant). En effet, en prenant le rotationnel des eq. (1.31), on obtient l’équation décrivant l’évolution de la vorticité absolue :

$$\frac{d}{dt}(\boldsymbol{\omega}_a) = -\boldsymbol{\omega}_a \cdot \nabla_h \mathbf{u}, \quad (1.32)$$

où $\nabla_h = (\partial_x, \partial_y, 0)$,

$$\boldsymbol{\omega}_a = \begin{pmatrix} -\partial_z v \\ \partial_z u \\ \zeta + f \end{pmatrix} \quad (1.33)$$

la vorticité absolue et $\zeta = \partial_x v - \partial_y u$ la vorticité relative. En prenant la divergence de la conservation

de la masse d'un fluide incompressible, on a également que

$$\frac{d}{dt}(\nabla b) = \nabla_h \mathbf{u} \cdot \nabla b, \quad (1.34)$$

où b est la flottabilité $b = -g\rho/\rho_0$. La somme ∇b .(eq. (1.32)) + ω_a .(eq. (1.35)) donne alors

$$\frac{d}{dt}(\omega_a \cdot \nabla b) = \frac{d}{dt}Q = 0, \quad (1.35)$$

la conservation de la vorticité potentielle d'Ertel. Cette dernière s'écrit dans sa version développée

$$Q = (f + \zeta)\partial_z \rho - (\partial_z v)(\partial_x b) + (\partial_z u)(\partial_y b). \quad (1.36)$$

Les propriétés de stabilité des écoulements océaniques peuvent être décrits à l'aide des variations spatiales de vorticité potentielle (Bretherton, 1966; Hoskins, 1974; Hoskins et al., 1985; Young & Chen, 1995; Morel et al., 2006). D'une part, un écoulement sans cisaillement vertical, peut être instable si le gradient de vorticité potentielle change de signe horizontalement, dans la direction perpendiculaire au courant. Il s'agit d'*instabilité barotrope*, ou instabilité de cisaillement. Dans le cas d'un tourbillon barotrope (*i.e.* homogène sur la vertical), cette condition s'exprime en coordonnée polaire comme " $\partial_r Q$ doit changer de signe sur l'horizontale". D'autre part, si la vorticité potentielle change de signe sur la verticale (*i.e.* entre différentes couches de densité homogène), le courant peut subir une *instabilité barocline*. Dans le cas d'un tourbillon cette condition s'exprime comme " $\partial_r Q$ doit changer de signe sur la verticale". Il est à noter que cette condition est une condition nécessaire mais pas suffisante. Pour diagnostiquer de manière complète un processus d'instabilité, il convient d'étudier en détail les transferts d'énergie au sein du fluide. Une étude détaillée des processus d'instabilité au sein d'un tourbillon isolé est présentée dans la section 5.1.

1.4.2 Le modèle quasi-géostrophique 2 couches

Dans ce paragraphe, nous dérivons le modèle quasi-géostrophique 2 couches de manière informelle. Cela permet de mettre en avant la philosophie de ce modèle, sans encombrer les pages de ce manuscrit. Une dérivation rigoureuse peut être trouvée dans Vallis (2017).

Ce modèle repose sur le principe suivant : les états observés dans l'océan sont à l'équilibre géostrophique. Autrement dit, $Ro \ll 1$ est respecté en tous temps. Il convient alors de remplacer $u \rightarrow u_g$, $v \rightarrow v_g$, et $\frac{d}{dt} \rightarrow \frac{d_g}{dt} = \partial_t + u_g \partial_x + v_g \partial_y$, où u_g et v_g sont les vitesses géostrophiques, décrites par les

équations du vent thermique

$$\begin{cases} \partial_x b = -f_0 \partial_z v_g \\ \partial_y b = -f_0 \partial_z u_g. \end{cases} \quad (1.37)$$

La dérivée matérielle géostrophique est bidimensionnelle car les écoulement géostrophiques sont 2D non divergents (*i.e.* $w_g = 0$). La transition entre les états équilibrés se fait par propagation d’ondes de gravité, qui ne sont pas incluses dans le modèle.

Partons de la forme de la vorticité potentielle d’Ertel exprimée en fonction de la flottabilité et dans laquelle les mouvements sont géostrophiques

$$Q_{qg} = (f + \zeta_g) \partial_z b - (\partial_z v_g)(\partial_x b) + (\partial_z u_g)(\partial_y b), \quad (1.38)$$

avec $\zeta_g = \partial_x v_g - \partial_y u_g$. En décomposant la flottabilité comme la somme d’une valeur moyenne constante $\bar{b}(z)$ et d’une anomalie par rapport à cette moyenne $b'(t, x, y, z)$, en se plaçant sur un plan- β et en linéarisant eq. (1.38) autour de l’état moyen, on obtient :

$$Q_{qg} = (f_0 + \beta y + \zeta) \partial_z \bar{b} + f_0 \partial_z b', \quad (1.39)$$

les autres terme étant d’ordre supérieur en Ro . On pose $N_0^2 = \partial_z \bar{b}$, la stratification moyenne, constante dans le temps et sur l’horizontale. Également, on définit la fonction de courant géostrophique ψ tel que

$$\begin{cases} \partial_x \psi = v_g \\ \partial_y \psi = -u_g. \end{cases} \quad (1.40)$$

Il en résulte simplement d’après les équations du vent thermique que $b' = f_0 \partial_z \psi$, et $\zeta_g = \Delta \psi$, et ainsi :

$$Q_{qg} = (\Delta \psi + f_0 + \beta_y) N_0^2 + f_0^2 \partial_{zz} \psi. \quad (1.41)$$

La vorticité potentielle étant conservée, on obtient alors directement

$$\frac{d_g}{dt} Q_{qg} = \frac{d_g}{dt} \left[\Delta \psi + f_0 + \beta_y + \frac{f_0^2}{N_0^2} \partial_{zz} \psi \right] = 0. \quad (1.42)$$

Formellement, il s’agit du modèles quasi-géostrophique pour lequel la stratification N_0^2 a été supposée constante. En effet, le terme de "vortex stretching" $\frac{f_0^2}{N_0^2} \partial_{zz} \psi$ ne comprend pas la dérivée verticale de la stratification. La dérivée matérielle géostrophique peut être exprimée entièrement en fonction de la

fonction de courant, tel que

$$\frac{d_g}{dt} Q_{qg} = \partial_t Q_{qg} + \mathcal{J}(\psi, Q_{qg}) = 0. \quad (1.43)$$

Au vu de la stratification typique de la colonne d'eau (Fig. 1.3), l'océan peut raisonnablement être considéré comme une superposition de deux couches de fluide de densités uniformes (Flierl, 1978), *i.e.* une couche supérieure de densité ρ_1 et d'épaisseur H_1 et une couche inférieure de densité $\rho_2 > \rho_1$ et d'épaisseur H_2 . Ainsi, $N_0^2 = -\frac{g}{\rho_0} \frac{\rho_1 - \rho_2}{\delta z} = \text{cste}$, où δz est la distance verticale sur laquelle s'effectue le changement de densité. La formulation de la vorticité potentielle quasi-géostrophique eq. (1.42), comprenant une stratification constante est donc raisonnable. Pour plus de généralité, on ajoute dans la couche profonde le terme comprenant les variations de bathymétrie $Q_{bath} = \frac{f_0 h_b}{H}$, où h_b est la hauteur des anomalies topographiques, et H la profondeur totale de la colonne d'eau. Ce terme est décrit en détail dans la section 6.3. Ainsi, si on pose $g' = \frac{\rho_1 - \rho_2}{\rho_0}$, il suit directement que l'écoulement peut être décrit par le système suivant

$$\begin{cases} (\partial_t \cdot + \mathcal{J}(\psi_1, \cdot)) \left[\Delta \psi_1 + f_0 + \beta_y + \frac{f_0^2}{g' H_1} (\psi_2 - \psi_1) \right] = 0 \\ (\partial_t \cdot + \mathcal{J}(\psi_2, \cdot)) \left[\Delta \psi_2 + f_0 + \beta_y + \frac{f_0^2}{g' H_2} (\psi_1 - \psi_2) + \frac{f_0 h_b}{H} \right] = 0. \end{cases} \quad (1.44)$$

Il s'agit du modèle quasi-géostrophique à deux couches avec un toit rigide (pour considérer une surface libre, le terme $-\frac{f_0^2}{g' H_1} \psi_1$ doit être ajouté dans l'expression de la vorticité potentielle de la première couche). Le rayon de déformation (analogue à R_D) est dans ce cadre défini comme $R_D^{qg} = f_0^{-1} \sqrt{g' H_1 H_2 / H}$.

Notons qu'ici, en se focalisant sur la formulation du modèle quasi-géostrophique à partir de la vorticité potentielle, nous ne représentons pas les phénomènes dont la vorticité potentielle est nulle (*i.e.* les ondes de Poincaré), qui composent une partie de la variabilité à méso- et sous-méso-échelle. Pour décrire ces derniers, il faut ajouter aux équations du vent thermique une équation sur la divergence de la vitesse. Dans la suite de ce manuscrit, nous ne nous intéressons pas à ces phénomènes en particulier, et n'entrons donc pas dans les détails ici.

Ce modèle est largement utilisé en océanographie, car il contient une grande partie des processus de méso-échelle et de grande échelle (Vallis, 2017), et il est notamment bien adapté pour l'étude des courants de méso-échelle intensifiés en surface (Flierl, 1978). Il a aussi l'avantage de n'avoir que 2 variables bi-dimensionnelles, qui déterminent l'état du système, ψ_1 et ψ_2 , à un instant donné.

1.5 Résumé

Ces principes théoriques, qui sont une partie du socle de la *Dynamique des Fluides Géophysiques* vont nous permettre de répondre aux questions soulevées pendant cette thèse. En particulier, nous réaliserons des simulations numériques, qui reposent sur le modèle des équations primitives (eq. (1.31)), afin d’étudier différents aspects de la dynamique des tourbillons de méso-échelle en mer d’Arabie. Également, nous utiliserons des simulations reposant sur le modèle quasi-géostrophique 2 couches (eq. (1.44)), pour décrire l’interaction de deux tourbillons proche d’une marche topographique. Le concept de Vorticité Potentielle sera largement utilisé, afin de déterminer les propriétés de stabilité des tourbillons et de décrire leur structure.

LES TOURBILLONS OCÉANIQUES ET LA MER D'ARABIE

Dans l'océan, des processus de différentes échelles spatiales et temporelles cohabitent. Ce manuscrit traite une partie de ces phénomènes : les tourbillons de méso-échelle et de sousméso-échelle. En particulier, nous nous intéressons à leur dynamique dans le contexte de la mer d'Arabie.

Cette partie, introductive également, présente un état de l'art bref et non exhaustif de l'étude des tourbillons océaniques. Nous introduisons les problématiques liées à la dynamique des tourbillons auxquels nous nous intéressons dans ce manuscrit : leur stabilité et leurs interactions avec leur environnement. Nous décrivons la dynamique des tourbillons de méso-échelle, puis mettons en avant les différences principales lorsque les tourbillons sont de sousméso-échelle. Ensuite, nous présentons le contexte de la mer d'Arabie, et mettons en avant l'importance de la dynamique tourbillonnaire pour la dynamique régionale, et la répartition des masses d'eau.

2.1 Les tourbillons océaniques

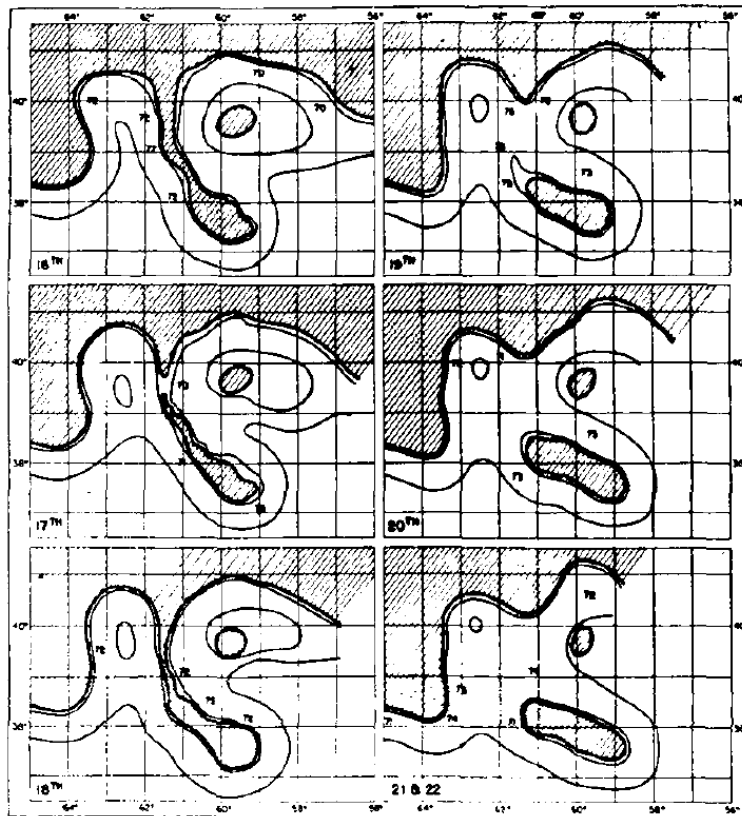


FIGURE 2.1 – Observation de la formation en Juin 1950 d'Edgar, un anneau du Gulf Stream, d'après Fuglister & Worthington (1951). Ce dernier se forme par décrochement d'un méandre du Gulf Stream. Les zones hachurées représentent les zones où $T < 18.3^{\circ}\text{C}$, dans les 200 premiers mètres de la colonne d'eau.

Les premiers tourbillons océaniques de méso-échelle observés, de manière détaillée, sont les anneaux du Gulf Stream (Fuglister & Worthington, 1951; Doblal & Cheney, 1977; Spence & Legeckis, 1981). Leur observation et leur caractérisation remonte aux années 1950. Par exemple, la campagne océanographique "Operation Cabot" (nom de code donné par l'U.S. Navy) durant laquelle plusieurs navires ont été déployés, a permis de déterminer la structure horizontale d'un anneau à coeur froid, *i.e.* un tourbillon cyclonique (Fuglister & Worthington, 1951), voir Fig. 2.1. Plus tard, dans les années 1970, les premières observations satellite de la température de la surface de l'océan par radiométrie ont permis de donner une représentation instantanée de la structure horizontale de tourbillons particuliers comme les anneaux du Gulf Stream (Richardson et al., 1973; Stumpf & Rao, 1975). Ces observations

ont ensuite motivé l'étude théorique et numérique du cycle de vie des tourbillons océaniques, qui reste depuis les années 1980 (*e.g.* Ikeda (1981); Le Groupe Tourbillon (1983); Gent & McWilliams (1986)) un sujet de recherche très actif dans la communauté scientifique.

C'est depuis l'arrivée des moyens d'observations altimétriques (les mesures par satellite de l'élévation du niveau de la mer) qu'une description globale des structures tourbillonnaires de méso-échelle est possible (Chelton, 2001; Chelton et al., 2007, 2011b), voir Fig. 2.2. À partir des cartes de hauteur du niveau de la mer (SSH), l'équilibre géostrophique eq. (1.28) permet d'obtenir la vitesse horizontale des courants de surface. Il est alors possible de repérer et de suivre les tourbillons de méso-échelle, et ainsi de caractériser leur structure horizontale et leur cycle de vie. Ces outils ont considérablement facilité l'observation de la structure verticale des tourbillons, par le biais de déploiements *in situ* dans leurs coeurs, *e.g.* Zhang et al. (2016).

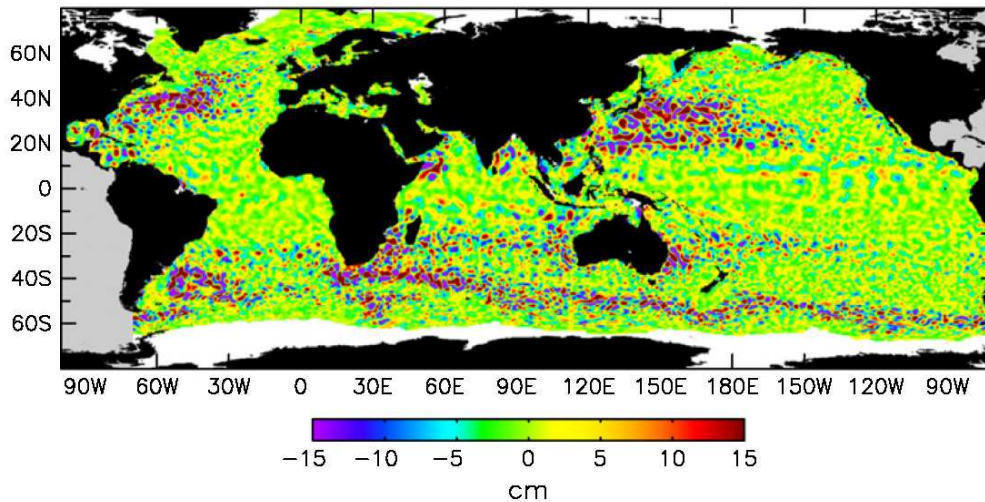


FIGURE 2.2 – Élévation du niveau de la mer observée le 28/08/1996 par satellite (merged T/P and ERS-1 data) d'après Chelton et al. (2011b). Les anomalies négatives (positives) correspondent à des tourbillons cycloniques (anticycloniques). Sur une période de 16 ans, 35 891 tourbillons ont une durée de vie de plus de 4 mois. Ces derniers ont, en moyenne, une durée de vie de 8 mois et se propagent sur une distance de 550 km vers l'ouest.

Les vingt dernières années de recherche ont montré que les tourbillons océaniques sont omniprésents dans l'océan (Chelton et al., 2011b), et ont un impact sur la circulation et les propriétés de la colonne d'eau à l'échelle globale. De par les importantes vitesses de rotation qu'ils induisent ($U \sim 1 \text{ m s}^{-1}$), les tourbillons advectent les traceurs comme la chlorophylle, et sont ainsi déterminants pour la répartition géographique des composants essentiels aux activités biologiques (Chelton et al., 2011a).

Du fait de leur structure cohérente, les tourbillons transportent également des masses d'eau (et les propriétés thermohalines associées *i.e.* T et S) (Dong et al., 2014), et de la chaleur (Sun et al., 2019) à travers l'océan. Le transport zonal de masse induit par les tourbillons de méso-échelle est du même ordre de grandeur que celui induit par les vents de grande échelle et la circulation thermohaline, soit environ 30-40 Sv (Zhang et al., 2014).

Les tourbillons sont un élément clef du système océan. Il convient alors de comprendre de manière détaillée leur cycle de vie. Il est notamment important de comprendre pourquoi ces structures restent cohérentes sur de longues périodes de temps : étudier leur *stabilité*. Au cours de leurs trajets, les tourbillons rencontrent également d'autres tourbillons, et éventuellement des anomalies bathymétriques ou le trait de côte. Ces *interactions* modifient leur comportement et ainsi les propriétés du milieu dans lequel ils évoluent. Nous décrivons dans la suite l'état actuel des connaissances concernant ces deux points.

2.1.1 La stabilité des tourbillons

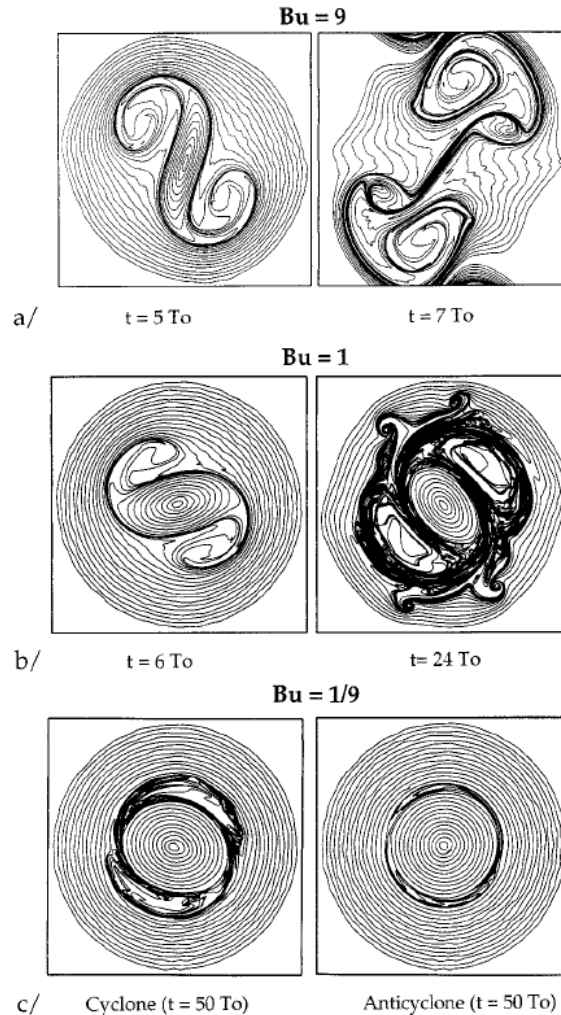


FIGURE 2.3 – Étude de stabilité à amplitude finie d'un tourbillon isolé, dans un modèle Shallow-Water 1 couche, d'après Stegner & Dritschel (2000). Les lignes noires représentent les isocontours de vorticité potentielle. Les tourbillons sont barotropes, initialement circulaires, et ont un nombre de Rossby $Ro < 0.1$. Ils ont initialement des profils de vitesse identiques, mais des nombres de Burger Bu différents. Dans tous les cas, le mode azimuthal 2 domine. (a) présente un cas de restabilisation sous la forme de deux dipôles, (b) un cas de restabilisation sous la forme d'un tripôle, et (c) l'asymétrie cyclone/anticyclone de la stabilité des tourbillons à petit Bu .

De nombreux tourbillons océaniques ont la particularité d'avoir une durée de vie longue durant laquelle ils restent cohérents. Ils sont ainsi présents toute l'année (ou une partie de l'année) à des endroits

donnés du globe. Des exemples de ce type de structures récurrentes peuvent être trouvés dans tous les bassins océaniques : les anneaux du Gulf Stream (Richardson, 1983) et les Meddies (Armi et al., 1989) dans l'Atlantique Nord, les anneaux des Aiguilles (Olson & Evans, 1986) dans l'Atlantique Sud, les tourbillons du canal du Mozambique (Halo et al., 2014) dans l'océan Indien, les anneaux du Kuroshio (Li et al., 1998) dans le Pacifique Nord, les anneaux du Loop Current (Meunier et al., 2018a) dans le golfe du Mexique, ou encore le dipôle de Ra's al Hadd (L'Hégaret et al., 2015, 2016) et le Great Whirl (Vic et al., 2014) en mer d'Arabie. Bien que continuellement entourés d'un champ de vitesse environnant dû aux autres structures cohérentes qui remplissent l'océan (Amores et al., 2017), ces tourbillons récurrents peuvent, en première approximation, être considérés comme *isolés*. On parlera dans la suite d'étude de tourbillon isolé lorsque le tourbillon étudié est seul dans un océan au repos et qu'il n'entraîne pas le fluide environnant en rotation. Depuis les années 1980, de nombreuses études se sont ainsi intéressées à la stabilité des tourbillons isolés, afin de comprendre la longue durée de vie des structures récurrentes. Ces travaux reposent principalement sur deux approches.

La première approche consiste à considérer un problème de *stabilité linéaire*. On suppose le tourbillon isolé initialement axisymétrique, et on se place en coordonnées cylindriques (r, θ, z) , référencées au centre du tourbillon. Ensuite, on décompose le courant comme

$$\mathbf{u}(t, r, \theta, z) = \mathbf{U}(r, \theta, z) + \mathbf{u}'(t, r, \theta, z), \quad (2.1)$$

où \mathbf{U} est le profil de vitesse du tourbillon dont on étudie la stabilité, et \mathbf{u}' une perturbation. Cette dernière a généralement la forme

$$\mathbf{u}'(t, r, \theta, z) = A(t)u_0(r)e^{im\theta}e^{ilz}, \quad (2.2)$$

où u_0 , m et l sont respectivement le profil radial, le mode azimuthal et le mode vertical de la perturbation. L'évolution temporelle de la perturbation est exponentielle pour des modes normaux :

$$A(t) = A_0 e^{t/\tau}, \quad (2.3)$$

et elle est linéaire pour des modes singuliers :

$$A(t) = A_0 \left(1 + \frac{t}{\tau}\right). \quad (2.4)$$

τ est le temps de croissance de la perturbation (Gent & McWilliams, 1986). En linéarisant les équations du mouvement *e.g.* eq. (1.44), autour de l'état moyen \mathbf{U} , on obtient un système matriciel, dont les inconnues sont u_0 et τ , pour chaque couple (m, l) donné. Ainsi, on obtient les modes de perturbation

les plus instables (*i.e.* ceux pour lesquels τ est minimal), et on peut anticiper la déformation que subira le tourbillon après un temps donné.

La stabilité d'un tourbillon dépend fortement de son profil radial de vitesse (Gent & McWilliams, 1986), *e.g.* Rankine, Gaussien, Lorentzien..., mais également de son profil vertical : barotrope (Gent & McWilliams, 1986; Flierl, 1988; Yim & Billant, 2015) ou barocline (Flierl, 1988; Hua, 1988; Nguyen et al., 2012; Yim et al., 2016; Yim & Billant, 2016; Mahdinia et al., 2017). La stratification ambiante, le nombre de Rossby Ro et le nombre de Burger Bu sont également des paramètres importants, influençant la stabilité des tourbillons pour un profil de vitesse donné (Mahdinia et al., 2017). À partir de ces études de stabilité linéaire, il a été montré que les perturbations instables au sein des tourbillons anticycloniques, ont généralement des temps de croissance τ beaucoup plus élevés que celles des cyclones (Mahdinia et al., 2017). Les tourbillons anticycloniques peuvent donc rester axisymétriques sur des temps longs. Cela peut expliquer pourquoi les tourbillons récurrents, à longue durée de vie, sont majoritairement anticycloniques.

Une deuxième approche consiste à utiliser des modèles numériques pour étudier l'évolution à amplitude finie des perturbations instables. De manière similaire à l'étude de stabilité linéaire, on impose au modèle numérique une condition initiale, composée d'un profil de vitesse moyen \mathbf{U} et d'une perturbation \mathbf{u}' . On lance ensuite une simulation "spin-down" (*i.e.* en laissant le système évoluer sans forçage), et on analyse la croissance des perturbations instables. La forme initiale de la perturbation peut être un bruit aléatoire, ou avoir une structure modale voulue. Cette approche a le bénéfice de pouvoir décrire la forme du tourbillon instable à temps longs contrairement à l'étude de stabilité linéaire qui ne décrit que le régime linéaire, *i.e.* à temps court, mais ne permet pas de remonter à une forme analytique de la perturbation. Il est cependant possible de déterminer la forme des modes les plus instables, en réalisant une décomposition de Fourier angulaire; plus de détails sur ce points sont donnés dans la section 5.1.

Ces études ont montré que, sur le plan- f , les perturbations de mode azimutal 2 sont généralement les plus instables. Elles mènent à l'elliptisation des tourbillons isolés (Fig. 2.3) par instabilités barotropes et baroclines, dépendamment du profil horizontal et vertical du tourbillon (Carton & McWilliams, 1989). L'un des résultats principaux de ces études de stabilité à amplitude finie est la re-stabilisation non-linéaire à temps longs des tourbillons instables (Lahaye & Zeitlin, 2015). Lorsque le mode 2 est le plus instable, cette re-stabilisation peut engendrer la formation d'un tripôle stable (Carton et al., 1989; Stegner & Dritschel, 2000; Lahaye & Zeitlin, 2015); de deux dipôles qui s'écartent l'un de l'autre (Stegner & Dritschel, 2000; Lahaye & Zeitlin, 2015), voir *e.g.* Fig. 2.3; ou de hétons elliptiques oscillants (Carton & McWilliams, 1996). Pour des perturbations de modes azimutaux plus élevés, on peut également assister à la formation de quadrupôles stables, et de pentapôles qui se déstabilisent ensuite

en formant 2 tripôles à temps très long (Carton, 2009). Sur le plan- β , la structure verticale de la Vorticité Potentielle est également déterminante pour la stabilité du tourbillon (Morel & McWilliams, 1997). Les perturbations de mode azimutal 1 sont généralement les plus instables, formant des "traînées d'ondes de Rossby" (McWilliams et al., 1986). En se couplant avec le monopôle de signe opposé formé par interaction avec cette onde de Rossby, la trajectoire du tourbillon n'est plus rectiligne, et peut former des boucles, des points de stagnation ou encore s'inverser (Sutyrin et al., 1994; Morel et al., 2006).

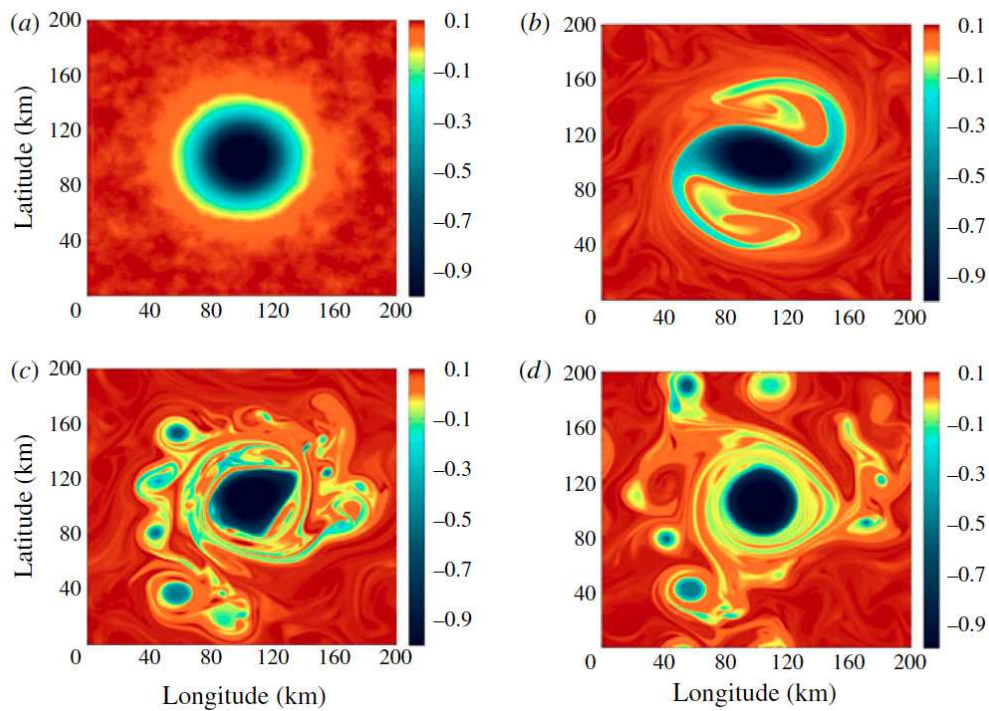


FIGURE 2.4 – Étude de stabilité à amplitude finie d'un tourbillon isolé, dans un modèle quasi-géostrophique continûment stratifié, à haute résolution, d'après Hua et al. (2013). La couleur présente l'anomalie de Vorticité Potentielle à la profondeur située au coeur du tourbillon au bout de (a) 0 jour, (b) 60 jours, (c) 120 jours, et (d) 240 jours. Le tourbillon est anticyclonique, initialement circulaire, et de profil Gaussien sur la verticale ("meddy-like"). Une perturbation aléatoire est superposée au champ de vitesse initiale (elle est visible en (a)). Le tourbillon est initialement instable vis-à-vis d'une perturbation de mode 2. Ensuite, des tourbillons et des filaments de sousmésos-échelle se forment par instabilités secondaires des bras spirales et du bord du tourbillon.

L'augmentation récente des moyens de calcul a permis de mener les études de stabilité à amplitude finie (*i.e.* en utilisant des modèles numériques) à des résolutions horizontales et verticales de plus

en plus importantes. Ainsi, il a été montré que des instabilités secondaires de sousmésos-échelle pouvait avoir lieu au sein des tourbillons instables (Brannigan et al., 2017; Ménesguen et al., 2018). Ces instabilités (barotrope, barocline et/ou symétrique) forment alors des filaments, des structures tourbillonnaires de sousmésos-échelle (Fig. 2.4), et également des variations de densité de petite échelle sur la verticale ("layering") (Hua et al., 2013). Elles sont alors très importantes pour la diffusion de traceurs, et peuvent mener à la dissipation à long terme des tourbillons après leur re-stabilisation non-linéaire. Dans ce manuscrit, c'est cette approche que nous utiliserons pour étudier la stabilité d'un tourbillon isolé (voir section 5.1).

2.1.2 Un cas d'interaction tourbillon-tourbillon : la fusion

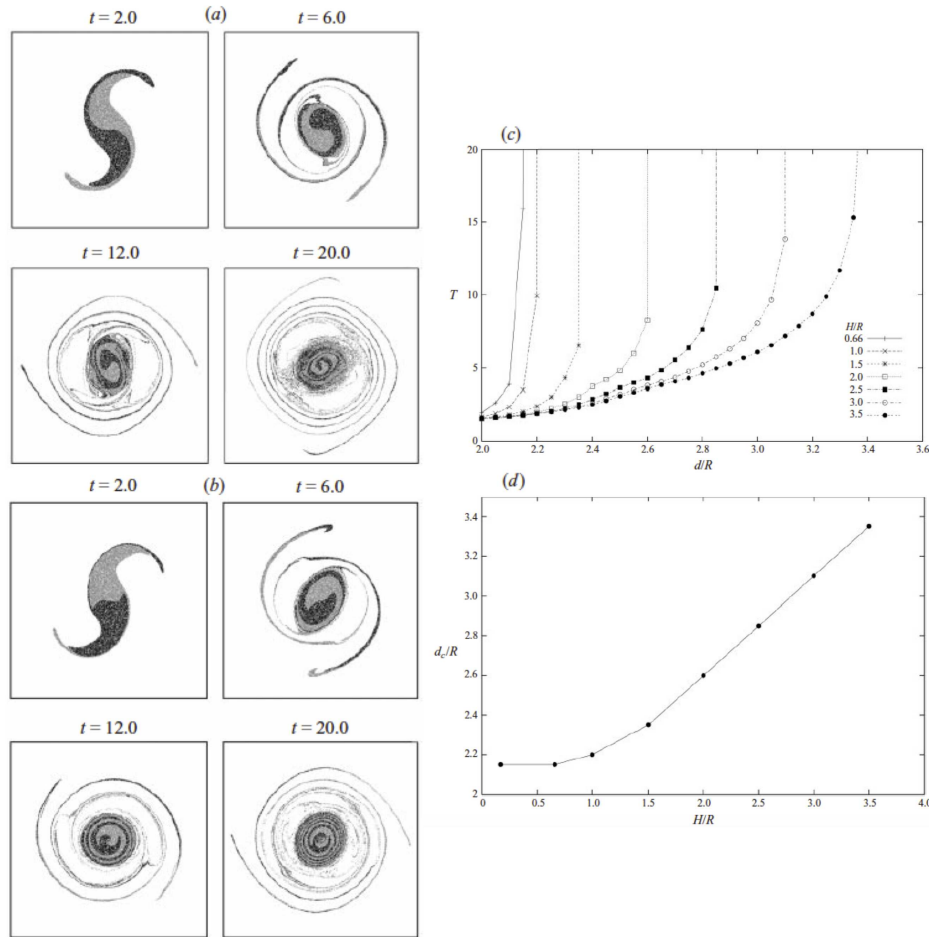


FIGURE 2.5 – Étude de la fusion de deux tourbillons dans un modèle quasi-géostrophique continûment stratifié, d'après von Hardenberg et al. (2000). (a) (resp. (b)) Position de particules initialement placées dans le cœur de deux tourbillons barotropes (resp. de rapport d'aspect $H/R = 1.5$) avant fusion. On peut voir le mélange latéral des masses d'eau induit par la fusion. (c) Temps de fusion en fonction du rapport d'aspect. (d) Distance critique de fusion d_c en fonction du rapport d'aspect H/R . À noter que $H/R = 3$ correspond à des tourbillons d'environ 900 m de hauteur.

Dans l'océan, les tourbillons ne sont généralement pas complètement isolés (Amores et al., 2017), voir *e.g.* Fig. 2.2. Lorsque deux tourbillons de polarités opposées se rencontrent, ils peuvent se coupler, et former un dipôle. Au contraire, s'ils sont de même signe ils peuvent entrer en co-rotation, et s'ils sont assez proche, fusionner (Deem & Zabusky, 1978; Leweke et al., 2016).

La *fusion de tourbillons* est ainsi omniprésente dans l'océan (Cui et al., 2019). Elle est d'une impor-

tance fondamentale pour la distribution et les transferts d'énergie à travers les échelles océaniques (Carnevale et al., 1991; Weiss & McWilliams, 1993; McWilliams et al., 1999; Kraichnan & Montgomery, 1980; Jiménez et al., 1996; Burgess et al., 2017) : la fusion est le processus clef pour la cascade inverse d'énergie (responsable de la présence de structure cohérente de méso-échelle dans l'océan) (McWilliams, 1984). Comme elle fournit un mécanisme de mélange latéral efficace *via* le mélange des masses d'eau en surface et en sub-surface (voir *e.g.* Fig. 2.5(a,b)), la fusion est également importante pour le transfert de chaleur et de traceurs vers les grandes échelles. Ainsi, depuis la première observation *in situ* d'une fusion de tourbillons océaniques dans les années 1980 (Cresswell, 1982), et les intenses débats qui s'en sont directement suivis (Gill & Griffiths, 1981; Nof, 1988; Cushman-Roisin, 1989), de nombreuses études théoriques et numériques ont été menées pour comprendre en détail le processus de fusion.

La plupart de ces travaux portent sur l'étude de la fusion de deux tourbillons isolés, dans laquelle l'influence des tourbillons alentours, des courants de grande échelle, de la topographie et de l'effet β sont négligés (Overman, 1982; Polvani et al., 1989; von Hardenberg et al., 2000; Dritschel, 2002; Reinaud & Dritschel, 2005; Carton et al., 2016; Ciani et al., 2016). Ces études ont montré que les tourbillons ne peuvent fusionner que lorsqu'ils sont suffisamment proche, *i.e.* lorsque leur distance mutuelle d normalisée par leur rayon R

$$d/R < d_c/R, \quad (2.5)$$

où d_c est la distance critique de fusion. L'étude de la fusion de tourbillons repose ainsi en majorité sur la compréhension de la valeur que peut prendre d_c , dépendamment (1) des caractéristiques des tourbillons (Ro , Bu , polarité, profil de vitesse), (2) de la stratification ambiante, et (3) du jeu d'équation considéré (*e.g.* eq. (1.31) ou eq. (1.44)). On peut ainsi trouver dans la littérature des valeurs de d_c variant du simple au double, fonction de ces paramètres. Pour donner un exemple d'étude se reposant sur des paramètres réalistes, on peut citer les études de von Hardenberg et al. (2000) et Dritschel (2002). Dans les deux cas, les auteurs ont considéré des tourbillons baroclines, de rapport d'aspect H/R , dans un modèle quasi-géostrophique continûment stratifié. La distance critique de fusion dépend dans ce cas fortement du rapport d'aspect : des tourbillons "fins" fusionneront plus difficilement que des tourbillons "épais", *i.e.* d_c augmente avec H/R (Fig. 2.5(c,d)). Si on considère l'adimensionnement de von Hardenberg et al. (2000) pour des tourbillons d'environ 900 m de hauteur, $d_c/R \sim 3.1$. Cette valeur est couramment utilisée lorsqu'il s'agit de prendre en compte la fusion de tourbillon dans la paramétrisation de modèles ou de programmes d'analyse de dynamique de tourbillons, *e.g.* Le Vu et al. (2018).

De nombreux efforts ont été faits pour étudier la fusion dans des conditions moins strictes que celle de deux tourbillons isolés (Carton, 2001; Perrot & Carton, 2010; Rodríguez-Marroyo et al., 2011). Malheureusement, le nombre de paramètres et la complexité du système dynamique résultant rend

cette tâche compliquée et fastidieuse. On peut aussi mentionner qu'à l'exception d'une étude dans un contexte 2D et très idéalisé (Bertrand & Carton, 1993), aucune étude n'a à ce jour pris en compte l'effet β dans le processus de fusion de tourbillons. Enfin, le manque d'observations globales et *in situ* du processus de fusion n'ont pas encore permis de tirer de conclusion sur la dynamique de fusion de tourbillons telle qu'elle apparaît réellement dans l'océan global. Le chapitre 6 de ce manuscrit traite de la fusion de tourbillons dans ce contexte, mêlé à celui de la mer d'Arabie, et vise à apporter des réponses supplémentaires à ce problème de fusion de tourbillons.

2.1.3 L'interaction des tourbillons avec les bords ouest

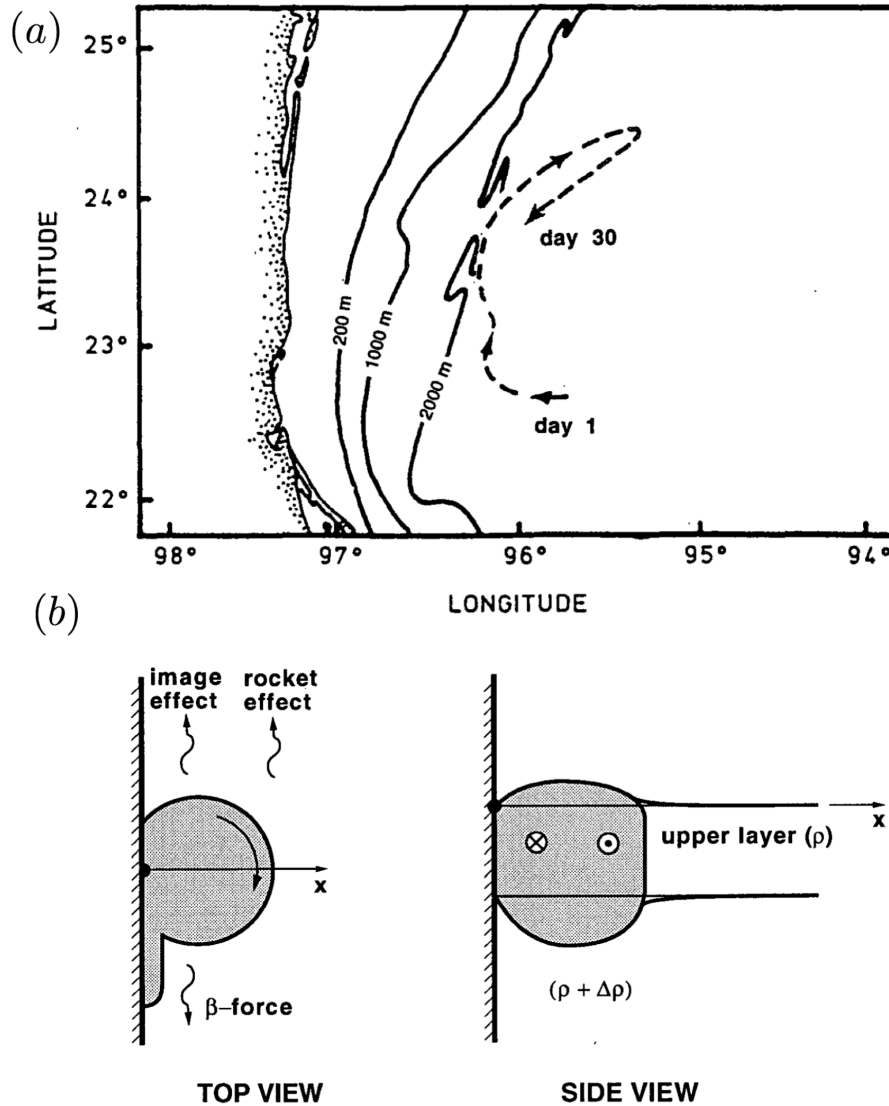


FIGURE 2.6 – D'après Shi & Nof (1994). (a) Observation du déplacement d'un anneau du Loop Current le long du bord ouest du golfe du Mexique en 1988. (b) Vu de dessus (gauche) et de côté (droite) d'un "wodon" : un tourbillon contraint le long d'un mur par l'effet β qui se déplace de manière constante dans la direction méridienne. Les trois forces en jeu sont représentées schématiquement. Dans le cas d'un anticyclone, la résultante des forces est orientée vers le nord.

Les tourbillons océaniques migrent continuellement vers l'ouest, influencés par l'effet β (Chelton et al., 2011b). Au terme de cette migration, ils interagissent inévitablement avec la topographie. Dans chaque bassin océanique, les bords ouest présentent ainsi des valeurs d'énergie cinétique turbulente importantes (Scharffenberg & Stammer, 2010), du fait des nombreux tourbillons qui s'y trouvent. Il existe une grande diversité de système de bord ouest : ils ont des bathymétries, des traits de côte différents, ainsi que des forçages et des dynamiques résultantes différents (*e.g.* présence de courants côtiers, d'un talus continental, de forçages atmosphériques locaux ou de grande échelle). Motivé par l'observation de la dérive d'anneaux du Gulf Stream et d'anneaux du Loop Current le long des frontières ouest des bassins (Shi & Nof, 1994), voir *e.g.* Fig. 2.6(a), l'interaction entre les tourbillons de méso-échelle et les bords ouest est un problème étudié à l'aide de simulations numériques depuis les années 1990. La pente continentale ayant généralement une faible extension horizontale $\mathcal{O}(10)$ km, en comparaison au rayon des tourbillons de méso-échelle $\mathcal{O}(50 - 100)$ km, le problème peut naturellement être simplifié en l'étude de l'interaction de tourbillons entraînés par effet β contre un mur méridien sur le bord ouest. Pour ces études, les effets frictionnels le long de la côte sont généralement négligés, car ils reposent sur des paramétrisations que l'on peut difficilement valider par l'observation.

Ce problème a été étudié dans des simulations très idéalisées (le problème tourbillon-mur sur plan- β , voir Shi & Nof (1993), Shi & Nof (1994), Sansón et al. (1998), Nof (1999), et Table 1 dans Shi & Nof (1994) qui résume les études plus anciennes). Des travaux ont également simulé des cas plus réalistes, inscrits dans le contexte de l'interaction entre les anneaux du Loop Current et le bord ouest du golfe du Mexique (Smith, 1986; Sutyrin et al., 2003; Frolov et al., 2004). Malgré les différences entre les hypothèses faites par ces auteurs, tous s'accordent sur le fait que lorsqu'un tourbillon rencontre un mur, celui-ci migre dans la direction méridienne sous l'influence de trois effets (Fig. 2.6(b)) : (1) l'effet image (l'advection du vortex image créé par le mur), (2) l'effet β (la différence d'intensité de la force de Coriolis entre la partie nord et sud du tourbillon), et (3) l'effet "rocket" (le tourbillon étant poussé vers le mur continuellement, il perd de la masse là où le courant du tourbillon converge vers le mur; il y a formation d'un petit jet, et propulsion du tourbillon dans le sens opposé, de manière analogue à une fusée, "rocket"). La résultante de ces trois forces est orientée vers le sud pour les cyclones, et le nord pour les anticyclones Shi & Nof (1994). Le système tourbillon-mur dérivant ainsi de manière stable est appelé "wodon" (contraction de "wall" et "modon"). Des études plus récentes ont montré dans des contextes différents que les courants anticycloniques peuvent générer des processus dissipatifs (et non visqueux) lors d'interactions entre le courant moyen et des ondes de gravité piégées à la côte (Dewar & Hogg, 2010; Gula & Zeitlin, 2010; Gula et al., 2010; Hogg et al., 2011; Deremble et al., 2016, 2017). En revanche, ces études n'ont pas été directement mises en relation avec la dérive des tourbillons sur les bords ouest. C'est dans ce contexte, mêlé à celui de la mer d'Arabie, que le travail présenté dans la

section 5.2.2 a été réalisé. Il vise à améliorer notre compréhension des interactions entre les tourbillons et les bords ouest à l'aide d'une approche 3D similaire aux études récentes mentionnées plus haut.

2.1.4 Par delà la méso-échelle : les tourbillons de sousméso-échelle

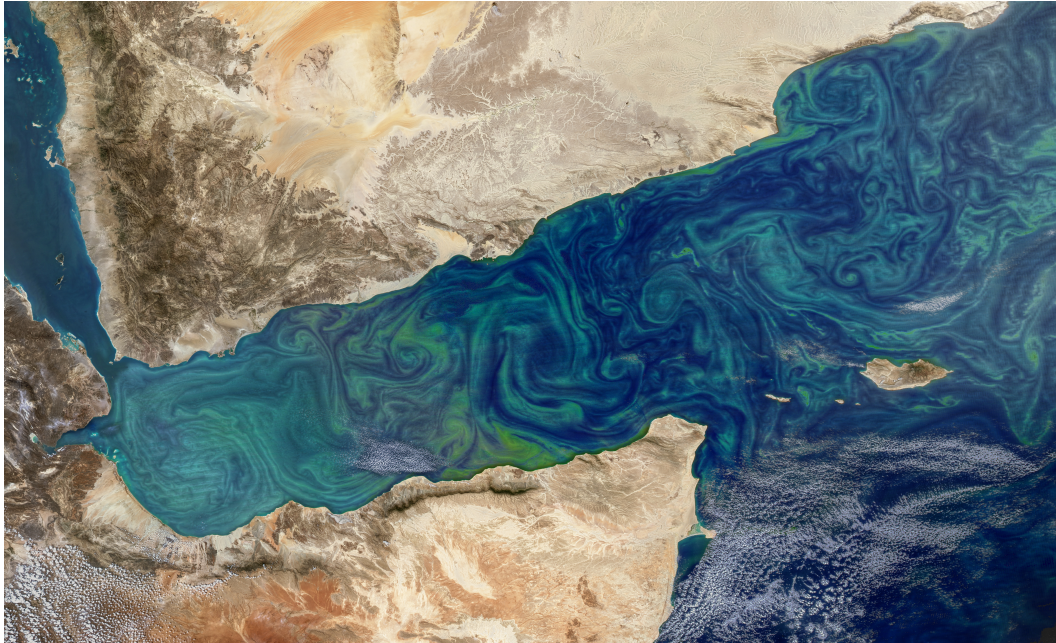


FIGURE 2.7 – Image de couleur de l'eau du golfe d'Aden (mer d'Arabie), prise par l'appareil MODIS (satellite Aqua) le 12/02/2018. La résolution est de 250 m horizontalement. On peut y voir la chlorophylle advectée par des filaments et des tourbillons de sousméso-échelle intensifiés en surface. Une description détaillée peut être trouvée dans Lévy et al. (2018). On notera l'évolution chronologique des moyens d'observations, et des tailles de structures tourbillonnaires observées entre Fig. 2.1 en 1950, Fig. 2.2 au début des années 2000, et Fig. 2.7 en 2018. Crédit : NASA Earth Observatory.

À sousméso-échelle, des structures cohérentes tourbillonnaires sont également présentes. Les phénomènes décrits plus hauts apparaissent également à ces échelles. Il faut cependant considérer des tourbillons dans un régime d'écoulement différent : (1) à grand nombre de Burger $Bu > 1$, (2) à grand nombre de Rossby $Ro > 1$, et ainsi (3) à l'équilibre cyclo-géostrophique (eq. (1.30)). De par leur faible extension horizontale, les tourbillons de sousméso-échelle ne peuvent pas actuellement être détectés par mesures altimétriques : il existe peu de mesures de la dynamique des tourbillons de sousméso-échelle, et en particulier, aucune mesure globale (instantanée ou non). C'est pourquoi, il existe encore peu d'études de processus orientées sur la dynamique des tourbillons de sousméso-échelle, et que les études mentionnées précédemment sont dans la plupart des cas mises en relation avec la dynamique de méso-échelle.

Les tourbillons de sousméso-échelle peuvent être séparés en deux classes. D'une part les tourbillons

intensifiés en surface : des mesures satellites ponctuelles de température et de couleur de l'eau (Fig. 2.7) permettent de reconstruire partiellement leur dynamique, et ainsi de décrire leur structure horizontale et de déployer des moyens d'observation *in situ* (Chavanne & Klein, 2010; Lévy et al., 2012; Buckingham et al., 2017). Les structures de sousmésos-échelle de surface ont ainsi été identifiées comme jouant un rôle important pour la production primaire (Lévy et al., 2018) et la re-stratification des couches superficielles de l'océan (Boccaletti et al., 2007).

D'autre part, les tourbillons de sousmésos-échelle intensifiés en sub-surface, généralement appelés Submesoscale Coherent Vortices (SCVs; McWilliams (1985)), ou intrathermocline eddies (ITEs; Dugan et al. (1982)) : ils n'ont souvent aucune signature à la surface (Ciani et al., 2015). Les mesures de telles structures sont donc très éparées, et dans beaucoup de cas, dues à la chance, voir *e.g.* Kostianoy & Belkin (1989); Lukas & Santiago-Mandujano (2001); L'Hégaret et al. (2016); Bosse et al. (2016, 2017); Meunier et al. (2018b); Gula et al. (2019). Un fait notable de ces structures est qu'elles apparaissent comme étant majoritairement anticycloniques. La raison pour cette observation est un sujet de recherche actuel, et une piste repose notamment sur l'asymétrie cyclone/anticyclone des propriétés de stabilité des tourbillons isolés : les anticyclones apparaissent plus stable que les cyclones (Stegner & Dritschel, 2000; Lazar et al., 2013b,a; Mahdinia et al., 2017).

Les tourbillons de sousmésos-échelles peuvent être générés de multiples façons : interaction d'un courant de bord avec la bathymétrie (D'Asaro, 1988), convection hivernale (Bosse et al., 2016), ou instabilité naturelle d'un courant de sousmésos-échelle (Gula et al., 2015; L'Hégaret et al., 2016). Dans la suite de ce manuscrit, nous nous intéresserons à la production de tourbillons de sousmésos-échelle, par instabilité secondaire d'un tourbillon de méso-échelle (section 5.1), et par interaction de tourbillons de méso-échelle le long d'un bord ouest (section 5.2.2). Nous reporterons également l'observation d'une structure profonde tourbillonnaire de sousmésos-échelle en mer d'Arabie, et discuterons les possibles mécanismes responsables de sa génération (section 5.3) .

2.2 La mer d'Arabie : un lieu dominé par la dynamique tourbillonnaire

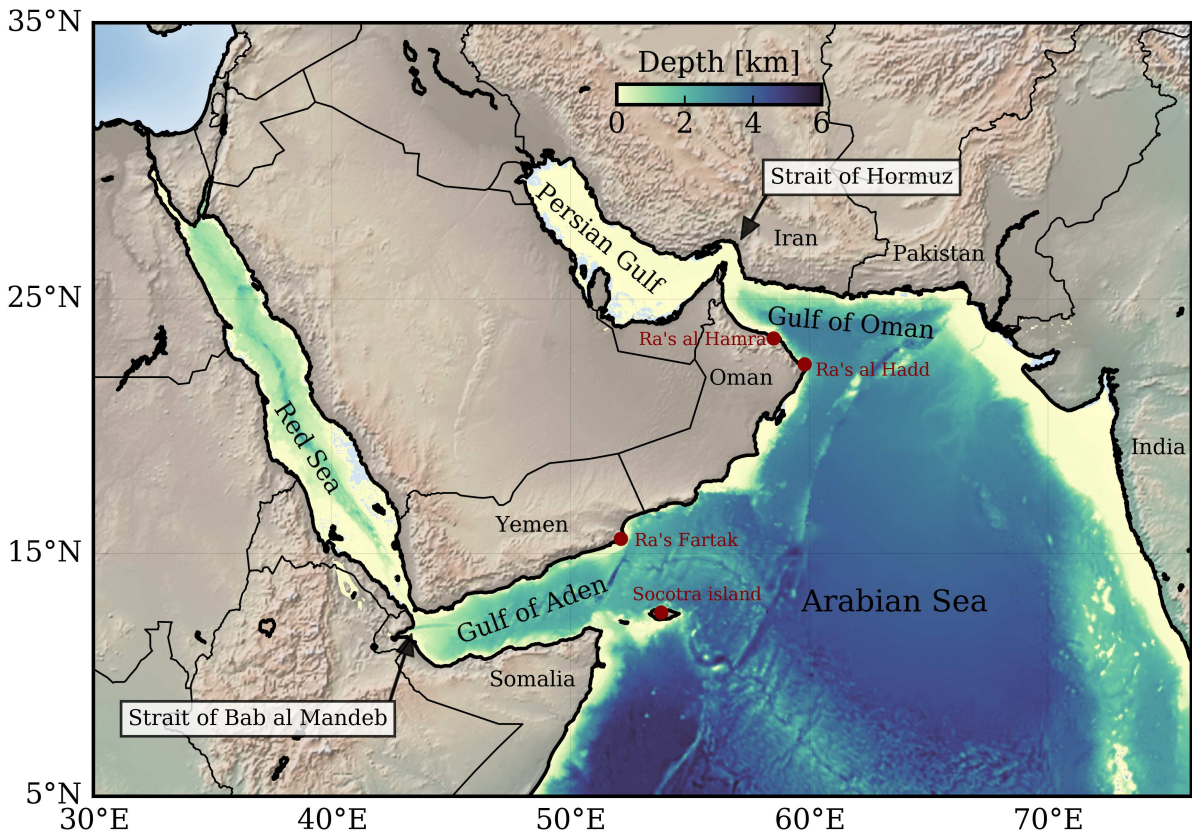


FIGURE 2.8 – Carte bathymétrique de la mer d'Arabie, indiquant les principaux lieux d'intérêts mis en avant dans ce manuscrit.

Nous avons vu que les tourbillons sont omniprésents dans l'océan, aussi bien à méso-échelle qu'à sous-méso-échelle, et ont une importance majeure dans sa dynamique. Ils ont une durée de vie limitée par leur stabilité, qui dépend de leur structure horizontale et verticale. Lorsqu'ils interagissent avec leur environnement, leur comportement peut être complexe. Il est essentiel d'étudier de manière fondamentale ce comportement, afin de comprendre les mouvements de masses induits par les structures tourbillonnaires dans l'océan.

Dans certaines régions, la dynamique tourbillonnaire domine la circulation océanique. C'est le cas de la mer d'Arabie, où le transport des propriétés de la colonne d'eau est dominé par le transport

induit par les tourbillons (Fischer et al., 2002). Comprendre la dynamique des structures de méso et sou-méso-échelle dans cette région est donc d'une importance fondamentale. Ce manuscrit traite de cette problématique. Nous présentons dans cette partie le contexte de la mer d'Arabie, afin d'introduire les concepts fondamentaux à la compréhension des études réalisées.

2.2.1 Généralités

La partie nord-ouest de l'Océan Indien (Fig. 2.8), délimitée au nord par la péninsule Arabique (Oman et Yémen), l'Iran et le Pakistan, au sud par l'équateur, à l'est par la Somalie, et à l'ouest par l'Inde, est communément appelée *mer d'Arabie* (بحر العرب). Du fait de l'activité géologique intense dans cette région, la bathymétrie en mer d'Arabie est chahutée. La profondeur moyenne est d'environ 4000 m, et trois principales anomalies topographiques sont présentes à l'intersection des plaques tectoniques : la dorsale de Carlsberg à l'ouest, atteignant 2000 m de profondeur, la zone de fracture d'Owen au nord-ouest, et une zone de convergence au nord, générant d'important monts sous-marins atteignant 1000 m de profondeur. Également, un important talus continental est présent le long de la côte omanaise, créant ainsi une région d'eaux peu profondes (< 1000 m) sur une extension horizontale de plusieurs centaines de kilomètres. À l'ouest, le golfe d'Aden, dont la profondeur évolue d'est en ouest de 3000 m à quelques centaines de mètres au niveau du détroit de Bab-el-Mandeb, constitue la connexion entre la mer d'Arabie et la Mer Rouge. De manière similaire, au nord, le golfe d'Oman, dont la frontière ouest est le détroit d'Ormuz, connecte la mer d'Arabie et le golfe Persique.

Les masses d'eau

Dans les deux mers marginales susmentionnées, la Mer Rouge et Le golfe Persique, des masses d'eau denses sont formées. Elles se propagent ensuite en mer d'Arabie *via* le Détroit de Bab-el-Mandeb et le détroit d'Ormuz, et participent fortement aux valeurs de température et de salinité climatologique en profondeur, dans le nord-ouest de l'Océan Indien.

Premièrement, la *Red Sea Water*, ou RSW, est formée au nord de la Mer Rouge, principalement par convection hivernale. Elle s'écoule ensuite dans le golfe d'Aden par le détroit de Bab-el-Mandeb (Sofianos & Johns, 2003), puis se stabilise entre les isopycnes 27 et 27.5 kg m^{-3} , à une profondeur de 500-700 m (Bower et al., 2000). Cette masse d'eau ne s'échappe que très peu du golfe d'Aden (Bower, 2002). En revanche, sa signature peut tout de même être trouvée le long des côtes omanaises (Carton et al., 2012), dans le bassin de Somalie (Warren et al., 1966), et jusqu'à 25°S (Quadfasel & Schott, 1982).

Deuxièmement, la *Persian Gulf Water*, ou PGW, est formée dans le golfe Persique par évaporation le long de la frontière ouest (Pous et al., 2015). Elle s'écoule à travers le Détroit d'Ormuz, et se stabilise

entre les isopycnes 26 et 27 kg m⁻³, soit entre 200 et 300 m de profondeur (Bower et al., 2000). Bien qu'elle soit principalement présente dans le golfe d'Oman, sa signature peut être trouvée le long des côtes omanaises (Carton et al., 2012), et plus au sud, jusqu'à 5-10°N (Quadfasel & Schott, 1982).

D'autres masses d'eau sont présentes en mer d'Arabie (Kumar & Mathew, 1997; Talley, 2011; L'Hégaret et al., 2018). Leur présence dépend de la période de l'année, et varie géographiquement. À la surface, des eaux très peu salées en provenance du golfe du Bengale, la *Bay of Bengal Water* (BBW), se propagent dans l'est de la mer d'Arabie en hiver, *via* le courant de mousson du nord-est. En sub-surface, on trouve principalement des eaux peu salées, l'*Indian Ocean Central Water* (IOCW), et des eaux salées, l'*Arabian Sea High Salinity Water* (ASHSW). Cette dernière est formée par convection hivernale au nord du bassin, et se propage ensuite au sud en sub-surface. Au fond, de l'*Indian Ocean Deep Water* (IODW) et de l'*Antarctic Bottom Water* (AABW) peuvent être trouvées. Ces masses d'eau profondes ont peu d'interactions avec la dynamique de méso-échelle à laquelle nous nous intéressons ici.

La circulation océanique en mer d'Arabie

Contrairement à l'Atlantique et au Pacifique, l'Océan Indien possède une frontière nord à moyenne latitude ($\sim 25^\circ\text{N}$). Cette propriété rend la dynamique atmosphérique au dessus de l'Océan Indien, et particulièrement de la mer d'Arabie unique. En effet, les vents de grande échelle s'inversent entre l'été et l'hiver, on parle du régime des vents de *mousson*. Une brève explication à ce phénomène est la suivante. La température de l'océan varie peu au cours de l'année. Le continent quant à lui est chaud en été et froid en hiver. La différence de pression entre les masses d'air océaniques et continentales génère ainsi des vents en direction du continent en été et de l'océan en hiver (Talley, 2011).

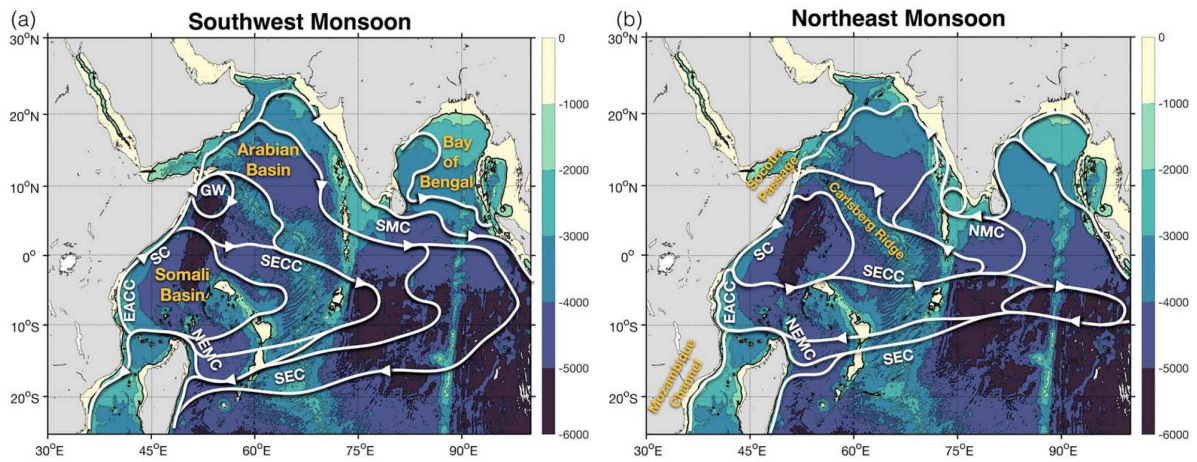


FIGURE 2.9 – Lignes de courant schématiques de la circulation moyenne de surface durant la mousson d'été (a) et la mousson d'hiver (b), d'après L'Hégaret et al. (2018). Les courants sont dérivés d'une climatologie mensuelle des courants, obtenue à l'aide de bouées dérivantes à 15 m de profondeur (Laurindo et al., 2017).

Plus précisément, deux régimes de vent différents peuvent être distingués (Findlater, 1969). D'une part, la mousson d'été (ou mousson de sud-ouest), caractérisée par des vents soufflant du sud-ouest vers le nord-est, principalement concentrés le long des côtes somaliennes, sous la forme du Jet Somalien (ou Jet de Findlater). C'est alors la saison humide, des pluies, sur le sous-continent indien et l'Asie du sud-est. D'autre part, la mousson d'hiver (ou mousson de nord-est), durant laquelle les vents soufflent de façon opposée, du nord-est vers le sud-ouest. Ces vents sont moins intenses que ceux de mousson d'été. Les périodes de transition entre la mousson d'été et la mousson d'hiver, les inter-moussons de printemps (Avril-Juin) et d'automne (Octobre-Novembre), sont rapides (4-6 semaines), et caractérisées par des vents très faibles au dessus de la mer d'Arabie.

De ce forçage atmosphérique unique, résulte une circulation à l'échelle du bassin changeant de direction selon la saison (Lee et al., 2000; L'Hégaret et al., 2018). En été, la circulation est anticyclonique (Fig. 2.9(a)). Le courant de Somalie (SC) s'écoule vers le nord, prolongé le long des côtes omanaise par un courant côtier. Le courant de mousson du sud-ouest (SMC) le long des côtes indiennes et le courant nord équatorial au sud ferment cette boucle. La circulation en hiver est cyclonique (Fig. 2.9(b)) avec des courants d'est ramenant des eaux peu salées du golfe du Bengale, coulant ensuite vers le nord, sous la forme du courant de mousson du nord-est (NMC), puis du nord-est vers le sud-ouest le long des côtes omanaises et somaliennes. Au sud de la mer d'Arabie, le contre-courant Sud-équatorial (SECC) s'écoulant d'ouest en est ferme cette boucle. Ainsi, de nombreux courants côtiers sont présents le long

des côtes omanaise et somaliennes. Ils changent de direction selon la saison. Ces courants sont la source des nombreux tourbillons de méso-échelle observés en mer d'Arabie.

2.2.2 La dynamique tourbillonnaire en mer d'Arabie

Dans la majorité des bassins océaniques, de nombreuses échelles cohabitent, de l'échelle du bassin à la sous-méso-échelle, chacune jouant un rôle particulier dans la régulation du système océanique. Comme exemple, on peut donner l'Atlantique Nord, où la circulation grande échelle forcées par le vent et les tourbillons de méso-échelle jouent un rôle équivalent dans le transport méridien de chaleur (Bryden & Hall, 1980; Sun et al., 2019).

En mer d'Arabie, la circulation grande échelle s'inverse selon la saison, et les courants côtiers sont instables. Ainsi, en moyenne, une circulation grande échelle est bien présente (celle présentée sur la Fig. 2.9), mais si on considère un instant donné, la mer d'Arabie est remplie de tourbillons de méso-échelle, avec entre 40 et 50 structures chaque jour (Trott et al., 2018). Contrairement à d'autres régions, ce sont alors les tourbillons qui dominent la dynamique, et déterminent le budget de chaleur (Fischer et al., 2002), la répartition des propriétés chimiques de la colonne d'eau (Queste et al., 2018) et des masses d'eau salées en profondeur (Bower, 2002).

À méso-échelle

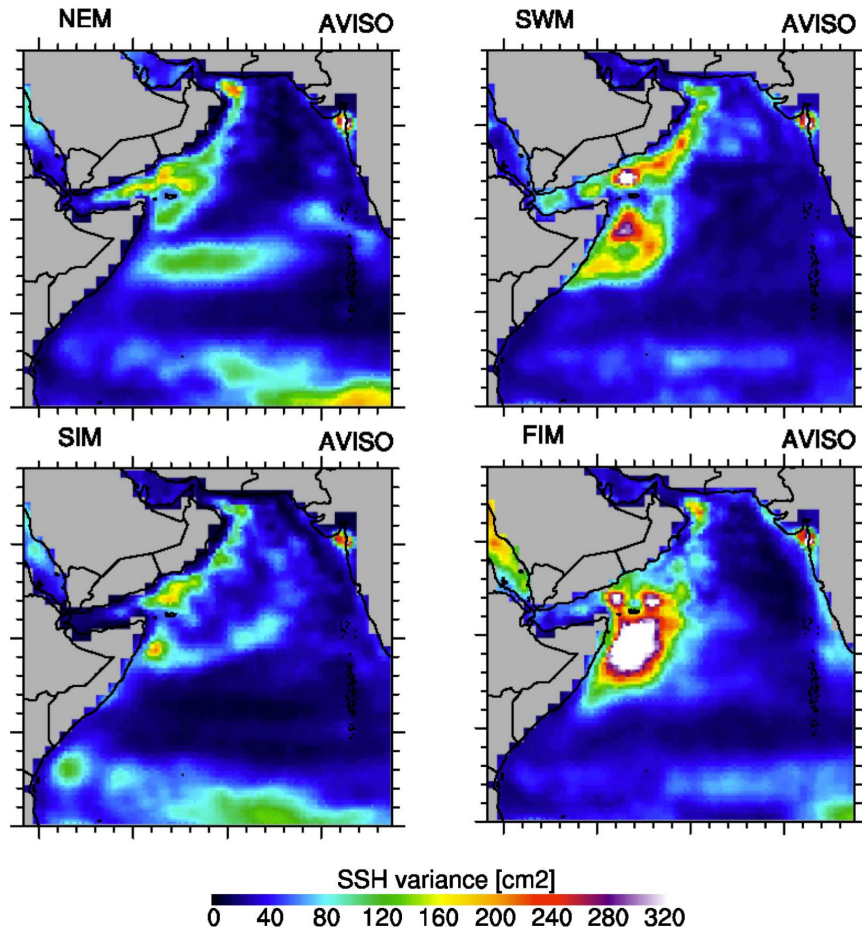


FIGURE 2.10 – Variance de SSH à partir de 10 ans de mesures altimétriques, pendant la mousson d’hiver (NEM), l’inter-mousson de printemps (SIM), la mousson d’été (SWM), et l’inter-mousson d’automne (FIM), d’après Vic et al. (2014). On peut y voir la prédominance de la dynamique tourbillonnaire sur le bord ouest du bassin et dans les golfes, en particulier durant la mousson d’été. La signature importante de variance dans le bassin de Somalie durant l’inter-mousson d’automne reflète la décroissance du Great Whirl.

La plupart des tourbillons de méso-échelle en mer d’Arabie peut être trouvée le long des côtes omanaise et yéménite, et dans le golfe d’Oman (Fig. 2.10). Ils ont des rayons compris entre 50 et 100 kilomètres, et génèrent des anomalies de SSH de 8-13 cm (Trott et al., 2018). Les mécanismes responsables de leur génération ne sont pas complètement compris, et restent sujets à débat. Une partie des tourbillons est générée par instabilité des courants côtiers, à la mise en place de la circulation de mousson.

Une autre partie est générée le long des côtes indiennes, puis propagée vers l'ouest sous forme d'ondes de Rossby. La propagation des ondes de Rossby vers l'ouest renforce alors les tourbillons présents sur le bord ouest du bassin (L'Hégaret et al., 2015; Trott et al., 2018). Un exemple de structure récurrente dans cette région est le dipôle de Ra's al Hadd, présent durant la mousson d'été entre l'entrée du golfe d'Oman et le sud des côtes omanaises. Le jet formé par ce dipôle est la structure la plus intense du nord de la mer d'Arabie, avec des courants de surface atteignant $U > 1 \text{ m s}^{-1}$, et un transport net d'ouest en est de 2-8 Sv (Flagg & Kim, 1998). Les tourbillons du nord de la mer d'Arabie sont déterminants pour l'export de PGW hors du golfe d'Oman (Carton et al., 2012; Vic et al., 2014; L'Hégaret et al., 2015), et ainsi pour l'augmentation de la salinité climatologique en profondeur entre les isopycnes 26 et 27 kg m^{-3} . Par exemple, durant l'inter-mousson de printemps, un tourbillon récurrent est formé proche du cap de Ra's al Hamra. Ce dernier advecte les eaux salées en profondeur des côtes omanaises jusqu'aux côtes iraniennes, et participe ainsi à la dilution de sel dans l'intégralité du golfe d'Oman. De manière similaire, lorsque la PGW a voyagé jusque dans l'ouvert du golfe d'Oman, le jet de Ra's al Hadd propulse ces eaux salées vers l'est, participant à la présence de PGW dans les valeurs climatologiques du nord de la mer d'Arabie. Il arrive ensuite que de la PGW expulsée au large des côtes Pakistanaïses de cette manière recircule au sud-ouest sous l'influence des tourbillons présents dans la région. De plus, il a été montré que l'advection générée par les tourbillons du golfe d'Oman contrôle les zones de dénitrification et de désoxygénation, avec les impacts sur la production primaire qui s'en suivent (Queste et al., 2018).

En mer d'Arabie, les tourbillons de méso-échelle les plus gros et intenses sont trouvés dans le bassin de Somalie (Trott et al., 2018). En particulier, durant la mousson d'été un anticyclone de grande taille est généré au sud de l'île de Socotra, le Great Whirl (GW). Ce dernier se développe dans la continuité du courant de Somalie aux alentours du mois de Juin. A cette époque son rayon est d'environ 350 km et atteint une profondeur de 200 m (Beal & Donohue, 2013). Ensuite, il se renforce et s'approfondit, sous l'influence de la circulation atmosphérique anticyclonique (Vic et al., 2014). À la fin du mois de septembre, où il est le plus intense, son rayon est d'environ 550 km, et sa profondeur de 1000 m (Beal & Donohue, 2013). Il induit alors un transport rotationnel de 60 Sv. Il disparaît ensuite durant l'inter-mousson d'automne, lorsque la circulation régionale change d'orientation (Vic et al., 2014). Durant la mousson d'hiver, il est courant d'observer en lieu et place du Great Whirl un cyclone de grande taille, moins intense que le Great Whirl, contraint le long de la côte.

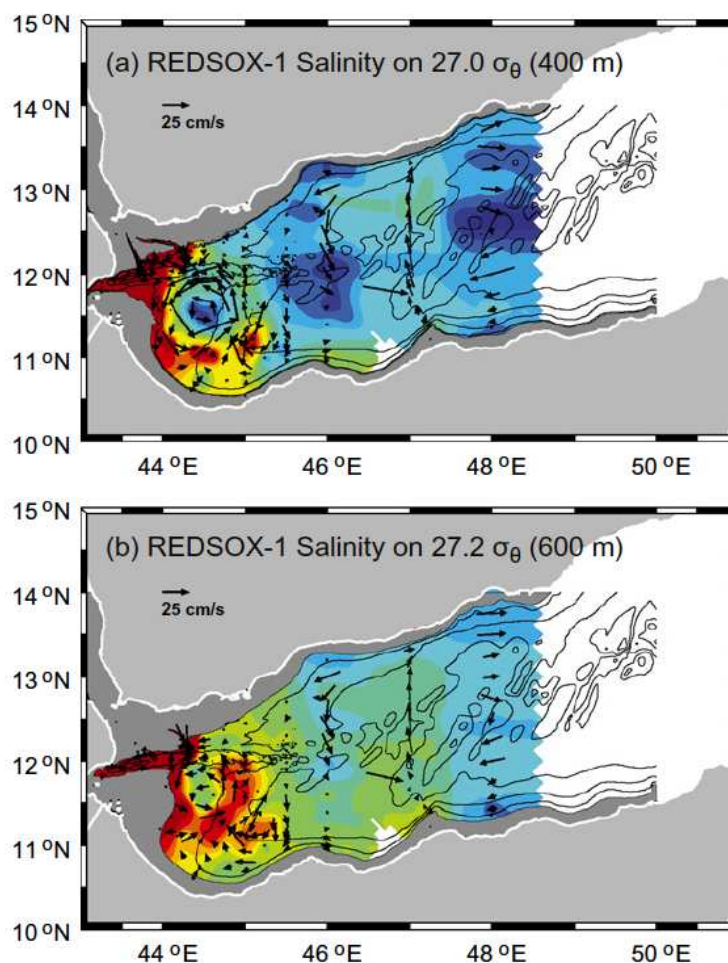


FIGURE 2.11 – Courants et salinité à 400 m (a) et 600 m (b) de profondeur dans le golfe d'Aden, d'après les données de la campagne REDSOX-1, comme présenté par Bower & Furey (2012); rouge foncé= 37 psu, bleu foncé=35.5 psu. On peut voir l'advection de la langue d'eau salée de RSW par un tourbillon de méso-échelle cyclonique. Ces observations *in situ* illustrent l'importance des tourbillons de méso-échelle en mer d'Arabie pour la répartition des masses d'eau salées en profondeur.

De nombreux tourbillons sont également présents à l'entrée et dans le golfe d'Aden. Les tourbillons récurrents de cette région sont généralement anticycloniques : le Lee Eddy et le Summer Eddy, qui se forment au début de la mousson d'été, restent stationnaires au nord de l'île de Socotra ou voyagent dans le golfe d'Aden (Bower & Furey, 2012); la gyre de Socotra, située à l'est ou au sud de l'île de Socotra en Septembre (Simmons et al., 1988); les anneaux du courant de Somalie, observés en Octobre (Fratantoni et al., 2006); et le Gulf of Aden Eddy, durant l'inter-mousson de printemps (Prasad et al., 2001). La présence de tourbillons cycloniques a également été mise en évidence (Bower, 2002; Al Saa-

fani et al., 2007; Bower & Furey, 2012). Leur présence est liée à la propagation dans le golfe d'Aden d'ondes de Rossby planétaires, dont le pôle négatif (d'après la SSH), constitue un tourbillon cyclonique. Également, ces cyclones naissent de l'interaction entre des anticyclones se propageant dans le golfe qui interagissent avec la côte et la bathymétrie (Morvan et al., 2020). Ces tourbillons ont généralement des durées de vie beaucoup plus faibles que les anticyclones dans cette région (~ 100 jours pour les anticyclones contre ~ 40 jours pour les cyclones). Ces tourbillons de méso-échelles (cycloniques et anticycloniques), de par leur profondeur d'intensification (~ 1000 m), ont un impact très important sur la propagation de la RSW (Bower, 2002; Ilıcak et al., 2011; Bower & Furey, 2012). En effet, lorsque les eaux salées s'écoulent du détroit de Bab-el-Mandeb, les tourbillons advectent et étirent la langue d'eau salée, voir *e.g.* Fig. 2.11. Ils sont alors responsables de la dilution de sel en profondeur à l'échelle du golfe, mais également des exports intermittents dans l'ouvert de la mer d'Arabie et dans le bassin de Somalie (Bower & Furey, 2012).

Enfin, bien que plus épars, des tourbillons sont présents au centre du bassin. Ces tourbillons ne sont pas stationnaires, et se propagent généralement vers l'ouest, advectés par les ondes de Rossby planétaires. Ces tourbillons sont peu connus et étudiés. Il est à noter qu'une partie de ces tourbillons, sont ceux décrits plus haut, avant qu'ils n'aient rejoint le bord ouest du bassin. Ils participent ainsi activement à l'activité tourbillonnaire en mer d'Arabie, en générant des courants profonds au centre du bassin, et en renforçant la dynamique le long du bord ouest et dans les golfes, à la fin de leurs voyages.

À sousméso-échelle

En mer d'Arabie, la dynamique tourbillonnaire de sousméso-échelle apparaît aussi comme étant omniprésente à la surface (voir *e.g.* Fig. 2.7), et en profondeur, où elle est primordiale pour la diffusion des masses d'eau salées.

En particulier, dans le golfe d'Oman, des tourbillons anticycloniques profonds de sousméso-échelles ont été observés transportant des eaux salées provenant de l'ouest du golfe (L'Hégaret et al., 2016). Ces lentilles, généralement appelés *Peddies* (la contraction de Persian Gulf et Eddies, de manière similaire aux *Meddies*), se forment par déstabilisation du courant profond de densité (L'Hégaret et al., 2016), ou par interaction des courants de méso-échelle avec la côte et la bathymétrie (Vic et al., 2015). Une fois formés, ils sont advectés par les tourbillons de méso-échelle et peuvent vivre plusieurs mois en restant cohérent (McWilliams, 1985), participant ainsi à l'export de PGW en mer d'Arabie.

De manière similaire, des tourbillons anticycloniques profonds de sousméso-échelle ont été observés aux alentours et dans le golfe d'Aden, des *Reddies* (Shapiro & Meschanov, 1991; Meschanov & Shapiro, 1998). Le mécanisme de génération de ces structures est encore discuté, mais il semblerait

qu'il soit similaire à celui des Peddies. Il est à noter, qu'aucune observation de tourbillon cycloniques profonds de sousmésos-échelle n'a jamais été réalisée en mer d'Arabie.

2.2.3 Plus généralement, en mer d'Arabie...

Outre ces questions d'intérêt scientifiques, la mer d'Arabie est un lieu stratégique, et d'intérêt économique pour le Moyen-Orient. En effet, les pays du Golfe (Arabie Saoudite, Émirats Arabes Unis, Irak, Iran, Koweït, Oman, Qatar) possèdent la moitié des ressources d'hydrocarbures mondiales. L'exportation au niveau mondial de ces ressources fait ainsi du golfe d'Oman en particulier, l'artère la plus importante en matière de transport d'hydrocarbures, avec environ 25% du trafic pétrolier mondial qui circule par le détroit d'Ormuz. Couplé aux problématiques de piraterie au large du Yémen et de la Somalie, la mer d'Arabie est donc une zone d'intérêt militaire prioritaire, où la circulation des bâtiments militaires est un enjeu stratégique pour la flotte. Les tourbillons océaniques, omniprésents dans cette région, impactent les propriétés dynamiques et acoustiques du milieu. Comprendre leur dynamique est donc primordial. D'une part pour aider à la navigation des navires de commerce. D'autre part pour améliorer la compréhension du milieu océanique dans lequel les bâtiments militaires opèrent pour la protection et la surveillance de la mer d'Arabie.

En dehors de ces dynamiques géopolitiques et militaires grande échelle, les habitants des côtes de la mer d'Arabie ont culturellement toujours subvenu à leurs besoins sans avoir recours aux grands groupes pétroliers qui exploitent les gisements d'hydrocarbures en mer et dans les terres. En particulier, grâce à l'abondance des ressources maritimes dont dispose cette région, il est estimé que la pêche est l'activité principale de 120 millions de personnes vivant sur les côtes de la mer d'Arabie. Les tourbillons transportent horizontalement et verticalement de l'oxygène et des nutriments (Queste et al., 2018), modulent les blooms de plancton (Tollefson, 2018) et la génération d'algues vertes (do Rosario Gomes et al., 2014). Ils interagissent également avec les upwellings côtiers présents au sud du sultanat d'Oman (Vic et al., 2017), qui induisent des vitesses verticales importantes au printemps et en été. Ainsi, ils affectent fortement la production primaire et les activités biologiques dans la région. Comprendre leur dynamique et leurs propriétés intrinsèques permet alors de donner des clefs physiques à la compréhension des processus biologiques à l'oeuvre dans ces régions où la pêche est importante pour la population.



FIGURE 2.12 – Vue depuis le petit port de pêche de Sifat al Sheikh (Oman), 50 km à l'est de Ra's al Hamra en Mai 2019. Au large, l'upwelling Omanais (Fischer et al., 2002) et le dipôle de Ra's al Hadd modulent les activités biologiques (Photo personnelle réalisée au cours de la campagne PHYSINDIEN 2019).

2.3 Les questions posées dans ce manuscrit

Comme nous avons vu dans la section 2.2, les tourbillons sont omniprésents en mer d'Arabie, et sont d'une importance particulière pour la dynamique et les propriétés de la colonne d'eau dans cette région. Dans ce manuscrit, nous nous intéressons aux tourbillons en mer d'Arabie par le prisme des précédentes études ayant analysé la dynamique des tourbillons de manière fondamentale. Nous nous intéressons aux processus en jeu à méso et sousméso-échelle dans lesquels les tourbillons de mer d'Arabie sont impliqués. Les différents processus auxquels nous nous intéressons sont résumés dans la Fig. 2.13.

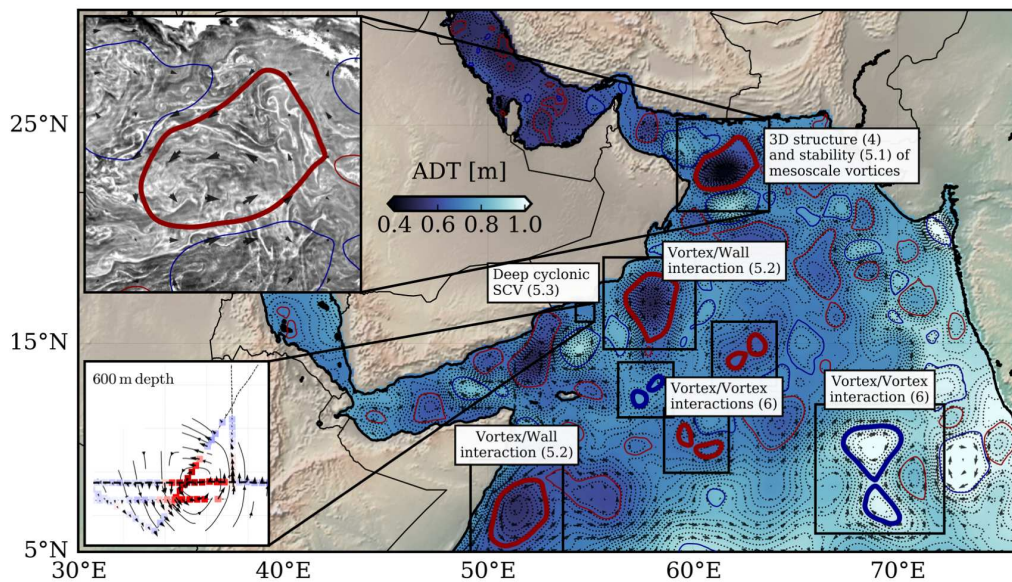


FIGURE 2.13 – Résumé des différents processus étudiés dans ce manuscrit concernant la dynamique des tourbillons en mer d'Arabie (numéros de section entre parenthèses). Carte de hauteur du niveau de la mer (SSH, en niveaux de bleu) à partir de laquelle sont détectés les tourbillons de méso-échelle avec AMEDA (contours bleus et rouges), le 14 Février 2015 : les tourbillons remplissent la mer d'Arabie et interagissent entre eux et avec leur environnement. L'encart en haut à gauche présente des données de couleur de l'eau obtenues par le satellite de la NASA Aqua, le 14 Février 2015 : il montre des structures de sousméso-échelle à la surface d'un imposant cyclone de méso-échelle. L'encart en bas à gauche présente les données récoltées durant la campagne PHYSINDIEN 2019, le 5 Mai 2019 : un tourbillon cyclonique profond de sousméso-échelle est présent au large des côtes omanaises.

Dans cette région, les propriétés de surface des tourbillons ainsi que la structure verticale de quelques specimens ont été déjà largement étudié. En revanche, une description complète de leur structure tridimensionnelle est manquante. Celle-ci permettrait de discuter de l'impact profond de ces structures sur la diffusion des masses d'eau, mais également de prédire leur comportement dynamique. Nous posons ainsi la première question :

Quelle est la structure 3D des tourbillons en mer d'Arabie ?

Également, on peut constater que les tourbillons en mer d'Arabie ne sont pas stationnaires : ils se déplacent, peuvent se dissiper, se détruire, qu'ils soient proche de la côte ou au centre du bassin. Ces phénomènes sont régulièrement accompagnés de l'observation de structures de sousmésos-échelle à la surface des tourbillons, ou en profondeur. Ainsi, pour déterminer l'impact des structures de mésos-échelle sur la dynamique locale, de méso et de sousmésos-échelle, nous posons la question suivante :

Quel est le cycle de vie des tourbillons isolés en mer d'Arabie ?

La mer d'Arabie étant remplie de tourbillons de méso-échelle, différentes interactions peuvent avoir lieu entre eux. Ces interactions influencent les propriétés dynamiques et thermohalines du milieu océanique, et sont donc importantes à grande échelle pour le transport des quantités de la colonne d'eau, notamment quand les tourbillons sont de même signe. À partir des observations, ces interactions apparaissent nombreuses en mer d'Arabie, et nous posons alors la question suivante :

Quelles sont les caractéristiques physiques des interactions entre tourbillons en mer d'Arabie ?

OBSERVER ET ÉTUDIER LA MER D'ARABIE

Pour répondre aux questions posées ci-dessus, et ainsi étudier la dynamique des structures tourbillonnaires de méso et de souméso-échelle en mer d'Arabie, différents outils ont été mis en place. Ces outils sont présentés dans ce chapitre. Nous présentons d'abord les moyens observationnels utilisés, et décrivons brièvement le principe de la mesure. Nous décrivons ensuite les moyens numériques : les modèles numériques utilisés, puis les configurations mises en places.

3.1 Les moyens observationnels

Afin de décrire la dynamique des structures de méso et sousméso-échelle en mer d'Arabie, nous utilisons différents moyens d'observation. Ils sont décrits dans cette section.

3.1.1 Altimétrie

Afin de déterminer la structure horizontale et la distribution des tourbillons de méso-échelle dans la région d'intérêt, nous utilisons un produit altimétrique régional, de résolution $1/8^\circ$, sur la période 2000-2015. Ce produit multi-mission combine les mesures altimétriques recueillies par différents satellites (Topex/Poseidon, ERS-2, GFOO, Jason-1, Envisat, Jason-2, Cryosat-2, Altika et HY2A), en les interpolant spatialement sur une grille Mercator, et temporellement (1 donnée par jour). Bien que ce produit fournisse une couverture complète de la mer d'Arabie, durant une période de 15 ans, certaines parties de la région ne sont en réalité pas mesurées directement par le satellite (*i.e.* elles ne sont pas sous la trace du satellite). Les données en ces lieux sont donc purement le produit du schéma d'interpolation utilisé pour fusionner les différentes données. Ainsi, des fluctuations du signal qui ne sont pas dues à des phénomènes physiques peuvent apparaître, et induisent une erreur $\mathcal{O}(1 - 5)$ cm (Le Traon et al., 1998; Le Vu et al., 2018).

À partir de ce produit altimétrique nous détectons les tourbillons de méso-échelle en mer d'Arabie grâce au Angular Momentum Eddy Detection and tracking Algorithm (AMEDA), développé par Le Vu et al. (2018). Cet algorithme a l'avantage de ne pas utiliser de seuils arbitraires pour la détection. Il peut également être appliqué sur différents produits, de résolutions temporelle et horizontale variables. Dans la suite, nous l'appliquerons également sur des sorties de modèles numériques. Une description complète peut-être trouvée dans Le Vu et al. (2018). En résumé il fonctionne comme suit : (a) à un pas de temps donné, à partir du champ de vitesse dérivé de l'altimétrie grâce à l'équilibre géostrophique, il calcule le moment angulaire local (LNAM, Mkhinini et al. (2014)), et le paramètre d'Okubo-Weiss local (LOW); (b) ensuite, il cherche les maxima locaux de LNAM dans les régions dominées par la vorticit  (i.e. o  $LOW < 0$); (c) si ces maxima sont entour s d'une ligne de courant ferm e, ils sont alors consid r s comme des centre de tourbillons; (d) les tourbillons sont ensuite suivis d'un pas de temps sur l'autre en minimisant une fonction de co t dans le p rim tre de chaque tourbillon, cela donne alors la trajectoire compl te des tourbillons, de leur g n ration   leur mort; (e) enfin, durant leur cycle de vie, les  v nements de fusion et de division des tourbillons sont report s, cela permet de compter *e.g.* combien de fusions de tourbillons ont eu lieu dans une zone donn e. Du fait de l'erreur des produits altim triques, la position du centre des tourbillons d tect e   partir de l'altim trie peut  tre erron e, avec une erreur $\mathcal{O}(1 - 5)$ km (Chaigneau et al., 2011; Kepler et al., 2018).

3.1.2 Plateformes autonomes

Afin d'avoir une estimation *in situ* des propriétés thermohalines et dynamiques de l'océan et de la mer d'Arabie en particulier, nous utilisons également les données recueillies par des plateformes autonomes.

Flotteurs dérivants

Du fait des erreurs sur les produits altimétriques, la vitesse des courants dérivées à partir de la hauteur du niveau de la mer, peut être mal évaluée, et une estimation *in situ* est alors nécessaire pour estimer la valeur des courants de surface de manière fiable. Pour se faire, nous utilisons les données de position et de vitesse récoltées par les flotteurs dérivant de surface (ancrés à 15 m pour éviter l'impact du vent) du Global Drifter Program. La mesure de vitesse est obtenue en suivant la position des flotteurs au cours du temps, et en inférant la vitesse du courant entre les positions successives. Une description complète de ce jeu de données peut être trouvée dans Lumpkin & Pazos (2007); Laurindo et al. (2017). Ce type de données a permis par exemple de donner une description *in situ* complète de la circulation de surface en mer d'Arabie, voir Fig. 2.9 d'après L'Hégaret et al. (2018).

Profileurs autonomes Argo

Afin d'estimer les propriétés thermohalines de la colonne d'eau, nous utilisons les données recueillies par les profileurs autonomes du réseau Argo (Argo, 2019). Le cycle de mesure de ce type de flotteur est présenté dans la Fig. 3.1, et le principe et les différents types de flotteurs sont décrits de manière très complète dans Ollitrault & Rannou (2013). Ce réseau de flotteurs permet d'obtenir des profils de température et de salinité jusqu'à une profondeur de 2000 m avec une couverture spatio-temporelle unique. En effet, grâce à un effort international, environ 3000 flotteurs sont présents en permanence dans l'océan. Ils ont permis de collecter environ un million de profils dans l'océan global entre 1999 et 2012; ce chiffre est en constante augmentation du fait du déploiement intensif de ce type de flotteurs dans de nombreuses campagnes océanographiques. En mer d'Arabie, 45978 profils ont été collectés entre 2000 et 2015, dont la moitié (21113) entre 2012 et 2015.

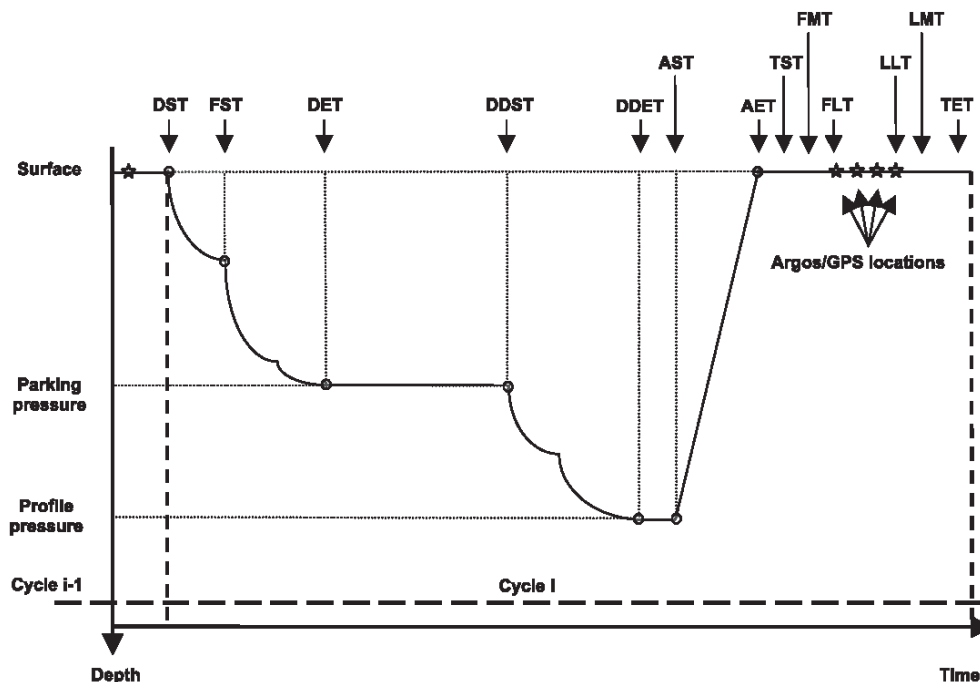


FIGURE 3.1 – Schéma du cycle d'un flotteur Argo : il dérive à une profondeur "de parking" durant un temps donné (généralement 10 jours à 1000 m de profondeur), effectue une plongée profonde jusqu'à la profondeur maximale choisie (généralement 2000 m), avant d'effectuer une remontée jusqu'à la surface au cours de laquelle il mesure la température, salinité et pression de la colonne d'eau. Ces données sont ensuite envoyées par connexion satellite avant que le flotteur ne reponde à la profondeur de parking.

3.1.3 La campagne océanographique PHYSINDIEN 2019

Historiquement, les propriétés de l'océan ont toujours été mesurées grâce à des déploiements de capteurs durant des campagnes à la mer à bord de navires océanographique dédiés. Ces mesures *in situ* restent aujourd'hui la source la plus fiable d'informations, car les capteurs sont calibrés à bord, et les mesures ciblées sur des phénomènes particuliers. En revanche, les campagnes sont coûteuses, et les mesures sont donc très ponctuelles. Elle ne permettent pas une couverture globale des phénomènes océanographiques contrairement aux mesures satellites et aux flotteurs autonomes décrits précédemment.

Dans ce manuscrit nous utilisons les données recueillies durant la campagne PHYSINDIEN 2019. Cette dernière avait pour objectif de mesurer la circulation de surface et de sub-surface en mer d'Arabie, au large des côtes Omanaises. Elle s'est déroulée au mois de Mai 2019 à bord du navire océanographique

de la Marine Nationale BHO Beautemps-Beaupré. La première partie de la campagne (Leg 1) a mesuré la structure des tourbillons de méso et de sousméso-échelle entre Salalah (Oman) et Mascate (Oman). La seconde partie de la campagne (Leg 2) a permis d'échantillonner les propriétés des eaux persiques dans le golfe d'Oman et de l'upwelling omanais, jusqu'à Duqm (Oman). Dans le présent travail, nous décrivons les mesures d'un tourbillon de sousméso-échelle profond récoltées au large de Salalah durant le Leg 1, entre le 4 et le 6 Mai 2019.



FIGURE 3.2 – L'équipe hydrographique (SHOM) et scientifique (UBO/SHOM/SQU) sur la plage arrière du BHO Beautemps-Beaupré durant la campagne PHYSINDIEN 2019.

3.2 Les moyens numériques

Afin d'avoir une vision complète des processus physiques à l'oeuvre dans l'océan, c'est à dire avoir accès aux champs physiques 3D à tout temps, les moyens d'observations décrits plus haut ne sont pas suffisants, et l'approche la plus directe est alors la simulation numérique. La plupart des études réalisées durant cette thèse reposent sur ce principe. Les différents types de simulations numériques sont décrits dans cette section.

3.2.1 CROCO

Principe du modèle numérique

Pour réaliser la plupart des études présentées dans ce manuscrit nous avons utilisé le modèle CROCO (Coastal and Regional Ocean COmmunity model). Ce dernier est une version du modèle ROMS (Regional Oceanic Modeling System) permettant de réaliser des simulations hautes résolutions, côtières et hauturières. Le modèle est décrit de manière complète dans la publication originale du modèle ROMS : Shchepetkin & McWilliams (2005). Les différentes options et tests du modèle ayant mené à la version du code utilisé ici sont présentés dans des publications complémentaires : Penven et al. (2006); Shchepetkin & McWilliams (2011); Debreu et al. (2012); Soufflet et al. (2016). Également, les détails techniques et les routines du modèle sont disponibles sur le site internet de CROCO : <https://www.croco-ocean.org>. Les simulations réalisées pour le présent travail sont des simulations très idéalisées, ne mettant pas en jeu de nombreuses parties du modèle (*i.e.* pas de forçage, de nesting, de couplage, de forçage aux frontières, ni de topographie). Également, nous avons utilisé les paramétrisations usuelles du modèle, déjà largement utilisées et décrites dans de précédentes études, *e.g.* Gula et al. (2015); Ménesguen et al. (2018). Ainsi, nous ne décrivons pas ici les méthodes numériques et toutes les paramétrisations possibles du modèle, mais plutôt le principe de la simulation, et les choix faits dans les différentes configurations.

Le modèle résout les équations primitives hydrostatiques (eq. 1.31) sur une grille Arakawa-C (Arakawa & Lamb, 1977) sur l'horizontale, et sur une grille décalée ρ - w sur la verticale. Les niveaux verticaux suivent la topographie; dans nos cas sans topographie ils sont donc équivalents à des niveaux de profondeur constante. Aux eq. 1.31, sont ajoutées la condition d'incompressibilité du fluide, et une équation d'état non-linéaire du type TEOS-10 (McDougall & Barker, 2011). Les équations sont écrites sous la forme de flux de quantité de mouvement de traceurs, permettant une meilleure conservation de ces derniers. La discrétisation temporelle utilise un schéma leapfrog Adams-Moulton. Les équations barotropes sont résolues sur des pas de temps plus courts que les équations 3D complètes, permettant un gain de temps conséquent sur la résolution du système total.

La diffusion de traceur et de moment sur (1) l'horizontale et (2) la verticale est gérée par (1) le schéma d'advection utilisé, qui induit une viscosité implicite, et (2) la fermeture turbulente verticale. D'une part, nous utilisons le schéma d'advection upwind d'ordre 5 pour les traceurs et le moment sur l'horizontale. Ce terme induit une viscosité implicite plus faible que pour le schéma upwind d'ordre 3, permettant ainsi une meilleure représentation des structures de sousmésos-échelle, *e.g.* les fronts et tourbillons (Ménesguen et al., 2018). La partie diffusive de l'opérateur d'advection est communément acceptée comme étant suffisamment diffusive pour ne pas avoir à ajouter de viscosité explicite (Shchepetkin & McWilliams, 1998). L'advection verticale est effectuée par une reconstruction parabolique centrée du quatrième ordre (Splines scheme). D'autre part, la fermeture turbulente est effectuée *via* le schéma K-Profile Parameterization (KPP, Large et al. (1994)) à la surface et dans l'intérieur. Ce dernier applique des coefficients de diffusion verticale dans la couche de mélange de surface et dans l'intérieur. La profondeur de la couche de mélange de surface est obtenue en comparant le nombre de Richardson avec une valeur critique. Dans l'intérieur, la diffusivité prend en compte les instabilités statique et verticale de cisaillement, ainsi que le déferlement d'ondes internes. Bien que les traceurs soient *a priori* conservés le long des isopycnes dans le système des équations primitives, les paramétrisations susmentionnées peuvent induire du mélange diapycnal de traceur et de quantité de mouvement, et donc également de PV.

Les différentes configurations

La philosophie des simulations présentées dans ce manuscrit est la suivante : effectuer les simulations numériques les plus idéalisées possible, puis ajouter un à un différents facteurs d'environnement (*e.g.* un trait de côte, un autre tourbillon...), afin d'isoler les processus physiques le plus efficacement possible. Ce sont des simulations dont on fixe l'état initial, puis que l'on laisse évoluer sans forçage ni intervention extérieure afin de suivre l'évolution des paramètres physiques au cours du temps. Dans ce cadre, différentes configurations ont été réalisées, dont les initialisations ont été mises en place avec des programmes Python développés seul ou en collaboration pendant la période de la thèse.

Premièrement, nous réalisons des simulations numériques mettant en jeu **un tourbillon réaliste isolé ou proche d'une côte**. Un tourbillon réaliste correspond à un tourbillon dont la structure 3D en vitesse, température et salinité n'est pas connue de manière analytique, mais obtenue à partir de données *in situ*. Pour ce faire, nous interpolons les données représentant un tourbillon (ici son anomalie de densité) sur une grille CROCO de résolution horizontale et verticale voulue. Après ajout d'une stratification moyenne, nous calculons la vitesse de rotation du tourbillon en tout point en utilisant les équations du gradient de vent (eq. 1.29), en suivant la procédure de Penven et al. (2014). Le tourbillon

se trouve alors dans un océan au repos, isolé, ou proche d'un trait de côte, puis évolue seul, fonction de ses propriétés intrinsèques. Ces simulations sont présentées et analysées de manière complète dans les sections 5.1 et 5.2.1, où le tourbillon réaliste est un cyclone composite extrait en mer d'Arabie. Les études ainsi réalisées constituent les premières réalisations de ce type de simulation dont le tourbillon simulé n'est pas initialisé analytiquement. Notons qu'à partir de ce travail et des scripts réalisés, différentes collaborations en cours visent à effectuer le même type d'études, pour d'autres tourbillons initiaux : des anneaux du Loop Current mesurés à l'aide de gliders autonomes, et le Christmas Eddy, mesuré à hautes latitudes.

Deuxièmement, nous réalisons des simulations numériques d'**un tourbillon analytique initialement isolé et proche d'une côte**. Pour ce faire, nous imposons un profil horizontal de vorticité relative en coordonnées polaires correspondant au tourbillon isolé, sous la forme

$$\omega(r) = \pm\omega_0 e^{-\left(\frac{r}{R}\right)^\alpha}, \quad (3.1)$$

où le signe dépend de la polarité, $r = \sqrt{(x - x_0)^2 + (y - y_0)^2}$ est la position radiale référencée au centre du tourbillon (x_0, y_0) et α est le paramètre de raideur du profil. $\omega_0 = V_0/R$, avec V_0 la vitesse azimutale maximale à une distance R du centre du tourbillon. Nous calculons ensuite la vitesse azimutale du tourbillon en intégrant radialement la vorticité, puis projetons le résultat sur la grille (cartésienne) CROCO de la simulation. L'anomalie de pression P' (et l'anomalie de température associée) est calculée en inversant la relation du gradient de vent (eq. 1.29). Finalement, une stratification analytique moyenne est ajoutée. Un trait de côte est ajouté sur le bord ouest de la simulation, à une distance donnée du centre du tourbillon. Ces simulations sont présentées et analysées de manière complète dans la section 5.2.2.

Troisièmement, nous réalisons des simulations de **fusion de deux tourbillons analytiques**. Le principe est le même que pour les simulations présentées ci-dessus, excepté que la procédure est effectuée deux fois, pour deux tourbillons initialement séparés d'une distance choisie. Ces simulations sont présentées et analysées de manière complète dans la section 6.2.2. Notons que ce travail et les scripts réalisés sont le départ d'une collaboration en cours, dont le but est d'étudier l'alignement de deux tourbillons de même signe initialement sur des niveaux verticaux différents.

3.2.2 Ré-analyse HYCOM 1/12°

Pour une étude particulière, nous avons utilisé les sorties de la réanalyse HYCOM + NCODA Global 1/12° reanalysis reposant sur l'assimilation de données *in situ* dans le modèle HYCOM. Ce dernier est un modèle aux équations primitives similaire à CROCO. Les différences principales sont que

(1) les niveaux verticaux sont hybrides (isopycnaux proche de la surface puis à profondeur constante au fond) et (2) une viscosité explicite est ajoutée. Ce jeu de données permet de considérer des champs de surface réalistes, avec une résolution horizontale satisfaisante. Il est fourni toutes les 3 heures sur une grille Mercator de résolution $1/12^\circ$ entre 40°S et 40°N . L'assimilation de données repose sur le Navy Coupled Ocean Data Assimilation system (NCODA, Cummings (2005); Cummings & Smedstad (2013)). NCODA utilise des prédictions à 24h HYCOM en première supposition, puis assimile les observations satellites et *in situ* disponible à la surface et dans la colonne d'eau en utilisant Improved Synthetic Ocean Profiles (Helber et al., 2012). Nous ne rentrons pas dans les détails numériques de la simulation utilisée, car celle-ci a déjà été entièrement validée, testée et utilisée dans de nombreuses précédentes études (Metzger et al., 2014; Yu et al., 2015; Thoppil et al., 2016; Metzger et al., 2017; Shinoda et al., 2019). Nous nous contentons ici d'utiliser les sorties du modèle disponible en ligne (<https://www.hycom.org/dataserver/gofs-3pt1/reanalysis>). L'analyse de cette simulation est présentée dans la section 6.2.2

3.2.3 Modèle QG 2 couches

Nous utilisons également un modèle numérique résolvant les équations quasi géostrophiques 2 couches (eq. 1.44). La résolution est pseudo-spectrale en espace, et mixte Euler-leapfrog en temps. Les simulations sont très idéalisées, avec un domaine carré, bipériodique, des grandeurs adimensionnées et une topographie analytique variant méridionalement. Deux tourbillons de vorticités potentielles uniforme pour $r < R$ et de même polarité sont initialisés proche du talus continental. Ces simulations ont l'avantage d'être peu coûteuses en temps et en espace de stockage, et permettent ainsi de faire varier de nombreux paramètres. Ces simulations sont présentées et analysées de manière complète dans la section 6.3.

LA STRUCTURE DES TOURBILLONS DE MÉSO-ÉCHELLE EN MER D'ARABIE

De précédentes études on présenté la structure horizontale typique des tourbillons de méso-échelle en mer d'Arabie (Trott et al., 2018), ou leur profils verticaux, de manière ponctuelle (Carton et al., 2012; L'Hégaret et al., 2016). En revanche, bien qu'essentielle pour comprendre l'impact sur la dynamique profonde des nombreuses structures observées par satellite, la détermination systématique de la structure 3D des tourbillons en mer d'Arabie n'a jamais été étudiée à l'aide de données *in situ*. Grâce aux nombreux flotteurs Argo aujourd'hui présents en mer d'Arabie, cette tâche est désormais possible. Cette partie présente l'étude de la structure 3D des tourbillons en mer d'Arabie, et répond aux questions suivantes : (1) Est ce que la position géographique des tourbillons influence leur structure verticale? (2) Quelle est la structure 3D moyenne des tourbillons en mer d'Arabie? (3) Quelles masses d'eaux peuvent être mesurées au coeur des tourbillons de méso-échelle en mer d'Arabie? Répondre à ces questions permet ainsi de donner un socle observationnel aux différentes études numériques réalisées plus loin.

4.1 Article publié dans *Deep Sea Research Part I*



Contents lists available at ScienceDirect

Deep-Sea Research Part I

journal homepage: www.elsevier.com/locate/dsri

On the 3D structure of eddies in the Arabian Sea

Charly de Marez*, Pierre L'Hégaret, Mathieu Morvan, Xavier Carton

Univ. Brest, Laboratoire d'Océanographie Physique et Spatiale (LOPS), IUEM, Rue Dumont D'urville, 29280, Plouzané, France



ARTICLE INFO

Keywords:
Mesoscale
Eddies
Oceanic vortices
Arabian sea
Argo
Sea of Oman

ABSTRACT

In the Arabian Sea, mesoscale eddies are prominent features of the circulation. They influence biological activities, tracer transport, and physical and chemical properties of the seawater. In particular, the pathways of salty water masses outflowing from the marginal seas are strongly impacted by the mesoscale eddies that evolve in the western part of the basin. The impact of mesoscale eddies on the different salty water masses has been investigated in previous studies with altimetric data and *in situ* data for short durations. In this study, we extend this analysis to most of the mesoscale eddies detected from altimetry data for the period 2000–2015. We use Argo floats colocalized with eddies to describe the 3D impact of mesoscale eddies on the dynamical and thermohaline properties of water masses in the Arabian Sea. The ~30,000 Argo stations used show a well characterized distribution of water masses in the different sub-basins of the Arabian Sea, with the Persian Gulf Water (PGW) flowing from the north and the Red Sea Outflow Water (RSOW) from the northwest. In addition, colocalizing Argo profiles in or out of these eddies allows for the extraction of temperature and salinity anomalies related to mesoscale eddies. Then, we present the vertical structure of density associated with these eddies. These results allow us to divide the Arabian Sea into areas depending on their hydrological and dynamical properties. In the Gulf of Oman and the Gulf of Aden, the water in the core of eddies is fresher than at their edge. Thus, most of eddies residing in these gulfs were generated in the Arabian Sea. In these eddies, the salinity anomalies corresponding to PGW and RSOW are on average stronger at their edge than in their core; this indicates that eddies in these gulfs impact outflow waters via advecting processes on their rim. Finally, we select the northern part of the Arabian Sea (including the Gulf of Oman), where most Argo profiles were collected. We calculate the composite 3D profiles of angular velocity and salinity anomaly for surface-intensified cyclonic eddies and subsurface anticyclonic eddies, with radii of about 100 km. The velocity profiles computed via the thermal wind equations are validated using surface velocities from altimetry and surface drifter measurements. On average, eddies in the northern Arabian Sea exhibit a clear pattern of PGW in their core. The comparison of these 3D composite structures with a particular cyclone near the Strait of Hormuz and a dipole sampled with a SeaSoar along the Omani Coast shows that they are representative of mesoscale eddies often observed in the area.

1. Introduction

Mesoscale eddies have a strong influence on the circulation in the Arabian Sea (Fischer et al., 2002). This basin, located in the Northern Indian Ocean between the African and Asian landmasses, is a region dominated by the monsoon wind regime. This forcing generates reversing alongshore currents and upwellings, which are an essential part of the regional circulation (Lee et al., 2000). The monsoon cycle is associated with strong and steady southwesterly winds across the basin in summer and with weaker northeasterly winds in winter (Findlater, 1969). This cycle leads to currents reversing in direction depending on the season, see Fig. 1 in L'Hégaret et al. (2018) which presents the mean

surface circulation. In this region, quantities related to the spatial structure and to the magnitude of mesoscale activity, such as eddy kinetic energy (Scharffenberg and Stammer, 2010) or eddy available potential Energy (Roulet et al., 2014), have values comparable with those of other eddy rich regions (e.g the Antarctic Circumpolar Current or the Agulhas Current). Indeed, the alongshore currents destabilize and form meanders with 100–200 km wavelengths; they produce eddies with similar diameters (Schott and McCreary, 2001). Wind stress forcing, and baroclinic Rossby waves generated at the eastern boundary of the Arabian Sea, can strengthen such eddies or contribute to their propagation (Al Saafani et al., 2007). The specific places mentioned in the article are indicated in Fig. 1. Also, we refer the reader to Fig. 2 in

* Corresponding author.

E-mail address: charly.demarez@univ-brest.fr (C. de Marez).<https://doi.org/10.1016/j.dsr.2019.06.003>

Received 17 December 2018; Received in revised form 4 June 2019; Accepted 5 June 2019

Available online 12 June 2019

0967-0637/ © 2019 Elsevier Ltd. All rights reserved.

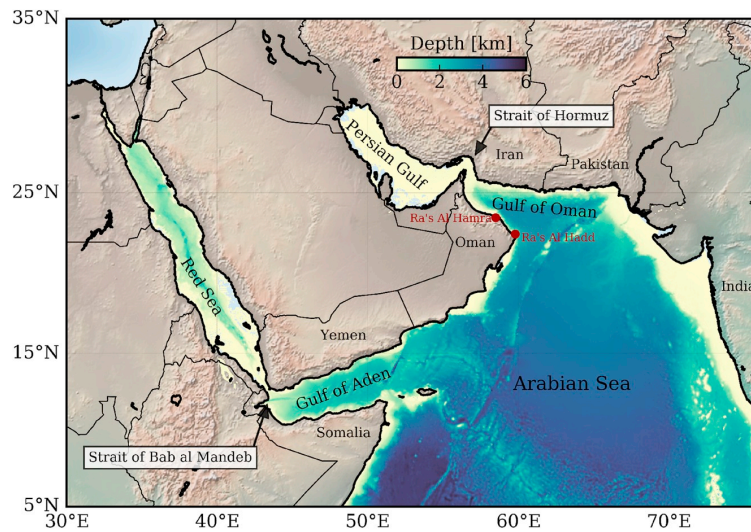


Fig. 1. Bathymetry in the Arabian Sea and adjacent gulfs from ETOPO2 (Smith and Sandwell, 1997).

Vic et al. (2014) for a description of the mean stationary eddies such as the Great Whirl and the dipole of Ras Al Hadd.

In the global ocean, mesoscale eddies influence biological activities (Chelton et al., 2011), tracer transport (Zhang et al., 2014), and physical and chemical properties of the water column (Dong et al., 2014). In the Arabian Sea, understanding the evolution of eddies is of primary importance: they carry and upwell/downwell (depending on the eddy polarity) oxygen and nutrients (Queste et al., 2018), and modulate plankton blooms (Tollefson, 2018) and green algae generation (do Rosario Gomes et al., 2014), which impact the fishing economy, sustaining 120 million people living on the rim of the Arabian Sea. Moreover, the eddy-driven circulation of the Arabian Sea strongly impacts the spreading of the dense salty water masses outflowing from the adjacent marginal seas (Bower and Furey, 2012; Carton et al., 2012).

In the Persian Gulf, a shallow (<100 m depth) semi-enclosed basin, warm and salty water is formed via evaporation near the western boundary (Pous et al., 2015). This water mass is called the Persian Gulf Water (PGW). After flowing through the Strait of Hormuz, the PGW stabilizes between 200 and 300 m depth and spreads into the Gulf of Oman and into the Arabian Sea (Bower et al., 2000). Similarly, the Gulf of Aden receives dense and saline water, the Red Sea Outflow Water (RSOW), which is formed in the Red Sea and outflows in the Arabian Sea through the shallow Strait of Bab al Mandeb (~150 m) before swiftly descending between 500 and 1000 m depth (Bower et al., 2000).

The common point between these two outflows is that the spreading of the saltier waters into the Arabian Sea strongly depends on the mesoscale structures lying in the gulfs (Bower et al., 2002; Bower and Furey, 2012; Ilicak et al., 2011; Vic et al., 2014). For instance, in the Gulf of Oman, during the spring intermonsoon, a recurrent cyclone near Ras al Hamra advects the outflowing water away from the coast of Oman, sending northward pulses of PGW from the Omani coast to the Iranian coast (L'Hégaret et al., 2015). Similar advective processes take place in the Gulf of Aden, where the outflow is stirred by gulf-size eddies (Bower et al., 2002; Ilicak et al., 2011). When the RSOW and the PGW reach the Arabian Sea, they can be detected far from the gulfs, as far south as 25°S for the RSOW and 5–10°N for the PGW (Quadfasel and Schott, 1982). In particular, these water masses have been observed in the core of mesoscale eddies, indicating that they may be trapped by such eddies, and that they can travel southward in them (L'Hégaret et al., 2015). Moreover, it has been shown that the salinity anomalies associated with waters flowing out of the Persian Gulf and of the Red Sea into the Arabian Sea have increased during the past fifty years. This

increase is concordant with the broad-scale surface warming and with the intensification of the global hydrological cycle (Durack and Wijffels, 2010). It is thus essential and timely to determine what is, on average, the 3D structure of eddies in the Arabian Sea to further discuss the physical processes involved in the mesoscale eddy/outflow interactions.

Previous observational studies provided a few snapshots of eddy vertical structure in the Arabian Sea (Carton et al., 2012; L'Hégaret et al., 2016), or showed the surface properties of such eddies (Trott et al., 2018). However, the systematic study of the 3D structure of eddies from *in situ* data in the Arabian Sea is lacking. To obtain the 3D structure of eddies in a specific area, several observational methods can be used. Either a given eddy can be sampled by many vertical profiles (Zhang et al., 2016; Souza et al., 2011); or, the 3D structure of a 'composite' eddy can be obtained via the analysis of Argo float data in the core of different eddies (Chaigneau et al., 2011; Yang et al., 2013; Pegliasco et al., 2015; Keppler et al., 2018). It is now possible to consider the latter method to study eddies in the Arabian Sea. New altimetric products with 1/8° resolution combining different missions are now available. They resolve more accurately eddies with radii twice or thrice the first baroclinic Rossby radius of deformation (which is between 50 and 100 km in the Arabian Sea). Furthermore, with the increase in Argo Float deployments, the water column properties are more densely sampled in the Arabian Sea. Thus, the vertical properties of eddies in this area can be studied more precisely.

In this paper, we study the 3D properties of eddies in the Arabian Sea. Unlike previous studies, we study the average structure of eddies using a composite approach. We address the following questions: (1) Do eddies in the Arabian Sea exhibit different vertical patterns depending on their geographic area? (2) What is the average 3D shape of mesoscale eddies in the Arabian Sea? (3) Which water masses of the Arabian Sea can be detected inside eddies?

In section 2, we present the dataset and the methods. Then, in section 3, we use Argo floats to study the dynamical and hydrological properties of eddies in the different sub-basins of the Arabian Sea, and to compute a composite 3D structure of eddies in the northern Arabian Sea.

2. Methods and materials

2.1. Argo floats

Profiles collected by Argo floats (Argo, 2019) in the period

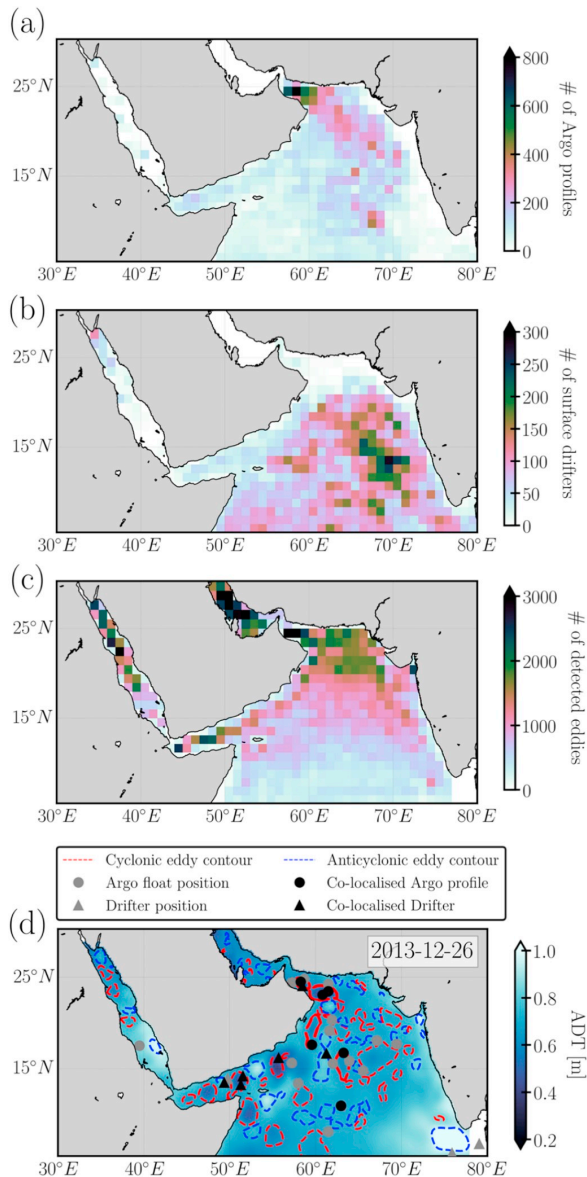


Fig. 2. Distribution of (a) Argo floats, (b) Surface drifters and (c) Detected eddies from the altimetry, for the period 2000–2015 in the Arabian Sea. (d) Snapshot of ADT from the altimetric product used for the detection of eddies. The contour of eddies from the AMEDA eddy detection (red and blue dashed lines), the positions of Argo profiles and Surface Drifters on the same date are superposed. (For interpretation of the references to color in this figure legend, the reader is referred to the Web version of this article.)

2000–2015 in the region of interest (30°E to 80°E and 5°N–30°N) are used to determine the vertical structure of the water column inside and outside mesoscale eddies. Only profiles containing both temperature (T) and salinity (S) data flagged as 'good' were downloaded from the Coriolis website (www.coriolis.eu.org). This dataset consists of 45,978 profiles (*i.e.* T, S and pressure (P) data at a given time) non-uniformly distributed in the region (Fig. 2 (a)). The number of profiles increases with time such that about half of the available profiles (21,113), were collected between 2012 and 2015. Contrary to this interannual trend, there is no seasonal bias in sampling: profiles are uniformly distributed

in time for each year, with a median of 4,162 profiles per month for the 2000–2015 period.

Once the data were downloaded from the Argo repository we did additional processing, as follows. Firstly, any profile containing fewer than five measurement or sampling less than 10% of the water column was discarded. These two conditions discarded profiles concentrated near the surface and thus diminish biases in statistics. Secondly, profiles with suspicious variations of salinity and temperature at the bottom were removed. 29,516 profiles representing 64% of the initial dataset remained after these quality controls. Then, the depth (z), the density (ρ), the conservative temperature (CT) and the absolute salinity (SA) at each station were computed from the T, S and P profiles using the Gibbs SeaWater (GSW) Oceanographic Toolbox (McDougall and Barker, 2011) which uses the TEOS-10 equation of state for seawater. The profiles were then linearly interpolated on 500 regularly spaced vertical levels in the range 0–2200 m, similar to the method used in Chaigneau et al. (2011). This interpolation retains small scale variations on the vertical, without creating artificial water masses where data are missing. In this study, data will be averaged over numerous profiles to extract mean T, S and ρ profiles inside and outside eddies.

2.2. Surface drifters

To obtain an *in situ* estimate of surface velocities in eddies, we use the position and horizontal velocity data from 15-m drogued drifters of the Global Drifter Program (GDP). The dataset consists in 39,247 values of velocities distributed over the regions of interest for the 2000–2015 period. For further information on these data see Lumpkin and Pazos (2007) and Laurindo et al. (2017). The density of drifters is directly related to the surface flow convergence and divergence, with a maximum number of drifters located where velocities are weak and the convergence is large (L'Hégaret et al., 2018). In our case, most drifters were located on the Eastern boundary of the Arabian basin and at latitudes lower than 20°N (Fig. 2(b)).

2.3. Eddy detection from altimetry

A regional 1/8° resolution altimetric product is used to detect mesoscale structures in the Arabian Sea for the 2000–2015 period. This specific altimetric series was processed by Collecte Localisation Satellites (CLS) and features interpolated absolute dynamical topography (ADT) and surface geostrophic velocities on a daily Mercator grid. It combines up-to-date datasets from different available missions (Topex/Poseidon, ERS-2, GFOO, Jason-1, Envisat, Jason-2, Cryosat-2, Altika and HY2A). A snapshot of ADT and surface velocity from this product in the region of interest is presented in Fig. 2(d). As discussed in previous studies (Le Traon et al., 1998; Le Vu et al., 2018), non-physical fluctuations or distortions in this 1/8° gridded product could be induced by the spatiotemporal heterogeneity of the satellites' tracks. This leads to errors of $O(1)$ cm, where the amplitude of the sea surface height is $O(50)$ cm. An estimation of the typical error induced by this heterogeneity in the Arabian Sea is shown in Fig. 15.

We used the Angular Momentum Eddy Detection and tracking Algorithm (AMEDA), recently developed and optimized by Le Vu et al. (2018) to detect mesoscale eddies in this area. One of the benefits of AMEDA is that it does not depend on arbitrary thresholding, which would require a fine-tuning of geometrical parameters. Also, the algorithm is robust with respect to the grid resolution and can thus be applied to a wide variety of velocity fields (experimental, numerical, altimetry...). This algorithm works as follows: (a) from the velocity fields, it computes the local normalized angular momentum (LNAM), as defined in Mkhinini et al. (2014) and the local Okubo-Weiss parameter (LOW) at each point; (b) then, it seeks LNAM local maxima where $LOW < 0$; (c) if these maxima are surrounded by a closed streamline, they are flagged as eddy centers. A full description of the algorithm is presented in Fig. 1 of Le Vu et al. (2018).

For a detected eddy, the algorithm gives, among other information, the position of the eddy center, its shape, defined as the largest closed streamline, its polarity, and the day of detection. As shown in Le Vu et al. (2018) the altimetric product detailed above allows the accurate detection of mesoscale eddies when their characteristic radius is larger than the local Deformation Radius R_D (Chelton et al., 1998), which is about 50 km in the northern Arabian Sea ($\sim 25^\circ\text{N}$) and 100 km in the southern part of our domain ($\sim 5^\circ\text{N}$).

Applied to altimetric data, AMEDA detected 489,562 eddy occurrences for the whole period. Eddy occurrences are not indicative of unique eddies. The AMEDA algorithm would identify an eddy occurring in the same location on two subsequent time steps as two eddy occurrences, although this would (most likely) be the same eddy. An example of such detection is shown in Fig. 2(d) at a given time (2013-12-26). As in Trott et al. (2018) the number of eddies in the Arabian Sea is roughly constant throughout the years, with a median of 30,450 eddies detected per year. The radius of detected eddies also increases as latitude decreases, with a standard deviation of the eddy radii of 172 km at 5°N , and 58 km at 25°N . The northern part of the basin, north of 17°N , is the region where AMEDA detected the most eddies (Fig. 2(c)); most likely because of the decrease of the eddy radius from the equator northward.

2.4. Methodology of colocalization

To characterize the 3D structure of eddies we implemented an algorithm of colocalization allowing to determine if either an Argo float or a surface drifter lies inside or outside an eddy detected by the AMEDA algorithm. The method is here illustrated with Argo profiles, but the algorithm works the same on surface drifters dataset. Every day, we seek all Argo profiles collected. Then, for each eddy detected on this day, we check if an Argo float has surfaced inside the streamline defining the eddy contour. To do so, the eddy contour is decomposed into a 20-vertex polygon. A 'point-in-polygon' algorithm is then used to determine if the float is inside the eddy. If this condition is met, the Argo profile is flagged as 'colocalized'. An example of such colocalization is presented in Fig. 3. We also collect the surface geostrophic velocity at the position of the Argo float from the altimetric dataset. All Argo profiles which have not been colocalized are flagged as 'out of eddies'; they will allow us to compute thermohaline climatologies out

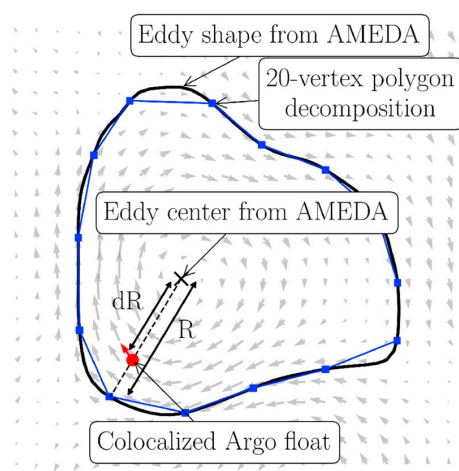


Fig. 3. Example of colocalization. Blue lines indicate the 20-vertex polygon into which the 'point-in-polygon' algorithm is processed. The gray-shaded arrows show the surface geostrophic velocity from altimetric data. The red arrow is the surface velocity collected at the location of the Argo float. (For interpretation of the references to color in this figure legend, the reader is referred to the Web version of this article.)

of eddies.

This method could lead to errors due to the misevaluation of the eddy position at the moment of Argo float sampling, due to the time interpolation of the altimetric product. Thus, we seek Argo floats surfacing within ± 12 hours around the time of eddy detection by altimetry. The tolerance is set knowing that the typical time for an Argo float to achieve a profile is about 5 hours (2000 m of ascent at $\sim 10 \text{ cm s}^{-1}$ for APEX and SOLO floats) and the transmission time varies between an hour and a dozen of hours (depending on the transmission system). As discussed in Chaigneau et al. (2011) or Keppler et al. (2018), this error may lead to a misevaluation of the distance between the center of the eddy and the profiles of $O(1 - 5)$ km. In the case of an Argo float lying close to the contour of an eddy, this error could cause a false classification of the profile inside or outside this eddy.

The dimensionless position with respect to the center of the eddy is computed for each colocalized Argo position (Fig. 3). The Euclidean distance between the center of the eddy and the Argo position defines a distance dR . We then compute a local radius of the eddy R by finding the intersection between the eddy contour and a straight line which passes through the center of the eddy and the Argo position. The dimensionless position is defined as $r = dR/R$. If $r = 0$, the profile is collected at the center of the eddy; if $r = 1$ the profile is collected on the edge of the eddy. This calculation allows us to calculate average density profiles in each radial section in a given eddy, without taking into account its actual shape (*i.e.* this means that we reshape each eddy to a circular form).

To summarize, for all eddies where Argo floats were colocalized, we have:

- The position of the center of the eddy;
- The horizontal shape of the eddy;
- Profiles of T, S, ρ and $P(z)$ collected by Argo floats within the eddy;
- Surface geostrophic velocities at the position of the floats;
- Dimensionless position of the profiles with respect to the center of the eddy r .

A similar approach of colocalization between eddies detected with the AMEDA algorithm and Argo floats has been done in the Mediterranean sea; see <https://www1.lmd.polytechnique.fr/dyned/>.

2.5. Composite eddy calculation

To determine the 3D structure of eddies, we need a vertical representation of the thermohaline and dynamic properties in the range $r \in [0,1]$. To do so we use a composite approach by considering numerous eddies in a given area, assuming that they have similar characteristics, as for instance in Chaigneau et al. (2011). This method is then applied to eddies lying in the northern Arabian Sea.

All the eddies considered are assumed axisymmetric. All profiles with the same r are localized on the same circle around the center of a 'normalized eddy'. If we assume that the properties of eddies do not depend on the angular position within the eddy, the circle of constant r collapses into a radial point. Therefore, we compute mean profiles of T, S and ρ for all r comprised in bins of dimensionless width 0.05. Note that the number of profiles per bin is higher towards the edge than at the center (Fig. 4(top)), giving a better confidence in the averages for $0.5 < r < 1$. For T, S and ρ we may thus compute 2D fields $T(r, z)$, $S(r, z)$ and $\rho(r, z)$ representing the variations of thermohaline properties in the core of the chosen eddies.

We assume that the stratification out of the composite eddy is well represented by the average of density profiles outside eddies in the area encompassing the composite. We use this mean profile for $\rho(r, z)$ where $r > 1$. Values for $r < 0$ are mirrored from values at $r > 0$. This method is used to smooth the density field at the center of the eddy (where $r = 0$) and at its edge, without discarding values at these locations during the smoothing (Fig. 4(bottom)).

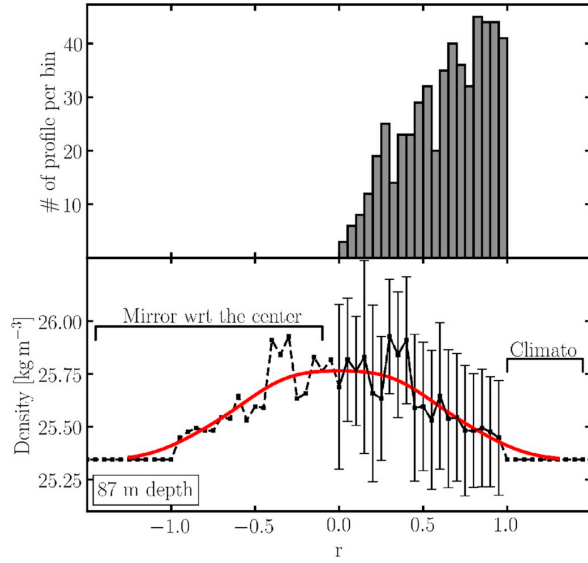


Figure 4. Smoothing procedure of the density for cyclonic eddies in the northern Arabian Sea. (top) Number of Argo in each bin. (bottom) Smoothing of the density at a given level. The dashed line fits the mean value of density at each depth used for the smoothing. Error bars indicate the standard deviation in each bin. The red thick line is the result of the smoothing used to compute the density anomaly and the geostrophic velocity.

The density $\rho(r, z)$ is horizontally smoothed using a Gaussian kernel of width $\sigma = 0.3$, removing all density variations over distances smaller than 4 measurement points, using altimetric data with $1/8^\circ$ resolution. In the area considered, the mean radius of eddies is about 120 km. The smoothing thus operates over scales smaller than 40 km. This smoothing removes sharp density gradients over small distances, which may have altered the geostrophic velocities calculation. We thus obtain a smooth density field $\rho_s(r, z)$ without assuming any analytic shape of eddies (contrary to [Keppler et al. \(2018\)](#)).

We use the thermal wind equations to compute the eddy-induced angular velocity. By considering geostrophic equilibrium and hydrostatics, the geostrophic velocities can be calculated in polar coordinates as:

$$f \partial_z u_\theta = \frac{-1}{\rho_0 g} \partial_r \rho_s(r, z), \quad (1)$$

where (r, θ) are respectively the radial and angular directions ([Gill, 2016](#)). The average Rossby number of the eddies in this study being weak, $R_o \sim 0.05$, no cyclogeostrophic correction is applied ([Ioannou et al., 2017](#)). R_o is calculated using the velocity of the altimetric dataset at the location of the Argo profiles we considered to compute the composite. We also assume that density varies only radially, so that $u_r = 0$. In the obtained sections, the density anomaly vanishes below the positive (resp. negative) anomalies for cyclones (resp. anticyclones). This results from density averaging at depth. We assumed a level of no motion at 1500 m depth ($u_\theta(-1500 \text{ m}) = 0$). This is the maximum common dive depth for the Argo floats considered in the northern Arabian Sea. This assumption, used in previous studies ([Chaigneau et al., 2011](#); [Keppler et al., 2018](#)), may underestimate the velocity since deep motion is assumed nil. Finally, we obtain the azimuthal velocity with:

$$u_\theta(r, z) = \frac{-f}{\rho_0 g} \int_{-1500 \text{ m}}^z \partial_r \rho_s(r, z) dz. \quad (2)$$

The error in density composite structure with respect to the density values of the Argo profiles is estimated. It is the relative Root Mean

Square Error between the value of density of the composite $\rho_s(x, y, z)$ and the actual Argo-collected value at the same location $\rho_A(x, y, z)$, such as:

$$\text{Relative error} = \frac{\sqrt{\rho_A(x, y, z)^2 - \rho_s(x, y, z)^2}}{\rho_A(x, y, z)}.$$

The horizontal extension of the composite structure is re-dimensionalized by the mean radius of eddies used for its creation, and is projected on the (x, y) coordinate following the usual polar to Cartesian coordinate transformation. Notice that in this calculation, the Argo profile locations with respect to the center of the eddy are expressed in Cartesian coordinates (x, y) , to take into account the actual distribution of floats in space.

2.6. The 2011 Phys-Indien experiment

We compare the 3D composite structures of eddies from this study with a cyclone and an anticyclone sampled during the Phys-Indien experiment in 2011 along the Omani coast. This experiment measured the circulation and water masses in the sub-basins around the Arabian Peninsula from February to April 2011 onboard French Navy's ship BHO Beautemps-Beaupré. This cruise used two CTD probes on a SeaSoar, and a VM-ADCP. More details about the campaign are discussed in [L'Hégaret et al. \(2016\)](#). Here we study the density computed from the conductivity and the temperature collected by a SeaSoar.

3. Results

We present here the results of our study. First, we show that the Arabian Sea can be divided into different areas, based on their thermohaline properties and the values of the First Baroclinic Rossby Radius of Deformation R_D . We then focus on the dynamical properties of eddies in the different areas and we isolate the surface cyclonic eddies (CE) and subsurface anticyclonic eddies (AE) with radii $R_D < R < 3 R_D$ in the northern Arabian Sea. We finally present the composite eddies computed for these two classes of eddies.

3.1. Distribution of water masses

The Arabian Sea is decomposed into 6 areas: 2 areas which directly cover the outflows from the Persian Gulf and the Red Sea: the Gulf of Oman and the Gulf of Aden; and 4 areas which have distinct water mass signatures, see [Fig. 5\(a\)](#). The number of Argo profiles collected in each area, depending on their position inside or outside eddies is presented in [Table 1](#). Though most Argo profiles were collected in the northern Arabian Sea, and at the southeastern boundary (area C), the number of profiles collected in each area is sufficient to describe the different water masses locally. Diagram of CT versus SA (TS-diagram here-after) are shown for each area in [Fig. 5\(b\)](#). The TS-diagrams we present correspond to the usual description of the water masses presented in [Fig. 1 of Quadfasel and Schott \(1982\)](#).

First of all, we isolate the two Gulfs at the western and the northern boundary of the basin: the Gulf of Aden (GA) and the Gulf of Oman (GO). These two areas are known as areas were RSOW and PGW flow out from the Red Sea and the Persian Gulf ([Bower et al., 2000](#); [Carton et al., 2012](#)). In the GA, TS-profiles exhibit a clear peak centered on the 27 kg m^{-3} σ_θ -level. This signature is typical of the Red Sea outflow which stabilizes between 600 and 1000 m depth in the GA ([Bower and Furey, 2012](#)). Similarly, the TS-diagram of the GO area reveals the PGW signature, with an anomaly centered at 300 m depth between the 26 and the 27 kg m^{-3} σ_θ -levels.

We compare the mean TS-profiles collected inside and outside eddies in these two areas ([Fig. 6](#)). We averaged profiles depending on their position in the eddy where they lay. Note that the number of profiles collected near the center of eddies, for $r < 0.25$ is much smaller

Table 1

Number of Argo profiles collected, depending on the area it was found in and its position inside or outside an eddy. Percentages indicate the fraction of profiles in a given area.

Area		Number of profiles			Outside eddies
		Inside eddies			
		$r < 0.25$	$0.25 < r < 0.5$	$0.5 < r < 1$	
Gulf of Aden (GA)		22 (1.8%)	58 (4.6%)	296 (23.7%)	872 (69.9%)
A		75 (3.9%)	169 (8.8%)	464 (24.2%)	1211 (63.1%)
B		89 (3.7%)	199 (8.4%)	639 (26.9%)	1447 (61%)
C		160 (1.4%)	594 (5.3%)	2106 (18.9%)	8272 (74.3%)
NAS	D	242 (2.4%)	704 (7%)	2751 (27.5%)	6306 (63%)
	Gulf of Oman (GO)	128 (4.5%)	288 (10.1%)	845 (29.8%)	1579 (55.6%)

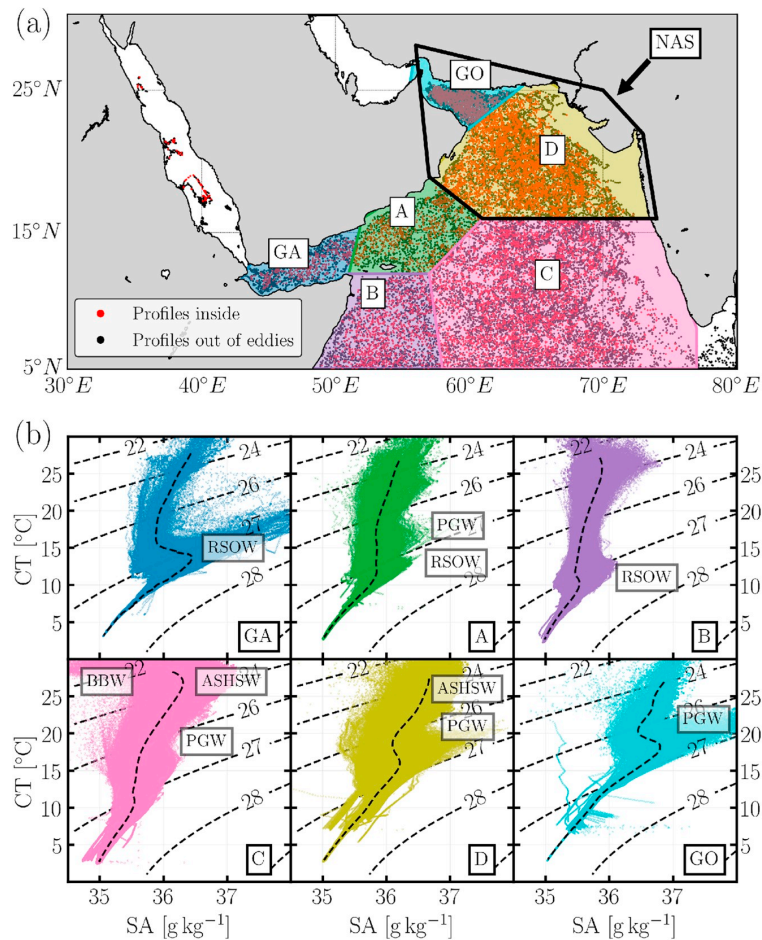


Fig. 5. (a) The different areas defined in our study, black (resp. red) dots shows the location of Argo profiles outside (resp. inside) mesoscale eddies. The black thick line indicates the northern Arabian Sea (NAS), where we compute the composite eddies. GA (resp. GO) is the abbreviation of Gulf of Aden (resp. Gulf of Oman). (b) TS-diagram of the different areas, dashed lines are averages for each area. Bold dashed lines are iso-density lines (*i.e.* σ_0 -level). The number of Argo profiles used to compute these diagrams is presented in Table 1. Water masses are abbreviated as follows: Red Sea Outflow Water (RSOW), Persian Gulf Water (PGW), Bay of Bengal Water (BBW) and Arabian Sea High Salinity Water (ASHSW). (For interpretation of the references to color in this figure legend, the reader is referred to the Web version of this article.)

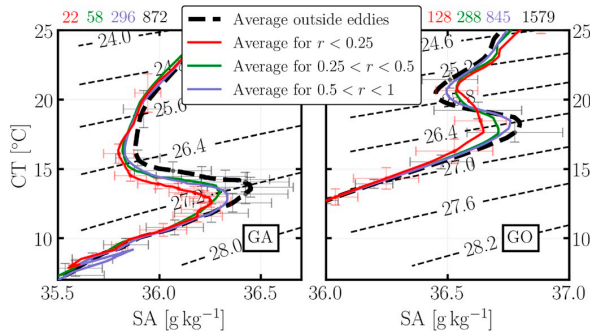


Figure 6. Averaged TS-diagrams in (left) the Gulf of Aden and (right) the Gulf of Oman. Black dashed lines indicate the mean TS-profiles outside eddies, and colored solid lines indicate the mean TS-profiles inside eddies. The color indicates the position of the Argo float with respect to the center of the eddy it was localized in. Numbers at the top of each panel indicate the number of profiles used to compute the averages. Black (resp. red) errorbars are the standard deviation of CT and SA associated with the mean profiles outside (resp. inside, $r < 0.25$) eddies.

than at their edges; also, more profiles were collected in the GO than in the GA, giving a better confidence in the results concerning the GO. The peaks on the TS-profiles corresponding to the RSOW and the PGW decrease radially inward in the eddies. Such eddies are often generated at the mouth of the gulfs, where the outflow salinity is weaker than west of the gulfs. Since these eddies propagate westward in the gulfs, they encounter saltier outflow waters (Al Saafani et al. (2007) in the GA) and thus the radial salinity difference increases. Nevertheless, due to their non uniform rotation, these eddies stir the external waters (the outflow waters) at their edge. PGW or RSOW are clearly present at the eddy rim (for $0.5 < r < 1$); a large number of profiles gives a fairly good confidence into these results (296 in the GA and 845 in the GO). Thus, the outflows are also steered by these eddies, as demonstrated in the GA by Bower et al. (2002) or Ilicak et al. (2011) and in the GO by Vic et al. (2015). Our results substantiate the idea that eddies influence the spreading of PGW and RSOW in the GO and the GA via advective processes.

Between the two Gulfs, along the southern coast of the Arabian Peninsula, we define area A, where outflows from the Red Sea and the Persian Gulf meet (see for instance Fig. 20 in Carton et al. (2012), which shows an Argo float, sampling both PGW and RSOW, near 55°E , 15°N). We confirm this by detecting weak peaks in the TS-diagram of this area at the σ_0 -levels of PGW and RSOW.

Then, we isolate the Somali Basin (area B), where in summer, the Great Whirl (GW), a large quasi-stationary eddy develops at the northern part of the Somali Current (see L'Hégaret et al. (2018) for a discussion on the circulation in this region, and Vic et al. (2014) for a description of the GW). Many water masses are present in this region; their distribution also depends on the season because of the monsoon regimes. However it has been shown that RSOW can clearly be identified there (Warren et al., 1966; Quadfasel and Schott, 1982). We observe RSOW in the TS-diagram of area B, with a peak at the 27 kg m^{-3} σ_0 -level; this peak is weaker than in the GA, showing that RSOW has been mixed with surrounding waters through its journey out of the GA.

Area C corresponds to the southeastern part of the Arabian Sea, where Bay of Bengal Water (BBW) flows into the Arabian Sea during the northern monsoon (winter), via the Northeast Monsoon Current (Kumar and Mathew, 1997; L'Hégaret et al., 2018). In the TS-diagram of this area, lighter and fresher water is detected at the surface. Its T/S properties show evidence of BBW in area C. Denser, saltier water, called Arabian Sea High-Salinity Water (ASHSW) is also found; it is formed in the north of the basin (near 20°N) in winter, and it spreads southward below the surface, on the 24 kg m^{-3} σ_0 -level (Kumar and Prasad, 1999).

A weak peak of PGW is also detected; therefore, water from the Persian Gulf may spread this far south.

Finally, we isolate the northern part of the Arabian Sea, called area D. As mentioned above, this place is the site of formation of ASHSW in winter, and we observe the presence of this water mass in the TS-diagram, with denser saltier water located in subsurface. As shown in Carton et al. (2012) (their appendix A), the salinity and the temperature at 300 m depth is larger north of 16°N , with a fairly constant zonal distribution. This pattern is mostly due to the spreading of PGW in this part of the basin. We confirm this by detecting a large peak of salinity at the σ_0 -level corresponding to the depth of stabilization of PGW in this area.

In the Arabian Sea, R_D varies meridionally and zonally. The mean values of R_D are thus different in areas A, B, C and D (Chelton et al., 1998). Therefore, the horizontal structure of eddies will be different depending on the area they lie into. In particular, areas B and C respectively have mean values of R_D of 141 and 131 km while areas A and D, have mean values of R_D of 66 and 51 km. This is due to the increase of R_D as latitude decreases. Similarly, the mean values of R_D are larger at the western boundary (area B compared to area C for instance). The Arabian Sea decomposition into specific areas we made thus takes into account these meridional and zonal gradients.

To further discuss the dynamical properties of eddies, we choose to merge the GO area and the area D, and we define a largest area representing the northern Arabian Sea (NAS area hereafter, see Fig. 5(a)). This area merging provides more Argo profiles to compute 3D composite structures of eddies. It is justified by the following observations. (1) As we can notice in Fig. 5(b), the TS-profiles of area D and GO are similar, even though the peak of PGW is weaker in area D because of its distance from the Persian Gulf. (2) In these two areas, R_D is roughly constant, with an average of about 48 km, and a standard deviation of 8 km, meaning that the horizontal properties of isolated eddies may be fairly homogeneous. (3) As mentioned above, and as shown in Fig. 6, eddies lying in the GO are most likely generated outside of the gulf. The merging of the two areas thus allows us to span the entire lifetime of eddies generated at the eastern part of the basin, and traveling westward into the GO.

3.2. Mean dynamical properties of eddies as revealed by argo floats

An outside-eddy density climatology is constructed by averaging all outside-eddy density profiles in a specific area. For each profile localized inside eddies, we compute density anomaly profiles with respect to this climatology, and we differentiate profiles collected inside a CE or AE.

As presented in Assassi et al. (2016) (see their Fig. 2), four classes of eddy may be observed: surface-intensified CE, surface-intensified AE, subsurface-intensified CE, and subsurface-intensified AE. Surface-intensified eddies are characterized by a maximum of density anomaly at the surface; positive for the CE, and negative for the AE. Subsurface-intensified eddies have a maximum density anomaly at depth. We filtered the profiles collected inside eddies depending on the depth of their maximum density anomaly. All profiles localized inside CE (resp. AE) with a maximum (resp. minimum) of density anomaly above 50 m depth are flagged as 'surface-intensified', while the profiles with a maximum (resp. minimum) between 600 m and 50 m depth are flagged as 'subsurface-intensified'. We then average anomalies depending on the distance r between the profile location and the center of the eddy (Fig. 7). We indicate in Fig. 7 the number of profiles used for each average, and the standard deviation associated with it. Notice that for some areas (e.g in the GA and surface-intensified eddies in area A, B and C), the number of profiles is weak with large standard deviations, giving a poor confidence in their density anomaly profiles. For instance in the GA the small number of profiles may lead to a bias due to the sampling of only a few eddies by Argo floats.

The density anomaly profiles obtained are in agreement with the

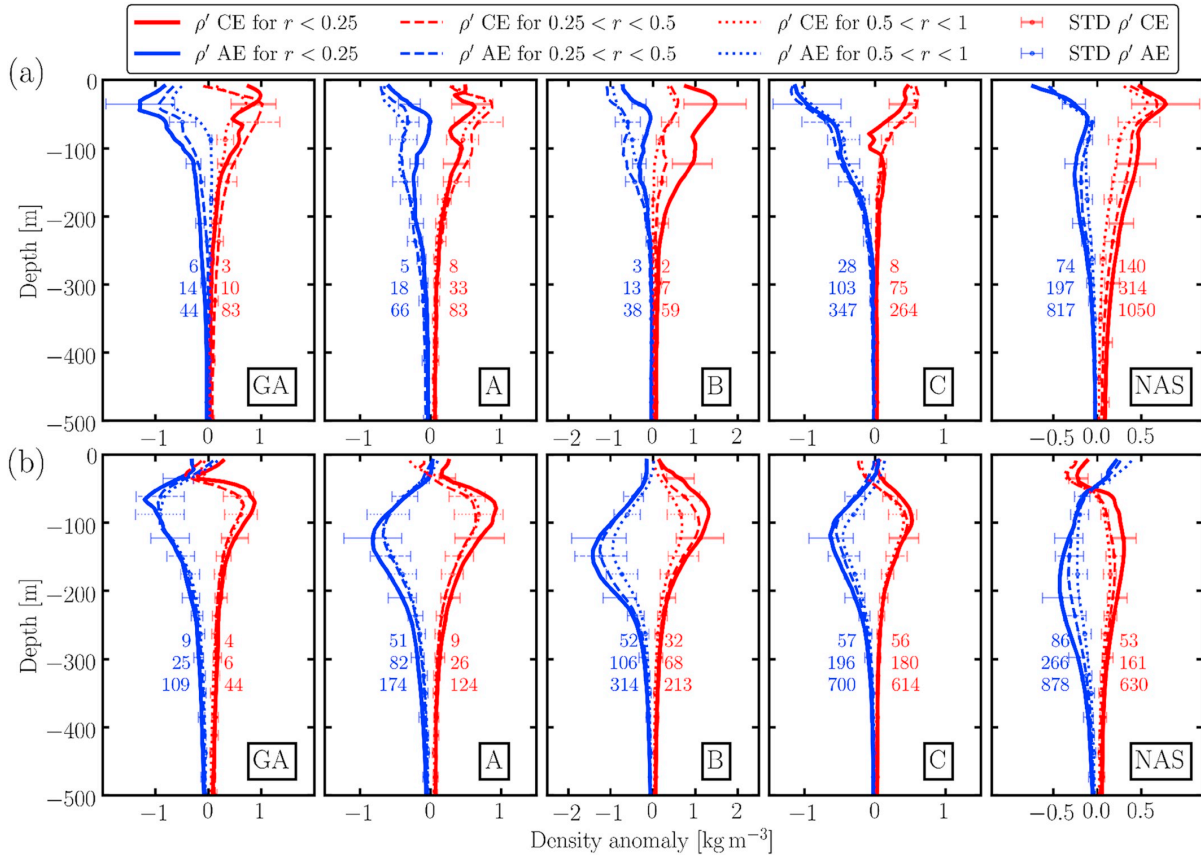


Fig. 7. Average density anomalies profiles inside (a) surface-intensified, and (b) subsurface-intensified AE (blue) and CE (red) in each area. Solid, dashed and point lines (resp. errorbars) present the averages (resp. standard deviation) for profiles colocalized at a distance $r < 0.25$, $0.25 < r < 0.5$ and $0.5 < r < 1$ from the center of the eddy it was colocalized in. Columns of numbers indicate the number of profiles used to compute the average profiles (top: $r < 0.25$, middle: $0.25 < r < 0.5$ and bottom: $0.5 < r < 1$). Notice that the x-scale of plots is not the same depending on the area. (For interpretation of the references to color in this figure legend, the reader is referred to the Web version of this article.)

standard structures of CE and AE in stratified and rotating flows (Vallis, 2017). Indeed, CE have a positive density anomaly while AE have a negative one, consistent with thermal wind balance (a surface-intensified cyclonic flow forces isopycnals to rise while an anticyclonic flow makes isopycnals dive creating respectively positive and negative density anomalies). Moreover, for each area where enough profiles were collected at the center of eddies, we clearly notice that the norm of the anomaly intensity decreases as r increases. It results from the fact that the density at the edge of eddies tends toward the climatology out of eddies.

The maximum density anomalies are observed for subsurface-intensified AE in area B, where the GW develops in summer. As shown in Trott et al. (2018), the GW has a radius and an intensity larger than those of most eddies in the Northwestern Indian Ocean. Its velocity maximum, up to 1 m s^{-1} , lies between 100 and 200 m depth (Beal and Donohue, 2013; Vic et al., 2014); at this depth, also lies the maximum of density anomaly of AE that we observe in area B.

To compute a 3D composite structure of eddies, we focus on the two categories of eddies with the highest sampling rate: surface-intensified CE and subsurface-intensified AE in the NAS. The maximum density anomaly of subsurface AE is relatively spread out there with a peak near 200 m depth, while surface-intensified CE have a well-marked peak near 30 m depth.

3.3. Isolating specific classes of eddies

We notice different spatial and seasonal patterns of eddies in the different regions (Fig. 8). In the GA, most eddies have radii between 100 and 150 km. Such eddies fill the whole Gulf of Aden, where they often form a row of alternate polarities (Bower and Furey, 2012). The size of eddies in this area is thus directly related to the size of the Gulf. Areas B and C being closer to the equator, R_D is large and so are the detected eddies in these regions (as shown for instance in Smith (2007)). In area B, we again notice the influence of the GW, with more floats colocalized during the summer and fall, in large AE (see purple line in the panel corresponding to AE with radii $R_D < R < 3 R_D$ in Fig. 8).

Nevertheless, most colocalized floats were found in eddies of radii $R_D < R < 3 R_D$, regardless of the region. Indeed, AMEDA more accurately detects eddies larger than R_D (Le Vu et al., 2018). The upper boundary ($3 R_D$) for single eddy detection is associated with eddy interactions, such as eddy merger or splitting into smaller ones, or dissipation by interaction with topography. Splitting and topographic bottom friction reduce the lifetime of eddies with large radii while merging extends it.

Hereafter, we focus on the region with the highest sampling rate by Argo floats: the northern Arabian Sea (NAS). We exclude eddies with radii smaller than R_D because these small eddies may result from

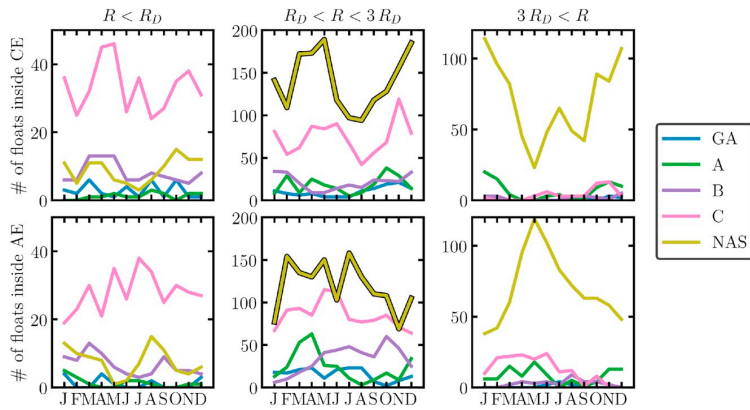


Fig. 8. Number of colocalized Argo stations, depending on the period of the year, the area and the radius of the eddy in which the float is colocalized, for CE (top row) and AE (bottom row). Each column corresponds to a different range of eddy radius. Colors indicate the area in which the eddy is located. The black contoured yellow lines correspond to the floats we consider to compute the composite structures. Notice that the y-scales are not the same depending on the radius classes. (For interpretation of the references to color in this figure legend, the reader is referred to the Web version of this article.)

detection errors, and may have dynamics more transient than that of larger mesoscale eddies. Eddies larger than $3 R_D$ are also excluded to avoid the inclusion of contours surrounding multiple close eddies. In the NAS we can also construct a generic 3D eddy shape during the whole year, since the number of floats colocalized is large throughout the year (>100 per month).

3.4. The 3D structure of eddies in the northern Arabian Sea

3.4.1. Composite structure

We search for a possible generic 3D structure of surface-intensified CE and subsurface-intensified AE with $R_D < R < 3 R_D$ in the NAS area,

by using the colocalized Argo profiles in such eddies. This represents 531 profiles for CE and 1130 profiles for AE.

The final composite 3D dynamical structures of typical CE and AE in the NAS are presented in Fig. 9(top row). CE have a maximal velocity localized at the surface, with a peak value of azimuthal velocity reaching 0.3 m s^{-1} near $r \sim 0.5$. AE are weaker, with a peak value of azimuthal velocity of about 0.2 m s^{-1} near 50 m depth and $r \sim 0.9$. Note that these structures do not correspond to all eddies in this area, but to an average shape of eddies. We finally notice that both CE and AE have a deep-reaching dynamical influence, with a velocity signature down to a thousand meters.

PGW and ASHSW are observed in the core of AE and CE. The mean

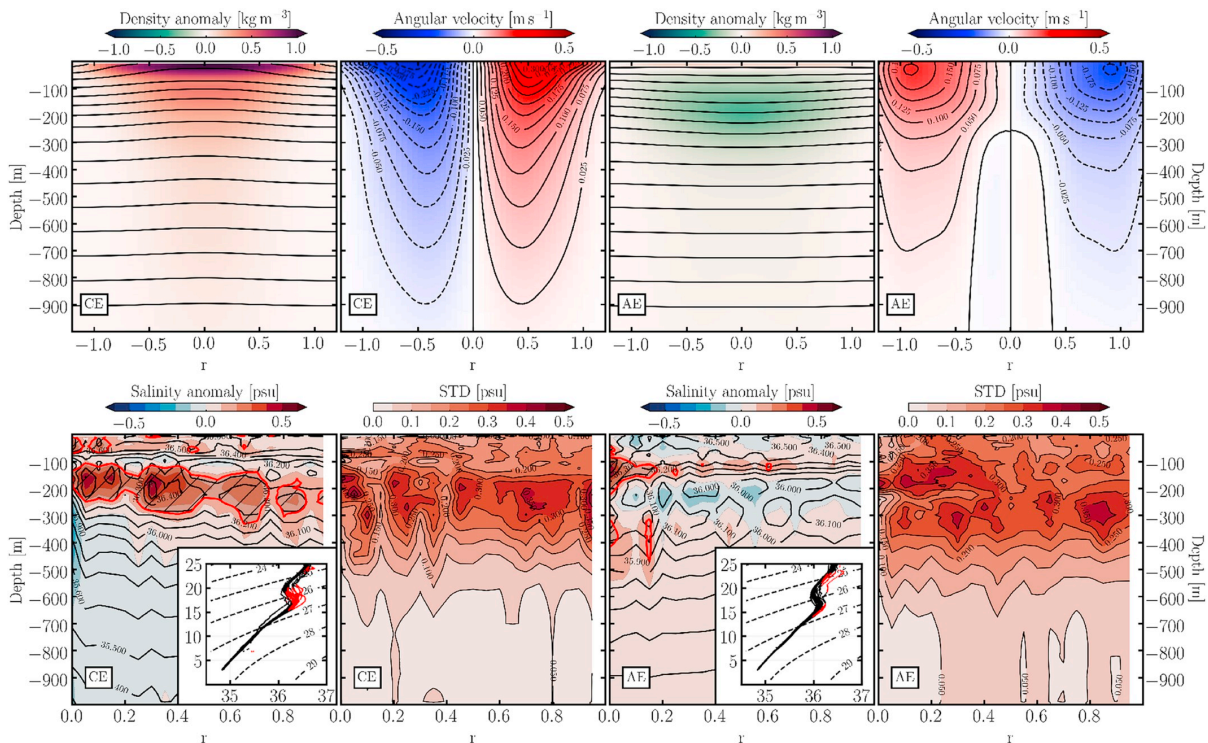


Fig. 9. 3D composite structure of eddies in the NAS area computed using 531 Argo profiles for the CE and 1130 ones for the AE. (top row) Anomaly of density (black contours indicate isopycnals separated of 0.5 kg m^{-3}) and angular velocities for CE and AE. (bottom row) Sections of salinity anomalies (with contours of salinity superposed) and standard deviation of salinity. Inserts are TS-diagram for the profiles of the composite structures. Dashed areas indicates areas with a salinity greater than 0.15 psu, also indicated with the red dots in the TS-diagrams.

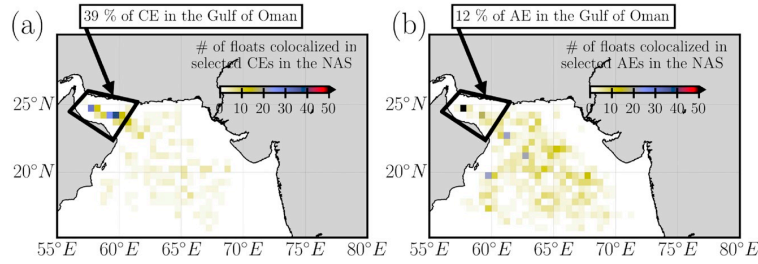


Fig. 10. Distribution of the position of eddies considered to compute the 3D composite (a) surface-intensified CE, and (b) subsurface-intensified AE, in the NAS. The black polygon indicates the area in which 39% of CE and 12% of AE were found.

salinity sections in CE and AE are computed within eddies: $S(r, z)$ (as explained in 2.5). Removing the average vertical distribution of salinity in the area gives salinity anomalies (Fig. 9). In both CE and AE, salinity anomalies and their associate standard deviations indicate the presence of ASHSW and PGW between the surface and 500 m depth (see TS-diagrams inserts in Fig. 9).

In CE, the ASHSW is found very close to the surface, above 50 m depth, and the PGW between 100 and 300 m depth. On the other hand, the water masses detected in AE are deeper than in CE because of the diving of isopycnals, with a PGW signature near 400 m depth. The signature of ASHSW is stronger while the signature of PGW is weaker than inside CE. Indeed, more CE were found near the Strait of Hormuz (39% of them in the Gulf of Oman), where the PGW is diluted, whereas only 12% of AE were found there (Fig. 10). Because we selected a large area to compute the composite structures, these 3D profiles present a large standard deviation, as shown in Fig. 9. This is due to the large number of eddies generated (and detected, see Fig. 10) along the eastern boundary of the Arabian Sea and propagating into the Gulf of Oman.

An estimation of the error between the initial Argo profiles and the composite structure is shown in Fig. 11. It is calculated on the density anomaly profiles where it reaches a peak, at 20 m depth for the CE and 200 m depth for the AE. The error thus obtained is related to the heterogeneity of the Argo floats positions, the intensity variation of

sampled eddies and their ellipticity (see Appendix D for its estimation). CE have a median error of 31% and AE of 56%. The larger this error is, the more the composite fails in representing the density anomaly sampled by a given Argo float. Both composites have large errors due to some profiles with very low density anomalies. This could be due to the fact that we did not consider the seasonal variability in our calculation, leading to some misevaluations of density anomalies. However, with a smaller error, the composite CE can be more trusted than the composite AE, and fairly represents the density anomalies of most of the 531 profiles used to compute it.

Surface velocities obtained from altimetry and surface drifters show accordingly good agreement with the surface angular velocity of the composite 3D structures of eddies, see Fig. 12. The surface geostrophic velocities collected during the colocalization of surface drifters with altimetry (see 2.4) are projected into an angular and a radial component with respect to each eddy. The angular component is then averaged in bins of width $dr = 0.05$ as for the density profiles. The relative error (see Fig. 12) shows that our calculation provides a fair estimate of the velocities in the ocean interior as well as at the surface. In particular, the agreement with the data is very good at the vortex edge ($r > 0.5$) with an error $< 25\%$, where structures are best sampled. At the eddy center the error is related as much to the inaccuracy in positioning the center as to the small number of Argo profiles.

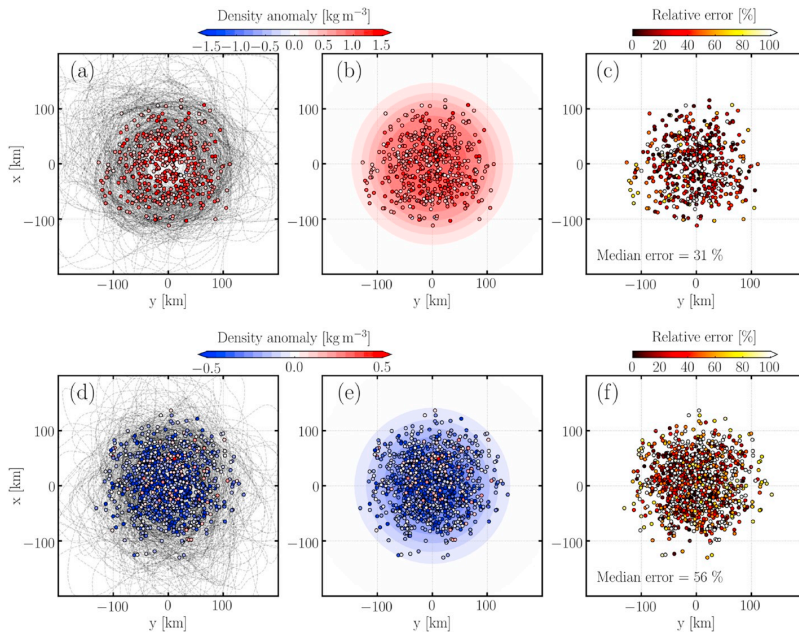


Fig. 11. Estimation of the error on the density anomaly between the composite CE (top) and AE (bottom), and the Argo profiles used for the creation of the composites. (a) (resp. (d)) Values of the density anomaly where it is maximal, at 20 m depth (resp 200 m) from the Argo profiles used to compute the composite CE (resp. AE). The perimeters of half the eddies considered for the creation of the composite are presented in thin dashed gray lines. (b,e) Same values of density anomalies as in (a,d), superposed over the density anomaly field of the composite at the same depth. Notice that the color-scale is different between CE and AE. The horizontal extension of the composites have been re-dimensionalized by the mean radius of eddies used for the creation of the composite, which is about 120 km for both CE and AE. (c,f) relative Root Mean Square Error between the value of density of the Argo profile, and of the composite at the same location. (For interpretation of the references to color in this figure legend, the reader is referred to the Web version of this article.)

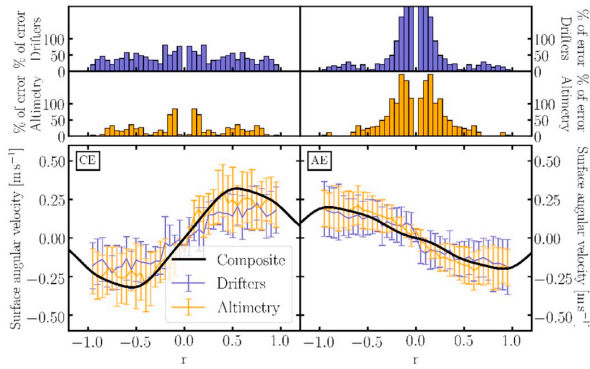


Fig. 12. Comparison between the surface velocity of the composite eddies and altimetric and drifter data. (top) Percentage of error between the composite eddy and data. (bottom) Angular velocity for each dataset. Errorbars are standard deviations in each bin. The velocity estimation from the altimetric (resp. surface drifters) data is computed using 531 (resp. 834) values for CE and 1130 (resp. 889) for AE. The maximum of error between the composite AE and the drifter data reaches 500% at the center of the eddy.

3.4.2. A particular cyclone in the Gulf of Oman

We compare the composite structure with a particular eddy detected in the Gulf of Oman. This eddy carried PGW in its core, and had a deep dynamical influence. It was detected via altimetry near the Strait of Hormuz (see Fig. 13(a)) nearly continuously for about a year. Its shape did not vary much during that time (see Fig. 13(b)), and an Argo float was trapped in it for about 40 cycles (*i.e.* 40 consecutive data transmissions).

Argo profiles in the eddy indicate that PGW is trapped in the core of the eddy. Indeed, the TS-diagram (Fig. 13(c)) peaks near 26.5 kg m^{-3} indicating a salty water with the same characteristics as those discussed in Fig. 5(b) for the GO. This water mass is located around 200 m depth (see the salinity profiles in Fig. 13(d)), as predicted by the 3D composite structure of salinity (Fig. 9 or Fig. 13(d)) and as discussed in Bower et al. (2000). The salinity signature of PGW can thus be well described by the 3D composite structure. Nevertheless, the salinity anomaly is greater than the salinity anomaly of the composite eddy. Indeed, the mean salinity near the Strait of Hormuz is larger than its climatological value in the NAS area. The occurrence of layering in salinity profiles in the eddy is likely due to stirring of the eddy water with ambient water (see for instance L'Hégaret et al. (2016) and Fig. 13(d)). We computed the difference between these salinity profiles and the profiles smoothed with a Gaussian kernel (the smoothing length is about 50 m) to

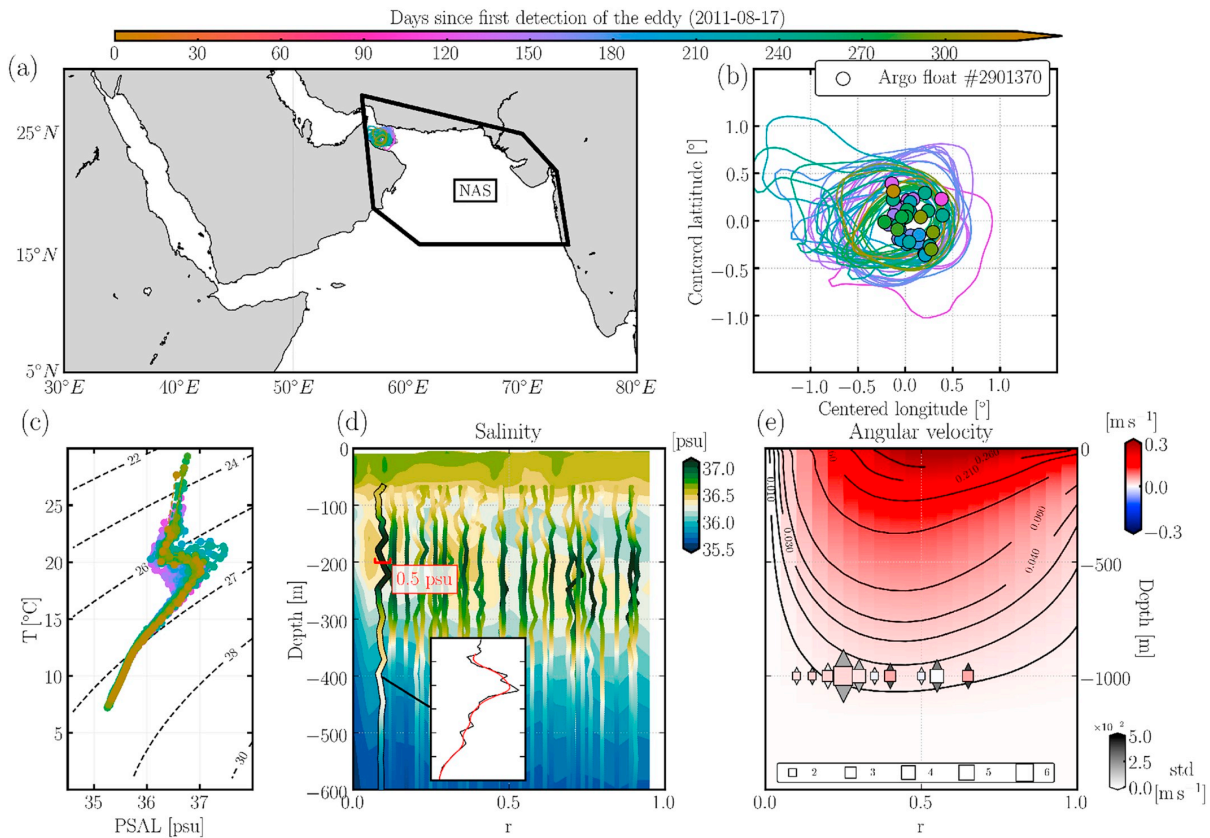


Fig. 13. Study of a particular CE in the Gulf of Oman. (a) Position of the eddy. (b) Evolution of the shape of the eddy, and position of the colocalized Argo float. (c) TS-diagram from profiles collected by the Argo float. The colorbar indicating the lifetime of the eddy when profiles are collected is used for (a), (b) and (c). (d) Profiles of salinity collected by the float superposed on the composite structure of salinity. Variations around these radial positions are the differences between the raw profiles (black line in insert) and a smoothed profiles (red line in insert). (e) Angular velocity of the Argo float with respect to the center of the eddy, compared with the composite structure of CE in the area. Each value of angular velocity is averaged in a bin of size $dr = 0.05$, the number of values used for the average is indicated by the size of the square and the standard deviation associated with the values is indicated by the color of the arrows. Note that the maximum depths of (d) and (e) are different.

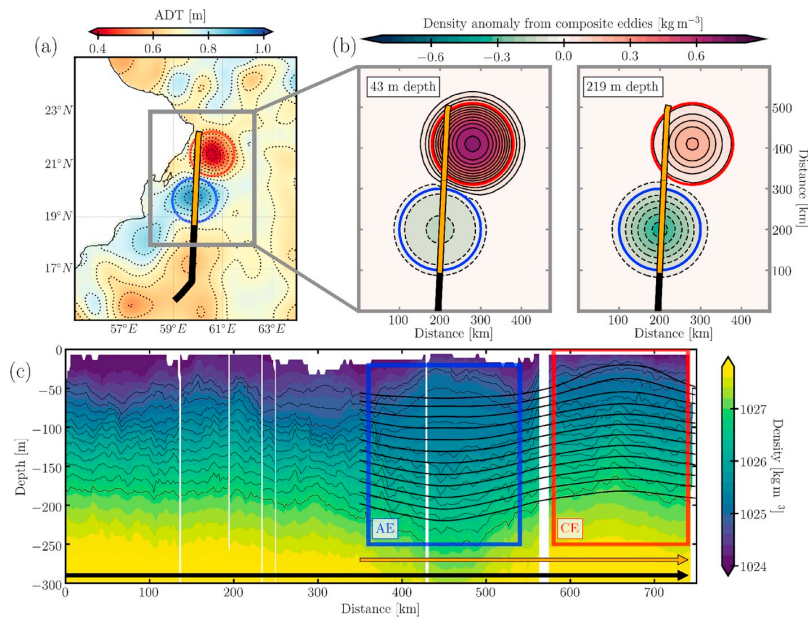


Fig. 14. Reconstruction of the 3D density field sampled during the Phys-Indien 2011 experiment. (a) ADT from altimetric data, location of the Phys-Indien transect and horizontal extension of composite eddies. (b) Density anomaly of the 3D reconstructed density field on 2 depth levels. (c) Vertical section of density. Thin black contours are contours of density from 1024.7 to 1026.9 kg m^{-3} every 0.2 kg m^{-3} from the Phys-Indien measures, while bold black contours are the same contours from the reconstructed field of density. Black and orange arrows show the length of sections presented in. Blue (resp. red) rectangle indicate the position of the AE (resp. CE). (For interpretation of the references to color in this figure legend, the reader is referred to the Web version of this article.)

highlight the spatial variations of salinity, see Fig. 13(d). Salinity steps at about 50 m depth exhibit jumps up to 1 psu. Such layering has already been observed in the same region; it may be due to different processes: double diffusion (Ghazi et al., 2017; Azizpour et al., 2017), salt fingering, convective diffusion (Schmitt, 1994), stirring by the eddy flow or breaking of internal waves generated on the shelf. Salt mixing in and near the eddies is thus responsible in part for the salinity distribution in the composite eddy.

The deep motion of the localized Argo float is consistent with a deep velocity of the CE, see Fig. 13(e). Since the float is parked at 1000 m depth during its drift, we can estimate the velocity at this depth. We compute the angular velocity of the float in the frame of reference of the eddy (see Appendix B). The float angular velocity is positive. Thus, it appears to be advected by the eddy even if lying at 1000 m depth. The magnitude of this velocity is in good agreement with the values predicted at this depth by the 3D composite structure of CE (though the standard deviation of this velocity is large and the velocity is weak). Physical processes such as topographic or coastal waves or deep gravity flows, or methodological problems (see Appendix B) can weaken this conclusion.

3.4.3. A specific dipole off the coast of Oman

We compute a vertical section from a 3D density field reconstructed with the composite shapes of AE and CE (see Appendix C). It shows good agreement with the section collected during the Phys-Indien experiment in 2011 by the SeaSoar, see Fig. 14(c). The bending of isopycnals associated with the CE is similar in the two cases, showing that our representation of CE in the area is consistent with observations. For the AE, though the bending of isopycnals at the bottom seems to match between the generic profile and the observed one, the vertical spacing between isopycnals near 100 m depth is not similar. Indeed, in the *in situ* measurement, the AE exhibits a positive anomaly of density at this depth resulting in a bending of isopycnals opposite to the composite AE. These differences are likely due to the fact that the AE observed in 2011 was deeper and more intense than the composite one, with an ADT anomaly about 4 times larger than the mean ADT of eddies we used to compute the composite AE. The method we used to compute the composite eddies did not take into account the reversal of the isopycnal bending, because we only consider profiles with a density anomaly

minimum localized at depth. To fit with the AE sampled in 2011, another criterion should be set to isolate eddies with large positive density anomaly at the surface, but this would discard a lot of profiles.

4. Discussion

We analyzed the thermohaline properties of the Arabian Sea eddies using about 30,000 Argo profiles during the 2000–2015 period, and we confirmed observations made in previous studies (e.g. Warren et al. (1966), Quadfasel and Schott (1982), Bower et al. (2000), Bower and Furey (2012) Carton et al. (2012), L'Hégaret et al. (2016)). The ASHSW is observed near its generation site (20°N), spreading towards the southeastern part of the Basin. In this latter region, the BBW coming from the Bay of Bengal is also observed. The RSOW is observed in the GA and in the southwestern part of the Arabian Sea: the Somali Basin and the southeastern coast of the Arabian Peninsula. Similarly, we observe the spreading of PGW in the GO and in the northern part of the basin (north of 16°N), with a high salinity (up to 39 psu) between the 26 and the 27 kg m^{-3} σ_θ -levels. A weak signature of PGW is also spotted in the southeast, suggesting that this water mass can spread out far from the Strait of Hormuz.

We added to the previous studies mentioned above the automatic identification of profiles in or out of eddies. It allowed us to discuss the average thermohaline properties inside eddies in comparison to those outside. The salinity anomaly corresponding to the signature of RSOW (resp. PGW) is on average larger out of the eddies than in their core when considering only the GA (resp. GO). Mesoscale eddies in the gulfs have thermohaline properties of the water masses out of the gulfs, consistent with a generation in the Arabian Sea.

Then, we focused on a larger area, from the GO to the Indian coast, where most Argo profiles were found. In this area, as previously shown in Carton et al. (2012), we observe intense PGW at depth. We investigated the mean thermohaline and dynamical properties of mesoscale surface-intensified CE and subsurface-intensified AE by computing the 3D composite profiles of eddies. We showed that eddies carry in their core a significant amount of PGW between 200 m and 400 m depth. This contrasts with the previous finding that in the GO, the PGW is preferentially found at the edge of eddies. This difference is due to the inhomogeneous sampling by Argo floats of the NAS and the eddies in

this region. Indeed, 52% (resp. 30%) of the profiles used for the composite salinity calculation with $r < 0.25$ (resp. $0.5 < r < 1$) were collected in the GO, in particular close to the Straits of Hormuz (see Table 1). Thus, the core of the composite eddy mostly represents the northwestern GO eddies, while its edge mostly represents the southwestern eddies of the NAS (in area D). Because we compute salinity anomalies with respect to the background climatology of the whole NAS, the composites exhibit intense salinity anomalies at their center. They are on average 0.4 psu in the CE core, with a standard deviation of about 0.3 psu. For the AE, the average salinity anomaly is much weaker, about 0.2 psu, but with a standard deviation up to 0.35 psu in the whole core of the eddy. Moreover, PGW is on average found preferentially in the core of CE than in AE. This is most likely due to the fact that (1) at the Strait of Hormuz where PGW is concentrated, more CE are found (e.g the cyclone discussed in section 3.4, and as shown in Fig. 10); and (2) the cyclone of the Ras Al Hadd's dipole is long lasting and can trap more concentrated PGW than its paired anticyclone (L'Hégaret et al., 2015), because it is closer to the Strait of Hormuz. This situation with a CE near the Strait of Hormuz and a dipole near Ras Al Hadd's can be seen in Fig. 2(d).

Though the area we considered is large, we could extract a composite 3D dynamical structure of eddies in the NAS that is fairly consistent with geostrophic velocities computed via the altimetry, the currents speed measured by surface drifters, and with *in situ* sampling of mesoscale eddies. These composites provide an estimate of the velocity field induced by eddies in the water column, from 1500 m up to the surface. Our results suggest that, on average, CE have a larger angular velocity than AE with a maximum of about 0.3 m s^{-1} for CE and of about 0.2 m s^{-1} for AE. The profiles of density anomalies in AE show that, on average, they are subsurface-intensified, with an angular velocity increasing from the surface to 50 m depth and vanishing at depth. Since we used a 3D method, our estimation of the typical maximal velocity of AE in this region is thus more accurate than if we only considered a surface-only product (e.g an altimetric dataset). CE are surface-intensified, and their maximum velocity is at the surface. Nevertheless, the estimated error of these composites is important, respectively 31% and 56% for the CE and the AE. It indicates that these composites do not represent all eddies in the area, and that mesoscale eddies in the NAS can have significantly different properties than the composites we present here.

5. Conclusion and future work

To summarize and to answer the questions we initially asked: this study aimed at extracting and characterizing the 3D structure of eddies in the Arabian Sea with a combined approach using altimetric data and Argo floats. Eddies were detected in the whole Arabian Sea and in adjacent gulfs using AMEDA, but the distributions of Argo floats and surface drifters were heterogeneous. With this dataset, we confirmed previous studies concerning the distribution of the important water masses in the different sub-basins of the region, and discussed the mean stratification one may find in eddies depending on the area (our first question). We then used a composite approach to find the mean 3D structure of mesoscale eddies of the NAS (our second question). We focus only on surface-intensified CE and subsurface-intensified AE, with

a radius $R_D < R < 3 R_D$, as these two categories had the greatest sampling/least error. This allowed us to extract composite 3D dynamical and thermohaline structures which are representative of these two types of eddies in the NAS. However, the composite CE can be more trusted than the composite AE, since its relative error is smaller. We show that the PGW is found at the edges of eddies in the GO, indicating a spreading of this water mass by stirring process, and in the core of eddies averaged in the whole NAS, indicating a possible trapping of this water mass out of the GO (our third question).

Our 3D computation will be improved in the future when more Argo floats are deployed in the Northern Indian Ocean. With more floats (combined with available altimetric products), the computation of statistically-robust composite structures will be possible in other parts of the Arabian Sea such as the Gulf of Aden. In addition, with the recent initiation of the Biogeochemical Argo program, biological parameters will be available (Gruber, 2010). Equivalent 3D composite structures such as the one discussed in this paper may thus be computed (using the same method of colocalization) for oxygen or chlorophyll and may determine the potential impact of eddies on biological activity.

A possible use of 3D structures as the one we extracted may be the reconstruction of an eddy-induced 3D density field in an area where the circulation is mainly driven by the mesoscale activity (e.g the Gulf of Aden or Oman). Such reconstruction may be done systematically by identifying each surface-detected eddy with a 3D structure computed from eddies of the same polarity, radius, location and depth of intensification, and use a similar reconstruction procedure as the one discussed in C. The applications of such a reconstruction are numerous and of possible great interest. As an example, this may allow us to use Lagrangian advection procedure on the resulting 3D velocity field to quantitatively estimate the contribution of eddies in the transport of tracers. Another example may be to isolate fine structures in transects (e.g submesoscale fronts or vortices, internal waves ...) by removing the contribution of mesoscale eddies.

The reconstruction of such 3D field requires an intensive sampling on the vertical to compute enough 3D composite structures which are representative of all eddies in an area. In the future, enough floats will allow us to measure in real time the structure of all eddies detected by satellite and to reconstruct their real time vertical structure.

Acknowledgments

This work was funded by the Direction Générale de l'Armement (DGA) via a full grant for Charly de Marez's PhD. We gratefully acknowledge B. Le Vu and A. Stegner's help, who provided the eddy detection algorithm AMEDA and its output on the Arabian Sea. AMEDA has been developed under the funding of the ANR-Astrid Project DYNED-Atlas (ANR 15 ASMA 0003 01). The altimeter products were produced by SSALTO/DUACS and distributed by AVISO, with support from CNES. This work is also a contribution to PRC 1069 'Meso and submesoscale vortices in the Atlantic and Indian Ocean', funded by CNRS and RFBR. The authors thank the five anonymous reviewers whose remarks widely improved the contents of this paper. In order to encourage readers to bring the 3D generic structure of eddies to life, the 3D field of the different quantities we computed are available with this paper (de Marez et al., 2019).

Appendix A. Formal error of the altimetric product

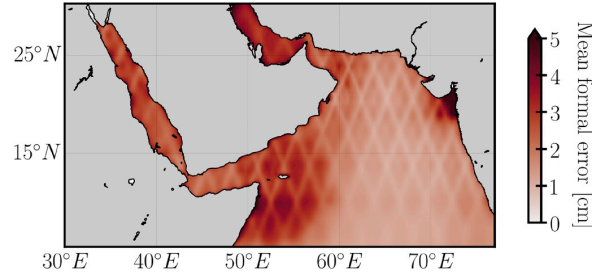


Fig. A.15. Formal mapping error of the altimetric product, averaged over the 2000–2015 period. It represents a purely theoretical mapping error which traduces errors induced by the constellation sampling capability and consistency with the spatial/temporal scales considered. For more details, see [Le Traon et al. \(1998\)](#).

Appendix B. Calculation of the deep velocity of an Argo float

We present the velocity computation of a specific Argo float (2901370) during its deep drift. Thus we can compare the 3D composite structure of eddies in the NAS with the Lagrangian advection of Argo float #2901370 by a particular eddy.

We start by positioning the float in the frame of reference of the drifting eddy: at each surfacing of the float, we remove the position of the eddy center at this date. This allows to remove the eddy drift velocity component from the deep velocity of the float. Then we calculate the Euclidean distance between surfacing positions every 5 days. Assuming that the Argo float trajectory is straight between two surfacings provides an estimate of the deep velocity of the float $\mathbf{u}^f = (u_x^f, u_y^f)$, with u_x^f (resp. u_y^f) the zonal (resp. meridional) component. Note that this assumption could lead to an under-estimation of the float velocity since its actual trajectory may be bent. Because distances between positions were computed in the frame of the eddy, \mathbf{u}^f is the relative velocity of the float with respect to the eddy.

The velocity of the float \mathbf{u}^f is then projected on an azimuthal and a radial component $(u_r^f, u_\theta^f) = (|\mathbf{u}^f| \cos \alpha, |\mathbf{u}^f| \sin \alpha)$, where α is the angle between the orientation of \mathbf{u}^f and the line between the center of the eddy and the Argo position. On average, $u_r^f = O(10^{-3}) \text{ m s}^{-1}$ and $u_\theta^f = O(10^{-2}) \text{ m s}^{-1}$ such that $u_r^f \ll u_\theta^f$. The deep velocity of the float is thus mostly azimuthal.

This deep velocity is computed between two successive surfacings, at a distance dR from the center of the eddy, which is then normalized by the local radius of the eddy (on average, $R \sim 53 \text{ km}$), giving the dimensionless position of this velocity measurement r . This calculation is similar to that discussed in section 2.5 for the positioning of Argo profiles. The angular component u_θ^f is finally averaged in bins of width $dr = 0.05$. If we assume that the float is only advected by the eddy, we can thus compare this deep azimuthal velocity with the composite CE in this area, see Fig. 13(e).

We remain cautious on the accuracy of this procedure. Firstly, the velocity of the float may be over-estimated because while transmitting its data, it drifts at the surface, advected by surface currents and/or wind. The value of the velocity may also be impacted by the errors in positioning the center of the eddy. Finally, as discussed in [Ollitrault and Rannou \(2013\)](#) the depth of Argo floats may be inaccurate, and it may vary substantially. Here we only know that the 1000 m parking depth (as indicated on the Coriolis website, bit.ly/2DtltM4) is consistent with the bathymetry of about 1200 m depth; thus we set the depth of drift to 1000 m.

Appendix C. Reconstruction of an instantaneous 3D density field

We present here the 3D density field reconstruction from the composite structures we computed in the NAS. This reconstruction was done to match a large anticyclone centered at 60°E , 20°N and a cyclone at 60.5°E , 21.5°N , sampled during the Phys-Indien experiment in 2011 along the Omani coast (see Fig. 14(a)). We assumed that the density field sampled by the Seasoar was only affected by the two eddies.

The reconstruction is done by executing the following steps. (1) We re-dimensionalize the radial coordinate of density anomalies presented in Fig. 9 with the estimated radii of the observed AE and CE, about 100 km (2) Because we assumed axisymmetry, the density anomaly in Cartesian coordinates is computed by rotating the (only-)radially-varying density anomaly field around the center. (3) We add up the AE and CE density anomalies at the estimated positions of the 2 eddies on a Mercator projection (see red and blue circles in Fig. 14(a) and (b)). This gives a 3D field of density anomaly with a horizontal distribution comparable with the Phys-Indien sampled eddies. (4) We finally add the density climatology of the NAS to represent the mean stratification.

Appendix D. Estimation of the ellipticity of sampled eddies

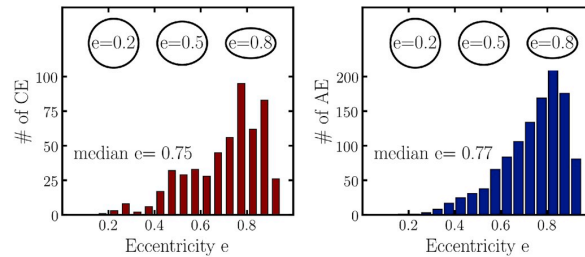


Fig. D.16. Eccentricity of the contour of CE (left) and AE (right) used to compute the 3D composite eddies presented in Fig. 9. Insert ellipses indicate the shape of ellipses for three values of eccentricity.

The eccentricity of a given eddy, describing its ellipticity, is computed by fitting an ellipse on its contour. This gives the semi-major and minor axes a and b . The eccentricity is then computed using the usual definition $e = \sqrt{1 - \left(\frac{b^2}{a^2}\right)}$. The distributions of the eccentricity of eddies used to compute the composite CE and AE are presented in Fig. 16. It shows that the median eccentricity of eddies considered is about 0.75. The composite structure computed in our study is thus a first approximation of the actual mean eddy which should be elliptic.

References

- Al Saafani, M.A., Shenoi, S.S.C., Shankar, D., Aparna, M., Kurian, J., Durand, F., Vinayachandran, P.N., 2007. Westward movement of eddies into the gulf of aden from the Arabian Sea. *J. Geophys. Res.* 112. <https://doi.org/10.1029/2006JC004020>.
- Argo, 2019. Argo Float Data and Metadata from Global Data Assembly Centre (Argo GDAC). SEANOE <https://doi.org/10.17882/42182>. <https://www.seanoe.org/data/00311/42182/> 2019-06-26.
- Assassi, C., Morel, Y., Vandermeersch, F., Chaigneau, A., Pegliasco, C., Morrow, R., Colas, F., Fleury, S., Carton, X., Klein, P., Cambra, R., 2016. An index to distinguish surface and subsurface intensified vortices from surface observations. *J. Phys. Oceanogr.* 46 (8), 2529–2552. <https://doi.org/10.1175/JPO-D-15-0122.1>. 0022-3670, 1520-0485.
- Azizpour, J., Chegini, V., Siadatmousavi, S.M., 2017. Seasonal variation of the double diffusion processes at the Strait of Hormuz. *Acta Oceanol. Sin.* 36, 26–34. <https://doi.org/10.1007/s13131-017-0990-6>.
- Beal, L.M., Donohue, K.A., 2013. The Great Whirl: observations of its seasonal development and interannual variability. *J. Geophys. Res.: Oceans* 118, 1–13. <https://doi.org/10.1029/2012JC008198>.
- Bower, A.S., Furey, H.H., 2012. Mesoscale eddies in the gulf of aden and their impact on the spreading of Red Sea outflow water. *Prog. Oceanogr.* 96, 14–39. <https://doi.org/10.1016/j.pocan.2011.09.003>. URL: <https://linkinghub.elsevier.com/retrieve/pii/S0079661111001145>.
- Bower, A.S., Hunt, H.D., Price, J.F., 2000. Character and dynamics of the Red Sea and Persian gulf outflows. *J. Geophys. Res.: Oceans* 105, 6387–6414. <https://doi.org/10.1029/1999JC900297>.
- Bower, A.S., Fratantoni, D.M., Johns, W.E., Hartmut, P., 2002. Gulf of aden eddies and their impact on Red Sea water. *Geophys. Res. Lett.* 29. <https://doi.org/10.1029/2002GL015342>.
- Carton, X., L'Hégaret, P., Baraille, R., 2012. Mesoscale variability of water masses in the Arabian Sea as revealed by Argo floats. *Ocean Sci.* 8, 227–248. <https://doi.org/10.5194/os-8-227-2012>. URL: <https://www.ocean-sci.net/8/227/2012/>.
- Chaigneau, A., Le Texier, M., Eldin, G., Grados, C., Pizarro, O., 2011. Vertical structure of mesoscale eddies in the eastern South Pacific Ocean: a composite analysis from altimetry and Argo profiling floats. *J. Geophys. Res.* 116. <https://doi.org/10.1029/2011JC007134>.
- Chelton, D.B., deSzoeke, R.A., Schlax, M.G., El Naggar, K., Siwertz, N., 1998. Geographical variability of the first baroclinic Rossby radius of deformation. *J. Phys. Oceanogr.* 28, 433–460. [https://doi.org/10.1175/1520-0485\(1998\)028<0433:GVOTFB>2.0.CO;2](https://doi.org/10.1175/1520-0485(1998)028<0433:GVOTFB>2.0.CO;2).
- Chelton, D.B., Gaube, P., Schlax, M.G., Early, J.J., Samelson, R.M., 2011. The influence of nonlinear mesoscale eddies on near-surface oceanic chlorophyll. *Science* 334, 328–332. <https://doi.org/10.1126/science.1208897>. <http://www.sciencemag.org/cgi/doi/10.1126/science.1208897>.
- de Marez, C., L'Hégaret, P., Morvan, M., Carton, X., 2019. On the 3d Structure of Eddies in the Arabian Sea. <https://doi.org/10.1016/j.dsr.2019.06.003>.
- do Rosario Gomes, H., Goes, J.I., Matondkar, S.G.P., Buskey, E.J., Basu, S., Parab, S., Thoppil, P., 2014. Massive outbreaks of Noctiluca scintillans blooms in the Arabian Sea due to spread of hypoxia. *Nat. Commun.* 5. <https://doi.org/10.1038/ncomms5862>. <http://www.nature.com/articles/ncomms5862>.
- Dong, C., McWilliams, J.C., Liu, Y., Chen, D., 2014. Global heat and salt transports by eddy movement. *Nat. Commun.* 5. <https://doi.org/10.1038/ncomms4294>. <http://www.nature.com/articles/ncomms4294>.
- Durack, P.J., Wijffels, S.E., 2010. Fifty-year trends in global ocean salinities and their relationship to broad-scale warming. *J. Clim.* 23, 4342–4362. <https://doi.org/10.1175/2010JCLI3377.1>. <http://journals.ametsoc.org/doi/abs/10.1175/2010JCLI3377.1>.
- Findlater, J., 1969. A major low-level air current near the Indian Ocean during the northern summer. *Q. J. R. Meteorol. Soc.* 95, 362–380. <https://doi.org/10.1002/qj.49709540409>.
- Fischer, A.S., Weller, R.A., Rudnick, D.L., Eriksen, C.C., Lee, C.M., Brink, K.H., Fox, C.A., Leben, R.R., 2002. Mesoscale eddies, coastal upwelling, and the upper-ocean heat budget in the Arabian Sea. *Deep Sea Res. Part II Top. Stud. Oceanogr.* 49, 2231–2264. [https://doi.org/10.1016/S0967-0645\(02\)00036-X](https://doi.org/10.1016/S0967-0645(02)00036-X). <http://linkinghub.elsevier.com/retrieve/pii/S096706450200036X>.
- Ghazi, E., Bidokhti, A.A., Ezam, M., Azad, M.T., Hassanzadeh, S., 2017. Physical properties of Persian gulf outflow thermohaline intrusion in the Oman sea. *Open J. Mar. Sci.* 07, 169–190. <https://doi.org/10.4236/ojms.2017.71013>.
- Gill, A.E., 2016. *Atmosphere Ocean Dynamics*. Elsevier.
- Gruber, N., 2010. Adding oxygen to Argo: developing a global in situ observatory for ocean deoxygenation and biogeochemistry. *Proceedings of OceanObs'09: Sustained Ocean Observations and Information for Society*. European Space Agency, pp. 432–441. <https://doi.org/10.5270/OceanObs09.cwp.39>. <http://www.oceanobs09.net/proceedings/cwp/cwp39>.
- Ilicak, M., Özgökmen, T.M., Johns, W.E., 2011. How does the Red Sea outflow water interact with gulf of aden eddies? *Ocean Model.* 36, 133–148. <https://doi.org/10.1016/j.ocemod.2010.10.006>. <https://linkinghub.elsevier.com/retrieve/pii/S1463500310001629>.
- Ioannou, A., Stegner, A., Le Vu, B., Taupier-Letage, I., Speich, S., 2017. Dynamical evolution of intense irapetra eddies on a 22 Year long period. *J. Geophys. Res.: Oceans* 122, 9276–9298. <https://doi.org/10.1002/2017JC013158>.
- Keppeler, L., Cravatte, S., Chaigneau, A., Pegliasco, C., Gourdeau, L., Singh, A., 2018. Observed characteristics and vertical structure of mesoscale eddies in the southwest tropical pacific. *J. Geophys. Res.: Oceans* 123, 2731–2756. <https://doi.org/10.1002/2017JC013712>.
- Kumar, P.H., Mathew, B., 1997. Salinity distribution in the Arabian Sea. *Indian J. Mar. Sci.* 27, 1–27.
- Kumar, S.P., Prasad, T.G., 1999. Formation and spreading of Arabian Sea high-salinity water mass. *J. Geophys. Res.: Oceans* 104, 1455–1464. <https://doi.org/10.1029/1998JC900022>.
- Laurindo, L.C., Mariano, A.J., Lumpkin, R., 2017. An improved near-surface velocity climatology for the global ocean from drifter observations. *Deep Sea Res. Oceanogr. Res. Pap.* 124, 73–92. <https://doi.org/10.1016/j.dsr.2017.04.009>. <https://linkinghub.elsevier.com/retrieve/pii/S0967063716302850>.
- Le Traon, P.Y., Nadal, F., Ducet, N., 1998. An improved mapping method of multisatellite altimeter data. *J. Atmos. Ocean. Technol.* 15, 522–534. [https://doi.org/10.1175/1520-0426\(1998\)015<0522:AIMMOM>2.0.CO;2](https://doi.org/10.1175/1520-0426(1998)015<0522:AIMMOM>2.0.CO;2).
- Le Vu, B., Stegner, A., Arsouze, T., 2018. Angular momentum eddy detection and tracking algorithm (AMEDA) and its application to coastal eddy formation. *J. Atmos. Ocean. Technol.* 35, 739–762. <https://doi.org/10.1175/JTECH-D-17-0010.1>. <http://journals.ametsoc.org/doi/10.1175/JTECH-D-17-0010.1>.
- Lee, C.M., Jones, B.H., Brink, K.H., Fischer, A.S., 2000. The upper-ocean response to monsoonal forcing in the Arabian Sea: seasonal and spatial variability. *Deep Sea Res. Part II Top. Stud. Oceanogr.* 47, 1177–1226. [https://doi.org/10.1016/S0967-0645\(99\)00141-1](https://doi.org/10.1016/S0967-0645(99)00141-1). <http://linkinghub.elsevier.com/retrieve/pii/S0967064599001411>.
- Lumpkin, R., Pazos, M., 2007. *Lagrangian Analysis and Prediction of Coastal and Ocean Dynamics*. Cambridge University Press, pp. 39–67.
- L'Hégaret, P., Duarte, R., Carton, X., Vic, C., Ciani, D., Baraille, R., Corrêard, S., 2015. Mesoscale variability in the Arabian Sea from HYCOM model results and observations: impact on the Persian Gulf Water path. *Ocean Sci.* 11, 667–693. <https://doi.org/10.5194/os-11-667-2015>. <https://www.ocean-sci.net/11/667/2015/>.
- L'Hégaret, P., Carton, X., Louazel, S., Boutin, G., 2016. Mesoscale eddies and sub-mesoscale structures of Persian Gulf Water off the Omani coast in spring 2011. *Ocean Sci.* 12, 687–701. <https://doi.org/10.5194/os-12-687-2016>. <https://www.ocean-sci.net/12/687/2016/>.
- L'Hégaret, P., Beal, L.M., Elipot, S., Laurindo, L., 2018. Shallow cross-equatorial gyres of the Indian ocean driven by seasonally reversing monsoon winds. *J. Geophys. Res.: Oceans*. <https://doi.org/10.1029/2018JC014553>. <https://onlinelibrary.wiley.com/doi/abs/10.1029/2018JC014553>.
- McDougall, T.J., Barker, P.M., 2011. *Getting Started with TEOS-10 and the Gibbs Seawater (GSW), Oceanographic Toolbox*.
- Mkhini, N., Coimbra, A.L.S., Stegner, A., Arsouze, T., Taupier-Letage, I., Béranger, K., 2014. Long-lived mesoscale eddies in the eastern Mediterranean Sea: analysis of 20 years of AVISO geostrophic velocities. *J. Geophys. Res.: Oceans* 119, 8603–8626. <https://doi.org/10.1002/2014JC010176>.
- Ollitrault, M., Rannou, J.-P., 2013. ANDRO: an argo-based deep displacement dataset. *J. Atmos. Ocean. Technol.* 30, 759–788. <https://doi.org/10.1175/JTECH-D-12-00073.1>. <http://journals.ametsoc.org/doi/abs/10.1175/JTECH-D-12-00073.1>.
- Pegliasco, C., Chaigneau, A., Morrow, R., 2015. Main eddy vertical structures observed in the four major Eastern Boundary Upwelling Systems. *J. Geophys. Res.: Oceans* 120, 6008–6033. <https://doi.org/10.1002/2015JC010950>.
- Pous, S., Lazure, P., Carton, X., 2015. A model of the general circulation in the Persian Gulf and in the Strait of Hormuz: intraseasonal to interannual variability. *Cont. Shelf Res.* 94, 55–70. <https://doi.org/10.1016/j.csr.2014.12.008>. <https://linkinghub.elsevier.com/retrieve/pii/S027844314100363X>.
- Quadfasel, D.R., Schott, F., 1982. Water-mass distributions at intermediate layers off the Somali coast during the onset of the southwest monsoon, 1979. *J. Phys. Oceanogr.* 12, 1358–1372. [https://doi.org/10.1175/1520-0485\(1982\)012<1358:WMDAIL>2.0.CO;2](https://doi.org/10.1175/1520-0485(1982)012<1358:WMDAIL>2.0.CO;2).
- Queste, B.Y., Vic, C., Heywood, K.J., Piontkovski, S.A., 2018. Physical controls on oxygen distribution and denitrification potential in the north west Arabian Sea. *Geophys. Res. Lett.* 45, 4143–4152. <https://doi.org/10.1029/2017GL076666>.
- Roulet, G., Capet, X., Maze, G., 2014. Global interior eddy available potential energy diagnosed from Argo floats. *Geophys. Res. Lett.* 41, 1651–1656. <https://doi.org/10.1002/2013GL059004>.
- Scharffenberg, M.G., Stammer, D., 2010. Seasonal variations of the large-scale geostrophic flow field and eddy kinetic energy inferred from the TOPEX/Poseidon and Jason-1 tandem mission data. *J. Geophys. Res.* 115. <https://doi.org/10.1029/2008JC005242>.
- Schmitt, R.W., 1994. Double diffusion in oceanography. *Annu. Rev. Fluid Mech.* 26, 255–285. <https://doi.org/10.1146/annurev.fl.26.010194.001351>. <http://www.annualreviews.org/doi/10.1146/annurev.fl.26.010194.001351>.

- Schott, F.A., McCreary, J.P., 2001. The monsoon circulation of the Indian Ocean. *Prog. Oceanogr.* 51, 1–123. [https://doi.org/10.1016/S0079-6611\(01\)00083-0](https://doi.org/10.1016/S0079-6611(01)00083-0). <http://linkinghub.elsevier.com/retrieve/pii/S0079661101000830>.
- Smith, K.S., 2007. The geography of linear baroclinic instability in Earth's oceans. *J. Mar. Res.* 65, 655–683. <https://doi.org/10.1357/002224007783649484>. <http://openurl.ingenta.com/content/xref?genre=article&issn=0022-2402&volume=65&issue=5&page=655>.
- Smith, W.H.F., Sandwell, D.T., 1997. Global sea floor topography from satellite altimetry and ship depth soundings. *Science* 277, 1956–1962. <https://doi.org/10.1126/science.277.5334>. <http://www.sciencemag.org/lookup/doi/10.1126/science.277.5334.1956>.
- Souza, J.M.A.C., de Boyer Montégut, C., Cabanes, C., Klein, P., 2011. Estimation of the Agulhas ring impacts on meridional heat fluxes and transport using Argo floats and satellite data. *Geophys. Res. Lett.* 38. <https://doi.org/10.1029/2011GL049359>.
- Tollefson, J., 2018. Ocean scientists work to forecast huge plankton blooms in Arabian Sea. *Nature* 555, 569–570. <https://doi.org/10.1038/d41586-018-03698-0>. <http://www.nature.com/doi/10.1038/d41586-018-03698-0>.
- Trott, C.B., Subrahmanyam, B., Chaigneau, A., Delcroix, T., 2018. Eddy tracking in the northwestern Indian ocean during southwest monsoon regimes. *Geophys. Res. Lett.* 45, 6594–6603. <https://doi.org/10.1029/2018GL078381>.
- Vallis, G.K., 2017. *Atmospheric and Oceanic Fluid Dynamics*. Cambridge University Press.
- Vic, C., Roulet, G., Carton, X., Capet, X., 2014. Mesoscale dynamics in the Arabian Sea and a focus on the Great Whirl life cycle: a numerical investigation using ROMS. *J. Geophys. Res.: Oceans* 119, 6422–6443. <https://doi.org/10.1002/2014JC009857>.
- Vic, C., Roulet, G., Capet, X., Carton, X., Molemaker, M.J., Gula, J., 2015. Eddy-topography interactions and the fate of the Persian gulf outflow. *J. Geophys. Res.: Oceans* 120, 6700–6717. <https://doi.org/10.1002/2015JC011033>.
- Warren, B., Stommel, H., Swallow, J., 1966. Water masses and patterns of flow in the Somali Basin during the southwest monsoon of 1964. *Deep Sea Res. Oceanogr. Abstr.* 13, 825–860. [https://doi.org/10.1016/0011-7471\(76\)90907-4](https://doi.org/10.1016/0011-7471(76)90907-4). <http://linkinghub.elsevier.com/retrieve/pii/0011747176909074>.
- Yang, G., Wang, F., Li, Y., Lin, P., 2013. Mesoscale eddies in the northwestern subtropical Pacific Ocean: statistical characteristics and three-dimensional structures. *J. Geophys. Res.: Oceans* 118, 1906–1925. <https://doi.org/10.1002/jgrc.20164>.
- Zhang, Z., Wang, W., Qiu, B., 2014. Oceanic mass transport by mesoscale eddies. *Science* 345, 322–324. <https://doi.org/10.1126/science.1252418>. <http://www.sciencemag.org/cgi/doi/10.1126/science.1252418>.
- Zhang, Z., Tian, J., Qiu, B., Zhao, W., Chang, P., Wu, D., Wan, X., 2016. Observed 3D structure, generation, and dissipation of oceanic mesoscale eddies in the south China sea. *Sci. Rep.* 6 <https://doi.org/10.1038/srep24349>. <http://www.nature.com/articles/srep24349>.

4.2 Supplément sur la signature de PGW dans le tourbillon composite

Les tourbillons composites extraits dans le nord de la mer d'Arabie présentent des anomalies de salinité en leur coeur, dû à la présence de PGW et de ASHSW en sub-surface dans cette région (voir Fig. 9 de la section précédente). Les composites étant calculés à partir d'une moyenne sur un ensemble de nombreux tourbillons, la présence de ces masses d'eaux n'indique pas obligatoirement que tous les tourbillons piègent en moyenne de la PGW ou de la ASHSW. En effet, la déviation de la salinité à la moyenne (*i.e.* au composite), à la profondeur de la PGW, montre que la salinité au sein des tourbillons est plus élevée dans le golfe d'Oman, que dans l'ouvert de la mer d'Arabie (Fig. 4.1 et Fig. 4.2). Cela montre que les hautes valeurs de salinité observées dans le coeur des tourbillons composites ne reflète pas un transport de PGW hors du golfe, mais plutôt l'impact de la salinité ambiante sur la salinité au coeur des tourbillons.

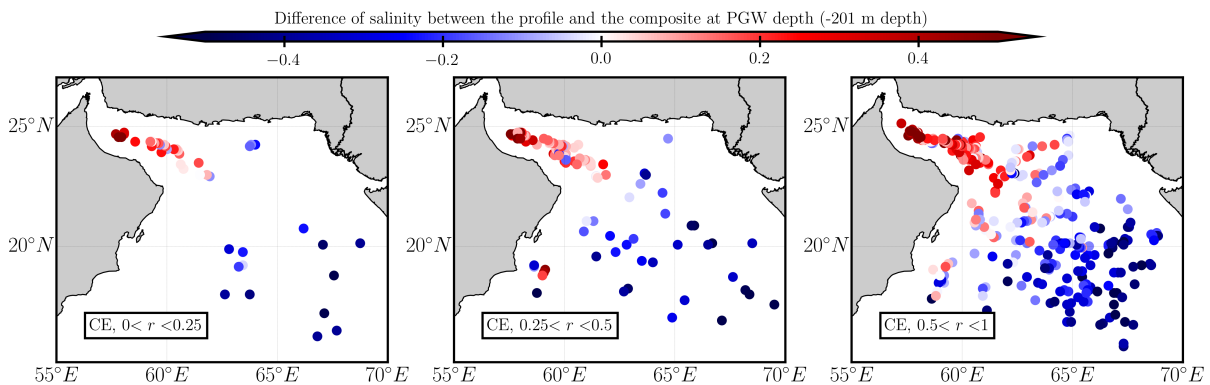


FIGURE 4.1 – Différence de salinité [en psu] entre les profils collectés dans le nord de la mer d'Arabie (co-localisé dans des cyclones), et le cyclone composite, à la profondeur de la PGW. Chaque sous-figure correspond à une gamme de distance entre le profil et le centre du tourbillon dans lequel il a été collecté.

Dans cette région, les tourbillons sont généralement formés dans l'ouvert de la mer d'Arabie, puis se propagent dans le golfe d'Oman par effet- β . Leur coeur est donc initialement moins salé que la stratification ambiante dans le golfe, lorsqu'ils y pénètrent. Les masses d'eaux salées se propagent vers le centre des tourbillons, par "*stirring*". Cela est confirmé par les valeurs de salinité proches de la périphérie des tourbillons (pour $0.5 < r < 1$) plus haute que lorsque $r \rightarrow 0$. Ainsi, les hautes valeurs de salinité présente au coeur des tourbillons composites sont dues aux tourbillons présents dans le golfe

d'Oman, qui ont advecté des masses d'eaux en leur centre.

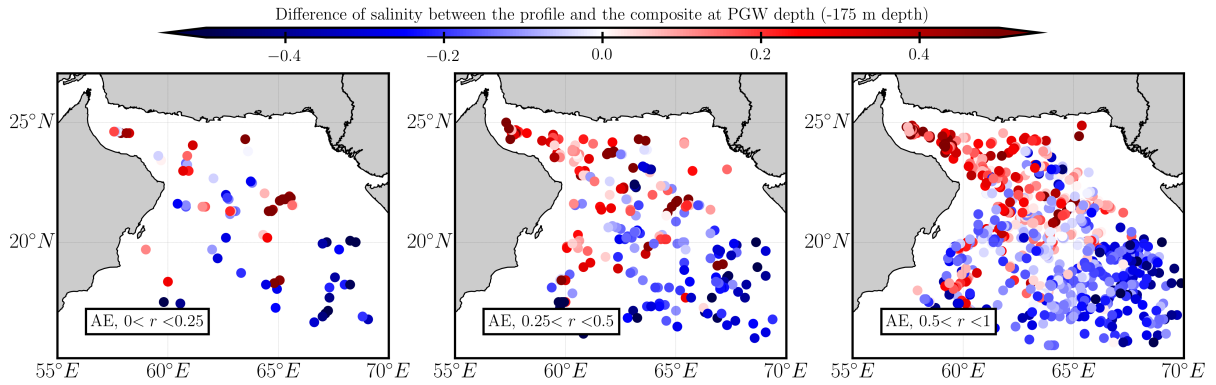


FIGURE 4.2 – Idem Fig. 4.1, pour la différence de salinité entre les profils collectés dans les anticyclones et l'anticyclone composite.

Enfin, il est intéressant de noter que pour $0.25 < r < 1$ certains profils présentent des valeurs de salinité importantes, assez loin du golfe. Ces observations sont le signe (1) de l'export de PGW par les tourbillons; ou (2) de la présence de structures de sousmésos-échelle formées dans le golfe d'Oman, qui sont ensuite advectées à la périphérie des structures de méso-échelle.

4.3 Conclusion sur la structure 3D des tourbillons en mer d'Arabie

Dans ce chapitre, nous avons présenté la structure tri-dimensionnelle des tourbillons de méso-échelle en mer d'Arabie, grâce à l'utilisation conjointe de mesures altimétriques et de mesures *in situ*. Ainsi, les résultats principaux sont ceux-ci :

- Les propriétés des masses d'eaux et les propriétés dynamiques des tourbillons permettent de diviser la mer d'Arabie en sept zones.
- Dans le golfe d'Oman et le golfe d'Aden, les eaux sont moins salées au centre des tourbillons qu'à leur périphérie, suggérant que les tourbillons présents dans les golfes sont générés en mer d'Arabie, puis advectent les masses d'eaux salées en leur coeur. Du fait de leur influence profonde, les tourbillons de méso-échelle ont donc, en moyenne, un impact important sur la distribution des masses d'eaux salées profondes de mer d'Arabie.
- Des tourbillons composites calculés à partir de nombreux tourbillons dans le nord de la mer d'Arabie, montrent une structure représentative des tourbillons fréquemment rencontrés dans cette région, sans hypothèse *a priori* sur leur structure.

LE CYCLE DE VIE DES TOURBILLONS ISOLÉS EN MER D'ARABIE

En première approche, il est raisonnable de supposer que les tourbillons de méso-échelle en mer d'Arabie, comme ceux observés par satellite dans le chapitre précédent, sont isolés. Bien que très forte, cette hypothèse permet d'étudier le comportement intrinsèque de ces tourbillons, fonction de leur propriétés. Nous présentons dans ce chapitre plusieurs études décrivant la dynamique des structures tourbillonnaires typiques de la mer d'Arabie, si l'on suppose que celles-ci sont isolées.

5.1 Stabilité

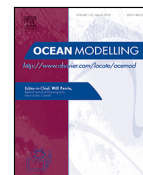
Les études de stabilité de tourbillons permettent de comprendre pourquoi ces structures vivent si longtemps dans l'océan (Chelton et al., 2011b). D'après les résultats du chapitre 4, le tourbillon composite cyclonique extrait dans le nord de la mer d'Arabie est représentatif des tourbillons cycloniques fréquemment observés dans cette région. Ce type de tourbillon peut vivre plusieurs mois, et peut être observé dans le golfe d'Oman ou dans l'ouvert de la mer d'Arabie, influençant ainsi la dilution des masses d'eaux venant du golfe Persique (voir *e.g.* la section 4.2 et L'Hégaret et al. (2015, 2016)), et les composants biologiques de la colonne d'eau (Queste et al., 2018). Cette section présente l'étude de la stabilité de ce type de tourbillon de méso-échelle, et permet ainsi de donner des clefs à la compréhension de la longue durée de vie de telles structures.

5.1.1 La stabilité du cyclone composite : Article publié dans *Ocean Modelling*



Contents lists available at ScienceDirect

Ocean Modelling

journal homepage: www.elsevier.com/locate/ocemod

Study of the stability of a large realistic cyclonic eddy

Charly de Marez^{a,*}, Thomas Meunier^b, Mathieu Morvan^a, Pierre L'Hégaret^a, Xavier Carton^a^a Univ. Brest, Laboratoire d'Océanographie Physique et Spatiale (LOPS), IUEM, Rue Dumont D'urville, 29280 Plouzané, France^b CICESE, Ensenada, B.C., Mexico

ARTICLE INFO

Keywords:

Mesoscale
Eddy
Instability
Submesoscale
Vortex

ABSTRACT

We investigate the stability of a composite cyclone representative of Arabian Sea eddies using a high resolution primitive equation model. We observe that the eddy is unstable with respect to a mixed barotropic/baroclinic instability, leading to the growth of an azimuthal mode 2 perturbation. The latter deforms the eddy, which eventually evolves into a tripole after about 4 months of simulation. The presence of a critical level for the most unstable mode generates sharp fronts in the surface mixed layer where the Rossby number is large. These fronts then become unstable, and this generates submesoscale cyclones and filaments. Near these fronts, diapycnal mixing occurs, causing the potential vorticity to change sign locally, and symmetric instability to develop in the core of the cyclonic eddy. Despite the instabilities, the eddy is not destroyed and remains a large-scale coherent structure for the last 6 months of the simulation. Looking at Sea Surface Height only, the composite eddy evolves little, and fairly represents the eddy observed in the altimetry which can live for several months. The study of this simulation thus illustrates the numerous kinds of instabilities which may occur in large cyclonic eddies but cannot be captured directly by altimetric data.

1. Introduction

Mesoscale eddies are a prominent feature of the ocean circulation. They have a strong influence on biological activity (Chelton et al., 2011), tracer transport (Zhang et al., 2014), and physical and chemical properties of the water column (Dong et al., 2014). Examples of long lived, coherent, and recurrent mesoscale eddies can be found in every oceanic basin: Gulf Stream rings in the western North Atlantic (Richardson, 1983), meddies in the eastern North Atlantic (Armi et al., 1989), Agulhas rings in the South Atlantic (Olson and Evans, 1986), Mozambique channel eddies in the Indian Ocean (Halo et al., 2014), Kuroshio rings in the western North Pacific (Li et al., 1998), Loop Current Eddies in the Gulf of Mexico (Meunier et al., 2018), the Ras al Hadd dipole in the northern Arabian Sea (L'Hégaret et al., 2015, 2016). All play an important role in the transport of heat and salt.

Mesoscale eddies have been intensively studied over the past 60 years. In particular, many studies have focused on their stability properties, using linear stability analysis (Gent and McWilliams, 1986; McWilliams et al., 1986; Nguyen et al., 2012; Yim and Billant, 2015), and numerical models to study the finite amplitude evolution of unstable perturbations (Carton and McWilliams, 1989; Stegner and Dritschel, 2000; Ménesguen et al., 2018). In these studies, eddies are modeled using analytical profiles, e.g. shielded vortices, Rankine vortices (Carton and McWilliams, 1989; Stegner and Dritschel, 2000), Gaussian vortices (McWilliams, 1985), or Lorentzian vortices (Hua et al., 2013; Meunier et al., 2018) assuming that they represent a

large range of observed eddies (Le Vu et al., 2018). The result of these stability analyses is strongly dependent on the initial profile imposed. In most cases, the eddy profiles are unstable, and can lead to the destruction of the eddy, the formation of dipoles, tripoles, or the long-time decay of the eddy (Carton et al., 1989; Stegner and Dritschel, 2000).

The increase of computational capabilities has led recent studies to implement very high resolution stability analyses in a 3D context. This allows the study of vortex stability beyond balanced mesoscale processes, and to observe how submesoscale features can emerge from the destabilization of mesoscale structures (Brannigan et al., 2017; Ménesguen et al., 2018). Such studies highlight a possible mechanism for the forward cascade of energy toward small scales.

In the past few years, it has become possible to determine the actual shape of oceanic eddies with a fairly good spatio-temporal resolution. Gridded multi-satellite altimetric products provide increased horizontal resolution (up to $1/8^\circ$) and resolve more accurately eddies with radii two or three times the first baroclinic Rossby radius of deformation (R_D hereafter) than older products with coarser horizontal resolution ($1/3^\circ$ or $1/4^\circ$). The rapid growth of the Argo database as well as the increase of the resolution of the vertical profiles significantly improved the sampling of the vertical structure of the global ocean. Combining the Argo and altimetry datasets, Chaigneau et al. (2011) have shown that *composite* methods are efficient in determining the average 3D shape of eddies and isolating classes of eddies in given areas. This effort

* Corresponding author.

E-mail address: charly.demarez@univ-brest.fr (C. de Marez).<https://doi.org/10.1016/j.ocemod.2019.101540>

Received 12 July 2019; Received in revised form 27 November 2019; Accepted 1 December 2019

Available online 9 December 2019

1463-5003/© 2019 Elsevier Ltd. All rights reserved.

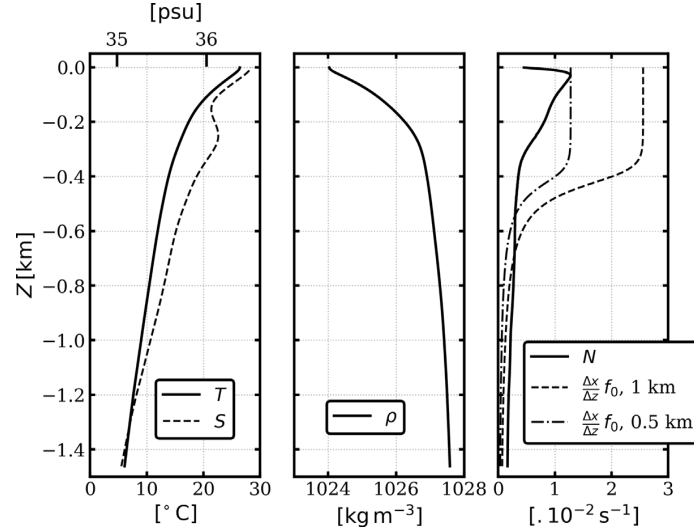


Fig. 1. Background temperature (left, solid), salinity (left, dashed), density (middle) and Brunt-Väisälä frequency N (right solid) profiles, after a short period of integration. This corresponds to the stratification as found by Argo floats in the northern Arabian Sea, and is used to initialize the simulations, with an additional thin surface mixed layer generated by the KPP scheme during the first days of the simulation (once created its depth is constant throughout time). The right panel shows in dashed lines the ratio $\frac{\Delta x}{\Delta z} f_0$ for two simulations, which can be compared to N ; Δx and Δz are the model grid spacings.

has been made in several regions, e.g. Chaigneau et al. (2011) in the eastern South Pacific Ocean, Keppler et al. (2018) in the Southwest Tropical Pacific ocean, and de Marez et al. (2019) in the Arabian Sea. In the latter study, the authors computed a composite eddy without *a priori* assumptions (e.g. a Gaussian pressure/velocity profile) and only from *in situ* measurements. Because the composite is a mean of a very varied population, it may not in fact be representative of all individual elements of the population. However, through comparison with altimetric and *in situ* – drifters, floats, and ship – measurements, authors showed that the composite cyclonic eddy is fairly representative of the Arabian Sea’s mesoscale cyclones already observed.

In this paper, we investigate the stability of a composite eddy, by running a high resolution primitive equation model initialized with a composite cyclone computed in the Arabian Sea. Contrary to previous studies, we do not use analytical initial conditions. The Arabian Sea, in the northern Indian Ocean, between the African and Asian landmasses, is a region dominated by the monsoon wind regime. This regime leads to seasonal along-shore current reversals. The alongshore currents destabilize and form meanders with 100–200 km wavelengths which eventually detach to form eddies with similar diameters (Schott and McCreary, 2001). Wind forcing and baroclinic Rossby waves generated at the eastern boundary of the Arabian Sea can strengthen the eddies and contribute to their propagation (Al Saafani et al., 2007). Eddies have a strong influence on the regional circulation. Mesoscale activity is reflected by high values of Eddy Kinetic Energy (Scharffenberg and Stammer, 2010) and Eddy Available Potential Energy (Roulet et al., 2014), nearly reaching the values in the Antarctic Circumpolar Current or the Agulhas Current. We refer the reader to Fig. 1 in L’Hégaret et al. (2018) which presents the mean surface circulation in this area, and Fig. 2 in Vic et al. (2014) for a description of the mean standing eddies there, such as the Great Whirl and the dipole of Ra’s Al Hadd.

This is the first time to our knowledge that the non-linear stability study of an isolated eddy is performed using *in situ* and satellite observed initial conditions. Here, we focus on physical processes underlying the long time evolution of the composite eddy. We address the following questions: (1) Is the composite cyclone stable in the primitive equation framework? (2) What are the physical mechanisms involved in the destabilization of the eddy? (3) Can the destabilization process, and the shape of the eddy after destabilization, be observed using altimetry and Argo data.

The paper is organized as follows. We present the composite eddy, and describe the numerical setup and tools used to study the simulation in Section 2. We present the results of the simulations, and describe the diagnostics performed to analyze the possible sources of instability in Section 3. We discuss sensitivity tests of our simulations in Section 4. Finally, the results are discussed in Section 5.

2. Context and methods

2.1. The composite eddy and its environment

The composite eddy was extracted using the following procedure: (1) Mesoscale eddies are detected from a $1/8^\circ$ altimetric product using the AMEDA algorithm (Le Vu et al., 2018) for the period 2000–2015. (2) A colocalization algorithm is then used to detect if an Argo float is located in or out of an eddy. (3) The background stratification of the region (Fig. 1) is computed by averaging Argo profiles located outside the eddies (7885 profiles). (4) 531 Argo profiles, collected inside surface-intensified Cyclonic Eddies of radius $R_D < R < 3 R_D$, are isolated. $R_D = 47$ km is the average First Baroclinic Rossby Radius of Deformation in the area (Chelton et al., 1998). (5) Density profiles are computed from Argo profiles and density anomalies are obtained by subtracting the background density in the area. (6) A dimensionless radial position $\tilde{R} = dR/R$ is computed for each profile, where dR is the distance between the center of the eddy and the position of the colocalized profile (dR), and R is the radius of the eddy. (7) The profiles are averaged depending on their value of \tilde{R} , in bins of width $\Delta R = 0.05$, yielding a composite vertical section of density anomaly $\tilde{\rho}(\tilde{R}, z)$. (8) For each depth, the density anomaly $\tilde{\rho}(\tilde{R}, z)$ is smoothed using a Gaussian Kernel of width 0.3. (9) Finally, this composite is extrapolated into a 3D structure, by assuming azimuthal symmetry. The horizontal extent of the composite is re-dimensionalized by the mean radius of all eddies used for the computation of the composite $\langle R \rangle = 100$ km.

The Structure of the composite Cyclonic Eddy is thus defined in terms of a density anomaly distribution. The sum of the density anomaly of the composite and the background stratification is shown in Fig. 2. Following the same procedure, a composite structure of salinity anomaly is computed (Fig. 2b). de Marez et al. (2019) show that these structures are representative of the typical mesoscale eddies observed in

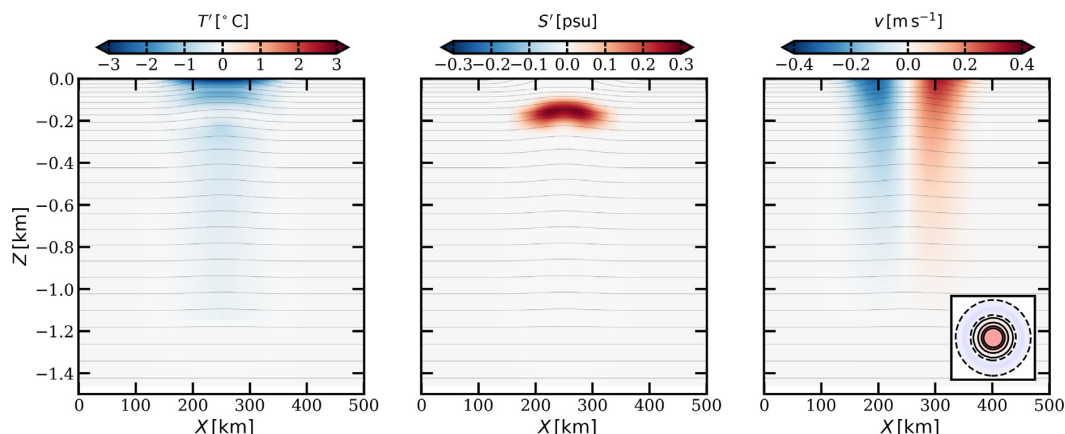


Fig. 2. Vertical section at the center of the domain ($y = 250$ km) at initialization, showing the shape of the composite eddy. (left) Temperature anomaly, (middle) salinity anomaly and (right) meridional (south–north) velocity v . Iso-density contours of the composite eddy, with a spacing of 0.4 kg m^{-3} , are superposed in all panels. Inset in the right panel shows the $-0.02, 0.02, 0.1, 0.2$ and 0.25 dynamic Rossby number ζ/f_0 contours at the surface; the colormap in the inset is the same as in Fig. 3.

the Arabian Sea. Details of the composite Cyclonic Eddy calculation and the associated validation are fully described in de Marez et al. (2019).

We compute the temperature anomaly field from the composite salinity and density, using the Gibbs SeaWater (GSW) Oceanographic Toolbox (McDougall and Barker, 2011), which uses the TEOS-10 equation of state for seawater (Fig. 2(a)). The background profiles shown in Fig. 1(a) are then added to the temperature and salinity anomaly fields (note that the surface mixed layer is initially not present). The velocity field is obtained via the cyclogeostrophic balance, following the procedure described in Penven et al. (2014), see Fig. 2(right). The numerical simulations are initialized with the temperature, salinity, and velocity fields corresponding to the composite eddy.

It is worth mentioning that by definition, the composite eddy has a coarse resolution. (1) On the horizontal direction: the averages of Argo-collected density profiles are made in bins of size $\Delta R = 0.05$. Once re-dimensionalized, this corresponds to a horizontal resolution of the composite eddy of 5 km. Since we perform high resolution numerical simulations, the composite eddy is interpolated on the fine grid of the simulation using a cubic-interpolation. (2) On the vertical direction: while the vertical resolution of Argo float profiles is irregular and $O(10)$ m, they were interpolated on a regularly spaced vertical grid, with a vertical spacing of 4.4 m. The composite is then linearly interpolated on the finer vertical grid of the simulation. In the simulation we will discuss, small scale variations of density and velocity are of $O(< 5)$ km on the horizontal and $O(< 10)$ m on the vertical. Such small scale features thus occur at scales that the composite computation could not capture.

The eddy is intensified at the surface, but has a deep-reaching influence down to about 1000 m depth. Its horizontal shape corresponds to a shielded vorticity monopole: a positive core of vorticity and a shield of negative vorticity (see inset in Fig. 2). Its radius, $R = 100$ km, is large compared to the mean regional R_D (47 km). The Burger number, defined as $Bu = \left(\frac{R_D}{R}\right)^2$ scales as $Bu = \left(\frac{47}{100}\right)^2 \sim 0.25 < 1$. In the following, mentions to ‘submesoscale’ refer to features and processes occurring at scales that are small compared to R_D (i.e. $Bu > 1$). Typically, the fronts and vortices generated around the eddy have a typical scale of $O(< 10)$ km. They are submesoscale features. The Coriolis parameter is kept constant in the simulations (f -plane), using the regional average value (latitude of 23°N): $f_0 = 5.2 \cdot 10^{-5} \text{ s}^{-1}$. The initial condition’s Rossby Number is small, $Ro = \frac{U_{\max}}{f_0 R_{\max}} \sim 0.13$, with U_{\max} the maximal velocity, at R_{\max} . Thus Ro/Bu is finite, and the eddy is frontal (Stegner and Dritschel, 2000). However, it has been shown that the dynamical Rossby number $\epsilon = \zeta/f_0$, with ζ the relative vorticity is a more pertinent parameter to study geostrophic

and ageostrophic dynamics in vortices (Stegner and Dritschel, 2000). In our case, $\epsilon \sim 0.3$ in the core of the eddy at initialization. Finally, the Froude number is $Fr = \frac{\epsilon}{\sqrt{Bu}} \sim 0.6$.

2.2. Numerical setup

To study the dynamics of the composite Cyclonic Eddy described in Section 2.1, we perform spindown idealized simulations, with the surface fluxes set to zero, using the Coastal and Regional Ocean Community model, CROCO (Shchepetkin and McWilliams, 2005). It solves the hydrostatic primitive equations (PE) for the velocity $\mathbf{u} = (u, v, w)$, temperature T , and salinity S , using a full equation of state for seawater (Shchepetkin and McWilliams, 2011). The potential density referenced at the surface ρ is computed offline from T and S using the TEOS-10 equation of state for seawater. From the potential density, we also compute the Brunt–Väisälä frequency defined by

$$N = \sqrt{-\frac{g}{\rho_0} \frac{\partial \rho}{\partial z}},$$

with $g = 9.81 \text{ m s}^{-2}$, and ρ_0 the mean density in the domain. The simulations performed integrate the PE for about 300 days on the f -plane, with a time step $dt = 120$ s, respecting the Courant Friedrichs Lewy (CFL) criterion. The numerical settings are similar to previous simulations performed in idealized contexts (Ménésguen et al., 2018): horizontal advection terms for tracers and momentum are discretized with fifth-order upwind advection schemes (UP5); the horizontal viscosity and diffusivity are set to zero, since the UP5 scheme damps dispersive errors; the vertical advection is discretized with a fourth-order centered parabolic spline reconstruction (Splines scheme); the vertical closure is done by adding a small vertical diffusion in the interior using a K-profile parameterization (KPP) (Large et al., 1994). Further discussion about these parameterizations can be found in Klein et al. (2008) or Ménésguen et al. (2018).

The KPP-scheme generates a thin surface mixed layer during the first days of the simulation. The latter is not present in the background stratification because it is computed as an average throughout the whole year. Once created (from $t \sim 20$ days), the surface mixed layer does not evolve, and it is consistent with the surface mixed layer observed in the density profiles of the Arabian Sea (except during the winter). It has a vertical extension of about 30 m depth, and can be seen in Fig. 1.

The domain size is 500×500 km on the horizontal. Taking a flat bottom at a depth of 1500 m is enough because the eddy has a

vertical extension of about 1000 m. We set open boundary conditions at the edges of the domain. This allows the radiation of gravity waves generated during the initial adjustment of the eddy. These waves are evacuated out of the domain at $t = 1$ day.

The vertical and horizontal resolutions are chosen to accurately resolve the frontal dynamics and the forward energy cascade at the surface. The simulation has 256 vertical levels stretched at the surface such that the vertical resolution is $\Delta z = 2$ m from the surface to about 400 m depth. Deeper, the vertical resolution decreases, with $\Delta z \sim 60$ m at the bottom. This choice was made to observe the vertical structure of the surface dynamics at high resolution. The stretching of the vertical levels can be seen in Fig. 1 (right). Different horizontal resolutions were tested: $\Delta x = 10, 5, 2, 1,$ and 0.5 km.

The primary destabilization of the eddy (studied in Section 3.2) depends relatively little on the horizontal resolution, since it is observed in all simulations for the range of values of Δx considered. The diagnosis performed to analyze this primary instability were all done on the $\Delta x = 1$ km simulation. Secondary instabilities are observed for the simulations with $\Delta x = 2, 1$ and 0.5 km. However, the time of apparition and the size of the small scale features (e.g the submesoscale vortices) differ in these simulations. To ensure that the model correctly resolves the frontal processes occurring at $t > 100$ days, and to fully resolve the $O(< 10)$ km structure, the diagnosis of the secondary instabilities (see Section 3.3) are performed on the $\Delta x = 0.5$ km simulation. For this one, the $\frac{\Delta x}{\Delta z}$ ratio is close to $\frac{N}{f_0}$ near the surface, see Fig. 1 (right). This avoids the presence of spurious gravity waves associated with intense frontal processes, and allows a better resolution of the forward energy cascade (Snyder et al., 1993; Nadiga, 2014; Ménesguen et al., 2018).

For the study of the primary instability (discussed in Section 3.2), the eddy is disturbed using two different methods. In the first one, the only source of perturbation is the numerical noise, due to the round-off errors at grid scale. In the second configuration we add a random noise. This noise is not spatially symmetric to avoid the dominant growth of specific azimuthal modes. The noise is introduced as a perturbation in the initial density and velocity fields. We define the random 2D perturbation $P(x, y)$ as a sum of 5000 random Gaussian functions in the horizontal plane:

$$P(x, y) = \sum_{i=0}^{5000} A_i e^{-\frac{(x-x_0^i)^2}{2\sigma_{x,i}^2} - \frac{(y-y_0^i)^2}{2\sigma_{y,i}^2}},$$

where $A_i, x_0^i, y_0^i, \sigma_{x,i}$ and $\sigma_{y,i}$ are chosen randomly and independently for each i , with $-1 < A_i < 1$; $50 < x_0^i, y_0^i < 450$ km; and $5 < \sigma_{x,i}, \sigma_{y,i} < 40$ km. Then, the initial density perturbation is computed as:

$$\rho_n(x, y, z) = \rho_{n,0} P(x, y) e^{z/h_n},$$

with $\rho_{n,0} = 0.01 \text{ kg m}^{-3}$ and $h_n = 500$ m. The depth $h_n = 500$ m is chosen so that the vertical extent of the perturbation is similar to the vertical extent of the perturbation at $t = 7$ days in the simulation without noise. The velocity perturbation is in cyclogeostrophic balance with the ρ_n field. This avoids the radiation of gravity waves during the first days of the simulation. The values of $\rho_{n,0}$ are chosen so that the domain integral of the random perturbation's kinetic energy E_k^i is about 10 times larger than the kinetic energy of the perturbation at $t = 7$ days in the simulation without noise. Thus, $E_k^i(t = 7 \text{ days, no noise}) = 1.9 \cdot 10^7 \text{ m}^5 \text{ s}^{-2}$ and $E_k^i(t = 7 \text{ days, noise}) = 29 \cdot 10^7 \text{ m}^5 \text{ s}^{-2}$. Notice that the energy of the perturbation is very weak compared to the total kinetic energy in the domain, which is about $1.8 \cdot 10^{11} \text{ m}^5 \text{ s}^{-2}$ at the initialization.

2.3. Definitions and tools for the study of the simulation

In this section, we describe the diagnostics performed. They allow us to characterize the dynamical processes involved in the destabilization of the eddy.

2.3.1. Different kinds of instabilities

The different instabilities which may occur in geophysical flow can be inferred from the Potential Vorticity structure. In the primitive equation framework, the relevant definition of Potential Vorticity is the Ertel Potential Vorticity (hereafter PV). It is materially conserved in the absence of friction or diapycnal processes (Hoskins et al., 1985; Vallis, 2017), and is defined as:

$$Q = \omega \cdot \nabla b, \quad (1)$$

where $b = -g \frac{\rho}{\rho_0}$ is the buoyancy, and ω is the 3D absolute vorticity of the flow, approximated here by

$$\omega = (-\partial_z v, \partial_z u, \zeta + f_0),$$

with $\zeta = (\partial_x v - \partial_y u)$ its z -component (relative vorticity hereafter). In the following, we will use the fully developed expression of the PV:

$$Q = (f_0 + \zeta) \partial_z b - (\partial_z v)(\partial_x b) + (\partial_z u)(\partial_y b). \quad (2)$$

An eddy with no vertical shear can be unstable with respect to barotropic (BT) instability. A necessary condition is that its radial gradient of PV, $\partial_r Q$, changes sign on the horizontal (i.e within a layer of constant density).

Also, an eddy can be unstable with respect to baroclinic (BC) instability. The necessary condition is that its radial gradient of PV, $\partial_r Q$, changes sign on the vertical (i.e between different layers). This latter change of sign can occur in the fluid interior (Phillips-type BC instability). If isopycnals outcrop, surface density gradients generate PV sheets (Bretherton, 1966) which, in turn, induce sharp PV gradients localized at the surface (Morel et al., 2006). The change of sign of the PV gradient can thus also occur between the surface and the interior (Charney-type BC instability), or between two sheet-type PV anomalies, at the surface and at the bottom (Eady-type instability) (Hoskins et al., 1985). In the mixed layer, the conditions for BC instability are changed and the theory described above is rather unsatisfactory. We refer the reader to Young and Chen (1995) for further description.

In geophysical flows, symmetric instability (SI) may also occur when the product of planetary vorticity and potential vorticity becomes negative ($fQ < 0$) (Fjørtoft, 1950; Hoskins, 1974; Bell, 2018). This is an overturning instability occurring in baroclinic currents, which results from an imbalance between the pressure gradients and the inertial forces (Thomas et al., 2013). It occurs where the dynamic is frontal and where the PV of the flow is negative (in the Northern hemisphere) because of the second and/or the third term of its expression (Eq. (2)). Following Thomas et al. (2013), a necessary condition for SI instability can be derived. First, we define the balanced Richardson number of the flow

$$Ri = \frac{f_0^2 N^2}{|\nabla b|^2}, \quad (3)$$

and the critical Richardson number

$$Ri_c = \frac{f_0}{\zeta_g}, \quad (4)$$

where ζ_g is the absolute vorticity of the geostrophic flow such as

$$\zeta_g = f_0 + (\partial_x v_g - \partial_y u_g), \quad (5)$$

where u_g and v_g are the zonal and meridional components of the geostrophic velocity in the simulation. PV of a geostrophic flow is negative when $Ri < Ri_c$. When this condition is met, SI can develop.

2.3.2. Energy transfer terms

The nature of the instabilities occurring in the flow may be investigated by studying the energy transfers. We assume that the flow may be decomposed as $\mathbf{u} = \langle \mathbf{u} \rangle + \mathbf{u}'$, where the brackets $\langle \cdot \rangle$ denote a mean state and the prime $'$ is the perturbation relative to this mean state.

First, the transfer from the mean kinetic energy (MKE) to the kinetic energy of the perturbation (EKE) may be expressed as:

$$(MKE \rightarrow EKE) = HRS + VRS, \quad (6)$$

where

$$HRS = -\langle u'^2 \rangle \partial_x \langle u \rangle - \langle u'v' \rangle \partial_y \langle u \rangle - \langle v'^2 \rangle \partial_y \langle v \rangle - \langle u'v' \rangle \partial_x \langle v \rangle \quad (7)$$

is the contribution from the Horizontal Reynolds Stress, and

$$VRS = -\langle u'w' \rangle \partial_z \langle u \rangle - \langle v'w' \rangle \partial_z \langle v \rangle \quad (8)$$

is the contribution of the Vertical Reynolds Stress. Note that Eq. (6) is obtained by integrating over the whole domain. Thus, formally, there are transport terms at the boundaries of the domain. In our simulations, these terms are null. Second, the transfer from the Potential Energy of the perturbation to the EKE is the Vertical Buoyancy Flux:

$$VBF = \langle w'b' \rangle. \quad (9)$$

The predominance of HRS, VRS, or VBF (> 0) in a region indicates a BT, Kelvin–Helmholtz type, or a BC instability respectively. More details on this decomposition and applications to the case of instabilities in the path of the Gulf Stream can be found in Gula et al. (2015, 2016). In our study, we use this decomposition to study (1) the primary instability of the eddy (Figs. 7 and A.17), and (2) the secondary instabilities occurring in the fronts around the eddy (Figs. A.18 and A.19).

In the first case, the mean flow defined by the variables $\langle u, v, w, b \rangle$ is assumed to be the initial state of the eddy. This choice allows to study the transfers of energy from the axisymmetric eddy to the perturbation. The perturbations u', v', w', b' are computed with respect to this initial state. Then, all time averaged products $\langle \cdot \cdot' \rangle$ are performed using a rolling time-mean average over a 1-month window (the growth time of the primary instability; see the following section).

In the second case, where we study the energy transfer to small scale structures (fronts and submesoscale vortices) rotating around the eddy, we project the variables in the frame of reference of the perturbation (rotating at a constant azimuthal velocity). $\langle \cdot \rangle$ is defined as a rolling time-mean average over a 10-days period in the rotating frame (the typical timescale of destabilization of the fronts). Perturbations \cdot' are computed with respect to this rolling time-mean average.

2.3.3. Normal mode decomposition

Perturbations are projected into azimuthal normal modes (Gent and McWilliams, 1986). Hereafter, the primed quantities denote the perturbation of A with respect to its initial value, such as

$$A'(t, x, y, z) = A(t, x, y, z) - A(t = 0, x, y, z).$$

Also, A^m is the decomposition of A into azimuthal normal modes. This decomposition is defined as follows:

$$A(t, r, \theta) = \sum_{m=0}^{m=\infty} A^m(t, r, \theta), \quad (10)$$

in the polar coordinates referenced at the center of the eddy (r, θ) , where

$$A^m(t, r, \theta) = a_m(t, r) \cos(m\theta + \phi_m(t, r)). \quad (11)$$

m is the azimuthal wavenumber and a_m and ϕ_m the amplitude and the phase of the mode, respectively. The phase velocity of the perturbation for the mode m is:

$$c_\phi^m(t, r) = \partial_t \phi_m(t, r). \quad (12)$$

The kinetic energy of the perturbation is defined as:

$$E'_k(t) = \frac{1}{2} \iiint dx dy dz (u_r'^2 + u_\theta'^2), \quad (13)$$

where u_r' and u_θ' are the radial and azimuthal velocity perturbations. Similarly, the kinetic energy of the mode m perturbation is:

$$E_k^m(t) = \frac{1}{2} \iiint dx dy dz ((u_r^m)^2 + (u_\theta^m)^2). \quad (14)$$

In these two expressions, the integrals are performed over the whole domain of the simulation. Using exponential notation, time evolution of normal mode perturbation velocity reads:

$$\mathbf{u}^m(t) = \mathbf{u}_0^m e^{im(\theta - ct)}, \quad (15)$$

which yields an exponential form for the energy growth:

$$E_k^m(t) = E_{k,0}^m e^{2\sigma t}. \quad (16)$$

Where $E_{k,0}^m$ is the initial perturbation and $\sigma = Re(-imc)$ is the growth rate. In our case, we choose to set $E_{k,0}^m = E_k^m(t = 7 \text{ days})$. This reference is chosen as close as possible from the beginning of the simulation, without having problem with division by zero when computing the growth time. In the simulations, perturbation growth rates are inferred from the amplification factor (λ):

$$\lambda_{E_k^m} = \frac{E_k^m(t)}{E_{k,0}^m}. \quad (17)$$

The growth time is defined as $\tau_{E_k^m} = \sigma_{E_k^m}^{-1}$ with

$$\sigma_{E_k^m} = \frac{1}{2t} \ln(\lambda_{E_k^m}). \quad (18)$$

Then,

$$\tau_{E_k^m}(t) = -2t \ln\left(\frac{E_k^m(t)}{E_{k,0}^m}\right). \quad (19)$$

When $\tau_{E_k^m}$ is small, the growth of the perturbation is rapid.

2.3.4. Critical level computation

The position of the critical level for azimuthal mode 2 at the surface is found by seeking the position where the phase speed of the mode 2 perturbations is equal to the angular velocity of the eddy. This latter is here an azimuthal average of the azimuthal velocity u_θ of the eddy. At each time we thus obtain the position of the critical level for the mode 2. We then average this position during the period $t = [50 : 70]$ days, to obtain the typical position of the critical level during the linear phase of the perturbation.

The energy of normal modes can concentrate within the critical level, as further described in Nguyen et al. (2012) or Riedinger and Gilbert (2014). In our study, we show that the presence of the critical level for mode 2 induces an intense stretching of the flow S . The latter is defined as the sum of the strain and the shear:

$$S = \underbrace{\partial_x u - \partial_y v + \partial_x v + \partial_y u}_{\text{Strain}} + \underbrace{\partial_x v + \partial_y u}_{\text{Shear}}.$$

It describes the tendency of the water parcels to be deformed by the ambient flow. Buoyancy gradients are steepened by this stretching. To describe the evolution of buoyancy gradients, we use the frontogenesis function F associated with the buoyancy. It is calculated using its standard definition as follows (Hoskins, 1982):

$$F(\mathbf{u}, b) = \partial_x u (\partial_x b)^2 + (\partial_x v + \partial_y u) \partial_x b \partial_y b + \partial_y v (\partial_y b)^2. \quad (20)$$

The opposite of F indicates the tendency of the buoyancy gradients to steepen:

$$-F(\mathbf{u}, b) = \frac{d}{dt} |\nabla b|^2.$$

3. Results

3.1. Overall course of the simulation

We present here the overall course of the simulation, and we separate the different stages of the eddy evolution that we will discuss in the following sections.

Fig. 3 shows the evolution of relative vorticity after 70, 100, 180, and 300 days of simulation (panels (a), (b), (c), and (d) respectively).

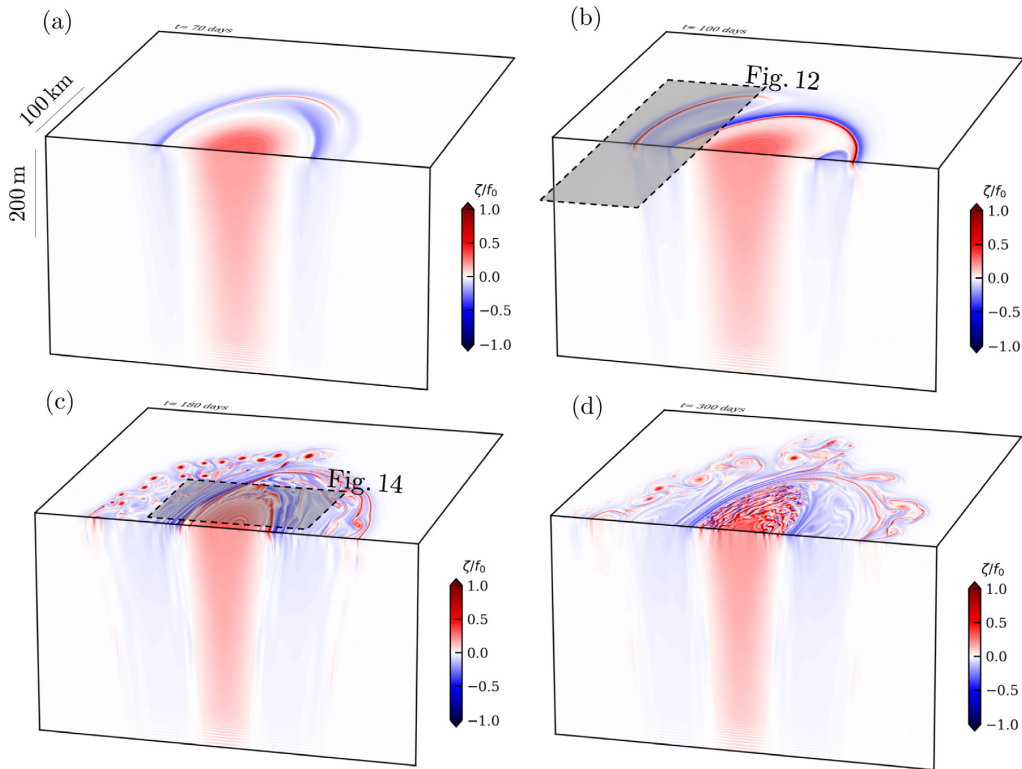


Fig. 3. Snapshots of the normalized relative vorticity ζ/f_0 at $t = 70, 100, 180$ and 300 days in the $\Delta x = 0.5$ km resolution simulation. Notice that the z -scale is very stretched to show the depth extension of the near-surface dynamics, see horizontal and vertical scalebars in panel (a). Gray rectangles in (b) and (c) show the regions studied in Figs. 12 and 14.

During the first part of the simulation (for $0 < t < 100$ days), a mixed BT/BC instability causes the eddy core to deform as spiral arms grow around it, see Fig. 3(a). Azimuthal mode 2 dominates, and the growth rate of the perturbation is roughly constant. The BC component of the instability leads to an intense frontogenesis at the edge of the eddy and in the spiral arms, see Fig. 3(b). Then, secondary instabilities occur in the surface mixed layer, see Fig. 3(c). In particular, shear instability develops in the spiral arms, generating series of small vortices of $O(10)$ km. The steepening of buoyancy gradients at the edge of the eddy also induces diapycnal mixing. This causes PV to change sign and yields SI. The latter erodes the edge of the eddy by creating fine scale structures of $O(2)$ km which are then ejected far away from the eddy, see Fig. 3(d). While secondary instabilities occur, the deepest part of the eddy ($z < -50$ m) remains a mesoscale tripole. It remains coherent during the last 6 months of the simulation. In Section 3.2, we describe the evolution of the cyclone from $t = 0$ to $t \sim 100$ days. Then, we present the secondary instabilities which occur in the surface mixed layer in Section 3.3.

3.2. Primary instability: the monopole becomes a tripole

3.2.1. Growth of normal modes

During the first 100 days of the simulation, the eddy destabilizes, with a domination of even azimuthal modes. To study the evolution of the perturbation, we compute its total kinetic energy at all times following Eq. (13), and for each azimuthal mode following Eq. (14), see (Fig. 4). The simulation without initial noise is compared to the simulation with a random noise.

No difference is discernible in terms of growth of the perturbation between the two cases, showing that the structure is intrinsically unstable regardless of the initial perturbations. The total kinetic energy

of the perturbation increases slowly at the first days of simulations. It then grows exponentially after $t \sim 50$ days, and tends to a plateau at $t \sim 150$ days.

The even modes have similar growth rates in the two simulations. In particular, the azimuthal mode 2 dominates, with values of energy close to the total energy of the perturbation. In the simulation where initial conditions are initially perturbed by a random noise, odd azimuthal modes are present at the initialization. These modes do not grow during the primary stage of the instability, meaning that they are stable. The processes involved in the primary destabilization of the eddy are well captured by the simulation without noise. In the following, we focus on the simulations performed without random noise.

The growth time of the perturbation is computed using Eq. (19) for the total kinetic energy of the perturbation, for modes 2, 4 and 6 (Fig. 5). The growth time of the total kinetic energy of the perturbation (*i.e.* for all modes) is, on average, around 30 days. From the beginning of the simulation, the growth time of mode 2 is almost equal to the growth time of the total perturbation, confirming that the instability is controlled by mode 2. Its growth time is roughly constant between day 50 and day 90, indicating that during this stage, mode 2 growth is exponential and evolves independently of the other modes (Gent and McWilliams, 1986).

At the beginning of the simulation, transient perturbations occur in the core of the eddy, mostly stemming from the initial adjustment of the eddy. They are evanescent and rapidly decay (Riedinger and Gilbert, 2014). However, during the first 20 days, their energy has similar magnitude to that of the unstable mode 2. They are believed to trigger mode 2. We next focus on the evolution of mode 2 since it dominates the instability. One can mention that for higher modes, nonlinear interactions most likely occur; their growth rates are not constant and have a similar evolution between each other.

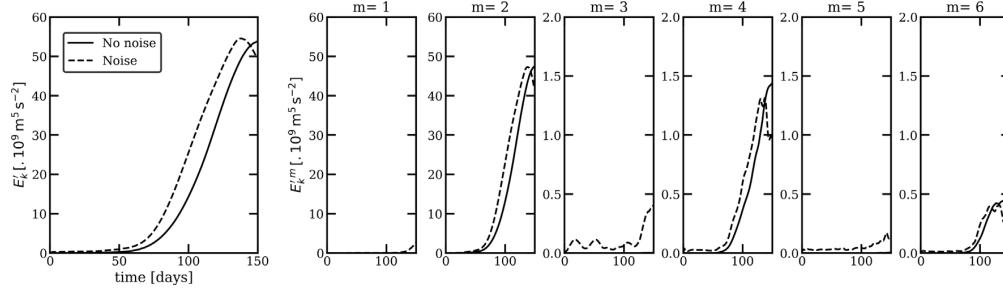


Fig. 4. Time evolution of the perturbation kinetic energy E_k' , for the simulation with random noise (dashed line) and without noise (solid line). The left panel shows the total kinetic energy of the perturbation (for all modes). The panels on the right show the kinetic energy of the first six azimuthal normal modes. Notice that the vertical scale for the perturbation energy is not the same for plots corresponding to $m > 2$.

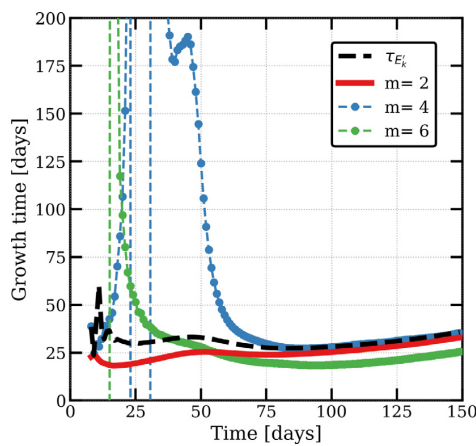


Fig. 5. Time evolution of the growth time (in days) of the total kinetic energy of the perturbation $\tau_{E_k'}$ (dashed line); and evolution of the growth time of the normal modes $\tau_{E_k^m}$ for mode 2 (red), 4 (blue) and 6 (green), for the simulation without noise.

3.2.2. Instability mechanism

The radial PV gradient $\partial_r Q$ is shown in Fig. 6. The horizontal change of sign of $\partial_r Q$ in the whole water column indicates that the structure may be barotropically unstable. At the center of the eddy, isopycnals outcrop (not shown), thus creating regions of high PV. Intersection lines between the surface and outcropping isopycnals are places of strong horizontal PV gradients. It can be seen in Fig. 6 at $z = -3$ m. This leads to a change of sign of $\partial_r Q$ in the vertical direction, between the surface and the interior PV gradients: the necessary condition for a Charney-type BC instability. The general stability conditions described by Pedlosky (1964), Eliassen (1983), Hoskins et al. (1985) and Ripa (1991), stating that

$$(u_\theta - \alpha)\partial_r Q < 0$$

and

$$N^2(\delta z_\rho)^2 > (u_\theta - \alpha)^2$$

in the whole domain, for any α , with δz_ρ the vertical displacement of isopycnals, are also not respected in the whole domain (not shown). All necessary conditions for BT or BC instabilities to occur are thus met. Such mixed BT/BC instabilities have already been observed in high resolution numerical simulations, in particular in the case of Meddy-like eddies, see for instance Ménesguen et al. (2018).

Here, while the instability is mainly BT, it is strengthened by a small baroclinic mode near the surface. The energy transfer terms (HRS, VRS and VBF) integrated along the horizontal directions are shown in

Fig. 7. During the growth of the instability, HRS and VBF dominate, confirming that the instability is both BT and BC as predicted by the structure of the PV profile (Fig. 6). The HRS term is deep reaching and shows that the BT instability dominates the formation of the tripole. This instability penetrates deeply, and drives the formation of the tripole in the whole water column during the first 100 days of the simulation. The structure of the tripole at depth can be seen in Fig. 3(d), with a strong barotropic component of the positive and negative poles, and an outer ring of positive vorticity (i.e. the spiral arms). The VBF term is maximum near the surface, at the interface between the SML and the interior. This suggests that the instability is intensified by a BC component at the surface. Maps of vertically integrated transfer terms are presented in Appendix A, in Fig. A.17. In summary, together Figs. 7 and A.17 show that the BC instability participates in forming intense spiral arms in the SML, while the BT instability leads to the deformation of the core of the eddy.

To understand the destabilization of the eddy, one can notice that the propagation of the unstable mode 2 is that of a Vortex Rossby wave (VRW), rotating around the eddy. This wave is supported by the radial gradient of PV of the eddy. This process is similar to planetary Rossby waves in the ocean, supported by the meridional PV gradient induced by the β -effect. The signature of the VRW in the simulation can be seen in the mode 2 component of the SSH. The VRW rotates about a quarter turn in 30 days (Fig. 8) giving $c_{VRW} = 0.05 \text{ rad days}^{-1}$. This value is consistent with the estimation of the phase speed of a baroclinic perturbation rotating around an unstable barotropic eddy in the quasi-geostrophic framework (see Appendix B). The mode 2 VRW exhibits different patterns depending on its position relative to the center of the eddy, see Fig. 9. It can be separated into two VRW rotating around the eddy at the same speed: an outer VRW (oVRW) at $r > 100$ km, and an inner VRW (iVRW) at $r < 100$ km. They are phase shifted. The oVRW is in advance compared to the iVRW. As these two waves interact, they amplify mutually, and the total perturbation rotating around the eddy grows (Flierl, 1988).

3.2.3. Critical level consequences

The presence of a critical level (CL) for mode 2 leads to an important frontogenesis at the edge of the eddy and in the spiral arms. As discussed in Nguyen et al. (2012), the azimuthal speed of the VRW which carry the perturbation is small compared to the maximal swirl angular velocity of the eddy. The critical level is thus located far from the center of the eddy, where its swirl velocity decreases outward (here on average at $r = 120$ km). This value was obtained during the linear stage, following the method described in Section 2.3.4. At the initial stage of the instability, for $t \sim 40$ –60 days, the perturbation is wrapped around the eddy in the form of long vorticity filaments near the critical level position (Fig. 10). At this time, the eddy is still mostly circular, since the radial velocity is weak. Then, the mode 2 component of radial velocity u_r' grows. It reaches a value of several kilometer per day (see Fig. 10). Since it is nearly in phase quadrature with the vorticity, this

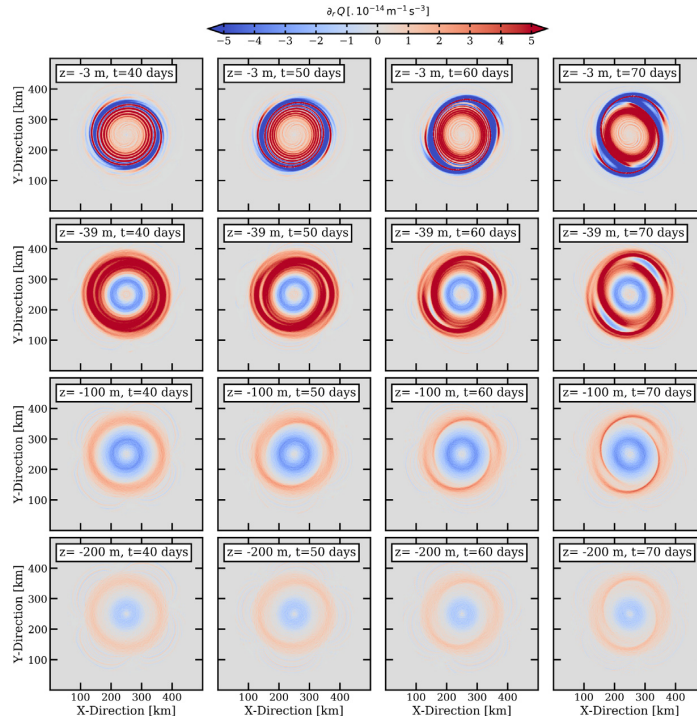


Fig. 6. Radial derivative of the PV at $t = 40, 50, 60,$ and 70 days (from left to right), at $3, 39, 100$ and 200 m depth (from top to bottom).

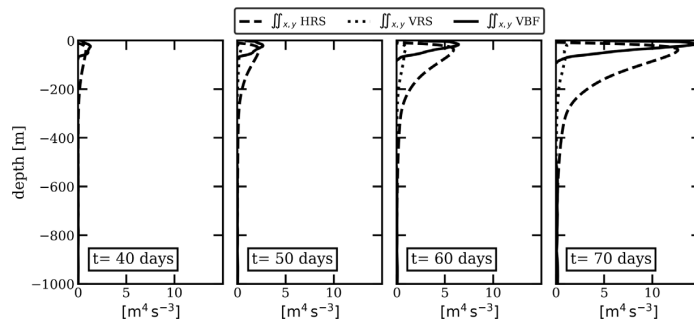


Fig. 7. Profiles of energy transfer terms integrated on the horizontal at $t = 40, 50, 60,$ and 70 days (from left to right). HRS, VRS, and VBF stand for Horizontal Reynolds Stress, Vertical Reynolds Stress, and Vertical Buoyancy Flux.

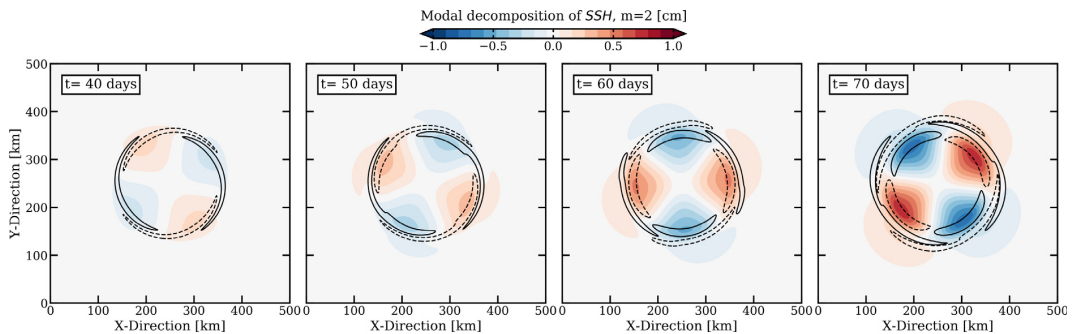


Fig. 8. Mode 2 of the SSH during the linear phase of the perturbation, at $t = 40, 50, 60,$ and 70 days. It shows the counter-clockwise rotation of the eddy Rossby Wave (VRW) around the eddy. This wave rotates of about a quarter turn in 30 days. We superposed the contours (± 0.02) of the mode 2 perturbation of normalized relative vorticity at the surface $\xi^{m=2}/f_0$.

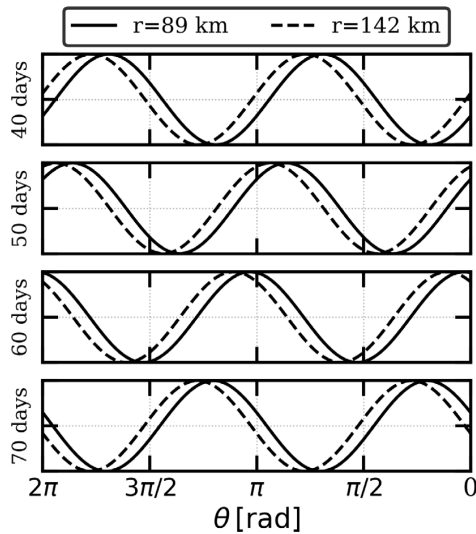


Fig. 9. Comparison between the phase of the outer VRW and the inner VRW, in the mode 2 component of the SSH. Solid (resp. dashed) black lines show cosinus with the phase of the mode 2 VRW at $r=89$ km (resp. 142 km) for the same times as in Fig. 8 (from top to bottom).

radial velocity perturbation leads to the ellipticization of the eddy, and to the creation of spiral arms around the eddy.

At $t \sim 100$ days, after the linear stage of the mode 2 perturbation, the eddy becomes elliptical, and two spiral arms form. These arms are very thin since they were initially elongated around the CL. Stretching dominates the flow at the edge of the eddy and in the spiral arms (Fig. 11 (a)). The flow generated by the primary instability thus forces the gradients to steepen, in particular, the buoyancy gradients. The frontogenesis function F associated with the buoyancy is computed at the surface and it is shown in Fig. 11(b). In the spiral arms and at the edges of the eddy, $-F$ is large. It reflects the steepening of the buoyancy gradients with time. Thus, the flow follows a frontal dynamic in these areas: the isopycnals outcrop and are very steep. Furthermore, the dynamical Rossby number $\epsilon = \zeta/f_0$ becomes locally larger than 1 (see Fig. 3), indicating that the circulation is mostly ageostrophic in these regions (Stegner and Dritschel, 2000). These observations are in agreement with the results of Nguyen et al. (2012) and Hua et al. (2013), who show that density gradients are enhanced at critical levels.

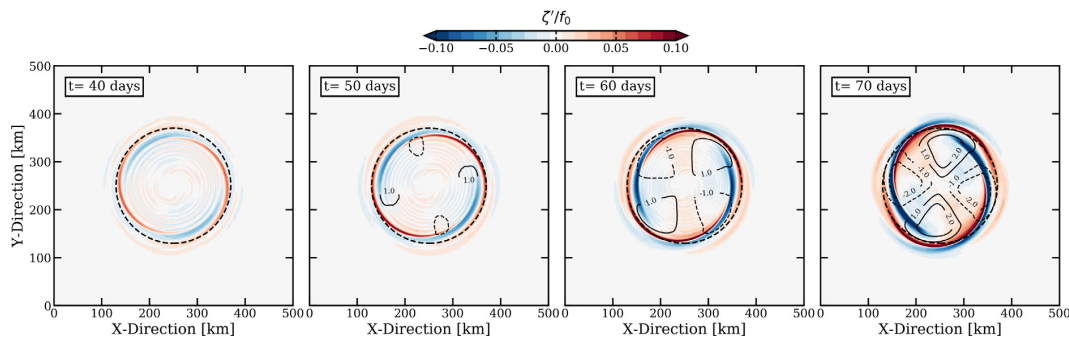


Fig. 10. Time evolution of the perturbation of relative vorticity at the surface, at $t = 40, 50, 60,$ and 70 days. Contours of the mode 2 component of the surface radial velocity $v_r^{m=2}$ for the values $-2, -1, 1,$ and 2 km day^{-1} are superposed. It shows that the perturbation of the radial velocity is nearly in phase quadrature with the vorticity. The position of the critical level for the mode 2 is shown with the dashed black circle, at $r = 120$ km.

3.3. Secondary instabilities and their impact on small scale structures

The primary BT/BC instability saturates at $t \sim 120$ days, after the initial monopole has evolved into a stable tripole; this tripole remains stable during the next 6 months of the simulation below the surface mixed layer. Inside the surface mixed layer, the intense frontogenesis leads to sharp fronts near the surface.

The small scale structures located in the surface mixed layer follow a Surface Quasi Geostrophic (SQG) dynamic. Because they have a small horizontal size, these surface features have a small vertical influence. Indeed, in the framework of the SQG model, following Isern-Fontanet et al. (2008), the streamfunction is $\Psi_{SQG} \propto e^{\frac{N_0 k}{f_0} z}$, where k is the horizontal wavenumber at the surface. The smaller horizontal scales decay in the vertical faster than larger ones. The vertical extension of surface structures scales as:

$$L_z = \frac{f_0 L}{2\pi N_0 f_0},$$

where L is the horizontal size of surface features and $N_0 \sim 10^{-2} \text{ s}^{-1}$ the typical stratification, leading to

$$L_z \sim 10^{-3} L.$$

In our case, filaments and submesoscale vortices which evolve at the surface have a size of $O(< 10)$ km. Therefore, they have a vertical influence over $O(< 10)$ m. This vertical scale applies to the stratified fluid below the surface mixed layer. It shows that the submesoscale is largely confined to the mixed layer, as it can be seen in Fig. 3 at $t \geq 100$ days.

3.3.1. Barotropic instability at the surface as a source of submesoscale

In the spiral arms, the steep PV gradients create favorable conditions for BT instability. BT instability occurs in a thin surface mixed layer in which the flow is confined, and leads to the destabilization of the spiral arms at $t \sim 110$ days. A mean PV section of a spiral arm (Fig. 12(b)) was computed by averaging 10 vertical sections at $t = 110$ days (Fig. 12(a)). The PV anomaly of the spiral arm is confined in the upper 10 m. The cross-filament derivative of the PV ($\partial_t Q$) changes sign along the section, signature of BT instability (Fig. 12(c)). Small ambient perturbations trigger instability, forming a row of small vortices of positive relative vorticity. The first ones appear at $t \sim 110$ days, at the tip of the arms. At $t \sim 130$ days, the whole arms destabilize (Fig. 12(a)), and evolve into a row of submesoscale vortices surrounding the main eddy (Fig. 3(c)). A few of the satellite vortices remain coherent for about 6 months. The energy transfer terms in the spiral arm are shown in Fig. A.18, see the calculation method in Section 2.3.2. It shows a strong signature of positive HRS in the arm when it becomes unstable, confirming that destabilization is due to a purely BT instability in the surface mixed layer. These observations show that BT instability of the spiral arms of

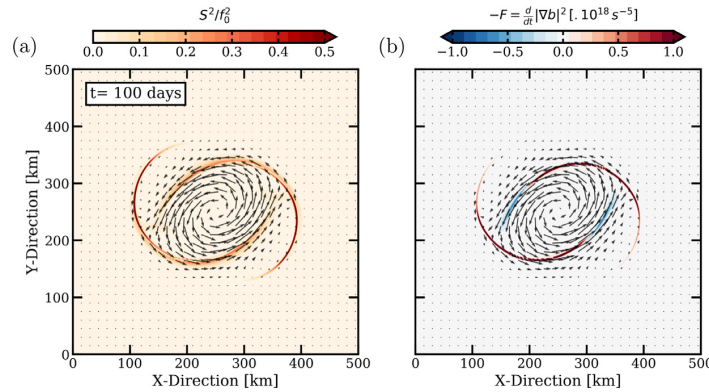


Fig. 11. Frontogenesis mechanism at $t = 100$ days. (a) Stretching at the surface normalized by the Coriolis frequency, and (b) opposite of the Frontogenesis function ($-F$) at the surface, reflecting the steepening of buoyancy gradients. The horizontal velocity at the surface is superposed in both panels.

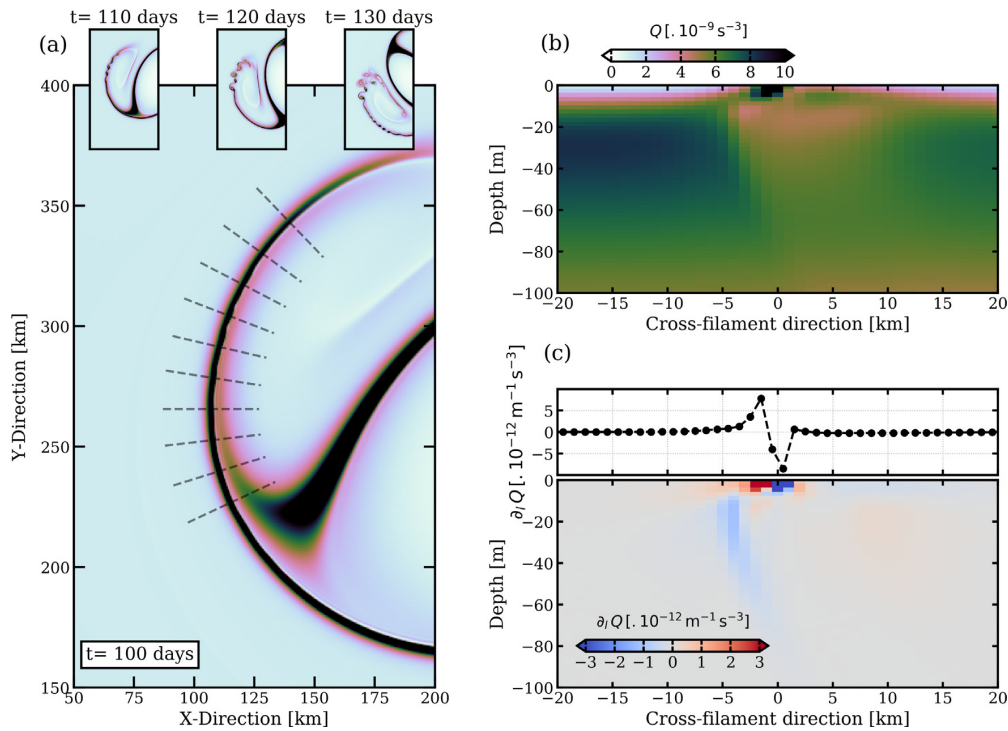


Fig. 12. (a) Snapshot of surface PV, at $t = 100$ days before the BT instability in the spiral arms. The domain shown is the western part of the eddy. Insets present snapshots of surface PV at $t = 110, 120$ and 130 days. (b) Mean vertical section of PV computed using 10 sections perpendicular to the spiral arm at $t = 100$ days (their position is indicated in (a) by the gray dashed lines). The colormap of (a) and (b) is the same. (c) Derivative of the PV along the axis of the section, at the surface (top), and in the first 100 meters (bottom).

a large unstable eddy is an efficient mechanism for the formation of submesoscale vortices.

To investigate the possibility of secondary instability to be triggered by grid-scale numerical noise, a sensitivity test was performed, adding a random noise in the simulation at $t = 90$ days. In this case, the arms destabilize slightly earlier, at $t = 105$ days, but in a similar way, still forming a row of small vortices. As for the primary instability of the vortex, the vorticity arms are intrinsically unstable.

At the edge of the eddy core, the cross-front PV gradient changes sign on the horizontal as well as on the vertical (not shown). Thus, the edge of the eddy is unstable with respect to a mixed BT/BC instability. Because the PV gradients are weaker, growth rates are slower than

observed in the arms. However, at $t \sim 150$ days, the small vortices generated around the eddy start to merge with the vortex edge, triggering instability. This is confirmed by large values of HRS and VBF at the edge, where the small eddies interact with the larger one (Fig. A.19). Then, a short wavelength elliptical VRW propagates around the eddy (see the deformation of the eddy's edge in Fig. 3(c)).

3.3.2. Evidence of symmetric instability at the edge of the eddy

A second phase of frontogenesis is triggered as the small scale VRW deforms the front at the edge of the eddy through intense stretching. Time evolution of the mean $-F$ at the surface is shown in Fig. 13(top). At $t = 160$ days, steepening of the buoyancy gradient starts to increase

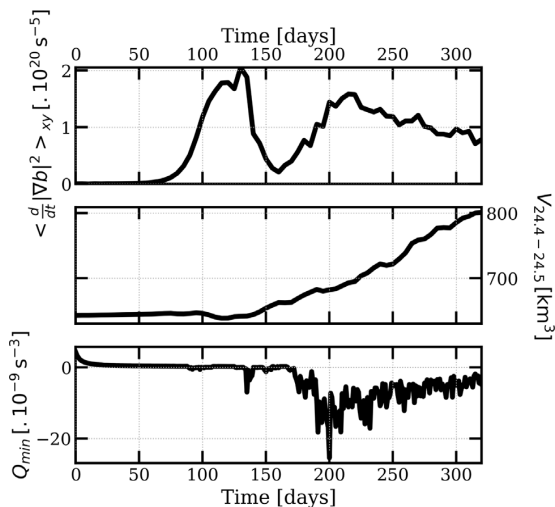


Fig. 13. Time evolution of (top) the average of $-F(u, b) = \frac{d}{dt} |\nabla b|^2$ at the surface, (middle) the volume between the $\rho = 1024.4 \text{ kg m}^{-3}$ and the $\rho = 1024.5 \text{ kg m}^{-3}$ isopycnals, and (bottom) the minimum of PV in the domain.

for a second time. The second and third terms of the PV (in Eq. (2)) become very intense locally, see e.g. Fig. 14(bottom). Indeed, the variations of velocity are localized at the surface, and variations of buoyancy occur at scales of $O(1)$ km. These terms are negative and of the same order of magnitude as the first term of the PV, see Fig. 14(middle), leading to a PV close to zero where the fronts are sharp (Fig. 14(top)).

The horizontal buoyancy variations occur at very fine scales (see the contours of $-F$ at $t = 180$ days in Fig. 14(bottom)). The circulation at

the edge of the eddy becomes strongly ageostrophic from $t \sim 160$ days, leading to diapycnal mixing at the edge of the eddy. The latter acts in decreasing stratification, leading to a PV sign change. In our model, since diapycnal mixing is parameterized through the KPP-scheme, we do not attempt to characterize it, and rather focus our attention on the dynamical processes resulting of the diapycnal mixing.

A first explanation for the decrease of the PV due to diapycnal mixing can be found by introducing changes of buoyancy in the expression of the PV. We present in Appendix C how the PV sign can change if it is initially close to zero.

A second explanation can be found in the integral formulation of the impermeability theorem derived in Haynes and McIntyre (1990) and discussed in Morel and McWilliams (2001):

$$\frac{d}{dt} \iiint_{\Omega} d\Omega \Delta Q = -f \frac{d\Omega}{dt}, \quad (21)$$

where Ω is a domain with periodic boundary conditions or with no normal flow (our case here), $d\Omega$ a volume element, ΔQ the PV anomaly with respect to the PV background, and $\frac{d\Omega}{dt}$ the volume variations of the layer. This formulation states that the bulk integral of the PV anomaly can only be changed by a loss or a gain of the volume inside a layer comprised between two isopycnals. At $t \sim 120$ days, the frontogenesis at the edge of the eddy has led to an isopycnal steepening at the surface. In particular, the layer between the $\rho = 1024.4 \text{ kg m}^{-3}$ and the $\rho = 1024.5 \text{ kg m}^{-3}$ isopycnals is thin, and slopes very steeply toward the surface. This specific layer is chosen because it represents isopycnals outcropping at the edge of the eddy. Then, after the destabilization of the eddy edge and diapycnal mixing, this layer has become thicker, and the front is less steep, see Appendix D, Fig. D.20. Following Eq. (21), this change of thickness leads to the decrease of the bulk integral of the PV, which explains the decrease of local PV, and the formation of negative PV. In Fig. 13, we present the time evolution of this layer volume. It is fairly consistent with the appearance of negative PV.

The presence of locally negative PV, along with an examination of the Richardson number show that the edge of the eddy is subject to

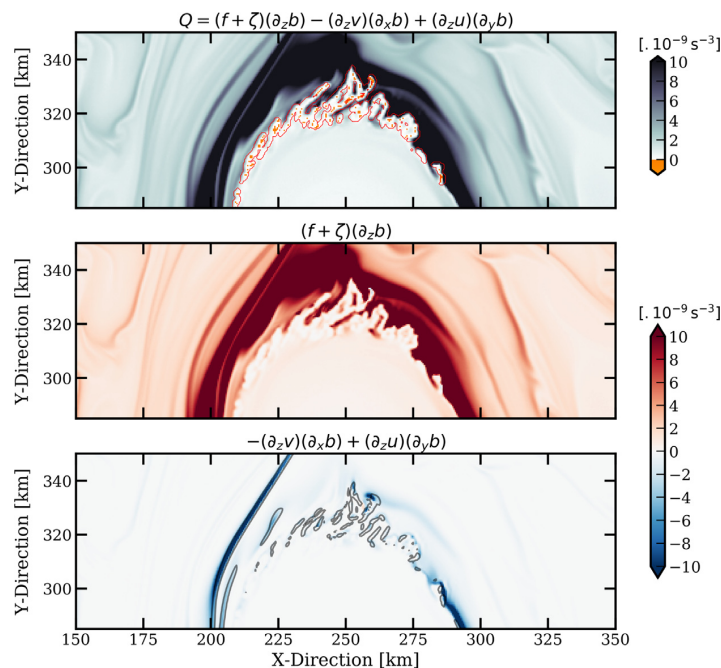


Fig. 14. Decomposition of the PV at $t = 180$ days, at the northern part of the eddy. (top) PV at the surface; the yellow indicates places where the PV is negative, and the red lines indicate regions where the criterion for SI to occur $Ri < Ri_c$ is respected. (middle) First term of the PV. (bottom) Second and third terms of the PV; contours of $-F = 10^{-18} \text{ s}^{-5}$ are superposed as gray thin lines.

SI. The area where $Ri < Ri_c$ is indicated in Fig. 14(top). In this area, the PV of the geostrophic flow is negative. When the PV changes sign, due to the second and third terms in Eq. (2), SI develops. From $t \sim 160$ days, the edge of the eddy thus becomes strongly deformed by vorticity changes over scales of $O(1)$ km. SI then propagates inward. At the end of the simulation, at $t = 300$ days, the SI pattern is present in the whole core of the eddy, at the surface, see Fig. 3(d).

4. Sensitivity study

We have performed other simulations to study the sensitivity of our results to the numerical setup. Hereafter, the ‘reference simulation’ refers to the simulation on the f -plane, with a cyclonic eddy, $\Delta x = 1$ km, 256 vertical levels, and the numerical settings discussed in Section 2.2. All the sensitivity tests are performed by varying one or several of these parameters. The details of these simulations are not shown in this paper, but we mention their most salient features.

Firstly, we changed the numerical settings of the model. Changing the horizontal advection scheme to a third-order upwind advection scheme (UP3) leads to a larger implicit viscosity, and the fronts at the surface are less intense and become unstable later than in the reference run. Fewer small vortices result from the instability and they are less intense. If we remove the KPP-scheme parameterization in the interior, an important noise appears at $t \sim 30$ days because of a lack of vertical turbulent closure. The sensitivity on the boundary conditions has been tested by running the model in a larger domain (1000×2000 km) with the eddy initialized at $(x_0, y_0) = (400, 300)$ km. This does not affect the dynamics of the eddy.

Secondly, we performed the reference simulation with a flat bottom at 4000 m with the same number and stretching of vertical levels. This does not affect the primary instabilities (the growth of mode 2 and the formation of row of small vortices), showing that a bottom at 1500 m is sufficient to describe the dynamic of the eddy. However, the SI occurs 30 days earlier. This is due to the fact that the spacing between the vertical levels is larger than in the reference run. The $\Delta x/\Delta z$ ratio is not close enough to N/f_0 , and the frontal dynamic is not well resolved.

Thirdly, we tested the cyclone–anticyclone asymmetry. We initialized the opposite composite density anomaly and recalculated the temperature and the velocity fields associated with it. This produces a warm core anticyclonic eddy. We put this structure in the same stratification as for the reference simulation, and we ran the model. We observed a different evolution than for the cyclonic case. At $t = 100$ days, the anticyclone was still stable, and its horizontal shape was similar to its initial shape. An azimuthal mode 2 then grew, as in the cyclonic case. It led to the formation of a tripole with spiral arms at $t \sim 280$ days. Then, the arms also became unstable and formed submesoscale vortices of negative relative vorticity. For the anticyclone, the growth of the perturbation was much slower than for the cyclone. Furthermore, the two satellites in the formed tripole were smaller than in the reference simulation. This asymmetry can be explained as follows. Considering the cyclogeostrophic balance, a cyclone and an anticyclone cannot have both antisymmetric velocity and density anomalies. Here, we initialized the anticyclone with the density anomaly. Thus, its swirling velocity was smaller than that of the cyclone, and the initial anticyclone had a weaker kinetic energy. In Stegner and Dritschel (2000), a comparison between the shape of tripoles obtained from the destabilization of a cyclone and an anticyclone can be seen in their Fig. 7.

Finally, we performed the reference simulation, but now on a β -plane, with $\beta = 2.1 \cdot 10^{-11} \text{ m}^{-1} \text{ s}^{-1}$ (the mean value of β in the area of the composite eddy). The primary instability of the eddy strongly differs from the f -plane simulations. After 20 days of simulation, the eddy starts drifting northwestward, with a trailing Rossby wave wake. The evolution of the eddy is similar to that shown in Fig. 3 of McWilliams et al. (1986). Then, mode 2 grows. At $t \sim 70$ days, two asymmetric arms are present around the initial eddy. They become unstable similarly as in the reference simulation, creating submesoscale vortices around the initial eddy.

5. Discussion

5.1. On the stability of the composite eddy

In this paper, we studied the stability of a composite cyclone as revealed by Argo floats in the northern Arabian Sea. With this simulation, we were able to study numerous kinds of instabilities, thanks to very high horizontal and vertical resolutions.

First, we observed that a deep azimuthal mode 2 barotropic instability deforms the eddy, which eventually evolves into a tripole after about 4 months of simulation. This kind of instability has already been observed for specific 2D analytical barotropic shielded vortices (Carton and McWilliams, 1989; Stegner and Dritschel, 2000), 3D meddy-like eddies (Yim and Billant, 2015; Meunier et al., 2015; Ménesguen et al., 2018), or surface eddies (Meunier et al., 2019). We show that in the vicinity of a realistic eddy intensified at the surface, azimuthal mode 2 perturbation is the main driver for its deformation.

Second, we showed that a baroclinic instability together with the presence of a critical level for the most unstable mode is the main cause for the generation of a highly ageostrophic flow around the eddy. This generates sharp fronts in the surface mixed layer where the Rossby number is large ($\epsilon > 1$).

Third, these fronts become unstable to a barotropic instability in the surface mixed layer. This leads to the generation of submesoscale cyclones and filaments. This highlights the predominance of secondary instabilities in the evolution of isolated eddies.

Finally, our results indicate that symmetric instability may be ubiquitous in large oceanic vortices, even cyclonic ones. Indeed, for small Bu vortices, the critical level is located near the edge of the eddy (Nguyen et al., 2012) where energy is concentrated. This leads to the formation of intense fronts. Near these fronts, a strongly imbalanced circulation occurs, and yields diapycnal mixing. As previously observed in the context of idealized simulations (Nadiga, 2014; Brannigan et al., 2017), this causes PV to change sign locally, and SI develops at the edge of the cyclonic eddy. This happens when the edge of the eddy becomes unstable due to the interaction between submesoscale vortices and the large eddy. It highlights the fact that in the real ocean the interactions between small scale features and large mesoscale eddies may play a key role in the stability of the latter.

Previous studies considering analytical vortices showed that when a vortex is unstable, it may break into smaller vortices, depending on its initial profile (Carton et al., 1989; Stegner and Dritschel, 2000). A major result of this study is that even if instabilities occur, the composite eddy is not destroyed and remains as a large scale coherent structure for the last 6 months of the simulation, similar to specific kind of analytical vortices (Hua et al., 2013; Ménesguen et al., 2018). The composite re-stabilizes into a tripolar structure for which the positive vorticity pole is slightly elliptical but coherent.

5.2. On the detectability of eddy instabilities

To infer the detectability in altimeter products of the series of instabilities described in this paper, we computed the SSH signature of the eddy at the beginning and at the end of the simulation, using a downgraded resolution similar to the one of the altimetric product (Fig. 15). The signature of the tripole at the end of the simulation is that of an elliptical cyclonic eddy, of ellipticity $e = 0.72$. The difference between the tripole and the initial cyclone is very weak, with variations of SSH of $O(1)$ cm, which is of the order of magnitude of the formal error induced by the spatio-temporal interpolation of altimetric products (see Appendix A in de Marez et al. (2019)). This indicates that the tripolar structures often observed in numerical studies may be present in the ocean but may not be observed due to the coarse resolution of the altimetry.

The mean ellipticity of eddies used to compute the composite was on average 0.75. The cyclone at the end of the simulation thus has

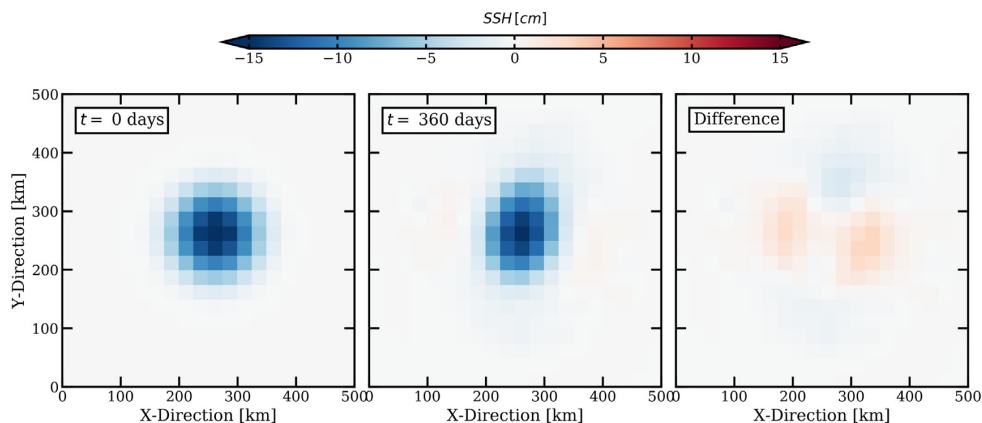


Fig. 15. SSH signature of the eddy at initialization (left), at the end of the simulation ($t = 360$ days) (middle), and the difference between the two. The resolution of the plot is downgraded to the same resolution as the altimetric product used to generate the composite eddy.

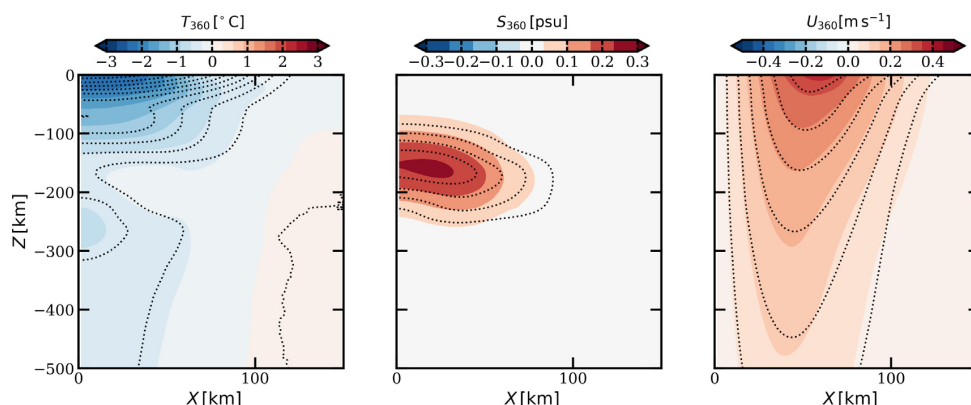


Fig. 16. Comparison between the azimuthal average of the final form of the eddy (at $t = 360$ days) and the composite. Color contours are azimuthal averages of the final eddy while black dashed contours indicate the same contours for the initial eddy.

an ellipticity comparable with the ellipticity of eddies observed in altimetric products, which were used to compute the composite. Since the composite was computed assuming axisymmetry, it is of interest to assess the impact of this hypothesis on the final state of the modeled eddy, by computing an azimuthal average (Fig. 16). The differences between the initialization and the final form act over scale of $O(10)$ km on the horizontal and $O(10)$ m on the vertical. Considering the very coarse resolution of the dataset available to study the 3D structure of eddies (e.g $O(10)$ km for the altimetric product and $O(10)$ m for Argo floats), and the error implied by the composite method $O(1 - 5)$ km (Chaigneau et al., 2011), these differences cannot be seen with *in situ* data.

The small scale features we observe during the secondary instabilities can be observed qualitatively on snapshots of true color (Lévy et al., 2018) or of sea surface temperature (Buckingham et al., 2017). However, no altimetric product allowing to predict the dynamical quantities at this resolution is currently available. This means that neither the primary instability nor the secondary instabilities can be clearly captured in a systematic way using the currently available altimetric and floats data. Considering SSH only, the composite eddy we studied evolves little, and fairly represents the eddy observed in the altimetry which can live for several months.

Declaration of competing interest

The authors declare that they have no known competing financial interests or personal relationships that could have appeared to influence the work reported in this paper.

CRediT authorship contribution statement

Charly de Marez: Conceptualization, Methodology, Software, Writing - original draft. **Thomas Meunier:** Conceptualization, Methodology, Writing - review & editing. **Mathieu Morvan:** Software, Writing - review & editing. **Pierre L'Hégaret:** Writing - review & editing. **Xavier Carton:** Writing - review & editing, Supervision, Funding acquisition.

Acknowledgments

This work was funded by the Direction Générale de l'Armement (DGA), France via a full grant for Charly de Marez's PhD. This work is also a contribution to PRC 1069 'Meso and submesoscale vortices in the Atlantic and Indian Ocean', funded by CNRS, France and RFBR, Russia. Simulations were performed using the HPC facilities DATARMOR of 'Pôle de Calcul Intensif pour la Mer' at Ifremer, Brest, France. The authors thank N. Lahaye for helpful discussions, and the two anonymous

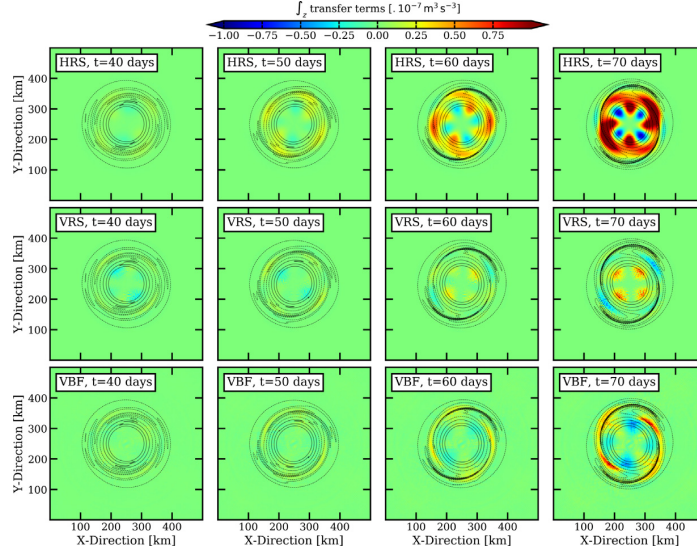


Fig. A.17. Snapshots of energy transfer terms integrated on the vertical at $t = 40, 50, 60,$ and 70 days (from left to right). HRS, VRS, and VBF stand for Horizontal Reynolds Stress, Vertical Reynolds Stress, and Vertical Buoyancy Flux.

reviewers whose remarks improved the contents of this paper. Model output is available upon request.

Appendix A. Maps of energy transfer terms

See Figs. A.17–A.19.

Appendix B. Estimating the phase velocity of the perturbation in the QG approximation

To estimate the value of the phase velocity of the mode 2 perturbation, one can use the framework of the continuously stratified quasi-geostrophic (QG) model (Vallis, 2017). We consider a mean state which is a circular barotropic eddy of azimuthal velocity U_θ and potential vorticity \bar{q} . We introduce a perturbation in the form of a normal mode, of potential vorticity q' and current function ψ' . Linearizing the system around the mean state gives (Pedlosky, 2013):

$$(U_\theta - c)q' - \psi' \bar{q}_r = 0 \quad (\text{B.1})$$

where c is the azimuthal velocity of the perturbation and \bar{q}_r is the radial derivative of \bar{q} . The potential vorticity of the perturbation is

$$q' = \Delta \psi' + \frac{f_0^2}{N_0^2} \partial_z \psi' = L \psi'. \quad (\text{B.2})$$

N_0 is the ambient stratification of the flow, which is in our case $\sim 10^{-2} \text{ s}^{-1}$. Using (B.1) and (B.2), the azimuthal velocity of the perturbation can be expressed as:

$$c = U_\theta - \frac{\psi' \bar{q}_r}{L \psi'}. \quad (\text{B.3})$$

For our purpose, we only discuss the order of magnitude of the velocity of the perturbation, which is:

$$c \sim U_\theta - \frac{\bar{q}_r}{\alpha}, \quad (\text{B.4})$$

where α approximates the operator L such as:

$$\alpha = \underbrace{\frac{4\pi^2}{R^2} + \left(\frac{m}{R}\right)^2}_{\alpha_{BT}} + \underbrace{\frac{f_0^2}{h N_0^2}}_{\alpha_{BC}}, \quad (\text{B.5})$$

with m the azimuthal mode of the perturbation, $R \sim 100$ km the radius of the eddy and $h \sim 50$ m the typical scale of variation of the perturbation. The first two terms (α_{BT}) represent the barotropic perturbation, while the third one (α_{BC}) corresponds to the vortex stretching induced by the baroclinicity of the flow.

In the case we study here, $\bar{q}_r \sim \frac{U_\theta^{max}}{(R/2)^2}$, with $U_\theta^{max} \sim 0.5 \text{ m s}^{-1}$ the value of U_θ at $\sim R/2$. This gives $\bar{q}_r \sim 2 \cdot 10^{-10} \text{ m}^{-1} \text{ s}^{-1}$, $\alpha_{BT} \sim 1.4 \cdot 10^{-9} \text{ m}^{-2}$ and $\alpha_{BC} \sim 5 \cdot 10^{-9} \text{ m}^{-2}$. At the edge of the eddy, $U_\theta \sim 0.1 \text{ m s}^{-1}$. Using Eq. (B.4) gives an estimation of the phase velocity $c \sim 0.06 \text{ m s}^{-1}$. This corresponds to a velocity of $0.06 \text{ rad days}^{-1}$, which is in fairly good agreement with the phase velocity computed in the simulation, and seen in Fig. 8. Notice that this estimation of the phase velocity depends on the values chosen for each quantity, and does not take into account the baroclinicity of the mean flow. However, it shows that to obtain a proper estimation, we need to consider both the BT and the BC components of the perturbation.

Appendix C. How can diapycnal mixing change the sign of the PV?

As pointed in Morel and McWilliams (2001), ‘when mixing does occur, it is not easy to predict the change of the PV for a fluid parcel’. Using the Ertel form of the PV, we assess here how can diapycnal mixing change the sign of the PV.

In the case of a front localized at the edge of an axisymmetric eddy, with no radial velocity, one can write the PV in polar coordinates as:

$$Q = \zeta_a \partial_z b + (\partial_z u_\theta)(\partial_r b),$$

with $\zeta_a = \zeta + f_0$. If we consider the Thermal Wind Balance, this becomes

$$Q = \zeta_a \partial_z b - f^{-1} (\partial_r b)^2.$$

We study the variations of PV when the buoyancy is modified by diapycnal mixing. We introduce $\Delta_z b$ and $\Delta_r b$ the variations of buoyancy respectively along the z and r axis. The value of Q may thus be approximated by:

$$Q = \frac{\Delta_z b}{\Delta z} \zeta_a - f^{-1} \left(\frac{\Delta_r b}{\Delta r}\right)^2. \quad (\text{C.1})$$

If diapycnal mixing occurs, the gradients of buoyancy diminish along the z -axis and/or the r -axis. In terms of variations of buoyancy, we thus

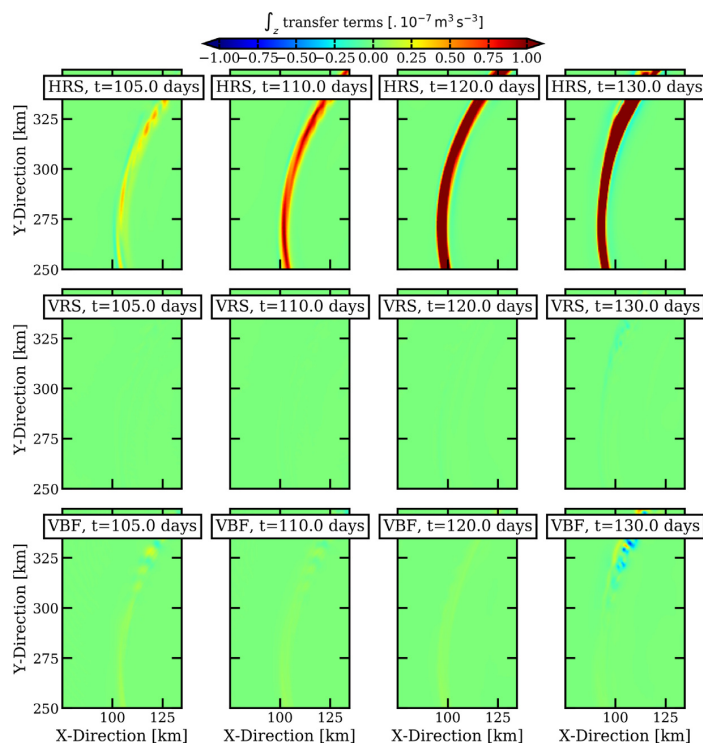


Fig. A.18. Snapshots of energy transfer terms integrated on the vertical, zoom on the left spiral arm which becomes unstable, at $t = 105, 110, 120,$ and 130 days (from left to right).

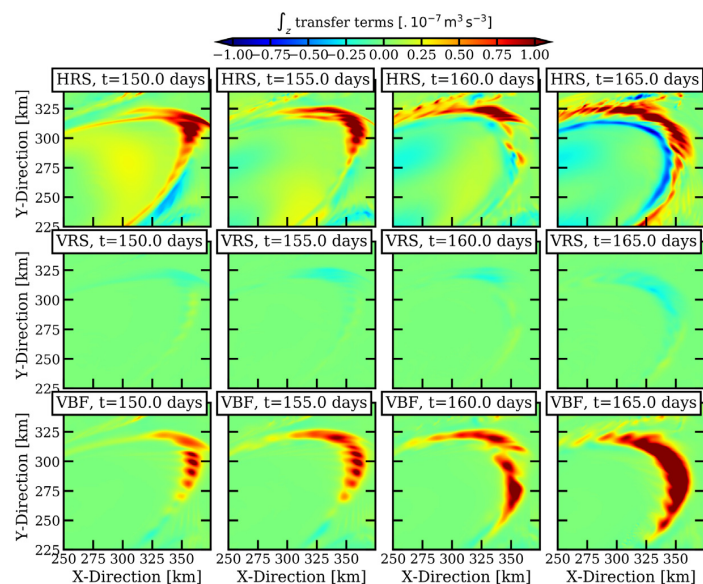


Fig. A.19. Snapshots of energy transfer terms integrated on the vertical, zoom on the edge of the eddy which becomes unstable, at $t = 150, 155, 160,$ and 165 days (from left to right).

have

$$\begin{cases} \Delta_z b \rightarrow \Delta_z b - b_z * \\ \Delta_r b \rightarrow \Delta_r b - b_r * \end{cases} \quad (C.2)$$

where $b_r, * > 0$ and $b_z, * > 0$ are the variations of buoyancy induced by the diapycnal mixing. They are positive since diapycnal mixing leads to a decrease of the variations of buoyancy. We assume here that during the time in which diapycnal mixing occurs, the flow does not vary, and

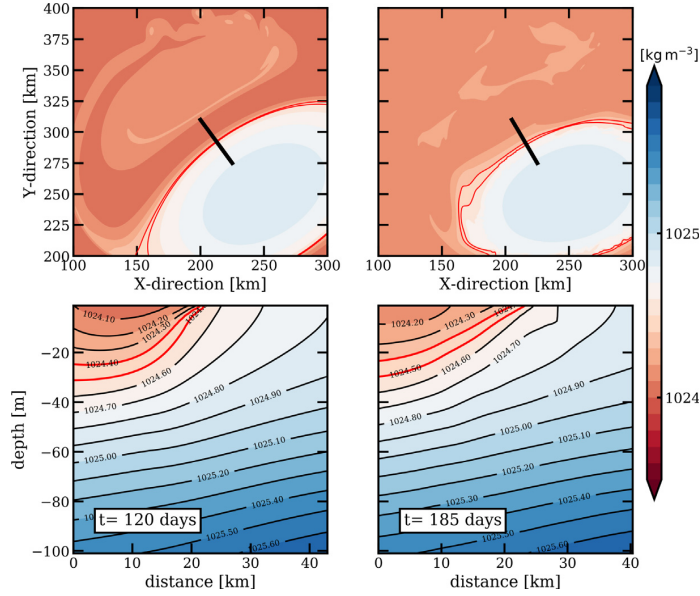


Fig. D.20. (top) Snapshots of density at the surface at $t = 120$ days (left) and $t = 185$ days (right). (bottom) Vertical sections of density at $t = 120$ days (left) and $t = 185$ days (right), their position is shown by the black thick lines in the top panels. Red contours indicate the isopycnals surrounding the layer we discuss, for which we compute the volume shown in Fig. 13.

Table C.1

Summary of the sign that can take ΔQ . CE and AE designate cyclonic and anticyclonic flow; vert. and horiz. indicate cases where the mixing only occurs on the vertical direction or the horizontal direction; ? indicates that the sign of ΔQ depends on the relative importance of the different terms.

	ΔQ_1	ΔQ_2	ΔQ_3	ΔQ
CE	< 0	< 0	> 0	?
AE	> 0	< 0	< 0	?
CE vert.	< 0	= 0	= 0	< 0
AE vert.	> 0	= 0	= 0	> 0
CE horiz.	= 0	< 0	> 0	?
AE horiz.	= 0	< 0	< 0	< 0

ζ_a thus remains constant. This strong assumption is not true at long times, when the new circulation is adjusted, but it allows to keep the calculation and the reasoning simple.

We define Q^* as the PV value after the diapycnal mixing. Introducing the new buoyancy variations (C.2) in the expression of the PV (C.1) gives:

$$Q^* = \underbrace{\frac{\Delta_z b}{\Delta z} \zeta_a - f^{-1} \left(\frac{\Delta_r b}{\Delta r} \right)^2}_{Q} - \frac{b_z^*}{\Delta z} \zeta_a - f^{-1} \left(\frac{b_r^*}{\Delta r} \right)^2 + 2f^{-1} \frac{\Delta_r b b_r^*}{(\Delta r)^2}.$$

The two first terms on the right hand side are the PV before the diapycnal mixing. We then define $\Delta Q = Q^* - Q$, the variation of PV during the diapycnal mixing. It is expressed such as:

$$\Delta Q = \underbrace{-\frac{b_z^*}{\Delta z} \zeta_a}_{\Delta Q_1} - \underbrace{f^{-1} \left(\frac{b_r^*}{\Delta r} \right)^2}_{\Delta Q_2} + \underbrace{2f^{-1} \frac{\Delta_r b b_r^*}{(\Delta r)^2}}_{\Delta Q_3}.$$

If the vorticity in the flow is positive, and if it is located in the northern hemisphere, $\zeta_a > 0$. Thus, both ΔQ_1 and ΔQ_2 are strictly negative. The sign of ΔQ_3 depends on the sign of $\Delta_r b$. In the case of a front leading to a positive velocity along the θ -axis (e.g at the edge of a cyclone), the buoyancy gradients along the r -direction are positive. Then, $\Delta Q_3 > 0$ and the sign of ΔQ thus depends on the relative

importance of its terms. The sign of ΔQ thus depends on the scale of variations and the values of the gradients. For instance, in a case where the mixing only occurs on the vertical, $b_r^* = 0$. The variation of PV thus reduces to $\Delta Q = \Delta Q_1 < 0$. In this case, the PV decreases. If before the mixing it was already close to 0, the decrease of the PV can thus lead to the generation of negative PV where the fluid has been mixed. A summary of the possible sign that ΔQ can take depending on the direction of the current, and the direction of the mixing is shown in Table C.1.

Appendix D. Section of the front at the edge of the eddy

See Fig. D.20.

References

- Al Saafani, M.A., Shenoi, S.S.C., Shankar, D., Aparna, M., Kurian, J., Durand, F., Vinayachandran, P.N., 2007. Westward movement of eddies into the Gulf of Aden from the Arabian Sea. *J. Geophys. Res.* 112, C11. <http://dx.doi.org/10.1029/2006JC004020>.
- Armi, L., Hebert, D., Oakey, N., Price, J.F., Richardson, P.L., Rossby, H.T., Ruddick, B., 1989. Two years in the life of a Mediterranean salt lens. *J. Phys. Oceanogr.* 19, 354–370. [http://dx.doi.org/10.1175/1520-0485\(1989\)019<0354:TYITLO>2.0.CO;2](http://dx.doi.org/10.1175/1520-0485(1989)019<0354:TYITLO>2.0.CO;2).
- Bell, M.J., 2018. Reduction of the linear stability problem for general zonal flows with any Rossby and Richardson numbers to a PDE. *Q. J. R. Meteorol. Soc.* 144, 2260–2276. <http://dx.doi.org/10.1002/qj.3352>.
- Brannigan, L., Marshall, D.P., Naveira Garabato, A.C., Nurser, A.J.G., Kaiser, J., 2017. Submesoscale instabilities in mesoscale eddies. *J. Phys. Oceanogr.* 47, 3061–3085. <http://dx.doi.org/10.1175/JPO-D-16-0178.1>.
- Bretherton, F.P., 1966. Critical layer instability in baroclinic flows. *Q. J. R. Meteorol. Soc.* 92, 325–334. <http://dx.doi.org/10.1002/qj.49709239302>.
- Buckingham, C.E., Khaleel, Z., Lazar, A., Martin, A.P., Allen, J.T., Naveira Garabato, A.C., Thompson, A.F., Vic, C., 2017. Testing Munk's hypothesis for submesoscale eddy generation using observations in the North Atlantic. *J. Geophys. Res. Ocean.* 122, 6725–6745. <http://dx.doi.org/10.1002/2017JC012910>.
- Carton, X.J., Flieri, G.R., Polvani, L.M., 1989. The generation of tripoles from unstable axisymmetric isolated Vortex structures. *Europhysics Letters (EPL)* 9, 339–344.
- Carton, X., McWilliams, J., 1989. Barotropic and baroclinic instabilities of axisymmetric vortices in a quasigeostrophic model. *Elsevier Oceanography Series*, vol. 50, 225–244. [http://dx.doi.org/10.1016/S0422-9894\(08\)70188-0](http://dx.doi.org/10.1016/S0422-9894(08)70188-0).

- Chaigneau, A., Le Texier, M., Eldin, G., Grados, C., Pizarro, O., 2011. Vertical structure of mesoscale eddies in the eastern South Pacific Ocean: A composite analysis from altimetry and Argo profiling floats. *J. Geophys. Res.* 116, C11. <http://dx.doi.org/10.1029/2011JC007134>.
- Chelton, D.B., deSzoeke, R.A., Schlax, M.G., El Naggar, K., Siwertz, N., 1998. Geographical variability of the first baroclinic rossby radius of deformation. *J. Phys. Oceanogr.* 28, 433–460. [http://dx.doi.org/10.1175/1520-0485\(1998\)028<0433:GVOTFB>2.0.CO;2](http://dx.doi.org/10.1175/1520-0485(1998)028<0433:GVOTFB>2.0.CO;2).
- Chelton, D.B., Gaube, P., Schlax, M.G., Early, J.J., Samelson, R.M., 2011. The influence of nonlinear mesoscale eddies on near-surface oceanic chlorophyll. *Science* 334, 6054. <http://dx.doi.org/10.1126/science.1208897>.
- de Marez, C., L'Hégaret, P., Morvan, M., Carton, X., 2019. On the 3D structure of eddies in the Arabian Sea. *Deep-Sea Res. I* 150, 103057. <http://dx.doi.org/10.1016/j.dsri.2019.06.003>.
- Dong, C., McWilliams, J.C., Liu, Y., Chen, D., 2014. Global heat and salt transports by eddy movement. *Nature Commun.* 5, 3294. <http://dx.doi.org/10.1038/ncomms4294>.
- Eliassen, A., 1983. The charney—stern theorem on barotropic—baroclinic instability. In: *Instabilities in Continuous Media*. pp. 563–572. http://dx.doi.org/10.1007/978-3-0348-6608-8_11.
- Fjørtoft, R., 1950. Application of Integral Theorems in Deriving Criteria of Stability for Laminar Flows and for the Baroclinic Circular Vortex. Grøndahl & søns boktr., I kommisjon hos Cammermeyers boghandel.
- Flierl, G.R., 1988. On the instability of geostrophic vortices. *J. Fluid Mech.* 197, 349–388. <http://dx.doi.org/10.1017/S0022112088003283>.
- Gent, P.R., McWilliams, J.C., 1986. The instability of barotropic circular vortices. *Geophys. Astrophys. Fluid Dyn.* 35, 209–233. <http://dx.doi.org/10.1080/03091928608245893>.
- Gula, J., Molemaker, M.J., McWilliams, J.C., 2015. Gulf stream dynamics along the southeastern U.S. seaboard. *J. Phys. Oceanogr.* 45, 690–715. <http://dx.doi.org/10.1175/JPO-D-14-0154.1>.
- Gula, J., Molemaker, M.J., McWilliams, J.C., 2016. Topographic generation of submesoscale centrifugal instability and energy dissipation. *Nature Commun.* 7, 12811. <http://dx.doi.org/10.1038/ncomms12811>.
- Halo, I., Backeberg, B., Penven, P., Ansonge, L., Reason, C., Ullgren, J., 2014. Eddy properties in the Mozambique channel: A comparison between observations and two numerical ocean circulation models. *Deep-Sea Res. II* 100, 38–53. <http://dx.doi.org/10.1016/j.dsr2.2013.10.015>.
- Haynes, P.H., McIntyre, M.E., 1990. On the conservation and impermeability theorems for potential vorticity. *J. Atmos. Sci.* 47, 2021–2031. [http://dx.doi.org/10.1175/1520-0469\(1990\)047<2021:OITCAIT>2.0.CO;2](http://dx.doi.org/10.1175/1520-0469(1990)047<2021:OITCAIT>2.0.CO;2).
- Hoskins, B.J., 1974. The role of potential vorticity in symmetric stability and instability. *Q. J. R. Meteorol. Soc.* 100, 480–482. <http://dx.doi.org/10.1002/qj.49710042520>, URL: <http://doi.wiley.com/10.1002/qj.49710042520>.
- Hoskins, B., 1982. The mathematical theory of frontogenesis. *Annu. Rev. Fluid Mech.* 14, 131–151. <http://dx.doi.org/10.1146/annurev.fl.14.010182.001023>.
- Hoskins, B.J., McIntyre, M.E., Robertson, A.W., 1985. On the use and significance of isentropic potential vorticity maps. *Q. J. R. Meteorol. Soc.* 111, 877–946. <http://dx.doi.org/10.1002/qj.49711147002>.
- Hua, B.L., Ménesguen, C., Le Gentil, S., Schopp, R., Marsset, B., Aiki, H., 2013. Layering and turbulence surrounding an anticyclonic oceanic vortex: in situ observations and quasi-geostrophic numerical simulations. *J. Fluid Mech.* 731, 418–442. <http://dx.doi.org/10.1017/jfm.2013.369>.
- Isern-Fontanet, J., Lapeyre, G., Klein, P., Chapron, B., Hecht, M.W., 2008. Three-dimensional reconstruction of oceanic mesoscale currents from surface information. *J. Geophys. Res. Ocean.* 113, C9. <http://dx.doi.org/10.1029/2007JC004692>.
- Keppeler, L., Cravatte, S., Chaigneau, A., Pegliasco, C., Gourdeau, L., Singh, A., 2018. Observed characteristics and vertical structure of mesoscale eddies in the southwest Tropical Pacific. *J. Geophys. Res. Ocean.* 123, 2731–2756. <http://dx.doi.org/10.1002/2017JC013712>.
- Klein, P., Hua, B.L., Lapeyre, G., Capet, X., Le Gentil, S., Sasaki, H., 2008. Upper ocean turbulence from high-resolution 3D simulations. *J. Phys. Oceanogr.* 38, 1748–1763. <http://dx.doi.org/10.1175/2007JPO3773.1>.
- Large, W.G., McWilliams, J.C., Doney, S.C., 1994. Oceanic vertical mixing: A review and a model with a nonlocal boundary layer parameterization. *Rev. Geophys.* 32, 363–403. <http://dx.doi.org/10.1029/94RG01872>.
- Le Vu, B., Stegner, A., Arsouze, T., 2018. Angular momentum eddy detection and tracking algorithm (AMEDA) and its application to coastal eddy formation. *J. Atmos. Ocean. Technol.* 35, 739–762. <http://dx.doi.org/10.1175/JTECH-D-17-0010.1>.
- Lévy, M., Franks, P.J.S., Smith, K.S., 2018. The role of submesoscale currents in structuring marine ecosystems. *Nature Commun.* 9, 4758. <http://dx.doi.org/10.1038/s41467-018-07059-3>.
- L'Hégaret, P., Beal, L.M., Elipot, S., Laurindo, L., 2018. Shallow cross-equatorial gyres of the Indian ocean driven by seasonally reversing monsoon winds. *J. Geophys. Res. Ocean.* 8902–8920. <http://dx.doi.org/10.1029/2018JC014553>.
- L'Hégaret, P., Carton, X., Louazel, S., Boutin, G., 2016. Mesoscale eddies and submesoscale structures of Persian Gulf Water off the Omani coast in spring 2011. *Ocean Sci.* 12, 687–701. <http://dx.doi.org/10.5194/os-12-687-2016>.
- L'Hégaret, P., Duarte, R., Carton, X., Vic, C., Ciani, D., Baraille, R., Corrêard, S., 2015. Mesoscale variability in the Arabian Sea from HYCOM model results and observations: impact on the persian Gulf water path. *Ocean Sci.* 11, 667–693. <http://dx.doi.org/10.5194/os-11-667-2015>.
- Li, L., Nowlin, W.D., Jilan, S., 1998. Anticyclonic rings from the kuroshio in the south China sea. *Deep-Sea Res. I* 45, 1469–1482. [http://dx.doi.org/10.1016/S0967-0637\(98\)00026-0](http://dx.doi.org/10.1016/S0967-0637(98)00026-0).
- McDougall, T.J., Barker, P.M., 2011. Getting Started with TEOS-10 and the Gibbs Seawater (GSW). *Oceanographic Toolbox*.
- McWilliams, J.C., 1985. Submesoscale, coherent vortices in the ocean. *Rev. Geophys.* 23, 165–182. <http://dx.doi.org/10.1029/RG023i002p00165>.
- McWilliams, J.C., Gent, P.R., Norton, N.J., 1986. The evolution of balanced, low-mode vortices on the β -plane. *J. Phys. Oceanogr.* 16, 838–855. [http://dx.doi.org/10.1175/1520-0485\(1986\)016<0838:TEOBML>2.0.CO;2](http://dx.doi.org/10.1175/1520-0485(1986)016<0838:TEOBML>2.0.CO;2).
- Ménesguen, C., Le Gentil, S., Marchesiello, P., Ducouso, N., 2018. Destabilization of an oceanic meddy-like vortex: Energy transfers and significance of numerical settings. *J. Phys. Oceanogr.* 48, 1151–1168. <http://dx.doi.org/10.1175/jpo-d-17-0126.1>.
- Meunier, T., Ménesguen, C., Carton, X., Le Gentil, S., Schopp, R., 2018. Optimal perturbations of an oceanic vortex lens. *Fluids* 3, 63. <http://dx.doi.org/10.3390/fluids3030063>.
- Meunier, T., Ménesguen, C., Schopp, R., Le Gentil, S., 2015. Tracer stirring around a Meddy: The formation of layering. *J. Phys. Oceanogr.* 45, 407–423. <http://dx.doi.org/10.1175/JPO-D-14-0061.1>.
- Meunier, T., Pallas-Sanz, E., Ruiz-Angulo, A., Ochoa-de-la-Torre, J., Tenreiro, M., 2019. Observations of layering under an anticyclonic warm-core ring in the Gulf of Mexico. *J. Phys. Oceanogr.* <http://dx.doi.org/10.1175/JPO-D-18-0138.1>.
- Meunier, T., Pallas-Sanz, E., Tenreiro, M., Portela, E., Ochoa, J., Ruiz-Angulo, A., Cusi, S., 2018. The vertical structure of a loop current eddy. *J. Geophys. Res. Ocean.* 123, 6070–6090. <http://dx.doi.org/10.1029/2018JC013801>.
- Morel, Y.G., Darr, D.S., Talandier, C., 2006. Possible sources driving the potential vorticity structure and long-wave instability of coastal upwelling and downwelling currents. *J. Phys. Oceanogr.* 36, 875–896. <http://dx.doi.org/10.1175/JPO2899.1>.
- Morel, Y., McWilliams, J., 2001. Effects of isopycnal and diapycnal mixing on the stability of oceanic currents. *J. Phys. Oceanogr.* 31, 2280–2296. [http://dx.doi.org/10.1175/1520-0485\(2001\)031<2280:EOIADM>2.0.CO;2](http://dx.doi.org/10.1175/1520-0485(2001)031<2280:EOIADM>2.0.CO;2).
- Nadiga, B.T., 2014. Nonlinear evolution of a baroclinic wave and imbalanced dissipation. *J. Fluid Mech.* 756, 965–1006. <http://dx.doi.org/10.1017/jfm.2014.464>.
- Nguyen, H.Y., Hua, B.L., Schopp, R., Carton, X., 2012. Slow quasigeostrophic unstable modes of a lens vortex in a continuously stratified flow. *Geophys. Astrophys. Fluid Dyn.* 106, 305–319. <http://dx.doi.org/10.1080/03091929.2011.620568>.
- Olson, D.B., Evans, R.H., 1986. Rings of the Agulhas current. *Deep-Sea Res.* A 33, 27–42. [http://dx.doi.org/10.1016/0198-0149\(86\)90106-8](http://dx.doi.org/10.1016/0198-0149(86)90106-8).
- Pedlosky, J., 1964. The stability of currents in the atmosphere and the ocean: part I. *J. Atmos. Sci.* 21, 201–219. [http://dx.doi.org/10.1175/1520-0469\(1964\)021<0201:TSOCIT>2.0.CO;2](http://dx.doi.org/10.1175/1520-0469(1964)021<0201:TSOCIT>2.0.CO;2).
- Pedlosky, J., 2013. *Geophysical Fluid Dynamics*. Springer Science & Business Media.
- Penven, P., Halo, I., Pous, S., Marié, L., 2014. Cyclogeostrophic balance in the Mozambique channel. *J. Geophys. Res. Ocean.* 119, 1054–1067. <http://dx.doi.org/10.1002/2013JC009528>.
- Richardson, P.L., 1983. Gulf stream rings. In: Robinson, A.R. (Ed.), *Eddies in Marine Science*. Springer Berlin Heidelberg, Berlin, Heidelberg, pp. 19–45. http://dx.doi.org/10.1007/978-3-642-69003-7_2.
- Riedinger, X., Gilbert, A.D., 2014. Critical layer and radiative instabilities in shallow-water shear flows. *J. Fluid Mech.* 751, 539–569. <http://dx.doi.org/10.1017/jfm.2014.303>.
- Ripa, P., 1991. General stability conditions for a multi-layer model. *J. Fluid Mech.* 222, 119–137. <http://dx.doi.org/10.1017/S0022112091001027>.
- Roulet, G., Capet, X., Maze, G., 2014. Global interior eddy available potential energy diagnosed from argo floats. *Geophys. Res. Lett.* 41, 1651–1656. <http://dx.doi.org/10.1002/2013GL059004>.
- Scharffenberg, M.G., Stammer, D., 2010. Seasonal variations of the large-scale geostrophic flow field and eddy kinetic energy inferred from the TOPEX/Poseidon and Jason-1 tandem mission data. *J. Geophys. Res.* 115, C2. <http://dx.doi.org/10.1029/2008JC005242>.
- Schott, F.A., McCreary, J.P., 2001. The monsoon circulation of the Indian ocean. *Prog. Oceanogr.* 51, 1–123. [http://dx.doi.org/10.1016/S0079-6611\(01\)00083-0](http://dx.doi.org/10.1016/S0079-6611(01)00083-0).
- Shchepetkin, A.F., McWilliams, J.C., 2005. The regional oceanic modeling system (ROMS): a split-explicit, free-surface, topography-following-coordinate oceanic model. *Ocean Model.* 9, 347–404. <http://dx.doi.org/10.1016/j.ocemod.2004.08.002>.
- Shchepetkin, A.F., McWilliams, J.C., 2011. Accurate Boussinesq oceanic modeling with a practical, “stiffened” equation of state. *Ocean Model.* 38, 41–70. <http://dx.doi.org/10.1016/j.ocemod.2011.01.010>.
- Snyder, C., Skamarock, W.C., Rotunno, R., 1993. Frontal dynamics near and following frontal collapse. *J. Atmos. Sci.* 50, 3194–3212. [http://dx.doi.org/10.1175/1520-0469\(1993\)050<3194:FDNAFF>2.0.CO;2](http://dx.doi.org/10.1175/1520-0469(1993)050<3194:FDNAFF>2.0.CO;2).
- Stegner, A., Dritschel, D.G., 2000. A numerical investigation of the stability of isolated shallow water vortices. *J. Phys. Oceanogr.* 30, 2562–2573. [http://dx.doi.org/10.1175/1520-0485\(2000\)030<2562:ANIOTS>2.0.CO;2](http://dx.doi.org/10.1175/1520-0485(2000)030<2562:ANIOTS>2.0.CO;2).

- Thomas, L.N., Taylor, J.R., Ferrari, R., Joyce, T.M., 2013. Symmetric instability in the Gulf stream. *Deep-Sea Res. II* 91, 96–110. <http://dx.doi.org/10.1016/j.dsr2.2013.02.025>.
- Vallis, G.K., 2017. *Atmospheric and Oceanic Fluid Dynamics*. Cambridge University Press.
- Vic, C., Rouillet, G., Carton, X., Capet, X., 2014. Mesoscale dynamics in the Arabian Sea and a focus on the Great Whirl life cycle: A numerical investigation using ROMS. *J. Geophys. Res. Ocean.* 119, 6422–6443. <http://dx.doi.org/10.1002/2014JC009857>.
- Yim, E., Billant, P., 2015. On the mechanism of the Gent–McWilliams instability of a columnar vortex in stratified rotating fluids. *J. Fluid Mech.* 780, 5–44. <http://dx.doi.org/10.1017/jfm.2015.426>.
- Young, W.R., Chen, L., 1995. Baroclinic instability and thermohaline gradient alignment in the mixed layer. *J. Phys. Oceanogr.* 25, 3172–3185. [http://dx.doi.org/10.1175/1520-0485\(1995\)025<3172:BIATGA>2.0.CO;2](http://dx.doi.org/10.1175/1520-0485(1995)025<3172:BIATGA>2.0.CO;2).
- Zhang, Z., Wang, W., Qiu, B., 2014. Oceanic mass transport by mesoscale eddies. *Science* 345, 322–324. <http://dx.doi.org/10.1126/science.1252418>.

5.1.2 Supplément sur l'asymétrie cyclone/anticyclone

Pour étudier l'asymétrie cyclone-anticyclone des structures tourbillonnaires comme étudiées dans la partie précédente, nous réalisons la même étude de stabilité que pour le composite cyclonique, mais en considérant un anticyclone. Pour ce faire, l'initialisation est effectuée avec un tourbillon d'anomalie de densité opposée, et des vitesses horizontales calculées à partir de l'équilibre cyclo-géostrophique. Ainsi, le cyclone et l'anticyclone ont des anomalies de densité symétriques, mais des vitesses de rotation de normes différentes. D'après eq. (1.30) on voit effectivement qu'un anticyclone aura une vitesse de rotation plus élevée.

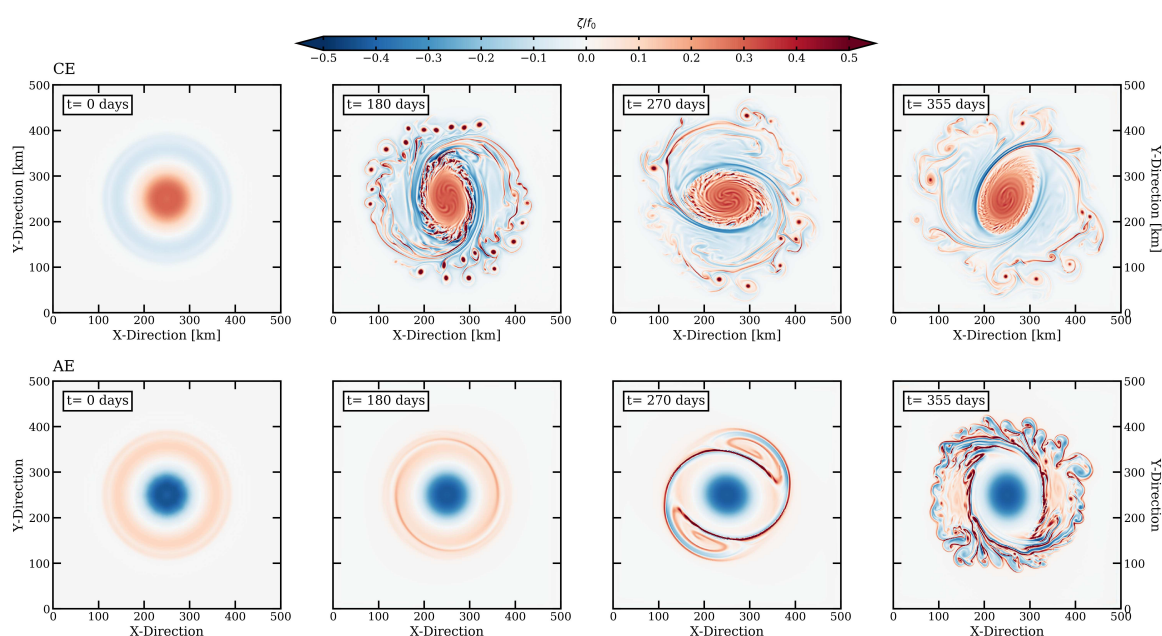


FIGURE 5.1 – Évolution de la vorticité relative ζ/f_0 au cours du temps pour (colonne du haut) le tourbillon composite original, et (bas) le tourbillon composite anticyclonique, pour lequel on a pris l'anomalie de densité opposé au cyclone. La résolution horizontale des simulations est $\Delta x = 1$ km.

On observe que l'anticyclone se déstabilise à des temps plus long (Fig. 5.1). Au bout de 100 jours, l'anticyclone est encore axisymétrique, et ce n'est qu'au bout d'environ 180 jours que des bras spirales apparaissent. Ensuite, les bras se développent, et de manière similaire au cas cyclonique, le tourbillon se restabilise et des structures de sous-méso-échelle sont formées en surface par instabilité secondaires.

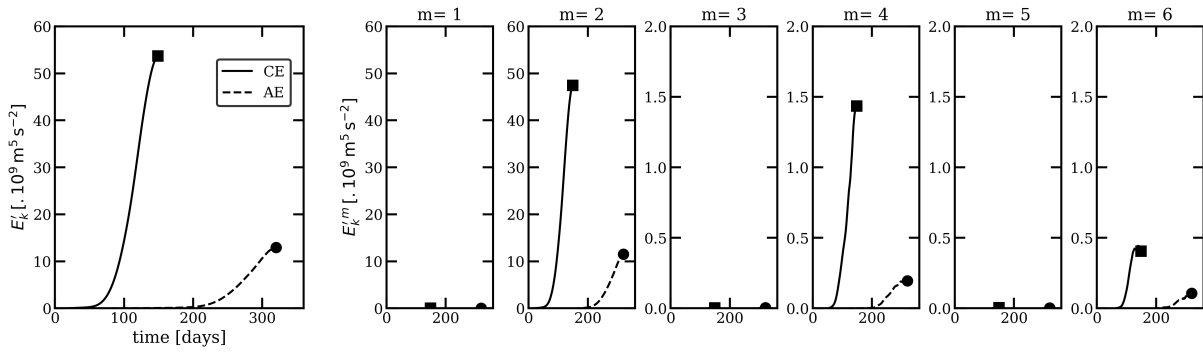


FIGURE 5.2 – Évolution temporelle de l'énergie cinétique de la perturbation totale (gauche) et par modes azimutaux, pour le cyclone (traits pleins) et l'anticyclone (traits pointillés), dans les simulations présentées dans la Fig. 5.1. Le temps de croissance de la perturbation totale est d'environ 30 jours pour le cyclone et 80 jours pour l'anticyclone. Le carré (resp. cercle) présente l'instant de restabilisation non-linéaire du cyclone (resp. anticyclone).

L'évolution modale de la perturbation est similaire dans le cas cyclonique et dans le cas anticycloniques, avec une croissance uniquement des modes paires (Fig. 5.2). En revanche, pour le cas anticyclonique (1) l'amplitude de la perturbation est plus faible, et (2) le temps de croissances est plus grand (d'environ un facteur 3). Avec cette expérience, nous confirmons ainsi les résultats de *e.g.* Stegner & Dritschel (2000) ou Mahdinia et al. (2017). En particulier, Mahdinia et al. (2017) a montré à partir d'une étude de stabilité linéaire pour des tourbillons ayant une anomalie de pression Gaussienne, que les perturbations instables au sein des tourbillons anticycloniques, ont généralement des temps de croissance beaucoup plus élevés que pour des cyclones. Nous observons un comportement similaire dans le cas de l'étude de stabilité du tourbillon composite (Fig. 5.2). En généralisant ce résultat à un cas représentatif des tourbillons observés en mer d'Arabie, nous donnons ainsi des clefs supplémentaires à la compréhension des temps de vie plus important des anticyclones que des cyclones, comme observé par exemple à l'entrée et dans le golfe d'Aden (Morvan et al., 2020). Nous montrons également que le processus de déstabilisation des tourbillons (cycloniques et anticycloniques) de méso-échelle en mer d'Arabie est une source importante de structure de sous-méso-échelle intensifiées en surface, comme régulièrement observé en mer d'Arabie (Lévy et al., 2018).

5.1.3 Supplément sur l'impact de l'effet- β pour la stabilité du cyclone composite

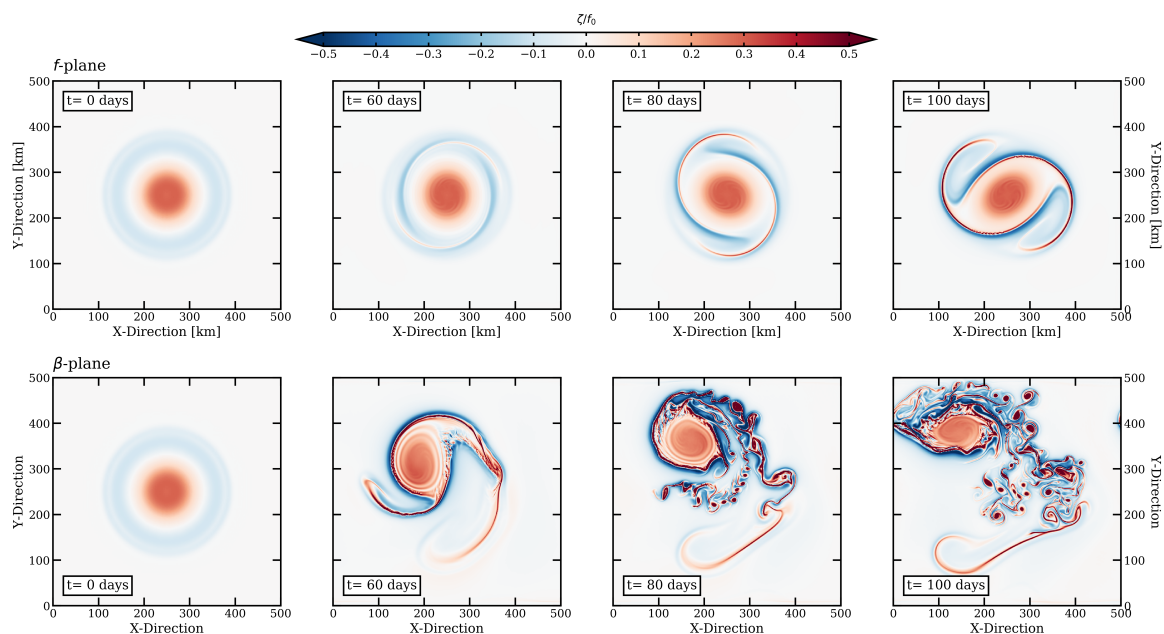


FIGURE 5.3 – Évolution de la vorticité relative ζ/f_0 au cours du temps pour le tourbillon composite sur (colonne du haut) le plan- f , et (bas) le plan- β . La résolution horizontale des simulations est $\Delta x = 1$ km.

À l'échelle d'un tourbillon de la taille du tourbillon composite présenté précédemment, l'effet- β n'est pas négligeable, avec une variation de f entre le bord sud, et le bord nord du tourbillon de

$$\frac{\beta 2R}{f_0} = \mathcal{O}(10)\%. \quad (5.1)$$

Comme proposé par *e.g.* McWilliams et al. (1986) ou Morel & McWilliams (1997), l'effet- β doit ainsi avoir un impact sur la stabilité du tourbillon.

Nous réalisons donc la même étude de stabilité que présenté précédemment, avec maintenant le cyclone composite initialisé sur le plan- β , où $\beta = 2.1 \cdot 10^{-11} \text{ m}^{-1} \text{ s}^{-1}$, la valeur moyenne dans la région où a été calculé le composite. L'évolution du tourbillon est alors très différente (Fig. 5.3). Tout d'abord, on constate que le tourbillon dérive vers le nord-ouest, comme prédit théoriquement (Morrow, 2004; Chelton et al., 2007). Cette dérive est due à la différence de force de Coriolis entre le nord et le sud du tourbillon, ou autrement dit, à l'advection du tourbillon par les ondes de Rossby planétaires.

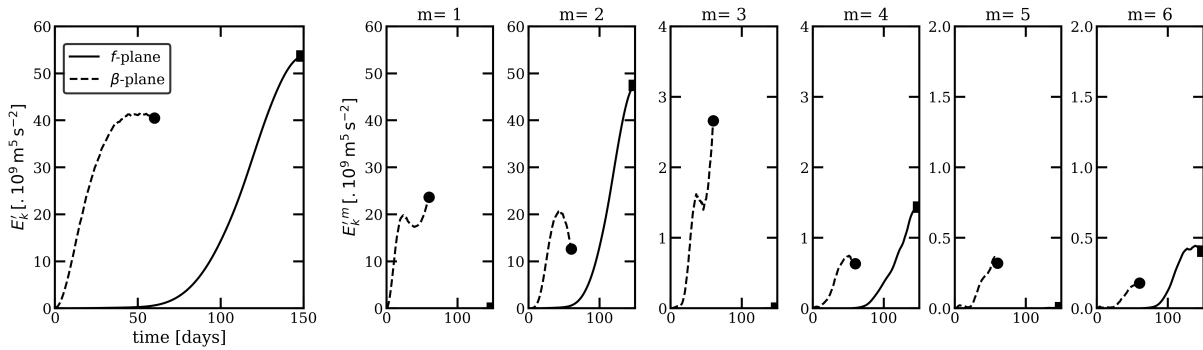


FIGURE 5.4 – Évolution temporelle de l'énergie cinétique de la perturbation totale (gauche) et par modes azimutaux, pour le cyclone sur le plan- f (traits pleins) et sur le plan- β (traits pointillés), dans les simulations présentées dans la Fig. 5.3. Le cercle présente l'instant où les instabilités secondaires se déclenchent dans le cyclone sur le plan- β .

La croissance des instabilités sur le plan- β est beaucoup plus rapide que sur le plan- f . En effet, au bout de 60 jours de simulation, les bras spiraux sont totalement développés, et au bout de 80 jours, le tourbillon se restabilise et les instabilités secondaires apparaissent. La décomposition azimutale révèle que les modes azimutaux impairs sont instables (Fig. 5.4). En particulier, la perturbation de mode 1 est du même ordre de grandeur que celle de mode 2, la perturbation de mode 3 du même ordre de grandeur que celle de mode 4... Le mode 1 correspond, comme suggéré par McWilliams et al. (1986), à la traînée de l'onde de Rossby planétaire ("trailing Rossby wave wake"), par laquelle le tourbillon transfère son énergie aux ondes de Rossby planétaire. La croissance des perturbations n'est pas exponentielle, et il est donc difficile de mesurer un temps de croissance comme défini précédemment. En revanche, qualitativement, on peut estimer que le temps de croissance sur le plan- β est au moins 2 fois inférieur à celui sur le plan- f . L'amplitude des modes 1 et 2 étant similaire, des interactions non-linéaires entre ces modes se produisent. Cela explique la plus forte intensité et taille du bras nord par rapport au bras sud. Ainsi, la croissance des modes dominants (modes 1 et 2) est plus courte, et la restabilisation non-linéaire du tourbillon apparaît plus tôt que sur le plan- f . La perturbation totale sur le plan- β atteint ainsi un niveau d'énergie plus faible que sur le plan- f . Cela suggère que, sur le plan- β , le tourbillon perd moins d'énergie par déstabilisation que sur le plan- f . Le mode 1 induit par le plan- β joue le rôle de "stabilisateur" de la perturbation de mode 2.

5.2 Interaction sur le bord ouest

Connaissant la structure typique des tourbillons en mer d'Arabie, nous avons pu observer que lorsqu'ils sont influencés par l'effet- β , ils sont déformés, et perdent de l'énergie par déstabilisation. Cependant, la structure tourbillonnaire méso-échelle se restabilise, demeure cohérente, et dérive vers le nord-ouest, influencé par les ondes de Rossby planétaires. En mer d'Arabie de telles structures finiront donc inévitablement leur voyage le long d'un mur (*e.g.* les côtes Omanaises ou Somaliennes). A partir d'observations et de modélisation numériques réalistes, on constate effectivement que la mer d'Arabie a la particularité de posséder de nombreux tourbillons sur sa frontière ouest (Fig. 2.10), plutôt qu'un courant de bord très intense (Vic et al., 2014; Trott et al., 2018). Une question naturelle à se poser est ainsi la compréhension du comportement intrinsèque de ce type de tourbillon lorsqu'ils sont contraint par effet- β le long d'une frontière physique.

5.2.1 L'interaction du tourbillon composite avec un bord ouest

Afin d'étudier le comportement des tourbillons de mer d'Arabie le long d'un bord ouest, nous réalisons la même expérience numérique que celle présentée en section 5.1.3, mais où la frontière ouest du domaine est un mur. Dans ce cas, le mur impose ainsi des conditions de flux et de vitesses normale au mur nulles. Cela implique qu'aucun effet visqueux n'est ajouté le long de cette frontière, et que des ondes de Kelvin peuvent se propager. La résolution du modèle est faible ($\Delta x = 5$ km, et 50 niveaux verticaux), pour s'affranchir d'une partie de la dynamique sousmésos-échelle (*e.g.* les fronts intenses), et gagner en temps de calcul. Nous réalisons une simulation pour le cyclone composite, et une pour l'anticyclone présenté en section 5.1.2. Dans les deux cas, le tourbillon est initialisé à une distance du mur de $4R$. Cela évite les recouvrements entre le mur et le champ de pression du tourbillon, tout en permettant au tourbillon d'atteindre rapidement ($\mathcal{O}(100)$ jours) le mur par effet- β .

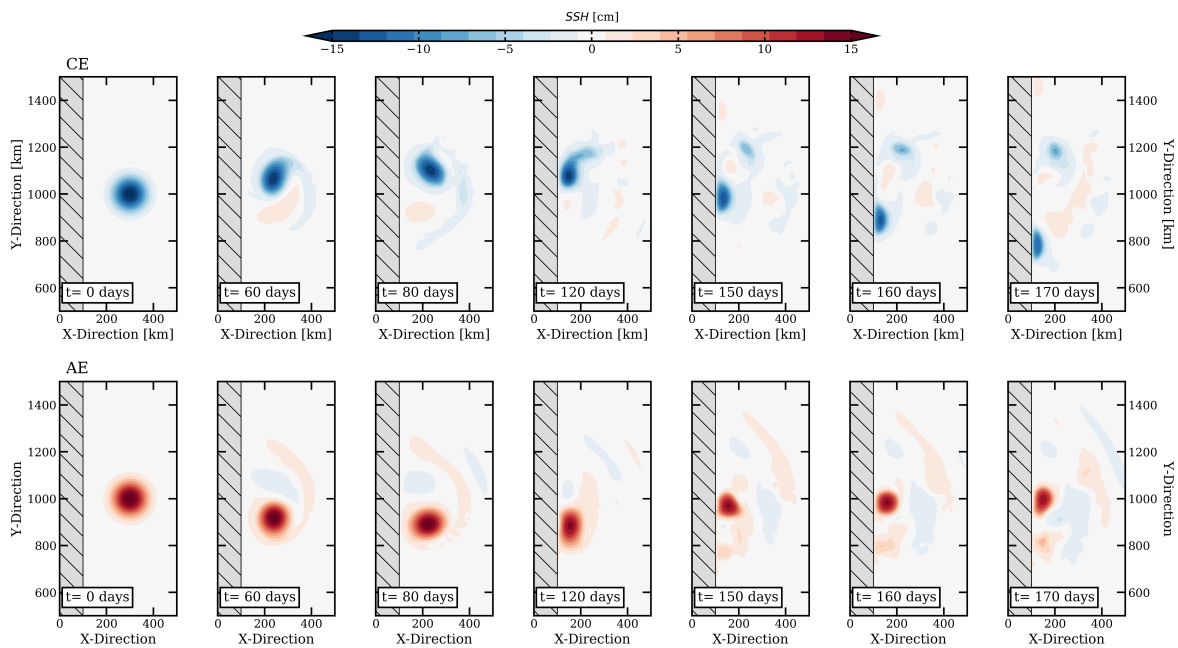


FIGURE 5.5 – Évolution de la SSH au cours du temps pour le tourbillon composite (haut) cyclonique, et (bas) anticyclonique, le long d'une frontière ouest, avec effet- β . La résolution horizontale des simulations est $\Delta x = 5$ km. Le cyclone se couple avec le mur sous la forme d'un "wodon", mais pas l'anticyclone.

Comme attendu, on observe au début de la simulation que le cyclone (resp. anticyclone) dérive vers le nord-ouest (resp. sud-ouest) jusqu'au mur, en un temps d'environ 4 mois (Fig. 5.5). Ensuite,



d'une part, dans le cas cyclonique, à $t \sim 120 - 150$ jours, le tourbillon se couple avec le mur et forme un wodon. La structure horizontale du wodon est qualitativement similaire à celle proposée dans des études passées, voir section 2.1.3. Le wodon dérive ensuite vers le sud sous l'action des trois forces en jeu (voir Fig. 2.6), comme attendu théoriquement. Au bout de $\sim 2 - 3$ mois de dérive, le wodon a parcouru 500 km le long du mur de manière stable. D'autre part, dans le cas anticyclonique, on voit qu'aux premiers instants d'interaction entre le tourbillon et le mur, il semble se former un wodon (voir Fig. 5.5 à $t = 120$ jours). En revanche, dans les jours suivants, on voit que le tourbillon ne se couple pas totalement avec le mur, il reste à distance, et il ne dérive pas vers le nord. Ainsi, alors que le cyclone parcourt 500 km en deux mois le long du mur, l'anticyclone reste à une latitude donnée et ne forme pas de wodon. Ces résultats vont à l'encontre des études réalisées précédemment concernant l'interaction tourbillon-mur sur un plan- β , *e.g.* Shi & Nof (1994), et semblent suggérer qu'une asymétrie cyclone-anticyclone existe dans l'interaction tourbillon-mur.

Afin de décrire en détail ce processus, et parce que la présence de tourbillons sur un bord ouest n'est pas seulement propre à la mer d'Arabie, nous réalisons dans la section suivante une étude paramétrique de ce problème en utilisant des profils de tourbillons plus généraux. Cela nous permet de tirer des conclusions générales sur le comportement des tourbillons de méso-échelle le long des bords ouest, dans l'océan.

5.2.2 Le problème général tourbillon-mur sur le plan- β : Article publié dans *Geophysical and Astrophysical Fluid Dynamics*



Vortex–wall interaction on the β -plane and the generation of deep submesoscale cyclones by internal Kelvin Waves–current interactions

Charly de Marez ^a, Thomas Meunier^b, Pauline Tedesco^a, Pierre L'Hégaret^a and Xavier Carton ^a

^aUniv. Brest, Laboratoire d'Océanographie Physique et Spatiale (LOPS), IUEM, Plouzané, France; ^bWoods Hole Oceanographic Institution, Falmouth, MA, USA

ABSTRACT

In this paper, we investigate the vortex–wall interaction on the β -plane, using a submesoscale and internal waves resolving model in an idealised context. Our results bring new insights on the dynamics of oceanic mesoscale eddies as they drift toward a western boundary. We show that there exists a strong cyclone/anticyclone asymmetry in the interaction, contrary to what was suggested in previous studies: anticyclones cannot drift meridionally along the wall because of internal Kelvin Waves–current interactions. This interaction is shown to be an efficient mechanism to generate small coherent submesoscale cyclones, which can travel hundreds of kilometres into the interior of the ocean.

ARTICLE HISTORY

Received 27 November 2019
Accepted 19 May 2020

KEYWORDS

Vortex; boundary;
wave–current interaction;
submesoscale

1. Introduction

The western boundaries of oceanic basins play a key role for the global circulation (Vallis 2017) and the energy budget closure (Zhai *et al.* 2010, Clément *et al.* 2016). All western boundary systems are different: they have different topography and coastline (see figure 1), as well as different regional forcing and resulting dynamics. As examples, one can cite (1) the Gulf Stream/Kuroshio/Agulhas/East Australian/Brazilian current areas, where intense boundary currents are forced by the large scale winds (Stommel 1976, Johns *et al.* 1990, Ridgway and Dunn 2003, Beal *et al.* 2011, Gula *et al.* 2015, Vallis 2017); (2) the Gulf of Mexico, where large anticyclones detach from the Loop Current and then drift toward the western coast of the gulf (Meunier *et al.* 2018); (3) the Arabian Sea and the Somalia basin, where coastal currents (L'Hégaret *et al.* 2018) as well as stationary vortices (Vic *et al.* 2014) are forced by the monsoon wind regimes (Findlater 1969) along the western boundary.

These western boundary systems share a common characteristics: they exhibit large values of Eddy Kinetic Energy (figure 1). This reflects the strong mesoscale activity occurring at western boundaries. Furthermore, examples of long lived, coherent and recurrent mesoscale vortices can be found in each of the western boundary systems, e.g. Gulf Stream

CONTACT Charly de Marez  charly.demarez@univ-brest.fr

© 2020 Informa UK Limited, trading as Taylor & Francis Group

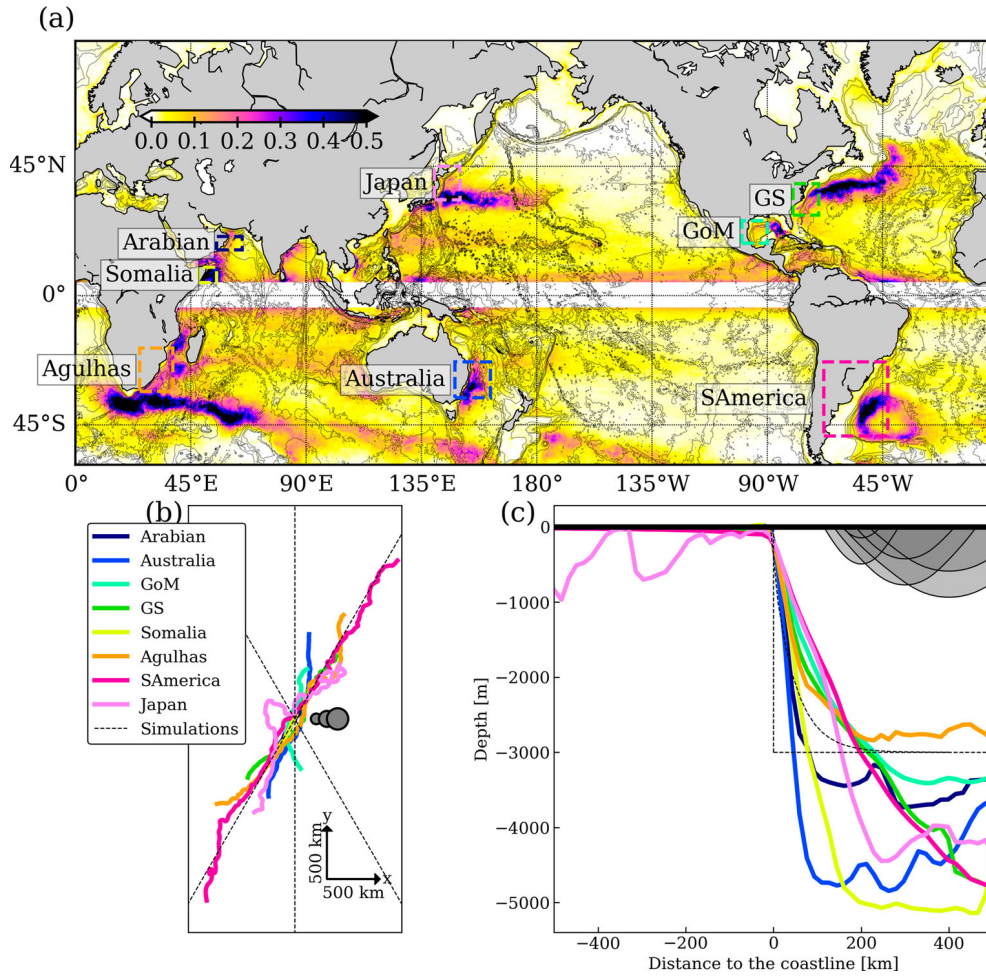


Figure 1. Western boundaries of the global ocean. (a) Time-average of the surface Eddy Kinetic Energy [$\text{m}^2 \text{s}^{-2}$] for the period 1 January 2000 to 31 December 2004, computed from the GOFs 3.1, 41-layer HYCOM+NCODA Global $1/12^\circ$ re-analysis (Metzger *et al.* 2014), using surface geostrophic velocities; dashed rectangles indicate example of western boundary areas. (b) Coastline of western boundary areas shown in (a), it is defined as the isobath 200 m from the ETOPO1 dataset (Amante 2009); thin dashed lines present the coastline orientations used in numerical simulations, with $\theta = -30, 0, \text{ and } 30^\circ$; grey circles show initial positions of eddies in numerical simulations, with varying radii $R = 50, 75, \text{ and } 100 \text{ km}$. (c) Along-coast averaged bathymetry in areas shown in (a) from the ETOPO1 dataset (Amante 2009); it is computed by averaging along the coastline the bathymetry in the normal direction to the coastline; thin dashed lines show the bathymetry shape used in numerical simulation: a wall or an exponential slope that fits with the average slope of all areas. Grey contours show initial positions of eddies in numerical simulations, with radii $R = 50, 75, 100 \text{ km}$, and initial azimuthal velocity $V_0 = 0.5, \text{ and } 1 \text{ m s}^{-1}$. (Colour online)

rings (Richardson 1983), Agulhas rings (Olson and Evans 1986), Mozambique channel eddies (Halo *et al.* 2014), Kuroshio rings (Li *et al.* 1998), Loop Current Eddies (Meunier *et al.* 2018), the Ras al Hadd dipole (L'Hégaret *et al.* 2015, 2016) or the great Whirl (Vic *et al.* 2014). Such mesoscale eddies are key features of the ocean circulation: they

impact biological activities (Chelton *et al.* 2011), tracer transport (Zhang *et al.* 2014) and properties of the water column (Dong *et al.* 2014).

Because of the β -effect, mesoscale eddies continuously migrate westward (Chelton *et al.* 2007, 2011). They eventually encounter a western boundary at the end of their journey, in particular when they are formed locally, e.g. Gulf Stream rings or Loop Current Eddies (Shi and Nof 1994). The dynamics of topographic interactions between mesoscale eddies and western boundaries is a problem of interest. The continental shelf has a relatively small extent ($O(10)$ km) in comparison to the mesoscale eddy radii ($O(50-100)$ km), see e.g. figure 1(c). The problem to address is therefore the “vortex–wall interaction on the β -plane”. This problem has already been addressed numerically, considering idealised 2D or quasi-2D dynamics (Shi and Nof 1993, 1994, Sansón *et al.* 1998, Nof 1999, and references therein; see e.g. table 1 in Shi and Nof 1994 that summarises older studies) or in more realistic setup (see Smith 1986, Sutyrin *et al.* 2003, Frolov *et al.* 2004). These studies all agree that once eddies have encountered the wall, they migrate meridionally under the influence of three effects, namely the image effect, the meridional asymmetry of the Coriolis force and the rocket effect, which together form so-called “wodons”. We refer the reader to the discussions made in Shi and Nof (1994) for a nice description of these three effects. According to these studies, there is no polarity bias in the wodon dynamics: cyclones and anticyclones behave symmetrically. However, more recent studies have shown, in other contexts, that anticyclonic flows along a wall-type boundary may undergo unbalanced processes, due to the interaction between Kelvin Waves trapped at the coast and the mean flow (Dewar and Hogg 2010, Gula and Zeitlin 2010, Gula *et al.* 2010, Hogg *et al.* 2011, Deremble *et al.* 2016, 2017). This suggests that the wodon regime may, in fact, be asymmetric. It is thus of interest to understand the vortex–wall interaction on the β -plane in a 3D model, which resolves such wave–current interactions, in order to understand the actual dynamics of both cyclonic and anticyclonic eddies on western boundaries. This paper is organised as follows: in section 2 we present our methods: we describe the idealised numerical simulations we perform and the theoretical tools we use; in section 3 we present the results of these simulations; and in section 4 we summarise the results and compare them with observations.

2. Methods

In this section, we present the idealised simulations performed for this study, and the diagnostics performed on their outputs. These simulations rely on a 3D primitive equation framework. We initialise an isolated surface-intensified eddy in a stratified ocean, on a β -plane, next to a western boundary (see figures 1(b),(c) that show the initial position of the eddies and boundaries in the simulations).

2.1. Numerical setup and domain

Idealised simulations are performed using the Coastal and Regional Ocean COmmunity model CROCO (Shchepetkin and McWilliams 2005). This model solves the hydrostatic primitive equations for the velocity, temperature and salinity, using a full equation of state for seawater (Shchepetkin and McWilliams 2011). The simulations performed integrate the primitive equations for 1 year. The numerical settings are similar to previous simulations

performed in an idealised context (see, e.g., Ménesguen *et al.* 2018): horizontal advection terms for tracers and momentum are discretised with fifth-order upwind advection schemes (UP5); the explicit horizontal viscosity and diffusivity are set to zero, since the UP5 scheme damps dispersive errors; the vertical advection is discretised with a fourth-order centered parabolic spline reconstruction (Splines scheme). Further discussion about these parameterisations can be found in Klein *et al.* (2008) or Ménesguen *et al.* (2018).

The horizontal domain size is 2000×2000 km. The bottom is flat, at 3000 m depth. We set a close boundary condition at the west of the domain, with a free slip condition (i.e. no normal velocities and mass fluxes). We also set open boundary conditions (i.e. radiative conditions see Marchesiello *et al.* 2001) at the north, east and south edges of the domain. This allows the radiation of waves. Simulations are performed on the β -plane using a linearly varying Coriolis parameter. To study the impact of the coastline orientation on the eddy dynamics, we vary the orientation of the beta effect with respect to the coastline. The Coriolis frequency is thus defined as

$$f = f_0 + \beta(\cos \theta y + \sin \theta x), \quad (1)$$

with x and y the zonal and meridional coordinates respectively; $f_0 = 5 \cdot 10^{-5} \text{ s}^{-1}$ and $\beta = 2 \cdot 10^{-11} \text{ m}^{-1} \text{ s}^{-1}$, the mean values representative of the dynamics in areas shown in figure 1(a); and θ the angle between the direction of the gradient of f and the coastline ($\theta = 0$ means that the coast is meridional).

In two particular simulations, we add a bottom slope along the western boundary. It is defined as an exponential fit of the average cross-coastline topography in the areas shown in figure 1(a). Its expression is

$$h_{\text{slope}} = H_t(1 - e^{x/L_t}),$$

with $H_t = 3000$ m and $L_t = 50$ km; it is shown in figure 1(c).

Simulations are performed with a 5 km horizontal resolution, and 50 vertical levels stretched at the surface. Exception is made for the simulation discussed in figure 8, which has a horizontal resolution of 2 km, and 128 vertical levels. In both cases, the vertical and horizontal resolutions are chosen to accurately resolve the frontal dynamics and the forward energy cascade at the surface, as the $\Delta x/\Delta z$ ratio is close to N/f_0 near the surface. This avoids the presence of spurious gravity waves associated with intense frontal processes and allows a better resolution of the forward energy cascade (Snyder *et al.* 1993, Nadiga 2014, Ménesguen *et al.* 2018). Also, the vertical resolution in the first 500 m below the surface allows to reasonably well resolve the internal wave dynamics with vertical wavelength $\lambda > 50$ m.

In this framework, the Ertel potential vorticity (PV in the text and Q in equations hereafter) is materially conserved in the absence of friction or diapycnal processes (Hoskins *et al.* 1985, Vallis 2017), and is defined as

$$Q = \boldsymbol{\omega} \cdot \nabla b, \quad (2)$$

where $b = -g\rho/\rho_0$ is the buoyancy, and $\boldsymbol{\omega}$ is the 3D absolute vorticity of the flow, approximated here by

$$\boldsymbol{\omega} = (-\partial_z v, \partial_z u, \zeta + f_0),$$

with $\zeta = (\partial_x v - \partial_y u)$ its z -component (relative vorticity hereafter).

If diapycnal processes occur (e.g. the mixing of tracers across isopycnals), PV can be modified locally. Following the impermeability theorem discussed in Haynes and McIntyre (1990), Morel and McWilliams (2001), and the results of Keyser and Rotunno (1990), Lamarque and Hess (1994), Legg *et al.* (1998), a loss or a gain of the volume inside a layer comprised between two isopycnals can lead to a local change of the PV. A relation proving this statement in the framework of the layered shallow water model used in Morel and McWilliams (2001) is derived in appendix B. Thus, if the volume between two isopycnals decreases, PV is prone to increase locally.

2.2. Simulation initialisation

We initialise an analytical background stratification $N(z)$, which fits the average ambient stratification in the areas shown in figure 1(a) – it is obtained from Argo floats profiles in the period 2000–2005. It has the form

$$N(z) = N_0 + N_1 e^{z/z_h}, \quad (3)$$

with z the vertical coordinate, $N_1 \approx 8 \cdot 10^{-3} \text{ s}^{-1}$, $z_h \approx 250 \text{ m}$ and $N_0 \approx 7 \cdot 10^{-3} \text{ s}^{-1}$. Integrating this stratification from the surface (where $\rho(z=0) = 1023 \text{ kg m}^{-3}$) gives the ambient density background $\rho(z)$; the temperature background $T(z)$ is obtained by inverting the TEOS-10 equation of state for seawater and assuming a constant salinity background $S(z) = 35 \text{ psu}$. The model is initialised with these temperature and salinity background profiles. In this study, the density ρ is the potential density referenced at the surface.

We initialise a surface intensified eddy of given relative vorticity profile. The initial profile of surface vorticity is

$$\omega(r) = \pm \omega_0 e^{-(r/R)^\alpha}, \quad (4)$$

with the sign depending on the eddy polarity, $r = \sqrt{(x - x_0)^2 + (y - y_0)^2}$, the radial coordinate referenced at the centre of the eddy (x_0, y_0) , and α the steepness parameter. $\omega_0 = V_0/R$, with V_0 the maximal azimuthal velocity at a distance R from the centre of the eddy. The surface azimuthal velocity of the eddy is computed using $v_\theta(r, 0) = r^{-1} \int dr \omega r$. By definition, this velocity vanishes slowly with r . To avoid the presence of spurious velocity at the edges of the domain, we apply a Hanning window on v_θ to make it smoothly tend to zero at $r > 3R$ (this generates a weak opposite-signed vorticity shield around the eddy that does not impact the processes discussed in the present study). The horizontal velocity decreases at depth such that $v_\theta(x, y, z) = v_\theta(x, y, 0) e^{-z/H}$, thus defining the height of the eddy H . The horizontal velocity field of the eddy (u, v) is obtained by projecting v_θ into Cartesian coordinates. The pressure anomaly field $P'(x, y, z)$ corresponding to this velocity field is computed *via* the Gradient Wind equation

$$2J(u, v) + f(\partial_x v - \partial_y u) = \rho^{-1} \Delta_h P', \quad (5)$$

with $J(u, v) = \partial_x u \partial_y v - \partial_y u \partial_x v$ the Jacobian operator, and Δ_h the horizontal Laplacian operator. From P' we determine the density and the temperature anomalies of the eddy.

We set the initial position of the eddy $(x_0, y_0) = (4R, L_y/2)$, with L_y the size of the domain along the meridional direction. This allows to set the eddy as close as possible to the coastline, without initial overlap of the eddy with the western boundary.

For our study, we vary the initial parameters as $R = [50, 75, 100]$ km, $V_0 = [0.5, 1.0]$ m s⁻¹ and $\theta = [-30, 0, 30]^\circ$, for both cyclonic and anticyclonic eddies. We set $H = 500$ m, and $\alpha = 24$, so that the eddy is surface intensified and its profile close to a Rankine vortex. This allows the eddy to not lose too much mass during its initial β -drift (contrary to, e.g. a Gaussian vortex, see McWilliams *et al.* 1986). Note that when isolated on an f -plane, the eddies studied here are stable during at least one year (not shown).

2.3. Vortex tracking

The position of eddies as they drift toward the west and along the western boundary is tracked using a dedicated algorithm that works as follows. At initialisation, and for each vertical level, we first get a density anomaly trigger value $\rho'_t(z)$. It is defined as the density anomaly value at the position where the radial gradient of relative vorticity is maximum. Then, at each time, the eddy contour at a given level z_0 is defined as the line enclosing the area, where

$$|\rho'(x, y, z_0)| > |\rho'_t(z_0)|.$$

The eddy centre at each level is obtained by finding the centroid of the eddy contour. Finally, the eddy centre positions at each level are vertically averaged to give the mean eddy centre at each time $(x_c(t), y_c(t))$. Also, the drift velocity of the eddy is defined as

$$U_w(t) = (dt)^{-1} \sqrt{(x_c(t+dt) - x_c(t))^2 + (y_c(t+dt) - y_c(t))^2},$$

where dt is the time spacing between simulation outputs.

2.4. Internal Kelvin waves dynamics

Along a western boundary, in a 3D flow, “internal Kelvin Waves” (iKW in the text hereafter) can propagate (Gill 1982). Their dispersion relation (see appendix A for the derivation) is given by

$$\omega = \frac{Nk_y}{k_z} = \frac{N\lambda}{2\pi} k_y, \quad (6)$$

with k_y and k_z the zonal and vertical wavenumber respectively, ω the frequency of the wave, and N the Brunt–Väisälä frequency. Also, $k_z = 2\pi/\lambda$, with λ the vertical wavelength of the wave. The angle of the rays along which the phase of these waves propagates is defined as $\tan \theta = k_y/k_z$. To characterise the propagation of iKW in our simulation outputs, we compute the (k_y, ω) power spectrum (dispersion diagram) of the horizontal velocity divergence $P^{\nabla \cdot u}$ at a given depth, along the western boundary. Energetic regions in the (k_y, ω) space are expected to follow the dispersion relation (6) of iKW.

Also, for the wave to have a finite energy, only the solution which propagates toward the south is acceptable. This wave has an amplitude that depends on the zonal coordinate x such that

$$\tilde{w}(x) = w_0 e^{-x/L_{\text{wave}}}, \quad (7)$$

where the zonal extension of the wave is $L_{\text{wave}} = N\lambda/2\pi f$.

The impact of waves on the mean flow can be characterised by the divergence of the Eliassen–Palm flux (EP flux hereafter) (Vallis 2017). Historically, this quantity has been used to describe the interaction between Rossby waves and mean current in the context of the Eady problem. More recently, this quantity has been extended to the interaction between internal gravity waves and the mean current in a 3D primitive equation framework by Liu *et al.* (2019), who showed that the EP flux is proportional to the group velocity of internal waves. Also, they showed in the context of a realistic atmospheric simulation that the EP flux divergence is an efficient proxy to understand the weakening/increasing of the mean current by wave–flow interactions (see, e.g. figure 4 in Liu *et al.* 2019). Thus, where the EP flux divergence is positive (resp. negative), the current is weakened (resp. increased) by wave–current interactions. Here, we use the EP flux divergence to describe the weakening of the mean current by Kelvin Waves. The EP flux divergence is estimated by computing the 3D divergence of the group velocity

$$\mathbf{c}_g = \left(0, \frac{N\lambda}{2\pi}, -\frac{N\lambda^2 k_y}{4\pi^2} \right), \quad (8)$$

assuming a given vertical wavelength λ , a meridional wavenumber k_y , and the actual 3D Brunt–Väisälä frequency $N(x, y, z)$.

3. Results

3.1. The cyclone/anticyclone asymmetry of the wodon regime

The interaction between a cyclonic eddy and the western boundary in numerical simulations is similar to the classical description made by Shi and Nof (1994) and Nof (1999). We describe the example case of a cyclone with $R = 50$ km, $V_0 = 0.5$ m s⁻¹ and $\theta = 0$. The eddy drifts northwestward, because of its interaction with planetary Rossby waves (McWilliams *et al.* 1986). As it encounters the western boundary, its direction reverses, and it starts drifting southward (see figure 2(a)). As explained in Shi and Nof (1994) and Nof (1999), this is due to the combination of both the image and the rocket effects which dominate over the β -induced drift. As it drifts southward along the wall, these three effects balance and the eddy takes the form of a “wodon”: the eddy has a semi-circular shape on the horizontal, with a part of the eddy’s fluid flowing northward (figure 2(b)). The eddy is not vertically tilted, and its vertical structure is similar to that at its initialisation (figure 2(c)). The drift velocity of the wodon along the wall is $U_w \approx 15$ km day⁻¹. This value is strongly dependent on the value of β , the size of the eddy, and its initial intensity, as suggested by earlier studies (Shi and Nof 1994).

At first glance, the anticyclonic eddy with $R = 50$ km, $V_0 = 0.5$ m s⁻¹, and $\theta = 0$ behaves quite similarly to the cyclone discussed above. The anticyclone drifts freely southwestward and is then deflected northward along the western boundary (figure 2(d)). This is expected by the fact that, an anticyclone should behave “exactly symmetrically” to a cyclone (Shi and Nof 1994, Nof 1999).

However, three differences exist between the anticyclonic and cyclonic cases. (1) The drift velocity of the anticyclone, $U_w \approx 10$ km day⁻¹, is slower than that of the cyclone. (2) The trajectory of the anticyclone along the wall is not straight, and it never has a semi-circular shape (figures 2(d),(e)). (3) A positive density anomaly is seen along the wall

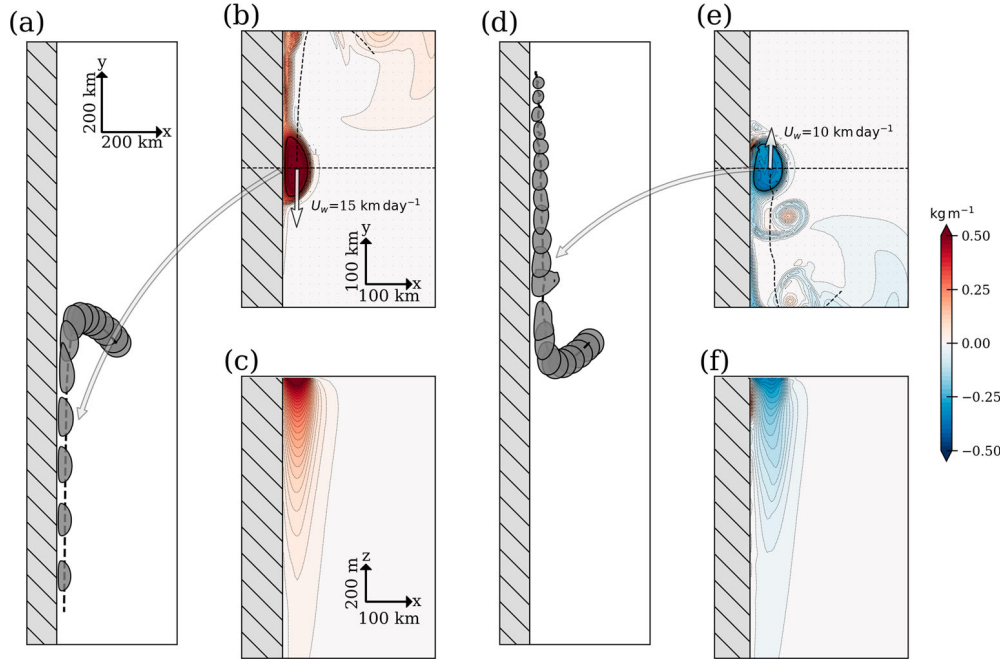


Figure 2. Eddy–wall interaction for a cyclonic (a,b,c) and an anticyclonic eddy (d,e,f), with $R = 50$ km, $V_0 = 0.5 \text{ m s}^{-1}$ and $\theta = 0$. (a,d) Time evolution of the eddy as it drifts along the wall, grey contours indicate the shape of the eddy at the surface (defined as the area where the density is greater than a trigger value, see Methods section); contours are shown from the start to the end of the simulation with an increment of 10 days. (b,e) Surface density anomaly at $t = 200$ days, the white arrow shows the drift velocity of the wodon. (c,f) Zonal vertical section of density anomaly at the centre of the eddy. The colourmaps in (b,c,e,f) are the same. (Colour online)

(figures 2(e),(f)). Note at this point that any viscous effects induced by the wall are excluded because a free-slip condition is chosen, and because it should have generated symmetric modification of both the cyclone and the anticyclone.

3.2. The anticyclonic regime: generation of submesoscale cyclones by wave–current interaction

To investigate the possible role of iKW, we describe the example case of the simulation of an anticyclonic eddy with $R = 50$ km, $V_0 = 0.5 \text{ m s}^{-1}$ and $\theta = 0$ (the same one that is shown in figures 2(d)–(f)). We compute the (k_y, ω) power spectrum of horizontal divergence along the western boundary between $t = 63$ and $t = 70$ days (figure 3), at 143 m depth – the depth at which we observe the positive density anomaly in figure 2(f). An energetic region is seen, in the $k_y < 0$ domain, which is consistent with a southward propagation, i.e. with the boundary on its right. The energy distribution is consistent with iKW dispersion relation, in particular for waves with $\lambda = 100$ m. At 143 m depth, intense vertical velocities are confined to the boundary, suggesting a trapping of the process along the wall, as expected for Kelvin Waves (see equation (7)). In vertical meridional sections, the vertical velocity shows a pattern typical of internal waves (figure 4(b)). The ray orientation is consistent with the expected orientation of iKW rays with $\lambda = 100$ m (see black

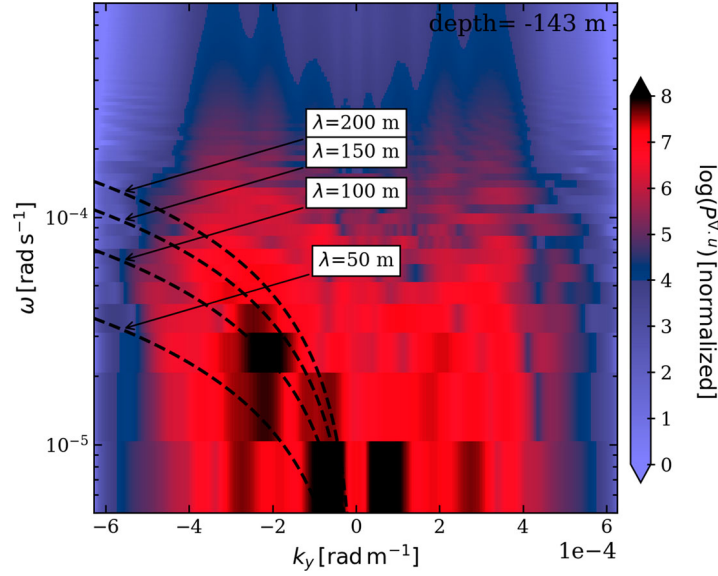


Figure 3. Dispersion diagram (k_y, ω spectrum) of the horizontal divergence at 143 m depth computed along the western boundary between $t = 63$ and $t = 70$ days, in the simulation with an anticyclonic eddy with $R = 50$ km, $V_0 = 0.5$ m s $^{-1}$ and $\theta = 0$; black dashed lines are Kelvin wave dispersion relation computed with meridionally averaged Brunt–Väisälä frequency along the boundary $N = 7.2 \cdot 10^{-3}$ s $^{-1}$ and the mean Coriolis frequency in the domain $f_0 = 5 \cdot 10^{-5}$ s $^{-1}$, for vertical wavelength $\lambda = 50, 100, 150$ and 200 m. (Colour online)

lines in figure 4(b)). From these results, it can be said that iKW are indeed observed in this numerical simulation. These waves are generated during the transient adjustment of the anticyclone, when it encounters the wall, at $t \sim 60$ days. Once generated, they propagate southward, at a (meridional) phase speed which closely matches the meridional velocity induced by the anticyclone (i.e. $c_\phi \approx -v$) along the wall. The waves are thus arrested by the flow, and trapped between the wall and the anticyclonic eddy as long as the eddy is constrained along the wall by the β -effect. Note that in the cyclonic case, no such waves are seen because even if they were generated, the waves would be expelled far from the eddy, since $c_\phi \approx v$, and then expelled out of the domain.

Weakening of the eddy's meridional velocity by iKW along the wall results in the generation of positive vorticity. In the experiment, regions of positive EP flux divergence coincide with regions of weak meridional velocity, suggesting a weakening of the current by iKW–mean current interaction (see figures 4(c),(d)). As the iKW are trapped along the wall, the velocity is weakened solely along the wall, and a shear is created by the wave-current interaction, which results in the generation of positive vorticity patches along the wall (see figures 4(e),(f)), and a pinching of isopycnals resulting from the PV conservation. This explains the positive density anomaly patch seen in figure 2(f) at depth.

The positive vorticity generation is enhanced by the breaking of the iKW. This breaking is due to the hydraulic jump generated where the iKW are locally arrested by the flow (Dewar and Hogg 2010): as the isopycnals steepen, the implicit diffusion induced by the horizontal advection of tracers leads to a mixing of tracers on the horizontal, and therefore across isopycnals. This leads to areas where $N^2 < 0$, where the isopycnals are the steepest

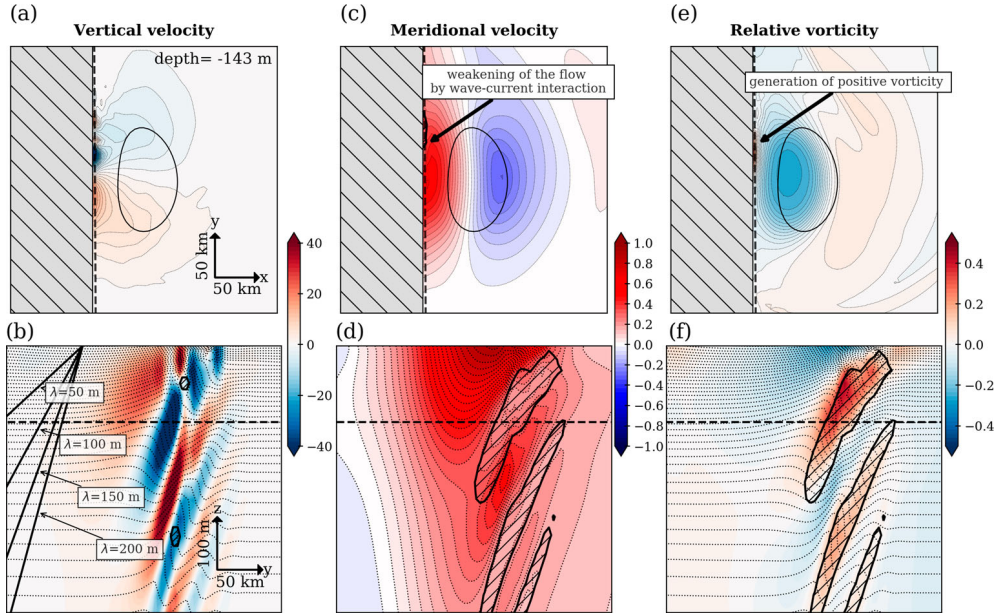


Figure 4. Interaction of internal Kelvin Waves with the mean current, in the simulation with an anticyclonic eddy, with $R = 50$ km, $V_0 = 0.5$ m s⁻¹ and $\theta = 0$. (a) Horizontal section of vertical velocity at 143 m depth and $t = 64$ days; black contours show the contour of the eddy at the surface (from the tracking procedure described in section 2.3); the dashed black line indicates the meridional vertical section shown in (b). (b) Meridional vertical section of vertical velocity [in m/day] along the boundary; black contours are isopycnals with a 0.06 kg m⁻³ spacing; black solid lines indicate the theoretical angle of internal Kelvin Waves rays, for vertical wavelength $\lambda = 50, 100, 150$ and 200 m. Hatched areas highlight positions where $N^2 < 0$. The dashed black line indicates the position of the horizontal section shown in (a). (c) Same as (a) for the meridional velocity [in m s⁻¹]. (d) Same as (b) for the meridional velocity; black contours are isovalues of meridional velocity. Hatched areas highlight positions where the Eliassen–Palm flux divergence is positive (meaning a weakening of the mean current by wave–current interactions). (e) Same as (a) for the relative vorticity normalised by f_0 . (f) Same as (b) for the relative vorticity normalised by f_0 ; black contours are isopycnals with a 0.06 kg m⁻³ spacing. Hatched areas highlight positions where the Eliassen–Palm flux divergence is positive. (Colour online)

(see figure 4(b)). Because diapycnal mixing occurs, the volume of some layers increases, while the volume of other layers decreases. For instance, the volume of the layer between the 1024.3 and 1024.8 kg m⁻³ isopycnals (that is the layer at approximately 143 m depth) decreases as iKW interact with the mean current (figure 5, solid line). Following the impermeability theorem Haynes and McIntyre (1990), Morel and McWilliams (2001), and the relation derived in appendix B, this acts in increasing the PV volume integral, and thus allows PV to increase locally (figure 5, dashed line). The diapycnal mixing therefore leads to an increase of the relative vorticity. We also refer the reader to Gula and Zeitlin (2010) and Gula *et al.* (2010) who also showed that the breaking of Kelvin Waves arrested by an anticyclonic flow, in a Shallow Water model, leads to the generation of positive PV patches.

The positive vorticity generated along the wall is advected toward the north while the wave–current interaction continues to generate vorticity (see figure 6 at $t = 68$ days). After some days, a patch of positive vorticity with a $O(30)$ km horizontal extent (a small cyclone) is present north of the anticyclone (see figure 6 at $t = 70$ days). The anticyclone thus slightly

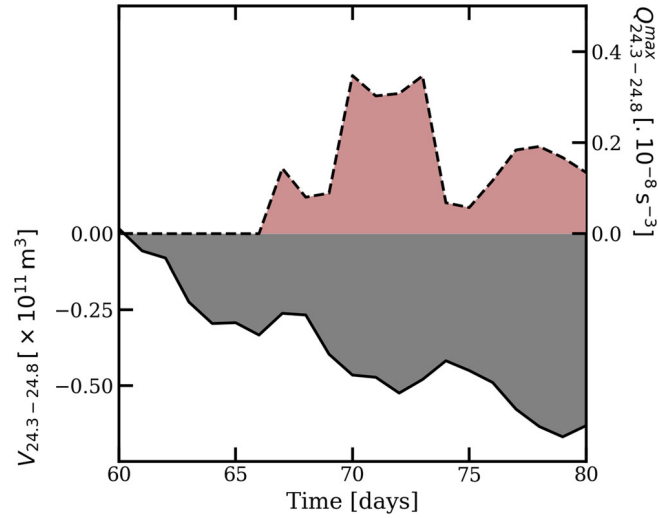


Figure 5. Time evolution of the maximum PV (dashed) and volume decrease (solid) in the layer between the 1024.3 and 1024.8 kg m⁻³ isopycnals. (Colour online)

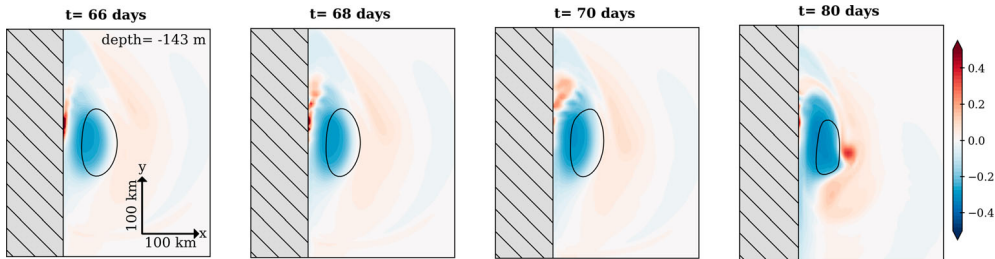


Figure 6. Time evolution of the relative vorticity at 143 m depth (normalised by f_0) for the anticyclone with $R = 50$ km, $V_0 = 0.5$ m s⁻¹, and $\theta = 0$; from left to right $t = 66, 68, 70,$ and 80 days. Note that the centre of the plot coincides with the detected centre of the eddy such that the window moves northward. (Colour online)

drifts eastward by dipolar coupling with the small cyclone. Because the anticyclone is much larger than the cyclone, this coupling does not last long, and the small cyclone is expelled toward the south while the anticyclone drifts back toward the wall due to the β -effect. The whole process then starts again with the generation of new positive vorticity patches along the wall (see figure 6 at $t = 80$ days).

For large/intense anticyclones, the small cyclones generated are larger and more intense; they are shown to have the signature of submesoscale (i.e. with a horizontal extent smaller than the deformation radius, about 50 km), namely intense cyclonic lenses. This can be seen, e.g. in the simulation with an anticyclone with $R = 100$ km, $V_0 = 1.0$ m s⁻¹ and $\theta = 0$ (see figure 7). The decrease of the meridional velocity by wave–current interactions is larger than for small anticyclones (because the initial swirling velocity of the eddy is larger), but this still acts on a small horizontal extent (because the iKW are trapped along the wall, see equation (7)). The positive vorticity generated, as well as the resulting cyclones, are thus more intense and with a larger horizontal extent than in the case described previously

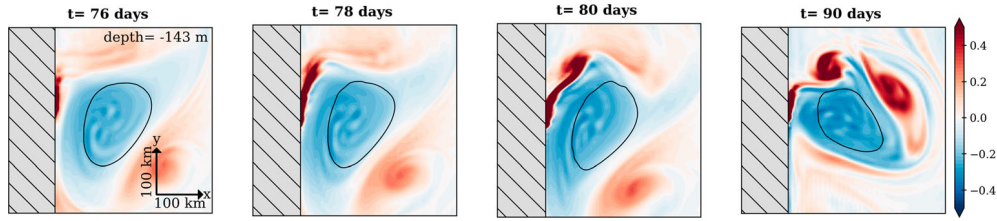


Figure 7. Same as figure 6, but for the anticyclone with $R = 100$ km, $V_0 = 1.0$ m s $^{-1}$, and $\theta = 0$, at $t = 76, 78, 80$, and 90 days. (Colour online)

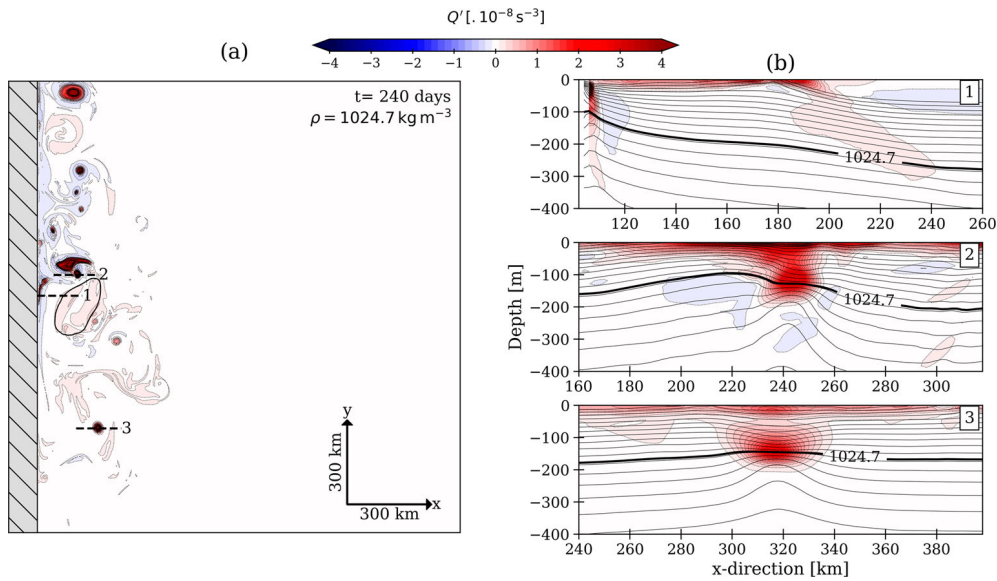


Figure 8. Generation of submesoscale vortices in the simulation with an anticyclone with $R = 100$ km, $V_0 = 1.0$ m s $^{-1}$ and $\theta = 0$, with a 2 km resolution. (a) PV anomaly on the 1024.7 kg m $^{-3}$ isopycnal, at $t = 240$ days; the black solid line shows the contour of the anticyclone (from the tracking procedure described in section 2.3). (b) Vertical section of PV anomaly at the three locations shown in (a) by the bold dashed lines; black contours are isopycnals with a 0.06 kg m $^{-3}$ spacing; the thick black line is the 1024.7 kg m $^{-3}$ isopycnal. The colourbar is the same in all four panels. In all panels, thin grey contours are PV anomaly contours. (Colour online)

(it can be seen by comparing figures 6 and 7). The small cyclones are generated on the 1024.7 kg m $^{-3}$ isopycnal all along the simulation (see figure 8(b)). This depth is set by the structure of the internal wave: the positive vorticity is generated where the wave-current interaction acts in decreasing the mean current (see figure 4(f)). An analysis of PV anomaly on the 1024.7 kg m $^{-3}$ isopycnal (figure 8) shows that the small cyclones generated during the early stages of the simulation are still present and coherent far from the generation spot. They indeed travelled on this isopycnal at a distance up to 500 km from the generation spot, for several months. The penetration distance in the open ocean of the submesoscale cyclones generated at the wall is about 300 km. Therefore, the iKW–anticyclone interaction is an efficient mechanism to generate small submesoscale coherent cyclonic vortices.

3.3. The cyclone and anticyclone different regimes

In this section, we show the different regimes of vortex/wall interaction on the β -plane that we observe in the parameter space.

When cyclones encounter a wall, independently of any parameters, they ultimately form a wodon, and drift toward the south (figure 9, solid lines). The dynamic is similar as the one discussed in previous studies (Shi and Nof 1994, Nof 1999). For some cases, for which $\theta = 30^\circ$, the cyclones first drift northwestward a long time before coupling with the wall. The dynamics of cyclonic wodons is not changed by the presence of a topographic slope (figure 9, solid red line), because topographic effects are weaker than the image effect (Shi and Nof 1994).

When anticyclones encounter a wall, the process described in the previous section prevent the formation of stable wodons (figure 9, dashed lines). First this process is enhanced in simulation with $\theta = -30^\circ$, because the coast acts as a springboard. In these cases, the coastline is tilted. The rocket and the image effect forces being oriented along the coastline, they thus have an eastward component. As these two effects are larger than the β -effect, this acts favourably in taking off the vortex from the wall. Also, the tilted coastline constrains the accumulation of positive vorticity between the wall and the eddy: the cyclones generated by iKW-current interactions become larger faster. Second, the process is also enhanced in simulations with anticyclones having intense initial swirling velocities V_0 . For these two cases, anticyclones never migrate zonally, but rather oscillate around a stationary position. To summarise, for a large variety of parameters, the anticyclonic wodon regimes does not exist. Adding a topographic slope, does not affect this process (figure 9, dashed red line).

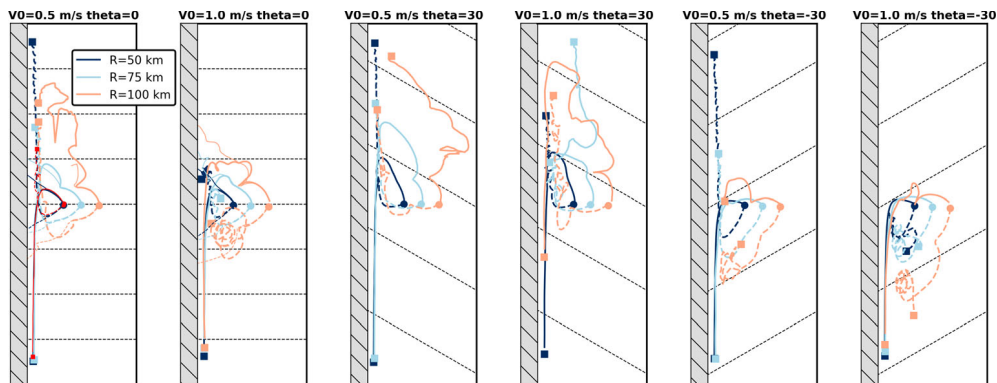


Figure 9. Drift of eddies along a western boundary. Each panel corresponds to given values of V_0 and θ . The hatched portion of the domain is the western boundary, black dashed contours are iso-values of Coriolis frequency. Circles show the initial position of eddies, bold solid (resp. dashed) lines show the evolution of the cyclonic (resp. anticyclonic) eddy centre during the simulations, squares show the end position of the eddies (either after 1 year of simulation or when eddies go out the domain). Colours of aforementioned features indicate the eddy radii at initialisation. Bold (resp. thin) lines present results of simulations ran with a western wall (resp. without western boundary, thus letting eddies drift away toward the west). Thin red solid (resp. dashed) lines show the results of simulations initialised with a cyclonic (resp. anticyclonic) eddy ($V_0 = 0.5 \text{ m s}^{-1}$, $R = 50 \text{ km}$), with a continental slope along the wall. Each panel show the whole domain in the meridional direction, i.e. 2000 km. (Colour online)

4. Summary and discussion

In this study, we have analysed the interaction between an isolated eddy and a western boundary. We have observed a strong cyclone/anticyclone asymmetry. On the one hand, cyclonic eddies couple with the western boundary, forming so-called wadons, which drift southward along the wall. This confirms previous findings (Shi and Nof 1994, Nof 1999, and references therein) and extends them to the 3D primitive equation framework. On the other hand, anticyclones do not become wadons as it was previously expected. This is due to the interaction between internal Kelvin Waves and the anticyclonic flow. iKW generated during the transient adjustment of the anticyclone are trapped at the coast and generate submesoscale cyclones through wave-current interactions. When the latter couple with the anticyclone, they prevent its northward drift, and force it to oscillate zonally. A similar process has already been observed in the dipole-wall interaction (Dewar and Hogg 2010, Hogg *et al.* 2011), and in the interaction between Rossby waves and a coast (Gula and Zeitlin 2010, Gula *et al.* 2010). Here, we show that in the vicinity of the vortex-wall interaction on the β -plane, the wave-current interaction observed in other contexts is of key importance for the dynamics of anticyclones, and may play an important role in the eddy dynamics on western boundaries. We also show that this process is efficient in generating submesoscale cyclones which can live for several months. The submesoscale vortices generated are dependent on the structure of the internal Kelvin Wave. This means that a wide variety of submesoscale cyclones may be generated depending on the ambient stratification, the shape of the coastline, and the shape of the forcing (i.e. the shape of the interacting eddy). In the ocean, most western boundaries form an angle close to 30° with the poleward axis (see figure 1(b)). The effect that we discuss in this study is enhanced for such wall orientation, thus suggesting that this effect may be ubiquitous in the ocean, and the generation of small submesoscale cyclones a common phenomenon. These findings go against studies that suggest that most submesoscale vortices in the ocean are anticyclonic (see, e.g. McWilliams 1985, Gula *et al.* 2019, and references therein). Thus it may be interesting to investigate on the existence of cyclonic submesoscale vortices near western boundaries, where isolated eddies interact with the coast, with *in situ* observations as well as realistic simulations.

Following Shi and Nof (1994)'s words, "a detailed comparison with observations is difficult because of the simplifications made in our models". Here we assumed, among other hypotheses, that (1) the eddies are isolated, (2) the boundary is a straight wall, and (3) there is no coastal current. Looking at figure 1(a) shows that almost every western boundary areas violate one of these hypotheses. However, exception can be made for the Gulf of Mexico, where (nearly isolated) large anticyclones drift toward a (nearly) straight wall: LCRs. Shi and Nof (1994) discussed the trajectory of a LCR tracked in the 1980's (see their figure 2). During the first stage of the LCR-wall interaction, the anticyclone drifted northward, supporting the wadon view. However, the LCR then left the coast and returned southward, invalidating the fact that the LCR has become a stable wadon. In figure 10, we show the trajectory of four LCRs, tracked from altimetry in 2004, 2008, 2009, and 2012. All of them freely β -drifted southwestward, before interacting with the wall, where they started to move northward. Then, two of them left the coast. One of these two was tracked long enough to see that it then returns southward, similarly as in the observations of Shi and Nof (1994). These observed trajectories show a qualitative agreement

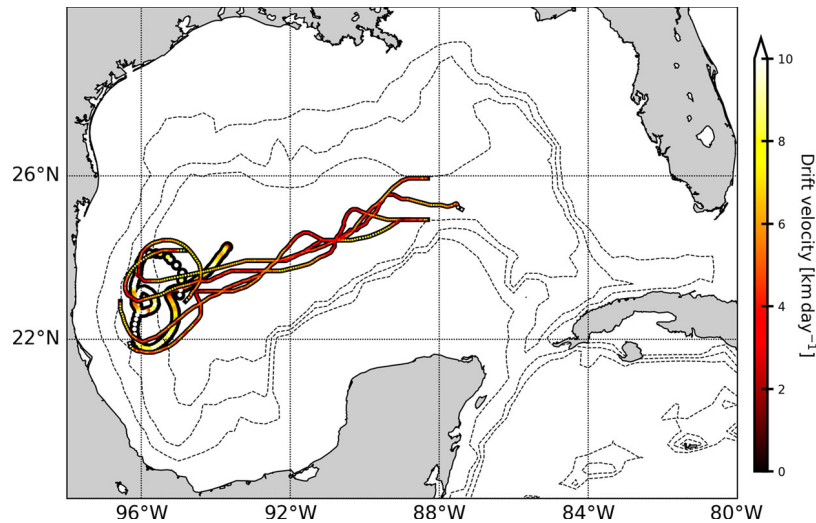


Figure 10. Trajectories of four Loop Current Rings detected from AVISO Absolute Dynamic Topography ($1/4^\circ$ resolution) data, in 2004, 2008, 2009 and 2012, using an eddy detection algorithm based on the detection of closed SSH contours (Chaigneau *et al.* 2008). Bold line shows the trajectory of the anticyclone in one of our simulations, with $R = 100$ km, $V_0 = 1.0$ m s $^{-1}$ and $\theta = 0$. Thin dashed lines are -3000 , -2000 , and -1000 m isobaths. (Colour online)

with the trajectory of anticyclones in our simulations. This would be speculative to go into further comparison. In particular, the drift velocity is lower in observations, most likely because of different values of β , eddy characteristics, background stratification, and perhaps of bottom topography. However, it is notable that the process explained in this study may give an explanation to the fact that LCRs appear not to drift northward until the northern coast of the Gulf of Mexico, but rather appear to oscillate around a stationary position.

Acknowledgements

This work was funded by the Direction Générale de l'Armement (DGA) via a full grant for Charly de Marez's PhD. This work is also a contribution to PRC 1069 "Meso and submesoscale vortices in the Atlantic and Indian Ocean", funded by CNRS and RFBR. Simulations were performed using the HPC facilities DATARMOR of "Pôle de Calcul Intensif pour la Mer" at Ifremer, Brest, France. Model outputs are available upon request. We gratefully acknowledge N. Lahaye and J. Gula for helpful discussions.

Absolute dynamic topography products were produced and distributed by the Copernicus Marine and Environment Monitoring Service (CMEMS) (<http://www.marine.copernicus.eu>). Global HYCOM re-analysis were downloaded from the dedicated repository <https://www.hycom.org/dataserver/gofs-3pt1/reanalysis>.

Disclosure statement

No potential conflict of interest was reported by the author(s).

Funding

This work was funded by the Direction Générale de l'Armement (DGA) via a full grant for Charly de Marez's PhD. This work is also a contribution to PRC 1069 "Meso and submesoscale vortices in the Atlantic and Indian Ocean", funded by CNRS and RFBR.

ORCID

Charly de Marez  <http://orcid.org/0000-0002-1712-729X>

Xavier Carton  <http://orcid.org/0000-0002-7849-6611>

References

- Amante, C. (2009). ETOPO1 1 arc-minute global relief model: procedures, data sources and analysis, Type: dataset.
- Beal, L.M., De Ruijter, W.P.M., Biastoch, A., Zahn, R. and Sa, S, and SCOR/WCRP/IAPSO Working Group 136, On the role of the Agulhas system in ocean circulation and climate. *Nature* **2011**, **472**, 429–436.
- Chaigneau, A., Gizolme, A. and Grados, C., Mesoscale eddies off Peru in altimeter records: identification algorithms and eddy spatio-temporal patterns. *Prog. Oceanogr.* **2008**, **79**, 106–119.
- Chelton, D.B., Gaube, P., Schlax, M.G., Early, J.J. and Samelson, R.M., The influence of nonlinear mesoscale eddies on near-surface oceanic chlorophyll. *Science* **2011**, **334**, 328–332.
- Chelton, D.B., Schlax, M.G. and Samelson, R.M., Global observations of nonlinear mesoscale eddies. *Prog. Oceanogr.* **2011**, **91**, 167–216.
- Chelton, D.B., Schlax, M.G., Samelson, R.M. and de Szoeke, R.A., Global observations of large oceanic eddies. *Geophys. Res. Lett.* **2007**, **34**, L15606.
- Clément, L., Frajka-Williams, E., Sheen, K.L., Brearley, J.A. and Garabato, A.C.N., Generation of internal waves by eddies impinging on the western boundary of the northatlantic. *J. Phys. Oceanogr.* **2016**, **46**, 1067–1079.
- Deremble, B., Dewar, W.K. and Chassignet, E.P., Vorticity dynamics near sharp topographic features. *J. Mar. Res.* **2016**, **74**, 249–276.
- Deremble, B., Johnson, E. and Dewar, W., A coupled model of interior balanced and boundary flow. *Ocean Modell.* **2017**, **119**, 1–12.
- Dewar, W.K. and Hogg, A.M., Topographic inviscid dissipation of balanced flow. *Ocean Modell.* **2010**, **32**, 1–13.
- Dong, C., McWilliams, J.C., Liu, Y. and Chen, D., Global heat and salt transports by eddy movement. *Nat. Commun.* **2014**, **5**, 1–6.
- Findlater, J., A major low-level air current near the Indian Ocean during the northern summer. *Q. J. R. Meteorolog. Soc.* **1969**, **95**, 362–380.
- Frolov, S.A., Sutyrin, G.G., Rowe, G.D. and Rothstein, L.M., Loop Current Eddy interaction with the western boundary in the Gulf of Mexico. *J. Phys. Oceanogr.* **2004**, **34**, 2223–2237.
- Gill, A.E., *Atmosphere-Ocean Dynamics*, 1982 (Academic press: Cambridge).
- Gula, J., Blacic, T.M. and Todd, R.E., Submesoscale coherent vortices in the Gulf Stream. *Geophys. Res. Lett.* **2019**, **46**, 2704–2714.
- Gula, J., Molemaker, M.J. and McWilliams, J.C., Gulf Stream dynamics along the southeastern U.S. seaboard. *J. Phys. Oceanogr.* **2015**, **45**, 690–715.
- Gula, J. and Zeitlin, V., Instabilities of buoyancy-driven coastal currents and their nonlinear evolution in the two-layer rotating shallow-water model. Part 1. Passive lower layer. *J. Fluid Mech.* **2010**, **659**, 69–93.
- Gula, J., Zeitlin, V. and Bouchut, F., Instabilities of buoyancy-driven coastal currents and their nonlinear evolution in the two-layer rotating shallow water model. Part 2. Active lower layer. *J. Fluid Mech.* **2010**, **665**, 209–237.

- Halo, I., Backeberg, B., Penven, P., Ansorge, I., Reason, C. and Ullgren, J., Eddy properties in the Mozambique channel: a comparison between observations and two numerical ocean circulation models. *Deep Sea Res. Part II* **2014**, **100**, 38–53.
- Haynes, P.H. and McIntyre, M.E., On the conservation and impermeability theorems for potential vorticity. *J. Atmos. Sci.* **1990**, **47**, 2021–2031.
- Hogg, A.M., Dewar, W.K., Berloff, P. and Ward, M.L., Kelvin wave hydraulic control induced by interactions between vortices and topography. *J. Fluid Mech.* **2011**, **687**, 194–208.
- Hoskins, B.J., McIntyre, M.E. and Robertson, A.W., On the use and significance of isentropic potential vorticity maps. *Q. J. R. Meteorolog. Soc.* **1985**, **111**, 877–946.
- Johns, W.E., Lee, T.N., Schott, F.A., Zantopp, R.J. and Evans, R.H., The North Brazil Current retroflection: seasonal structure and eddy variability. *J. Geophys. Res.* **1990**, **95**, 22103.
- Keyser, D. and Rotunno, R., On the formation of potential-vorticity anomalies in upper-level jet-front systems. *Mon. Weather Rev.* **1990**, **118**, 1914–1921.
- Klein, P., Hua, B.L., Lapeyre, G., Capet, X., Le Gentil, S. and Sasaki, H., Upper ocean turbulence from high-resolution 3D simulations. *J. Phys. Oceanogr.* **2008**, **38**, 1748–1763.
- Lamarque, J.F. and Hess, P.G., Cross-tropopause mass exchange and potential vorticity budget in a simulated tropopause folding. *J. Atmos. Sci.* **1994**, **51**, 2246–2269.
- Legg, S., McWilliams, J. and Gao, J., Localization of deep ocean convection by a mesoscale eddy. *J. Phys. Oceanogr.* **1998**, **28**, 944–970.
- L'Hégaret, P., Beal, L.M., Elipot, S. and Laurindo, L., Shallow cross-equatorial gyres of the Indian Ocean driven by seasonally reversing monsoon winds. *J. Geophys. Res. C: Oceans* **2018**, **123**, 8902–8920.
- L'Hégaret, P., Carton, X., Louazel, S. and Boutin, G., Mesoscale eddies and submesoscale structures of Persian Gulf Water off the Omani coast in spring 2011. *Ocean Sci.* **2016**, **12**, 687–701.
- L'Hégaret, P., Duarte, R., Carton, X., Vic, C., Ciani, D., Baraille, R. and Corréard, S., Mesoscale variability in the Arabian Sea from HYCOM model results and observations: impact on the Persian Gulf Water path. *Ocean Sci.* **2015**, **11**, 667–693.
- Li, L., Nowlin, W.D. and Jilan, S., Anticyclonic rings from the Kuroshio in the South China Sea. *Deep Sea Res. Part I* **1998**, **45**, 1469–1482.
- Liu, L., Ran, L. and Gao, S., A three-dimensional wave activity flux of inertia-gravity waves and its application to a rainstorm event. *Adv. Atmos. Sci.* **2019**, **36**, 206–218.
- Marchesiello, P., McWilliams, J.C. and Shchepetkin, A., Open boundary conditions for long-term integration of regional oceanic models. *Ocean Modell.* **2001**, **3**, 1–20.
- McWilliams, J.C., Submesoscale, coherent vortices in the ocean. *Rev. Geophys.* **1985**, **23**, 165–182.
- McWilliams, J.C., Gent, P.R. and Norton, N.J., The evolution of balanced, low-mode vortices on the β -plane. *J. Phys. Oceanogr.* **1986**, **16**, 838–855.
- Ménesguen, C., Le Gentil, S., Marchesiello, P. and Ducoussou, N., Destabilization of an oceanic meddy-like vortex: energy transfers and significance of numerical settings. *J. Phys. Oceanogr.* **2018**, **48**, 1151–1168.
- Metzger, E.J., Smedstad, O.M., Thoppil, P., Hurlburt, H., Cummings, J., Walcraft, A., Zamudio, L., Franklin, D., Posey, P., Phelps, M., Hogan, P., Bub, F. and DeHaan, C., US Navy operational global ocean and Arctic ice prediction systems. *Oceanography* **2014**, **27**, 32–43.
- Meunier, T., Pallas-Sanz, E., Tenreiro, M., Portela, E., Ochoa, J., Ruiz-Angulo, A. and Cusí, S., The vertical structure of a Loop Current Eddy. *J. Geophys. Res. C: Oceans* **2018**, **123**, 6070–6090.
- Morel, Y. and McWilliams, J., Effects of isopycnal and diapycnal mixing on the stability of oceanic currents. *J. Phys. Oceanogr.* **2001**, **31**, 2280–2296.
- Nadiga, B.T., Nonlinear evolution of a baroclinic wave and imbalanced dissipation. *J. Fluid Mech.* **2014**, **756**, 965–1006.
- Nof, D., Strange encounters of eddies with walls. *J. Mar. Res.* **1999**, **57**, 739–761.
- Olson, D.B. and Evans, R.H., Rings of the Agulhas current. *Deep Sea Res. Part A* **1986**, **33**, 27–42.
- Richardson, P.L., Gulf stream rings. In *Eddies in Marine Science*, edited by A.R. Robinson, pp. 19–45, 1983 (Springer Berlin Heidelberg: Berlin, Heidelberg).

- Ridgway, K. and Dunn, J., Mesoscale structure of the mean East Australian Current system and its relationship with topography. *Prog. Oceanogr.* **2003**, **56**, 189–222.
- Sansón, L.Z., Graef, F. and Pavia, E.G., Collision of anticyclonic, lens-like eddies with a meridional western boundary. *J. Geophys. Res.: Oceans* **1998**, **103**, 24881–24890.
- Shchepetkin, A.F. and McWilliams, J.C., The regional oceanic modeling system (ROMS): a split-explicit, free-surface, topography-following-coordinate oceanic model. *Ocean Modell.* **2005**, **9**, 347–404.
- Shchepetkin, A.F. and McWilliams, J.C., Accurate Boussinesq oceanic modeling with a practical, “stiffened” equation of state. *Ocean Modell.* **2011**, **38**, 41–70.
- Shi, C. and Nof, D., The splitting of eddies along boundaries. *J. Mar. Res.* **1993**, **51**, 771–795.
- Shi, C. and Nof, D., The destruction of lenses and generation of wadons. *J. Phys. Oceanogr.* **1994**, **24**, 1120–1136.
- Smith, D.C., A numerical study of Loop Current Eddy interaction with topography in the western Gulf of Mexico. *J. Phys. Oceanogr.* **1986**, **16**, 1260–1272.
- Snyder, C., Skamarock, W.C. and Rotunno, R., Frontal dynamics near and following frontal collapse. *J. Atmos. Sci.* **1993**, **50**, 3194–3212.
- Stommel, H., *The Gulf Stream*, 1976 (Univ. of Calif. Press: Berkeley).
- Sutyrin, G.G., Rowe, G.D., Rothstein, L.M. and Ginis, I., Baroclinic eddy interactions with continental slopes and shelves. *J. Phys. Oceanogr.* **2003**, **33**, 283–291.
- Vallis, G.K., *Atmospheric and Oceanic Fluid Dynamics*, 2017 (Cambridge University Press: Exeter).
- Vic, C., Roulet, G., Carton, X. and Capet, X., Mesoscale dynamics in the Arabian Sea and a focus on the Great Whirl life cycle: a numerical investigation using ROMS. *J. Geophys. Res. C: Oceans* **2014**, **119**, 6422–6443.
- Zhai, X., Johnson, H.L. and Marshall, D.P., Significant sink of ocean-eddy energy near western boundaries. *Nat. Geosci.* **2010**, **3**, 608–612.
- Zhang, Z., Wang, W. and Qiu, B., Oceanic mass transport by mesoscale eddies. *Science* **2014**, **345**, 322–324.

Appendices

Appendix A. Derivation of the dispersion relation of internal Kelvin Waves

Along a western boundary, in a 3D flow, internal Kelvin Waves (iKW in the text) can propagate. There, the velocity normal to the boundary is null, and the primitive equations are simply

$$-fv = -\frac{1}{\rho_0}\partial_x P, \quad \frac{Dv}{Dt} = -\frac{1}{\rho_0}\partial_y P, \quad \partial_z P = -\rho g, \quad (\text{A.1})$$

where $\mathbf{u} = (u, v, w)$ is the flow velocity, $D/Dt \equiv \partial_t + \mathbf{u} \cdot \nabla$ is the material derivative, P is the pressure, ρ is the density linked to the temperature and the salinity by an equation of state for seawater, ρ_0 is a mean density and f the Coriolis frequency. The continuity equation is

$$-\frac{g}{\rho_0} \frac{D\rho}{Dt} + N^2 w = 0, \quad (\text{A.2})$$

where N is the Brunt–Väisälä frequency. The non divergence of the flow is expressed as

$$\partial_y v + \partial_z w = 0. \quad (\text{A.3})$$

From (A.1)–(A.3) we obtain two evolution equations for the vertical velocity, namely

$$\partial_{tzz} w - N^2 \partial_{yy} w = 0 \quad (\text{A.4})$$

and

$$\partial_{tx} w + f \partial_y w = 0. \quad (\text{A.5})$$

Assuming that the flow is a monochromatic wave propagating meridionally from north to south, the vertical velocity as the form

$$w(x, y, z, t) = \tilde{w}(x) e^{i(k_y y + k_z z + \omega t)}, \quad (\text{A.6})$$

where k_y and k_z are the zonal and vertical wavenumbers respectively, and ω is the frequency of the wave. We also have $k_z = 2\pi/\lambda$, where λ is the vertical wavelength of the wave. Substituting (A.6) into (A.4) gives the iKW dispersion relation

$$\omega = \frac{Nk_y}{k_z} = \frac{N\lambda}{2\pi}k_y. \quad (\text{A.7})$$

Appendix B. How is potential vorticity impacted by a local change of volume?

In the ocean, the layer between two isopycnals can change because of numerous effects, including diapycnal mixing. If we consider such a layer of height h , far from boundaries, in the framework of Morel and McWilliams (2001) (e.g. in a layered shallow water model) the time evolution of the layer volume $V = Sh$, with S the surface of the layer, can be written as

$$So = \frac{DV}{Dt} = S\frac{Dh}{Dt} + h\frac{DS}{Dt} = S\frac{Dh}{Dt} + hS(\partial_x u + \partial_y v), \quad (\text{B.1})$$

because $S^{-1}DS/Dt = \partial_x u + \partial_y v$, where u and v are the horizontal velocity components in the layer. Thus we obtain the evolution equation of the layer height

$$\frac{Dh}{Dt} + h(\partial_x u + \partial_y v) = \frac{So}{S}, \quad (\text{B.2})$$

with a source term on the right-hand side. Taking the curl of the momentum equation in the layer gives the evolution equation

$$\frac{DA}{Dt} + A(\partial_x u + \partial_y v) = 0 \quad (\text{B.3})$$

of the absolute vorticity $A = \zeta + f$, in which ζ is the relative vorticity and f is the Coriolis parameter.

Finally, taking $h \times (\text{B.3}) - A \times (\text{B.2})$ gives a relation for the temporal evolution of the Potential Vorticity in the layer $Q = A/h$

$$\frac{DQ}{Dt} = -\frac{So}{Sh^2}A. \quad (\text{B.4})$$

It states that if $Q > 0$ in the layer, a decrease of volume of the layer (e.g. $So < 0$) leads to a local increase of the Potential Vorticity. This phenomenon is observed in our simulations, as shown in figure 5.

5.3 Observation d'un tourbillon cyclonique profond de sousmésos-échelle

Lors de la campagne PHYSINDIEN 2019, un tourbillon de sousmésos-échelle a été observé le long des côtes Omanaise. Ce tourbillon étant cyclonique, comme ceux formés par interaction entre les ondes de Kelvin et les tourbillons anticycloniques sur un bord ouest (voir section précédente), nous présentons ici sa structure, et discutons des mécanismes possible ayant mené à sa génération.

5.3.1 L'observation : Article publié dans *Geophysical Research Letters*

Geophysical Research Letters

RESEARCH LETTER

10.1029/2020GL087881

Key Points:

- A deep submesoscale cyclone was observed in the Arabian Sea
- The cyclone contained Red Sea Water on its rim
- This cyclone was generated at the mouth of Gulf of Aden, as a local current interacted with the bottom topography

Correspondence to:

C. de Marez,
charly.demarez@univ-brest.fr

Citation:

de Marez, C., Carton, X., Corréard, S., L'Hégaret, P., & Morvan, M. (2020). Observations of a deep submesoscale cyclonic vortex in the Arabian Sea. *Geophysical Research Letters*, 47, e2020GL087881. <https://doi.org/10.1029/2020GL087881>


Received 9 MAR 2020

Accepted 20 MAY 2020

Accepted article online 30 MAY 2020

©2020. American Geophysical Union.
All Rights Reserved.

Observations of a Deep Submesoscale Cyclonic Vortex in the Arabian Sea

Charly de Marez¹ , Xavier Carton¹, Stéphanie Corréard², Pierre L'Hégaret¹, and Mathieu Morvan¹

¹Univ. Brest, Laboratoire d'Océanographie Physique et Spatiale (LOPS), IUEM, Plouzané, France,

²SHOM/DOPS/STM/DTO, Toulouse, France

Abstract Submesoscale coherent vortices (SCVs) are numerous in high-resolution numerical simulations, but their observations are scarce. Among the few in situ available measurements of SCVs, a vast majority concern anticyclones. No cyclonic SCV with large dynamical Rossby number ($|\zeta/f| > 1$) has ever been sampled. This suggested that such small cyclones may lack robustness. Here, we present in situ measurements of an intense cyclonic SCV in the Arabian Sea. This eddy lay at 600 m depth, with a Rossby number $Ro = \mathcal{O}(1)$ and a dynamical Rossby number $|\zeta/f| > 1.5$. This cyclone was most likely generated at the mouth of the Gulf of Aden. It trapped and advected Red Sea Water, from there on. This highlights the role of deep SCVs in the spreading of salty waters across the Arabian Sea.

Plain Language Summary Numerical simulations of the ocean reveal the presence of numerous submesoscale eddies, vortices with radii smaller than, or equal to, 10 km. Nevertheless, their observations at depth are scarce because sampling their hydrological and dynamical structures requires very high resolution measurements. The present study presents measurements of a deep submesoscale cyclone in the Arabian Sea, collected during the PHYSINDIEN 2019 experiment. This intense, submesoscale, subsurface cyclone was centered at 600 m depth; most likely, it was formed at the mouth of the Gulf of Aden. Then it carried highly saline waters from the Red Sea toward the open Arabian Sea. We underline that conditions leading to the formation of such submesoscale eddies are often met in this region. Thus, such deep eddies should be recurrent in this region and should play a key role in spreading salty waters.

1. Introduction

Mesoscale eddies (with radii ~ 100 km) are known as oceanic coherent structures. The increase in remote sensing capabilities (Chelton et al., 2007, 2011) helped improve the deployment of in situ sensors in the core of surface eddies. Altimetry and infrared radiometry allowed the tracking of such eddies in near real time and provided their characteristics at the ocean surface. Both surface- and subsurface-intensified eddies have a significant impact on biological activities, tracer transport, and properties of the water column (Chelton et al., 2011; Dong & McWilliams, 2007; Zhang et al., 2014).

At scales below the mesoscale, in particular at submesoscale (0.3–30 km horizontally), numerous physical phenomena, and in particular smaller coherent structures, play an important role in the evolution of the ocean. Submesoscale oceanic structures can be generated by the interaction of regional currents with the topography, or by the interaction of mesoscale structures, or by the instability of mesoscale currents. External forcings—for example, outflows, extreme wind events, and thermal vents—can also yield submesoscale structures (D'Asaro, 1988; de Marez et al., 2020; McWilliams, 2019). These submesoscale features, among which vortices and filaments (with a typical size on the order of 10 km), are more arduous to detect than mesoscale eddies, all the more so as they lie below the ocean surface.

Surface-intensified submesoscale features can be located via satellite measurements. With this information, sensors can be accurately deployed to measure the vertical structure of these small vortices and filaments (Buckingham et al., 2017; Chavanne & Klein, 2010; Lévy et al., 2012). Surface submesoscale features play a key role in the ocean primary production (Lévy et al., 2018) and in the restratification of surface layers (Boccaletti et al., 2007).

By contrast, the quantification and dynamics of subsurface-intensified submesoscale structures are much less known because measurements are scarce, all the more so for deep (>300 m depth) structures, whose presence cannot be detected by satellites. Their in situ sampling thus relies on either an accurate knowledge of deep dynamical processes (sampling locations must be chosen based on what we know about submesoscale structure formation) or luck (a sampling not specifically targeting the submesoscale but with sufficient resolution to encounter them).

Submesoscale coherent vortices (SCVs; McWilliams, 1985), also named intrathermocline eddies (ITEs; Dugan et al., 1982), are a type of such subsurface submesoscale structures. Their radii are smaller than the Rossby deformation radius, their velocity maxima are localized at depth (McWilliams, 1985), and they have high values of vorticity ζ , locally reaching the Coriolis frequency f , that is, $|\zeta/f| = \mathcal{O}(1)$ (McWilliams, 2019). A few in situ experiments succeeded in measuring SCVs with a sufficient horizontal resolution (see, e.g., Bosse et al., 2016, 2017; Gula et al., 2019; Kostianoy & Belkin, 1989; L'Hégaret et al., 2016; Lukas & Santiago-Mandujano, 2001; Meunier et al., 2018, and the references therein). Among these, only a few observations of cyclonic SCVs were reported (Bosse et al., 2016), but with weak horizontal velocities, and therefore $|\zeta/f| \ll 1$. Thus, in observations, intense SCVs appeared as strictly anticyclonic. This view was also supported by numerical and theoretical studies, which claim that isolated cyclonic vortices are more unstable than anticyclonic ones, with growth rates of most unstable perturbation being larger for cyclones than for anticyclones (Lazar, Stegner, & Heifetz, 2013; Lazar, Stegner, Caldeira, et al., 2013; Mahdinia et al., 2017; Stegner & Dritschel, 2000). However, it is currently not possible to definitely conclude on SCV stability properties with respect to their polarity, because of the lack of cyclonic SCV observations. Furthermore, most of SCV observations were impaired by a lack of direct velocity measurements preventing an accurate estimate of SCVs' dynamical structure.

SCVs can be generated by the interaction of boundary currents with topography (D'Asaro, 1988), by winter-time deep convection (Bosse et al., 2016), or by the natural or forced instability of deep flows (L'Hégaret et al., 2016). They are generated in numerous places, and they should be rather ubiquitous in the world oceans. In particular, SCVs can play a key role in salt transport. As examples, Lukas and Santiago-Mandujano (2001) measured an SCV that transported salty water from the coast of Baja California to Hawaii, thus increasing the local salinity by >0.5 psu. L'Hégaret et al. (2016) showed that, occasionally, SCVs formed at the mouth of the Persian Gulf can induce salinity anomalies up to 1 psu in the open Arabian Sea.

Due to strong evaporation, salty waters are formed in the marginal seas of the Arabian Sea; they are called the Persian Gulf Water (PGW) and the Red Sea Water (RSW). After flowing via the Strait of Hormuz or the Strait of Bab el Mandeb into the Arabian Sea, they settle at 300 and 600 m depths, respectively (Bower et al., 2000). In the Arabian Sea, the pathways and spreading of PGW and RSW are controlled by the deep dynamical influence of surface mesoscale eddies (Bower & Furey, 2012; L'Hégaret et al., 2015, 2016). SCVs have also been shown to carry PGW (L'Hégaret et al., 2016) and RSW (Meschanov & Shapiro, 1998; Shapiro & Meschanov, 1991) far from the straits. This suggests that deep submesoscale processes are important for the spreading of salty outflows in the Arabian Sea.

In this paper, we present an observation of an intense deep submesoscale cyclone in the Arabian Sea. It is intensified at the depth of the RSW, with this water mass characteristic; thus, it participates in the spreading of RSW in the Arabian Sea. In Section 2, we present the PHYSINDIEN experiment and the other data sets used in the study. In Section 3, we present in details the measured deep submesoscale cyclone. In Section 4, we discuss the possible generation mechanism of this cyclone. Finally, we summarize observations and conclude on the potential impact of these measurements in Section 5.

2. Data and Methods

2.1. The PHYSINDIEN 2019 Experiment

During the PHYSINDIEN 2019 experiment in May 2019, the French Navy oceanographic vessel BHO Beautemps-Beaupré measured the surface and subsurface circulation off the Omani coast (western Arabian Sea). The first part of the experiment (Leg 1) started from Salalah (Oman) on 2 May 2019 and reached Muscat (Oman) on 12 May 2019. During Leg 1, several devices were deployed including a vessel-mounted acoustic Doppler current profiler with 38 kHz frequency (RDI 38 kHz VM-ADCP) and a RapidCAST (off-the-shelf Teledyne product).

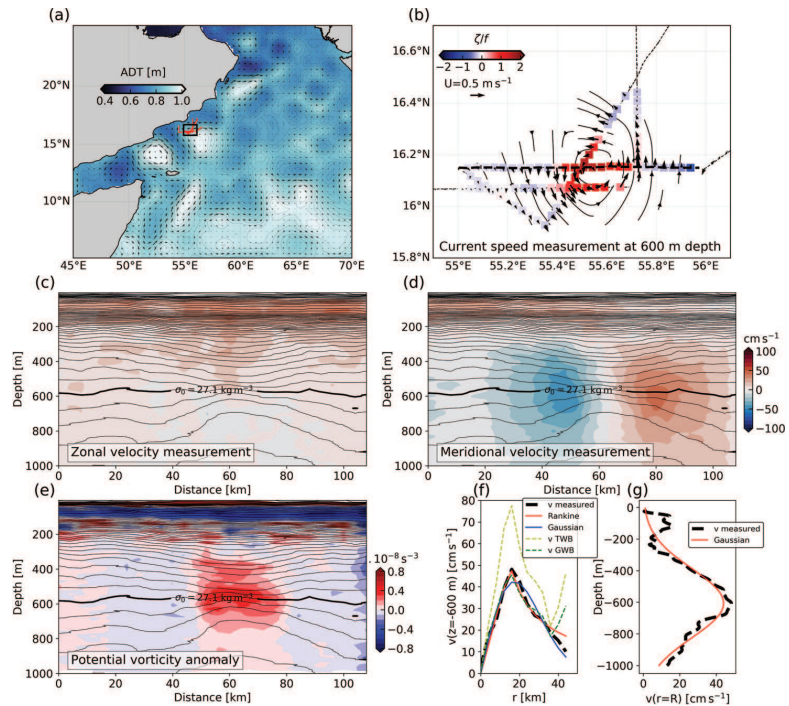


Figure 1. Dynamical structure of the deep submesoscale cyclone sampled off Omani coast. (a) Sea-level anomaly from AVISO and derived geostrophic surface current (black arrows) on 5 May 2019; the red lines indicate the ship track, and the black rectangle shows the position of panel (b). (b) Current speed measurement at 600 m depth from VM-ADCP measurements (black arrows) and normalized vorticity ζ/f along the ship track (colored squares) estimated from a linear optimal interpolation of horizontal velocities at 600 m depth (black streamlines); the thin dashed lines indicate the ship track, and the bold dashed line indicates the position of the vertical section shown in panels (c)–(e). (c) Vertical section of zonal velocity from VM-ADCP measurements along the east-west section shown bold in (b); thin black contours show isopycnals with a spacing of 0.1 kg m^{-3} , and thick black contour shows the $\sigma_\theta = 27.1 \text{ kg m}^{-3}$ isopycnal. (d) Same as (c) for the meridional velocity along the east-west section shown bold in (b). (e) Same as (c) for the potential vorticity anomaly PVA along the east-west section shown bold in (b). (f) Profile of azimuthal velocity of the cyclone at 600 m depth from VM-ADCP measurements (dashed black), compared with estimates of the velocity using the thermal wind balance (TWB, dashed yellow) and the gradient wind balance (GWB, dashed green); fit of a Rankine vortex profile (solid red), with $R = 15.2 \pm 0.3 \text{ km}$, $V_0 = 0.50 \pm 0.01 \text{ m s}^{-1}$, and $\chi = 0.0328 \text{ m s}^{-1}$; fit of a Gaussian vortex profile (solid blue), with $R = 12.4 \pm 0.2 \text{ km}$, $V_0 = 0.49 \pm 0.01 \text{ m s}^{-1}$, and $\chi = 0.0345 \text{ m s}^{-1}$. (g) Vertical profile of velocity at the radius of maximum velocity ($r = 16 \text{ km}$) from ADCP measurements; fit of a vertical Gaussian profile, with $z_0 = -605 \pm 2 \text{ m}$, $H = 309 \pm 3 \text{ m}$, $V_0 = 0.44 \pm 0.01 \text{ m s}^{-1}$, and $\chi = 0.046 \text{ m s}^{-1}$.

During the whole Leg 1, the VM-ADCP measured the current velocity from ~ 40 to about 1,000 m depth. The vertical averaging of raw data is made over 16 m. On the horizontal, data are averaged every 200 m, with a ship speed of $\sim 4 \text{ m s}^{-1}$. This leads to an accuracy of velocity measurements of about $1.5 \times 10^{-2} \text{ m s}^{-1}$ (Jimenez-Gonzalez et al., 2003). The data were first linearly interpolated on a regularly spaced grid, with a horizontal resolution of 0.25 km and a vertical resolution of 1 m. Then, a low-pass filter with a cutting length of 5 km was applied on the horizontal to remove spurious fine-scale signals.

The RapidCAST sampled the salinity and the temperature of the water column during one particular section of Leg 1 (see bold dashed line in Figure 1b). This device is an automated profiler that performs CTD casts down to $\sim 500 \text{ m}$ at 5 knots and to $\sim 1,000 \text{ m}$ at 1 knot, without the requirement of an operator on deck. Along the section, 30 profiles, down to $\sim 1,000 \text{ m}$ depth, were acquired, spaced of 2 nautical miles ($< 4 \text{ km}$). The vertical resolution is here $\sim 1 \text{ m}$; it depends on the speed of the ship. The data were linearly interpolated on a regularly spaced grid, with a horizontal resolution of 4 km and a vertical resolution of 5 m.

The potential density referenced at the surface σ_0 was computed along this section, from the absolute salinity S_A and conservative temperature Θ , using the TEOS-10 equation of state for seawater (McDougall & Barker, 2011). Along this section, the VM-ADCP measurements were interpolated on the RapidCAST grid, in order to estimate the potential vorticity (PV) anomaly associated with the measured structure. PV is calculated via (Hoskins, 1974)

$$Q = \left(f + \frac{\partial v}{\partial x} \right) \frac{\partial b}{\partial z} - \frac{\partial v}{\partial z} \frac{\partial b}{\partial x}, \quad (1)$$

where x is the zonal position, v the VM-ADCP measured meridional velocity, f the Coriolis frequency, and $b = -g\sigma_0/\sigma_0^*$ the buoyancy (g is the gravity and σ_0^* the mean value of density). The PV anomaly (PVA) is computed by subtracting a climatological value of PV from the local PV, on each isopycnal; climatological PV is defined as $Q_{\text{clim}} = f \frac{\partial}{\partial z} b_{\text{clim}}$ —where b_{clim} is estimated from the WOA 2018 database (see details below). We performed several sections initially to confirm that the RapidCAST section passes through the center of the vortex.

2.2. Other Data Sets and Methods

To estimate the climatological thermohaline properties of the water column in the area of interest, we used the WOA 2018 database, supplied by NOAA. Temperature and salinity are provided for each month of the year, over the whole Arabian Sea. Its horizontal resolution is 0.25° , and its vertical resolution in the upper 1,500 m of the ocean is about 3 m.

We also used the MERCATOR reanalysis, to describe the ocean dynamics at depth and to obtain the fine-scale variations of thermohaline properties in the area of interest. This product, processed by CMES, supplies physical fields on a $1/12^\circ$ grid and 50 vertical levels, for the period 27 December 2006 to present. The salinity and the horizontal velocity field were linearly interpolated on the $\sigma_0 = 27.1 \text{ kg m}^{-3}$ isopycnal—near which RSW propagates (Bower et al., 2000).

We ran a particle advection simulation, using the aforementioned MERCATOR reanalysis data interpolated on the $\sigma_0 = 27.1 \text{ kg m}^{-3}$ isopycnal, with the set of Python classes Parcels (Probably A Really Computationally Efficient Lagrangian Simulator). This software simulates the advection of an ensemble of particles, using a given 2-D or 3-D velocity field. This tool has been widely used in the past few years, and it is fully described in Lange and van Sebille (2017) and Delandmeter and van Sebille (2019) and in the references therein.

3. The Submesoscale Cyclonic Vortex

3.1. Dynamical Structure

At the edge of a surface-intensified mesoscale anticyclone (see Figure 1a), measurements of horizontal currents were performed during the PHYSINDIEN 2019 experiment between 3 and 5 May 2019; they showed a velocity signal intensified at 600 m depth, off the Omani coast. The ship made several passes over the signal in a time lapse of about 24 hr, thus ensuring a synoptic sampling of the structure. Based on these measurements, the structure can be identified as a deep cyclonic vortex (Figure 1b). Its horizontal extent was about half the local first baroclinic Rossby radius of deformation (which is about 60 km in this region; see Chelton et al., 1998): It is a submesoscale cyclone (SCY hereafter in the text).

From these measurements, we find that the core of the SCY has vorticity values $\zeta/f > 1.5$ (see Figure 1b). Along sections performed through the SCY's center, isopycnals have a concave lens shape, typical of subsurface-intensified cyclones (Assassi et al., 2016; see Figures 1c–1e). Also, the SCY's PVA is that of an isolated cyclonic lens, relatively well isolated from the surrounding flow (see Figure 1e). The PVA reaches a peak value of $\mathcal{O}(10^{-8}) \text{ s}^{-3}$, and it is centered around the $\sigma_0 = 27.1 \text{ kg m}^{-3}$ isopycnal. The radial distribution of azimuthal velocity at 600 m depth is shown in Figure 1f. In its core, the SCY has a radial profile of azimuthal velocity close to that of a Rankine vortex profile:

$$v_{\text{Rankine}}(r) = V_0 \left(\frac{r}{R} \right) \text{ for } r < R, \quad (2)$$

where $R = 15.2 \text{ km}$ is the radius of the maximal azimuthal velocity $V_0 = 0.5 \text{ m s}^{-1}$. This can also be seen in the horizontal distribution of ζ (Figure 1b); relative vorticity is positive and does not vary much in the SCY's core. At the SCY's edge, the velocity profile is closer to that of a Gaussian vortex:

$$v_{\text{Gaussian}}(r) = V_1 \left(\frac{r}{R_1} \right) e^{-r^2/(4R_1^2)}, \quad (3)$$

with $R_1 = 12.4$ km and $V_1 = 0.49$ m s⁻¹ than to that of a Rankine vortex

$$v_{\text{Rankine}}(r) = V_0 \left(\frac{R}{r} \right) \text{ for } r > R. \quad (4)$$

This is most likely due to the background flow (Amores et al., 2017), which generates an opposite-signed vorticity shield around the eddy (Figure 1b) and therefore a Gaussian-like velocity profile. Over the whole vortex, the cumulative error of the Rankine fit, estimated as

$$\chi = \sqrt{\frac{1}{\int dr} \int dr (v_{\text{measured}} - v_{\text{fit}})^2},$$

is smaller than the error of the Gaussian fit. This difference is not statistically significant, as the profiles are different only over a few points. However, the observed SCY can rather be well represented by a Rankine vortex profile. The dependency of the azimuthal velocity with depth z follows a Gaussian law

$$v(R, z) = V_0 e^{-(z-z_0)^2/H^2}, \quad (5)$$

with $z_0 = -605$ m and $H = 309$ m, the depth and thickness of the SCY, respectively (see Figure 1g). The Gaussian shape of SCVs commonly used in past studies since McWilliams (1985) is thus rather satisfying to represent the SCY on the vertical, even if the actual profile of velocity is little skewed relative to the analytical shape.

From these characteristics, we estimate that the Rossby number $Ro = V_0/fR$, associated with the SCY, is $\mathcal{O}(1)$. Along with the value of the dynamical Rossby number $|\zeta/f| \sim 1.5$ (which is the relevant parameter to quantify ageostrophic effects; see Stegner & Dritschel, 2000), this suggests that the vortex is not in geostrophic balance. This is confirmed by the comparison between an estimate of the SCY's velocity, from its density signature, using (1) the thermal wind balance or (2) the gradient wind balance (Figure 1f). The gradient wind balance velocity is closer to the measured velocity of the SCY. The centrifugal acceleration due to eddy curvature balances in part the radial pressure gradient. This acts to decrease the azimuthal velocity of the cyclone.

3.2. Thermohaline Structure

The temperature and salinity profiles (Figures 2a and 2b) reveal that the SCY is surrounded by salty (>36 g kg⁻¹) and warm ($>11^\circ\text{C}$) water, in comparison to climatological values (Figure 2e). This water mass has the thermohaline signature of RSW, and it is centered around the $\sigma_0 = 27.1$ kg m⁻³ isopycnal (Figure 2e) (Bower et al., 2000).

Layering is seen in the high salinity profiles that surround the SCY (Figure 2c), suggesting that double diffusive processes occur. This is confirmed by the values of Turner angle Tu (Ruddick, 1983; Turner, 1979), defined a

$$Tu = \tan^{-1} \left(\frac{\delta + 1}{\delta - 1} \right), \quad (6)$$

with $\delta = \frac{\beta \alpha_\theta S_\Delta}{\alpha_\theta \theta}$, where β and α are the thermal expansion coefficient and the saline contraction coefficient, respectively. Where $-90^\circ < Tu < -45^\circ$, the water column is diffusively unstable: Warm and salty waters are found below colder and fresher waters leading to stable diffusive convection; where $45^\circ < Tu < 90^\circ$, warm and salty waters are found above colder and fresher ones, leading to favorable conditions for salt fingering; and where $-45^\circ < Tu < 45^\circ$, the water column is stable with respect to double diffusion.

The upper core of the SCY (i.e., between 200 and 600 m depth) is stable. However, the lower core of the SCY (i.e., between 600 and 1,000 m depth), as well as its edge, exhibits values of Tu in the range $-90^\circ < Tu < -45^\circ$ (Figure 2d). The SCY is thus subject to double diffusive convection, which can in turn lead to a vertical homogenization of the water column properties. Such processes are supposed to induce a long-time decay of the SCY (McWilliams, 1985).

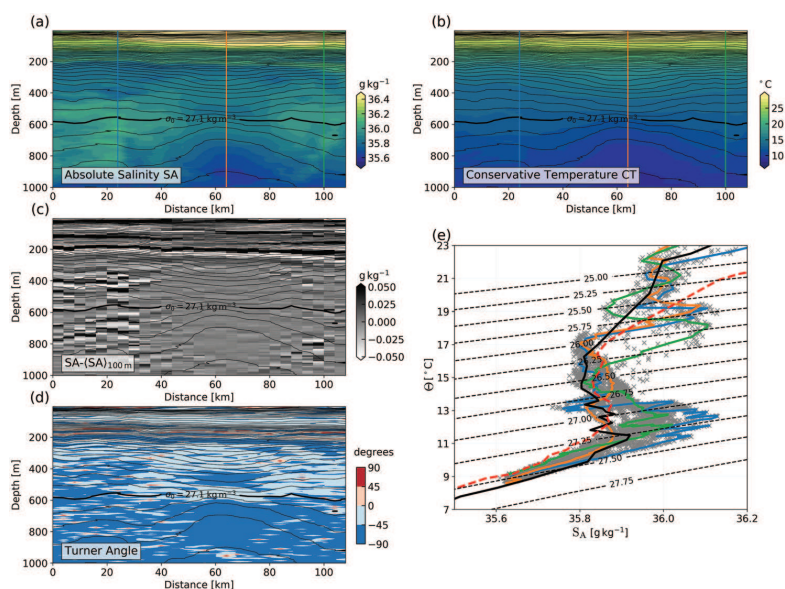


Figure 2. Thermohaline structure of the deep submesoscale cyclone. (a) Same as Figure 1c for the absolute salinity S_A from RapidCAST measurements. (b) Same as (a) for the conservative temperature Θ . (c) Same as (a) for the difference between the measured S_A and vertically low-passed $S_A \langle S_A \rangle_{100\text{m}}$ with a cutting length of 100 m. (d) Same as (a) for the Turner angle Tu . (e) Temperature-salinity diagram containing all profiles shown in panels (a) and (b); the blue and green (resp. orange) profiles show profiles collected at the edge (resp. center) of the cyclone (see their position in panels a and b), and the thick solid black (resp. dashed red) profile shows the TS profile (from the WOA 2018 database) at the proposed site of generation (resp. site of observation) shown in Figures 3a–3d by the red (resp. green) cross.

4. Discussion on the Origin of the Vortex

Unfortunately, the only available information about the SCY comes from measurements performed once at the observation site, as described in Section 3. Its past life is unknown. No Argo profiling float sampled it. During the 3 months prior to SCY discovery, the only data available at this location were satellite data. Since the SCY has no surface signature, satellite data do not provide information on its origin nor on its path.

However, a numerical model that assimilates satellite data such as MERCATOR can provide realistic surface fields with a satisfactory horizontal resolution, along with an estimate of thermohaline and dynamical properties of the ocean at depth. Thus, we assume here that the SCY evolved passively, on a given isopycnal, advected by the mean current from its generation site to its observation site (the green cross in Figures 3a–3c). This assumption is reasonable, since the SCY has a lens-like structure and a coherent core; past studies have shown that SCVs are robust; they can live for several months steadily or advected by large-scale or mesoscale flows (McWilliams, 1985).

Starting from this assumption, we release particles around the observation site and advect them backward during 3 months using the MERCATOR reanalysis velocities on the $\sigma_0 = 27.1 \text{ kg m}^{-3}$ isopycnal. Thus, we obtain an estimate of the previous path of water particles trapped inside the SCY. A large amount of particles (17%) comes from the easternmost part of the Gulf of Aden; they passed close to a prominent topographic feature, the Ra's Fartak cape (see the red cross in Figures 3a–3c), on average on mid-March of 2019. Other particles remained in the open ocean, far away from the coast.

The SCY has plausibly been generated at the entrance of the Gulf of Aden, by interaction between the mean flow and the Ra's Fartak cape. Other generation sites can be excluded for two reasons. First, the impermeability theorem (Haynes & McIntyre, 1990) states that no PV transport is possible across isopycnal surfaces, except if frictional or diapycnal processes occur. Thus, the high PVa values of the SCY on the $\sigma_0 = 27.1 \text{ kg m}^{-3}$ isopycnal must have been generated by deep nonconservative or diabatic effects

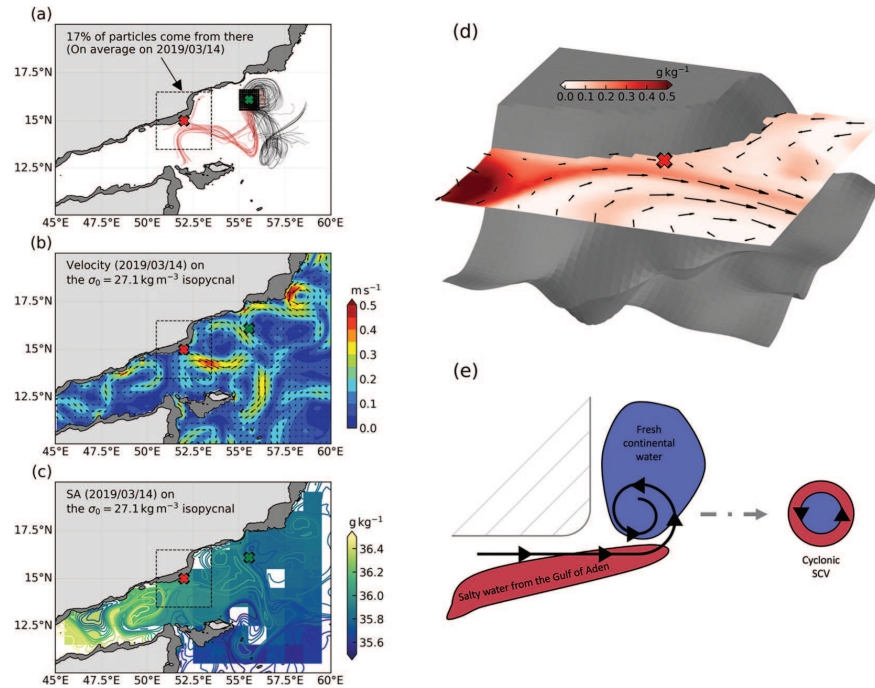


Figure 3. Proposed mechanism of generation of the deep subsurface cyclone. (a) Trajectories of 100 particles initially placed at the observation site (green cross) and advected backward using the velocities of the MERCATOR reanalysis on the $\sigma_0 = 27.1 \text{ kg m}^{-3}$ isopycnal; red lines indicate the trajectories of particles that passed close to the proposed generation site, the Ra's Fartak cape (red cross), during their journey. (b) Horizontal velocity from the MERCATOR reanalysis on the $\sigma_0 = 27.1 \text{ kg m}^{-3}$ isopycnal, on the average date when advected particles passed close to the generation site (14 March 2019); the color shows the intensity of the current and arrows the direction. (c) Absolute salinity from the WOA 2018 database (color) and from the MERCATOR reanalysis (color contours), on the $\sigma_0 = 27.1 \text{ kg m}^{-3}$ isopycnal, on the same date than (b). (d) 3-D view of the generation site on 14 March 2019; the gray 3-D surface shows the bathymetry, the color plot shows the salinity anomaly (i.e., the difference from the WOA 2018 database), and the black arrows show the horizontal velocity, on the $\sigma_0 = 27.1 \text{ kg m}^{-3}$ isopycnal from the MERCATOR reanalysis. (e) Schematic of the proposed mechanism of generation of a deep cyclone by interaction with the topography, inspired from D'Asaro (1988).

(McWilliams, 1985). Following the particle trajectories, the only place where such a PV injection is possible is Ra's Fartak cape, via frictional effects at the bottom. Second, the thermohaline properties of the SCY's core are comparable with the climatological values at Ra's Fartak cape (see Figure 2e). If the SCY had been generated in the open Arabian Sea (following other particle trajectories), its core would have been fresher.

The proposed mechanism of generation is the following. Mid-March 2019, an anticyclonic mesoscale eddy at the mouth of the Gulf of Aden induced an intense current along Ra's Fartak cape, reaching 0.15 m s^{-1} at depth. As this current flowed eastward (see Figures 3b and 3d), with the coast on its left, frictional torques generated a positive vorticity strip close to the topography. This strip subsequently rolled up into small cyclones in the lee of the cape, possibly via inertia and the D'Asaro mechanism (D'Asaro, 1988) and/or by centrifugal and barotropic shear instabilities (Srinivasan et al., 2019). Frictional generation of vorticity near the coast has been intensively studied, using idealized (Dong et al., 2007; Morvan et al., 2019; Srinivasan et al., 2019) and realistic (Contreras et al., 2019; Dong & McWilliams, 2007; Gula et al., 2019, 2015; McWilliams, 2019; Vic et al., 2015) numerical simulations. It has been identified as an efficient mechanism to form deep subsurface vortices in gradient wind balance, with high values of $|\zeta/f|$ (Srinivasan et al., 2019), and a lens-like shape (Morvan et al., 2019).

In particular, Srinivasan et al. (2019) showed that the value of $|\zeta/f|$ for a submesoscale vortex generated in the lee of a seamount scales as

$$|\zeta/f| \sim \frac{U}{fL} \mathcal{O}(h\sqrt{N}), \quad (7)$$

with N the ambient stratification and U the intensity of the current flowing over a seamount of height h and width L . We apply this scaling assuming that the Ra's Fartak cape induces the same dynamics than half of a seamount. We take $U = 0.15 \text{ m s}^{-1}$, $h = 1,500 \text{ m}$, $L = 50 \text{ km}$, $N = 2.5 \times 10^{-2} \text{ s}^{-1}$ (estimated with the WOA 2018 climatology), and $f = 3.77 \times 10^{-5} \text{ s}^{-1}$. This gives $1 < |\zeta/f| < 10$, which is in satisfactory agreement with the high values of $|\zeta/f|$ in the core of the observed SCY. Concomitantly with this vorticity generation, a tongue of salty water from the Gulf of Aden, with the signature of RSW, was advected along the coast (see Figures 3c and 3d) by the local current. This salty water wrapped around the newly formed SCY and, in turn, formed the ring of RSW observed around the SCY. The whole generation process is summarized in Figure 3e.

5. Conclusion

In this paper, we have presented an original observation of a deep SCY in the Arabian Sea. It was plausibly formed at the mouth of the Gulf of Aden, near Ra's Fartak cape, where the interaction of a mesoscale anticyclone with the steep topography provided a source of positive vorticity that subsequently generated a deep cyclone. During its formation, the cyclone entrained salty RSW (from the Gulf of Aden) along its rim. Then, it traveled for about 2 months, entering the Omani waters, where it was sampled. Temperature and salinity measurements show that the water surrounding the cyclone is saltier and warmer than the climatological value (see Figure 2e). The passage of the cyclone has thus—locally and transiently—contributed to increase the deep salinity and temperature of the Arabian Sea, by carrying RSW seaward. Moreover, if the cyclone has dissipated just after its observation, it could have had a lasting impact on salinity in that location.

Mesoscale anticyclones are regularly observed in the mouth of the Gulf of Aden, near Ra's Fartak cape (Morvan et al., 2020): the Summer Eddy, which is formed at the beginning of the summer monsoon and then travels into the Gulf of Aden (Bower & Furey, 2012); the Somali Current Rings, observed in October (Fratantoni et al., 2006); and the Gulf of Aden Eddy during the spring intermonsoon (Prasad et al., 2001). Therefore, the generation of deep SCYs may be a common phenomenon, though little observed for the moment due to their small size and to the absence of surface signature. Along Omani coasts, salinity peaks at the depth of RSW have been observed in the past (Carton et al., 2012; de Marez et al., 2019). They could be related to submesoscale structures carrying RSW away from their generation spot. Anticyclonic SCVs carrying salty RSW have already been observed in the Arabian Sea (Meschanov & Shapiro, 1998; Nof et al., 2002; Shapiro & Meschanov, 1991). They were most likely generated by the instability of the outflowing RSW tongue. Thus, several mechanisms that can lead to the generation of coherent SCVs are at play, in the Gulf of Aden. These results altogether suggest that deep submesoscale eddies may contribute substantially to the transport of RSW out of the Gulf of Aden and to the mean stratification at depth.

More generally, the observations presented in this paper show that, even if anticyclonic SCVs seem to be predominant in the deep ocean, cyclones can also be generated and remain coherent for several months. Here, the cyclone has a Rossby number $Ro = \mathcal{O}(1)$. This cyclone is thus very intense and highly ageostrophic. Its 3-D structure is close to theoretical profiles (close to that of a Rankine vortex radially and Gaussian vertically). The universality of such profiles should be studied with more real or simulated data. Further, we should study the mechanisms for polarity bias in SCVs, in particular intense ones, if such a bias is confirmed. For instance, stability studies could be conducted, using these simple analytical profiles, to further describe the processes at play in intense anticyclonic and cyclonic SCVs.

Data Availability Statement

The altimeter products were produced by SSALTO/DUACS and distributed by AVISO, with support from CNES. The WOA 2018 data set, the MERCATOR reanalysis, and the Parcels tool can be found online (<https://www.nodc.noaa.gov/OC5/woa18/woa18data.html>, <https://marine.copernicus.eu>, and <https://oceanparcels.org>). Processed data can be obtained on the author's GitHub (<https://github.com/demarez/DATA>; see de Marez, 2020).

Acknowledgments

This work was funded by the Direction Générale de l'Armement (DGA) via a full grant for Charly de Marez's PhD. The authors gratefully acknowledge helpful discussions with C. Vic, C. Buckingham, and T. Meunier. Finally, and most importantly, we address special thanks to the captain and crew of the oceanographic vessel BHO Beautemps-Beaupré, whose dedication allowed us to obtain the fine measurements presented here.

References

- Amores, A., Monserrat, S., Melnichenko, O., & Maximenko, N. (2017). On the shape of sea level anomaly signal on periphery of mesoscale ocean eddies. *Geophysical Research Letters*, *44*, 6926–6932. <https://doi.org/10.1002/2017GL073978>
- Assassi, C., Morel, Y., Vandermeersch, F., Chaigneau, A., Pegliasco, C., Morrow, R., & Cambra, R. (2016). An index to distinguish surface- and subsurface-intensified vortices from surface observations. *Journal of Physical Oceanography*, *46*(8), 2529–2552. <https://doi.org/10.1175/JPO-D-15-0122.1>
- Boccaletti, G., Ferrari, R., & Fox-Kemper, B. (2007). Mixed layer instabilities and restratification. *Journal of Physical Oceanography*, *37*(9), 2228–2250. <https://doi.org/10.1175/JPO3101.1>
- Bosse, A., Testor, P., Houpert, L., Damien, P., Prieur, L., Hayes, D., & Mortier, L. (2016). Scales and dynamics of Submesoscale Coherent Vortices formed by deep convection in the northwestern Mediterranean Sea: Vortices in the NW Mediterranean Sea. *Journal of Geophysical Research: Oceans*, *121*, 7716–7742. <https://doi.org/10.1002/2016JC012144>
- Bosse, A., Testor, P., Mayot, N., Prieur, L., D'Ortenzio, F., Mortier, L., & Raimbault, P. (2017). A submesoscale coherent vortex in the Ligurian Sea: From dynamical barriers to biological implications. *Journal of Geophysical Research: Oceans*, *122*, 6196–6217. <https://doi.org/10.1002/2016JC012634>
- Bower, A. S., & Furey, H. H. (2012). Mesoscale eddies in the Gulf of Aden and their impact on the spreading of Red Sea Outflow Water. *Progress in Oceanography*, *96*(1), 14–39. <https://doi.org/10.1016/j.pocean.2011.09.003>
- Bower, A. S., Hunt, H. D., & Price, J. F. (2000). Character and dynamics of the Red Sea and Persian Gulf outflows. *Journal of Geophysical Research*, *105*(C3), 6387–6414. <https://doi.org/10.1029/1999JC900297>
- Buckingham, C. E., Khaleel, Z., Lazar, A., Martin, A. P., Allen, J. T., Naveira Garabato, A. C., & Vic, C. (2017). Testing Munk's hypothesis for submesoscale eddy generation using observations in the North Atlantic. *Journal of Geophysical Research: Oceans*, *122*, 6725–6745. <https://doi.org/10.1002/2017JC012910>
- Carton, X., L'Hégaret, P., & Baraille, R. (2012). Mesoscale variability of water masses in the Arabian Sea as revealed by ARGO floats. *Ocean Science*, *8*(2), 227–248. <https://doi.org/10.5194/os-8-227-2012>
- Chavanne, C. P., & Klein, P. (2010). Can oceanic submesoscale processes be observed with satellite altimetry? *Geophysical Research Letters*, *37*, L22602. <https://doi.org/10.1029/2010GL045057>
- Chelton, D. B., deSzoeke, R. A., Schlax, M. G., El Naggar, K., & Siwertz, N. (1998). Geographical variability of the first baroclinic Rossby radius of deformation. *Journal of Physical Oceanography*, *28*(3), 433–460. [https://doi.org/10.1175/1520-0485\(1998\)028<0433:GVOTFB>2.0.CO;2](https://doi.org/10.1175/1520-0485(1998)028<0433:GVOTFB>2.0.CO;2)
- Chelton, D. B., Gaube, P., Schlax, M. G., Early, J. J., & Samelson, R. M. (2011). The influence of nonlinear mesoscale eddies on near-surface oceanic chlorophyll. *Science*, *334*(6054), 328–332. <https://doi.org/10.1126/science.1208897>
- Chelton, D. B., Schlax, M. G., & Samelson, R. M. (2011). Global observations of nonlinear mesoscale eddies. *Progress in Oceanography*, *91*(2), 167–216. <https://doi.org/10.1016/j.pocean.2011.01.002>
- Chelton, D. B., Schlax, M. G., Samelson, R. M., & de Szoeke, R. A. (2007). Global observations of large oceanic eddies. *Geophysical Research Letters*, *34*, L15606. <https://doi.org/10.1029/2007GL030812>
- Contreras, M., Pizarro, O., Dewitte, B., Sepulveda, H. H., & Renault, L. (2019). Subsurface mesoscale eddy generation in the ocean off central Chile. *Journal of Geophysical Research: Oceans*, *124*, 5700–5722. <https://doi.org/10.1029/2018JC014723>
- D'Asaro, E. A. (1988). Generation of submesoscale vortices: A new mechanism. *Journal of Geophysical Research*, *93*(C6), 6685. <https://doi.org/10.1029/JC093iC06p06685>
- de Marez, C. (2020). Submesoscale cyclone dataset. <http://github.com/demarez/DATA>. doi: 10.5281/zenodo.3824500.
- de Marez, C., L'Hégaret, P., Morvan, M., & Carton, X. (2019). On the 3D structure of eddies in the Arabian Sea. *Deep Sea Research Part I: Oceanographic Research Papers*, *150*, 103057. <https://doi.org/10.1016/j.dsr.2019.06.003>
- de Marez, C., Meunier, T., Morvan, M., L'Hégaret, P., & Carton, X. (2020). Study of the stability of a large realistic cyclonic eddy. *Ocean Modelling*, *146*, 101,540. <https://doi.org/10.1016/j.ocemod.2019.101540>
- Delandmeter, P., & van Sebille, E. (2019). The Parcels v2.0 Lagrangian framework: New field interpolation schemes. *Geoscientific Model Development*, *12*(8), 3571–3584. <https://doi.org/10.5194/gmd-12-3571-2019>
- Dong, C., & McWilliams, J. C. (2007). A numerical study of island wakes in the Southern California Bight. *Continental Shelf Research*, *27*(9), 1233–1248. <https://doi.org/10.1016/j.csr.2007.01.016>
- Dong, C., McWilliams, J. C., & Shchepetkin, A. F. (2007). Island wakes in deep water. *Journal of Physical Oceanography*, *37*(4), 962–981. <https://doi.org/10.1175/JPO3047.1>
- Dugan, J. P., Mied, R. P., Mignerey, P. C., & Schuetz, A. F. (1982). Compact, intrathermocline eddies in the Sargasso Sea. *Journal of Geophysical Research*, *87*(C1), 385. <https://doi.org/10.1029/JC087iC01p00385>
- Fratantoni, D. M., Bower, A. S., Johns, W. E., & Peters, H. (2006). Somali Current rings in the eastern Gulf of Aden. *Journal of Geophysical Research*, *111*, C0903. <https://doi.org/10.1029/2005JC003338>
- Gula, J., Blacic, T. M., & Todd, R. E. (2019). Submesoscale coherent vortices in the Gulf Stream. *Geophysical Research Letters*, *46*, 2704–2714. <https://doi.org/10.1029/2019GL081919>
- Gula, J., Molemaker, M. J., & McWilliams, J. C. (2015). Topographic vorticity generation, submesoscale instability and vortex street formation in the Gulf Stream. *Geophysical Research Letters*, *42*, 4054–4062. <https://doi.org/10.1002/2015GL063731>
- Haynes, P. H., & McIntyre, M. E. (1990). On the conservation and impermeability theorems for potential vorticity. *Journal of the Atmospheric Sciences*, *47*(16), 2021–2031. [https://doi.org/10.1175/1520-0469\(1990\)047<2021:OTCAIT>2.0.CO;2](https://doi.org/10.1175/1520-0469(1990)047<2021:OTCAIT>2.0.CO;2)
- Hoskins, B. J. (1974). The role of potential vorticity in symmetric stability and instability. *Quarterly Journal of the Royal Meteorological Society*, *100*(425), 480–482. <https://doi.org/10.1002/qj.49710042520>
- Jimenez-Gonzalez, S., Mayerle, R., & Egozoue, J. (2003). On the accuracy of acoustic Doppler current profilers for in-situ measurements. A proposed approach and estimations for measurements in tidal channels. <https://doi.org/10.1109/CCM.2003.1194311>
- Kostianoy, A., & Belkin, I. (1989). A survey of observations on intrathermocline eddies in the world ocean. *Elsevier Oceanography Series* (Vol. 50, pp. 821–841). Moscow: Elsevier. [https://doi.org/10.1016/S0422-9894\(08\)70223-X](https://doi.org/10.1016/S0422-9894(08)70223-X)
- L'Hégaret, P., Carton, X., Louazel, S., & Boutin, G. (2016). Mesoscale eddies and submesoscale structures of Persian Gulf Water off the Omani coast in spring 2011. *Ocean Science*, *12*(3), 687–701. <https://doi.org/10.5194/os-12-687-2016>
- L'Hégaret, P., Duarte, R., Carton, X., Vic, C., Ciani, D., Baraille, R., & Corréard, S. (2015). Mesoscale variability in the Arabian Sea from HYCOM model results and observations: Impact on the Persian Gulf Water path. *Ocean Science*, *11*(5), 667–693. <https://doi.org/10.5194/os-11-667-2015>
- Lange, M., & van Sebille, E. (2017). Parcels v0.9: Prototyping a Lagrangian ocean analysis framework for the petascale age. *Geoscientific Model Development*, *10*(11), 4175–4186. <https://doi.org/10.5194/gmd-10-4175-2017>

- Lazar, A., Stegner, A., Caldeira, R., Dong, C., Didelle, H., & Viboud, S. (2013). Inertial instability of intense stratified anticyclones. Part 2. Laboratory experiments. *Journal of Fluid Mechanics*, 732, 485–509. <https://doi.org/10.1017/jfm.2013.413>
- Lazar, A., Stegner, A., & Heifetz, E. (2013). Inertial instability of intense stratified anticyclones. Part 1. Generalized stability criterion. *Journal of Fluid Mechanics*, 732, 457–484. <https://doi.org/10.1017/jfm.2013.412>
- Lévy, M., Ferrari, R., Franks, P. J. S., Martin, A. P., & Riviere, P. (2012). Bringing physics to life at the submesoscale. *Geophysical Research Letters*, 39, L14602. <https://doi.org/10.1029/2012GL052756>
- Lévy, M., Franks, P. J. S., & Smith, K. S. (2018). The role of submesoscale currents in structuring marine ecosystems. *Nature Communications*, 9(1), 4758. <https://doi.org/10.1038/s41467-018-07059-3>
- Lukas, R., & Santiago-Mandujano, F. (2001). Extreme water mass anomaly observed in the Hawaii ocean time-series. *Geophysical Research Letters*, 28(15), 2931–2934. <https://doi.org/10.1029/2001GL013099>
- Mahdinia, M., Hassanzadeh, P., Marcus, P. S., & Jiang, C. H. (2017). Stability of three-dimensional Gaussian vortices in an unbounded, rotating, vertically stratified, Boussinesq flow: Linear analysis. *Journal of Fluid Mechanics*, 824, 97–134. <https://doi.org/10.1017/jfm.2017.303>
- McDougall, T. J., & Barker, P. M. (2011). Getting started with TEOS-10 and the Gibbs Seawater (GSW) oceanographic toolbox. *SCOR/IAPSO WG*, 127, 1–28.
- McWilliams, J. C. (1985). Submesoscale, coherent vortices in the ocean. *Reviews of Geophysics*, 23(2), 165–182. <https://doi.org/10.1029/RG023i002p00165>
- McWilliams, J. C. (2019). A survey of submesoscale currents. *Geoscience Letters*, 6(1). <https://doi.org/10.1186/s40562-019-0133-3>
- Meschanov, S., & Shapiro, G. (1998). A young lens of Red Sea Water in the Arabian Sea. *Deep Sea Research Part I: Oceanographic Research Papers*, 45(1), 1–13. [https://doi.org/10.1016/S0967-0637\(97\)00018-6](https://doi.org/10.1016/S0967-0637(97)00018-6)
- Meunier, T., Tenreiro, M., Palls-Sanz, E., Ochoa, J., Ruiz-Angulo, A., Portela, E., & Carton, X. (2018). Intrathermocline eddies embedded within an anticyclonic vortex ring. *Geophysical Research Letters*, 45, 7624–7633. <https://doi.org/10.1029/2018GL077527>
- Morvan, M., L'Hégaret, P., Carton, X., Gula, J., Vic, C., de Marez, C., & Koschel, K. (2019). The life cycle of submesoscale eddies generated by topographic interactions. *Ocean Science*, 15(6), 1531–1543. <https://doi.org/10.5194/os-15-1531-2019>
- Morvan, M., L'Hégaret, P., de Marez, C., Carton, X., Corréard, S., & Baraille, R. (2020). Life cycle of mesoscale eddies in the Gulf of Aden. *Geophysical & Astrophysical Fluid Dynamics*, 1–19. <https://doi.org/10.1080/03091929.2019.1708348>
- Nof, D., Paldor, N., & Gorder, S. V. (2002). The Reddy maker. *Deep Sea Research Part I: Oceanographic Research Papers*, 49(9), 1531–1549. [https://doi.org/10.1016/S0967-0637\(02\)00040-7](https://doi.org/10.1016/S0967-0637(02)00040-7)
- Prasad, T. G., Ikeda, M., & Kumar, S. P. (2001). Seasonal spreading of the Persian Gulf Water mass in the Arabian Sea. *Journal of Geophysical Research*, 106(C8), 17,059–17,071. <https://doi.org/10.1029/2000JC000480>
- Ruddick, B. (1983). A practical indicator of the stability of the water column to double-diffusive activity. *Deep Sea Research Part A: Oceanographic Research Papers*, 30(10), 1105–1107. [https://doi.org/10.1016/0198-0149\(83\)90063-8](https://doi.org/10.1016/0198-0149(83)90063-8)
- Shapiro, G., & Meschanov, S. (1991). Distribution and spreading of Red Sea Water and salt lens formation in the northwest Indian Ocean. *Deep Sea Research Part A: Oceanographic Research Papers*, 38(1), 21–34. [https://doi.org/10.1016/0198-0149\(91\)90052-H](https://doi.org/10.1016/0198-0149(91)90052-H)
- Srinivasan, K., McWilliams, J. C., Molemaker, M. J., & Barkan, R. (2019). Submesoscale vortical wakes in the lee of topography. *Journal of Physical Oceanography*, 49(7), 1949–1971. <https://doi.org/10.1175/JPO-D-18-0042.1>
- Stegner, A., & Dritschel, D. G. (2000). A numerical investigation of the stability of isolated shallow water vortices. *Journal of Physical Oceanography*, 30(10), 2562–2573. [https://doi.org/10.1175/1520-0485\(2000\)030<2562:ANIOTS>2.0.CO;2](https://doi.org/10.1175/1520-0485(2000)030<2562:ANIOTS>2.0.CO;2)
- Turner, J. S. (1979). Buoyancy effects in fluids.
- Vic, C., Rouillet, G., Capet, X., Carton, X., Molemaker, M. J., & Gula, J. (2015). Eddy-topography interactions and the fate of the Persian Gulf Outflow. *Journal of Geophysical Research: Oceans*, 120, 6700–6717. <https://doi.org/10.1002/2015JC011033>
- Zhang, Z., Wang, W., & Qiu, B. (2014). Oceanic mass transport by mesoscale eddies. *Science*, 345(6194), 322–324. <https://doi.org/10.1126/science.1252418>

5.3.2 Supplément sur la possibilité de génération de ce tourbillon par interaction tourbillon-ondes de Kelvin sur le bord ouest

Le tourbillon de sousmésos-échelle mesuré au large des côtes Omanaises, est (1) cyclonique et intensifié en profondeur, et (2) vraisemblablement généré par l'interaction d'un anticyclone de mésos-échelle avec la côte Yéménite. Il a des propriétés semblables à celles des tourbillons de sousmésos-échelle générés dans des simulations idéalisées d'interaction d'un tourbillon anticyclonique avec un bord ouest (voir section 5.2.2). Ces tourbillons ont une durée de vie longue et restent cohérents en profondeur durant plusieurs mois. Ainsi, il est probable que l'interaction courant-ondes de Kelvin ait participé à la génération du tourbillon observé. Le faible nombre de données *in situ* en mer d'Arabie dans les mois précédents la campagne PHYSINDIEN, ainsi que la dynamique complexe dans la région ne permet pas de conclure de manière certaine sur ce point. Effectuer une simulation réaliste de la zone possible de génération (de manière similaire à *e.g.* Vic et al. (2015)), proche du cap de Ra's Fartak, serait alors un moyen efficace de déterminer si de nombreuses structures similaires sont générées dans cette région.

5.4 Conclusion sur la dynamique des tourbillons isolés

Dans ce chapitre, nous avons discuté du cycle de vie des tourbillons en mer d'Arabie, en fonction de leur caractéristiques intrinsèques. Pour ce faire, nous avons supposé que les structures de méso-échelle observées en mer d'Arabie sont isolées, et que le cyclone composite calculé dans le chapitre 4 est représentatif des tourbillons intensifiés en surface dans cette région. Ainsi, nous avons pu réaliser des études de stabilité du composite, et déterminer les instabilités pouvant avoir lieu en son sein. Également, nous avons mis en avant l'impact de la polarité et de l'effet- β pour sa stabilité. Ensuite, nous avons étudié le comportement de ce type de structures lorsque celles-ci sont contraintes le long d'une frontière ouest. Enfin, nous avons présenté la mesure d'un tourbillon de sousméso-échelle, et nous avons discuté de ses potentiels causes de génération. Les résultats principaux sont alors ceux-ci :

- Lorsqu'ils sont isolés sur le plan- f , les tourbillons méso-échelle cycloniques typiques de mer d'Arabie se déforment sous l'action d'une instabilité mixte barotrope/barocline.
- Cette déformation est plus lente dans le cas d'anticyclones, et plus rapide sur le plan- β .
- La restabilisation non-linéaire de la structure méso-échelle prévient la destruction à temps long des tourbillons.
- Des instabilités secondaires au sein des tourbillons de méso-échelle sont des sources de génération de structures de sousméso-échelle intensifiées en surface.
- Une asymétrie cyclone/anticyclone est présente lorsque des tourbillons isolés rencontrent une frontière solide à l'ouest des bassins, y compris en mer d'Arabie.
- Des structures profondes de sousméso-échelle sont générées par interaction anticyclone-ondes de Kelvin, prévenant la dérive au nord des anticyclones, et expliquant possiblement les observations de tourbillons cycloniques de sousméso-échelle effectuées durant la campagne PHYSINDIEN 2019.

LES INTERACTIONS ENTRE TOURBILLONS EN MER D'ARABIE

Les tourbillons de méso-échelle en mer d'Arabie ne sont en réalité pas isolés. En particulier, de nombreux tourbillons de même signes sont proches les uns des autres, interagissent, et éventuellement fusionnent. Dans ce chapitre, nous questionnons ce processus de fusion dans le contexte de la mer d'Arabie, et étudions en détail les mécanismes à l'oeuvre dans de tels événements.

6.1 La fusion de tourbillons en mer d'Arabie

Une des propriétés du programme AMEDA, utilisé dans le chapitre 4 pour détecter les tourbillons de méso-échelle, est qu'il peut détecter et répertorier les événements de fusion entre deux tourbillons détectés (Le Vu et al., 2018). Utilisant les mêmes sorties d'AMEDA que présenté dans le chapitre 4, nous avons ainsi pu mesurer le nombre de fusions de tourbillons de méso-échelle qui se sont produites en mer d'Arabie sur la période 2000-2015, voir Fig. 6.1

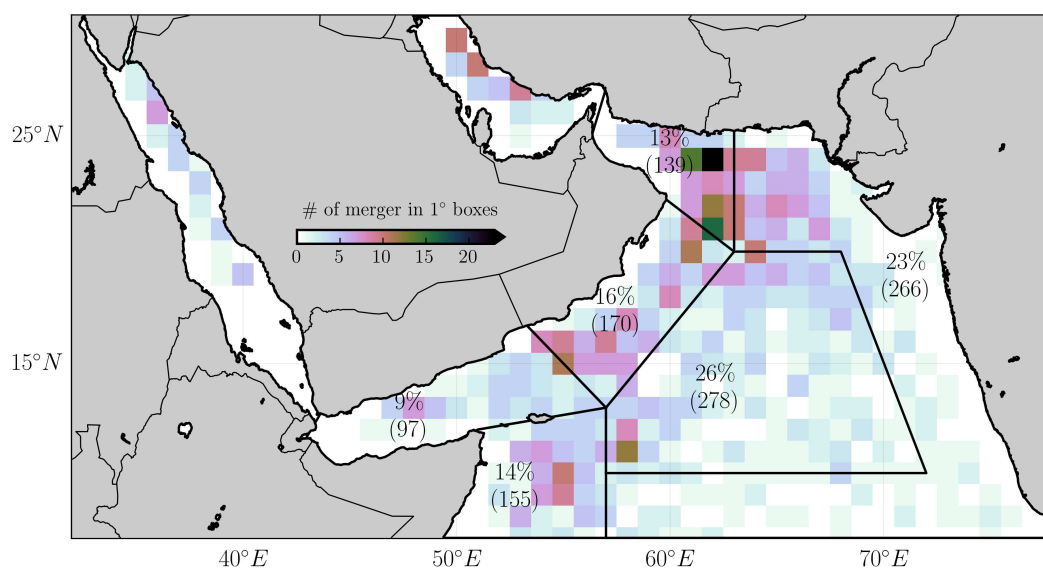


FIGURE 6.1 – Répartition des fusions de tourbillons en mer d'Arabie, détectées par AMEDA dans l'altimétrie sur la période 2000-2015. Un quart des fusions se trouvent dans l'océan ouvert et la moitié le long du bord ouest du bassin (dont 16% proche du talus continental Omanais).

Sur une période de 15 ans, nous détectons 1105 évènements de fusions de tourbillons en mer d'Arabie. Ce chiffre est sous-estimé car la résolution du produit altimétrique ne permet pas d'étudier les structures inférieures à R_D , voir les détails de la détection au chapitre 4. Ainsi, en moyenne, une fusion se produit tous les 5 jours en mer d'Arabie. Les tourbillons étant déterminant pour la répartition des propriétés physiques, chimiques et biologiques dans cette région, il est donc clair que la fusion de tourbillons est primordiale pour la répartition spatiale des masses d'eaux, des écosystèmes et de la quantité de mouvement en mer d'Arabie.

6.2 Les mécanismes de la fusion dans l'océan ouvert

6.2.1 De la mer d'Arabie à l'océan global

Un nombre significatif de fusions (26%, soit 278 événements de fusion, voir Fig. 6.1) survient dans l'ouvert de la mer d'Arabie, *i.e.* loin des côtes et des anomalies topographiques (Fig. 6.1). Ces événements de fusion respectent ainsi les hypothèses effectuées dans de nombreuses études passées, étudiant la dynamique de la fusion de deux tourbillons *isolés* (voir section 2.1.2). Les mécanismes en jeu dans la fusion de tourbillons au centre de la mer d'Arabie sont donc *a priori* bien décrit par ces études, en particulier par la distance critique de fusion de deux tourbillons isolés sur le plan- f . Nous proposons ici de tester la validité des différentes approximations susmentionnées, afin de mettre en avant les processus clés en jeu lors de la fusion de deux tourbillons dans cette région.

La dynamique dans l'ouvert de la mer d'Arabie n'est pas spécifique à cette région. Elle est commune à toute les régions de moyenne latitude dans lesquelles la dynamique est turbulente, et où il n'y a pas de courants intenses (*e.g.* loin des bords ouest des bassins, ou des zones d'upwelling). Nous questionnons ainsi la pertinence des hypothèses effectuées pour discuter de la fusion de deux tourbillons isolés, dans un contexte global, plutôt que régional. Cela permet de tirer des conclusions générales sur la fusion de tourbillons dans l'océan ouvert. Ce travail est conduit à partir de l'analyse des fusions de tourbillons ayant eu lieu dans la période 2000-2005 au centre des cinq bassins océaniques majeurs, et de simulations numériques dont les approximations et paramètres choisis sont cohérents avec la situation dans l'ouvert de la mer d'Arabie.

6.2.2 Est ce que la fusion de tourbillons peut être considérée comme isolée? Article publié dans *Scientific Reports*

Les informations supplémentaires de cette étude sont présentées dans l'appendice B.

OPEN

Oceanic vortex mergers are not isolated but influenced by the β -effect and surrounding eddies

Charly de Marez^{1*}, Xavier Carton¹, Pierre L'Hégaret¹, Thomas Meunier², Alexandre Stegner³, Briac Le Vu³ & Mathieu Morvan¹

Oceanic vortices are ubiquitous in the ocean. They dominate the sub-inertial energy spectrum, and their dynamics is key for the evolution of the water column properties. The merger of two like-signed coherent vortices, which ultimately results in the formation of a larger vortex, provides an efficient mechanism for the lateral mixing of water masses in the ocean. Understanding the conditions of such interaction in the ocean is thus essential. Here, we use a merger detection algorithm to draw a global picture of this process in the ocean. We show that vortex mergers are not isolated, contrary to the hypothesis made in most earlier studies. Paradoxically, the merging distance is well reproduced by isolated vortex merger numerical simulations, but it is imperative to consider both the β -effect and the presence of neighbouring eddies to fully understand the physics of oceanic vortex merger.

Oceanic vortices, named *eddies*, impact biological activities¹, tracer transport², and properties of the water column³. It has become clear that the mesoscale (10–100 km) eddy field, is at least as energetic as the large scale circulation⁴, essential for the air-sea interactions⁴, and thus for the evolution of climate⁵. Eddy-eddy interactions therefore play a central role in the evolution of the ocean/atmosphere physics and biology. In particular, *vortex merger*—the physical process in which two like-signed coherent vortices collapse, ultimately resulting in a larger vortex—is of key importance for the distribution and the transfers of energy across scales in the ocean^{6–11}. Since the 80's, an important effort has been undertaken to understand the physics of oceanic vortex merger, including *in situ*¹², laboratory^{13,14}, and numerical¹⁵ observations, associated with intense theoretical debates^{16–18}. Most fundamental studies addressed the 'isolated vortex merger' problem, omitting the influence of neighbouring eddies, large scale currents, or boundary, topographic, and planetary effects^{19–25}. Efforts to include more physical effects in studies of vortex merger^{26–29} were often impaired by the lack of general observations in the global ocean, or by the complexity of the resulting dynamical system. Despite recent trials³⁰ and pointwise observations^{12,31–33}, a global description of vortex merger in the ocean is lacking.

In this paper, we present an analysis of merging events in the global ocean, using a global 1/12° re-analysis dataset. This study was conducted over a five-year period, in five domains in the middle of each major oceanic basins—these domains *a priori* respect the hypothesis of isolated vortex merger studies: they are far away from the coastlines, topographic features, and strong currents, and are located at mid-latitudes (see Fig. 1). From 5,867 detected merging events, we infer the actual characteristics of mesoscale eddies that merge, and test the isolated vortex merger problem hypotheses. Further, we compare this analysis with the outcome of 1,600 idealized numerical simulations. The latter rely on a 3D primitive equations model, both on the f -plane and on the β -plane, using a realistic open ocean parameterization (e.g. a realistic stratification, and numerical parameters used in regional numerical simulations^{34,35}). To allow for a direct comparison, we use the same merging event detection algorithm in both datasets.

Here, we show that in the five study areas, vortex mergers are not isolated; they are influenced by neighbouring eddies as well as by the β -effect. Paradoxically, the merging process in the ocean is well represented by very simple simulations of Gaussian eddies a thousand meters deep on an f -plane, at least as far as the critical distance of merging is concerned. The necessary inclusion of β -effect for realism leads to a discrepancy with the global analysis: the advection of eddies by planetary Rossby waves weaken the critical distance of merging. Thus, another physical effect is at work in the real ocean: the ubiquitous density of the mesoscale eddy field, which prevent the eddies to drift away during the merger. These findings have important implications for the future understanding of eddy-eddy interactions.

¹Univ. Brest, Laboratoire d'Océanographie Physique et Spatiale (LOPS), Plouzané, France. ²CICESE, Ensenada, B.C., Mexico. ³Laboratoire de Météorologie Dynamique, CNRS Ecole Polytechnique, Palaiseau, France. *email: charly.demarez@univ-brest.fr

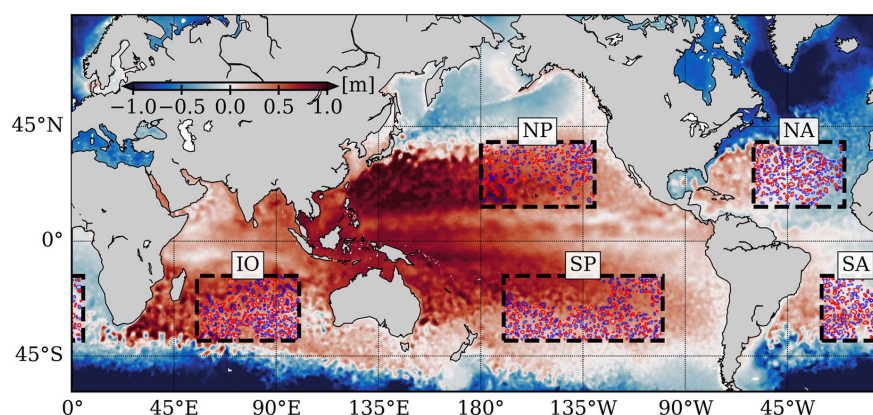


Figure 1. Definition of the five study areas. The color map represents a snapshot of Sea Surface Height on 01/05/2000 from the HYCOM dataset. Eddies detected on this date are presented by the red and blue contours (for cyclonic and anticyclonic eddies respectively). NP, SP, NA, SA, and IO are abbreviations for North Pacific, South Pacific, North Atlantic, South Atlantic, and Indian Ocean.

Results

Vortex merging analysis in the ocean: are interacting vortex pairs isolated from the surrounding? 5,867 merging events were detected, *viz.* 605, 605, 1,797, 937, and 1923 in the NP, SP, NA, SA, and IO areas, respectively (Fig. 1). They were identified and extracted over a five year period, from the 1/12° HYCOM re-analysis dataset (hereafter 'HYCOM dataset', see 'Methods' section for the dataset, the detection algorithm, hereafter AMEDA, and Supplementary Fig. 2A and 9 for an example of merging event detection). The dataset relies on the assimilation of altimetric and *in situ* data in a mesoscale resolving numerical model, ensuring realistic surface fields with a satisfying horizontal resolution. 1,031, 1,037, 2,647, 1,445, and 2,779 different eddies were involved in the detected merging events, out of 4,051, 4,641, 6,079, 4,222, and 6,131 detected eddies (*i.e.* individual trajectories), thus implying a probability of an eddy undergoing a merging event of 25%, 22%, 44%, 34%, and 45% in the NP, SP, NA, SA, and IO areas, respectively. Eddies are thus more prone to merge in the NA and IO areas, because of the proximity of strong currents that generate numerous eddies³⁰, *i.e.* the Gulf Stream and the Antarctic Circumpolar Current. Merging eddies have Rossby and Burger numbers (Ro and Bu , see 'Methods' section) in the ranges $0.03 < Ro < 0.1$ and $0.1 < Bu < 1.5$, with a probability density maximum at $Ro = 0.05$ and $Bu = 0.5$ (Fig. 2B). As $Ro \ll 1$, estimations of the velocities from the geostrophic balance using the Sea Surface Height is accurate³⁶. The upper limit of Bu corresponds to the limit of accurate eddy detection by AMEDA³⁷. Eddies are not frontal ($Ro/Bu \ll 1$), meaning that there is no strong polarity bias in the stability of eddies³⁸. Still, more mergers of anticyclonic eddies (AEs) than cyclonic eddies (CEs) are detected (Fig. 2A), independently of the number of detected eddies. However, results depend on the area considered, with maximum values of 56.4% and 54.6% for AEs merger respectively in the SP and in the SA (Supplementary Figs. 3–7). 60.4% and 54.9% of mergers involve AEs with $Bu < 0.5$ and $0.5 < Bu < 1$ respectively, while the trend is reversed for $Bu > 1$, with 57.3% of mergers for CEs (Supplementary Fig. 8), suggesting that AEs with small Bu are more prone to merging than CEs. Because most of the merging events we detected involved eddies with $Bu < 1$, the global statistics reflect the behavior of eddies at small Bu . The orientation of the eddy pairs shows that a larger proportion of them are oriented meridionally (Fig. 2C). A CEs/AEs asymmetry is seen in the orientation, with more AEs (resp. CEs) with an orientation near 60° (resp. 120°). This indicates that when they merge, AE (resp. CE) pairs are more likely to be orientated Southwest-Northeast (resp. Northwest-Southeast). Note that the standard deviation is large because of the orientation variability observed between the different regions. This pattern has a clearer signature in the southern hemisphere than in the northern hemisphere, in particular in the SA and the IO areas (see Supplementary Figs. 6, 7), where AEs (resp. CEs) propagate northwestward (resp. southwestward)³⁹. However, it would be speculative to attribute this CEs/AEs asymmetry to the β -drift propagation of eddies only, as other processes such as the eddy generation may play a role in the orientation of merging eddies.

These results provide important information to test the validity of usual assumptions used in isolated vortex merger studies. First, the ratio of the Ro of the two merging eddies (Fig. 2D), a proxy of the symmetry of the system, shows that a significant number ($>10\%$) of merging events occur with one eddy having a Rossby number 1.5 times larger than the other eddy. Most of the merging events studied here are nonetheless symmetric, as about 45% of merging events have a Ro ratio lower than 1.2. This may also be related to the resolution of the HYCOM dataset, which does not allow for extreme asymmetric events (*e.g.* with Ro ratio > 2). Second, the Coriolis parameter varies by about 3–5% (Fig. 2E) around eddies: meridional asymmetry is intrinsic to the system. Third, the vorticity variance (Fig. 2F) around eddies is important for a significant number of merging events. For isolated merging events, the latter is zero, because no background flow is present. Thus, merging eddies are not isolated, and the merging process is influenced by other structures located close to the two merging eddies. In particular, other coherent eddies are detected in the periphery of merging eddies (Fig. 2G), with an average of two CEs (resp. AEs)

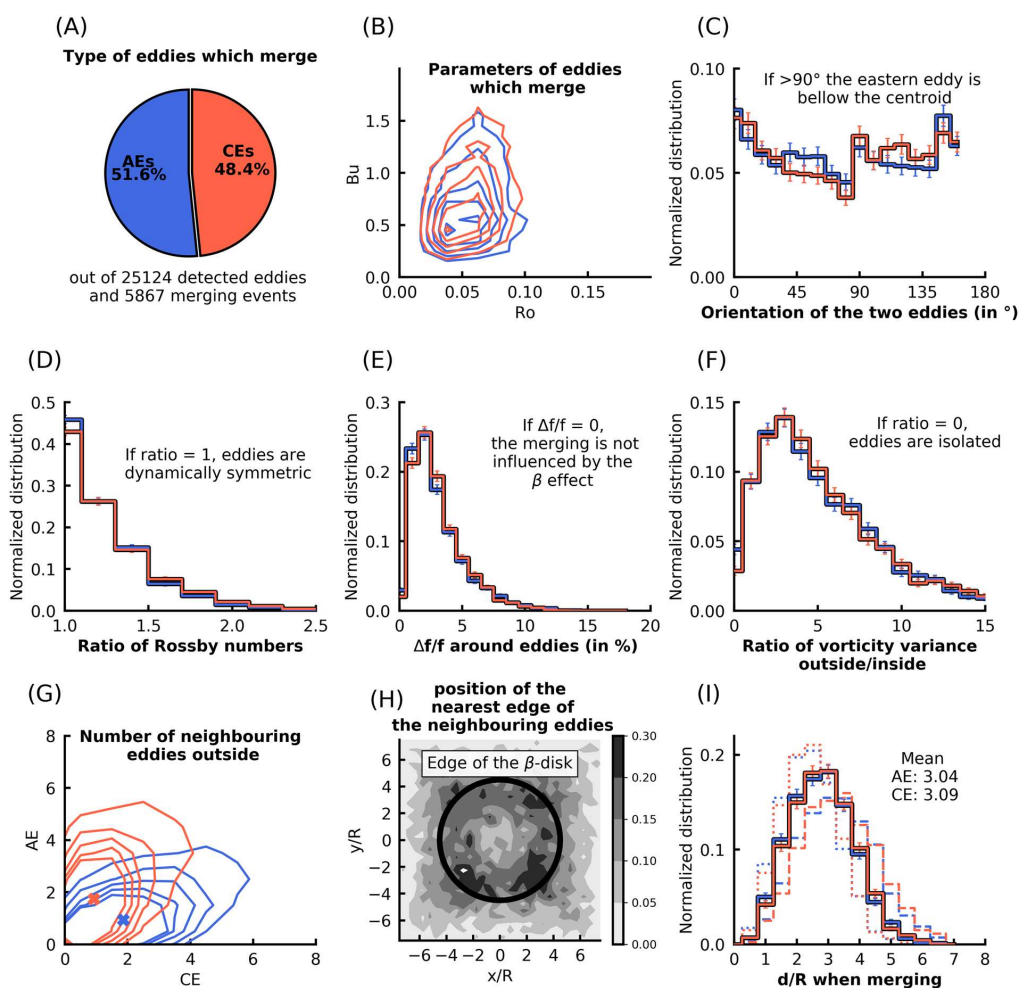


Figure 2. Characteristics of the merging events from the HYCOM dataset. In each panel, blue and red indicate Anticyclonic Eddies (AEs) and Cyclonic Eddies (CEs) respectively. (A) Type of eddies which merge; the distribution is normalized by the number of eddies per type (we take into account the fact that more AEs are detected). (B) Ro and Bu distribution, contours are [1,2,3,4,5] % values of 2D histograms. (C) Normalized distribution of the orientation of merging eddies; a bin reaching 0.2 means that it represents 20% of the total merging events for a given polarity. Errorbars show \pm the standard deviation in each bin using a Monte Carlo Bootstrapping method with 10,000 re-sampling. (D) Same as (C) for the Ro ratio between merging eddies. (E) Same as (C) for the standard deviation of the Coriolis parameter outside eddies, divided by the mean value of Coriolis parameter in the same area —the ‘outside’ is defined as the area inside a circle of radius two times the distance between the merging eddies. (F) Same as (C) for the vorticity variance ratio between the areas outside and inside merging eddies, as defined in Eq. (4) —the ‘inside’ area corresponds to the area defined by the two eddy contours when the merging is detected. (G) Same as (B), for the number of neighbouring eddies detected outside eddies, depending on their polarity. Blue and red crosses indicate the mean number of neighbouring eddies for AEs and CEs respectively: on average, 0.93 (resp. 1.74) AEs, and 1.86 (resp. 0.92) CEs surround merging AEs (resp. CEs). (H) Position of the nearest edges of the neighbouring eddies; the grey scale indicates the value of a 2D histogram, and the black bold circle presents the chosen edge of the β -disk in idealized simulations. (I) Same as (C) for the merging distance $d_m = d/R$, where d is the Euclidean distance between the two eddy centers when they merge, and R is the average of the R values between the first detection of the eddy and the merger; dashed and dotted lines show the distributions of d_m for which R is equal to the mean value of R in each bin, plus or minus the standard deviation of R in this bin. Details about the calculation of quantities in each panel are presented in the ‘Methods’ section.

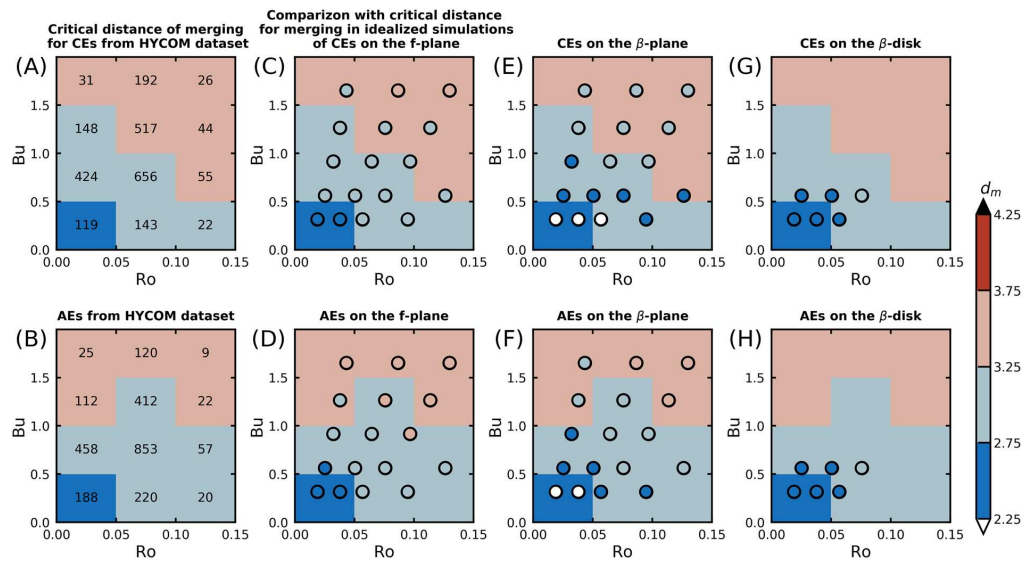


Figure 3. Comparison between the mean distance of merging in the HYCOM dataset, and the maximal initial distance between eddies for which they merge in the idealized simulations. (A) Mean distance of merging d_m for CEs in the HYCOM dataset, depending on Ro and Bu . The numbers of values used to compute averages are indicated for each range of Ro and Bu . (B) Same as (A) for AEs in the HYCOM dataset. (C) Maximum distance of merging d_m^i observed in numerical simulations of CEs with $\alpha = 2$ and $H = 1000$ m on the f -plane (the results are shown by the circle colors). The color background is the same as in (A) to allow a comparison between numerical simulations and the HYCOM dataset analysis. (D) Same as (C) for AEs on the f -plane. (E) Same as (C) for CEs on the β -plane. (F) Same as (C) for AEs on the β -plane. (G) Same as (C) for CEs on the β -disk. (H) Same as (C) for AEs on the β -disk.

detected around merging AEs (resp. CEs). The polarity asymmetry in the number of neighbouring eddies results from the CE/AE asymmetry due to previous merging events (*i.e.* close eddies with the same polarity are more likely to have already merged). Surrounding eddies are close to the merging eddies: their median edge is located at $4.5R$ from the centroid of the interacting pair (Fig. 2H). Merging eddies are thus *constrained* inside a sea of eddies. Note here that AMEDA does not take into account 3-eddy merging events. It thus underestimates the number of merging events, and maybe overestimates the number of like-signed eddies around the two merging eddies. In summary, the usual hypotheses for symmetric, isolated vortex merger —*i.e.* two identical eddies on the f -plane, isolated from the surrounding— are not verified in the HYCOM dataset.

Comparing the merging distance between the global ocean and idealized simulations. In the HYCOM dataset, the average normalized merging distance d_m is of 3.04 for AEs and 3.09 for CEs (Fig. 2I). This distance is obtained on the first day of interaction between the merging eddies, when they start to influence each other (see ‘Methods’ section). It thus reflects the critical distance below which their velocity fields interfere constructively, ultimately causing the collapse of the vortex system. This distance depends on the Ro and Bu of merging eddies (Fig. 3A,B). d_m increases with Ro and Bu , such that $d_m \approx 2.5$ for $Ro < 0.05$ and $Bu < 0.5$, and $d_m \approx 3.5$ for $Ro > 0.1$ and $Bu > 1$. For a given eddy radius (*i.e.* a constant Bu), Ro increases with the maximal swirl velocity of the eddy. As the latter becomes larger, the advective timescale induced by the eddies decreases, causing a quicker collapse of the eddies. This leads to increasing the minimum distance for which eddies can interact and merge, and explains the increase of d_m with Ro . The variations of d_m as a function of Bu are related to the baroclinic component of the flow.

In idealized simulations, merger strongly depends on the Ro and the Bu of eddies at initialization (Figs. 3C–H, see ‘Methods’ section for details about simulations, and Supplementary Figs. 2B,C and 10,11 for example of merging events in these simulations). We compute the maximum initial distance between the two eddies at which merging occurs d_m^i . The latter increases with Ro and Bu , and merging is thus easier for smaller eddies than for large ones. Independently of other parameters, the radial steepness of the velocity profile α and the height of the eddies H have a strong influence on the interaction between eddies (Supplementary Fig. 12). Indeed, the steeper the eddy velocity profile is (or/and thinner it is), the smaller d_m^i is: (1) eddies with smaller α interact with farther structures; (2) as H decreases, the baroclinic modes take over the barotropic mode, therefore decreasing its horizontal influence^{21,22}. On the f -plane, a clear AEs/CEs asymmetry is evident: d_m^i is larger for AEs than for CEs. Using the cyclogeostrophic balance, for a given velocity field, a given pressure anomaly has a larger extent for AEs than for CEs, causing AEs to interact at larger distances.

The β -effect reduces d_m^i , especially for larger eddies. The physical mechanism responsible for the decrease of d_m^i can be described as follows. With the β -effect, meridionally aligned eddies generate a Rossby wave composed of meridionally elongated Sea Surface Height patches with zonally alternating sign (e.g. Supplementary Fig. 2C). This wave creates a southward (resp. northward) velocity east of the two AEs (resp. CE); thus, the southern (resp. northern) eddy moves southward (resp. northward), weakening the merging efficiency. Supplementary Figs. 10, 11 illustrate this phenomenon. The opposite situation would happen if one has considered a situation in the southern hemisphere. Modifying the orientation of the two eddies at initialization (not shown) tends to slightly reduce this effect. However, even when eddies are zonally aligned, an intense shear generated by Rossby waves leads to the stretching of the two eddies along the zonal axis. This also acts in reducing the merging efficiency.

Running simulations with β -effect and a circular wall around the eddies (β -disk simulations, see 'Methods' section), allows to simulate the situation where solitary eddies drift during a long time period³⁹, and are then constrained by neighbouring eddies when they interact—the free-slip wall acts as an image vortex⁴⁰, and prevent the eddies to drift away. In such simulations, merging eddies can exchange more vorticity as the wall prevents them to drift far away. This increases the merging efficiency as well as d_m^i .

The merging distances observed in the HYCOM dataset are reproduced by the idealized simulations on the f -plane: the values of d_m^i match well the observed d_m for all *Ro* and *Bu* studied (in particular for simulations with $H = 1000$ m and $\alpha = 2$, as expected—in the ocean, eddies are mostly Gaussian³⁷, and about 1000 m deep^{41–44}). With the β -effect, if eddies are not constrained by a disk, d_m in the HYCOM dataset is significantly larger than the d_m^i values observed in idealized simulations, especially for small *Bu* and *Ro*. In this parameter range, β -disk simulations with $H = 1000$ m and $\alpha = 2$ are found closer to the measures made in the HYCOM dataset.

Discussion

The hypotheses of 'isolated vortex merger' studies are rarely verified in the global ocean. First, a significant number of merging situations are not symmetric. Some merging events may thus be influenced by 'vortex thinning' events⁴⁵, where the largest eddy causes the smallest one to wrap around it⁴⁶. This supports the view of ref. ⁴⁷, that vortex thinning rather than vortex merger may play a significant role in the inverse energy cascade. Second, the β -effect plays an important role in the merging process. It modifies the shapes and motions of eddies before the merger, as they drift westward instead of co-rotating. Third, opposite-signed coherent structures were found close to most merging eddies. This result together with the findings of ref. ⁴⁸, which showed that isolated eddies are surrounded by opposite-signed coherent structures, shows that the turbulent open ocean is thus closer to a dense 'sea of modons'⁴⁹ rather than pairs of isolated eddies. This is a key result since opposite-sign eddies can couple with any of the merging eddies, thus reducing or increasing their critical distance of interaction, and modifying momentum transfer between them²⁸. After merger, eddies are stabilized by such dipolar couplings. Also, as eddies are surrounded by neighbouring eddies, they can not drift as freely as if they were isolated: the merger is constrained in a finite area. The physical properties of the flow during the merger significantly differ from those observed in isolated vortex merger studies.

Comparison between the critical distance observed in the global ocean and the values found in idealized simulations highlights a paradox with strong implication on the understanding of vortex merger in the global ocean. The critical distances of merging found for f -plane simulations involving 1000 m deep Gaussian eddies are close to the observed distance of merging in the global ocean (for the present range of *Ro* and *Bu*). Furthermore, the mean critical distance of $3.05R$ found in the global ocean is consistent with values found in the literature when considering 3D quasi-geostrophic simulations of two isolated vortices on an f -plane^{21,22}. As merger is influenced by the β -effect, one would expect that considering β -plane simulations would give a better accuracy in the merger distance estimation. We observe the opposite, with a distance of merger significantly lower in β -plane simulations than observed in the ocean. Other mechanisms are thus at work, which tend to increase the critical distance of merging. The results of our simulations suggest that these mechanisms are related to the proximity of neighbouring eddies, which prevent the eddies to drift away—by β -effect—during the merger. Indeed, if we consider that the merger is constrained in a finite area, on the β -plane, the critical distance is found to be closer to the global ocean analysis. Furthermore, in the real ocean, merger may also be impacted by the coupling of one or two of the eddies with opposite-signed companions. Considering all the actual parameters in the ocean, the vortex merger is thus best described by *non*-isolated idealized situations. This paradox shows that focusing on the critical distance of merging to describe merging events in the ocean may lead to a misvaluation of the physical mechanisms involved in the merger.

The numerous merger we studied, together with previous studies^{6–11}, suggests that the merger of large mesoscale eddies are key for the transfer of heat and energy to large scales, through the mixing of water masses in surface and sub-surface. Recent studies suggested that, in the ocean, the number of vortex splitting is comparable to that of the vortex merger³⁰. This other kind of events should therefore play an important role in the ocean energy budget as well, opposite to the role of the vortex merger, as it transfers heat and energy toward small scales. A similar study as the one presented here could thus be conducted, in order to describe the modalities of the splitting process in the global ocean. In particular, the AMEDA algorithm used here is suitable for such a task, as it allows to get the historic of splitting events that eddies went through, exactly similarly as for the merger³⁷.

To accurately describe the vortex splitting, as well as to extend the present study to smaller vortices (i.e. for larger *Ro* and *Bu*), a higher-resolution dataset should be used. Indeed, with a higher resolution, smaller vortices are detected. The study of smaller structures could allow to describe the interaction regimes between eddies at horizontal scales below the mesoscale. Using a regional model in several regions of the ocean, rather than a global one, could ensure to have a correct representation of both the mesoscale and the submesoscale dynamics, and therefore an unprecedented description of the vortex-vortex interactions.

Methods

Global ocean analysis, and the definition of the five study areas. We use the Sea Surface Height and the surface horizontal velocities in the period 01/01/2000 to 31/12/2004, in the five study areas shown in Fig. 1, from the GOFS 3.1, 41-layer HYCOM+NCODA Global 1/12° re-analysis. The product is supplied every three hours on a 0.08° resolution Mercator grid between 40°S and 40°N. For our study, a five-year period is sufficient to obtain robust statistics. We consider one output per day for our study, to decrease the computational time.

This HYCOM re-analysis data have been intensively validated⁵⁰ and used^{51–54} in several contexts during the past ten years. The global HYCOM re-analysis uses the Navy Coupled Ocean Data Assimilation (NCODA) system^{55,56} for data assimilation. NCODA uses the 24-hour HYCOM forecast⁵⁷ as a first guess in a 3D variational scheme and assimilates available satellite altimeter observations, satellite, and *in situ* sea surface temperature as well as *in situ* vertical temperature and salinity profiles from XBTs, Argo floats and moored buoys. Surface information is projected downward into the water column using Improved Synthetic Ocean Profiles⁵⁸.

We focus on areas respecting the hypothesis of isolated vortex merger studies. First, areas are far away from the coastlines, topographic features, and strong currents (to avoid coastal, topographic, or current/eddy interactions). We also exclude areas close to islands —this explains blank areas *e.g.* in the northern part of the SP area around Marquesas Islands. Second, the five areas are located at mid-latitudes (to avoid equatorial dynamics and ice related phenomena). The mean values of the Coriolis frequency f , of the depth of the seafloor, and of the first baroclinic Rossby radius of deformation $R_D \sim 45$ km⁵⁹ are similar in the five areas. Also, as revealed by Argo floats⁶⁰, the mean annual stratification (represented by the Brunt-Väisälä frequency) of the five areas are similar (Supplementary Fig. 1). The characteristics of merging events vary little between the study areas (Supplementary Figs. 3–7). We thus mostly consider statistics over all areas. Note that the five study areas are similar to the one discussed in ref. 48.

Numerical simulations of vortex merger. *Numerical setup.* We perform idealized simulations of isolated vortex merger using the Coastal and Regional Ocean COmmunity model (CROCO)⁶¹. This model solves the hydrostatic primitive equations for the velocity, temperature, and salinity, using a full equation of state for seawater⁶². The simulations performed integrate the primitive equations for 50 days. The time step is 900 s. The horizontal domain size is 1200 × 1200 km. The bottom is flat, at 3000 m depth. The boundaries of the domain do not affect the dynamics of the eddies that are surface intensified and initially set at the center of the domain. The horizontal resolution is 5 km. 32 vertical levels are chosen, stretched at the surface. The coarse resolution is consciously chosen since our aim is to perform numerous simulations to cover up as well as possible the parameters space. Simulations performed on the f -plane use Coriolis parameter $f_0 = 6.6 \times 10^{-5} \text{ s}^{-1}$; simulations on the β -plane use a linearly varying Coriolis parameter $f = f_0 + \beta y$, with y the meridional coordinate and $\beta = 2 \times 10^{-11} \text{ m}^{-1} \text{ s}^{-1}$. f_0 and β are the mean value of the 5 study areas, and are representative of the northern hemisphere mid-latitude dynamics.

The numerical settings are similar to previous simulations performed in an idealized context^{63,64}: horizontal advection terms for tracers and momentum are discretized with fifth-order upwind advection schemes (UP5); the explicit horizontal viscosity and diffusivity are set to zero, since the UP5 scheme damps dispersive errors; the vertical advection is discretized with a fourth-order centered parabolic spline reconstruction (Splines scheme). Further discussion about these parameterizations can be found in⁶³ or⁶⁵. No vertical diffusion is added; this allows to avoid numerically parameterized diabatic effects, which can affect the conservation of Potential Vorticity⁶⁶.

Simulations initialization. We initialize an analytical background stratification $N(z)$, which fits the average ambient stratification in the five selected study areas (Supplementary Fig. 1):

$$N(z) = N_0 + N_1 e^{z/z_h}, \quad (1)$$

with $z < 0$ the vertical coordinate, $N_1 = 9 \times 10^{-3} \text{ s}^{-1}$, $z_h = 150$ m, and $N_0 = 7 \times 10^{-3} \text{ s}^{-1}$. Integrating this stratification from the surface (where $\rho(z=0) = 1030 \text{ kg m}^{-3}$), gives the ambient density background $\rho(z)$; the temperature background $T(z)$ is obtained by inverting the TEOS-10 equation of state for seawater⁶⁷ and assuming a constant salinity background $S(z) = 35$ psu. The model is initialized with these temperature and salinity background profiles.

We initialize surface intensified eddies of given relative vorticity profile. For each eddy, we set the initial profile of surface vorticity:

$$\omega(r) = \pm \omega_0 e^{-\left(\frac{r}{R}\right)^\alpha}, \quad (2)$$

with the sign depending on the eddy polarity, $r = \sqrt{(x - x_0)^2 + (y - y_0)^2}$ the radial coordinate referenced at the center of the eddy (x_0, y_0) , and α the steepness parameter. $\omega_0 = V/R$, with V the maximal azimuthal velocity at a distance R from the center of the eddy. The surface azimuthal velocity of the eddy is computed using $v_\theta(r, 0) = \frac{1}{r} \int dr \omega r$. By definition, this velocity vanishes slowly with r , contrary to *e.g.* Rankine vortices. To avoid the presence of spurious velocity at the edges of the domain, we apply a Hanning window on v_θ to make it smoothly tend to zero at $r > 3R$. The horizontal velocity decreases at depth such that $v_\theta(x, y, z) = v_\theta(x, y, 0) e^{-z/H}$, thus defining the height of the eddy H . The horizontal velocity field of the eddy (u, v) is obtained by projecting v_θ into Cartesian coordinates. The pressure anomaly field $P(x, y, z)$ corresponding to this velocity field is computed via the Gradient Wind equation:

$$2J(u, v) + f(\partial_x v - \partial_y u) = \frac{1}{\rho} \Delta_h P', \quad (3)$$

with $J(u, v) = \partial_x u \partial_y v - \partial_y u \partial_x v$ the Jacobian operator, and Δ_h the horizontal Laplacian operator. From P' we determine the density and the temperature anomalies of the eddy. These anomalies are computed for the two eddies, at positions $x_0 = x_c$, and $y_0 = y_c \pm d/2$, thus defining the initial distance between the eddies d . x_c and y_c are the coordinates of the center of the domain. Note that the eddies are stable during the whole simulation.

This initialization uses only few parameters for eddies: α defines the steepness of the velocity profile ($\alpha = 2$ corresponding to a Gaussian vortex); H is related to the baroclinicity of the eddy. For our study, we vary the initial parameters as $R = [35, 40, 47, 60, 80]$ km, $V = [0.1, 0.2, 0.3, 0.5, 0.7]$ m s⁻¹, $\alpha = [2, 4]$, and $H = [500, 1000]$ m, for both cyclonic and anticyclonic eddies. For each set of parameters, we also vary the initial distance between the two eddies in the range $d/R = [2.5, 3.0, 3.5, 4.0]$, and we run simulations on both the f -plane and the β -plane. Hence, we are able to know the maximum value of d/R (with an accuracy of ± 0.25) for which eddies with given initial parameters merge (this value is noted d_m^i in the text). We scan 400 different sets of parameters, and a total of 1600 simulations. We downgrade the resolution of the outputs to 0.08°, and we consider one output per day to have a dataset consistent with the HYCOM outputs.

To study the vortex merger in a context where eddies are not isolated but packed, surrounded by neighbouring eddies, we perform a few simulations with a boundary around the two main eddies. The boundary is a circular wall with a radius of $4.5R$ from the center of the domain. These simulations are referred to as β -disk simulations in the text. The radius of the disk is chosen as the median distance between the merging eddies centroid and the closest neighbouring eddies edge (see Fig. 2H). A free-slip condition is chosen such as no frictional effect are induced by the boundary.

Our definition of vortex merging events with AMEDA. To identify the merging events both in the HYCOM dataset and in idealized simulations, the Angular Momentum Eddy Detection and tracking Algorithm (AMEDA³⁷) is used. One of the benefits of AMEDA is that it does not depend on arbitrary thresholding, which would require a fine-tuning of geometrical parameters. Also, the algorithm is robust with respect to the grid resolution and can thus be applied to a wide variety of velocity fields (experimental, numerical, altimetry...). This algorithm has been used and validated in previous studies in the past few years^{36,37,44,68}, see also an example of application of AMEDA in <https://www1.lmd.polytechnique.fr/dyned/>. To detect eddies, we use the Sea Surface Height, to avoid false detections due to mixed-layer related phenomena. Note that considering only the Sea Surface Height may underestimate the velocity of detected eddies since the algorithm only takes into account the geostrophic part of the velocity field. A full description of the algorithm is presented in Fig. 1 and Fig. 13 of³⁷. In particular, the detection of merging works as follows: the algorithm identifies the couples of eddy centers that are encompassed by a closed streamline (*i.e.* a shared contour), and it checks if one of the two eddy trajectories ends after the interaction period. If these two conditions are met, the merging event is counted and one can access the characteristics of the two eddies when merging occurs.

This method provides the characteristics of each detected eddy from its generation (or first detection) to the last time it was detected (either its death due to destabilization or interaction with broader scale structures (topography, currents...), or until it merges with another eddy): the position of the eddy center, its shape, its polarity, its radius R (defined as the mean radius of the maximum velocity contour), the mean maximum velocity along this contour V , and the ID of eddies that would have merged with it. Example of merging events are shown for the HYCOM dataset, an f -plane simulation, and a β -plane simulation in Supplementary Figs. 2A–C respectively.

The definition of merger is the same for both the HYCOM dataset and the idealized simulations. As discussed in previous studies^{21,25}, defining whether merging occurred may be tricky, mainly for three reasons. First, they can rotate around each other and exchange momentum, but keep two vorticity maxima. The distinction between close co-rotating eddies and a single eddy resulting from the merger can thus be arduous. Second, in the case of Gaussian eddies, two co-rotating eddies will always merge after an infinite period of time. Third, several types of regimes can be observed when co-rotating vortex pairs interact: elastic interaction, complete merger, partial merger, partial straining out, and complete straining out^{31,46,69,70}. For this study, we abstain from these ambiguities by considering that merging occurred if AMEDA detected a merging event during the lifetime of detected eddies. We thus only differentiate a merging event *versus* no merging event, similarly as ref. ²³. In the case of partial merger, the detection of the merger will depend on the merger efficiency. Indeed, as this one increases, the smallest eddy is too small to be detected, and AMEDA indicates a merging event. We do this in both HYCOM dataset and in idealized simulations, thus giving a consistent definition of merging in the two cases. In the case of the idealized simulations, if eddies have not merged during the first 50 days of simulation, they are considered as independent. This duration has been chosen knowing that the median lifetime of eddies before merging in the HYCOM dataset is 40 days. Note that in the HYCOM dataset, to be sure that we consider merging events of two stable vortices, we only consider eddies with a lifetime larger than 10 days.

Common definitions: dimensionless numbers and distance of merging. The definitions of R and V in both the initialization of idealized simulations, and AMEDA detections in the HYCOM dataset are consistent. From R and V , one can compute the Rossby and Burger numbers of the merging eddies. They are respectively defined as $Ro = V/(f_0 R)$ and $Bu = (R_D/R)^2$. Ro is a proxy of the surface intensity of the dynamic core¹; Bu indicates the importance of stratification against rotation. The values of R and V chosen for the initialization of the idealized simulations give a range of Rossby numbers varying between $Ro = 0.019$ and $Ro = 0.3$, and Burger numbers between $Bu = 0.32$ and $Bu = 1.65$. This covers the parameter space of eddies which merge in the HYCOM dataset (see Fig. 2B). Note that for the study of eddies detected in the HYCOM dataset, R is in fact the average of the R values between the first detection of the eddy and the merger. This average is done because the radius of eddies before the merging may vary substantially due to the strong interactions between eddies (see *e.g.* Supplementary Fig. 2). To compute Bu for each detected eddy in the HYCOM dataset, we interpolate the value of R_D from the ref. ⁵⁹'s global estimation at the position of the detected eddy.

The normalized distance between eddies when they merge in the HYCOM dataset d_m is defined as the Euclidean distance between the two eddy centers (Fig. 2I) when AMEDA detects the merger (on the first day of interaction between the two merging eddies). It is normalized by the mean radius of the two eddies. Since the two radii may differ, and because their value is impacted by the merging events, d_m is subject to variations. Thus, we present also in Fig. 2I the distributions of d_m , for which R is equal to the mean value of R in each bin, plus or minus the standard deviation of R in this bin. They are respectively the dotted and the dashed step lines. d_m is defined such as it can be compared with the maximum initial distance between eddies, for which they are observed to merge in idealized simulations d_m^i (for a given set of parameters).

Other quantities used to describe merging events in the HYCOM dataset. From the eddy characteristics extracted by AMEDA in the HYCOM dataset, we compute quantities to describe the merging events occurring in the global ocean (Fig. 2). In the following we denote by \bullet_1 and \bullet_2 the quantities corresponding to the two eddies implied in a specific merging event.

We compute the ratio of the Rossby numbers for each pair of eddies (Fig. 2D) as $\max(R_{01}, R_{02})/\min(R_{01}, R_{02})$. Thus, for each pair, this ratio is always greater than 1, with 1 corresponding to eddies with equal Rossby numbers.

The orientation of the two eddies with respect to the meridional direction (Fig. 2) is computed from the positions of the two eddies on a Mercator projection. The orientation is computed modulo 180° so that the angle does not depend on which eddy is east or west of the system.

The other quantities described hereafter are computed in two particular domains around eddies. These two domains are specified in the text and in Fig. 2F,G as 'inside' and 'outside'. The 'inside' area corresponds to the area defined by the two eddy contours when the merging is detected, hereafter \mathcal{C}_1 and \mathcal{C}_2 (see red bold contours in Supplementary Fig. 2A). The 'outside' is defined as the area inside a circle of radius two times the distance between the merging eddies, hereafter \mathcal{D} (see black thin line in Supplementary Fig. 2A), from which we subtract the inside area. With these definitions of areas we compute the ratio of vorticity variance (Fig. 2F) as:

$$\frac{\int_{\mathcal{D}} dx dy \omega_s^2(x, y) - \int_{\mathcal{C}_1 + \mathcal{C}_2} dx dy \omega_s^2(x, y)}{\int_{\mathcal{C}_1 + \mathcal{C}_2} dx dy \omega_s^2(x, y)}, \quad (4)$$

with $\omega_s(x, y) = \partial_x v - \partial_y u$ the relative vorticity at the surface. This quantity thus describes whether the environment of the two merging eddies is turbulent or not. To be more specific about this point, we also count the number of neighbouring eddies detected by AMEDA for which the center is located in the outside area (Fig. 2G). The distance between the centroid of the merging eddies and nearest edge of neighbouring eddies is computed (Fig. 2H). For each neighbouring eddy, it is defined as the distance between the centroid of the merging eddies and the center of the neighbour, from which we subtract the radius of the neighbour. As this distance depends on the radius of merging eddies, it is normalized by R .

Also, we compute the variation of the Coriolis frequency $\Delta f/f$ around eddies (Fig. 2E) by computing the standard deviation of $f(x, y)$ inside the \mathcal{D} contour, divided by the mean value of $f(x, y)$ in the same area.

Received: 30 October 2019; Accepted: 16 January 2020;

Published online: 19 February 2020

References

- Chelton, D. B., Gaube, P., Schlax, M. G., Early, J. J. & Samelson, R. M. The Influence of Nonlinear Mesoscale Eddies on Near-Surface Oceanic Chlorophyll. *Science* **334**, 328–332. <https://doi.org/10.1126/science.1208897> (2011).
- Zhang, Z., Wang, W. & Qiu, B. Oceanic mass transport by mesoscale eddies. *Science* **345**, 322–324. <https://doi.org/10.1126/science.1252418> (2014).
- Dong, C., Mc Williams, J. C., Liu, Y. & Chen, D. Global heat and salt transports by eddy movement. *Nature Communications*, **5**, <https://doi.org/10.1038/ncomms4294> (2014).
- Small, R. *et al.* Air-sea interaction over ocean fronts and eddies. *Dynamics of Atmospheres and Oceans* **45**, 274–319. <https://doi.org/10.1016/j.dynatmoce.2008.01.001> (2008).
- Palter, J. B. The Role of the Gulf Stream in European Climate. *Annual Review of Marine Science* **7**, 113–137. <https://doi.org/10.1146/annurev-marine-010814-015656> (2015).
- Carnevale, G. F., Mc Williams, J. C., Weiss, J. B. & Young, W. R. Evolution of vortex statistics in two-dimensional turbulence. *Physical Review Letters* **66**, 2735–2737. <https://doi.org/10.1103/PhysRevLett.66.2735> (1991).
- Weiss, J. B. & Mc Williams, J. C. Temporal scaling behavior of decaying two-dimensional turbulence. *Physics of Fluids A: Fluid Dynamics* **5**, 608–621. <https://doi.org/10.1063/1.858647> (1993).
- Mc Williams, J. C., Weiss, J. B. & Yavneh, I. The vortices of homogeneous geostrophic turbulence. *Journal of Fluid Mechanics* **401**, 1–26. <https://doi.org/10.1017/S0022112099006382> (1999).
- Kraichnan, R. H. & Montgomery, D. Two-dimensional turbulence. *Reports on Progress in Physics* **43**, 547. [10.1088%2F0034-4885%2F43%2F5%2F001](https://doi.org/10.1088%2F0034-4885%2F43%2F5%2F001). (1980).
- Jiménez, J., Moffatt, H. K. & Vasco, C. The structure of the vortices in freely decaying two-dimensional turbulence. *Journal of Fluid Mechanics* **313**, 209–222. <https://doi.org/10.1017/S0022112096002182> (1996).
- Burgess, B. H., Dritschel, D. G. & Scott, R. K. Vortex scaling ranges in two-dimensional turbulence. *Physics of Fluids* **29**, 111104. <https://doi.org/10.1063/1.4993144> (2017).
- Cresswell, G. R. The Coalescence of Two East Australian Current Warm-Core Eddies. *Science*, **215**, 161–164. <https://doi.org/10.1126/science.215.4529.161> (1982).
- Griffiths, R. W. & Hopfinger, E. J. Coalescing of geostrophic vortices. *Journal of Fluid Mechanics* **178**, 73–97. <https://doi.org/10.1017/S0022112087001125> (1987).
- Nof, D. & Simon, L. M. Laboratory Experiments on the Merging of Nonlinear Anticyclonic Eddies *Journal of Physical Oceanography* **17** 343–357 [https://doi.org/10.1175/1520-0485\(1987\)017<0343:LEOTMO>2.0.CO;2](https://doi.org/10.1175/1520-0485(1987)017<0343:LEOTMO>2.0.CO;2) (1987).

15. Mc Williams, J. C. The emergence of isolated coherent vortices in turbulent flow. *Journal of Fluid Mechanics* **146**, 21–43, <https://doi.org/10.1017/S0022112084001750> (1984).
16. Gill, A. & Griffiths, R. Why should two anticyclonic eddies merge. *Ocean Modelling* **41**, 501–518 (1981).
17. Nof, D. The Fusion of Isolated Nonlinear Eddies. *Journal of Physical Oceanography*, **18**, 887–905, [https://doi.org/10.1175/1520-0485\(1988\)351018<0887:TFOINE>2.0.CO;2](https://doi.org/10.1175/1520-0485(1988)351018<0887:TFOINE>2.0.CO;2) (1988).
18. Cushman-Roisin, B. On the Role of Filamentation in the Merging of Anticyclonic Lenses. *Journal of Physical Oceanography*, **19**, 253–258, [https://doi.org/10.1175/1520-0485\(1989\)019<0253:OTROFI>2.0.CO;2](https://doi.org/10.1175/1520-0485(1989)019<0253:OTROFI>2.0.CO;2) (1989).
19. Overman, E. A. Evolution and merger of isolated vortex structures. *Physics of Fluids* **25**, 1297, <https://doi.org/10.1063/1.863907> (1982).
20. Polvani, L. M., Zabusky, N. J. & Flierl, G. R. Two-layer geostrophic vortex dynamics. Part 1. Upper-layer V-states and merger. *Journal of Fluid Mechanics* **205**, 215, <https://doi.org/10.1017/S0022112089002016> (1989).
21. von Hardenberg, J., Mc Williams, J. C., Provenzale, A., Shchepetkin, A. & Weiss, J. B. Vortex merging in quasi-geostrophic flows. *Journal of Fluid Mechanics* **412**, 331–353, <https://doi.org/10.1017/S0022112000008442> (2000).
22. Dritschel, D. G. Vortex merger in rotating stratified flows. *Journal of Fluid Mechanics* **455**, 83–101, <https://doi.org/10.1017/S0022112001007364> (2002).
23. Reinaud, J. N. & Dritschel, D. G. The critical merger distance between two co-rotating quasi-geostrophic vortices. *Journal of Fluid Mechanics* **522**, 357–381, <https://doi.org/10.1017/S0022112004002022> (2005).
24. Carton, X., Ciani, D., Verron, J., Reinaud, J. & Sokolovskiy, M. Vortex merger in surface quasi-geostrophy. *Geophysical & Astrophysical Fluid Dynamics* **110**, 1–22, <https://doi.org/10.1080/03091929.2015.1120865> (2016).
25. Ciani, D., Carton, X. & Verron, J. On the merger of subsurface isolated vortices. *Geophysical & Astrophysical Fluid Dynamics* **110**, 23–49, <https://doi.org/10.1080/03091929.2015.1135430> (2016).
26. Carton, X. Hydrodynamical modeling of Oceanic Vortices. *Surveys in Geophysics* **22**, 179–263, <https://doi.org/10.1023/A:1013779219578> (2001).
27. Perrot, X. & Carton, X. 2d vortex interaction in a non-uniform flow. *Theoretical and Computational Fluid Dynamics* **24**, 95–100, <https://doi.org/10.1007/s00162-009-0127-4> (2010).
28. Rodríguez-Marroyo, R., Viúdez, A. & Ruiz, S. Vortex Merger in Oceanic Tripoles. *Journal of Physical Oceanography* **41**, 1239–1251, <https://doi.org/10.1175/2011JPO4582.1> (2011).
29. de Marez, C., Carton, X., Morvan, M. & Reinaud, J. The Interaction of Two Surface Vortices Near a Topographic Slope in a Stratified Ocean. *Fluids* **2**, 57, <https://doi.org/10.3390/fluids2040057> (2017).
30. Cui, W., Wang, W., Zhang, J. & Yang, J. Multicore structures and the splitting and merging of eddies in global oceans from satellite altimeter data. *Ocean Science* **15**, 413–430, <https://doi.org/10.5194/os-15-413-2019> (2019).
31. Yasuda, I. Geostrophic Vortex Merger and Streamer Development in the Ocean with Special Reference to the Merger of Kuroshio Warm Core Rings. *Journal of Physical Oceanography*, **25**, 979–996, [https://doi.org/10.1175/1520-0485\(1995\)025<0979:GVMA SD>2.0.379.CO;2](https://doi.org/10.1175/1520-0485(1995)025<0979:GVMA SD>2.0.379.CO;2) (1995).
32. Schultz Tokos, K. L., Hinrichsen, H.-H. & Zenk, W. Merging and Migration of Two Meddies. *Journal of Physical Oceanography*, **24**, 2129–2141, [https://doi.org/10.1175/1520-0485\(1994\)024<2129:MAMOTM>2.0.CO;2](https://doi.org/10.1175/1520-0485(1994)024<2129:MAMOTM>2.0.CO;2) (1994).
33. Carton, X., Daniault, N., Alves, J., Cherubin, L. & Ambar, I. Meddy dynamics and interaction with neighboring eddies southwest of Portugal: Observations and modeling. *Journal of Geophysical Research*, **115**, <https://doi.org/10.1029/2009JC005646> (2010).
34. Gula, J., Molemaker, M. J. & Mc Williams, J. C. Gulf Stream Dynamics along the Southeastern U.S. Seaboard. *Journal of Physical Oceanography* **45**, 690–715, <https://doi.org/10.1175/JPO-D-14-0154.1> (2015).
35. Gula, J., Molemaker, M. J. & Mc Williams, J. C. Topographic generation of submesoscale centrifugal instability and energy dissipation. *Nature Communications*, **7**, <https://doi.org/10.1038/ncomms12811> (2016).
36. Ioannou, A., Stegner, A., Le Vu, B., Taupier-Letage, I. & Speich, S. Dynamical Evolution of Intense Ierapetra Eddies on a 22 Year Long Period. *Journal of Geophysical Research: Oceans* **122**, 9276–9298, <https://doi.org/10.1002/2017JC013158> (2017).
37. Le Vu, B., Stegner, A. & Arsouze, T. Angular Momentum Eddy Detection and Tracking Algorithm (AMEDA) and Its Application to Coastal Eddy Formation. *Journal of Atmospheric and Oceanic Technology* **35**, 739–762, <https://doi.org/10.1175/JTECH-D-17-0010.1> (2018).
38. Stegner, A. & Dritschel, D. G. A Numerical Investigation of the Stability of Isolated Shallow Water Vortices. *Journal of Physical Oceanography* **30**, 2562–2573, [https://doi.org/10.1175/1520-0485\(2000\)030<2562:ANIOTS>2.0.CO;2](https://doi.org/10.1175/1520-0485(2000)030<2562:ANIOTS>2.0.CO;2) (2000).
39. Chelton, D. B., Schlax, M. G., Samelson, R. M. & de Szoeke, R. A. Global observations of large oceanic eddies: GLOBAL OBSERVATIONS OF OCEANIC EDDIES. *Geophysical Research Letters* **34**, <https://doi.org/10.1029/2007GL030812> (2007).
40. Shi, C. & Nof, D. The Destruction of Lenses and Generation of Wodons. *Journal of Physical Oceanography*, **24**, 1120–1136, [https://doi.org/10.1175/1520-0485\(1994\)024<1120:TDOLAG>2.0.CO;2](https://doi.org/10.1175/1520-0485(1994)024<1120:TDOLAG>2.0.CO;2) (1994).
41. Chaigneau, A., Le Texier, M., Eldin, G., Grados, C. & Pizarro, O. Vertical structure of mesoscale eddies in the eastern South Pacific Ocean: A composite analysis from altimetry and Argo profiling floats. *Journal of Geophysical Research*, **116**, <https://doi.org/10.1029/2011JC007134> (2011).
42. Pegliasco, C., Chaigneau, A. & Morrow, R. Main eddy vertical structures observed in the four major Eastern Boundary Upwelling Systems. *Journal of Geophysical Research: Oceans* **120**, 6008–6033, <https://doi.org/10.1002/2015JC010950> (2015).
43. Keppler, L. et al. Observed Characteristics and Vertical Structure of Mesoscale Eddies in the Southwest Tropical Pacific. *Journal of Geophysical Research: Oceans* **123**, 2731–2756, <https://doi.org/10.1002/2017JC013712> (2018).
44. de Marez, C., L'Hégaret, P., Morvan, M. & Carton, X. On the 3D structure of eddies in the Arabian Sea. *Deep Sea Research Part I: Oceanographic Research Papers* <https://doi.org/10.1016/j.dsr.2019.06.003>.
45. Sutyryn, G. G. On vortex intensification due to stretching out of weak satellites. *Physics of Fluids*, **31**, 075103, <https://doi.org/10.1063/1.5098068> (2019).
46. Dritschel, D. G. & Waugh, D. W. Quantification of the inelastic interaction of unequal vortices in two-dimensional vortex dynamics. *Physics of Fluids A: Fluid Dynamics* **4**, 1737–1744, <https://doi.org/10.1063/1.858394> (1992).
47. Xiao, Z., Wan, M., Chen, S. & Eyink, G. L. Physical mechanism of the inverse energy cascade of two-dimensional turbulence: a numerical investigation. *Journal of Fluid Mechanics* **619**, 1–44, <https://doi.org/10.1017/S0022112008004266> (2009).
48. Amores, A., Monserrat, S., Melnichenko, O. & Melnichenko, N. On the shape of sea level anomaly signal on periphery of mesoscale ocean eddies. *Geophysical Research Letters* **44**, 6926–6932, <https://doi.org/10.1002/2017GL037978> (2017).
49. Stern, M. Minimal properties of planetary eddies. *Journal of Marine Research* **33**, 1–13 (1975).
50. Metzger, E. et al. Global ocean forecast system 3.1 validation test. Tech. Rep., Naval research lab stennis detachment stennis space center ms stennis space center united states (2017).
51. Metzger, E. J. et al. US Navy Operational Global Ocean and Arctic Ice Prediction Systems. *Oceanography* **27**, 32–43, <https://doi.org/10.5670/oceanog.2014.66> (2014).
52. Yu, Z. et al. Seasonal cycle of volume transport through Kerama Gap revealed by a 20-year global HYbrid Coordinate Ocean Model reanalysis. *Ocean Modelling* **96**, 203–213, <https://doi.org/10.1016/j.ocemod.2015.10.012> (2015).
53. Thoppil, P. G., Metzger, E. J., Hurlburt, H. E. & Smedstad, O. The current system east of the Ryukyu Islands as revealed by a global ocean reanalysis. *Progress in Oceanography* **141**, 239–258, <https://doi.org/10.1016/j.poccean.2015.12.013> (2016).
54. Shinoda, T., Zamudio, L., Guo, Y., Metzger, E. J. & Fairall, C. W. Ocean variability and air-sea fluxes produced by atmospheric rivers. *Scientific Reports*, **9**, <https://doi.org/10.1038/s41598-019-38562-2> (2019).

55. Cummings, J. A. Operational multivariate ocean data assimilation. *Quarterly Journal of the Royal Meteorological Society* **131**, 3583–3604, <https://doi.org/10.1256/qj.05.105> (2005).
56. Cummings, J. A. & Smedstad, O. M. Variational Data Assimilation for the Global Ocean. In *Data Assimilation for Atmospheric, Oceanic and Hydrologic Applications vol.II*, 303–343, <https://doi.org/10.1007/978-3-642-35088-7-13> (Springer Berlin Heidelberg, 2013).
57. Bleck, R. An oceanic general circulation model framed in hybrid isopycnic–Cartesian coordinates. *Ocean Modelling* **4**, 55–88, [https://doi.org/10.1016/S1463-5003\(01\)00012-9](https://doi.org/10.1016/S1463-5003(01)00012-9) (2002).
58. Helber, R., Carnes, M., Townsend, T., Barron, C. & Dastugue, J. Validation test report for the improved synthetic ocean profile (ISOP) system, part I: Synthetic profile methods and algorithm (2012).
59. Chelton, D. B., deSzoeke, R. A., Schlax, M. G., El Naggar, K. & Siwertz, N. Geographical Variability of the First Baroclinic Rossby Radius of Deformation. *Journal of Physical Oceanography*, **28**, 433–460, (1998).
60. Argo. Argo float data and metadata from Global Data Assembly Centre (Argo GDAC), <https://doi.org/10.17882/42182> (2019). Type: dataset.
61. Shchepetkin, A. F. & Mc Williams, J. C. The regional oceanic modeling system (ROMS): a split-explicit, free-surface, topography-following-coordinate oceanic model. *Ocean Modelling* **9**, 347–404, <https://doi.org/10.1016/j.ocemod.2004.08.002> (2005).
62. Shchepetkin, A. F. & Mc Williams, J. C. Accurate Boussinesq oceanic modeling with a practical, “Stiffened” Equation of State. *Ocean Modelling* **38**, 41–70, <https://doi.org/10.1016/j.ocemod.2011.01.010> (2011).
63. Ménesguen, C., Marchesiello, P. & Ducousso, N. Destabilization of an Oceanic Meddy-Like Vortex: Energy Transfers and Significance of Numerical Settings. *Journal of Physical Oceanography* **48**, 1151–1168, <https://doi.org/10.1175/jpo-d-17-0126.1> (2018).
64. de Marez, C., Meunier, T., Morvan, M., L’Hégaret, P. & Carton, X. Study of the stability of a large realistic cyclonic eddy. *Ocean Modelling* **146**, 101540, <https://doi.org/10.1016/j.ocemod.2019.101540> (2020).
65. Klein, P. et al. Upper Ocean Turbulence from High-Resolution 3D Simulations. *Journal of Physical Oceanography* **38**, 1748–1763, <https://doi.org/10.1175/2007JPO3773.1> (2008).
66. Morel, Y. & Mc Williams, J. Effects of Isopycnal and Diapycnal Mixing on the Stability of Oceanic Currents. *Journal of Physical Oceanography*, **31**, [https://doi.org/10.1175/1520-0485\(2001\)031<2280:EOIADM>2.0.CO;2](https://doi.org/10.1175/1520-0485(2001)031<2280:EOIADM>2.0.CO;2) (2001).
67. Mc Dougall, T. J. & Barker, P. M. Getting started with teos-10 and the gibbs seawater (gsw) oceanographic toolbox. *SCOR/IAPSO WG 127*, 1–28 (2011).
68. Garreau, P., Dumas, F., Louazel, S., Stegner, A. & Le Vu, B. High-Resolution Observations and Tracking of a Dual-Core Anticyclonic Eddy in the Algerian Basin. *Journal of Geophysical Research: Oceans* **123**, 9320–9339, <https://doi.org/10.1029/2017JC013667> (2018).
69. Prieto, R., McNoldy, B. D., Fulton, S. R. & Schubert, W. H. Classification of Binary Tropical Cyclone-Like Vortex Interactions. *Monthly Weather Review*, **131**, 2656–2666, [https://doi.org/10.1175/1520-0493\(2003\)131<2656:ACOBTC>2.0.CO;2](https://doi.org/10.1175/1520-0493(2003)131<2656:ACOBTC>2.0.CO;2) (2003).
70. Kuo, H.-C., Schubert, W. H., Tsai, C.-L. & Kuo, Y.-F. Vortex Interactions and Barotropic Aspects of Concentric Eyewall Formation. *Monthly Weather Review* **136**, 5183–5198, <https://doi.org/10.1175/2008MWR2378.1> (2008).

Acknowledgements

This work was funded by the Direction Générale de l’Armement (DGA) via a full grant for Charly de Marez’s PhD. This work is also a contribution to PRC 1069 ‘Meso and submesoscale vortices in the Atlantic and Indian Ocean’, funded by CNRS and RFBR. Simulations were performed using the HPC facilities DATARMOR of “Pôle de Calcul Intensif pour la Mer” at Ifremer, Brest, France. AMEDA has been developed under the funding of the ANR-Astrid Project DYNED-Atlas (ANR 15 ASMA 0003 01). AMEDA is available online, <https://github.com/briaclevu/AMEDA>. Global HYCOM re-analysis were downloaded from the dedicated repository <https://www.hycom.org/dataserver/gofs-3pt1/reanalysis>. Model outputs are available upon request. We gratefully acknowledge C. Vic for his helpful comments on the manuscript.

Author contributions

C.d.M. designed the experiments, performed the numerical simulations and led the analysis of the results and writing. P.L., T.M. and X.C. provided guidance in the interpretation of the results of the numerical simulation, and contributed to the writing of the manuscript. B.L.V. and A.S. provided guidance on the use of AMEDA and on interpretation of its outputs. M.M. provided guidance on the use of HYCOM outputs and on the initialization of numerical simulations.

Competing interests

The authors declare no competing interests.

Additional information

Supplementary information is available for this paper at <https://doi.org/10.1038/s41598-020-59800-y>.

Correspondence and requests for materials should be addressed to C.d.M.

Reprints and permissions information is available at www.nature.com/reprints.

Publisher’s note Springer Nature remains neutral with regard to jurisdictional claims in published maps and institutional affiliations.



Open Access This article is licensed under a Creative Commons Attribution 4.0 International License, which permits use, sharing, adaptation, distribution and reproduction in any medium or format, as long as you give appropriate credit to the original author(s) and the source, provide a link to the Creative Commons license, and indicate if changes were made. The images or other third party material in this article are included in the article’s Creative Commons license, unless indicated otherwise in a credit line to the material. If material is not included in the article’s Creative Commons license and your intended use is not permitted by statutory regulation or exceeds the permitted use, you will need to obtain permission directly from the copyright holder. To view a copy of this license, visit <http://creativecommons.org/licenses/by/4.0/>.

© The Author(s) 2020

6.3 L'impact d'une marche topographique sur la fusion de tourbillons

Bien qu'un quart des fusions ait lieu dans l'ouvert de la mer d'Arabie, une majorité de ces événements a lieu le long des côtes. En particulier, nombreuses sont les fusions ayant lieu le long du talus continental Omanais (16%, soit 170 événements, voir Fig. 6.1). Ces fusions ne sont alors plus isolées (au sens conventionnel du terme), mais contraintes le long de la côte. Lorsqu'elles fusionnent, les structures peuvent éventuellement passer au dessus du talus qui en retour modifie l'écoulement. Nous présentons dans cette partie l'impact de la présence d'un talus continental sur la fusion de deux tourbillons, afin de décrire l'impact potentiel du talus Omanais sur les fusions de tourbillons ayant lieu dans cette région.

6.3.1 Article publié dans *Fluids*



Article

The Interaction of Two Surface Vortices Near a Topographic Slope in a Stratified Ocean

Charly de Marez ¹, Xavier Carton ^{2,*} , Mathieu Morvan ² and Jean N. Reinaud ³ 

¹ École Normale Supérieure de Lyon, 69007 Lyon, France; charly.de-marez@ens-lyon.fr

² Laboratoire d'Océanographie Physique et Spatiale, Institut Universitaire Européen de la Mer, Université de Bretagne Occidentale, 29200 Brest, France; mathieu.morvan@univ-brest.fr

³ Vortex Dynamics Group, Mathematical Institute, University of St Andrews, Scotland KY16 9SS, UK; jnr1@st-andrews.ac.uk

* Correspondence: xcarton@univ-brest.fr; Tel.: +33-290-915-509

Received: 21 July 2017; Accepted: 17 October 2017; Published: 25 October 2017

Abstract: We study the influence of bottom topography on the interaction of two identical vortices in a two-layer, quasi-geostrophic model. The two vortices have piecewise-uniform potential vorticity and are lying in the upper layer of the model. The topography is a smooth bottom slope. For two cyclones, topography modifies the merger critical distance and the merger efficiency: the topographic wave and vortices can advect the two cyclones along the shelf when they are initially far from it or towards the shelf when they are initially closer to it. They can also advect the two cyclones towards each other and thus favour merger. The cyclones deform, and the potential vorticity field undergoes filamentation. Regimes of partial vortex merger or of vortex splitting are then observed. The interaction of the vorticity poles in the two layers are analysed to explain the evolution of the two upper layer cyclones. For taller topography, two new regimes appear: vortex drift and splitting; and filamentation and asymmetric merger. They are due to the hetonic coupling of lower layer vorticity with the upper layer vortices (a heton is a baroclinic vortex dipole, carrying heat and momentum and propagating horizontally in the fluid), or to the strong shear that the former exerts on the latter. The interaction of two anticyclones shows regimes of co-rotation or merger, but specifically, it leads to the drift of the two vortices away from the slope, via a hetonic coupling with oppositely-signed vorticity in the lower layer. This vorticity originates in the breaking of the topographic wave. The analysis of passive tracer evolution confirms the inshore or offshore drift of the fluid, the formation of tracer fronts along filaments and its stirring in regions of vortex merger. The trajectories of particles indicate how the fluid initially in the vortices is finally partitioned.

Keywords: vortex interaction; topography; quasi-geostrophic model

1. Motivation of the Study

Vortices are prevalent and long-lived features of ocean dynamics. They play a key role in the transport of momentum, heat, salt, chemical tracers and biological species, across the ocean basins. They can be surface intensified, like the warm-core rings of the Gulf Stream, or thermocline-intensified vortices, like meddies (eddies of Mediterranean outflow water) in the Northeastern Atlantic Ocean [1]. Oceanic vortices can exist both at the mesoscale (with radii comparable to the first internal deformation radius) and at the submesoscale (with smaller radii; [2]). Vortices can be generated at the submesoscale and then merge to grow in size to the mesoscale [3]. The merging process is that by which two like-signed vortices, at the same depth, collapse to form a larger vortex. Vortex merger has been observed in the ocean for Gulf Stream rings [4] and also for meddies [5–7].

The process of vortex merger has been studied in simple configurations; the evolution of two equal vortices, or of two unequal vortices, with initially axisymmetric velocities, in the absence of external currents, has been investigated in two-dimensional incompressible flows [8–16] and in rotating, stratified flows [17–26]. In these studies, the two vortices interacted in the absence of bottom topography.

Interactions of like-signed oceanic vortices have also been observed near coasts. Figure 1 shows the interaction of two anticyclones near the east coast of Australia.

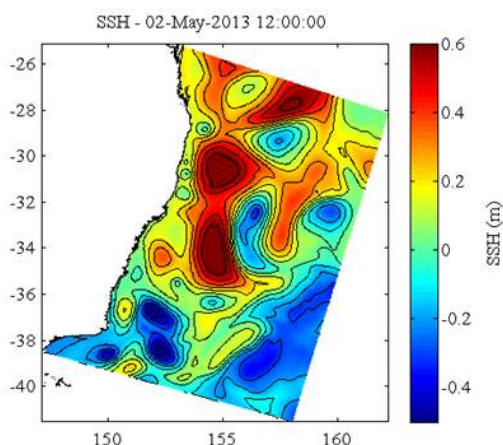


Figure 1. Altimetric map showing the interaction of eddies near the east coast of Australia; notice the close interaction of two anticyclones near the coast (Archiving, Validation and Interpretation of Satellite Oceanographic Data altimetry).

In such a case, each vortex not only interacts with its partner, but also with the coastal bathymetry.

The interaction of a single vortex with a topographic step has already been studied. McDonald [27] showed that cyclones are drawn towards the shallow region (also called “the shelf” hereafter) and that anticyclones are repelled away from it, into the deep region. Indeed, a cyclone (referred to as a “primary cyclone” hereafter) advects fluid from offshore onto the shelf to its right and shelf fluid offshore to its left. The former fluid column is squeezed vertically and develops anticyclonic relative vorticity, while the latter is stretched vertically and becomes cyclonic. These fluid columns, which have acquired vorticity, are called “secondary vortices”. The flow field created by this secondary dipole advects the primary cyclone shoreward (see also Figure 2a of [28]). The opposite effect holds for anticyclones, which are advected offshore by these secondary vortices. Dunn et al. (2001) [29] showed that, for a tall topographic step, vortices can drift with the topographic wave in a steady motion. Zhang et al. (2011) [30] also studied the transport of shelf water, associated with the topographic wave-vortex interaction. They found that the topographic vortex created by a cyclone remains near the shelf, while that created by an anticyclone couples with it and moves offshore; therefore anticyclones are more capable of advecting water away from the shelf. It has been shown that the interaction of ocean vortices with the bottom slope can produce smaller (submesoscale) vortices by forcing and then destabilising a bottom boundary layer [31,32].

Vortex merger near a topographic step in a stratified fluid has however not yet been addressed. This process raises several questions:

- (1) Under which conditions can two surface vortices merge near a topographic step or slope?
- (2) What are the other nonlinear regimes they can undergo and why?
- (3) What are the consequences of these various interactions on the cross-shelf transport?

This problem is complex due to the number of parameters involved (vortex radius, intensity, mutual distance of the vortices, distance to the shelf, topographic slope, height of the shelf, planetary beta effect). Here, we reduce the problem to a simple configuration to render it tractable. We consider two vortices, with piecewise uniform potential vorticity, in a two-layer quasi-geostrophic model on the f -plane. The slope is a hyperbolic tangent in the meridional direction.

The paper is organised as follows: Section 2 presents the methods and models. Section 3 describes the various nonlinear regimes for the interaction of two cyclones. Section 4 analyses these regimes and the influence of topographic height. Section 5 is devoted to the interaction of two anticyclones. Section 6 addresses the evolution of tracer and particles in the flow field and their exchange across the slope. Finally, conclusions are presented in Section 7.

2. The Mathematical Model

2.1. Model Governing Equations

The quasi-geostrophic equations govern the dynamics of stratified flows strongly constrained by planetary rotation (flows with small Froude and Rossby numbers) and with moderate meridional extent. Denoting U the horizontal velocity magnitude, L the horizontal length scale, H the thickness of the flow, N the buoyancy frequency, $f = f_0 + \beta y$ the Coriolis parameter in the domain (at any latitude) (f_0 being the Coriolis parameter at the centre of the domain, y the meridional distance to this centre, β the meridional gradient of the Coriolis parameter), the Froude number is $Fr = U/NH \ll 1$, the Rossby number is $Ro = U/fL \ll 1$ and the meridional extent of the flow, L , is bounded by $L \ll f_0/\beta$.

In a fluid composed of two superimposed layers of uniform (but different) densities, these quasi-geostrophic equations are written:

$$\partial_t q_j + \vec{u}_j \cdot \vec{\nabla} q_j = \nu_4 \nabla^4 \omega_j \quad (1)$$

where $j = 1, 2$ is the upper, lower layer index. The right-hand side of Equation (1) is the biharmonic dissipation of vorticity, implemented numerically to remove vorticity accumulation at small scales, and ν_4 is called hyperviscosity. The layer-wise total potential vorticity is:

$$q_j = \nabla^2 \psi_j + F_j (\psi_k - \psi_j) + f + \delta_{j,2} f h_b / H_2 \quad (2)$$

where ψ_j is the stream function in layer j . We used $k = 3 - j$.

Due to the small meridional extent of the domain considered in this study, we keep $f = f_0$ here. The layer coupling coefficients are $F_j = f_0^2 / (g' H_j)$ with H_j the thickness of layer j and $g' = g(\rho_2 - \rho_1) / \rho_0$ the reduced gravity. ρ_0 is an average density, and $\delta_{i,j}$ is the Kronecker symbol. The internal deformation radius is $R_d = \sqrt{(g' H_1 H_2) / H} / f_0$, and its inverse is called $\gamma = 1/R_d$. Here, equal layer thicknesses are chosen $H_1 = H_2 = 0.5, H = 1$. The two-layer model is appropriate for surface-intensified flows in the ocean (Flierl, 1978).

The topographic height (from the deepest bottom) is $h_b(y)$ here (see its mathematical form in Section 2.2; note that the choice of direction for the topographic gradient is arbitrary with respect to the f -plane). The relative vorticity is:

$$\zeta_j = \partial_x v_j - \partial_y u_j = \nabla^2 \psi_j \quad (3)$$

the horizontal velocity being:

$$u_j = -\partial_y \psi_j, \quad v_j = \partial_x \psi_j \quad (4)$$

From this velocity, we can define the velocity shear in layer j :

$$S_j = \partial_x v_j + \partial_y u_j \quad (5)$$

the strain rate in layer j :

$$T_j = \partial_x u_j - \partial_y v_j \quad (6)$$

and finally the Okubo–Weiss quantity:

$$OW_j = S_j^2 + T_j^2 - \zeta_j^2 \quad (7)$$

It distinguishes regions where deformation is dominant from those of concentrated vorticity.

We remind that the vertical (barotropic and baroclinic) modes are defined by:

$$\psi_t = (H_1 \psi_1 + H_2 \psi_2) / H, \quad \psi_c = \psi_1 - \psi_2 \quad (8)$$

For convenience, we call:

$$q_{dj} = \zeta_j + F_j(\psi_k - \psi_j) \quad (9)$$

the potential vorticity anomaly (note that $q_{d1} = q_1$).

We call topographic vorticity the term:

$$q_{topo} = f_0 h_b / H_2 \quad (10)$$

In our analyses, we use the quantity:

$$q_{2i} = \zeta_2 - F_2 \psi_2 \quad (11)$$

that we call the “equivalent barotropic” potential vorticity of the lower layer. From this quantity, the lower layer stream function (velocity) can be directly diagnosed (by inverting a Helmholtz operator).

2.2. Numerical Model

Equations (1) and (2) for the quasi-geostrophic model have been implemented numerically in a square, biperiodic domain, using a pseudo-spectral technique in space and a mixed Euler-leapfrog scheme in time. The time step is bounded by the Courant–Friedrich–Levy condition, $\Delta t < \Delta x / U_{max}$. The domain length and width used are $L = 4\pi$ (with $x, y \in [-2\pi, 2\pi]$). Model simulations are performed with 512 collocation points. Very weak biharmonic viscosity is applied in the model ($\nu_4 = 5 \times 10^{-8}$). This viscosity does not alter the physical results of the model and only removes small-scale noise.

The initial conditions of this model are a pair of identical, circular vortices of radius $R = 0.5$, enclosing uniform quasi-geostrophic relative vorticity $q_1 = 1$ (when we investigate the interaction of two cyclones) or $q_1 = -1$ (when we study the interaction of two anticyclones), lying at a distance d from each other and at a distance d_c from the topography. Elsewhere, $q_1 = q_{d2} = 0$ (see Figure 2).

As an application to the ocean, the East Australian eddies have a peak velocity $V \sim 0.5$ m/s at a radius $R \sim 50$ km. Using an estimate of vorticity $q \sim 2\zeta \sim 4V/R = 4 \times 10^{-5} \text{ s}^{-1}$, length and time are scaled between the model and the ocean via $L_s = 10^5 \text{ m}$ and $T_s = 2.5 \times 10^4 \text{ s}$. At 35°S , $f_0 = 8.34 \times 10^{-5} \text{ s}^{-1}$, so that $q/f_0 = 0.5$ (note that $Ro = 0.12$). The radius of deformation is about 50 km so that the Burger number $Bu \sim 1$. The relative influence of the beta-effect is weak, since the vortices are mesoscale features; here, $\beta L / f_0 \sim 1.2 \cdot 10^{-2}$, and the vortex radius is small compared with the Rhines scale $L_{Rh} = \sqrt{V/\beta}$, a scale above which the beta effect is influential on the dynamics. Here, $L_{Rh} \sim 160$ km.

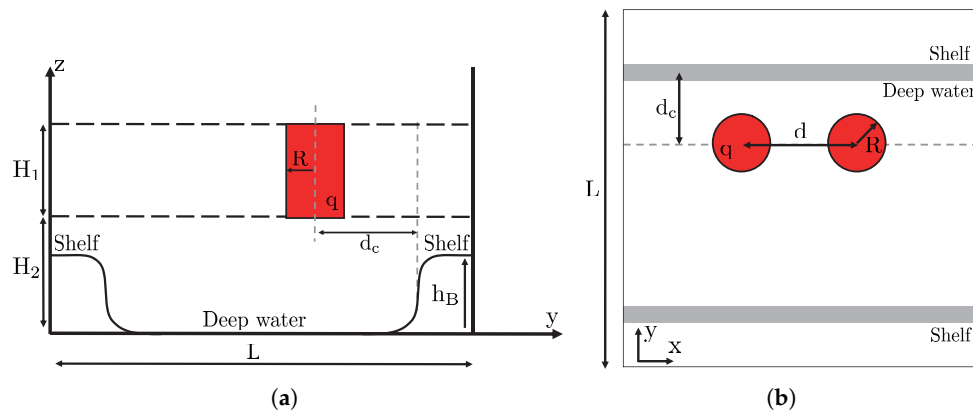


Figure 2. Sketch of model and vortex configuration; (a) side view; (b) top view.

In the model, the dimensionless value of f_0 is therefore 2.0, which scales the topographic vorticity $f_0 h_b / H_2$ in Equation (3). The maximal value of h_{b0} / H_2 , used in this study is 0.3. Note that the quasi-geostrophic model assumptions are met since the Rossby number is small, the Burger number is unity, the beta effect is weak and the topographic amplitude remains moderate.

Nevertheless, this validity is limited to mesoscale vortices, near low shelves, at mid-latitudes. The interaction between smaller vortices, near taller shelves, should be investigated in a primitive equation model.

The bathymetry is a smooth slope both north and south (for positive and negative y 's):

$$h_b(y) = h_{b0} [1.0 + 0.5 \tanh((y - y_t) / L_t) - 0.5 \tanh((y + y_t) / L_t)] \quad (12)$$

The topographic gradient thus defines the meridional direction. The choice of parameter values for cyclonic solutions is $y_t = 3, L_t = 0.25$ and $y_t = 5, L_t = 0.25$ for anticyclones. The shallow region is wider in the former case, because cyclones tend to climb on topographic slopes; therefore, a significant part of their evolution is expected to take place in the shallow region (the “shelf”), if they are not too far away from it initially. Due to meridional periodicity of the domain (the isobaths giving the zonal direction), the shelf forms a single region.

To track fluid masses, a passive tracer, with initial distribution equal to one over the shelf and to minus one in the deep region, is used to study the evolution of shallow and deep fluid masses. Note that the passive scalar field has the same resolution and undergoes the same dissipation as vorticity.

Furthermore, 10,000 particles were seeded in the flow (over the shelf, in the deep region and in the vortices). Their advection (via a Euler scheme) and tracking allow us to follow the fluid from the vortex cores.

3. Interaction of Two Cyclones: Nonlinear Regimes

Three hundred numerical simulations have been performed varying the non-dimensional distance between the two cyclones d/R , their distance to the slope d_c/R , the rescaled density stratification γR and the topographic vorticity $f_0 h_{b0} / H_2$. Figure 3 summarises the main regimes in the parameter space.

The left-hand panel in Figure 3a is similar to the results obtained by Polvani (1989) [33], for vortex merger over a flat bottom in a two-layer quasi-geostrophic model: in this case, merger occurs for $d/R < 3.3$. The invariance of the nondimensional critical merger distance $d^* = d/R$ with respect to stratification in this study is related to the vortex initialisation as a disk of constant potential vorticity. When vortices are initially disks of uniform relative vorticity, the critical merger distance depends on stratification via hetonic effects [18,19,34–37]. Indeed, relative vorticity in one layer induces interface

deviation between layers and thus potential vorticity of opposite sign in the other layer. This in turn can lead to vertical coupling of these vorticity poles and to their self-advection, counter-acting the merging process.

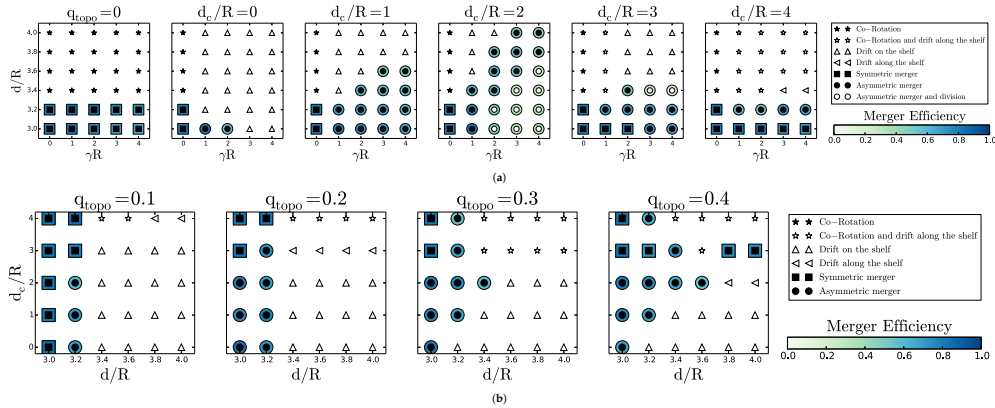


Figure 3. Regime diagram for the interaction of two surface cyclones with: (a) given d_c/R (see above each plot) in the $\gamma R, d/R$ plane for $f_0 h_{b0} H_2 = 0.3$; (b) given topographic vorticity (see above each plot) in the $d/R, d_c/R$ plane. Black stars indicate co-rotation; white stars represent co-rotation and drift along the shelf/slope; black squares indicate symmetric merger; black circles represent asymmetric merger; white circles denote asymmetric merger and vortex splitting; upward pointing triangles represent drift towards and on the slope and shelf; and triangles pointing left represent drift along the shelf/slope. The blue shading provides the value of the merger efficiency, when relevant.

In the presence of topography, the two cyclone evolution is similar to that over a flat bottom, if they lie far away from the slope. Merger occurs again for $d^* = 3.3$; the weak influence of topographic waves leads to asymmetric merger. If the two cyclones are initially more distant from each other than d^* , co-rotation and drift along the slope are the main evolutions. Note that, in the large d_c/R limit, the co-rotating cyclone pair can drift steadily along the topography.

An analytical solution for a point vortex doublet drifting steadily along a step-like shelf can be obtained, with approximations (see Appendix A). This solution shows that (1) stationary drift of a vortex doublet is possible far away from the shelf and (2) this doublet induces a wave in topographic vorticity, which displaces the doublet.

If the vortex pair is initially close to the slope, new regimes appear:

- (i) Asymmetric, partial merger can occur as negative potential vorticity in the lower layer creates a flow in the upper layer; this flow advects one cyclone towards the other; then, the two cyclones merge. Thus, merger occurs for two cyclones initially more distant than $3.3R$. However, the lower layer vorticity poles exert a shear on the upper layer cyclones, which filament. Therefore, the efficiency of the merging process is reduced. We define merger efficiency as the ratio of the final (merged) vortex area integral of potential vorticity (in Layer 1), to that of the two initial vortices:

$$ME = \frac{\int \int q_{final} dS}{\int \int q_{initial} dS}$$

(the area is bounded by the outermost closed vorticity contour). This efficiency is maximal for the evolution called complete vortex merger, during which nearly all the fluid contained in the two initial vortices (and the potential vorticity of these fluid particles, which is a Lagrangian invariant) goes into the final, merged, vortex. Indeed, during this evolution, only a small percentage of the initial vortex fluid (usually less than 5%) is finally contained in the peripheral filaments, which ensure angular momentum conservation.

Figure 3 shows that asymmetric merger is less efficient than symmetric merger.

- (ii) Asymmetric merger and splitting: The vortex resulting from merger is elongated and subject to intense shear from its cyclonic partner and from topographic vortices (topographic vortices are formed by the amplification, steepening and breaking of topographic waves); this merged vortex splits into two parts. This evolution can occur when γR is large enough to couple the motions vertically. In this case, the merger efficiency is very small.
- (iii) Drift towards the slope and on the shelf: when the vortices are close enough to the slope, the topographic wave and subsequently formed vortices (in the lower layer) can advect both upper layer vortices upon the shelf. Again, this requires sufficient layer coupling (i.e., large values of γR).

Figure 3b describes the regimes in the $d/R, d_c/R$ plane for various values of topographic vorticity q_{topo} . For small values of q_{topo} , the regime diagram shows that the critical merger distance is $d^* = 3.3$, as for a flat bottom, but the vortex pair is influenced by the topographic waves and can climb on the shelf if $d/R > 3.3$.

As the topographic height increases, two main effects are noticed:

- (a) The efficiency of the merger of the two cyclonic vortices is reduced by filamentation, and the merger is only partial.
- (b) Merger occurs for initially more distant cyclones; this is related to the advection of one cyclone towards the other by topographic vortices.

We summarise our results in Figure 4 by plotting the normalised critical merger distance d^* against the stratification γR , for the various values of the distance of the vortex pair to the topographic slope d_c/R .

This figure confirms that far from the slope, the critical merger distance is similar to that over a flat bottom. When the vortices are initially very close to the slope, this critical distance is reduced (the vortices are pushed apart by the topographic wave). For intermediate distances from the slope ($d_c/R \in [1, 2]$), the topographic vortices advect the two vortices towards each other and favour merger. This effect is all the stronger as layer coupling (stratification) is strong.

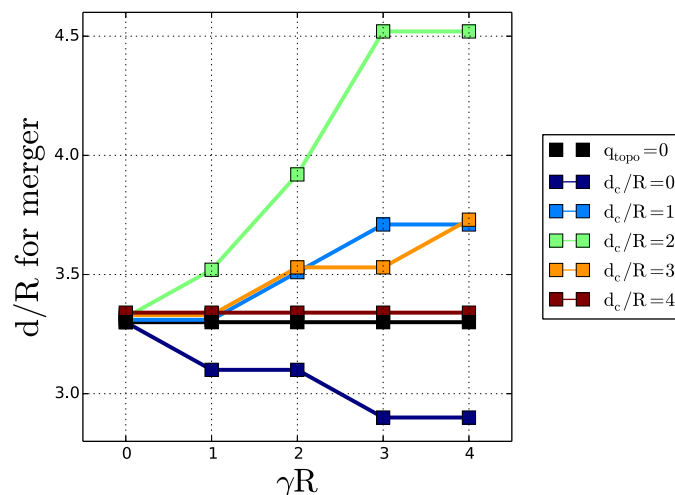


Figure 4. Critical merger distance d^* , with respect to stratification, for various distances of the cyclone pair to topography.

4. Analysis of Main Regimes for the Two Cyclone Interaction

Here, the topographic vorticity is $f_0 h_{b0}/H = 0.3$. We analyse in detail selected examples, the three regimes of interaction specific to the case with bottom topography, which are not observed over a flat bottom, for two equal vortices.

4.1. Partial Merger

Firstly, we analyse the case of a partial merger ($d/R = 3.4, \gamma R = 1, d_c/R = 2$); we present the vorticity and velocity shear fields, in each layer, in Figure 5.

Figure 5a shows the vortices in the upper layer (in relative vorticity distribution). Initially, the two vortices start co-rotating; the easternmost vortex climbs on the slope; it is elongated and starts to merge with its companion vortex. However, finally, the cyclone above the shelf drifts away from its partner in the deep region. This indicates that the topographic effects are stronger than the mutual vortex interaction. This topographic effect is due to the lower layer flow across the topography and to its coupling to the upper layer. Indeed, it can be seen that a perturbation of the interface with large zonal scale grows first in the lower layer (as predicted by Appendix A), but then, as the evolution is unsteady, this wave grows, changes form and couples with the upper layer vortex on the shelf. To assess this coupling, the vorticity and velocity shear distributions in the lower layer are next examined.

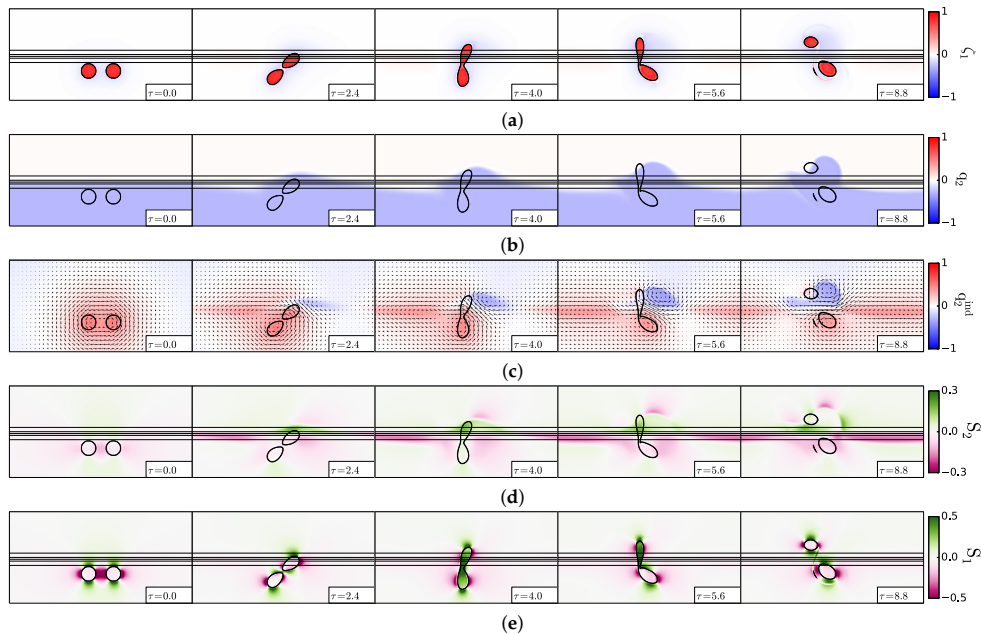


Figure 5. Partial merger of two cyclones, case $d/R = 3.4, \gamma R = 1, d_c/R = 2$. (a) Upper layer relative vorticity (Equation (3)); (b) lower layer potential vorticity (Equation (2)); (c) lower layer “equivalent barotropic” potential vorticity and velocity field (Equations (4) and (11)); (d) lower layer velocity shear (Equation (5)); (e) upper layer velocity shear (Equation (5)). In (a,b,d,e), the black contours indicate the topographic slope (Equation (12); straight lines) and the upper layer vorticity contours showing the two vortex evolution. In each plot, x varies between -2π and $+2\pi$, and y varies between 0 and $+2\pi$.

Figure 5b shows the total, deep, potential vorticity. It only comprises topographic vorticity initially. This vorticity is advected on the slope by the upper layer cyclonic motion, via vortex stretching. To better identify the effects of this deep vorticity advection, we plot, in Figure 5c, the lower layer “equivalent barotropic” potential vorticity, to which the deep motion is directly related (the deep vorticity field is indicated). In this deep “equivalent barotropic” potential vorticity, one can easily

identify the topographic wave, which develops along the slope, with a positive vorticity pole (to the west) and a negative one (to the east). These vorticity poles match the difference in total deep potential vorticity, between the instantaneous and initial values along the slope. A negative vorticity pole grows below and east of the upper layer cyclone on the slope. This deep anticyclone is responsible for (a) the elongation of the upper layer cyclone on the slope (via the shear exerted on it) and (b) the drift of this cyclone towards the shelf (via the hetonic coupling).

Finally, we also compute the velocity shear generated by these deep vorticity poles (Figure 5d); at $\tau = 4.0$ and $\tau = 5.6$ (τ is the normalised time, equal to the model time divided by the eddy time scale; the latter is chosen as $T = 4\pi/q_{1max} = 4\pi$), intense shear is created exactly below the upper layer cyclone on the slope. This lower layer shear is felt in the upper layer via the density interface. Figure 5e indicates how strong the upper layer shear is, in the vortex on the slope, at $\tau = 4.0$ and $\tau = 5.6$.

Since the deep flow and potential vorticity play a key role in coupling the upper layer vortices and the topography, some further analysis is devoted to their time evolution. In particular, we write the lower layer potential “equivalent barotropic” vorticity equation as:

$$\partial_t q_{2i} = -J(\psi_2, q_{2i}) - F_2 \partial_t \psi_1 - J(\psi_2, F_2 \psi_1) - J(\psi_2, f_0 h_b / H_2) \quad (13)$$

neglecting dissipation. Here, $J(f, g) = \partial_x f \partial_y g - \partial_x g \partial_y f$ is the Jacobian operator.

This equation states that the lower layer “equivalent barotropic” potential vorticity (that related directly to the deep flow) varies owing to its advection by this deep flow, to the rate of change of the upper layer flow (via layer coupling), to the baroclinic advection of the barotropic flow and to the interaction of the lower layer flow with the topography.

Indeed, the third term in the right-hand side, $-F_2 J(\psi_2, \psi_1)$ can also be written $F_2 J(\psi_c, \psi_t)$. This term also represents the barotropic advection of interface deviation. These three components are presented below (Figure 6).

In Figure 6a, the first term in the equation, the advection of lower layer “equivalent barotropic” potential vorticity, is northward, as indicated by the dipole at the middle of the domain.

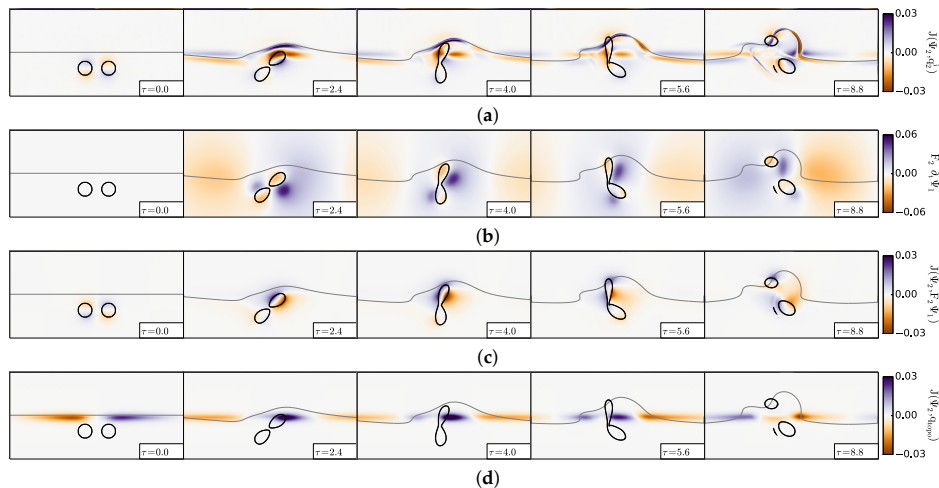


Figure 6. Partial merger of two cyclones, case $d/R = 3.4, \gamma R = 1, d_c/R = 2$. Analysis of the terms contributing to the rate of change of the lower layer “equivalent barotropic” potential vorticity (Equation (13)): (a) lower layer advection of this potential vorticity; (b) rate of change of the upper layer flow (via layer coupling); (c) baroclinic advection of the barotropic flow (with layer coupling coefficient); (d) interaction of the lower layer flow with the topography. In all sub-plots, the black contours indicate the front of lower layer potential vorticity anomaly (straight line at $\tau = 0$) and the upper layer vorticity contours showing the two-cyclone evolution.

The second term, the rate of change of the upper layer flow (multiplied by the layer coupling coefficient), is initially related to the rotation of the upper layer vortex pair (see Figure 6b). At later times, it becomes zonally dipolar, corresponding to the meridional advection of one upper layer cyclone to the north. This dipolar structure is related to the growth of a dipole in q_{2i} (see Figure 5c at $\tau = 4$ and $\tau = 5.6$). This rate of change is twice as strong as the first term. The third term (barotropic advection of interface deviation) is also related to the rotation of the two vortices initially, but then becomes predominant in the northern cyclone for which the northward motion and the velocity shear become strong (see Figure 6c). This term is weaker than the second term. Finally, the last term represents the topographic wave (see Figure 6d). It is concentrated along the slope. It is of the same order as the first and third terms. In summary, though the third term is larger than the other terms, all terms contribute to the upper layer cyclones' motion and deformation, to the deformation of the lower layer potential vorticity and to the growth of the topographic wave.

The distance between the geometric centres of the upper layer cyclones (see Figure 7) decreases sharply at early times in the presence of the topographic slope, whereas it would remain constant over a flat bottom. After they have joined, the two cyclones diverge spatially; this corresponds to the rapid growth of this distance with time.

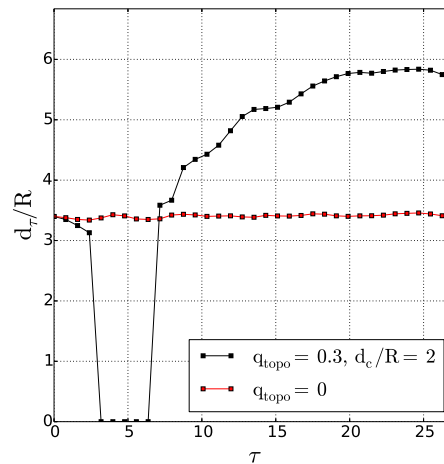


Figure 7. Time evolution of the distance between cyclone centres for the partial merger of two cyclones; case $d/R = 3.4$, $\gamma R = 1$, $d_c/R = 2$; comparison between the evolutions with and without the topography.

4.2. Merger and Splitting

Secondly, we analyse a case of merger and splitting ($d/R = 3.4$, $\gamma R = 3$, $d_c/R = 2$); we present the vorticity and velocity shear, in the two layers, in Figure 8. Figure 8a shows that the upper layer vortices merge asymmetrically (between $\tau = 0$ and $\tau = 10.3$). Then, the merged vortex becomes more elongated (see $\tau = 13.5$ and $\tau = 17.5$), before splitting into two vortices of nearly equal sizes ($\tau = 23.9$). The lower layer “equivalent barotropic” potential vorticity shows a negative pole on the slope, between two positive poles, east and west (see Figure 8b; $\tau = 10.3$). A strong shear flow appears between these poles, in particular at the location of the merged vortex. This vortex elongates around this negative pole of q_{2i} and breaks. In the lower layer, the velocity shear is initially the strongest in the periphery of the vortices (see Figure 8c; $\tau = 0$). As the merged vortex elongates, this shear reaches its positive maximum inside this vortex (at $\tau = 13.5$ and $\tau = 17.5$). After splitting, the shear is intense between the vortices.

This deformation is reflected in the upper layer Okubo–Weiss quantity (see Figure 8d). Initially, the two vortex cores are the loci of vorticity concentration, while the shear and strain rates are stronger

on their rim. At later times ($\tau = 13.5$ and $\tau = 17.5$), the deformation rate is not negligible, compared with vorticity, in the merged vortex core. A qualitative model for upper layer vortex splitting is presented in Appendix B. In the two-layer quasi-geostrophic framework, it is possible to estimate the shear created in the upper layer by a lower layer (topographic) vortex and to compare this shear with that necessary to break an upper layer vortex. It occurs that here, the shear is strong enough to induce this splitting. Once split, the two upper layer cyclones are again a region of vorticity concentration.

The distance between the vortices (see Figure 9) decreases sharply with time and vanishes, in the presence of topography; this corresponds to the merging process. Note that the time series is stopped before splitting occurs. Over a flat bottom, merger does not occur, and the distance between vortices does not substantially vary with time.

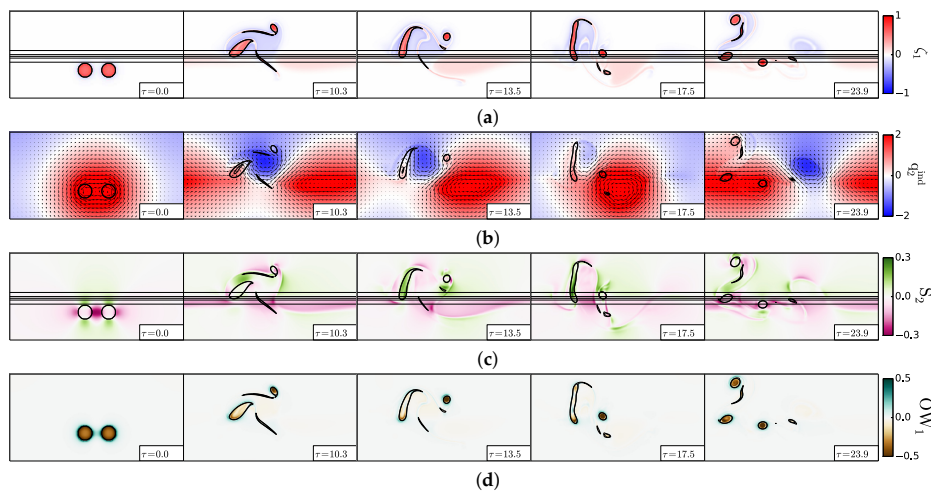


Figure 8. Merger and splitting of two cyclones, case $d/R = 3.4, \gamma R = 3, d_c/R = 2$. (a) Upper layer relative vorticity (Equation (2)); (b) lower layer “equivalent barotropic” potential vorticity (Equation (11)); (c) lower layer velocity shear (Equation (5)); (d) upper layer Okubo–Weiss quantity (Equation (7)). The black contours indicate the topographic slope (Equation (12); straight lines) and the upper layer vorticity contours showing the two vortex evolution.

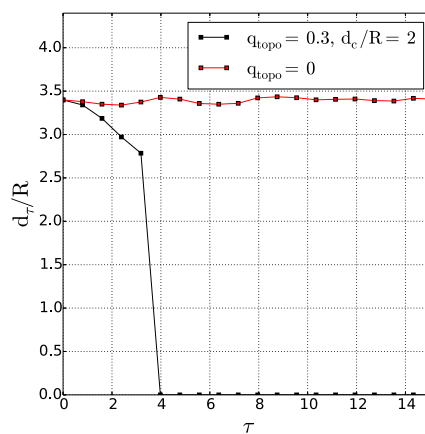


Figure 9. Time evolution of the distance between vortex centres for the merger and splitting of two cyclones; case $d/R = 3.4, \gamma R = 3, d_c/R = 2$; comparison between the evolutions with and without the topography.

4.3. Drift towards the Shelf

Finally, we study a case where two cyclones, initially close to each other, drift apart on the shelf ($d/R = 3.2, \gamma R = 1, d_c/R = 0$); we present the vorticity and velocity shear, in the two layers, in Figure 10.

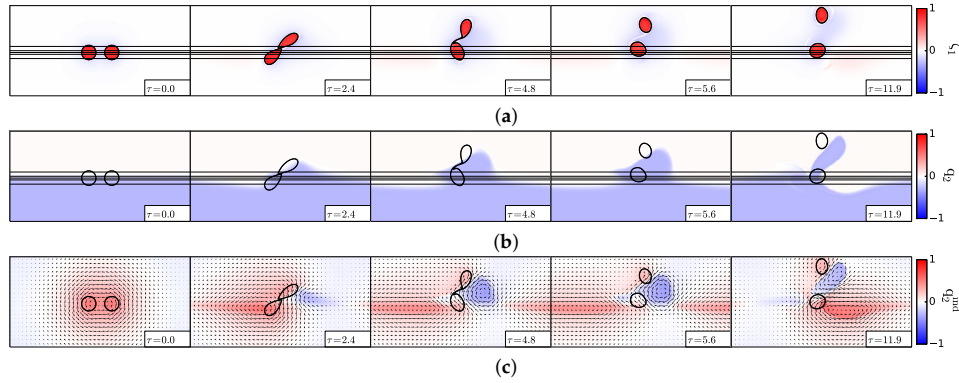


Figure 10. Separation of two cyclones, case $d/R = 3.2, \gamma R = 1, d_c/R = 0$. (a) Upper layer relative vorticity (Equation (3)); (b) lower layer potential vorticity (Equation (2)); (c) lower layer “equivalent barotropic” potential vorticity (Equation (11)). The black contours indicate the topographic slope (Equation (12); straight lines) and the upper layer vorticity contours showing the two vortex evolution.

Figure 10a indicates that the two cyclones, initially located on the topographic slope, join at their mid-point, but only briefly ($\tau = 2.4$). Soon, they drift apart, being connected only by a filament ($\tau = 4.8$). This filament is rapidly dissipated, and the two cyclones become progressively more distant from each other, one remaining on the slope, the other moving northward onto the shelf ($\tau = 5.6$ and $\tau = 11.9$).

The explanation for this evolution lies in the lower layer (see Figure 10b): the anticlockwise motion of the upper layer vortex pair drives the deep fluid upslope, to its east and downslope to its west. The fluid moving upslope acquires the negative potential vorticity anomaly (to compensate the vertical squeezing of the fluid columns). This negative vorticity tongue couples with both upper cyclones, but as it extends northward, it pairs more efficiently with the northern cyclone. This is confirmed by the structure of the lower layer “equivalent barotropic” potential vorticity (Figure 10c), whose negative pole amplifies north of the slope, east of the two cyclones, and then drifts northeastward with the northern cyclone.

These lower layer potential vorticity poles result from the amplification of the vorticity front deviation; this deviation encompasses two terms, one due to lower layer (topographic) vortices and one due to topographic waves. Note that, at early times, there are no topographic vortices. This deviation is analysed via a Fourier transform of the difference in potential vorticity between any given time and the initial state. This Fourier analysis is performed in the lower layer, over the topographic slope:

$$q_2'(x, y, t) = q_2(x, y, t) - q_2(x, y, 0) = \sum_{n=0}^N A_n(y, t) \cos(2n\pi x/L) + B_n(y, t) \sin(2n\pi x/L) \quad (14)$$

for $y_t - L_t < y < y_t + L_t$, and:

$$a_n(t) = \frac{1}{2L_t} \int_{y_t-L_t}^{y_t+L_t} A_n(y, t) dy, \quad b_n(t) = \frac{1}{2L_t} \int_{y_t-L_t}^{y_t+L_t} B_n(y, t) dy \quad (15)$$

The time series of a_n and b_n are shown in Figure 11: at early time, the longest wave grows, forced by the vortex pair. This can be seen in the early maps of lower layer potential vorticity. Then, harmonics (shorter waves) develop, as the upper layer vortices come nearer to the slope and as nonlinear interactions transfer energy from one wave to another. Among these harmonics, the first

and second are dominant. These harmonics are due to the steepening and finally to the breaking of the topographic wave, which produces a topographic vortex. The higher harmonics have an amplitude comparable to that of the initial wave, when breaking occurs. The wavelength of the second harmonic is nearly equal to the horizontal extent of the vortex pair. Note that, once formed, the topographic vortices not only couple with upper layer vortices and advect them away, but they also deform them.

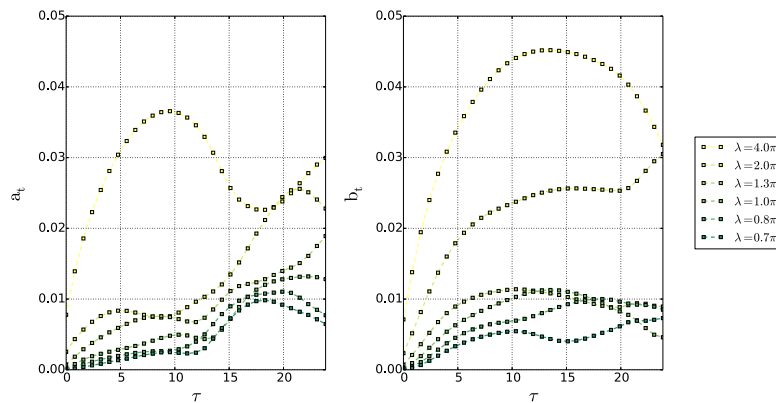


Figure 11. Fourier transform of the lower layer potential vorticity, on the slope, in the case $d/R = 3.2$, $\gamma R = 1, d_c/R = 0$. The modal coefficients $a_n(t)$ and $b_n(t)$ (Equation (15)) are plotted versus time, for several wavelengths $\lambda = L/n = 4.0\pi/n$.

The time evolution of the distance between the two vortices (Figure 12) shows indeed that the two vortices touch each other, but then drift apart. This separation and drift is due to the presence of the topographic vortices in the lower layer; they create the hetonic effect, which propels the two vortices apart from each other. Indeed, over a flat bottom, the two vortices touch, and merge irreversibly. It can be noticed that (a) there is little difference between the two initial evolutions (over a flat bottom and over the shelf) in terms of vortex separation; but (b) when topography is present, the vortices are finally much more distant than they were initially. The hetonic effect has prevailed over the merging tendency due to the closeness of the vortex pair with the shelf (merging did not have time to occur before the topographic effects set in).

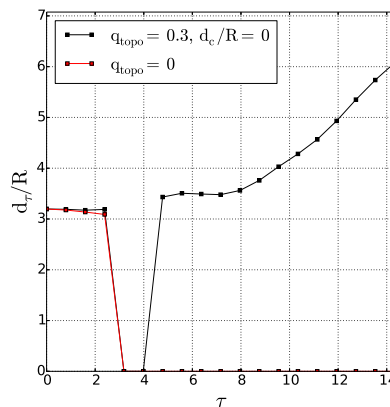


Figure 12. Time evolution of the distance between vortex centres for the drift of two cyclones on the shelf; case $d/R = 3.2, \gamma R = 1, d_c/R = 0$; comparison between the evolutions with and without the topography.

4.4. Influence of Topographic Height

The regime diagram is shown for $f_0 h_{b0} / H_2 = 0.6$ in Figure 13. Compared with that for $f_0 h_{b0} / H_2 = 0.3$ (Figure 3), asymmetric merger is favoured, both when the two cyclones lie above the slope, or far away from it. Two new regimes appear: vortex drift and splitting, filamentation and asymmetric merger. We describe them hereafter. Note also that by increasing the topographic height, the topographic slope is increased, which favours the growth of topographic waves and of topographic vortices.

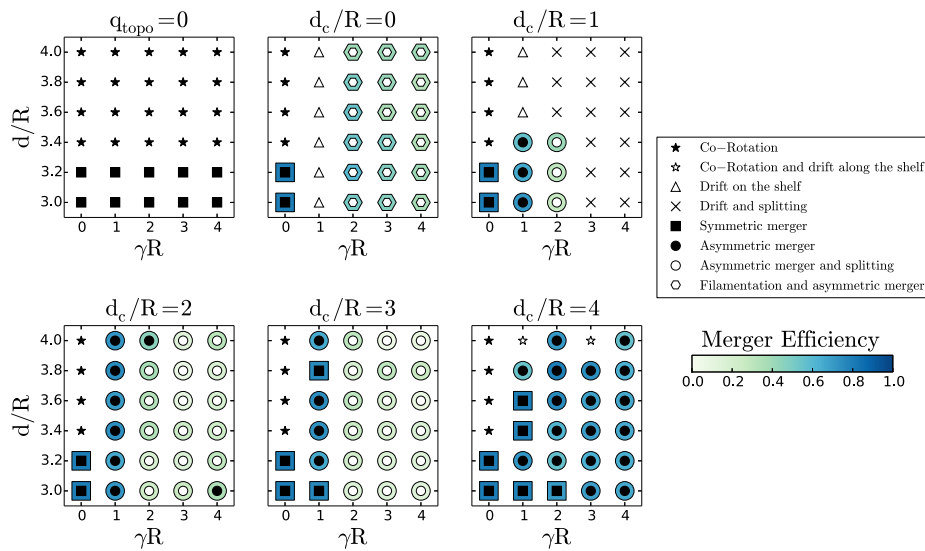


Figure 13. Regime diagram for the interaction of two surface cyclones given d_c/R (see above each plot), in the $\gamma R, d/R$ plane, for $f_0 h_{b0} / H_2 = 0.6$. Black stars indicate co-rotation; white stars represent co-rotation and drift along the shelf/slope; black squares indicates symmetric merger; black circles represent asymmetric merger; white circles denote asymmetric merger and vortex splitting; triangles represent drift towards and on the slope and shelf; hexagons indicate filamentation and asymmetric merger; and crosses denote vortex drift and splitting. The blue shading provides the value of the merger efficiency, when relevant.

4.4.1. Vortex Drift and Splitting

For $d/R = 3.6, \gamma R = 2.0, d_c/R = 1.0$, the two upper layer cyclones drift towards the shelf (see Figure 14a); the easternmost vortex splits above the slope. Finally, three main vortex fragments drift along the slope. This evolution is due to the influence of the lower layer vorticity (Figure 14b). As the upper layer vortices move across the slope, a topographic wave is formed in the lower layer (see, for instance, $\tau = 10.3$). At this moment, the easternmost upper vortex is located above and between two lower potential vorticity poles of opposite polarities. These two poles create an intense shear on the upper vortex, which breaks (see again Appendix B for a description and qualitative estimation of this effect). The lower and upper layer shears (Figure 14c,d) indicate a strong shear associated with the topographic wave and also a strong shear on the vortex, which breaks (at $\tau = 10.3$).

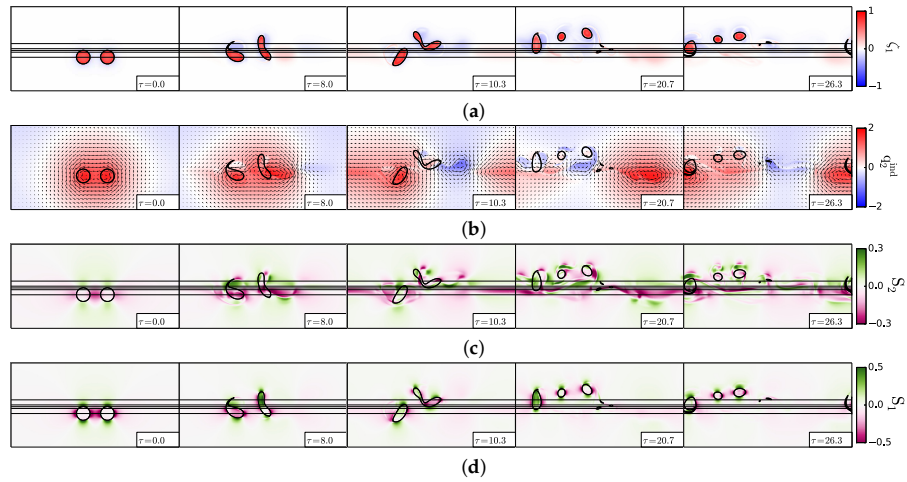


Figure 14. Drift and splitting of two cyclones, case $d/R = 3.6, \gamma R = 2, d_c/R = 1$. (a) Upper layer relative vorticity (Equation (3)); (b) lower layer “equivalent barotropic” potential vorticity and velocity field (Equations (4) and (11)); (c) lower layer velocity shear (Equation (5)); (d) upper layer velocity shear (Equation (5)). In (a,c,d), the black contours indicate the topographic slope (Equation (12); straight lines) and the upper layer vorticity contours showing the two vortex evolution.

4.4.2. Filamentation and Asymmetric Merger

The second “new” regime, which appears for taller topographies, is filamentation and asymmetric merger. It is obtained for the same vortex parameters as in the previous case ($d/R = 3.6, \gamma R = 2.0$), but for vortices initially closer to the topography $d_c/R = 0$. This regime is shown in Figure 15.

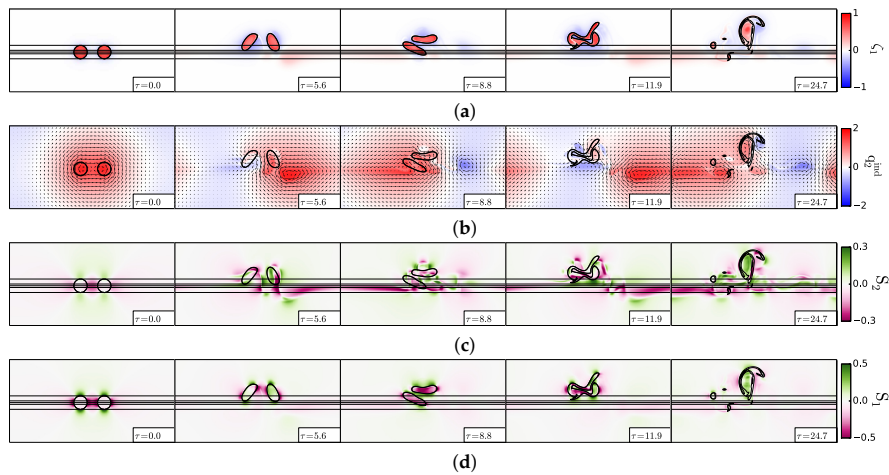


Figure 15. Filamentation and asymmetric merger of two cyclones, case $d/R = 3.6, \gamma R = 2, d_c/R = 0$. (a) Upper layer relative vorticity (Equation (3)); (b) lower layer “equivalent barotropic” potential vorticity and velocity field (Equations (4) and (11)); (c) lower layer velocity shear (Equation (5)); (d) upper layer velocity shear (Equation (5)). In (a,c,d), the black contours indicate the topographic slope (Equation (12); straight lines) and the upper layer vorticity contours showing the two vortex evolution.

Initially, the two vortices head towards each other and towards the shelf (see Panel (a) of this figure). Then, they are strongly elongated; they filament, but the tangle of filaments and small eddies finally merges to form one large vortex and peripheral debris.

Again, the explanation of this behaviour is given by the structure of the lower layer “equivalent barotropic” potential vorticity, composed of an alternation of opposite-signed poles (see Panel (b) of the figure). The upper vortices lie above and between these poles (at $\tau = 5.6$). The shear is thus strong, and vortex splitting is also favoured by hetonic coupling. This is confirmed by the structure of the shear in both layers (in particular in the lower layer at $\tau = 5.6$ and in the upper layer at $\tau = 8.8$). Merger occurs only when the filaments and vortices are located above a negative lower layer vorticity pole ($\tau = 11.9$).

Finally, the merged vortex is again located above and between a cyclone and an anticyclone of the lower layer and is strongly elongated.

5. Interaction of Two Anticyclones

Previous studies have shown that a single anticyclone tends to drift away from a continental shelf. Thus, it is expected that the interaction of two anticyclones will be accompanied by such a drift.

We study the interaction of two identical anticyclones, with $q_{topo} = 0.3$. The regime diagram is presented in Figure 16. Compared with the interaction of two cyclones, two new regimes appear here; they are the drift of the two vortices away from the slope, without or with merger. In the case of merger, the critical distance can increase substantially, $d^* > 7$, for $d_c/R = 4$ (see an example of such a merger for two distant anticyclones in Figure 17).

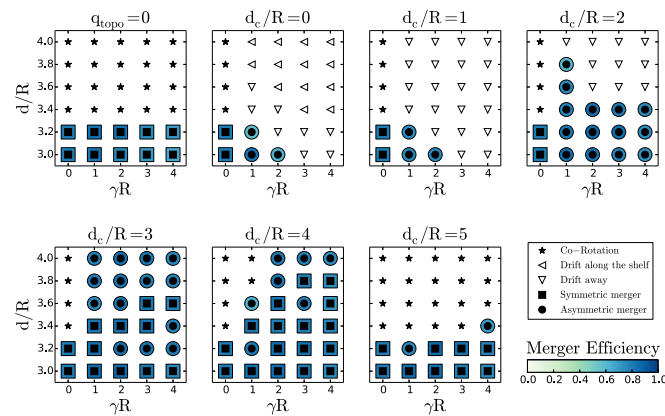


Figure 16. Regime diagram for the interaction of two surface anticyclones, in the $(\gamma R, d/R)$ plane, for fixed d_c/R (for each sub-plot). Black stars indicate co-rotation. Black squares for symmetric merger; black circles for asymmetric merger and triangles for vortex drift, away from the slope (triangle pointing down) or along the slope (triangle pointing left).

First, we present the drift of two anticyclones away from the slope for $d/R = 3.4$, $d_c/R = 1$, $\gamma R = 1$ in Figure 18. In this regime, one anticyclone remains near the slope while the other one drifts away from the slope (see Figure 18a). This evolution is due to the coupling of this anticyclone with a positive potential vorticity pole in the lower layer (see Figure 18b,c). This lower cyclone separates the two upper anticyclones. The upper layer anticyclone close to the slope interacts successively with a lower layer cyclone and then with a lower layer anticyclone. The other upper layer anticyclone drifts offshore, coupled as a heton with a bottom cyclone.

Next, we present the merger of two upper layer anticyclones, initially separated by $d = 3.8R$, in Figure 19. The two upper layer anticyclones start rotating, and the westernmost one tears a filament of lower layer fluid offshore of the shelf (see Figure 19a,b). This lower layer filament couples with this upper layer anticyclone and advects it towards the easternmost anticyclone. Thus, the two anticyclones merge and shed filaments in the upper layer. The lower layer filament, which had been torn away from the shelf, then wraps around the merged anticyclone (see Figure 19b,c). The vertical coupling between layers (Figure 19d) is maximal between the westernmost anticyclone and the lower layer filament.

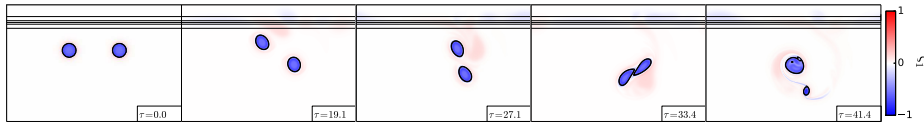


Figure 17. Merger of two anticyclones initially separated by $d = 7.2R$ for $\gamma = 3, d_c/R = 4.0$; time series of the upper layer relative vorticity (Equation (3)).

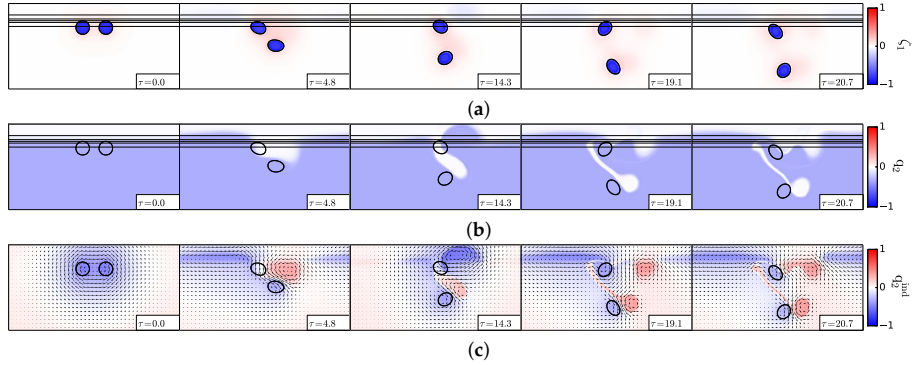


Figure 18. Drift of two anticyclones away from the slope for $d/R = 3.4, \gamma R = 1, d_c/R = 1$. (a) Upper layer relative vorticity (Equation (3)); (b) lower layer potential vorticity (Equation (2)); (c) lower layer velocity and “equivalent barotropic” potential vorticity (Equations (4) and (11)). In (a,b), the black contours indicate the topographic slope (Equation (12); straight lines) and the upper layer vorticity contours showing the two vortex evolution.

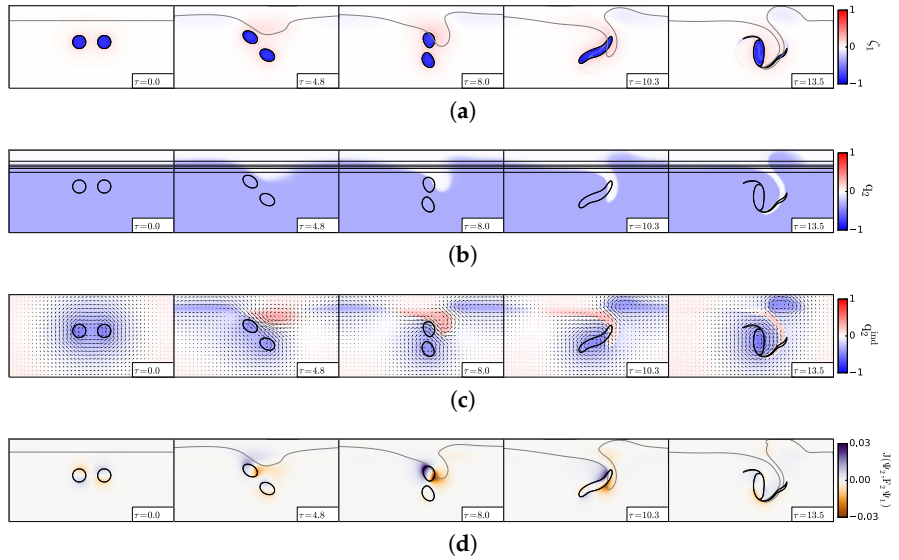


Figure 19. Merger of two anticyclones away from the slope for $d/R = 3.8, \gamma R = 1, d_c/R = 3$. (a) Upper layer relative vorticity (Equation (3)); (b) lower layer potential vorticity (Equation (2)); (c) lower layer velocity and “equivalent barotropic” potential vorticity (Equation (11)); (d) Jacobian term of layer coupling $F_2J(\psi_2, \psi_1)$. In (a,b,d), the black contours indicate the topographic slope (Equation (12); straight lines) and the upper layer vorticity contours showing the two vortex evolution.

6. Evolution of Tracer and Particles across the Slope

The advection of the passive tracer and of the particles injected in the flow has been studied for all the regimes analysed above (for both the cyclones and the anticyclones). We next illustrate this advection during the interaction of two cyclones for the regimes of merger and splitting shown in Figure 8.

The tracer evolution, from the initial state with positive unit value in the deep region and negative unit value over the shelf, shows two essential patterns (see Figure 20):

- (1) The tracer distribution mostly follows the lower layer vorticity front initially; its gradient forms a double front, which also follows the vorticity filaments. This occurs in both layers (see Figure 20a,b). The concentration of tracer often occurs where the lower layer strain is intense and aligned with the tracer gradient (see Figure 20c).
- (2) There is considerable stirring of the tracer in the area where the two cyclones have merged, over the shelf (see again Figure 20a,b). This stirring is related to the intensity of the shear in this region.

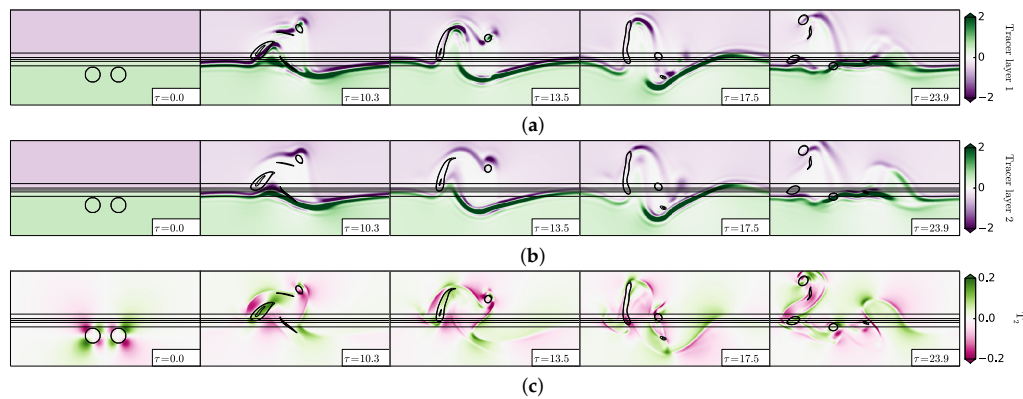


Figure 20. Tracer and strain evolution during the interaction of two cyclones for $d/R = 3.4$, $\gamma R = 3$, $d_c/R = 2$. (a) Tracer in the upper layer; (b) tracer in the lower layer; (c) strain field T_2 in the lower layer (Equation (6)). The black contours indicate the topographic slope (Equation (12); straight lines) and the upper layer vorticity contours showing the two cyclone evolution.

Next, we analyse the time evolution of the particles initially seeded in both regions (shallow and deep) and in the vortex cores.

Results are presented in Figure 21 for both layers. Note that, due to the strong layer coupling in this case ($\gamma R = 3.0$), the global pattern of particle evolution is similar in the two layers. The particles initially trapped in the cyclones are located only in the upper layer. Two main elements can be noted:

- (1) The particle evolution in the lower layer follows closely that of the tracer and of the lower layer potential vorticity, previously shown;
- (2) There are exchanges of particles between the two cyclones; the merged vortex contains particles from both of them, but with a majority of particles from the westernmost cyclone (that which is less deformed during the interaction). Similarly, the fragments (small vortex and filaments) mostly contain particles from the easternmost cyclone.

The number of particles crossing the slope inwards and outwards, in both layers, is shown in Figure 22. This number is maximal as the vortices cross the slope and merge. Then, it decreases as the merged upper layer cyclone elongates above the shelf, away from the slope. The number of particles crossing the slope reaches a nearly uniform value as two cyclones finally drift along the slope. The rotation associated with these cyclones generates a constant flux of particles in and out of the shelf.

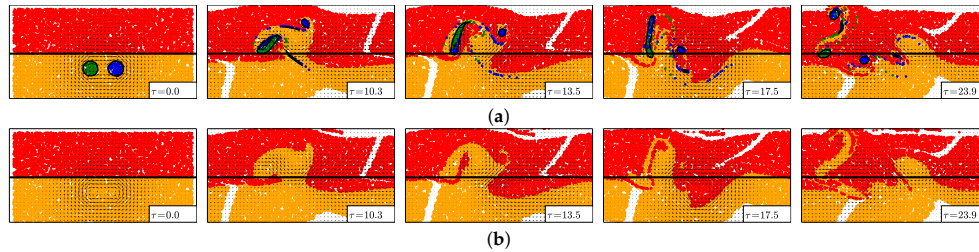


Figure 21. Particle evolution during the interaction of two cyclones for $d/R = 3.4$, $\gamma R = 3$, $d_c/R = 2$. (a) Particles in the upper layer; (b) particles in the lower layer. The black contours indicate the topographic slope (Equation (12); straight lines) and the upper layer vorticity contours showing the two cyclone evolution.

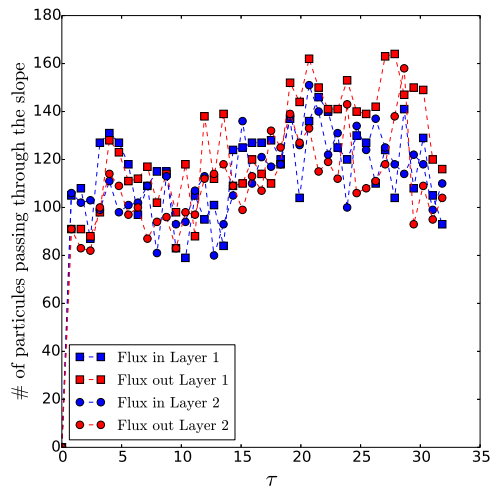


Figure 22. Number of particles crossing the slope inward and outward, in both layers, during the interaction of two cyclones for $d/R = 3.4$, $\gamma R = 3$, $d_c/R = 2$.

7. Discussion and Conclusions

We have analysed the impact of a bottom slope on the interaction of two vortices (potential vorticity anomalies) located in the upper layer of a two-layer quasi-geostrophic model. The cases of cyclones and of anticyclones were successively addressed.

In the presence of a bottom topography of moderate height, but lying initially far away from the slope, two cyclones merge only for $d/R < 3.3$ as above a flat bottom. However, then, they do not simply co-rotate around a fixed point; they also drift along the slope. An approximate steady state analytical solution was provided, which also shows that a large-scale deviation of the potential vorticity front appears over the topography. This was confirmed by numerical results.

When the two cyclones lie initially closer to the slope, the influence of the bottom topographic wave and vortices is more intense and leads to new dynamical regimes: asymmetric merger, splitting or drift towards the shelf. Asymmetric merger results from the different evolution of the two cyclones in their initial stage, as they co-rotate near the slope. The easternmost cyclone is elongated and can split into two parts, one of which can merge with the westernmost cyclone. Vortex elongation results from the shear induced by the bottom (topographic) vortices. A simple and approximate analytical model to assess the strength of this shear and the possible cyclone splitting is provided in Appendix B.

Globally, as the two cyclones are positioned initially closer to the slope, their critical merger distance increases, except when the two vortices lie exactly above the slope axis. Then, vortex separation can occur, again due to coupling with lower layer topographic vortices.

When the bottom topography is taller, two other regimes are observed, namely vortex drift and splitting, filamentation and asymmetric merger. The former occurs when the two cyclones are initially close to the slope, and it is due to the shearing effect of the bottom topographic vortices. The latter occurs when the two cyclones initially lie above the slope axis. It is a complex process by which the cyclones, being initially elongated, split; but all resulting fragments remain close to one another and finally merge together.

The interaction of two anticyclones brings about two other regimes, the drift of the two cyclones away from the slope, with or without merger. This drift is due to the tearing of a positive vorticity pole from the slope in the lower layer. This deep cyclone couples with one or both anticyclones and advects them away from the slope, as a heton. These results are qualitatively insensitive to horizontal resolution and to the choice of hyperviscosity, as long as the vortex profile is not altered by viscous effects.

Finally, the evolution of tracer closely follows that of the potential vorticity. In the lower layer, the tracer is mixed in the region of vortex merger, while tracer fronts follow the strong gradients of potential vorticity, in particular the filaments. Based on the experiments, the fluid (or tracer) from the deep domain can easily be advected onto the shelf and be efficiently mixed there by the two-cyclone interactions. On the other hand, the interaction of two anticyclones, remaining essentially in the deep domain, is less efficient in advecting offshore fluid from the shelf, except if the two anticyclones are initially very close to the shelf break (a radius away).

Note that there is similarity between these results and vortex merger near a bottom slope in a homogeneous fluid, with quasi-2D dynamics [28]. The cyclones drift shorewards, and the anticyclones' offshore and vortex merger are favoured (in particular asymmetric vortex merger). However, 2D dynamics allows less complexity in dynamical regimes and has a simpler dynamical mechanisms due to the absence of stratification. The present results also bear similarity with those of a previous study of vortex merger on the beta-plane [38], in that it also showed regimes of asymmetric vortex merger for two vortices initially more distant than $3.3 R$. This was explained in that case by the beta drift of the two vortices, which could bring them close to each other, and by the energy loss by the vortices to the Rossby wave field.

Though this study already provided new results, it will have to be extended to address other important questions. Firstly, it would be interesting to use a quasi-geostrophic model with a finer vertical resolution (e.g., with three layers or with a continuous stratification) to evaluate the vertical deformation of the upper layer vortices during the interaction and also the three-dimensional structure of the deep potential vorticity poles. Note that secondary instabilities can then occur and split the vortices before they can interact; the results can be different [21].

Secondly, the case of very tall topographies (when the step height is comparable with the lower layer thickness) should be addressed with a primitive equation model. In this model, inertia-gravity waves and asymmetry between cyclone and anticyclone dynamics (the representation of which is banned by the geostrophic approximation in our model) may modify the present results. In particular, very tall topographies act as walls for the flow, associated with the influence of "ghost vortices" across the wall.

Associating both dynamical elements (primitive equation dynamics and fine vertical resolution) would allow the study of bottom boundary layers on the slope, which have been shown to generate submesoscale vortices [32].

Studying the interaction of smaller and more intense vortices than the mesoscale ones, that is vortices with $Ro \sim 1$ and/or $Bu \sim Ro$, would provide even richer phenomenology, including strong topographic vortices able to break the initial vortices, strong dependence to the vertical location of the initial vortex cores and again cyclone/anticyclone asymmetry in terms of stability or ability to interact (even in the absence of a shelf).

Lastly, this study will also have to be extended to reach the complexity of oceanic situations. Several dynamical elements will be added for oceanographic application: in particular, unequal layer thicknesses, capes or promontories in the shelf, the planetary beta effect, which supports planetary Rossby waves. All these effects can impact vortex merger near a coast as seen south of the Arabian Peninsula. However, it is presently difficult to make predictions from our simple study for oceanic situations with much larger complexity. This will be the subject of further studies.

Acknowledgments: This work is a contribution to the PHYSINDIEN research program funded by SHOM (French Hydrographic and Oceanographic Service). PHYSINDIEN investigates the structure and dynamics of mesoscale features in the Arabian Sea and adjacent seas.

Author Contributions: Xavier Carton and Jean N. Reinaud conceived of and designed the experiments. Charly de Marez performed the experiments. Xavier Carton, Charly de Marez, Mathieu Morvan and Jean N. Reinaud analysed the results and wrote the paper.

Conflicts of Interest: The authors declare no conflict of interest.

Appendix A. Analytical Model of an Upper Layer Point Dipole Interaction with a Bottom Step-Like Shelf, in the Long-Range Limit

We compute the effect of two point vortices in the upper layer, on a topographic vorticity front in the lower layer, in the long-range limit. Here, the topography is a step with a vorticity jump $q_{topo} = -f_0 h_{b0}/H_2$. The vortices and topography lie in the same position as in Figure 2; the two vortices are pointwise: they have a null radius, but a finite strength Γ_1 (area integral of potential vorticity). The distance d between the two vortices is assumed very small compared with their distance d_c to the topographic step; this justifies the long-range approximation for calculations.

In that respect, we can use the lowest order of a dipolar expansion of the stream function induced by the two upper layer vortices in the lower layer. Similarly, we can apply the Gauss theorem to the vorticity distribution. Thus, the far field of the stream function, in the lower layer, at the topographic step, is:

$$\psi(x, y = 0) = \frac{h_1 \Gamma_1}{2\pi} \text{Log}[x^2 + d_c^2] \quad (\text{A1})$$

We can now follow the theory of the vortex-potential vorticity front interaction developed in Stern and Flierl (1987) [39], in the particular case where there is no basic zonal flow. Using the linear theory (for large distances between the point dipole and the front), the meridional velocity of the front v_2' is equal to and opposite of the meridional velocity induced by the vortex pair v_{2p} . Calling $\eta_2(x)$ the deviation of the potential vorticity interface from its initial position $y = 0$, its shape is defined by the Fredholm integral equation of the first kind:

$$\int_{-\infty}^{+\infty} \left[\frac{1}{x' - x} + \gamma K_1(\gamma|x' - x|) \right] \eta_2(x') dx' = \frac{4h_1 \Gamma_1 x}{q_{topo}(x^2 + d_c^2)} \quad (\text{A2})$$

where the integral excludes $x' = x$.

In the absence of the modified Bessel function, the integral is simply π times the Hilbert transform of η_2 , while the right-hand side is $4h_1 \Gamma_1 d_c / q_{topo}$ times the Hilbert transform of $1/(x^2 + d_c^2)$. Then, one easily recovers a result similar to that of Stern and Flierl (1987) [39]:

$$\eta_2(x) = \frac{4h_1 \Gamma_1 d_c}{\pi q_{topo}(x^2 + d_c^2)} \quad (\text{A3})$$

The presence of the modified Bessel function renders the problem more difficult mathematically (the Fourier transform of η_2 is a complicated function). A rough approximation of the solution can be obtained using the asymptotic expansion $K_1(x) \sim 1/x$, which is valid when x is small. Note that,

unfortunately, $K_1(x) \ll 1/x$ when x is large. Under this approximation, the solution would be half that written above.

Further work should try to provide a more accurate approximation.

We also recall that, in a two-layer model with zero mean flow, and a bottom topographic step of height h_{b0} , the phase speed of free topographic waves is:

$$c = -\frac{f_0 R_d h_{b0} H}{H_2^2} \quad (\text{A4})$$

This can be obtained by linearizing the potential vorticity equations (Equations (1) and (2)) around a state of rest.

Appendix B. Qualitative Model for Upper Layer Vortex Splitting in the Shear Exerted by Two Bottom Topographic Vortices

Let us assume that the topographic wave has broken into two topographic vortices, one over the shelf and one in the deep region, near the slope. Call R_t the radius of these topographic vortices. We assume that these two vortices lie at a distance $2R_t$ from each other. Their potential vorticity is $q_{topo} = f_0 h_b / H_2$. Finally, we call $\Gamma_2 = \pi R_t^2 q_{topo}$ the strength of each vortex.

The velocity induced by one such vortex in the upper layer is:

$$v_1 = \frac{h_2 \Gamma_2}{2\pi} \left[\frac{1}{r} - \gamma K_1(\gamma r) \right] \quad (\text{A5})$$

From this, we can calculate the shear exerted by these two topographic vortices, in the upper layer, at the mid-point between them (point of maximal shear), that is for $r = R_t$. This shear is:

$$\frac{dv_1}{dr} = h_2 q_{topo} \left[-1 + (\gamma R_t)^2 \left(\frac{1}{\gamma R_t} K_1(\gamma R_t) - K_0(\gamma R_t) \right) \right] \quad (\text{A6})$$

It is easy to see that for large γR_t , the terms with the two modified Bessel functions are small, so that the shear reaches the value $h_2 q_{topo}$, while if $\gamma R_t \sim 1$, the modified Bessel function term is positive and decreases the shear.

For $q_{topo} = 0.3$ and $\gamma R_t = 3.0$, the upper layer shear is then about 0.15 compared with $q_1 = 1$. This shear intensity is then sufficient to split the upper layer vortex (see also [2]).

References

1. Richardson, P.L.; Bower, A.S.; Zenk, W. A census of Meddies tracked by floats. *Prog. Oceanogr.* **2000**, *45*, 209–250.
2. Carton, X. Hydrodynamical modeling of oceanic vortices. *Surv. Geophys.* **2001**, *22*, 179–263.
3. Aguiar, A.C.B.; Peliz, A.; Carton, X. A census of meddies in a long-term high-resolution simulation. *Prog. Oceanogr.* **2013**, *116*, 80–94.
4. Masina, S.; Pinardi, N. Merging of barotropic symmetric vortices. A case study for gulf stream rings. *Il Nuovo Cimento C* **1991**, *14*, 539–553.
5. Schultz-Tokos, K.L.; Hinrichsen, H.H.; Zenk, W. Merging and migration of two meddies. *J. Phys. Oceanogr.* **1994**, *24*, 2129–2141.
6. Carton, X.; Daniault, N.; Alves, J.; Chérubin, L.; Ambar, I. Meddy dynamics and interaction with neighboring eddies southwest of Portugal : Observations and modeling. *J. Geophys. Res.* **2010**, *115*, doi:10.1029/2009JC005646.
7. L'Hegaret, P.; Carton, X.; Ambar, I.; Menesguen, C.; Hua, B.L.; Chérubin, L.; Aguiar, A.; Le Cann, B.; Daniault, N.; Serra, N. Evidence of Mediterranean Water dipole collision in the Gulf of Cadiz. *J. Geophys. Res.* **2014**, *119*, 5337–5359.

8. Overman, E.A., II; Zabusky, N.J. Evolution and merger of isolated vortex structures. *Phys. Fluids* **1982**, *25*, 1297–1305.
9. Dritschel, D.G. The stability and energetics of corotating uniform vortices. *J. Fluid Mech.* **1985**, *157*, 95–134.
10. Dritschel, D.G. The nonlinear evolution of rotating configurations of uniform vorticity. *J. Fluid Mech.* **1986**, *172*, 157–182.
11. Carton, X. On the merger of shielded vortices. *EPL (Europhysics Letters)* **1992**, *18*, 697.
12. Melander, M.V.; Zabusky, N.J.; McWilliams, J.C. Asymmetric vortex merger in two dimension: Which vortex is “victorious”? *Phys. Fluids A* **1987**, *30*, 2610–2612.
13. Melander, M.V.; Zabusky, N.J.; McWilliams, J.C. Symmetric vortex merger in two dimensions: Causes and conditions. *J. Fluid Mech.* **1988**, *195*, 303–340.
14. Yasuda, I.; Flierl, G.R. Two-dimensional asymmetric vortex merger: Merger dynamics and critical merger distance. *Dyn. Atmos. Oceans* **1997**, *26*, 159–181.
15. Yasuda, I.; Flierl, G.R. Two-dimensional asymmetric vortex merger: Contour dynamics experiments. *J. Oceanogr.* **1995**, *51*, 145–170.
16. Meunier, P.; Ehrenstein, U.; Leweke, T.; Rossi, M. A merging criterion for two-dimensional co-rotating vortices. *Phys. Fluids* **2002**, *14*, 2757–2766.
17. Griffiths, R.W.; Hopfinger, E.J. Coalescing of geostrophic vortices. *J. Fluid Mech.* **1987**, *178*, 73–97.
18. Verron, J.; Valcke, S. Scale-dependent merging of baroclinic vortices. *J. Fluid Mech.* **1994**, *264*, 81–106.
19. Valcke, S.; Verron, J. Interactions of baroclinic isolated vortices: The dominant effect of shielding. *J. Phys. Oceanogr.* **1997**, *27*, 524–541.
20. Sokolovskiy, M.A.; Verron, J. Finite-core hetons: Stability and interactions. *J. Fluid Mech.* **2000**, *423*, 127–154.
21. Von Hardenberg, J.; McWilliams, J.C.; Provenzale, A.; Shchepetkin, A.; Weiss, J.B. Vortex merging in quasi-geostrophic flows. *J. Fluid Mech.* **2000**, *412*, 331–353.
22. Dritschel, D.G. Vortex merger in rotating stratified flows. *J. Fluid Mech.* **2002**, *444*, 83–101.
23. Reinaud, J.N.; Dritschel, D.G. The merger of vertically offset quasi-geostrophic vortices. *J. Fluid Mech.* **2002**, *469*, 297–315.
24. Reinaud, J.N.; Dritschel, D.G. The critical merger distance between two co-rotating quasi-geostrophic vortices. *J. Fluid Mech.* **2005**, *522*, 357–381.
25. Bambrey, R.R.; Reinaud, J.N.; Dritschel, D.G. Strong interactions between two co-rotating quasi-geostrophic vortices. *J. Fluid Mech.* **2007**, *592*, 117–133.
26. Ozugurlu, E.; Reinaud, J.N.; Dritschel, D.G. Interaction between two quasi-geostrophic vortices of unequal potential-vorticity. *J. Fluid Mech.* **2008**, *597*, 395–414.
27. McDonald, N.R. The motion of an intense vortex near topography. *J. Fluid Mech.* **1998**, *367*, 359–377.
28. Carton, X.; Morvan, M.; Reinaud, J.N.; Sokolovskiy, M.A.; L'Hegaret, P.; Vic, C. Vortex Merger near a Topographic Slope in a Homogeneous Rotating Fluid. *Reg. Chaot. Dyn.* **2017**, *22*, 455–478.
29. Dunn, D.C.; McDonald, N.R.; Johnson, E.R. The motion of a singular vortex near an escarpment. *J. Fluid Mech.* **2001**, *448*, 335–365.
30. Zhang, Y.; Pedlosky, J.; Flierl, G.R. Shelf Circulation and Cross-Shelf Transport out of a Bay Driven by Eddies from an Open-Ocean Current. Part I: Interaction between a Barotropic Vortex and a Steplike Topography. *J. Phys. Oceanogr.* **2011**, *41*, 889–910.
31. Molemaker, M.J.; McWilliams, J.C.; Dewar, W.K. Submesoscale instability and generation of mesoscale anticyclone near a separation of the California Undercurrent. *J. Phys. Oceanogr.* **2015**, *45*, 613–629.
32. Vic, C.; Rouillet, G.; Capet, X.; Carton, X.; Molemaker, M.J.; Gula, J. Eddy-topography interactions and the fate of the Persian Gulf Outflow. *J. Geophys. Res.* **2015**, *120*, 6700–6717.
33. Polvani, L.M.; Zabusky, N.-J.; Flierl, G.R. Two layer geostrophic vortex dynamics. Part 1. Upper layer V-states and merger. *J. Fluid Mech.* **1989**, *205*, 215–242.
34. Gryanik, V.M. Dynamics of localized vortex perturbations on vortex charges, in a baroclinic fluid. *Izv. Atmos. Ocean. Phys.* **1983**, *19*, 347–352.
35. Gryanik, V.M. Dynamics of singular geostrophic vortices in a two-layer model of the atmosphere (ocean). *Izv. Atmos. Ocean. Phys.* **1983**, *19*, 171–179.
36. Hogg, N.G.; Stommel, H.M. The Heton, an Elementary Interaction Between Discrete Baroclinic Geostrophic Vortices, and Its Implications Concerning Eddy Heat-Flow. *Proc. Royal Soc. A* **1985**, *397*, 1812, doi:10.1098/rspa.1985.0001.

37. Griffiths, R.W.; Hopfinger, E.J. Experiments with baroclinic vortex pairs in a rotating fluid. *J. Fluid Mech.* **1986**, *173*, 501–518.
38. Bertrand, C.; Carton, X. Vortex merger on the beta plane. *C. R. Acad. Sci. Paris Ser. II* **1993**, *316*, 1201–1206.
39. Stern, M.E.; Flierl, G.R. On the interaction of a vortex with a shear flow. *J. Geophys. Res. C* **1987**, *92*, 10733–10744.



© 2017 by the authors. Licensee MDPI, Basel, Switzerland. This article is an open access article distributed under the terms and conditions of the Creative Commons Attribution (CC BY) license (<http://creativecommons.org/licenses/by/4.0/>).

6.4 Conclusion sur la fusion de tourbillons

Dans ce chapitre, nous avons discuté d'une partie des interactions entre tourbillons qui se produisent en mer d'Arabie, les fusions. Plutôt que de décrire des événements particuliers observés, nous avons décrit le processus de fusion de manière générale, notamment en le remettant en contexte dans l'océan global. Avec ce type d'étude paramétrique, nous avons ainsi pu décrire les mécanismes à l'oeuvre dans la fusion de tourbillons, qu'ils se produisent loin des côtes, ou proche d'un talus continental. Les résultats principaux sont alors ceux-ci :

- La fusion de tourbillons dans l'océan ouvert est impactée par la présence de tourbillons adjacents, et de l'effet- β .
- Comparer la distance critique de fusion des tourbillons dans les zones turbulentes au centre des bassins, avec des études idéalisées de fusion de deux tourbillons isolés sur un plan- f omet les mécanismes principaux impliqués dans la fusion.
- Lorsque les tourbillons sont proches d'un talus continental, la génération d'ondes de Rossby topographiques génère de nombreux autre régimes, et conduit à la réduction ou à l'augmentation de la distance critique de fusion dépendamment de la polarité, et de la position des tourbillons par rapport au talus.

CONCLUSION ET PERSPECTIVES

Dans ce manuscrit de thèse, nous nous sommes intéressés aux processus en jeu à méso et sous-méso-échelle dans lesquels les tourbillons de mer d'Arabie sont impliqués.

Nous avons tout d'abord présenté la structure tridimensionnelle des tourbillons de méso-échelle en mer d'Arabie, grâce à l'utilisation conjointe de mesures altimétriques et de mesures *in situ*. Cela a permis d'accroître la connaissance de la structure typique du champs tourbillonnaire dans cette région jusque là seulement décrite en surface ou ponctuellement en profondeur. De ce travail, il apparaît que dans le golfe d'Oman et le golfe d'Aden, les eaux sont moins salées au centre des tourbillons qu'à leur périphérie, suggérant que les tourbillons présents dans les golfes sont générés en mer d'Arabie, puis advectent les masses d'eaux salées en leur coeur. Du fait de leur influence profonde, les tourbillons de méso-échelle ont donc, en moyenne, un impact important sur la distribution des masses d'eaux salées profondes de mer d'Arabie. Des tourbillons composites calculés à partir de nombreux tourbillons dans le nord de la mer d'Arabie, montrent une structure représentative des tourbillons fréquemment rencontrés dans cette région, sans hypothèses *a priori* sur leur structure.

Partant de ce constat, nous avons ensuite décrit le cycle de vie des tourbillon en mer d'Arabie, sous l'hypothèse que ceux ci-sont isolés du reste de la dynamique, en utilisant le tourbillon composite susmentionné. Cela a permis de réaliser des simulations très idéalisées, mais pour la première fois représentatives de la dynamique tourbillonnaire d'une région particulière. Nous avons ainsi vu que lorsqu'ils sont isolés sur le plan- f , les tourbillons méso-échelle cycloniques typiques de mer d'Arabie se déforment sous l'action d'une instabilité mixte barotrope/barocline. La croissance de cette instabilité est plus lente dans le cas d'anticyclones, et plus rapide sur le plan- β . Cependant, à long terme, la destruction du tourbillon est prévenue par le phénomène de restabilisation non-linéaire. Cela explique donc en partie pourquoi dans cette région les tourbillons peuvent rester cohérent, et avoir des durées de vie de plusieurs années. Après restabilisation, des instabilités secondaires sont néanmoins spontanément générées du fait de la structure instable du tourbillon. Cela conduit à la génération de structures de sous-méso-échelle intensifiées en surface. Nous avons également montré que lorsque ce type de tourbillons de méso-échelle se propage en direction d'une frontière ouest solide sous l'influence de l'effet- β , une asymétrie cyclone/anticyclone apparaît : les tourbillons cycloniques se propagent de manière stationnaire vers le sud, alors que les anticyclones vont avoir tendance à osciller autour d'une latitude moyenne, et générer des structures profondes de sous-méso-échelle par interaction anticyclone-ondes

de Kelvin. Ces résultats donnent des clefs à la compréhension de la présence d'un tourbillon cyclonique de sousmésos-échelle observé durant la campagne PHYSINDIEN 2019. Cette observation est la première observation d'un cyclone profond de sousmésos-échelle d'une telle intensité.

Comme les tourbillons de méso-échelle ne sont en réalité pas isolés du reste du champ tourbillonnaire, très dense en mer d'Arabie, nous avons finalement discuté d'une partie des interactions entre tourbillons qui se produisent : les fusions. Plutôt que de décrire des événements particuliers observés, nous avons décrit le processus de fusion de manière générale, notamment en le remettant en contexte dans l'océan global. Avec ce type d'étude paramétrique, nous avons ainsi pu décrire les mécanismes à l'oeuvre dans la fusion de tourbillons, qu'ils se produisent loin des côtes, ou proche d'un talus continental. Le résultat principal de cette étude est que la fusion de tourbillons dans l'océan ouvert est fortement impactée par la présence des tourbillons adjacents au système fusionnant, ainsi que par l'effet- β . De ce fait, la comparaison habituellement faite entre la distance critique pour laquelle deux tourbillons dans l'océan fusionnent, et celle obtenue à partir d'études idéalisées de fusion de deux tourbillons isolés sur un plan- f (les études classiques réalisées théoriquement et numériquement) omet les paramètres principaux impliqués dans la fusion : le champ turbulent ambiant et l'effet- β . De plus, lorsque l'on ajoute la présence d'un talus continental aux abords des tourbillons qui fusionnent, la génération d'ondes de Rossby topographiques conduit à la réduction ou à l'augmentation de la distance critique de fusion, dépendamment de la polarité et de la position des tourbillons par rapport au talus. Cela ajoute donc de la complexité au phénomène de fusion, dont la compréhension complète dans le contexte océanique se révèle un défi toujours actuel.

Les travaux réalisés au cours de cette thèse ont permis d'augmenter nos connaissances sur la dynamique des tourbillons en mer d'Arabie. Nous n'avons pas répondu à une question précise car la problématique est vaste et constitue un pan à part entière de l'océanographie physique. Afin de compléter ces travaux de thèse, de nombreux axes peuvent être envisagés. Il serait erroné de ne donner que quelques axes d'études supplémentaires en assurant qu'ils permettront une compréhension totale de la dynamique de cette région. En revanche il est intéressant de noter qu'elles sont les avancées futures qui permettront d'aller plus loin dans cette direction.

Premièrement l'acquisition de nouvelles données *in situ* grâce aux moyens d'observations autonomes (ARGO, bouées dérivantes...) déployés actuellement est prometteuse. Certaines régions de mer d'Arabie, comme le golfe d'Aden, sont notamment pauvres en données, et la structure des tourbillons de méso-échelle en profondeur est mal connue. Le déploiement de nouveaux appareils, notamment par le SHOM, permettra l'acquisition de nouvelles données, et ainsi l'échantillonnage de manière plus importante des tourbillons de ces régions. De plus, la réalisation de campagnes océanographiques dans des régions riches en phénomènes de sousmésos-échelle, comme ceux présentés dans la section 5.3

permettront de valider et comparer les phénomènes étudiés dans les simulations numériques, qui ne reposent pour l'instant que sur des suppositions théoriques, et dont la paramétrisation peut s'avérer arbitraire par construction.

Deuxièmement, la mise en place de simulation réalistes haute résolution de la région dans la lignée de Vic et al. (2014) ou Morvan et al. (2020) permettrait de décrire de manière tri-dimensionnelle les phénomènes de méso et sous-méso-échelle échantillonnés grâce aux mesures *in situ*, et qui sont pour l'heure difficile à discuter de manière statistique. Ce genre de simulations pourra également permettre de remettre en contexte les analyses effectuées dans les simulations idéalisées présentées dans ce manuscrit, et qui s'émancipent volontairement de la multitude de phénomènes présent dans l'océan réel. La réalisation de ce genre de simulation serait très pertinente dans les régions où a par exemple été observé le tourbillon cyclonique de sous-méso-échelle présenté dans la section 5.3. Cela permettrait de discuter quantitativement et statistiquement l'impact de la génération de sous-méso-échelle en profondeur sur l'export de RSW dans l'ouvert de la mer d'Arabie. De plus, la réalisation de simulations biogéochimiques dans les régions côtières où les tourbillons sont omniprésents, comme au large d'Oman, permettrait de quantifier l'impact de la dynamique tourbillonnaire sur l'évolution des écosystèmes marins. Cela permettrait de discuter quantitativement de l'importance des tourbillons pour les activités de pêche qui nourrissent des millions de personnes sur les cotes de la mer d'Arabie.

SUR L'IMPACT ACOUSTIQUE DES STRUCTURES TOURBILLONNAIRES

Comme mentionné dans la section 2, la mer d'Arabie est un lieu stratégique, et d'intérêt économique pour le Moyen-Orient, et le monde économique. Les pays du Golfe (Arabie Saoudite, Émirats Arabes Unis, Irak, Iran, Koweït, Oman, Qatar) possédant la moitié des ressources d'hydrocarbure mondiale, l'exportation au niveau mondiale de ces ressources fait du golfe d'Oman en particulier l'artère la plus importante en matière de transport d'hydrocarbure. Couplé aux problématiques de piraterie au large du Yémen et de la Somalie, la mer d'Arabie est donc une zone d'intérêt militaire prioritaire, où la circulation des bâtiments militaires est un enjeu stratégique de la flotte. Les tourbillons océaniques, omniprésents dans cette région, impactent les propriétés dynamiques et acoustiques du milieu.

En effet, les propriétés thermohalines du milieu (la température et la salinité) sont modifiées par la présence de tourbillons : des eaux plus (resp. moins) denses sont présentes en leur coeur pour des cyclones (resp. anticyclones). La vitesse du son dans le milieu marin (la célérité c) étant une fonction de ces variables et de la pression $c(T, S, P)$, la présence de tourbillons modifie le profil de célérité. Cette modification peut alors modifier de manière significative la propagation du signal sonore sous marin. Or, sur un théâtre d'opération militaire, l'outil acoustique est primordial pour la sécurité des bâtiments : les navires de surface ont besoin de détecter la potentielle présence de menaces sous-marines, et les navires sous-marins ont besoin de surveiller la surface pour les mêmes raisons évidentes. Sous l'eau, seule la surveillance acoustique est possible, et la présence d'un tourbillon de méso-échelle peut théoriquement permettre à un sous-marin de rester indétectable pour une frégate ennemie. Ainsi, dans une région d'intérêt militaire majeur comme la mer d'Arabie, la connaissance des structures de méso-échelle permet d'anticiper les potentielles modifications de la propagation du son, et donc déterminer quelles sont les structures qui sont à *risque* pour les bâtiments militaires.

Le principal impact de la modification du profil de célérité sur la propagation sonores est la création ou disparition de *chenaux acoustiques*. En effet, la présence de gradients verticaux (ou non) de célérité sur la verticale va générer des réflexions des rayons acoustiques, et ainsi créer des niveaux d'im-

perméabilité au signal sonore.

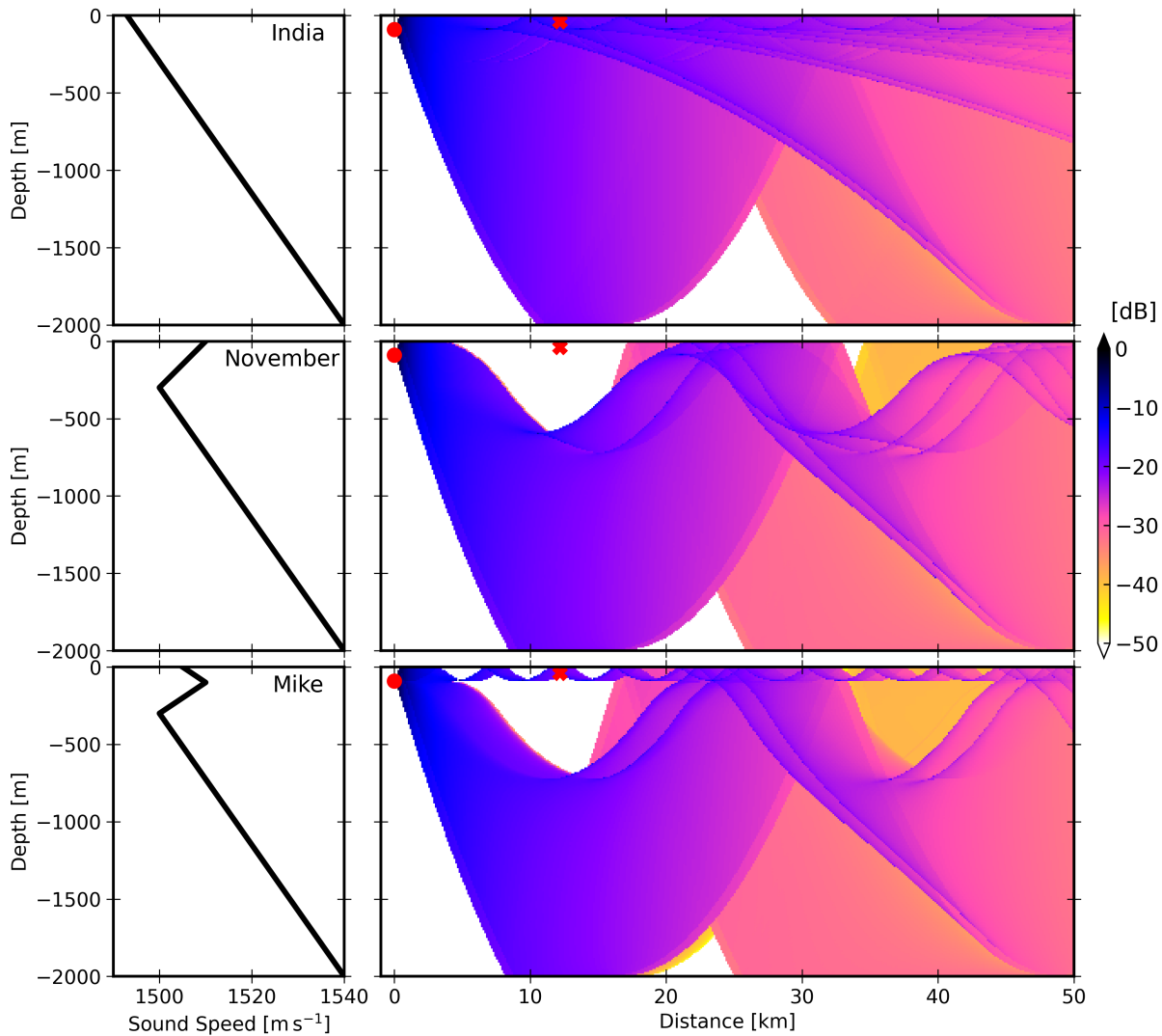


FIGURE A.1 – Atténuation du signal acoustique en fonction du profil de célérité. (gauche) Profils de célérité en fonction de la profondeur. (droite) Champs d'atténuation du signal acoustique prédit par le modèle de propagation acoustique Bellhop (Etter, 2018) pour le profil de célérité 1D correspondant. Le point rouge indique la position de la source (par exemple un sous-marin émettant un bruit de moteur), et la croix rouge la position d'un navire de surface cherchant à détecter des signaux acoustiques sous-marins.

Dans un milieu où le profil de célérité est constant horizontalement, mais varie avec la profondeur (cas 1D), trois profils verticaux typiques de célérité peuvent être définis : India (variation constante de

célérité), November (un changement de signe du gradient de célérité) et Mike (deux changement de signe du gradient de célérité), voir Fig. A.1(gauche). Dans l'océan profond au repos, les profils moyens de célérité sont généralement du type November ou Mike, avec une ou plusieurs inversion du gradient proche de la surface dû à la présence d'une thermocline ou d'un front de température. La présence de deux inversions de gradient proche de la surface (profil Mike) génère un chenal acoustique en surface, dans lequel le signal acoustiques est piégé et peu atténué, voir Fig. A.1(droite). Ainsi, un sous-marin émettant un son à la position indiquée par le point rouge dans Fig. A.1(droite) ne sera pas détecté par une frégate en surface à la position indiquée par la croix rouge dans le cas d'un profil November, mais sera détecté dans le cas d'un profil Mike (car un chenal acoustique en surface aura été créé).

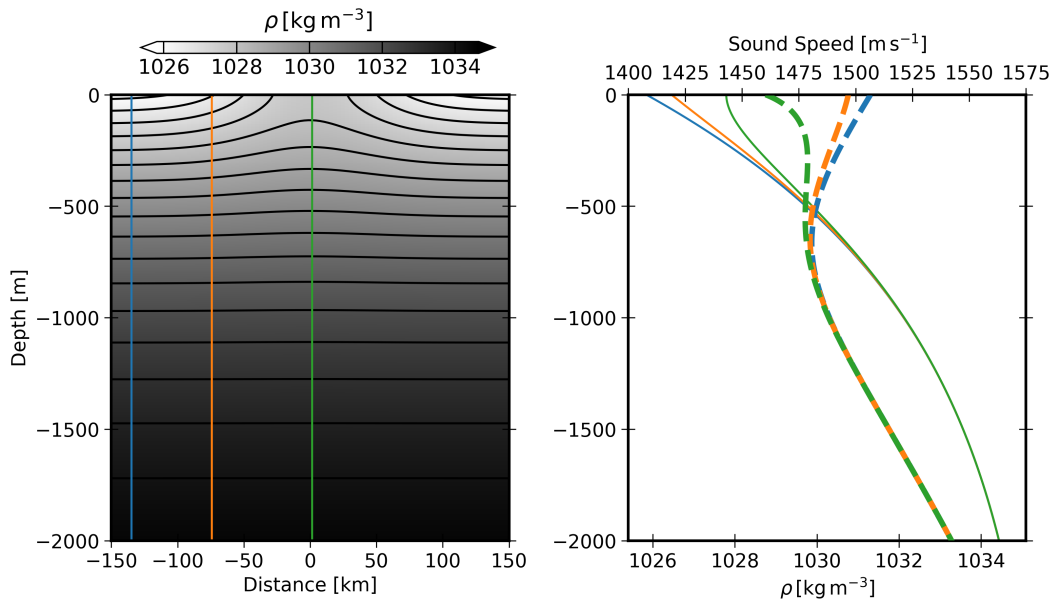


FIGURE A.2 – (Gauche) Section verticale de densité d'un tourbillon cyclonique théorique. (Droite) Profils de densité (traits pleins) et de célérité associée (traits gras pointillés) aux positions indiquées par les lignes de couleur dans le panneau gauche.

Les structures de méso et sousméso-échelle dans l'océan modifient la stratification ambiante, et de fait le profil de célérité local. Pour illustrer l'impact acoustique d'une structure de méso-échelle, nous présentons le cas théorique d'un tourbillon cyclonique d'anomalie de densité Gaussienne, plongé dans une stratification ambiante exponentielle, voir Fig. A.2. La présence de ce dernier modifie drastiquement le comportement acoustique du milieu. En effet, la stratification ambiante est caractérisée par un profil de célérité November : il n'y a pas de chenal acoustique en surface, et le son se propagera de manière privilégiée en profondeur. Au centre du tourbillon en revanche, l'anomalie de densité créé

une inversion du gradient vertical de célérité, et le profil est alors du type Mike : un chenal de surface est présent en surface. Ainsi, la présence de ce tourbillon peut causer la détection d'un bâtiment militaire présent en son centre, et cette structure est donc à risque. La variété de structure à risque d'un point de vue acoustique est très grande. Ce risque dépend (1) de la stratification ambiante et (2) de l'anomalie de densité créé par la présence de la structure. Le risque sera principalement caractérisé par un changement du type de profil de célérité en fonction de la position par rapport au centre de la structure.

De manière opérationnelle, la détermination du risque acoustique sur un théâtre d'opération se déroule comme suit. Le bâtiment mesure à sa position des profils de température et de salinité afin de connaître de manière précise le profil de célérité sous la coque. Ensuite, des profils de célérité sont estimés au coeur et en périphérie des structures dynamiques alentours. Des modèles mathématiques empiriques sont utilisés pour ajuster ces profils et obtenir un champs 2D de célérité. Ainsi, du fait de la variété de structures et de stratifications ambiantes, et de l'évolution rapide des structures océanique, l'impact de la dynamique sur la propagation acoustique est la plupart du temps estimé en temps réel sur le théâtre d'opération.

Dans le cadre de cette thèse, nous avons étudié une variété importante de structures de méso et de sous-méso-échelle. Nous avons montré que la vision climatologique (*i.e.* une vision moyenne et "lissée") des structures peut s'avérer erronée dans des cas réel, du fait de la présence d'instabilités géophysiques ou de structures adjacentes qui modifient la dynamique. Ces travaux sont d'intérêt pour la prédiction de l'impact acoustique des structures. En effet, la connaissance de nouveaux types de structures pouvant intervenir dans la dynamique locale de la mer d'Arabie permet d'anticiper de nouvelles situations à risque.

Les structures de méso-échelle étudiées dans la section 4, et notamment les composites extraits, sont par définition des moyennes spatiotemporelles regroupant des dizaines de structures. Ainsi, les profils verticaux au coeur et en périphérie des tourbillons étudiés sont très lisses. L'impact acoustique de ce genre de profils moyen présente peu d'intérêt car les gradients verticaux de célérité ne vont être que très peu être modifiés par la présence de tels structures. De plus, l'étude de l'impact acoustique ayant pour but une application opérationnelle, il est intéressant d'étudier des événements particuliers, plutôt que des situations moyennes.

Nous discutons ci-dessous qualitativement l'impact acoustique de trois situations particulières étudiées au cours de cette thèse : la déstabilisation d'un tourbillon cyclonique, la présence d'un cyclone profond de sous-méso-échelle et la fusion de deux tourbillons en présence d'un champs externe de tourbillons. Le lecteur se rendra compte que l'impact de tels événements est très limité, et ne mérite donc pas une étude approfondie. Nous donnons simplement ici des pistes d'exploration aux futures

études acoustiques menées dans cette direction.

Impact de la déstabilisation d'un tourbillon cyclonique sur le profil périphérique Nous avons montré dans la section 5.1 que malgré le fait qu'il ne puisse pas être détecté par satellite, un champ turbulent de sousmésos-échelle peut être présent en périphérie des tourbillons de méso-échelle en mer d'Arabie, du fait d'instabilités barotropes, baroclines et symétriques. Ainsi, la vision schématique de la Fig. A.2(gauche) utilisé habituellement pour discuter de l'impact acoustique d'une structure peut être erronée. Dans un cas comme celui présenté dans la section 5.1, le profil périphérique au tourbillon (ligne orange dans la Fig. A.2) peut potentiellement être modifié par la présence de fronts et de tourbillons de sousmésos-échelle. Il faudrait ainsi prendre en compte ce type d'instabilité (qui modifie potentiellement le profil de célérité aux abords du tourbillon) dans l'étude de l'impact de ces structures sur la propagation du son.

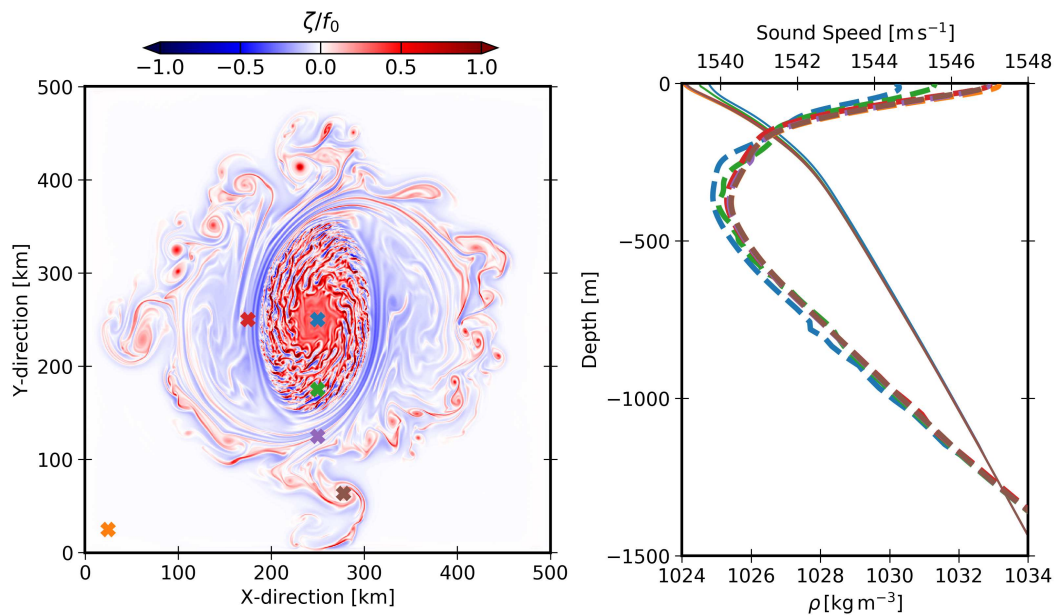


FIGURE A.3 – (Gauche) Vorticité relative normalisée à la surface, après 300 jours de simulation ($\Delta x = 500\text{m}$, voir détails de la simulation dans la section 5.1). (Droite) Profils de densité (traits pleins) et de célérité associée (traits gras pointillés) aux positions indiquées par les croix de couleur dans le panneau gauche.

En pratique, les structures présentes en périphérie du tourbillon étudié dans la section 5.1 modifient très peu le profil de célérité. Bien que ces structures soient très intenses ($|\zeta/f_0| > 1$), elles sont localisées à la surface, et ont des signatures en densité faibles comparativement au champ dominant de

méso-échelle (voir Fig. A.3). Les profils de célérité sont donc peu modifiés par ce champ de sousmésos-échelle, et l'ensemble des profils sont du type Mike, avec un chenal de surface très mince, d'épaisseur $O(10)$ m. Le cas étudié ici présente donc un faible risque stratégique. En revanche, il illustre le fait que le champs de sousmésos-échelle présent en périphérie de la plupart des tourbillons doit *a priori* être pris en compte lorsque l'on choisi le profil de célérité de transition entre le coeur du tourbillon et le milieu au repos. Cette problématique est une voix d'amélioration possible pour la prédiction des risques acoustiques dû à la présence de tourbillons.

Impact de la présence d'un cyclone profond de sousmésos-échelle Les structures profondes de sousmésos-échelle (*i.e.* les SCVs) sont une menace potentielle forte pour les bâtiments militaires, car ils ne peuvent pas être repérés depuis la surface (par exemple par satellite), et peuvent avoir un impact important sur les profils locaux de célérité. Il a par exemple été montré que les Meddies (les SCVs générés au niveau du détroit de Gibraltar qui se propagent ensuite dans l'Atlantique Nord chargés d'eaux méditerranéennes, voir *e.g.* Carton et al. (2010)) peuvent modifier fortement les profils de célérité localement, et sont ainsi des structures à risque.

Dans la section 5.3, nous avons étudié un autre type de SCV : un tourbillon cyclonique de sousmésos-échelle mesuré en profondeur au large d'Oman. Cette structure ne peut pas être repérée par satellite, et a une signature importante en salinité et en vitesse. Lorsque l'on trace les profils de célérité en périphérie et au centre du tourbillon, on constate cependant que le profil de célérité est très peu modifié par la présence du tourbillon, voir Fig. A.4. À l'extérieur comme à l'intérieur du tourbillon, les profils de célérité sont de type November, et les variations de célérité induites par le pincement des isopycnes sont de $O(1)$ m s^{-1} . Ainsi, ce tourbillon, plongé dans cette stratification ambiante, ne peut pas créer de chenal acoustique, et a donc un impact faible sur la propagation du son. Nous pouvons donc affirmer que d'un point de vue acoustique, cette structure n'est pas à risque.

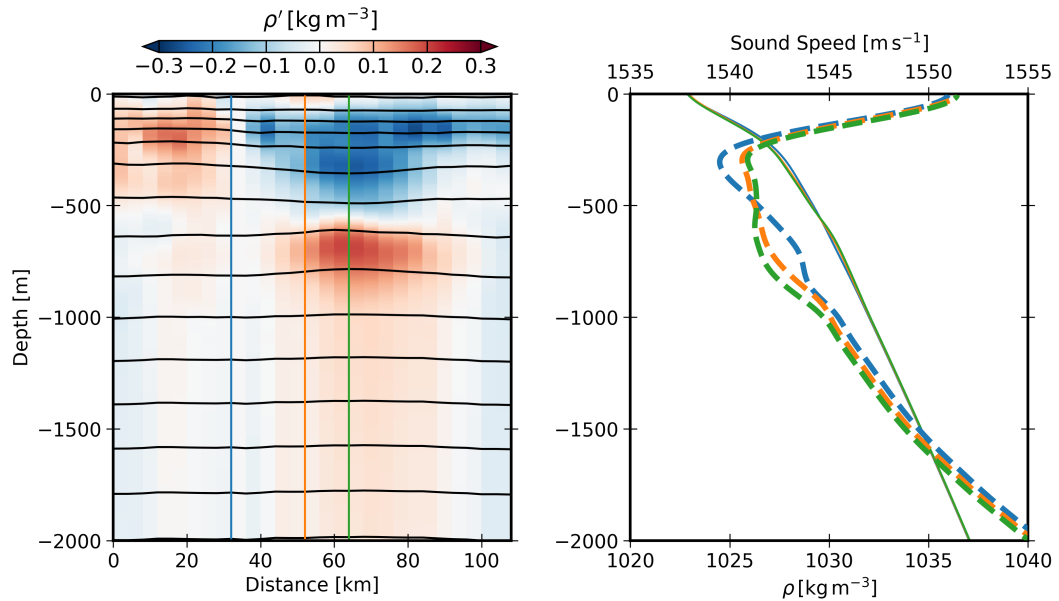


FIGURE A.4 – (Gauche) Section verticale d’anomalie de densité du cyclone profond de sousmésos-échelle mesuré en mer d’Arabie au cours de la campagne PHYSINDIEN 2019 (voir section 5.3). (Droite) Profils de densité (traits pleins) et de célérité associée (traits gras pointillés) aux positions indiquées par les lignes de couleur dans le panneau gauche.

Impact des tourbillons périphériques lors de la fusion de tourbillons Dans la plupart des études théoriques et numériques, les processus géophysiques d’intérêt sont considérés comme isolés de leur environnement. C’est le cas par exemple dans la section 5 du présent manuscrit. Or, l’océan est un système hautement turbulent, et les interactions entre les différents processus sont constants. Considérer des processus isolés est donc une approximation qui dans certains cas omet des paramètres important. C’est le cas pour la fusion de tourbillon. Nous avons en effet montré dans la section 6.2.2 que la fusion entre deux tourbillons de même signe est fortement influencé par la présence d’autre structures cohérentes, majoritairement de signe opposé.

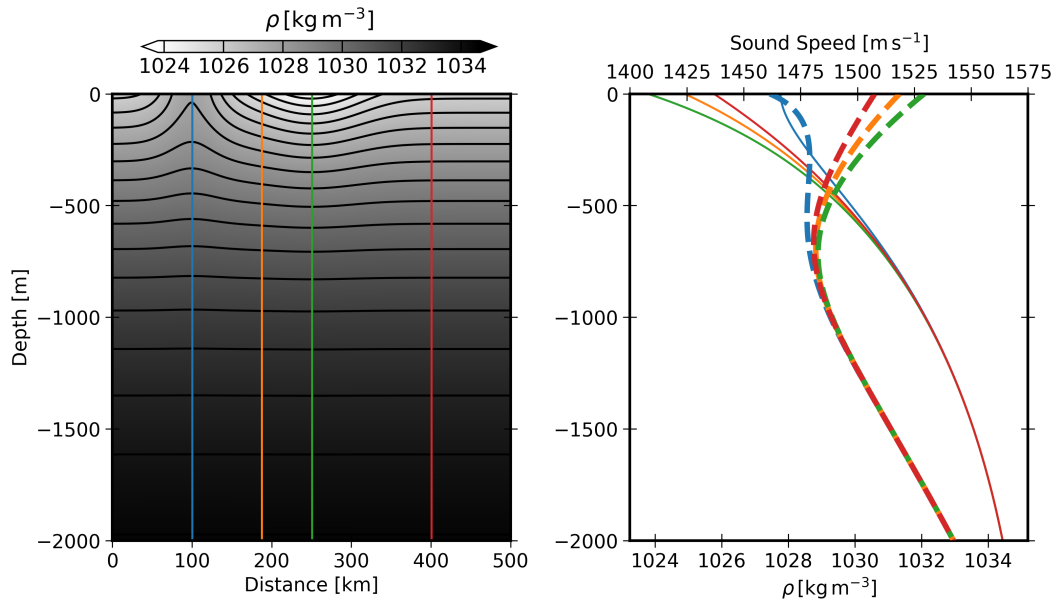


FIGURE A.5 – (Gauche) Section verticale de densité d'un tourbillon anticyclonique théorique (au centre), et d'un tourbillon cyclonique adjacent. (Droite) Profils de densité (traits pleins) et de célérité associée (traits gras pointillés) aux positions indiquées par les lignes de couleur dans le panneau gauche.

Dans le cadre d'études de l'impact acoustique de structures de méso et de sousméso-échelle, le choix du profil de stratification ambiante est primordial (*e.g.* le profil bleu dans la Fig. A.2). Le travail présenté dans la section 6.2.2 nous indique que dans la plupart des cas de fusions dans l'océan ouvert, il faudra considérer un profil extérieur comportant la signature en densité d'un tourbillon de signe opposé. Dans l'exemple schématisé de la Fig. A.5, le tourbillon anticyclonique au centre du domaine représente un tourbillon résultant d'une fusion entre deux anticyclones. Si l'on considère un profil d'environnement au repos (profil rouge), il n'y a pas de changement de type de profil de célérité. En revanche, si on suppose qu'il est probable que cette fusion soit adjacente à un tourbillon cyclonique, il faudra considérer un profil modifié par la présence d'un tel tourbillon (*e.g.* le profil bleu). Dans ce cas il y a un changement de type de profil de célérité, avec un profil November au centre du système fusionnant et un profil Mike à l'extérieur. Un couple de tourbillon anticyclonique qui fusionnent n'est donc pas à risque tant que ceux-ci ne sont pas adjacents à d'autre tourbillon (ce qui n'est jamais le cas dans l'océan réel). Ce point est donc à prendre en compte pour les études futures relative à la modélisation théorique et empirique de l'impact acoustique des fusions de tourbillons.

INFORMATIONS SUPPLÉMENTAIRES POUR LA SECTION 6.2.2

Supplementary information for
"Oceanic vortex mergers are not isolated but influenced by the
 β -effect and surrounding eddies"

Charly de Marez, Xavier Carton, Pierre L'Hégaret, Thomas Meunier,
Alexandre Stegner, Briac Le Vu, and Mathieu Morvan

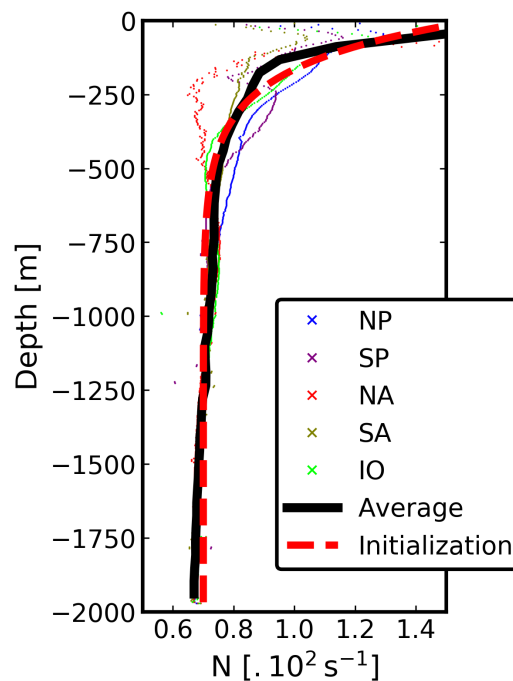


Figure 1: Brunt-Väisälä frequency N profiles in the five study areas. Black bold lines are the average profiles of each quantity over the five areas. Red dashed lines are the profiles used for the initialization of the idealized simulations. Profile in areas NP, SP, NA, SA, and IO are averaged over all available Argo profiles on the 2000-2005 period in each area. This represents respectively 11355, 11580, 6437, 4473, and 7084 profiles from 195, 221, 178, 97, and 165 different Argo floats.

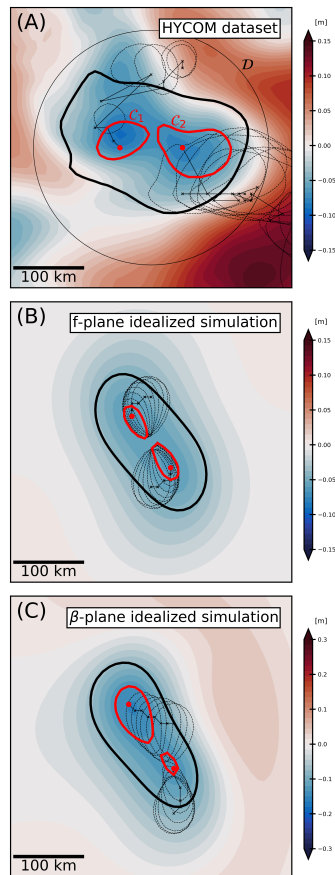


Figure 2: Example of merging detection with AMEDA, in the HYCOM dataset (A), in idealized simulations on the f -plane (B), and on the β -plane (C). The color background is the Sea Surface Height (at the merging moment) used by AMEDA for the eddy detection and tracking. Black crosses and black dashed lines are centers and contours of the two eddies before the merging event; red dots and red bold lines are the centers and the contours of the two eddies when merging occurs (as defined by AMEDA); the black bold contour is the contour of the eddy resulting of the merging (here 2 days after the merging event). Note that the domain shown in B and C is not the whole simulation domain (which is three times larger in both directions).

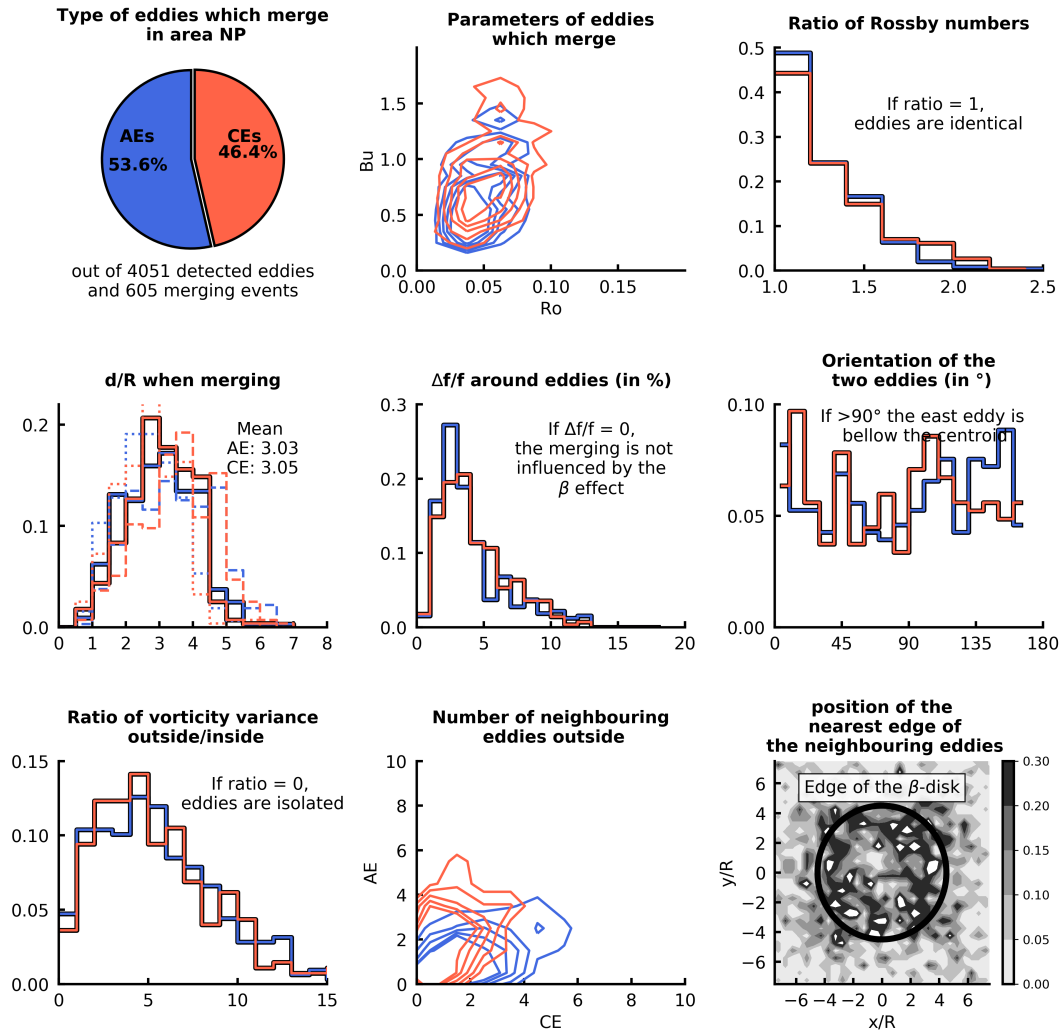


Figure 3: Same as Fig. 2 of the main manuscript, but for area NP

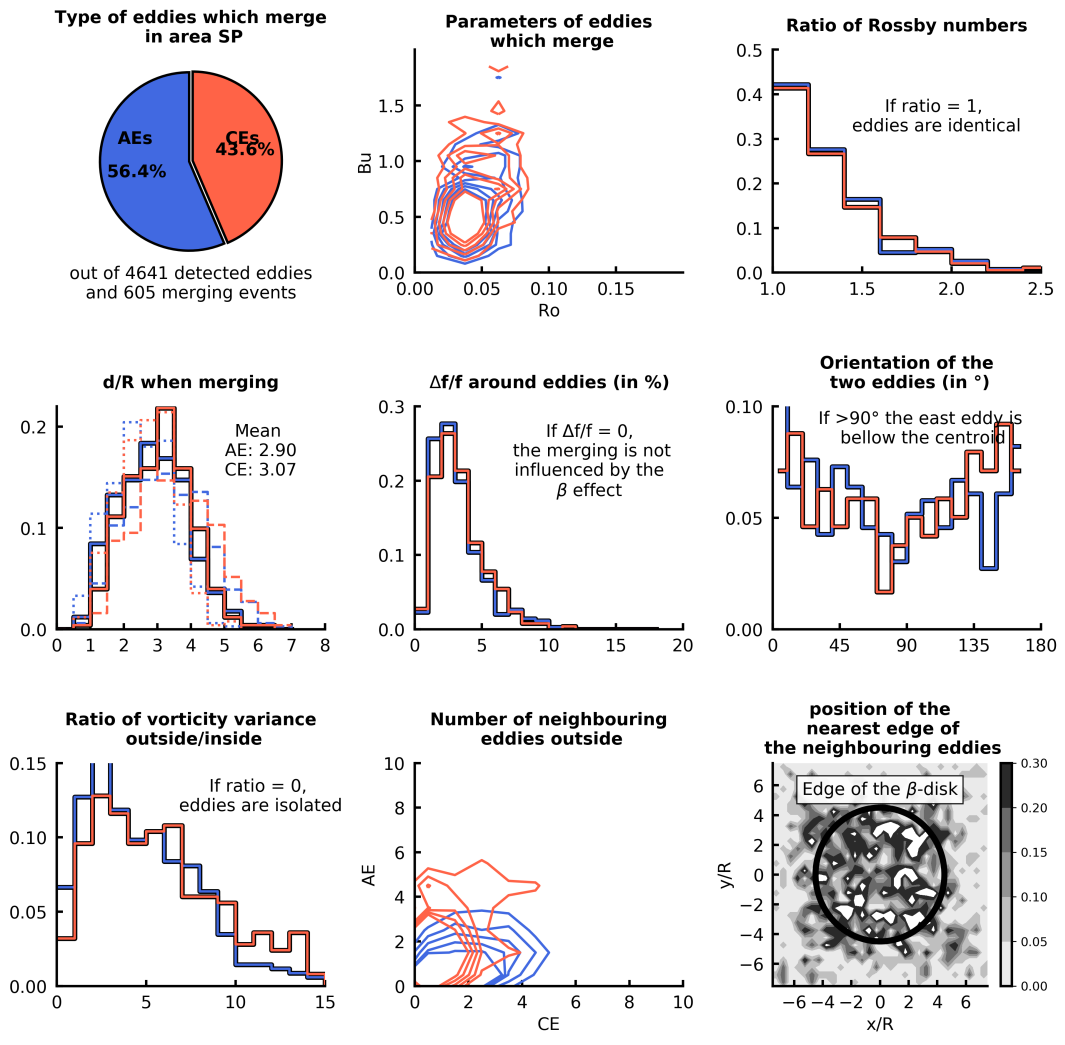


Figure 4: Same as Fig. 2 of the main manuscript, but for area SP

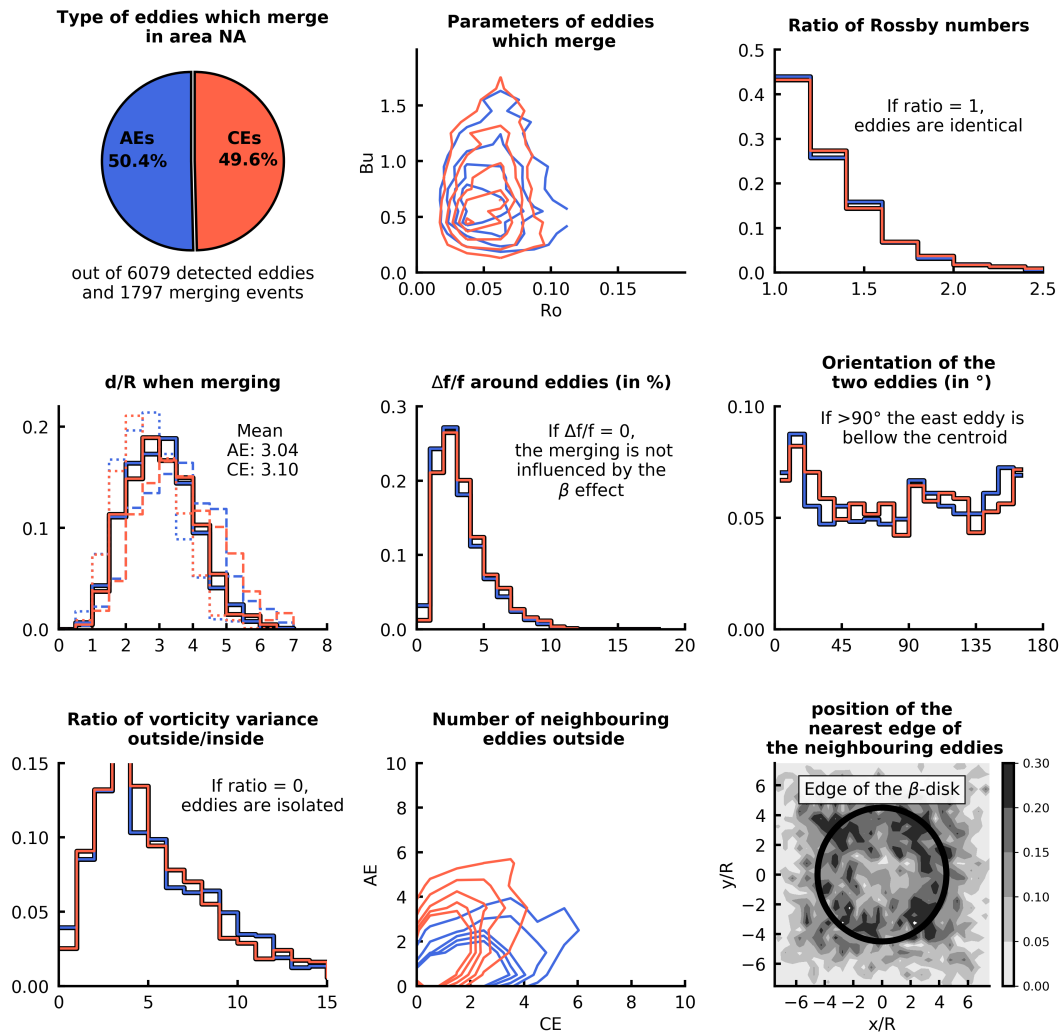


Figure 5: Same as Fig. 2 of the main manuscript, but for area NA

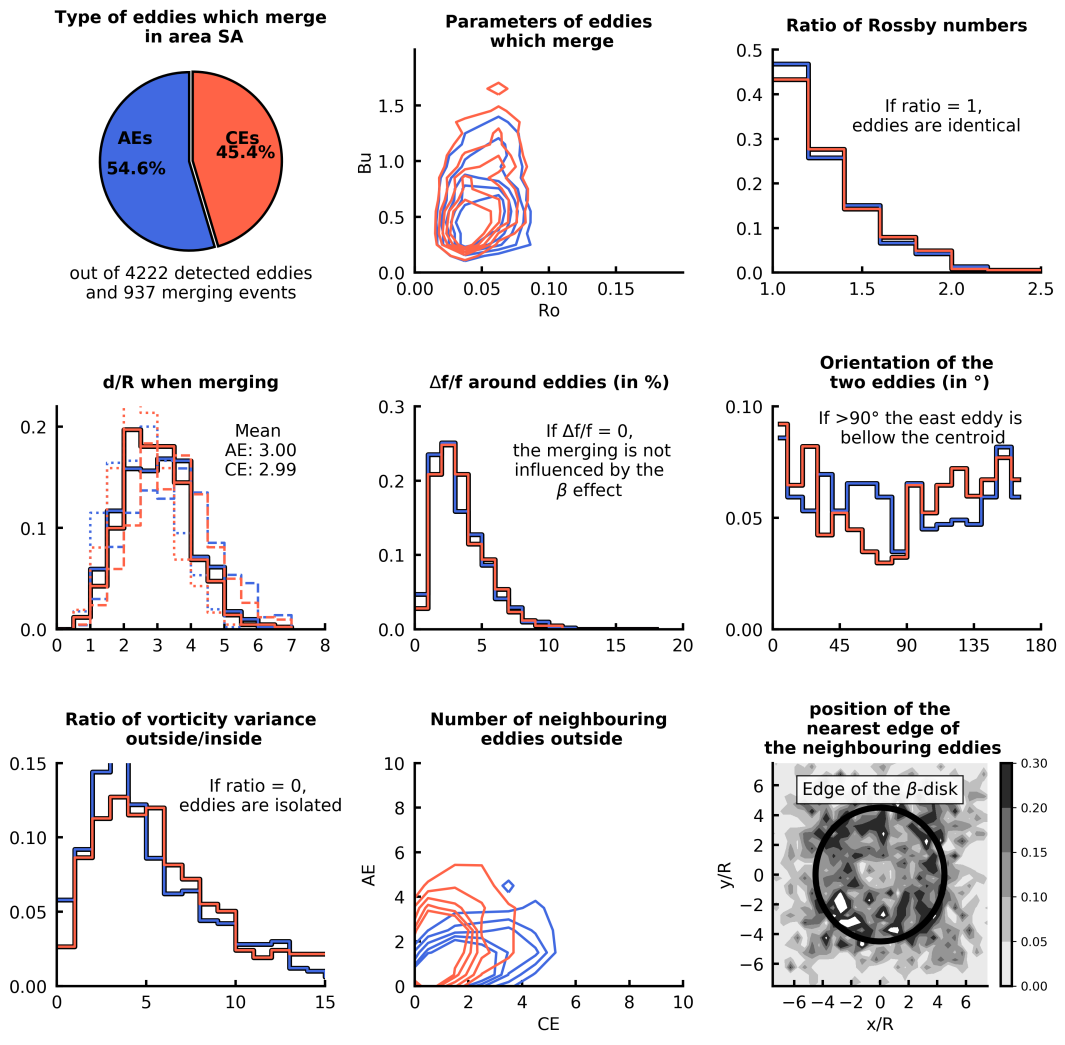


Figure 6: Same as Fig. 2 of the main manuscript, but for area SA

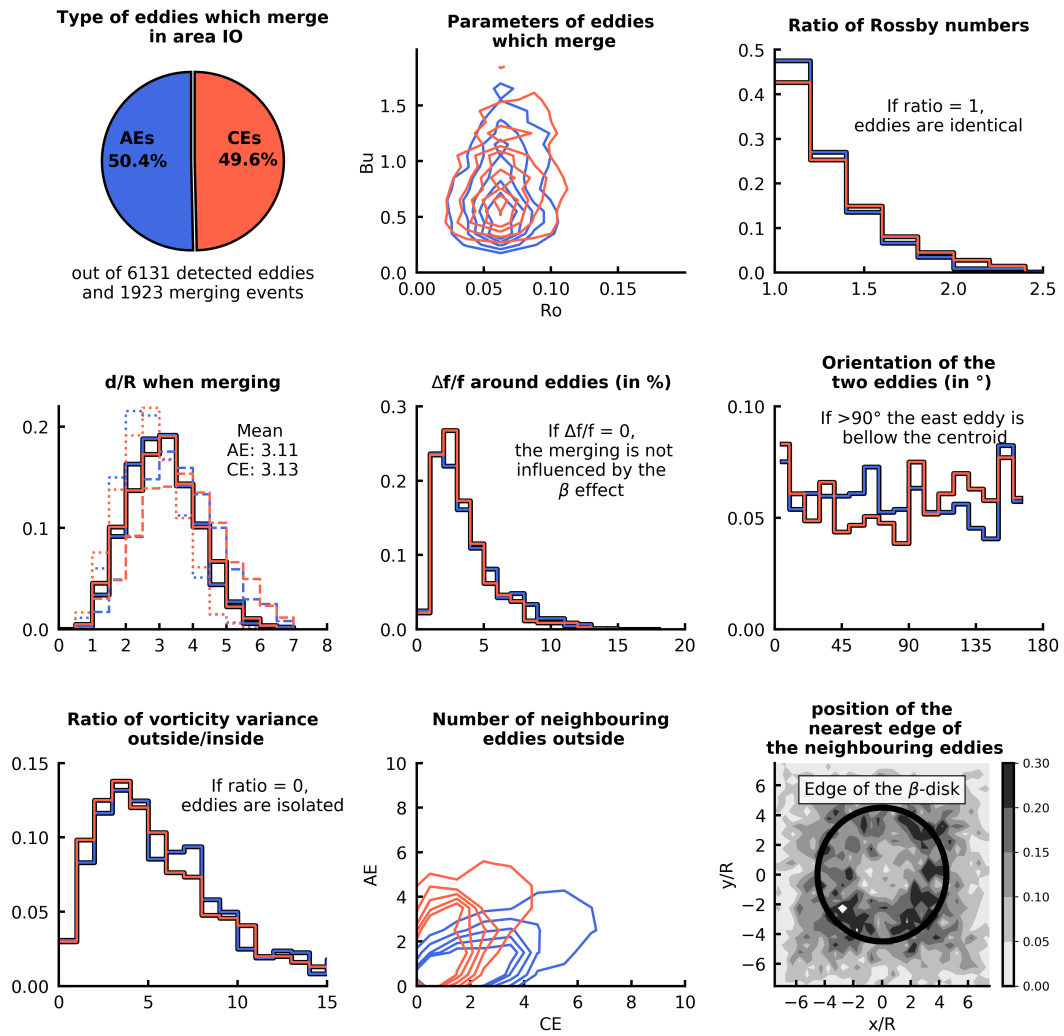


Figure 7: Same as Fig. 2 of the main manuscript, but for area IO

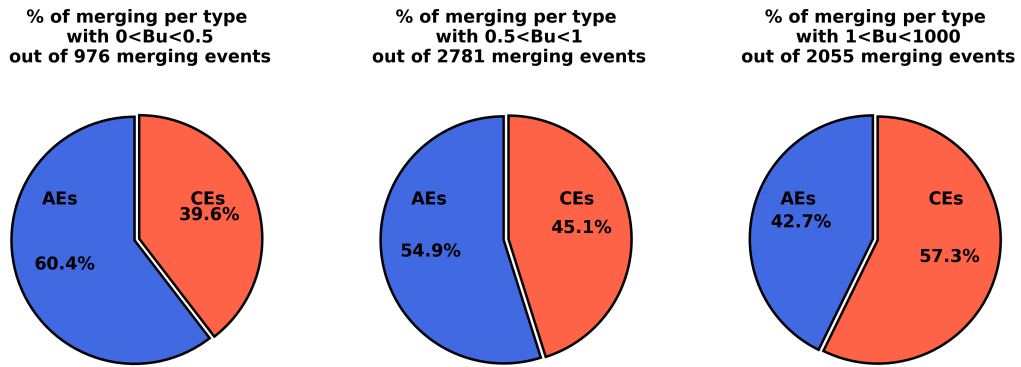


Figure 8: Same as Fig. 2A of the main manuscript, but only for merging eddies with $0 < Bu < 0.5$ (left), $0.5 < Bu < 1$ (middle), $1 < Bu$ (right).

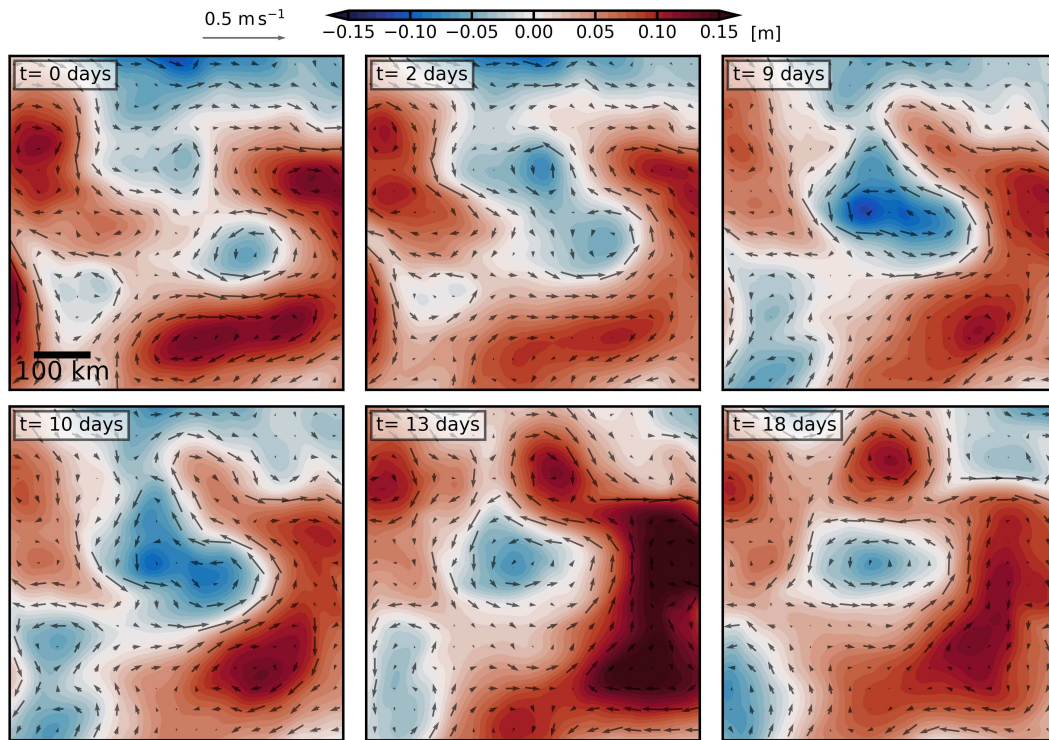


Figure 9: Time evolution of the sea surface height in the HYCOM dataset during the merger of two CEs detected by AMEDA in the North Pacific (NP) area). Each panel is centered around 136.48°W , 19.68°N . The first panel shows the sea surface height on 2003/04/10. Black arrows indicate the surface geostrophic velocity computed from the sea surface height anomaly. This example illustrates the impact of neighbouring AEs on the merger.

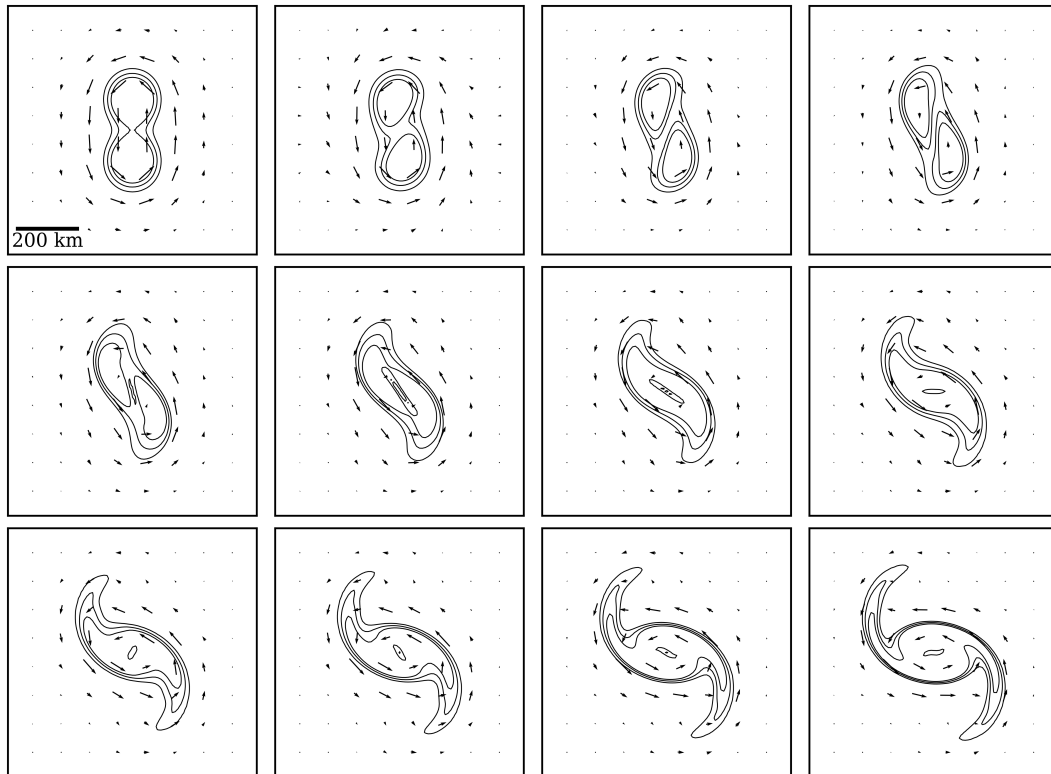


Figure 10: Time evolution of the surface relative vorticity in an idealized 'isolated vortex merging' simulation on the f -plane. The initialization consists of two CEs, with $d/R = 2.5$, $R = 80 \text{ km}$, $V = 0.3 \text{ m s}^{-1}$, $H = 1000 \text{ m}$, and $\alpha = 2$. Black contours correspond to normalized surface relative vorticity $\omega_s/f = [0.03, 0.05, 0.07]$; black arrows indicate the surface velocity field. Time goes from left to right and from top to bottom, with a time spacing between panels of 2 days. Note that not the whole domain of the simulation is shown. For this simulation, merger occurs.

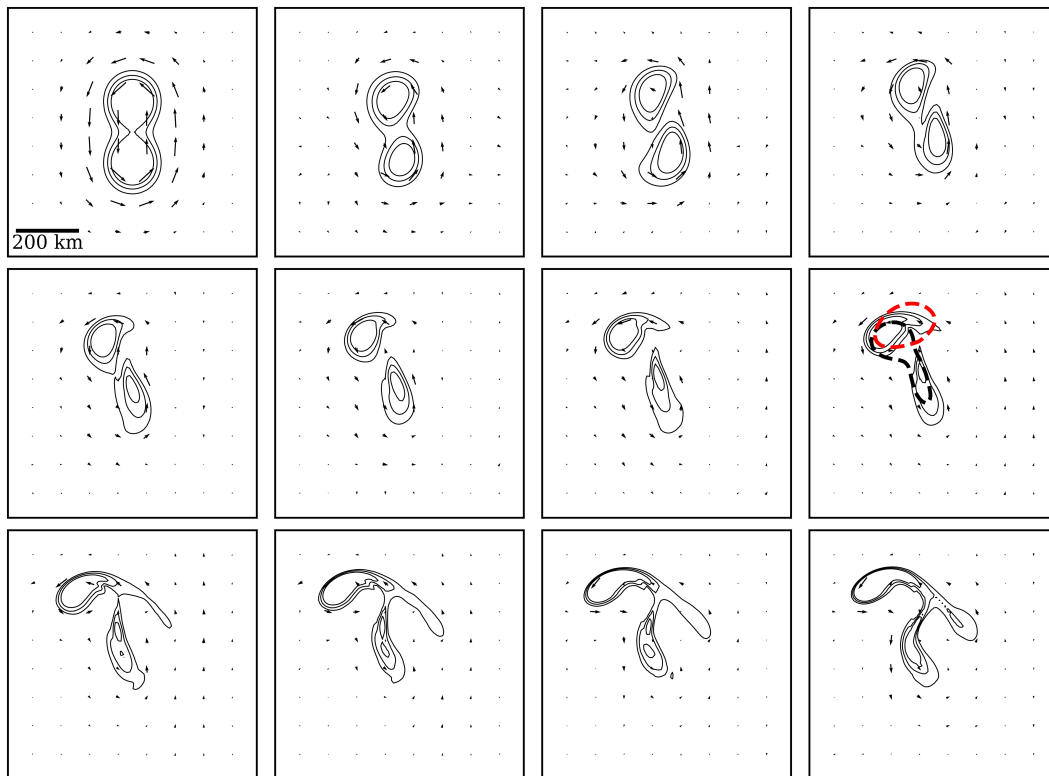


Figure 11: Same as Fig. 10, but for which the simulation was ran on the β -plane. In this case, merger does not occur. The meridionally aligned eddies generate Rossby wave composed of meridionally elongated Sea Surface Height patches with zonally alternating sign (*e.g* Supplementary Fig. 2C). This wave creates a northward velocity east of the two CEs, seen on day 4; thus, the northern eddy moves northward, weakening the merging efficiency. Modifying the orientation of the two eddies at initialization (not shown) tends to slightly reduce this effect. However, even when eddies are zonally aligned, an intense shear generated by Rossby waves leads to the stretching of the two eddies along the zonal axis. This also acts in reducing the merging efficiency. Bold dashed contours in the eighth panels are -0.2 m contours of SSH for the β -plane simulation (black) and the β -disk simulation (red) with the same parameters. For this latter, the merging efficiency is increased and merging is detected.

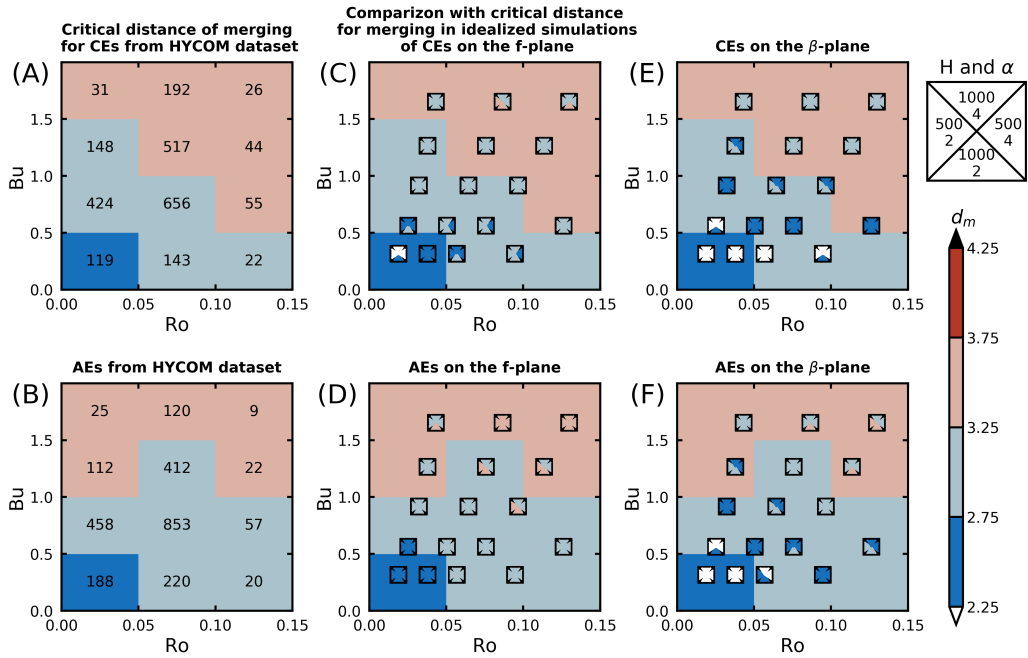


Figure 12: Comparison between the mean distance of merging in the HYCOM dataset, and the maximal initial distance between eddies for which they merge in the idealized simulations. (A) Mean distance of merging d_m for CEs in the HYCOM dataset, depending on Ro and Bu . The numbers of values used to compute averages are indicated for each range of Ro and Bu . (B) Same as (A) for AEs in the HYCOM dataset. (C) Maximum distance of merging d_m^i observed in numerical simulations of CEs on the f -plane. Results are presented as black squares in which 4 grey scale triangles are inserted. Each square corresponds to a given value of Ro and Bu , and the different triangles in this square corresponds to different values of H and α (see top right insert, which indicates the values of H (in meters) and α). The color background is the same as in (A) to allow a comparison between numerical simulations and observations from the HYCOM dataset. (D) Same as (C) for AEs on the f -plane. (E) Same as (C) for CEs on the β -plane.

LA SPHÉRICITÉ DE LA TERRE ET SON IMPACT SUR LA DYNAMIQUE OCÉANIQUE

Nous présentons ici une étude annexe à la thématique principale de la thèse. A partir de simulations réalistes de l'Atlantique Nord, réalisées avec le modèle CROCO, nous questionnons l'importance de la sphéricité terrestre pour la dynamique océanique. Nous revisitons ainsi le problème de Stommel (Stommel, 1948), dans un contexte réaliste. Cette partie permet alors d'illustrer le concept d'effet- β introduit dans la section 1.2.1. Ici, nous posons la question, surprenante, mais non moins intellectuellement stimulante : est ce que d'après les courants océaniques, la Terre pourrait être plate ?

CAN THE EARTH BE FLAT ? A PHYSICAL OCEANOGRAPHER'S PERSPECTIVE

Charly de Marez

Université de Bretagne Occidentale
Laboratoire d'Océanographie Physique et Spatiale
IUEM
Rue Dumont D'Urville
charly.demarez@univ-brest.fr

Mathieu Le Corre

Université de Bretagne Occidentale
Laboratoire d'Océanographie Physique et Spatiale
IUEM
Rue Dumont D'Urville
mathieu.lecorre@univ-brest.fr

January 7, 2020

ABSTRACT

According to a recent survey, 2% of the U.S. population is convinced that the earth is flat. This idea is heralded by members of the Flat Earth Society, and promulgated through Internet forums and other public media channels. Children and young students are easy targets. As a science teacher confronted by these ideas, it can be a challenge to firmly confront their fundamentally flawed foundation while still remaining compassionate towards those who espouse such beliefs. While we do not purport to have the answer for such difficult situations, as two scientists studying ocean physics, we attempt to lend a helping hand to the interested instructor. Here, we use the most advanced computational tools of the physical oceanography community to show that the properties of the ocean that we observe from ships, satellites, and autonomous observing platforms should not exist if the earth were flat. In particular, using *the first* realistic simulation of the ocean on a flat Earth, we show that the North Atlantic gyre, appears entirely different on a flat Earth. For members of the physical oceanography community, the results presented here are obvious; however, for the Flat Earth Society community, it may present an intellectual challenge.

1 Introduction

For the past 10 years, the idea that the earth may be flat has experienced a revival. While concrete numbers are arduous to find, rough estimates suggest that only 84% of the U.S. population agreed with "I have always believed the world is round" (<https://bit.ly/2wePEmI>). Moreover, according to this survey, 2% of the pool was deeply convinced that the earth is flat. Even if one have to be cautious with these unpublished results, it is not rare to find —if we know where to seek— people confident about the fact that the earth is flat, even if their scientific expertise is low. Supporters of the flat Earth theory are convinced that the governments and the scientific community is lying to the public by spreading false data and information. This idea is heralded by members of the Flat Earth Society (FES). Children and young students are easy targets. As a teacher, it is difficult to be confronted to these ideas because they may be supported by students' close family, friends, or favorite artists. Following the call of the American Association of Physics Teacher [1], it is timely to give scientific proofs, "in a calm and respectful way, to show that someone other than the science deniers" are listening to the questions of doubting people.

If the earth were flat, the dynamics of the ocean would be deeply different. Indeed, the large-scale circulation relies on physical mechanisms which are directly related to the sphericity of the earth. In this study, we propose to use state-of-the-art computational tools to compare the ocean dynamics on (1) the spherical Earth and (2) the flat Earth. This allows a proof, *by contradiction*, that the actual properties of the ocean should not exist if the earth were flat. We conduct this study by using some of the most advanced tools used by the physical oceanography community today: high resolution ($\Delta x \sim 6$ km) basin-scale realistic simulations, as well as satellite and large *in situ* observation databases. To our knowledge, no one has tried to model the flat Earth. We thus present the first (and hopefully the last) realistic simulation of the ocean on a flat Earth. For most of the members of our Earth and planetary sciences

community, the results presented here are obvious. Despite this, we estimate that this may have a pedagogic purpose, since we illustrate textbook-concepts phenomena in a realistic context. Also, our approach may provide high school and university-level science teachers with critical tools to confront and compassionately question FES views in the classroom. Coincidentally, our presentation may help students to understand that a flat Earth is not compatible with what is actually occurring in the oceans. To tackle this enormous task, we have tried to conduct our study in a way that it follows as much as possible the beliefs and data espoused by the FES.

Model the flat flat Earth

Understanding how the global ocean circulation might appear on a flat Earth is conceptually challenging, and we thus limit our study to the North Atlantic. Indeed, as presented by the FES on their website: "The Flat Earth is laid out like a North-Azimuthal projection. The North Pole is at the center while Antarctica is at the rim. The continents are spread out around the North Pole." The comparison between the oceanic currents on a flat Earth or a spherical one is made difficult because they have different horizontal extensions. Also, as the primary source of energy of the ocean is the atmosphere (through solar radiations and winds), one needs to consider atmospheric data to impulse energy at the surface of our simulated oceans. Looking at flat Earth official maps, one observes that the North Atlantic closely resemble the maps of the spherical Earth that others utilize (see for instance <https://bit.ly/2m4XuJN>). This would not be the case if one have examined for instance the North Pacific, or any basin in the southern hemisphere. This allows us, without loss of belief, to consider the North Atlantic as our study domain for both cases (spherical and flat Earth scenarios), utilizing atmospheric forcing and geography frequently encountered in this region.

We now discuss the circulation in the North Atlantic as might be found on a spherical or flat Earth. Here, we focus on the shape and intensity of the Gulf Stream, which is a strong boundary current found on the eastern coast of the United States. This latter current system is intense, flowing northward along the U.S. continental shelf from the Strait of Florida to Cape Hatteras near 40°N, where it leaves the coast (see *e.g* [2], [3], and references therein). Studying the occurrence of this current is convenient because (1) its signature can clearly be seen at the surface of the ocean, (2) it is present throughout the whole year with little variations, and (3) its presence is accepted by the FES, such that its use is permitted within our arguments.

Our discussion is organized as follows. In section 2, we present a set of equations that allows us to describe the ocean in a dynamical manner; in these equations, we approximate the earth as spherical and flat Earth, depending on the particular case examined. In section 3, we present our method, which includes a description of the numerical simulations and datasets used. In section 4, we compare the outputs of the two simulations with observations, and particularly the location and intensity of the Gulf Stream in order to help answer the question, "Is the earth flat?". In section 5, we discuss the simulation outputs, highlighting the physical mechanisms that modify the position and intensity of the Gulf Stream. Finally, we conclude in section 6.

2 Governing equations for the ocean dynamics

The dynamics of a fluid in an inertial frame of reference is described by the Navier-Stokes equations [4]:

$$\rho \frac{d\mathbf{u}_i}{dt} = -\nabla P + \mu \Delta \mathbf{u}_i + \mathbf{F}_{ext}, \quad (1)$$

where ρ is the density of the fluid (determined by an equation of state), P its pressure, μ its viscosity, \mathbf{F}_{ext} any external forces applied to the fluid, and $\frac{d\mathbf{u}_i}{dt}$ the acceleration of the fluid in the inertial frame. The earth can be considered as an inertial frame of reference. Indeed, its rotation around the sun is slow (in comparison to the time scale of the fluid movements we consider, typically greater than one week), as is the rotation of the sun within the galaxy. In the flat Earth model, the earth is the center of the universe, and gravity does not exist. However, the earth is moving upward with a constant acceleration called "Universal Acceleration". By construction, this model reproduces an earth in an inertial frame of reference, with a constant force acting on all objects moving at its surface, as the gravity does.

The acceleration of a rotating fluid can be expressed in the inertial frame of reference such as:

$$\frac{d\mathbf{u}_i}{dt} = \frac{d\mathbf{u}}{dt} + \underbrace{2\boldsymbol{\Omega} \times \mathbf{u}}_{\text{Coriolis force}} + \underbrace{\boldsymbol{\Omega} \times (\boldsymbol{\Omega} \times \mathbf{x}_i)}_{\text{Centrifugal force}}. \quad (2)$$

$\mathbf{u} = (u, v, w)$ is the velocity of the fluid in the rotating frame of reference, $\boldsymbol{\Omega}$ is the rotation vector expressed in the inertial frame, and \mathbf{x}_i is the position of the fluid in the inertial frame. The centrifugal force is small, and can be

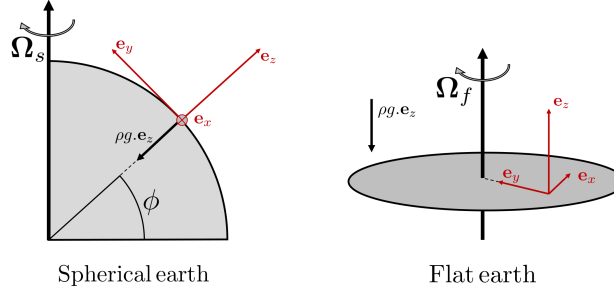


Figure 1: Frame of reference for the spherical Earth (left) and the flat Earth (right). In each panel, $(\mathbf{e}_x, \mathbf{e}_y, \mathbf{e}_z)$ are the axis of the rotating frame of reference, in which the rotation vectors are projected.

considered as a small deviation of the gravity (or equivalent) force. It is of $O(1)\%$ compared to $g = 9.81 \text{ m s}^{-2}$. The Coriolis force is a fictitious force that comes from the change of coordinates and cannot be neglected. Thus, the study of a fluid at the surface of a rotating body is done by using the Navier-Stokes equation in a rotating frame of reference,

$$\rho \frac{d\mathbf{u}}{dt} = -\nabla P + \mu \Delta \mathbf{u} + \mathbf{F}_{ext} - 2\boldsymbol{\Omega} \times \mathbf{u}. \quad (3)$$

At this point it is worth mentioning two points. (1) In many flat Earth models, the earth is not rotating. The Coriolis force thus does not act on planetary fluids. (2) The FES questions the existence of the Coriolis force (at a fundamental level), by stating that this is an "effect" which has never been observed experimentally (see https://wiki.tfes.org/Coriolis_Effect). If we consider this two points as the truth, all Newtonian mechanics and Geophysical Fluid Dynamics collapse. Here, we thus assume that Earth is rotating and that the Coriolis force does exist.

To derive equation (3), there is no need to assume any position for the rotating frame of reference. It can thus be placed on either a sphere or a disk. The only difference between the two cases is the projection of $\boldsymbol{\Omega}$ in the rotating frame. Considering the 2 frames of reference $(\mathbf{e}_x, \mathbf{e}_y, \mathbf{e}_z)$ shown in Fig. 1, we obtain $\boldsymbol{\Omega}_s = (0, \Omega_e \cos \phi, \Omega_e \sin \phi)$ for a spherical Earth, and $\boldsymbol{\Omega}_f = (0, 0, \Omega_{fe})$ for a flat Earth. Ω_e is the rotation rate of the spherical Earth, ϕ the latitude on the spherical Earth, and Ω_{fe} the rotation rate of the flat Earth. Applying the cross product to compute the form of the Coriolis force leads to a set of equations for the two cases. To keep equations simple, we discard viscosity and external forcings in equations. Also, the gravity (or equivalent) force is defined such as $\mathbf{F}_{ext} = \rho g \mathbf{e}_z$. This gives

$$\begin{cases} \frac{d}{dt}u - fv + f^*w = -\frac{1}{\rho}\partial_x P \\ \frac{d}{dt}v + fu = -\frac{1}{\rho}\partial_y P \\ \frac{d}{dt}w - f^*u = -\frac{1}{\rho}\partial_z P - g \end{cases} \quad (4)$$

for a spherical Earth, with $f = 2\Omega \sin \phi$ and $f^* = 2\Omega \cos \phi$, respectively the traditional and non traditional components of the Coriolis frequency. They represent the projection of $\boldsymbol{\Omega}$ on the normal and meridional (*i.e* North-South) directions of the local plane.

For the flat Earth, equations are

$$\begin{cases} \frac{d}{dt}u - \hat{f}v = -\frac{1}{\rho}\partial_x P \\ \frac{d}{dt}v + \hat{f}u = -\frac{1}{\rho}\partial_y P \\ \frac{d}{dt}w = -\frac{1}{\rho}\partial_z P - g \end{cases} \quad (5)$$

with $\hat{f} = 2\Omega_{fe}$. Because the equations governing the acceleration of fluid parcels on a flat Earth neglect the meridional component of Coriolis—the so-called traditional approximation—we have elected to do the same for the case of the spherical Earth ($f^* = 0$). This is also justified on account of the distance from the Equator and pronounced stratification in our domain.

Conceptually, the difference between a flat Earth and a spherical one can be summarized as follows: *on a flat Earth there is no planetary β -effect*. Performing a Taylor expansion of the Coriolis frequency around a mean latitude ϕ_0 on a sphere gives

$$f = f_0 + \beta y + O[(\phi - \phi_0)^2], \quad (6)$$

with y the meridional direction, $f_0 = 2\Omega_e \sin \phi_0$, and $\beta = 2\Omega_e \cos \phi_0 / R_e$ with R_e the radius of the spherical Earth.

On the other hand, on a flat Earth, the Coriolis frequency will not vary:

$$\hat{f} = \hat{f}_0 = \text{constant}, \quad (7)$$

with $\hat{f}_0 = 2\Omega_{fe}$. That is, the difference between the spherical and flat Earth is comprised in the existence of β .

To *turn off* the impact of Earth's spherical nature on the dynamics, one need only set the Coriolis parameter, f , to a constant value. We will consider in the following the hydrostatic primitive equations to describe the planetary fluid [5]. This is a common simplification of Navier-Stokes equations, widely used in physical oceanography, which relies on the Boussinesq and the hydrostatic assumptions. This means, respectively, that (1) density is taken constant except in the gravity term, and (2) vertical acceleration of the fluid is considered small compared to the vertical pressure gradient. This gives (again discarding viscosity and external forcing terms for simplicity)

$$\begin{cases} \frac{d}{dt}u - fv = -\frac{1}{\rho_0}\partial_x P \\ \frac{d}{dt}v + fu = -\frac{1}{\rho_0}\partial_y P \\ \partial_z P = -\rho g, \end{cases} \quad (8)$$

with

$$\begin{cases} f = 2\Omega_e \sin \phi \rightarrow \text{spherical Earth} \\ f = \hat{f}_0 \rightarrow \text{flat Earth.} \end{cases} \quad (9)$$

For slowly varying phenomena and large scale dynamics, the pressure gradients is in equilibrium with the Coriolis force term (in equation (8)), this is the so-called *geostrophic balance*. If we introduce a typical timescale and a horizontal lengthscale of fluid movements T and L , this is true for $T \gg 1$ day and $L > 100$ km. Assuming that the pressure at the surface is linked to the sea surface height (hereafter SSH in the text, and η in equations) by $\eta = \rho_s g P(z = 0)$, this reads

$$\begin{cases} -fv_s = -g\partial_x \eta \\ +fu_s = -g\partial_y \eta, \end{cases} \quad (10)$$

where the subscript A_s designates the surface value of A —*i.e.* (u_s, v_s) are the horizontal components of the surface velocity of the fluid. These (purely diagnostic) equations are useful because they allow us to describe the surface ocean dynamics simply by measuring the SSH. At large horizontal scales, this can presently be done using satellites. For example, a positive (negative) SSH anomaly corresponds to anticyclonic (cyclonic) surface currents. In the Northern hemisphere, anticyclonic currents rotate clockwise, whereas cyclonic currents rotate counter-clockwise. At lateral

scales of $O(10 - 100)$ km, these rotating currents are referred to as anticyclonic *mesoscale eddies*. We refer the reader to [6, 7] for an example of study where mesoscale eddies are described from their SSH signature. At basin scales, we refer to such rotating currents as *gyres*. In the following, we use the SSH as well as the norm of the surface velocity, $|U| = \sqrt{u_s^2 + v_s^2}$, as diagnostic quantities to describe the large scale currents.

3 Simulating and observing the ocean

We performed realistic simulations of the North Atlantic using the Coastal and Regional Ocean COmmunity model (CROCO, [8]). This model solves the hydrostatic primitive equations, *i.e.* the set of equations (8), in which the surface forcing and the bottom friction is added. The density is computed using the full equation of state for seawater [9]. The horizontal advection terms for tracers and momentum are discretized with third-order upwind advection schemes (UP3), see *e.g.* [10] for a further description. This parameterization implies implicit dissipation and it damps dispersive errors. The horizontal resolution is $\Delta x \sim 6$ km such that mesoscale eddies are reasonably well resolved. Simulations have 50 vertical levels following the topography. The calculations are performed in a vertically stretched coordinate such that the resolution near the surface and bottom are higher than within the ocean interior. The bathymetry is constructed from the SRTM30 PLUS dataset [11]. The simulations are initialized, and forced at boundaries with the SODA dataset [12]. At the surface, the forcing is taken from the daily ERA-INTERIM dataset [13]. The model parameterization are the same as the one described in [14] and [15]. We also refer the reader to the latter references for a full validation of the numerical settings.

We run two simulations. In the first one, we consider the Coriolis frequency f of a spherical Earth, which varies with latitude. This simulation thus reproduces the ocean dynamics on a spherical Earth, including the β -effect. This simulation is called BETA hereafter in the text. We run a second simulation considering that the earth is flat, thus having a constant Coriolis frequency $f = \hat{f}_0$. This simulation is called FLAT hereafter in the text. The choice of \hat{f}_0 is tricky because it determines the mesoscale dynamics (10-100 km) through the Rossby radius of deformation [16]. Choosing a value of \hat{f}_0 thus sets the eddy scale and also influences wave propagation speeds. We choose to set $\hat{f}_0 = 10^{-4} \text{ s}^{-1}$ since we want to study in particular the mid-latitudes dynamics.

Simulations are run from January 1, 2000 to March 3, 2008. We consider a spin-up period of 2 years to allow the large-scale circulation to be at equilibrium. In the following, the time period we consider is thus from January 1, 2002 to March 3, 2008 (~ 5 year period). Averages of SSH and $|U|$ are made over the entire simulations. Averages of sea surface temperature (SST) during the winter are made for the months of December, January, and February.

We also compute the meridional heat transport of the Gulf Stream during the winter, defined by

$$\text{heat transport} = \int_{-1000\text{m}}^0 dz \int_{80^\circ\text{W}}^{60^\circ\text{W}} dx \rho_0 c_p \langle v_s T \rangle_t, \quad (11)$$

where the integral is performed vertically and zonally (*i.e.* along the East-West direction — x is the zonal coordinate), T is the temperature, $\rho_0 = 1030 \text{ kg m}^{-3}$ is the mean density, $c_p = 3850 \text{ J kg}^{-1} \text{ K}^{-1}$ is the specific heat capacity, and $\langle \cdot \rangle_t$ is a wintertime average over the whole period. It thus gives an estimation of the heat transport (in Watts) varying in latitude. We do the calculation between 30°N and 40°N . The domain considered for this calculation is shown in Fig. 4 (see black dashed rectangle).

We compare the simulation outputs with *in situ* and satellite data. Surface currents are derived from the NOAA 15 m-drogued drifters dataset. For further information on these data see [17] and [18]. Values of horizontal velocities are averaged in bins of size $0.5^\circ \times 0.5^\circ$ for the period 2002-2008. The median number of (u_s, v_s) data per bin is 1250, with about 5000 data per bin in the Gulf Stream region. The mean SSH is estimated by averaging the absolute dynamic topography of the AVISO dataset supplied on a daily mercator grid for the period 2002-2008. This product was produced and distributed by the Copernicus Marine and Environment Monitoring Service (CMEMS) (<http://www.marine.copernicus.eu>).

4 Is the earth flat ?

The outputs from the BETA run shows a very good agreement with satellite data, as a clear zonal dipolar structure is seen in the SSH (Fig. 2). This reflects the signature of the anticyclonic subtropical gyre of the North Atlantic [19]. In FLAT, this circulation does not set up. Also, the near-equator circulation appears to be dominated by eddies. This is not in accordance with satellite data, and is due to the fact that f does not have the correct value in this region. Indeed, on a sphere, $f \rightarrow 0$ at the equator, the geostrophic equilibrium (10) therefore does not stand, and no coherent eddies should be seen.

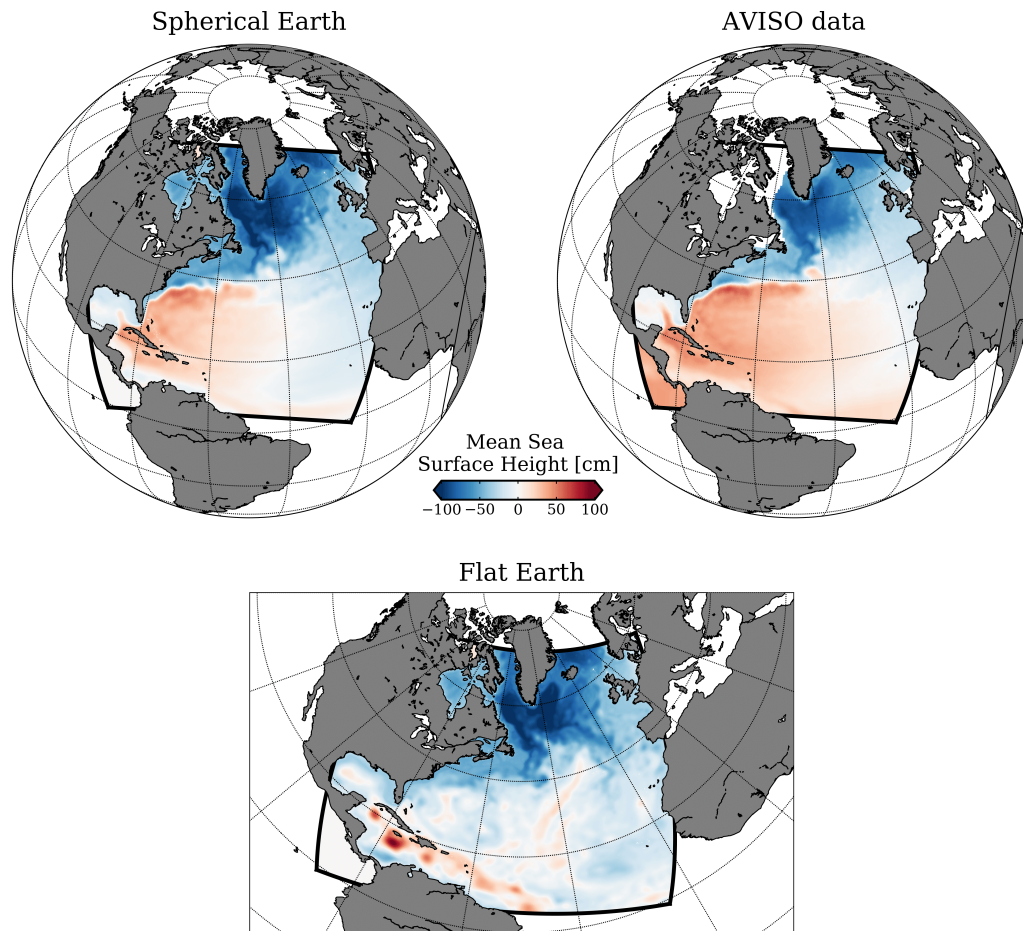


Figure 2: Mean SSH in the BETA simulation (top left), the FLAT simulation (bottom), and satellite observations (top right). Averages are done over a five year period after a 2-year spin up. The BETA simulation outputs and satellite observations are projected on a sphere, while the FLAT simulation outputs are presented on a North-Azimuthal projection (following Fat Earth Society maps).

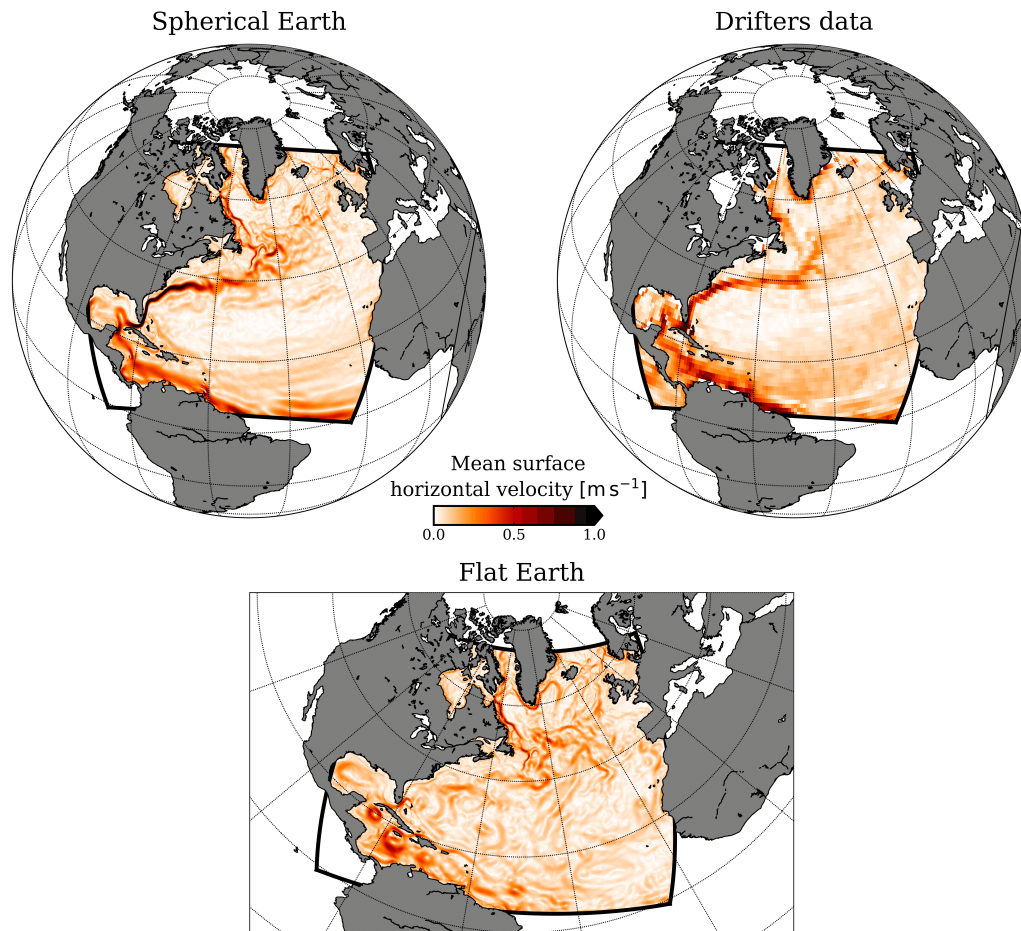


Figure 3: Mean surface horizontal velocity $|U|$ in the BETA simulation (top left), the FLAT simulation (bottom), and the drifters dataset (top right). Averages are done over a five year period after a 2-year spin up. The BETA simulation outputs and drifter measurements are projected on a sphere, while the FLAT simulation outputs are presented on a North-Azimuthal projection (following Fat Earth Society maps).

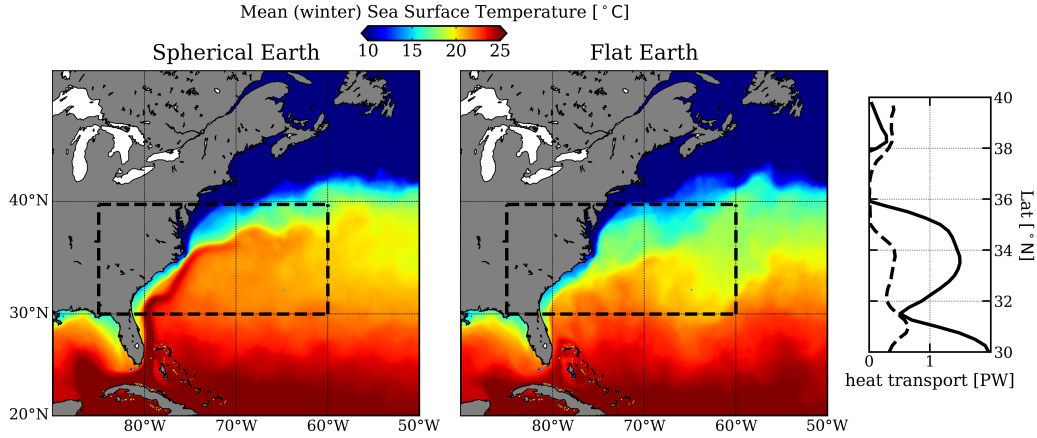


Figure 4: (left) Winter averages of the SST in the BETA and the FLAT run; black dashed area indicates the area in which the heat transport is estimated. (right) Estimation of the heat transport induced by the Gulf Stream. Black solid lines corresponds to the BETA simulation while black dashed line corresponds to the FLAT simulation. To allow a finest comparison, simulation outputs are visualized with a Mercator projection.

The western part of the subtropical gyre is the Gulf Stream. Its signature is clearly seen in both the SSH (Fig. 2) and the surface currents (Fig. 3) of the BETA simulation. This signature is in good agreement with drifter measured surface velocities. The intensity and the width of the Gulf Stream are well reproduced near 30°N, off the coasts of Florida, with surface velocities reaching 2 m s^{-1} . In the FLAT simulation, the Gulf Stream signature is not seen. Furthermore, the retroflection of the Loop Current in the Gulf of Mexico [20], the production and the western propagation of Loop Current rings in the Gulf of Mexico [21], Meddies at the Southwest of Portugal [22], and Gulf Stream rings [23] are well reproduced in the BETA simulation but not in FLAT (not shown).

From these two simplistic comparisons, one concludes that Earth must not be flat. If it were not, the basin-scale circulation of the North Atlantic would disappear, and so would the Gulf Stream. The loss of such an intense current would have impacts clearly visible on the North Atlantic climate. Indeed, the Gulf Stream carries warm tropical water northward, particularly during winter (see Fig. 4). This creates a positive meridional heat transport [24]. This latter phenomenon is important for the whole atmosphere dynamics [25] and the European climate [26]. In the FLAT simulation, we observe that if the earth were flat, the meridional heat transport in the region of the Gulf Stream, between 30 and 36°N, would be divided by a factor of 8 (see Fig. 4, right panel). As further evidence that the Earth is not flat, one can put forth that European as well as east U.S. climate would be significantly different (and temperature most likely cooler in winter) on a flat Earth.

5 Discussion: why does the sphericity matter so much ?

We have seen in a realistic context that the sphericity of the earth is of key importance for the large scale dynamics in the ocean, and particularly for the occurrence of western boundary currents such as the Gulf Stream. Note that similar observations could be made in other basins, such as the North Pacific, where the western boundary current occurring there is the Kuroshio [27]. In this section, we use basic textbooks theories to illustrate why the sphericity of Earth matters for the basin scale dynamics.

The occurrence of the North Atlantic subtropical gyre can be explained using the *Sverdrup relation*. As previously mentioned, the ocean mostly gains energy from the wind stress. Assuming that movements are slow and with a large horizontal extent ($T \gg 1 \text{ day}$ and $L > 100 \text{ km}$), and considering a wind stress $\tau = (\tau_x, \tau_y)$, the horizontal components of equations (8) become

$$\begin{cases} -\rho_0 f v = -\partial_x P + \partial_z \tau_x \\ +\rho_0 f u = -\partial_y P + \partial_z \tau_y. \end{cases} \quad (12)$$

If we vertically integrate these equations over the whole water column (considering a flat bottom), taking the curl of the result leads to

$$\partial_x(fU) + \partial_y(fV) = \nabla \times \tau|_z, \quad (13)$$

where $\mathbf{U} = (U, V) = \int dz \rho_0 \mathbf{u}$ represents the barotropic component of the velocity (*i.e* the part of the velocity which is homogeneous throughout the whole water column). Considering the β -plane approximation (6) and the non divergence of \mathbf{U} leads to the Sverdrup relation:

$$\beta V = \nabla \times \tau|_z. \quad (14)$$

Because the winds are mainly zonal, this can be simplified as

$$\beta V = -\partial_y \tau_x. \quad (15)$$

Integrating the non-divergence $\partial_x U + \partial_y V = 0$ zonally from west to east (with a reference $U = 0$ at the western part of the basin) leads to an equation on the zonal velocity:

$$\beta U = (x - L) \partial_{yy}^2 \tau_x, \quad (16)$$

with x the meridional coordinate, and L the meridional size of the basin. Notice that integrating from east to west gives a wrong result. This can be fixed by adding a bottom friction to equations (Stommel equations).

Above the North Atlantic, winds are from west to east in the northern part of the basin, and in the opposite direction near the Equator. Following equations (15) and (16) thus leads to a theoretical anticyclonic barotropic circulation at the basin-scale: the subtropical gyre. From this circulation results a positive anomaly of SSH. This is what we see for the spherical Earth simulation in Fig. 2. On a flat Earth, $\beta = 0$, and equations (15) and (16) are no longer valid. The basin scale circulation is not set up, even if the wind blows the same way. This can be seen in the FLAT simulation outputs.

In the primitive equations framework, a generalization of the Sverdrup relation (14) can be obtained by integrating equations (8) —in which we add all friction terms— and cross-differentiating the result [28]. This gives the so-called full barotropic vorticity balance equation:

$$\frac{\partial \Omega}{\partial t} = \overbrace{-\nabla \cdot (f\mathbf{U})}^A + \underbrace{\nabla \times \tau|_z}_B + \frac{\overbrace{\mathbf{J}(P_b, h)}^C}{\rho_0} + \underbrace{\nabla \times \tau^{\text{bot}}|_z}_D + \mathcal{D}_\Sigma + \mathcal{A}_\Sigma. \quad (17)$$

The left hand side of this relation is the temporal variation of the barotropic vorticity $\Omega = \partial_x V - \partial_y U$. The terms A and B are respectively the planetary vorticity advection and the wind curl. Because we consider long time averages, $\nabla \cdot (f\mathbf{U}) \approx \beta V$, and $\frac{\partial \Omega}{\partial t} \approx 0$. The balance between these two terms is the Sverdrup relation (14). The term C is the bottom pressure torque with \mathbf{J} the Jacobian operator, P_b the pressure anomaly along a contour line of fixed topography, and h the topography. This term represents the local steering of oceanic currents by topographic features. The term D is the bottom drag curl. Finally, \mathcal{D}_Σ and \mathcal{A}_Σ are the horizontal diffusion term (induced by the horizontal advective scheme of the numerical model), and the nonlinear advection term respectively. Details about the last term, and how each term is computed from the model outputs can be found in [28].

We horizontally integrate the time averages of the different terms of equation (17) for the BETA and the FLAT simulations (Fig. 5). The integration domain corresponds to the subtropical gyre of the North Atlantic observed in the BETA simulation (a closed contour of streamfunction). The Gulf Stream is excluded from this domain, to only consider the Sverdrup-type circulation.

In the BETA simulation, we mainly observe a balance between the wind stress and the planetary vorticity, as suggested by the Sverdrup relation. In the FLAT simulation, because of the lack of β , the wind stress has to be compensated by other terms: here by the bottom pressure torque. The small topographic features are thus key for the basin scale circulation on a flat Earth.

In summary, the sphericity of the earth allows the basin scale circulation to set up, through a balance between the wind stress and the planetary vorticity induced by the existence of β .

As seen in the calculation of equation (16), an asymmetry appears in the ocean when considering the west to east direction or the east to west one. This is due to the propagation of *Rossby waves*, which transport energy at large scales from east to west. To describe them theoretically, it is useful to simplify the primitive equations, to obtain the so-called

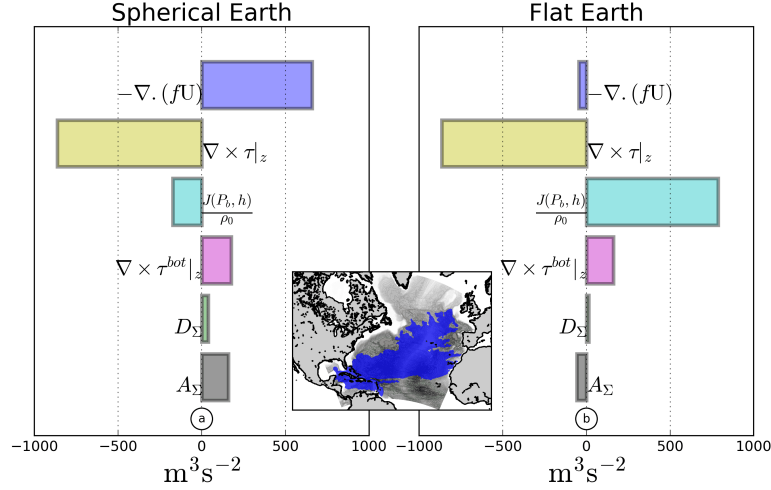


Figure 5: Horizontally integrated terms of the barotropic vorticity balance equation for (left) the BETA simulation and (right) the FLAT simulation. The domain for the integration is shown by the blue contour in the middle insert.

quasi-geostrophic model. It can be done by assuming a flow with $T \gg 1$ day, $L > 100$ km, and a small aspect ratio ($H/L \ll 1$, with H the mean depth of the ocean). The development can be found in [5]. We consider here a one-layer ocean (an ocean which is not stratified), for simplicity, with no bottom topography, and the β -plane approximation. The governing equation reads:

$$\frac{d_g}{dt} \left[\Delta \Psi - \frac{\Psi}{R^2} + \beta y \right] = 0, \quad (18)$$

where Ψ is the streamfunction (proportional to SSH, $\Psi = g\eta/f_0$), $R = \sqrt{gH/f_0^2}$ is the barotropic radius of deformation, and $\frac{d_g}{dt}$ is the material derivative considering only the geostrophic velocities. Linearizing (18) around a rest state, and introducing a perturbation of SSH as a monochromatic wave, gives the dispersion relation for Rossby waves:

$$\omega = \frac{-\beta k}{k^2 + l^2 + R^{-2}}, \quad (19)$$

with k and l the zonal and meridional wavenumbers of the wave, and ω its pulsation. For large-scale motions ($k^2 + l^2 \ll R^{-2}$), this can be simplified as

$$\omega = -\beta k R^2, \quad (20)$$

which is the dispersion relation of long Rossby waves. The most salient feature of this equation is that the group velocity and the phase velocity of the wave are equal, $c = -\beta R^2$, and strictly negative. This means that the wave as well as its energy always travel toward the west. If the earth were flat, with $\beta = 0$, Rossby waves are absent from the ocean.

In the real ocean, the water column is stratified such that the water is heavier at the bottom than at the surface. Thus, one has to take into account the vertical density variations in the expression of the dispersion relation of long Rossby waves. This can be done, in the simplest way, by replacing the barotropic radius of deformation R by the first Rossby radius of deformation $R_d = NH/f$ that takes into account the local value of stratification N , depth H , and Coriolis parameter f . We refer the reader to [16] for a full description of R_d .

Long Rossby waves propagating westward are seen in the BETA simulation. Indeed, the Hovmöller diagram (time versus space diagram) of the SSH at the latitude of the Gulf Stream (30°N), shows a streak pattern orientated westward (Fig. 6). The slope of the streaks is in good accordance with the theoretical prediction of the phase speed of long Rossby waves. The time evolution of the SSH in the BETA simulation (not shown, see animation in supplementary materials) shows a westward movement of mesoscale structures. This movement is explained by the occurrence of long Rossby waves which advect eddies toward the west. As the energy is carried toward the west by Rossby waves, physical

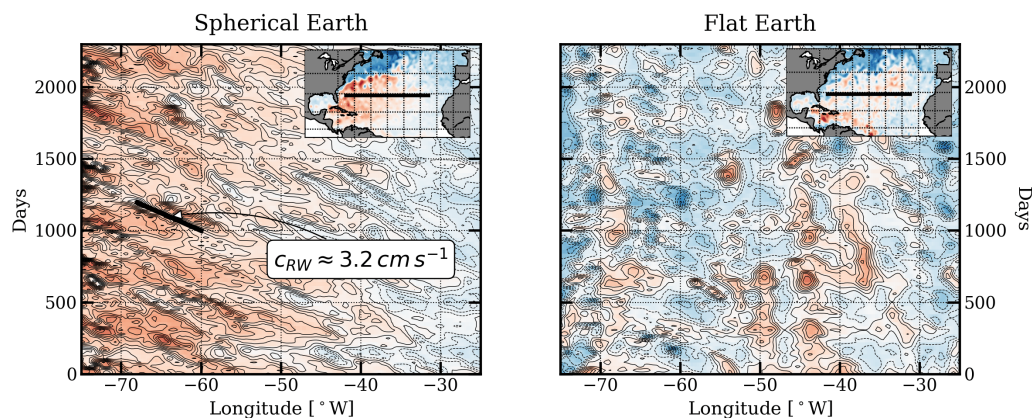


Figure 6: Hovmöller diagrams of the SSH along a line located at 30°N (see inserts), for the BETA run (left) and the FLAT run (right). The black bold line in the left panel indicates the phase line of a theoretical long Rossby Wave with a phase velocity $c_{RW} = -\beta R_d^2$; R_d is an estimation of the First Rossby Radius of deformation near 30°N from [16].

processes are intensified at the western boundary of the basin. This explains why the North Atlantic gyre is intensified at the western boundary of the basin, forming the Gulf Stream. In the FLAT simulation, no Rossby waves are seen. No Rossby wave can propagate because of the lack of β . The currents are not intensified at the western boundary, and mesoscale structures are nearly stationary.

In summary, the sphericity of the earth makes the energy travel towards the west. This explains the westward propagation of structures in the ocean as well as the western intensification of the oceanic currents.

6 Conclusion

With this study we have shown that a flat Earth cannot accurately reproduce the observed dynamics of the North Atlantic Ocean. Indeed, on a flat Earth, numerous phenomena which have been intensively studied and observed in the past 70 years are not seen. Specific examples include the North Atlantic gyre, the Gulf Stream, the formation of mesoscale eddies, and their propagation toward the west.

To be complete, it should be mentioned that the accuracy of the data and approximation of the governing equation of motions as implemented in the models may be questioned by supporters of the flat Earth. Here, we have focused on the Gulf Stream because its existence in the ocean is accepted by the Flat Earth Society. Explaining why the presence of the Gulf Stream requires the sphericity of the earth thus appeared to be a straightforward way toward the global *re-acceptation* of the sphericity of the earth.

Acknowledgments

We thank X. Carton for helpful discussions, and for his support in this unusual project. We also thank C. Buckingham for his precious comments that greatly improved the quality of the manuscript. Simulations were performed using the HPC facilities DATARMOR of “Pôle de Calcul Intensif pour la Mer” at Ifremer, Brest, France. Model outputs are available upon request, for people who are interested in using it, as well as for skeptics from all walks of life.

References

- [1] American Association of Physics Teachers. Calling all physicists. *American Journal of Physics*, 87(9):694–695, September 2019.
- [2] Henry M Stommel. *The Gulf Stream: a physical and dynamical description*. Univ of California Press, 1958.
- [3] F.C. Fuglister. Gulf stream '60. *Progress in Oceanography*, 1:265–373, January 1963.
- [4] LD Landau and EM Lifshitz. *Fluid Mechanics*, 1987.

- [5] Geoffrey K Vallis. *Atmospheric and oceanic fluid dynamics*. Cambridge University Press, 2017.
- [6] Dudley B. Chelton, Michael G. Schlax, Roger M. Samelson, and Roland A. de Szoeke. Global observations of large oceanic eddies. *Geophysical Research Letters*, 34(15), August 2007.
- [7] Dudley B. Chelton, Michael G. Schlax, and Roger M. Samelson. Global observations of nonlinear mesoscale eddies. *Progress in Oceanography*, 91(2):167–216, October 2011.
- [8] Alexander F. Shchepetkin and James C. McWilliams. The regional oceanic modeling system (ROMS): a split-explicit, free-surface, topography-following-coordinate oceanic model. *Ocean Modelling*, 9(4):347–404, January 2005.
- [9] Alexander F. Shchepetkin and James C. McWilliams. Accurate Boussinesq oceanic modeling with a practical, “Stiffened” Equation of State. *Ocean Modelling*, 38(1-2):41–70, January 2011.
- [10] Patrice Klein, Bach Lien Hua, Guillaume Lapeyre, Xavier Capet, Sylvie Le Gentil, and Hideharu Sasaki. Upper Ocean Turbulence from High-Resolution 3D Simulations. *Journal of Physical Oceanography*, 38(8):1748–1763, August 2008.
- [11] J. J. Becker, D. T. Sandwell, W. H. F. Smith, J. Braud, B. Binder, J. Depner, D. Fabre, J. Factor, S. Ingalls, S-H. Kim, R. Ladner, K. Marks, S. Nelson, A. Pharaoh, R. Trimmer, J. Von Rosenberg, G. Wallace, and P. Weatherall. Global Bathymetry and Elevation Data at 30 Arc Seconds Resolution: SRTM30_plus. *Marine Geodesy*, 32(4):355–371, November 2009.
- [12] James A. Carton and Benjamin S. Giese. A Reanalysis of Ocean Climate Using Simple Ocean Data Assimilation (SODA). *Monthly Weather Review*, 136(8):2999–3017, August 2008.
- [13] D. P. Dee, S. M. Uppala, A. J. Simmons, P. Berrisford, P. Poli, S. Kobayashi, U. Andrae, M. A. Balmaseda, G. Balsamo, P. Bauer, P. Bechtold, A. C. M. Beljaars, L. van de Berg, J. Bidlot, N. Bormann, C. Delsol, R. Dragani, M. Fuentes, A. J. Geer, L. Haimberger, S. B. Healy, H. Hersbach, E. V. Hólm, L. Isaksen, P. Kållberg, M. Köhler, M. Matricardi, A. P. McNally, B. M. Monge-Sanz, J.-J. Morcrette, B.-K. Park, C. Peubey, P. de Rosnay, C. Tavolato, J.-N. Thépaut, and F. Vitart. The ERA-Interim reanalysis: configuration and performance of the data assimilation system. *Quarterly Journal of the Royal Meteorological Society*, 137(656):553–597, April 2011.
- [14] Mathieu Le Corre, Jonathan Gula, A. Smilenova, and L. Houper. On the dynamics of a deep quasi-permanent anticyclonic eddy in the rockall trough. *French Congress of Mechanics*, 2019.
- [15] Mathieu Le Corre, Jonathan Gula, and Anne Marie Treguier. Barotropic vorticity balance of the north atlantic subpolar gyre in an eddy-resolving model. *Ocean Science*, in review, 2019.
- [16] Dudley B. Chelton, Roland A. deSzoeke, Michael G. Schlax, Karim El Naggar, and Nicolas Siwertz. Geographical Variability of the First Baroclinic Rossby Radius of Deformation. *Journal of Physical Oceanography*, 28(3):433–460, March 1998.
- [17] R. Lumpkin and M. Pazos. *Lagrangian Analysis and Prediction of Coastal and Ocean Dynamics*. pages 39–67. Cambridge University Press, 2007.
- [18] Lucas C. Laurindo, Arthur J. Mariano, and Rick Lumpkin. An improved near-surface velocity climatology for the global ocean from drifter observations. *Deep Sea Research Part I: Oceanographic Research Papers*, 124:73–92, June 2017.
- [19] Lynne D Talley. *Descriptive physical oceanography: an introduction*. Academic press, 2011.
- [20] H. E. Hurlburt and J. Dana Thompson. A Numerical Study of Loop Current Intrusions and Eddy Shedding. *Journal of Physical Oceanography*, 10(10):1611–1651, October 1980.
- [21] W. Sturges and R. Leben. Frequency of Ring Separations from the Loop Current in the Gulf of Mexico: A Revised Estimate. *Journal of Physical Oceanography*, 30(7):1814–1819, July 2000.
- [22] X. Carton, N. Daniault, J. Alves, L. Cherubin, and I. Ambar. Meddy dynamics and interaction with neighboring eddies southwest of Portugal: Observations and modeling. *Journal of Geophysical Research*, 115(C6), June 2010.
- [23] P. L. Richardson. Gulf Stream Rings. In Allan R. Robinson, editor, *Eddies in Marine Science*, pages 19–45. Springer Berlin Heidelberg, Berlin, Heidelberg, 1983.
- [24] H. L. Bryden and M. M. Hall. Heat Transport by Currents Across 25 N Latitude in the Atlantic Ocean. *Science*, 207(4433):884–886, February 1980.
- [25] Shoshiro Minobe, Akira Kuwano-Yoshida, Nobumasa Komori, Shang-Ping Xie, and Richard Justin Small. Influence of the Gulf Stream on the troposphere. *Nature*, 452(7184):206–209, March 2008.
- [26] Jaime B. Palter. The Role of the Gulf Stream in European Climate. *Annual Review of Marine Science*, 7(1):113–137, January 2015.

- [27] Keisuke Mizuno and Warren B. White. Annual and Interannual Variability in the Kuroshio Current System. *Journal of Physical Oceanography*, 13(10):1847–1867, October 1983.
- [28] Jonathan Gula, M. Jeroen Molemaker, and James C. McWilliams. Gulf Stream Dynamics along the Southeastern U.S. Seaboard. *Journal of Physical Oceanography*, 45(3):690–715, March 2015.

ÉTUDE DE L'INTERACTION TOURBILLON-UPWELLING

Nous présentons ici une étude menée au cours de la troisième année de thèse, et publiée dans le journal *Regular and Chaotic Dynamics*, traitant de l'interaction entre un front d'upwelling (modélisé par un jet zonal), et un champs tourbillonnaire. Cette problématique revêt une importance particulière en mer d'Arabie. En effet, le système principal d'upwelling de la région (l'upwelling Omanais) se trouve sur le bord Ouest du Bassin. De part la présence d'ondes de Rossby planétaire, les tourbillons finissent leur vie sur le bord ouest, et donc lorsque l'upwelling est présent (au printemps), ils interagissent avec celui-ci (Vic et al., 2017). L'étude repose sur la réalisation de simulation idéalisée avec le modèle CROCO, de la même manière que dans les sections 5 et 6.



Interaction of an Upwelling Front with External Vortices: Impact on Cross-shore Particle Exchange

Charly de Marez^{1*} and Xavier Carton^{1**}

¹Univ. Brest, Laboratoire d'Océanographie Physique et Spatiale (LOPS),
IUEM, Rue Dumont D'urville,
29280 Plouzané, France

Received July 14, 2021; revised August 17, 2021; accepted August 30, 2021

Abstract—Coastal upwellings, due to offshore Ekman transport, are more energetic at the western boundaries of the oceans, where they are intensified by incoming Rossby waves, than at the eastern boundaries. Western boundary upwellings are often accompanied by a local vortex field. The instability of a developed upwelling front and its interaction with an external vortex field is studied here with a three-dimensional numerical model of the hydrostatic rotating Navier-Stokes equations (the primitive equations). The baroclinic instability of the front leads to the growth of meanders with 100-200 km wavelength, in the absence of external vortex. On the f -plane, these waves can break into a row of vortices when the instability is intense. The β -effect is stabilizing and strongly decreases the amplitude of meanders. Simulations are then performed with a front initially accompanied by one or several external vortices. The evolutions in this case are compared with those of the unstable jet alone. On the f -plane, when an external vortex is close to the front, this latter sheds a long filament which wraps up around the vortex. This occurs over a period similar to that of the instability of the isolated front. Cyclones are more efficient in tearing such filaments offshore than anticyclones. On the β -plane, the filaments are short and turbulence is confined to the vicinity of the front. At long times, waves propagate along the front, thus extending turbulence alongshore. The initial presence of a vortex alley leads to a stronger destabilization of the front and to a larger cross-shore flux than for a single vortex, with many filaments and small vortices pushed far offshore. In the ocean, this cross-shore exchange has important consequences on the local biological activity.

MSC2010 numbers: 8096

DOI: 10.1134/S1560354721050063

Keywords: coastal upwelling front, vortices, filaments, baroclinic instability, frontal waves, particle motion and tracking

1. INTRODUCTION

The Arabian Sea, in the North-Western Indian Ocean, is the seat of oceanographic processes which interact dynamically (see Fig. 1). These physical processes, in turn, influence the regional biological activity of the ocean. This sea evolves under the influence of monsoon winds [north-easterlies in winter and south-westerlies in summer; 41] and of a strong evaporation rate [39]. The strong winds induce a cyclonic regional circulation in winter and an anticyclonic regional one in summer. Moreover, these winds generate Rossby waves near the western coast of India [5]. These waves propagate westward and they can strengthen large, long-lived eddies, like the Great Whirl near the coast of Somalia [53] and the Ras al Hadd dipolar eddy South of Oman [2] (eddies are oceanic vortices). The Arabian Sea is populated with many eddies [1, 7, 48]. Such eddies are formed in particular by the instability of coastal currents and of the regional gyre currents.

A second main feature of the Arabian Sea are two western boundary upwellings (near Somalia and South of Oman), as the wind blows parallel to the coast and northwestward in summer [6, 12, 14, 15, 37, 40, 44, 52]. In upwellings, the Ekman drift due to the wind pushes the surface water

*E-mail: charly.demarez@univ-brest.fr

**E-mail: xcarton@univ-brest.fr

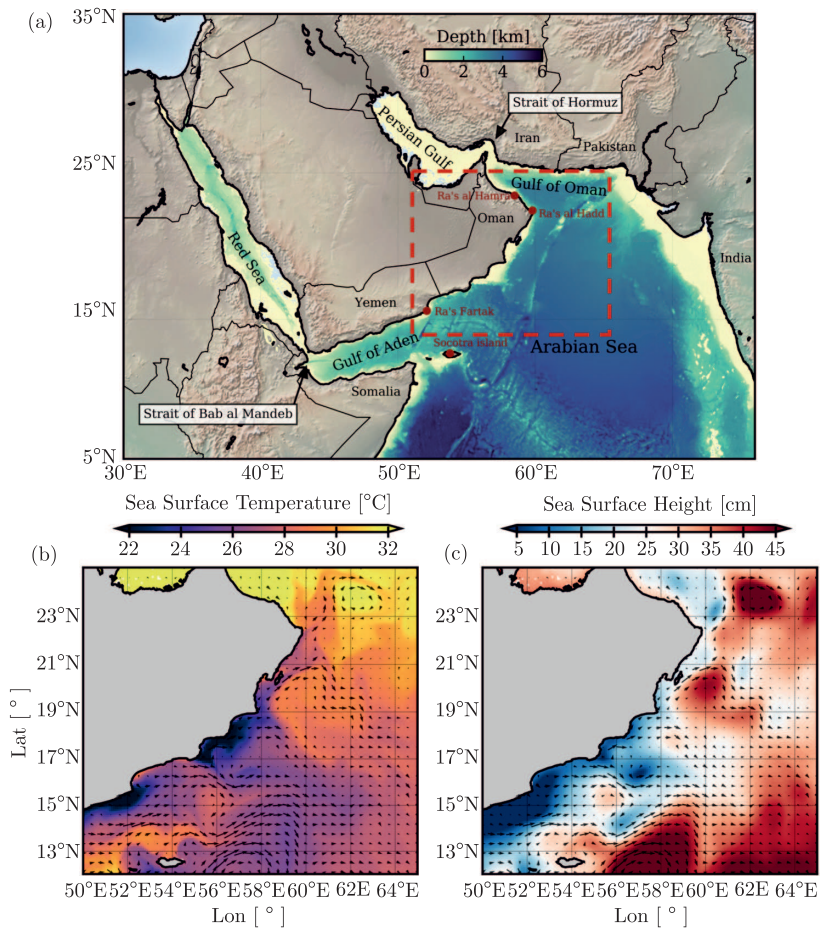


Fig. 1. (a) Bathymetry in the Arabian Sea and adjacent gulfs from ETOPO2 [45], dashed rectangle shows the geographic position of panels (b), (c). (b) Sea Surface Temperature and (c) Sea Surface Height (SSH) along the Omani coast in the Arabian Sea on 05/08/2020. Arrows show the geostrophic velocity derived from SSH. Cold filaments resulting from the steering of the upwelling by mesoscale eddies are seen near 56°E 16°N . Data are from Operational Mercator global ocean analysis and forecast system (downloaded on the Copernicus website).

offshore, leading to an outcropping of deeper and colder water from depths of 150 m. This cold water (which can be 5°C cooler than the Arabian Sea surface water) is rich with nutrients, favoring the local biological activity. And indeed, this upwelling region is an intense fishing area. When the upwelling is developed (in August/September), the sea surface height near the coast can lie 30 cm below the offshore sea surface and a northeastward current, the Oman Coastal Current, flows offshore. Western boundary upwellings are more energetic than their eastern boundary counterparts because they absorb energy from incoming Rossby waves. The temperature and salinity fronts which bound the upwelling region offshore are not steady. They often meander and they may form cold filaments. Capes play an important role in the offshore growth and protrusion of cold filaments from upwellings [12, 32, 44]. These filaments can extend offshore over more than 250 km and bring nutrients into the oligotrophic surface ocean [24]. South of Oman, the upwelling lasts for the whole summer and interacts with the local eddy field [see Fig. 5 of 44]. The upwelling front and current can form meanders and eddies, either by instability or *via* the interaction with the eddies [see Fig. 5 of 40]. The evolution of an upwelling front and coastal current in the presence of external vortices,

and its comparison with the evolution of an unstable front in the absence of such vortices, is the subject of the present paper, with application to the Arabian Sea (again, see Fig. 1).

The structure and stability of upwelling systems, with fronts and currents, have been the subject of many previous studies [11, 17, 29, 33, 54, to name a few]. The first studies were aimed at understanding the spin-up of the upwelling as the wind starts to blow and before it becomes a well established front associated with a geostrophic current. In particular, the role of the frictional boundary layers in the formation of the upwelling was investigated [33]. The importance of the topographic constraint on the deep boundary layer was analyzed [34, 35]. Analytical solutions of the density and velocity structure were provided for a time-varying wind stress forcing the upwelling. In particular, the formation of a subsurface countercurrent was studied with regard to the vertical mixing of heat and momentum [29]. For an upwelling south of a zonal coast, an eastward baroclinic current builds up as the offshore front steepens. When the wind stress has a longshore variation, Kelvin waves propagate along the coast, away from the upwelling region. The alongshore flow deviates from geostrophy. Ageostrophic velocities perpendicular to the coast then form a two-cell vertical circulation [47].

In our study, we investigate the instability of the geostrophic current associated with the offshore upwelling front, or how it interacts with an external eddy field; we assess the consequences of these interactions on cross-shore transport. The interaction between a zonal current and a single external eddy has been the subject of several studies. Pratt & Stern [38] studied the growth and detachment of an eddy from a potential vorticity front in a one-layer model. Stern & Flierl [46] considered the interaction between a single eddy and a zonal potential vorticity front in a one-layer model (with finite or infinite radius of deformation). They showed that, in the linear stage of the interaction, the surface integral of vorticity in the meander of the front is equal and opposite to the area integral of the eddy vorticity. This leads to a dipolar effect which can advect the eddy along the front. Vandermeersch et al. [50, 51] determined the conditions under which an eddy can cross a potential vorticity front meridionally, in one and two-layer models. The existence of a stagnation point (a hyperbolic point in the flow field) was found as a necessary condition for this crossing. This condition is identical for the detachment of an eddy from an unstable front [8]. These latter authors found that the circulation of the detached eddy was proportional to that enclosed within a wavelength of the meandering front, extending offshore to the stagnation point.

This paper is organized as follows. Section 2 describes the numerical model and the analysis tools. In particular, the novelty of this paper lies in the use of a three-dimensional model (see supplementary information for the presentation of the 3D evolution of some simulations discussed in this study). Section 3 details the numerical results of the upwelling current instability, in the absence of vortices. The results are analyzed with respect to the characteristic wavelengths of the meanders growing on the current and of the inshore and offshore transports. Section 4 considers the nonlinear evolution of the front in the presence of a single vortex offshore. Cyclone-anticyclone asymmetry is considered since the flow is not quasi-geostrophic. Section 5 considers the situation where multiple vortices exist south of the front, as observed in the Arabian Sea. Section 6 characterizes the cross-shore exchanges with particle tracking. Conclusions follow.

2. METHODS

2.1. The Numerical Simulations

In this section, we present the idealized model runs performed for this study. The aim of these runs is to study the instability of an upwelling front and to simulate the interaction of an upwelling front with one or several vortices.

2.1.1. Numerical setup and domain

The simulations are carried out in a 3D hydrostatic primitive equation framework. They are performed using the Coastal and Regional Ocean Community (CROCO) model [42]. This model solves the hydrostatic primitive equations for the velocity, temperature, and salinity, using a full equation of state for seawater [43]. The simulations performed integrate the primitive equations for 1 year. The numerical settings are similar to previous simulations performed in an idealized context (see, e. g., [27, 31]): horizontal advection terms for tracers and momentum are discretized with fifth-order upwind advection schemes (UP5); the explicit horizontal viscosity and diffusivity are set to

zero, since the UP5 scheme damps dispersive errors; the vertical advection is discretized with a fourth-order centered parabolic spline reconstruction (splines scheme). Further discussion about these parameterizations can be found in Klein et al. [20] or Ménesguen et al. [31]. Vertical mixing of tracers and momentum is done using a K-profile parameterization [KPP, 22], and there is no bottom friction. Simulations have 32 terrain-following vertical levels, which are stretched such that the vertical resolution is $\Delta z \sim 8$ m at the surface, and $\Delta z \sim 120$ m at the bottom. The horizontal resolution is 5 km. The domain is square, with a length $L_{\text{domain}} = 2000$ km or $L_{\text{domain}} = 3000$ km in vortex alley simulations (see details below). The bottom is flat and 2000 m deep. We set the Coriolis parameter to $f = f_0 = 10^{-4} \text{ s}^{-1}$ or $f = f_0 + \beta y$, with $\beta = 2 \times 10^{-11} \text{ m}^{-1} \text{ s}^{-1}$ and y the meridional coordinate. The northern and southern boundaries are closed, with a 10 km wide sponge layer to avoid the generation of spurious boundary dynamics. A zonal periodic condition is chosen at the eastern and western boundaries such that the domain is a zonal channel.

We initialize an analytical background stratification $N(z)$, which fits the average ambient stratification in the five major oceanic basins, similarly as in de Marez et al. [25, 28]:

$$N(z) = N_0 + N_1 e^{z/z_h}, \quad (2.1)$$

with $z < 0$ the vertical coordinate, $N_1 = 9 \times 10^{-3} \text{ s}^{-1}$, $z_h = 150$ m, and $N_0 = 7 \times 10^{-3} \text{ s}^{-1}$. Integrating this stratification from the surface (where $\rho(z=0) = 1030 \text{ kg m}^{-3}$), gives the ambient density background $\rho(z)$; the temperature background $T(z)$ is obtained by inverting the TEOS-10 equation of state for seawater [30] and assuming a constant salinity background $S(z) = 35$ psu. The model is initialized with these temperature and salinity background profiles.

2.1.2. Components of simulations

Upwelling front. We chose to study the evolution of the upwelling front once it is established by the wind forcing. This established front is the initial condition of our simulations, which are then run in free decay. These simulations determine the further, unforced, evolution of this front. Not adding surface forcing in the simulations allows us to analyze specifically the front instability or the front-vortex interaction as a classical initial-value problem. Our simulations have an application to the ocean when the time scales of the evolution are shorter than those of the forcing. For other cases, simulations with forcing, or with a relaxation towards a prescribed state, will be performed in a follow-up of this study. It must be noted that free-decay simulations have often been used in studies of oceanic flow stability, since they produce instability waves which depend only on the current and not on the forcing.

We simulate the presence of an upwelling front by initializing a zonal jet of a given velocity profile, similarly as in Barth [4]; this velocity profile has the form:

$$u_{up} = V_0^{up} e^{z/H} e^{-\left(\frac{y-y_0^{up}}{L}\right)^2}, \quad (2.2)$$

with V_0^{up} the initial velocity of the upwelling jet, $y_0^{up} = L_{\text{domain}}/2$ the latitude of the upwelling jet, and H and L the vertical and zonal extent of the upwelling jet, respectively. This current is then geostrophically adjusted with the density field and the sea surface height. This leads to a temperature front separating cooler waters in the north from warmer waters in the south.

In the simulations discussed in this study, we set $V_0^{up} = 0.2 \text{ m s}^{-1}$, $H = 200$ m, and $L = 50$ km. These values correspond to those chosen in previous studies (see, e. g., [4, 52]) for the study of upwellings.

Sinusoidal perturbation. To trigger the upwelling front instability, we add a sinusoidal perturbation along the front, directly in the initialization of a few experiments. This disturbance idealizes the observed perturbations due to the surrounding flow, or to the atmospheric influence, on the upwelling front. It is usual to choose a single wave as a perturbation in the linear, normal-mode theory of flow stability. This disturbance is here a temperature anomaly centered around y_0 , and of the form

$$T_{\text{pert}} = 0.5 e^{-z/500} e^{-\left(\frac{y-y_0^{up}}{50 \cdot 10^3}\right)^2} \cos\left(\frac{2\pi}{\lambda_{\text{pert}}} x\right), \quad (2.3)$$

with x the zonal direction, and $\lambda_{\text{pert}} = [50, 100, 250, 500, 1000]$ km. Varying the wavelength allows the determination of the fastest growing disturbance. The choice of a perturbation deeper than the

mean flow is motivated by the likeliness that it is triggered by neighboring currents which are deeper than the upwelling: vortices or marginal sea outflow currents or baroclinic Rossby waves. A density anomaly is then computed assuming that the perturbation has no signature in salinity. The velocity field associated with this density anomaly is then obtained *via* the thermal wind balance.

Vortex. To address the main objective of this article (the interaction of an upwelling front with a pre-existing vortex field), we initialize one or several surface-intensified vortices south of the upwelling front (offshore), in the vortex-front interaction simulations. When several vortices are initialized, they are aligned along the coast offshore of the front. These vortices are initialized in azimuthal velocity (or in vorticity) as in de Marez et al. [25, 28]. For each vortex, we set the initial profile of surface vertical vorticity:

$$\omega(r) = \pm\omega_0 e^{-\left(\frac{r}{R}\right)^\alpha}, \quad (2.4)$$

with the sign depending on the vortex polarity, $r = \sqrt{(x - x_c)^2 + (y - y_c)^2}$ the radial coordinate referenced at the center of the vortex (x_c, y_c) , and α (usually an integer) the steepness parameter.

The surface azimuthal velocity of the vortex can be computed using $v_\theta(r, 0) = \frac{1}{r} \int r dr \omega r$. In general it takes the complicated form $v_\theta(r) = (\omega_0 R^2 / (\alpha r)) \gamma((2/\alpha), (r/R)^\alpha)$, where $\gamma(s, x)$ is the incomplete gamma function. In the well-known case of a Gaussian vertical vorticity, with $\alpha = 2$, the azimuthal velocity is $v_\theta(r) = \omega_0 \frac{R^2}{r} [1 - e^{-r^2/R^2}]$. In this case, this velocity grows linearly with r , for $r \ll R$, similarly to Rankine vortices. Far from the center, it decays at best as $1/r$ (that is, slower than for a Rankine vortex). To avoid the presence of spurious velocity at the edges of the domain, we apply a Hanning window on v_θ to make it smoothly tend to zero at $r > 3R$. The horizontal velocity decreases at depth such that $v_\theta(x, y, z) = v_\theta(x, y, 0) e^{-z/H_{\text{vortex}}}$, thus defining the height of the vortex H_{vortex} . We denote (u, v) the horizontal Cartesian components of the velocity of the vortex. The pressure anomaly field $P'(x, y, z)$ corresponding to this velocity field is computed *via* the gradient wind equation:

$$2J(u, v) + f(\partial_x v - \partial_y u) = \frac{1}{\rho} \Delta_h P', \quad (2.5)$$

with $J(u, v) = \partial_x u \partial_y v - \partial_y u \partial_x v$ the Jacobian operator, and Δ_h the horizontal Laplacian operator. From P' we determine the density and the temperature anomalies of the vortex. These anomalies are computed for as many vortices as we want, at positions x_c and y_c . Note that such vortices are robust during the whole simulation.

We set $H_{\text{vortex}} = 1000$ m, as surface-intensified vortices are mostly about 1000 m deep in this part of the ocean [9, 19, 26, 36], and $\alpha = 24$, so that the vortex has a profile close to a Rankine vortex (also called a top-hat vortex, as in, e.g., [28]). For our study, we vary other initial parameters as $R = [50, 100]$ km, and $V_0^{\text{vortex}} = [0.2, 0.4, 0.6]$ m s⁻¹ for both cyclonic and anticyclonic vortices. For each set of parameters, we also vary the initial distance between the vortices and the upwelling front as $d/R = [2.0, 3.0, 4.0, 5.0]$, thus setting y_c .

In simulations with an isolated vortex, we set $x_c = L_{\text{domain}}/2$. For simulations with a zonal vortex alley (i.e., an alley of vortices of alternated polarities, at a given latitude, with a constant spacing between their centers) we also vary the distance between each vortex $d_{\text{btw}}/R = [2.0, 3.0, 4.0]$ and the number of vortices $N = [2, 4, 6]$. In these cases, the center (in the zonal direction) of the vortex alley is at the center of the domain $L_{\text{domain}}/2$. Therefore, $L_{\text{domain}} = N \times d_{\text{btw}}$.

A summary of the three kinds of simulations we ran, with the different parameters we varied, is shown in Fig. 2.

2.2. Diagnostics

2.2.1. Modal decomposition

To analyze the growth of perturbations on the upwelling front, we decompose its deviation from a straight front in zonal Fourier series. We apply this analysis to the surface temperature field at each time step

$$T(x, y) - \langle T(y) \rangle = \sum_{j=0}^{j=\infty} [c_j(y) \cos(jx) + s_j(y) \sin(jx)] \quad (2.6)$$

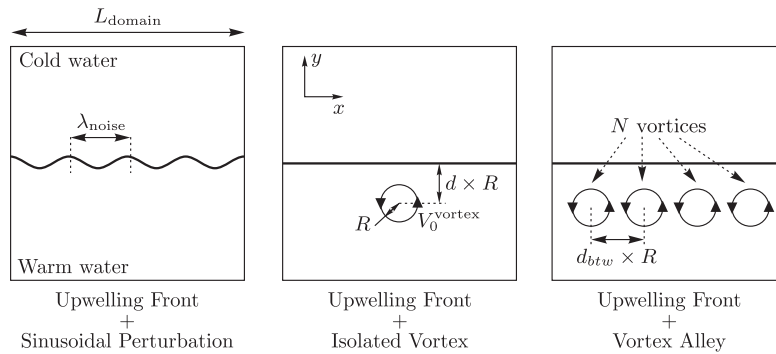


Fig. 2. Scheme of the three kinds of simulations we performed and the different physical parameters we varied.

where $\langle T(y) \rangle$ is the straight temperature front corresponding to $u^{up}(y, z = 0)$. Then, to examine only the modes of the upwelling front, we average c_j and s_j in a 100 km wide meridional band. This gives the time-varying amplitude of each mode $\langle c_j^2 + s_j^2 \rangle_y(t)$. In the following, we present and discuss the wavelength of each mode $\lambda = L_{\text{domain}}/j$, with L_{domain} the size of the domain (2000 km).

2.3. The Frontogenesis Function

To characterize the evolution of buoyancy gradients, we calculate the frontogenesis function F associated with the buoyancy. It is defined as follows [18]:

$$F(\mathbf{u}, b) = \partial_x u (\partial_x b)^2 + (\partial_x v + \partial_y u) \partial_x b \partial_y b + \partial_y v (\partial_y b)^2.$$

The opposite of the function F indicates the tendency of the buoyancy gradients to steepen:

$$-F(\mathbf{u}, b) = \frac{d}{dt} |\nabla b|^2.$$

2.4. Particle Advection

We ran particle advection simulations, using the outputs of CROCO simulations, with the set of python classes Parcels (Parcels stands for “Probably A Really Computationally Efficient Lagrangian Simulator”). This software simulates the advection of an ensemble of particles using a given 2D or 3D velocity field. This tool has been widely used in the past few years, and it is fully described in Delandmeter & van Sebille [13], Lange & van Sebille [21] and in references therein.

The surface velocity field is used here, and the forward advection is computed with a fourth-order Runge–Kutta scheme (time spacing $dt = 5$ minutes). Particles are initially set at $t = 0$ days on a regular grid, at $100 \leq x \leq 1900$ km and $500 \leq y \leq 1500$ km, with a spacing between particles of 25 km. Thereby, a total of 2993 particles are advected throughout the year of simulation.

3. ANALYSIS OF THE UPWELLING FRONT INSTABILITY

3.1. Modal Analysis of Growing Perturbations

Firstly we studied the instability of the straight upwelling front alone (in the absence of any initial vortex). Only a sinusoidal perturbation was added along the front, to trigger its instability (see Section 2.1.2 and Fig. 2(left)). The modal amplitude of the growing perturbations (the unstable waves on the front) for various perturbation wavelengths, when one neglects the β -effect (i. e., on the f -plane), is shown in Fig. 3a. We distinguish the time series of amplitudes for a mode with a given wavelength initially (λ_{pert}), from those for the mode which is finally the most unstable one (λ_{max}), and has this wavelength (see also the figure caption). If the initial wave grows the fastest, then $\lambda_{\text{pert}} = \lambda_{\text{max}}$.

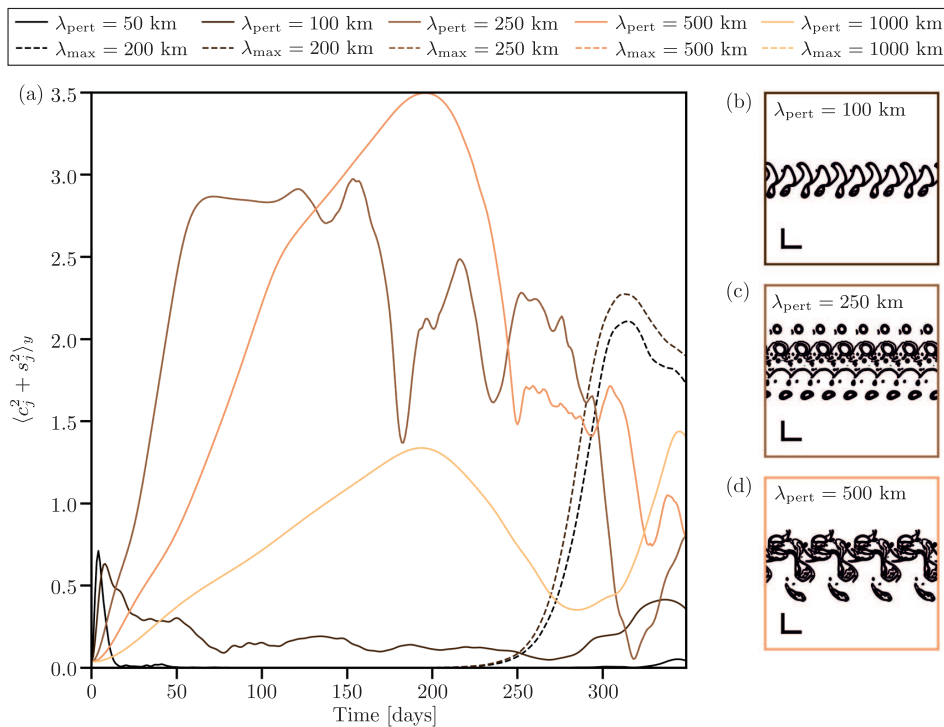


Fig. 3. (a) Time evolution of the amplitude of modes from the modal decomposition of the surface temperature, in simulations with an upwelling front and an initial sinusoidal perturbation, for $L = 50$ km, $H = 200$ m, and $V_0^{up} = 0.2 \text{ m s}^{-1}$. The color of the line indicates the wavelength of the wave at initialization (λ_{pert}), such that one color designates one simulation. The solid lines show the evolution of the mode with the same wavelength as the initial perturbation (λ_{pert}), while the dashed lines show the evolution of the mode that reaches the largest amplitude (with a wavelength λ_{max}). If the solid and dashed lines are superposed, the mode that reaches the largest amplitude has the same wavelength as the initial perturbation. (b), (c), and (d) Surface temperature contours after one year in the simulations with $L = 50$ km, $H = 200$ m, and $V_0^{up} = 0.2 \text{ m s}^{-1}$, and $\lambda_{\text{pert}} = 100, 250, \text{ and } 500$ km. Sizebars in the bottom left of each panel show a distance of 200×200 km.

When they are forced initially, waves shorter than the most unstable one also grow, but decay rapidly; thus they do not reach large amplitudes. They dominate at short time for fast jets and may thus be related to horizontal shear flow instability. On the contrary, longer waves reach larger amplitudes with time, either within a month or within 8 months. In particular, waves with 200–250 km wavelength are the most unstable over a 1–3 months period; they are followed in amplitude by 500 km long waves. With an internal radius of deformation close to 50–60 km in this oceanic region [10], a wavelength of $2\pi R_d = 300\text{--}350$ km is characteristic of baroclinic instability. Therefore, the growth of these long waves in the first months of simulation can be related to the development of baroclinic instability along the jet. When long waves grow after a longer period (e.g., 8 months), their origin is rather to be searched for in wave-wave interaction, since the flow is not forced.

A similar modal analysis but now including the β -effect is shown in Fig. 4a. The β -effect renders flows zonal so that long waves are damped (see, e.g., Flierl et al. [16] or the well-known Phillips model of baroclinic instability [49]). As a result, the most unstable waves in our simulations lie near ~ 100 km wavelength. In fact, the dimensionless value of β is $\beta L^2/U = L^2/L_{\text{Rhines}}^2$. For the same geophysical value of $\beta = 2 \times 10^{-11} \text{ m}^{-1} \text{ s}^{-1}$, this damping effect will be weak for a fast jet such as the Gulf Stream ($U = 1 \text{ m s}^{-1}$), but stronger for the jet associated with a typical upwelling front (in our simulations, $U = 0.2 \text{ m s}^{-1}$). Therefore, meanders on the upwelling front are expected to have a shorter wavelength than those of intense jets such as western boundary currents.

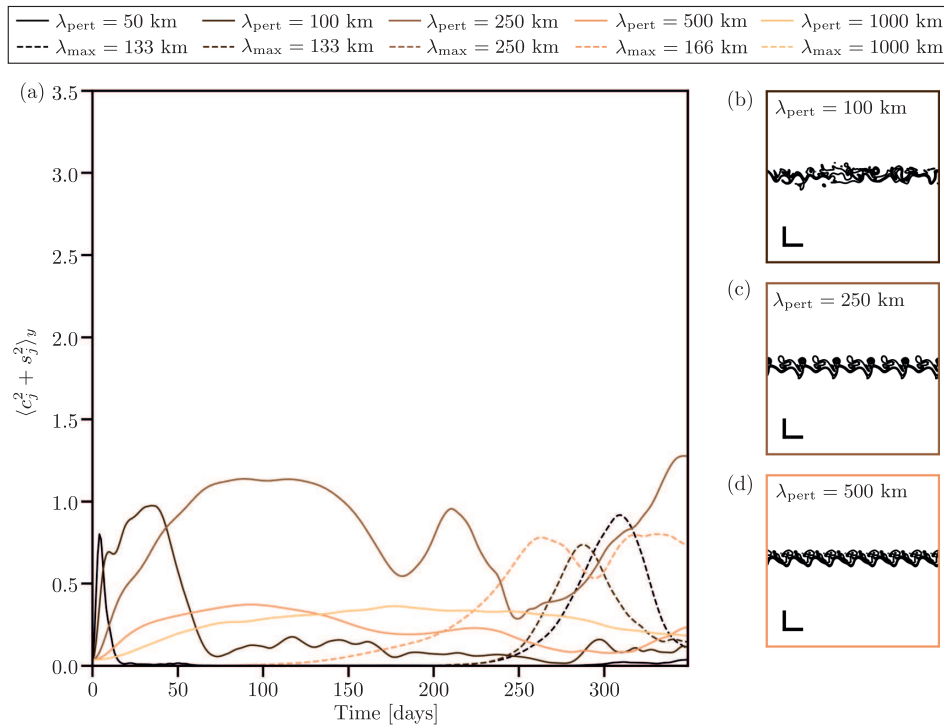


Fig. 4. Same as Fig. 3, but with a β -effect added in the simulation.

3.2. Spatial Structure of the Front with Growing Perturbations

3.2.1. In the absence of β -effect

When short waves are forced initially, they can grow even if they are shorter than the linearly most unstable wave. This growth will only be transient. These short waves saturate in amplitude without breaking and then slowly decay. Longer waves break and form vortices of about 200 km diameter (see Fig. 3b). We note that northward extending (anticyclonic) meanders do not form vortices, while southward (cyclonic) meanders do. This north-south asymmetry of meanders on a front can be explained by (1) the difference in local deformation radius (smaller to the north than to the south if the upper ocean layer is thinner to the north); for baroclinic instability, a smaller deformation radius favors the growth of shorter waves (and conversely); and (2) the curvature vorticity $V/r \partial_r V$, which contrary to the geostrophic vorticity is parity biased (here V is the jet velocity magnitude in the meander and r is the radius of curvature of the meander). These arguments can explain the growth of longer waves than those initialized, south of the jet, thus leading to the breaking of meanders into vortices. Such asymmetries do not appear in quasi-geostrophic simulations of jet instability.

The most unstable wave is determined by computing its growth during the early stage of the evolution. When this wave is initialized (e. g., $\lambda_{\text{pert}} = 250$ km), it grows up to breaking the front, generating vortices of ~ 200 km diameter. Since the most unstable perturbation is initialized everywhere, vortices form both north and south of the jet. Along the central latitude, the jet comes back to a quasi-zonal state once the vortices have detached. This effect has been explained in previous studies [3] and it can be clearly seen in Fig. 3c.

If a longer wave is initialized, shorter waves emerge via nonlinear wave-wave interactions, and finally vortices of ~ 200 km diameter form. These nonlinear wave interactions also generate other features such as filaments and smaller vortices (see Fig. 3d).

3.2.2. In the presence of the β -effect

When the β -effect is added, long waves do not grow and shorter waves dominate the evolution of the flow. This leads to the generation of filaments and of small vortices (of ~ 50 km diameter). The most unstable waves form vortices of ~ 100 km diameter. Since the β -effect renders flows zonal, meanders grow less north and south, and the perturbations remain confined near the front axis, see Figs. 4b–4d. Even long waves imposed initially on the front bifurcate towards smaller meanders. Still, they do not form very small scale features and thus the flow pattern is spatially more regular.

4. UPWELLING FRONT EVOLUTION IN THE PRESENCE OF A SINGLE VORTEX

Now that the instability of the front, without external vortex, has been studied, we investigate the influence of a single vortex on this same front. The vortex is initialized south of the front and it replaces the perturbation added to the front in the previous section (see Section 2.1.2 and Fig. 2(middle)). This vortex deforms the front along its own spinning motion. Here, we do not perform a Fourier analysis of the front perturbation; indeed, the wavelength which is the most unstable on the straight front in the absence of external vortex is now perturbed by the presence of the vortex. Performing this analysis here would in particular reflect the vortex size. For the simulations discussed here, the vortex position, polarity, radius, and velocity are varied. The evolution of the front on the f -plane and on the β -plane is now presented. The position of the front is chosen as the isotherm corresponding to the average of the northern and southern temperature after 100 (resp. 200) days of simulated time in Fig. 5 (resp. Fig. 6).

4.1. The Reference Cases

To further study the influence of the vortex parameters on the front stability, we define reference cases, for which the vortex can have either polarity, a radius $R = 100$ km (corresponding to the radius of vortices formed by the instability of the front previously described), a distance to the front $d = 2R$, and an azimuthal velocity $V_0^{\text{vortex}} = \pm 0.2 \text{ m s}^{-1}$ initially. The front positions in these cases are shown by solid color lines in Figs. 5 and 6.

In this case, on the f -plane, the presence of a vortex south of the front induces a meridional deformation of the front in its vicinity, but not over the whole length of the domain, during the first three months of simulation. At later times (200 days), this filament extrudes offshore and detaches from the front. Also, the most unstable wave of the front grows, leading to small scale perturbations along the whole front.

After 3 months, we observe that, if the vortex is cyclonic, the front is more deformed than if the vortex were anticyclonic. This can be explained by the following. Though their relative vorticities are initially antisymmetric, their Ertel potential vorticities are asymmetric. Indeed, even at first order beyond quasi-geostrophy the absolute vorticity multiplies the density anomaly, and we can write this first-order Ertel potential vorticity anomaly as

$$\delta Q = \omega + (f_0 + \omega)b/N^2,$$

where b is the buoyancy anomaly associated with the vortex, and N the Brunt–Väisälä frequency $N^2 = -\frac{\partial b}{\partial z}$. δQ characterizes the vortex ability to remotely influence its environment. Since ω and b are antisymmetric at first order for cyclones and anticyclones, δQ is larger in modulus for cyclones. Again at first order, this potential vorticity anomaly is conserved in time. In [46] it is shown that, in two-dimensional flows, a vorticity front develops a meander with equal and opposite circulation to that of the vortex deforming it. Applying this principle here explains why fronts extrude longer and/or larger filaments when nearing a cyclone than an anticyclone; this can be seen after 100 simulated days. After 200 days, the perturbation breaks down nonlinearly and becomes spatially more convoluted and intricate. These nonlinear effects can also lead to the production of long offshore filaments by fronts under the influence of anticyclones, but this effect is weaker than after 100 days. Meanders and filaments are much smaller in the presence of the β -effect than in its absence.

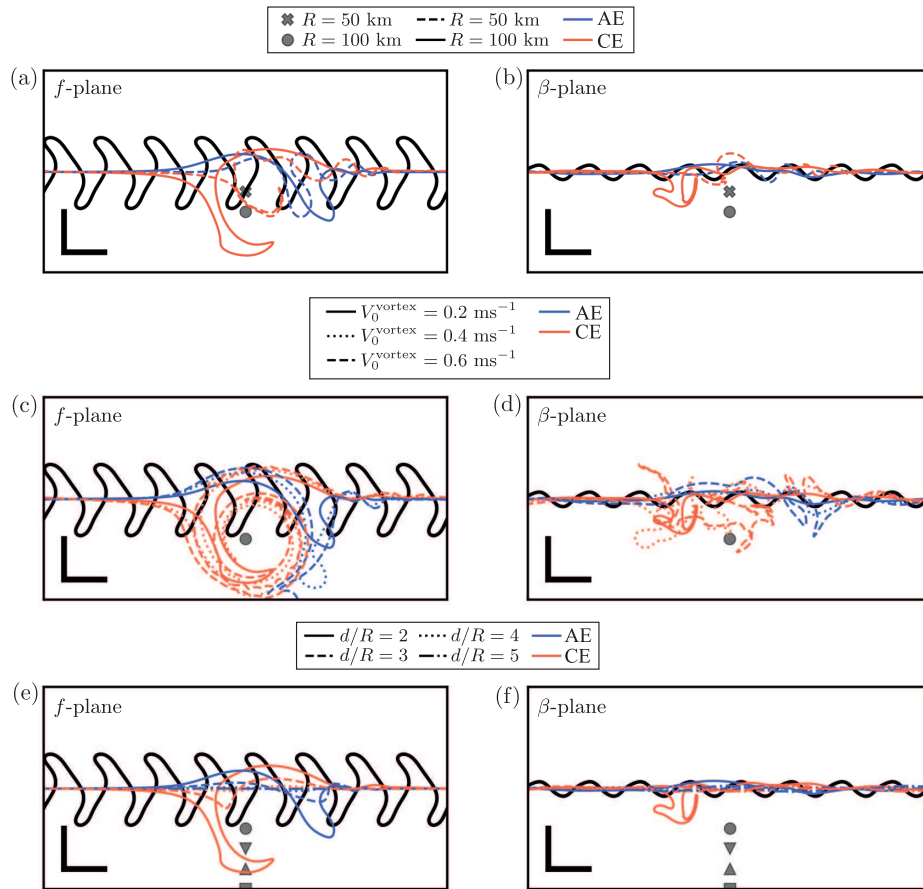


Fig. 5. Position of the upwelling front (initially $L = 50$ km, $H = 200$ m, and $V_0^{\text{up}} = 0.2 \text{ m s}^{-1}$) at $t = 100$ days, in simulations with an isolated vortex of parameters (a), (b) $d/R=2$, $V_0^{\text{vortex}} = 0.2 \text{ m s}^{-1}$, and different values of vortex radius R ; (c), (d) $d/R = 2$, $R = 100$ km, and different values of azimuthal velocity V_0^{vortex} ; (e), (f) $V_0^{\text{vortex}} = 0.2 \text{ m s}^{-1}$, $R = 100$ km, and different values of upwelling-vortex distance $dR/$. The left (resp. right) column shows simulations without (resp. with) β -effect. Note that, for each column, solid lines of a given color show the same simulation. In all panels, the black line shows the upwelling front initialized along with a sinusoidal perturbation ($\lambda_{\text{pert}}=250$ km), the red (resp. blue) lines show the upwelling front initialized along with a cyclonic (resp. anticyclonic) vortex, markers show the initial position of the vortex, and sizebars in the bottom left show a distance of 200×200 km.

4.2. Sensitivity to the Vortex Radius

The influence of the vortex radius R on the flow evolution is studied for a vortex lying at a distance $d = 2R$ from the front, with an azimuthal velocity $V_0^{\text{vortex}} = \pm 0.2 \text{ m s}^{-1}$ initially, see Figs. 5a, 5b and 6a, 6b. Under these conditions, wider vortices lead to longer filaments offshore both after 100 and 200 days. On the f -plane, smaller vortices yield more wave amplification downstream, and in particular more coastal intrusion of open ocean fluid (i. e., south of the front). The growth of a longer filament in the presence of a larger vortex is also associated with a weaker growth of the 200 km long wave on the front; the evolution of the front under the influence of the vortex supersedes the unstable evolution of the front (alone). At long times, the long frontal wave recovers its strength of the jet instability case, for both small and large vortices. In the presence of the β -effect, cyclonic vortices drift northwestward and thus come closer to the front, while anticyclonic vortices drift away from the front on the β -plane, explaining the difference in the generated filament

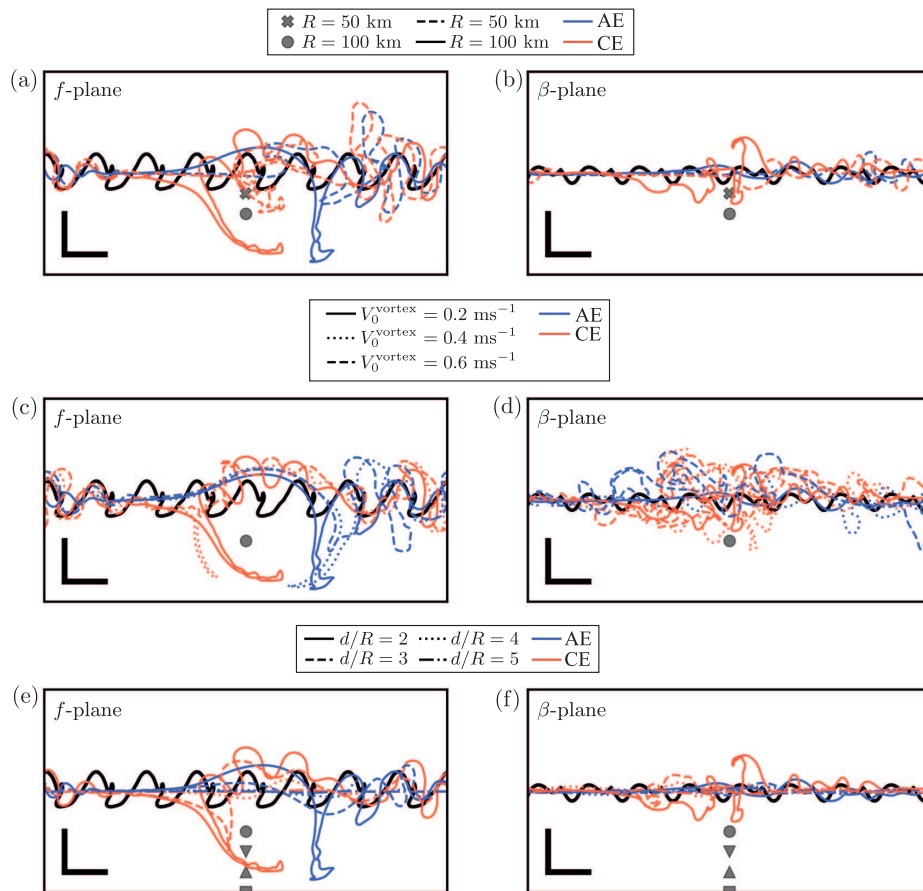


Fig. 6. Same as Fig. 5 at $t = 200$ days.

lengths. Again, the zonal straightening effect of β on streamlines prevails, so that shorter filaments are generated on the β -plane than on the f -plane.

4.3. Sensitivity to the Vortex Intensity

The influence of the vortex intensity V_0^{vortex} is studied for a vortex lying at a distance $d = 2R$ from the front, with a radius $R = 100$ km initially, see Figs. 5c, 5d and 6c, 6d. When V_0^{vortex} increases, so does the vortex dynamical influence on the front. Thus, the filaments growing from the front increase in size.

On the f -plane, after 100 days, the filaments wrap up around the vortex. Though the perturbation is concentrated around the quasi-steady vortex, this interaction leads to much offshore export of coastal fluid. Again, cyclones disturb the front more deeply than anticyclones do. After 200 days, filaments still protrude far offshore on the f -plane, but forced waves have now propagated along the front axis so that much offshore-coastal fluid exchange occurs, all along the front axis.

On the β -plane, short waves develop on the front, with smaller amplitude than on the f -plane. The most intense external vortices induce more small scale turbulent features. Again, more small-scale features are induced by cyclones than by anticyclones. After 100 days, these small-scale features remain trapped between the front and the vortex and do not drift far offshore. This can be related to the flow straightening by the β -effect and to the westward vortex drift which, for the front and its meanders, displaces the external deformation field. After 200 days, turbulence has

developed from its state at $t = 100$ days. It extends all along the front and the inshore-offshore fluid exchange is amplified. Still, no coastal fluid is advected offshore beyond the vortex. Here, the meridional gradient of upper layer vortex stretching (across the front) is positive, which increases the westward Rossby wave speed so that frontal meanders are located more to the West than on the f -plane.

4.4. Sensitivity to the Vortex Distance to the Front

The influence of the distance between the vortex and the front d/R is studied for a vortex with a radius $R = 100$ km, and an azimuthal velocity $V_0^{\text{vortex}} = \pm 0.2 \text{ m s}^{-1}$ initially, see Figs. 5e, 5f and 6e, 6f. The same observations as in the previous subsection hold here. On the f -plane, after 100 days, long waves grow and large meanders break into offshore filaments when the vortex is close to the front ($d/R = 2$ or 3). After 200 days, shorter waves develop and affect the whole length of the front. Here again, cyclones induce more pronounced deformations and longer filaments than anticyclones. When $d/R = 4$ or 5, very little deformation of the front occurs, both on the f - and on the β -plane. As a consequence, vortices lying 400 km away from the upwelling front influence it very little, as could be anticipated from the calculation of the velocity field. On the β -plane, the stabilizing effect of the planetary vorticity gradient confines the waves and the turbulence to the vicinity of the front.

5. INTERACTION OF AN UPWELLING FRONT WITH A VORTEX ALLEY

Though the interaction of a single vortex with an upwelling front is an important step in our study, and though analyzing this case provides important and general conclusions, sea surface measurements in the Arabian Sea show that the southern Omani upwelling is rarely bordered by only one vortex; multiple vortices surround the front (see, e. g., Fig. 1). Therefore, we generalize the previous case to that of a vortex alley along the front (see Section 2.1.2 and Fig. 2(right)). We use the physical vortex parameters of the most significant case previously analyzed: $V_0^{\text{vortex}} = 0.2 \text{ m s}^{-1}$, $R = 100$ km, and $d/R = 2$. Here we vary the alongshore distance between the vortices d_{btw} , the number of vortices N , and the presence or absence of the β -effect.

5.1. Sensitivity to the Number of Vortices

We present the case with $d_{\text{btw}}/R = 4$, which shows the highest efficiency for filament production, for $N = 2 - 6$ vortices, see Figs. 7a, 7b and 8a, 8b. On the f -plane, at $t = 100$ days, the effect for each vortex is comparable to that of a single vortex, i. e., long filaments protrude offshore from the front. The velocity field resulting from the addition of the vortices is stronger at the center of the domain, and thus the filaments are longer there. Filaments are advected southward between an anticyclone (to the west) and a cyclone (to the east). On the contrary, the front is pushed northwards and forms a wide meander to the north, between a cyclone (to the west) and an anticyclone (to the east). At $t = 200$ days, the filaments have been cut, and some of them are brought closer to the front by the velocity field of the zonal jet. We can also see (as in the reference cases, see Section 4.1), the development of shorter waves, which now grow on the wide meanders. This state is comparable to that of the nonlinear evolution of the unstable front in the absence of external vortices initially. Note a difference between the present case and that with a single external vortex: here, the front is shifted north, which did not occur with only one vortex. On the β -plane, again, shorter and less prominent meanders and filaments are produced after 100 days. These waves break into a turbulent field, in the vicinity of the front, after 200 days.

5.2. Sensitivity to the Distance Between Vortices

The influence of the distance between vortices within the vortex alley d_{btw}/R is studied for a vortex alley of 6 vortices (i. e., $N=6$, this corresponds to cases with the most intense deformation of the front), see Figs. 7c, 7d and 8c, 8d. We do not detail each figure individually, but we note that, for short times, the larger the intervortex distance, the stronger the offshore mass transport. Indeed, the alongshore extent of the front deformation and the filament widths increase with d_{btw} . At longer time, the northward displacement of the front is larger for small d_{btw} because the vorticity dipoles which are generated are more intense (the distance between the centers of the two vortices in the dipole being smaller). On the contrary, on the β -plane, the front shows more long wave (200 km length) instability when d_{btw} is larger (the vortices triggering longer waves). Again, the β -effect reduces the amplitude of meanders and intensifies turbulence in the vicinity of the front.

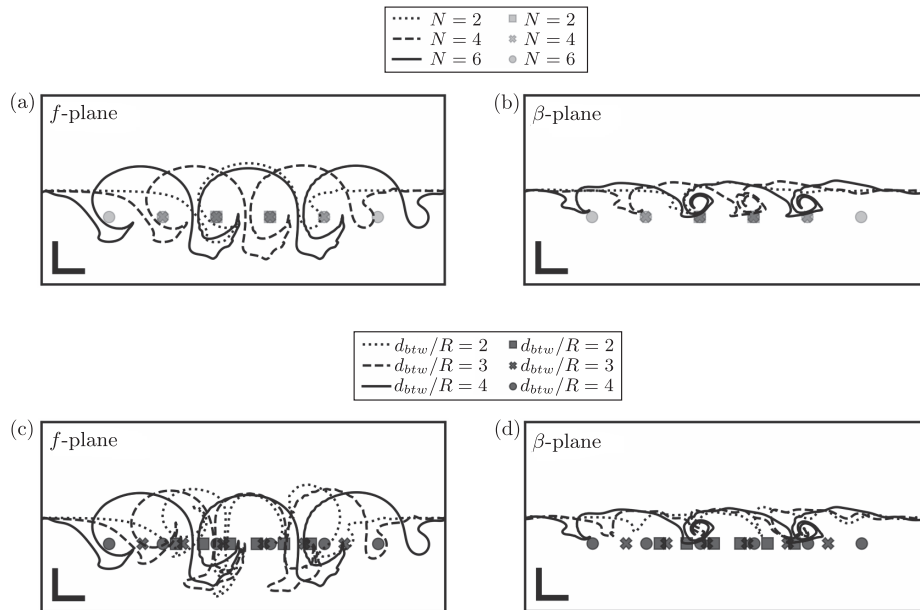


Fig. 7. Position of the upwelling front (initially $L = 50 \text{ km}$, $H = 200 \text{ m}$, and $V_0^{\text{up}} = 0.2 \text{ m s}^{-1}$) at $t = 100$ days, in simulations with a vortex alley of parameters (a), (b) $d/R=2$, $V_0^{\text{vortex}} = 0.2 \text{ m s}^{-1}$, $R = 100 \text{ km}$, $d_{btw}/R = 4$, and different number N of vortices; (c), (d) $d/R=2$, $V_0^{\text{vortex}} = 0.2 \text{ m s}^{-1}$, $R = 100 \text{ km}$, $N = 6$, and different values of distance between vortices d_{btw}/R . The left (resp. right) column shows simulations without (resp. with) β -effect. Note that, for each column, solid lines show the same simulation. The markers show the initial position of vortices, and sizebars in the bottom left show a distance of $200 \times 200 \text{ km}$.

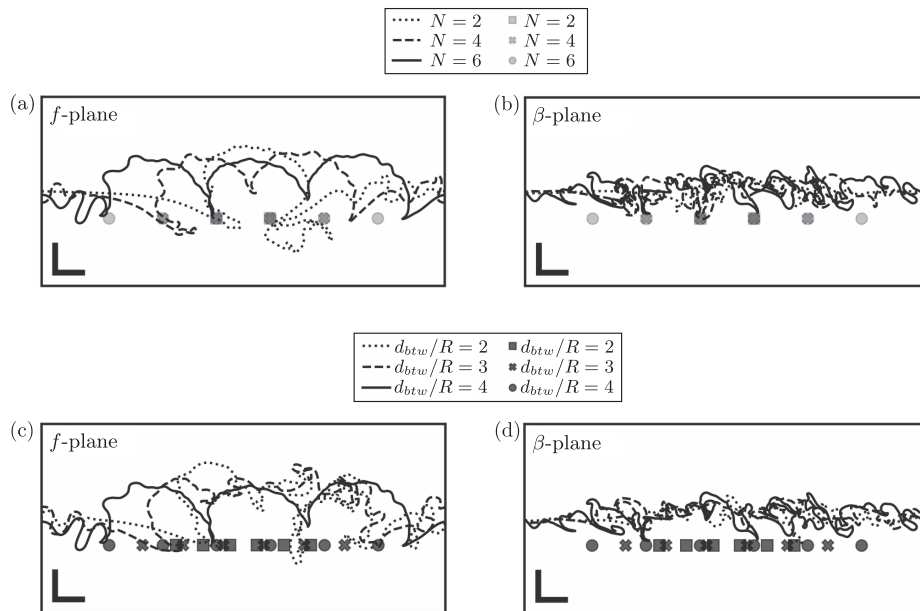


Fig. 8. Same as Fig. 7 at $t = 200$ days.

6. DISCUSSION: CROSS-SHORE EXCHANGE OF PARTICLES

We discuss here the impact of vortices and of upwelling destabilization on the transport of fluid particles in the domain. In particular, we present the export and import of particles across the y -position of the upwelling, to assess the role of the different dynamical elements in the particle transport off-shore (from north to south) and onshore (from south to north). This point is key to the local dynamics of upwelling rich regions because this can trigger phytoplankton blooms [23, 44].

To do so, we ran particle advection simulations (see Section 2.4 for details) in 4 particular CROCO simulations, which are the most representative of the upwelling-vortex interactions behavior. For further use, we define onshore as shorewards of the front (i.e., north of the front), and offshore conversely. The particle evolution with time is presented for an upwelling front with a sinusoidal perturbation (a), in the presence of a cyclone (b), of an anticyclone (c), or of a vortex alley (d), on the f -plane (Fig. 9) or on the β -plane (Fig. 10).

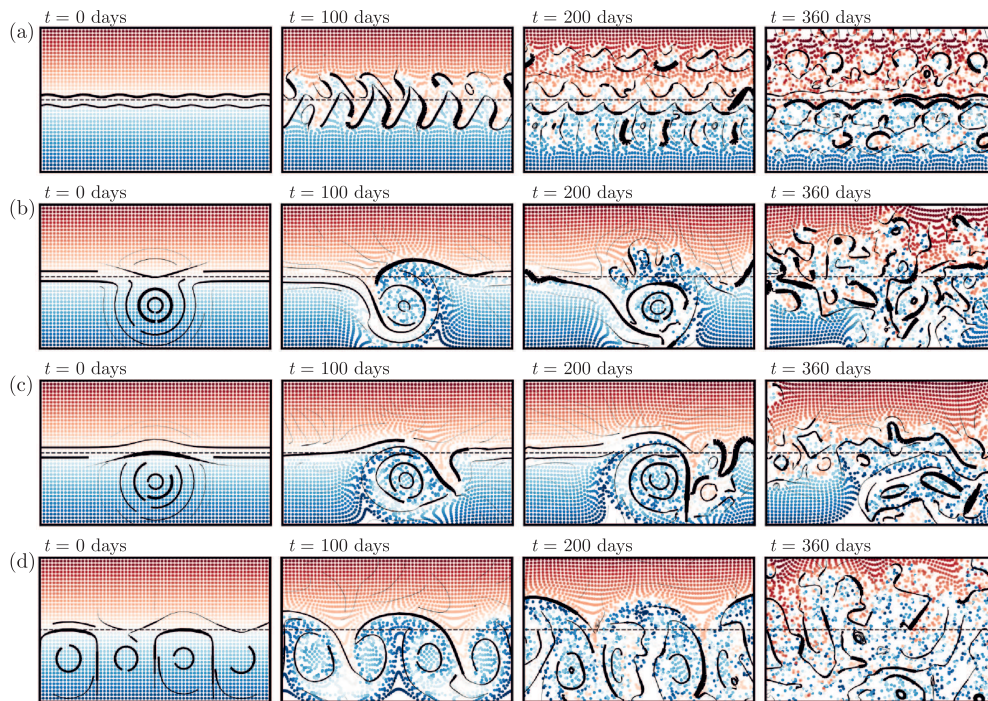


Fig. 9. Snapshots of particle advection simulations with an upwelling front of parameters $L = 50$ km, $H = 200$ m, and $V_0^{\text{up}} = 0.2 \text{ m s}^{-1}$, and (a) a sinusoidal perturbation ($\lambda_{\text{pert}} = 250$ km), (b) (resp. (c)) an isolated cyclonic (resp. anticyclonic) vortex ($R = 100$ km, $H_{\text{vortex}} = 1000$ m, $V_0^{\text{vortex}} = 0.2 \text{ m s}^{-1}$, and $d/R = 2$), and (d) a vortex alley ($R = 100$ km, $H_{\text{vortex}} = 1000$ m, $V_0^{\text{vortex}} = 0.2 \text{ m s}^{-1}$, $d/R = 2$, $N = 6$, and $d_{\text{btw}}/R = 4$). The particle color indicates the initial y -position of particles. The black solid lines show streamlines of the surface velocity field from the CROCO simulations used for the particle advection. The black dashed lines show the initial y -position of the upwelling front, which defines the frontier between offshore (south) and onshore (north) regions. Each panel is centered at the center of the domain and is 1600×1000 km wide.

For the perturbed front, the particles drift onshore and offshore nearly equally on the f -plane, while the cross-shore exchange is strongly reduced on the β -plane (as expected). When the front faces a single cyclone, on the f -plane, offshore particles are trapped in a meander which wraps counterclockwise and shoreward, after 100 days. After 200 days, this meander undergoes instability and produces shorter scale meanders; it breaks and gives birth to many small vortices inshore of the front. The offshore meander at $t = 100$ days produces a long-wave perturbation on the front, leading to the offshore motion of onshore particles. This meander also breaks into smaller

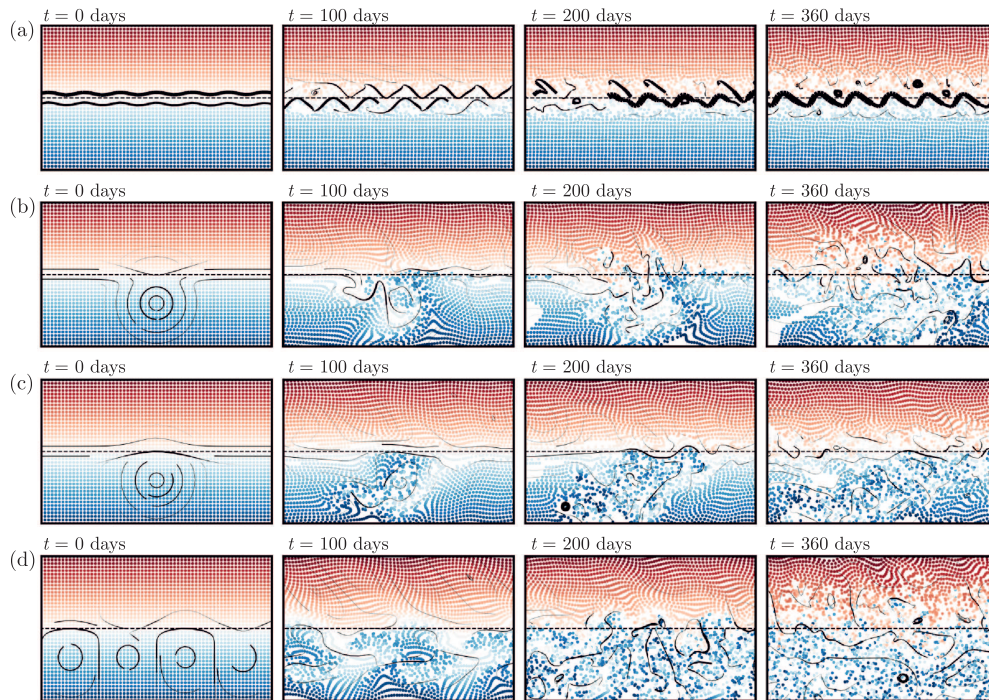


Fig. 10. Same as Fig. 9 but with β -effect added in simulations.

fragments (small vortices and filaments). Such fragments are seen on Chlorophyll-a images of the Oman upwelling front (such an image can be found in lecture 17 of Lisa Beal’s oceanography course: <https://beal-agulhas.rsmas.miami.edu/teaching/courses/lecture-seventeen/index.html>). On the β -plane, the cross-shore displacement of particles and their meridional flux are strongly reduced, but small-scale patches of displaced particles are still present on both sides of the front. When the front faces an anticyclone on the f -plane, a large meander of coastal water is pulled offshore and carries passive particles across the front after 100 days. This meander breaks into a coherent, medium scale cyclone, next to the anticyclone. After 360 days, both the vortex interactions and the front breaking lead to the production of small-scale filaments and vortices offshore. This phenomenon is considerably weakened on the β -plane where only three small vortices containing coastal water are found offshore after 200 days. After 360 days, particles have been displaced inside the offshore region, but little cross-front exchange has taken place. In the presence of a vortex row, on the f -plane, the intrusion and extrusion of fluid *via* the front meanders and the subsequent filaments lead to substantial cross-front exchange, in particular *via* small-scale features. On the β -plane, the cross-front flux is still the largest of all simulations, visually.

The median particle export distance for each case, in the onshore and offshore direction, and the percentage of exported particles are shown in Fig. 11. On the f -plane, the front with a vortex alley or with a cyclone displace more particles than the unstable front or the front with an anticyclone, but the front with a cyclone advects particles only close to the front. On the β -plane, much fewer particles are advected across the front and the export distance is strongly reduced. Again, the front with a cyclone or with a vortex alley advect more particles. The latter case is the most efficient to horizontally stir particles. Finally, the frontogenesis function computed in the front-vortex alley case (Fig. 12) indicates that the frontogenetic tendency is large around the small vortices and formed filaments.

For a comparison of these results with the upwelling and vortices off Oman (see Fig. 1), we can see that the cyclone lying offshore of the front (at 17°N, 57°E) pulls a long filament away from the front. On the SST map (Fig. 1a) cold water extends offshore at least over 300 km. South of the main cyclone, a smaller cyclone, containing cold water, is found. Another filament, shorter than

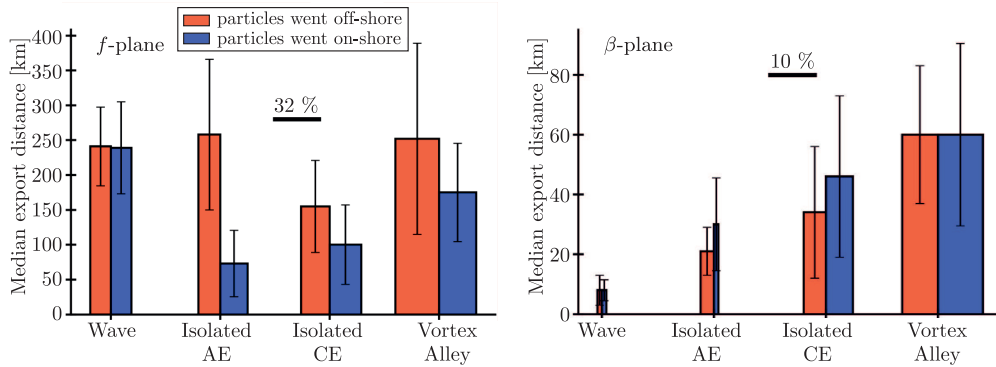


Fig. 11. Median export distance of particles after one year of advection in different simulations on the f -plane (left) or the β -plane (right). The error bars show the standard deviation of export distance, and the width of boxes indicates the percentage of exported particles (see the size bar in each panel). Note that scales are different in each panel. All simulations have initially an upwelling front with $L = 50$ km, $H = 200$ m, and $V_0^{\text{up}} = 0.2 \text{ m s}^{-1}$; “wave” corresponds to simulations with a sinusoidal perturbation ($\lambda_{\text{pert}} = 250$ km), “isolated CE (resp. AE)” corresponds to simulations with an isolated cyclonic (resp. anticyclonic) vortex ($R = 100$ km, $H_{\text{vortex}} = 1000$ m, $V_0^{\text{vortex}} = 0.2 \text{ m s}^{-1}$, and $d/R = 2$), and “vortex alley” corresponds to simulations with a vortex alley ($R = 100$ km, $H_{\text{vortex}} = 1000$ m, $V_0^{\text{vortex}} = 0.2 \text{ m s}^{-1}$, $d/R = 2$, $N = 6$, and $d_{\text{btw}}/R = 4$). Note that the simulations discussed in this figure are the same as those shown in Fig. 9 and in Fig. 10.

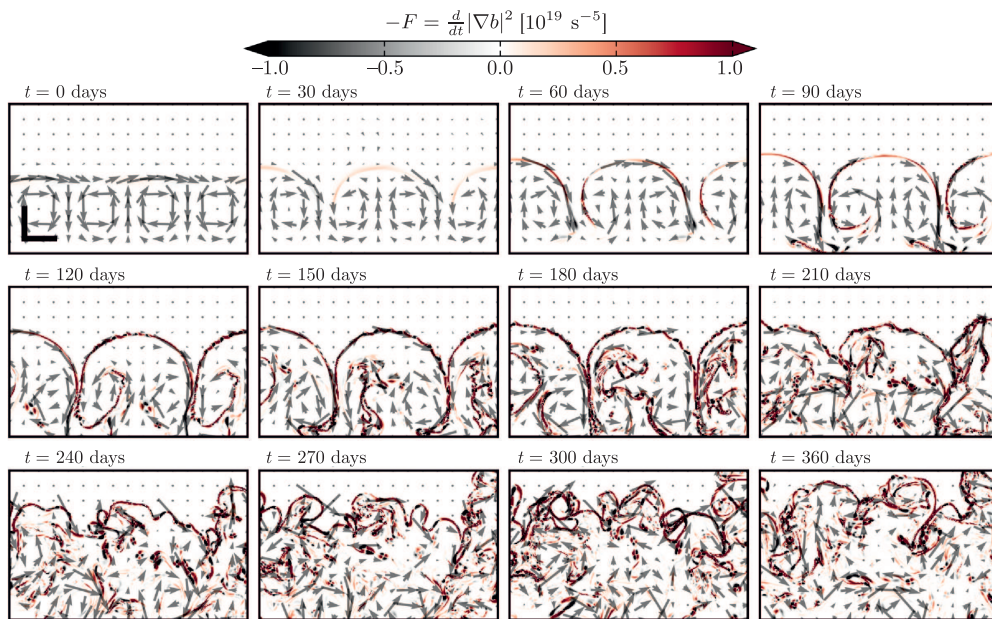


Fig. 12. Time evolution of $-F$ in the simulation with an upwelling front of parameters $L = 50$ km, $H = 200$ m, and $V_0^{\text{up}} = 0.2 \text{ m s}^{-1}$, and a vortex alley ($R = 100$ km, $H_{\text{vortex}} = 1000$ m, $V_0^{\text{vortex}} = 0.2 \text{ m s}^{-1}$, $d/R = 2$, $N = 6$, and $d_{\text{btw}}/R = 4$), i. e., the “vortex alley” case in Fig. 11. The grey arrows show the surface velocity field. The size bars in the bottom left show a distance of 200×200 km. Each panel is centered at the center of the domain and is 1600×1000 km wide.

the former, is torn away from the upwelling front by the anticyclone lying at 20°N and 60°E . On the SST and SSH maps, contrary to our model, more vortices lie farther offshore of those close to the front. They also carry cold water away from the coast and make it recirculate.

These results suggest that the impacts of upwelling front instability or front interaction with a vortex field on biological activity are expected to be important. Firstly, nutrient rich onshore waters will be exported offshore by the meanders which then break into filaments and into small vortices. These flow structures will be the seat of intense biological activity (blooms) favored by the further vertical uplift of nutrients to the surface, related to frontogenesis. Secondly, exchange of coastal and deep water species will be achieved by these horizontal exchanges, leading to a possible modification of local ecosystems, and to possible competitive exclusion of species, in an otherwise protected environment for them.

7. CONCLUSIONS

We have studied the evolution of an unstable upwelling front and of a front in the presence of vortices offshore. We have not considered a stable front in the presence of external vortices, because upwelling fronts are naturally unstable. The characteristic wavelengths and coherent structures produced by these evolutions have been determined. Their impact in terms of horizontal fluxes of particles has been studied. In particular, wavelengths of 100 or 200 km appear on the front, and small-scale filaments and vortices are finally produced. Frontogenesis is strong around them. Mesoscale vortices and smaller scale features advect particles across the front. The timescales of 3–6 months considered here can be made shorter by considering faster frontal currents (e. g., in the linear approximation, a $0.4\text{--}1\text{ m s}^{-1}$ frontal jet will reduce the timescales by factors of 2 to 5, leading to periods of about 1 month for the formation of meanders and filaments). Numerical simulations using particles advection have shown that a vortex alley is the most efficient perturbation to the upwelling front, in terms of cross-front transport (compared with a single vortex or with the instability of the front alone).

Still, this study remains idealized in terms of flow conditions. First and foremost, it has only considered the inertial (unforced) evolution of the front. We will extend these results in a following study by adding wind stress and/or the front relaxation to a prescribed state to assess the energetic balance between atmospheric forcing and mean flow instability. Bottom topography and coastal irregularities should also be added as they can alter or favor the formation of filaments and of vortices from upwelling fronts [32]. The wind variability is also essential in the evolution of upwelling fronts, by either weakening them or amplifying them. Further studies with nested models of the Arabian Sea and of the region south of Oman will be done in the near future. They will benefit from *in situ* measurements performed during the Physindien 2019 experiment south of the Sultanate of Oman for their validation.

FUNDING

This work was funded by the Direction Générale de l'Armement (DGA) via a full grant for Charly de Marez's PhD. This work is also a contribution to PRC 1069 "Meso and submesoscale vortices in the Atlantic and Indian Ocean", funded by CNRS and RFBR. Simulations were performed using the HPC facilities DATARMOR of "Pôle de Calcul Intensif pour la Mer" at Ifremer, Brest, France. Model outputs are available upon request.

CONFLICT OF INTEREST

The authors declare that they have no conflicts of interest.

AUTHORS' CONTRIBUTIONS

The authors declare their participation in the study, CdM for conception, numerical work and contribution to the paper writing, XC for conception, participation in the analyses and paper writing.

REFERENCES

1. Al Saafani, M. A., Shenoi, S. S. C., Shankar, D., Aparna, M., Kurian, J., Durand, F., and Vinayachandran, P. N., Westward Movement of Eddies into the Gulf of Aden from the Arabian Sea, *J. Geophys. Res. Oceans*, 2007, vol. 112, C11004, 12 pp.
2. Ayouche, A., De Marez, Ch., Morvan, M., L'Hégaret, P., Carton, X., Le Vu, B., and Stegner, A., Structure and Dynamics of the Ras al Hadd Oceanic Dipole, *Oceans*, 2021, vol. 2, no. 1, pp. 105–125.
3. Baey, J.-M., Rivière, P., and Carton, X., Ocean Jet Instability: A Model Comparison, *ESAIM: Proc.*, 1999, vol. 7, pp. 12–23.
4. Barth, J. A., Short-Wave Length Instabilities on Coastal Jets and Fronts, *J. Geophys. Res. Oceans*, 1994, vol. 99, no. C8, pp. 16095–16115.
5. Brandt, P., Stramma, L., Schott, F., Fischer, J., Dengler, M., and Quadfasel, D., Annual Rossby Waves in the Arabian Sea from TOPEX/POSEIDON Altimeter and in Situ Data, *Deep Sea Res. Part 2 Top. Stud. Oceanogr.*, 2002, vol. 49, pp. 1197–1210.
6. Bruce, J. G., Some Details of Upwelling Off the Somali and Arabian Coasts, *J. Mar. Res.*, 1974, vol. 32, pp. 419–423.
7. Bruce, J. G., Johnson, D. R., and Kindle, J. C., Evidence for Eddy Formation in the Eastern Arabian Sea during the Northeast Monsoon, *J. Geophys. Res. Oceans*, 1994, vol. 99, no. C4, pp. 7651–7664.
8. Capet, X. and Carton, X., Nonlinear Regimes of Baroclinic Boundary Currents, *J. Phys. Oceanogr.*, 2004, vol. 34, no. 6, pp. 1400–1409.
9. Chaigneau, A., Le Texier, M., Eldin, G., Grados, C., and Pizarro, O., Vertical Structure of Mesoscale Eddies in the Eastern South Pacific Ocean: A Composite Analysis from Altimetry and Argo Profiling Floats, *J. Phys. Oceanogr.*, 2011, vol. 116, C11025, 16 pp.
10. Chelton, D. B., deSzoeke, R. A., Schlax, M. G., El Naggar, K., and Siwertz, N., Geographical Variability of the First Baroclinic Rossby Radius of Deformation, *J. Phys. Oceanogr.*, 1998, vol. 28, no. 3, pp. 433–460.
11. Csanady, G. T., On the Structure of Transient Upwelling Events, *J. Phys. Oceanogr.*, 1982, vol. 12, no. 1, pp. 84–96.
12. Currie, R., Circulation and Upwelling Off the Coast of South-East Arabia, *Oceanol. Acta*, 1992, vol. 15, no. 1, pp. 43–60.
13. Delandmeter, P. and van Sebille, E., The Parcels v2.0 Lagrangian Framework: New Field Interpolation Schemes, *Geosci. Model Dev.*, 2019, vol. 12, no. 8, pp. 3571–3584.
14. Elliott, A. J. and Savidge, G., Some Features of the Upwelling Off Oman, *J. Mar. Res.*, 1990, vol. 48, pp. 319–333.
15. Fischer, A. S., Weller, R. A., Rudnick, D. L., Eriksen, C. C., Lee, C. M., Brink, K. H., Fox, C. A., and Leben, R. R., Mesoscale Eddies, Coastal Upwelling, and the Upper-Ocean Heat Budget in the Arabian Sea, *Deep Sea Res. Part 2 Top. Stud. Oceanogr.*, 2002, vol. 49, pp. 2231–2264.
16. Flierl, G. R., Carton, X. J., and Messenger, Ch., Vortex Formation by Unstable Oceanic Jets, *ESAIM: Proc.*, 1999, vol. 7, pp. 137–150.
17. Hidaka, K., Physical Oceanography of Upwelling, *Geoforum*, 1972, vol. 3, no. 3, pp. 9–21.
18. Hoskins, B., The Mathematical Theory of Frontogenesis, *Ann. Rev. Fluid Mech.*, 1982, vol. 14, pp. 131–151.
19. Keppler, L., Cravatte, S., Chaigneau, A., Pegliasco, C., Gourdeau, L., and Singh, A., Observed Characteristics and Vertical Structure of Mesoscale Eddies in the Southwest Tropical Pacific, *J. Geophys. Res. Oceans*, 2018, vol. 123, no. 4, pp. 2731–2756.
20. Klein, P., Hua, B. L., Lapeyre, G., Capet, X., Le Gentil, S., and Sasaki, H., Upper Ocean Turbulence from High-Resolution 3D Simulations, *J. Phys. Oceanogr.*, 2008, vol. 38, no. 8, pp. 1748–1763.
21. Lange, M. and van Sebille, E., Parcels v0.9: Prototyping a Lagrangian Ocean Analysis Framework for the Petascale Age, *Geosci. Model Dev. Discuss.*, 2017, vol. 10, pp. 4175–4186.
22. Large, W. G., McWilliams, J. C., and Doney, S. C., Oceanic Vertical Mixing: A Review and a Model with a Nonlocal Boundary Layer Parameterization, *Rev. Geophys.*, 1994, vol. 32, no. 4, pp. 363–403.
23. Liao, X., Zhan, H., and Du, Y., Potential New Production in Two Upwelling Regions of the Western Arabian Sea: Estimation and Comparison, *J. Geophys. Res. Oceans*, 2016, vol. 121, no. 7, pp. 4487–4502.
24. Manghnani, V., Morrison, J. M., Hopkins, T. S., and Böhm, E., Advection of Upwelled Waters in the Form of Plumes Off Oman during the Southwest Monsoon, *Deep Sea Res. Part 2 Top. Stud. Oceanogr.*, 1998, vol. 45, nos. 10–11, pp. 2027–2052.
25. de Marez, C., Carton, X., L'Hégaret, P., Meunier, T., Stegner, A., Le Vu, B., and Morvan, M., Oceanic Vortex Mergers Are Not Isolated but Influenced by the β -Effect and Surrounding Eddies, *Sci. Rep.*, 2020, vol. 10, no. 1, Art. No. 2897, 11 pp.
26. de Marez, Ch., L'Hégaret, P., Morvan, M., and Carton, X., On the 3D Structure of Eddies in the Arabian Sea, *Deep Sea Res. Part 1 Oceanogr. Res. Pap.*, 2019, vol. 150, 103057, 16 pp.
27. de Marez, Ch., Meunier, T., Morvan, M., L'Hégaret, P., and Carton, X., Study of the Stability of a Large Realistic Cyclonic Eddy, *Ocean Model.*, 2020, vol. 146, 101540, 18 pp.

28. de Marez, Ch., Meunier, Th., Tedesco, P., L'Hégaret, P., and Carton, X., Vortex Wall Interaction on the β -Plane and the Generation of Deep Submesoscale Cyclones by Internal Kelvin Waves Current Interactions, *Geophys. Astrophys. Fluid Dyn.*, 2020, vol. 114, nos. 4–5, pp. 588–606.
29. McCreary, J., A Linear Stratified Ocean Model of the Coastal Undercurrent, *Philos. Trans. R. Soc. Lond. Ser. A Math. Phys. Eng. Sci.*, 1981, vol. 302, no. 1469, pp. 385–413.
30. McDougall, T. J. and Barker, P. M., *Getting Started with TEOS-10 and the Gibbs Seawater (GSW) Oceanographic Toolbox*, SCOR/IAPSO WG127 (2011).
31. Ménesguen, C., Le Gentil, S., Marchesiello, P., and Ducoussou, N., Destabilization of an Oceanic Meddy-Like Vortex: Energy Transfers and Significance of Numerical Settings, *J. Phys. Oceanogr.*, 2018, vol. 48, no. 5, pp. 1151–1168.
32. Meunier, T., Rossi, V., Morel, Y., and Carton, X., Influence of Bottom Topography on an Upwelling Current: Generation of Long Trapped Filaments, *Ocean Model.*, 2010, vol. 35, no. 4, pp. 277–303.
33. Pedlosky, J., Longshore Currents and the Onset of Upwelling over Bottom Slope, *J. Phys. Oceanogr.*, 1974, vol. 4, no. 3, pp. 310–320.
34. Pedlosky, J., An Inertial Model of Steady Coastal Upwelling, *J. Phys. Oceanogr.*, 1978, vol. 8, no. 2, pp. 171–177.
35. Pedlosky, J., A Nonlinear Model of the Onset of Upwelling, *J. Phys. Oceanogr.*, 1978, vol. 8, no. 2, pp. 178–187.
36. Pegliasco, C., Chaigneau, A., and Morrow, R., Main Eddy Vertical Structures Observed in the Four Major Eastern Boundary Upwelling Systems, *J. Geophys. Res. Oceans*, 2015, vol. 120, no. 9, pp. 6008–6033.
37. Piontkovski, S. and Al-Jufaili, S., Coastal Upwellings and Mesoscale Eddies of the Western Arabian Sea: Some Biological Implications, *Int. J. Oceans Oceanogr.*, 2013, vol. 7, no. 2, pp. 93–115.
38. Pratt, L. J. and Stern, M. E., Dynamics of Potential Vorticity Fronts and Eddy Detachment, *J. Phys. Oceanogr.*, 1986, vol. 16, no. 6, pp. 1101–1120.
39. Privett, D., Monthly Charts of Evaporation from the North Indian Ocean (including the Red Sea and the Persian Gulf), *Q. J. R. Meteorol. Soc.*, 1959, vol. 85, no. 366, pp. 424–428.
40. Sastry, J. and d'Souza, R., Upwelling and Upward Mixing in the Arabian Sea, *Indian J. Mar. Sci.*, 1972, vol. 1, pp. 17–27.
41. Schott, F. A. and Fischer, J., Winter Monsoon Circulation of the Northern Arabian Sea and Somali Current, *J. Geophys. Res. Oceans*, 2000, vol. 105, no. C3, pp. 6359–6376.
42. Shchepetkin, A. F. and McWilliams, J. C., The Regional Oceanic Modeling System (ROMS): A Split-Explicit, Free-Surface, Topography-Following-Coordinate Oceanic Model, *Ocean Model.*, 2005, vol. 9, no. 4, pp. 347–404.
43. Shchepetkin, A. F. and McWilliams, J. C., Accurate Boussinesq Oceanic Modeling with a Practical, “Stiffened” Equation of State, *Ocean Model.*, 2011, vol. 38, no. 1, pp. 41–70.
44. Shi, W., Morrison, J. M., Böhm, E., and Manghnani, V., The Oman Upwelling Zone during 1993, 1994 and 1995, *Deep Sea Res. Part 2 Top. Stud. Oceanogr.*, 2000, vol. 47, nos. 7–8, pp. 1227–1247.
45. Smith, W. H. F. and Sandwell, D. T., Global Sea Floor Topography from Satellite Altimetry and Ship Depth Soundings, *Science*, 1997, vol. 277, no. 5334, pp. 1956–1962.
46. Stern, M. E. and Flierl, G. R., On the Interaction of a Vortex with a Shear Flow, *J. Geophys. Res. Oceans*, 1987, vol. 92, no. C10, pp. 10733–10744.
47. Suginohara, N., Upwelling Front and Two-Cell Circulation, *J. Meteor. Soc. Japan*, 1977, vol. 33, pp. 115–130.
48. Trott, C. B., Subrahmanyam, B., Chaigneau, A., and Roman-Stork, H. L., Eddy-Induced Temperature and Salinity Variability in the Arabian Sea, *Geophys. Res. Lett.*, 2019, vol. 46, no. 5, pp. 2734–2742.
49. Vallis, G. K., *Atmospheric and Oceanic Fluid Dynamics: Fundamentals and Large-Scale Circulation*, 2nd ed., Cambridge: Cambridge Univ. Press, 2017.
50. Vandermeersch, F., Carton, X., and Morel, Y., Interaction between an Eddy and a Zonal Jet: P. 2. Two-and-a-Half-Layer Model, *Dynam. Atmos. Oceans*, 2003, vol. 36, no. 4, pp. 271–296.
51. Vandermeersch, F., Carton, X., and Morel, Y., Interaction between an Eddy and a Zonal Jet: P. 1. One-and-a-Half-Layer Model, *Dynam. Atmos. Oceans*, 2003, vol. 36, no. 4, pp. 247–270.
52. Vic, C., Capet, X., Roulet, G., and Carton, X., Western Boundary Upwelling Dynamics Off Oman, *Ocean Dyn.*, 2017, vol. 67, pp. 585–595.
53. Vic, C., Capet, X., Roulet, G., Carton, X., Molemaker, M. J., and Gula, J., Eddy-Topography Interactions and the Fate of the Persian Gulf Outflow, *J. Geophys. Res. Oceans*, 2015, vol. 120, pp. 6700–6717.
54. Yoshida, K., Coastal Upwelling Off the California Coast, *Rec. Oceanogr. Works Japan (N. S.)*, 1955, vol. 2, no. 2, pp. 8–20.

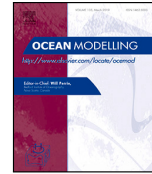
ÉTUDE IDÉALISÉE DU CYCLE DE VIE D'UN TOURBILLON SEMI-PERMANENT

Nous présentons ici une étude menée au cours de la troisième année de thèse, et publiée dans le journal *Ocean Modelling*, en collaboration avec J. Gula et M. Le Corre. Cette étude, bien que pas directement liée au sujet de la thèse, s'inscrit dans la continuité de l'étude de la dynamique tourbillonnaire dans l'océan. Nous étudions ici le cycle de vie d'un tourbillon anticyclonique semi-permanent, comme celui présent dans le Rockall Trough au large des côtes Irlandaises, ou du Lofoten Eddy dans les Mers Nordiques. Nous montrons à partir de simulations idéalisées que ce type de tourbillon est entretenu par des fusions avec des tourbillons de sousmésos-échelle. Ces fusions sont intensifiées en présence de convection, et sont fortement impactées par la stratification ambiante. Nous montrons également qu'à temps long, ces tourbillons peuvent perdre de l'énergie du fait de la friction au fond et de l'apparition d'instabilités géophysiques. Cette partie permet donc une autre illustration des phénomènes présentés dans les sections 5.1 et 6.2.2, à propos d'instabilités et de fusion de tourbillons.



Contents lists available at ScienceDirect

Ocean Modelling

journal homepage: www.elsevier.com/locate/ocemod

The influence of merger and convection on an anticyclonic eddy trapped in a bowl

Charly de Marez^{a,*}, Mathieu Le Corre^{a,c}, Jonathan Gula^{a,b}^a Univ. Brest, Laboratoire d'Océanographie Physique et Spatiale (LOPS), IUEM, Rue Dumont D'urville, 29280 Plouzané, France^b Institut Universitaire de France (IUF), France^c LEGOS, University of Toulouse, IRD, CNRS, CNES, UPS, Toulouse, France

ARTICLE INFO

Keywords:
Mesoscale
Vortex
Merger
Convection

ABSTRACT

We investigate the impact of several parameters on the lifecycle of an anticyclonic eddy lying in a topographic depression (a bowl), similar to the Lofoten Vortex and the Rockall Trough eddy cases. We observe that the vortex merger with submesoscale coherent vortices generated at depth allows the eddy to grow in size, and intensify at depth. Wintertime convection is also shown to directly intensify the eddy by deepening isopycnals. Also, convection indirectly affects the shape of the eddy. It enhances the number of merger (1) at the surface, with small vortices generated in the convectively-deepened surface mixed-layer, and (2) at depth, because the vertical distance between the main eddy's core and small companion vortices is reduced, thus increasing the merging efficiency. These processes altogether contribute to the maintaining of the eddy. On the other hand, the bottom drag is the main process contributing to the decay of the eddy. Our study thus shows that the sustaining for several years of such eddies trapped in a bowl is mainly due to the balance between merger and bottom drag.

1. Introduction

Mesoscale eddies are a prominent feature of the ocean circulation. They have a strong influence on biological activity (Chelton et al., 2011), tracer transport (Zhang et al., 2014), and physical and chemical properties of the water column (Dong et al., 2014). In some regions, semi-permanent eddies can be seen throughout the year, at a nearly constant position. Among other examples, two particular cases are the Lofoten Vortex (LV), and the Rockall Trough eddy (RT eddy). These two semi-permanent eddies have the peculiarity to be anticyclonic, and located above a topographic depression – a bowl. The formation of such vortices has recently been examined by Solodoch et al. (2021). Authors showed using idealized simulations that successive merging events form a permanent anticyclone lying in the topographic depression. The dynamics of the resulting vortex depends on the ratio of eddy's vorticity to topography's potential vorticity. However, the mechanisms that sustain semi-permanent anticyclones in bowl-like topography such as the LV and the RT eddy are not yet fully understood.

The LV can be found in the Lofoten Basin in the Nordic Seas. It appears as a large anticyclone at the center of the basin. It was first detected by *in situ* data between 1970 and 1990 (Ivanov and Korablev, 1995). The LV is intensified between 700 and 900 m depth and has a radius of about 30 km (Yu et al., 2017). Two processes are candidate to explain the long lifetime of the LV. First, from observational data, Ivanov and Korablev (1995) and Bosse et al. (2019)

argued that wintertime intensification resulting from convection plays a determinant role in sustaining the LV. Second, model studies showed that the LV is sustained by the merger and alignment with smaller vortices generated by unstable boundary currents (Köhl, 2007; Trodahl et al., 2020). In the current state of knowledge, the relative importance of each process is not clear. One of the aims of the present study is to give new answers to this question.

The RT eddy is located in the Rockall Trough, off Ireland in the North Atlantic. It has a clear signature at the sea surface (Heywood et al., 1994; White and Heywood, 1995; Volkov, 2005; Xu et al., 2015), but also at depth with high values of eddy available potential energy (Roulet et al., 2014). This eddy is less sampled than the LV and less known. However, thanks to recent *in situ* deployments, it has been shown that it is intensified at depth, with a maximum azimuthal velocity of $\sim 0.3 \text{ m s}^{-1}$ near 500 m depth (Smilenova et al., 2020). It has a radius of approximately 40 km and can reach down to 1500 m. Its lifecycle, as well as the mechanisms that sustain it are yet poorly documented. However, recent model studies by Le Corre et al. (2019) and Smilenova et al. (2020) have shown some evidences that (1) the RT eddy formation is the result of successive mergers of deeply generated submesoscale vortices along the Porcupine Bank, (2) the merger of the RT eddy with these small vortices as well as wintertime convection sustain the RT eddy, and allow it to remain semi-permanent in the Rockall Trough.

* Corresponding author.

E-mail address: charly.demarez@univ-brest.fr (C. de Marez).<https://doi.org/10.1016/j.ocemod.2021.101874>

Received 20 April 2021; Received in revised form 19 July 2021; Accepted 30 July 2021

Available online 5 September 2021

1463-5003/© 2021 Elsevier Ltd. All rights reserved.

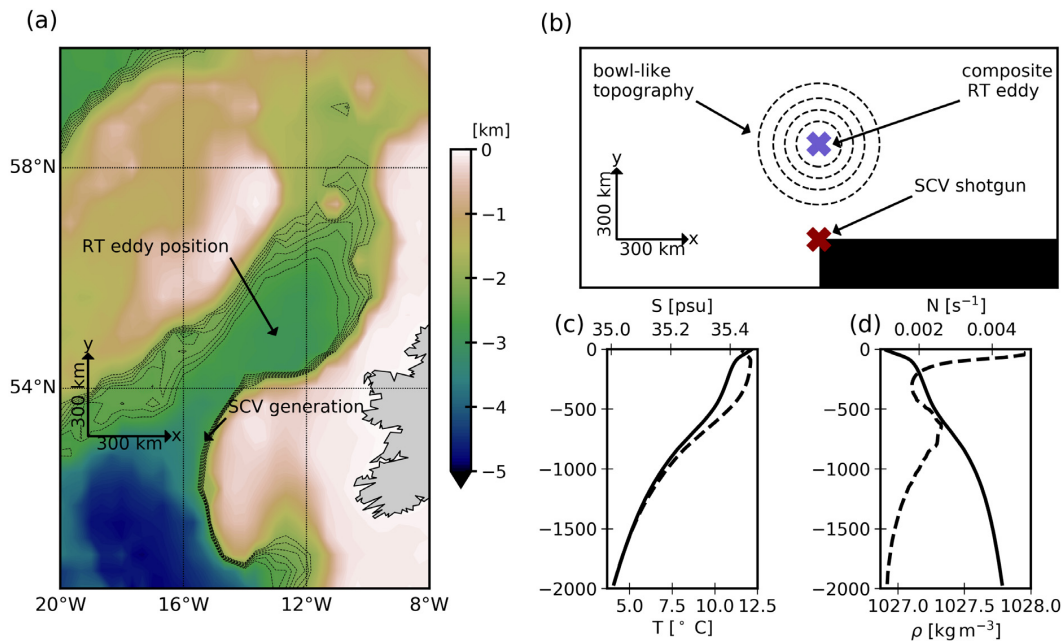


Fig. 1. (a) Rockall Trough bathymetry; dashed contours show isobaths 2500 to 2000 m depth with a 100 m interval. (b) Scheme of idealized simulation setup; dashed contours show same isobaths as in (a). (c) Climatological background temperature (solid) and salinity (dashed) used in idealized simulations. (d) Climatological background potential density (solid) and corresponding Brunt-Väisälä frequency (dashed) used in idealized simulations.

In this paper, we investigate the impact of several parameters on the lifecycle of an anticyclonic eddy lying in a topographic depression. In particular, we discuss the impact of merger and convection on the lifetime and shape of the anticyclone. To explore the parameter space, we use an idealized approach based on the Rockall Trough Eddy case. This allows to (1) discuss on the general behavior of anticyclonic eddies in a bowl, and (2) give insights in the particular case of the Rockall Trough Eddy that is yet poorly documented. In Section 2 we present the methods, the numerical simulation setup and the diagnostics performed on outputs. In Section 3 we present the results of our study, the impact of the different parameters on the vortex dynamics. In Section 4 we summarize and discuss the results.

2. Methods

2.1. The numerical simulations

In this section, we present the idealized simulations performed for this study. The aim of these simulations is to simulate schematically the dynamics occurring in the Rockall Trough area: a semi-permanent anticyclone (the RT eddy) lying in a bowl-like topography, fed by anticyclonic Submesoscale Coherent Vortices (SCVs) generated hundreds of kilometers away from the main eddy (hereafter, the main eddy designates the eddy that lies approximately in the center of the bowl-like topography, and merges with smaller SCVs). We detail each aspect of the simulation in the following subsections.

2.1.1. Numerical setup and domain

The simulations rely on a 3D primitive equation framework. They are performed using the Coastal and Regional Ocean Community model CROCO (Shchepetkin and McWilliams, 2005). This model solves the hydrostatic primitive equations for the velocity, temperature, and salinity, using a full equation of state for seawater (Shchepetkin and McWilliams, 2011). The simulations integrate the primitive equations for about 7 and a half years. The numerical settings are similar

to previous simulations performed in an idealized context (see, e.g., Ménesguen et al., 2018): horizontal advection terms for tracers and momentum are discretized with fifth-order upwind advection schemes (UP5); the explicit horizontal viscosity and diffusivity are set to zero, since the UP5 scheme damps dispersive errors; the vertical advection is discretized with a fourth-order centered parabolic spline reconstruction (Splines scheme). Further discussion about these parameterizations can be found in Klein et al. (2008) or Ménesguen et al. (2018). Vertical mixing of tracers and momentum is done using a K-profile parameterization (KPP, Large et al., 1994), and the effect of bottom friction is parameterized through a logarithmic law of the wall (with the same parameters than in e.g. Gula et al. (2015) or Le Corre et al. (2020)). Some simulations are run without this bottom drag to study its impact on the vortex dynamics. Simulations have 64 terrain-following vertical levels, which are stretched such that the resolution increases in the depth range where the main eddy lies, giving $\Delta z \sim 20$ m from surface to 1000 m depth, and $20 < \Delta z < 90$ m below. The horizontal resolution is $\Delta x = 5$ km.

The domain is chosen so that it represents schematically the RT area, see Fig. 1(a,b). The domain is 2000 km and 1000 km wide zonally and meridionally, respectively. A bowl-like topography is placed at the center of the domain, to represent the RT topographic depression. It is modeled by a Gaussian function

$$h = h_0 + h_1 \exp(-r^2/(2R)^2),$$

with $r = \sqrt{(x - x_0)^2 + (y - y_0)^2}$, $x_0 = 1000$ km, $y_0 = 600$ km, $R = 100$ km, $h_0 = 2000$ m, and $h_1 = 500$ m, such that the simulation is 2000 m deep everywhere, except in the bowl where it reaches 2500 m deep. The background stratification is the average stratification in the RT area, see Fig. 1(c,d). It is defined as the average stratification in the RT from Le Corre et al. (2020)'s simulation. A return to this background stratification is set in the boundaries. At these boundaries a 10 km wide sponge layer avoid the generation of spurious boundary dynamics.

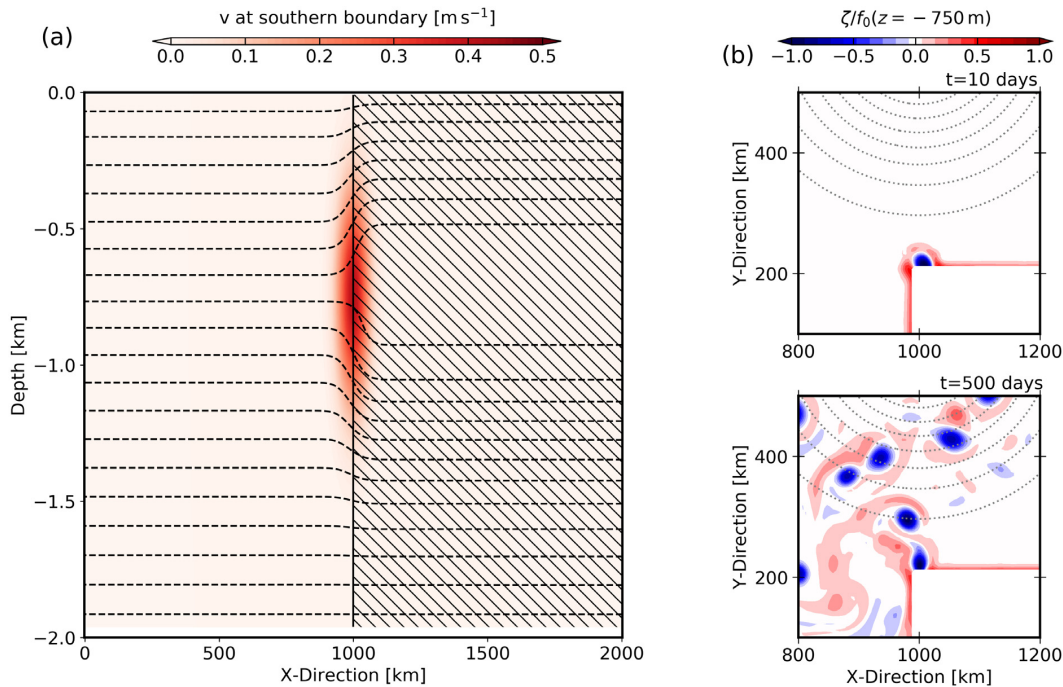


Fig. 2. (a) Meridional velocity at the southern boundary for the “middle” case; black lines indicate isopycnals with a 0.5 kg m^{-3} spacing; hatched area indicate the position of the mask. (b) Snapshots of normalized relative vorticity at $t = 10$ and $t = 500$ days, at 750 m depth, showing the SCV generation at the mask corner in the “middle” case.

2.1.2. The SCV shotgun

In the RT, SCVs are generated along the Porcupine Bank (Smilenova et al., 2020). To simulate this SCV generation, we designed a “SCV shotgun”, that continuously generates SCVs at a given depth during the simulation. It is placed at 300 km from the bowl-like topography center. This distance is chosen so that it is similar to the one between the Porcupine Bank and the RT eddy position in reality, see Fig. 1(a,b).

The SCV shotgun is based on the principle fully described in Deremble et al. (2016): at boundary singularities such as corners, vorticity is injected into the domain even for free-slip boundary conditions. We add a land mask forming a corner (*i.e.* a boundary singularity) at the south of the domain, with a free-slip condition along this mask. Then, we impose a meridional current at depth along the mask (see Fig. 2(a)), of the form:

$$v = v_0 \exp(-(x - x_0)^2 / (2L)^2) \exp(-(z - z_0)^2 / (2H)^2),$$

with $v_0 = 0.4 \text{ m s}^{-1}$, $L = 30 \text{ km}$, and $H = 200 \text{ m}$. As discussed in Deremble et al. (2016), the horizontal extension and intensity of generated SCVs are mainly controlled by the sub-grid parameterization and horizontal discretization, such that L and v_0 poorly control the shape of SCVs. After sensitivity tests, we chose the aforementioned values for v_0 , L , and H such that the model stability is satisfying, and that the properties and the frequency of generation of SCVs are similar to the one observed in realistic simulations of the Rockall Trough (Smilenova et al., 2020), *i.e.* about 10 SCVs are generated each year. We also vary $z_0 = [-1250, -1000, -750, -500, -250] \text{ m}$, to discuss the impact of the SCV depth on the merging process. They are called “deep”, “middle deep”, “middle”, “middle surf”, and “surf” cases respectively in the following. Note that the middle case is the one representative of RT SCV generation (see *e.g.* Fig. 11 in Smilenova et al. (2020)). This current is geostrophically adjusted with the density field at the southern boundary, see Fig. 2(a). Examples of SCV generation in the middle case are shown in Fig. 2(b,c).

2.1.3. The Rockall Trough anticyclone

As discussed in the introduction, a semi-permanent anticyclonic eddy is present in the RT throughout the whole year: the RT eddy. To simulate this presence, we add in some simulations, at initialization, a composite anticyclone representative of the RT eddy above the center of the bowl-like topography (at $x = x_0$ and $y = y_0$, the blue cross position in Fig. 1(b)).

This composite was extracted from a realistic simulation representing the Subpolar North Atlantic gyre. It is fully described in Le Corre et al. (2020). The 2011 vertical properties of the simulated RT eddy being close to ship-board Conductivity–Temperature–Depth (CTD) data collected in January 2011 (see the supplementary material of Smilenova et al. (2020)), this simulation is assumed to represent well the RT eddy dynamics. An example of RT eddy occurrence in the simulation is shown in Fig. 3(a). We tracked the RT eddy by following the maximum SSH value in the area. After isolating the eddy, we took its temporal main structure and azimuthally averaged it to obtain the main composite structure of the RT eddy (Fig. 3(b,c,d,e)).

2.1.4. Add convection

The wintertime convection may play an important role in the intensification and the maintenance of anticyclonic eddies (Gelderloos et al., 2011; Bosse et al., 2016, 2019), in particular in high latitude areas such as the RT. To discuss the impact of the convection on the intensity of the RT eddy, we ran simulations with a surface net heat flux (SNHF) representative of the RT area. It is calculated as an average of the SNHF (from Carton et al., 2018) in the area of latitude and longitude comprised respectively between 53°N and 57°N , and 15°W and 11°W . The annual variation of SNHF imposed in the simulations with convection is shown in Fig. 4.

2.1.5. Sum up

A total of 16 simulations have been run and analyzed, to study the impact of the different parameters (presence and depth of the SCV

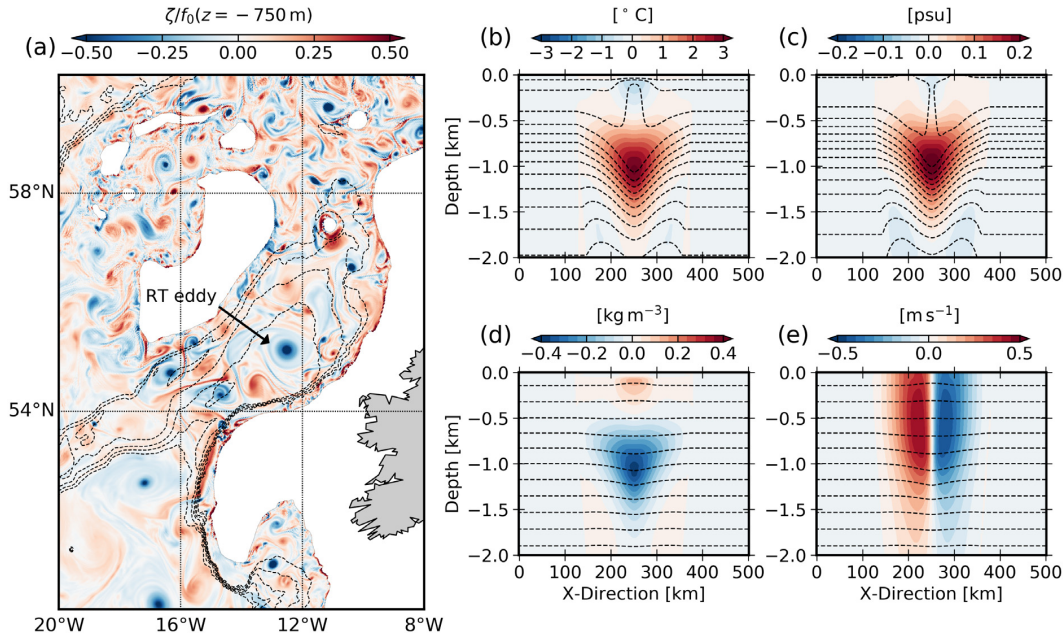


Fig. 3. (a) Snapshot of normalized relative vorticity at 750 m depth in the Rockall Trough area, from the realistic simulation (Le Corre et al., 2020) in which the composite anticyclone was extracted; dashed contours show isobaths from 3500 to 2000 m depth with a 250 m interval. (b,c,d,e) Temperature anomaly, salinity anomaly, density anomaly, and azimuthal velocity of the composite anticyclone; dashed contours show isolines of temperature (b), salinity (c), and density (d,e).

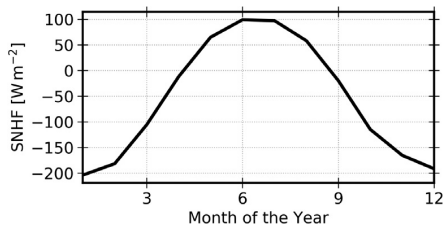


Fig. 4. Surface net heat flux imposed in idealized simulations with convection.

shotgun, presence of the RT eddy at initialization, convection, bottom drag) on the RT eddy intensity and dynamics. The different simulations are summarized in Table 1.

mRTDC is the simulation closest to the reality, as it includes all features and forcings occurring in the RT area: SCVs generated at a realistic depth, convection, bottom drag, and a anticyclonic eddy at the center of the bowl-like topography.

2.2. Diagnostics

We describe in this section the diagnostics performed on the simulation outputs.

2.2.1. Detection of the main eddy

In each simulation, we detect the main eddy using the Angular Momentum Eddy Detection and tracking Algorithm (AMEDA, Le Vu et al., 2018). One of the benefits of AMEDA is that it does not depend on arbitrary thresholding, which would require a fine-tuning of geometrical parameters. Also, the algorithm is robust with respect to the grid resolution and can thus be applied to a wide variety of velocity fields (experimental, numerical, derived from altimetry). This algorithm has been used and validated in previous – observational and numerical –

studies (Ioannou et al., 2017; Le Vu et al., 2018; Garreau et al., 2018; de Marez et al., 2019; de Marez et al., 2020), see also an example of application of AMEDA in <https://www1.lmd.polytechnique.fr/dyned/>. This algorithm works as follows: (a) from the velocity fields, it computes the local normalized angular momentum (LNAME, Mkhini et al., 2014) and the local Okubo–Weiss parameter (LOW) at each point; (b) then, it seeks LNAME local maxima where LOW < 0; (c) if these maxima are surrounded by a closed streamline, they are flagged as eddy centers. A full description of the algorithm is presented in Fig. 1 of Le Vu et al. (2018). In this study, the detection is done using daily velocity fields, at –250, –500, –750, –1000, and –1250 m depth for surf, middle surf, middle deep, and deep cases respectively. Choosing the depth of detection as equal to the depth of SCV generation ensures an accurate estimation of the radius increase of the main eddy when it merges with SCVs. The main eddy’s edge is defined as its contour of maximal velocity. The mean radius of this contour at a given time is R_{max} . We use this contour to compute volume integrated quantities, assuming that the eddy is roughly cylindrical.

In simulations with a composite anticyclonic eddy at initialization, the main eddy is simply the initial eddy, that we follow in time. For simulations with no eddy at $t=0$, the main eddy is defined as the first SCV that reaches the center of the bowl-like topography and then grow in size due to merging with other SCVs.

2.2.2. Kinetic energy budget

In the primitive equation framework, the kinetic energy (KE) equation can be obtained by taking the inner product of the horizontal velocities with the momentum equations. It follows:

$$\frac{1}{2} \partial_t u_i^2 + u_j \partial_j (\frac{1}{2} u_i^2) + w \partial_z (\frac{1}{2} u_i^2) = \frac{u_i}{\rho_0} \partial_i P + \mathcal{V}_i u_i + D_i u_i + S_i u_i, \quad (1)$$

with summation convention, $i = 1, 2$, and $j = 1, 2$, u_i are the horizontal component of velocity, ∂_i the components of the vector differential operator, \mathcal{V}_i the components of the parameterized vertical mixing, D_i the components of the horizontal diffusion, and S_i other sources and sinks (due to restoring, nudging, boundary conditions...). This equation is then vertically integrated, and we define:

Table 1
Parameters of the analyzed simulations.

Name	SCV shotgun	RT eddy at initialization	Bottom drag	Convection
dD	deep	–	yes	–
mD	middle	–	yes	–
m	middle	–	–	–
sD	surf	–	yes	–
RTD	–	yes	yes	–
RT	–	yes	–	–
RTDC	–	yes	yes	yes
dRTD	deep	yes	yes	–
dRTDC	deep	yes	yes	yes
mdRTD	middle deep	yes	yes	–
mRTD	middle	yes	yes	–
mRT	middle	yes	–	–
mRTDC	middle	yes	yes	yes
msRTD	middle surf	yes	yes	–
sRTD	surf	yes	yes	–
DC	–	–	yes	yes

- $hadv = \int dz u_j \partial_j (\frac{1}{2} u_i^2)$,
- $vadv = \int dz w \partial_z (\frac{1}{2} u_i^2)$,
- $Prsgrd = \int dz \frac{u_i}{\rho_0} \partial_i P$,
- $vmix = \int dz \mathcal{V}_i u_i$,
- $hmix =$ explicit part of $\int dz \mathcal{D}_i u_i$,
- $hdiff =$ implicit part of $\int dz \mathcal{D}_i u_i$,
- $nudg = \int dz S_i u_i$,
- $cor = \int dz (fuv - fvu)$,
- $vol =$ the depth integrated KE variations due to the grid breezing,
- $Drag =$ contribution of the bottom drag parameterization in the $vmix$ term.

All these terms are computed online (Gula et al., 2016). The closed KE budget is:

$$\partial_t \int dz \frac{1}{2} u_i^2 = hadv + vadv + Prsgrd + vmix + hmix + hdiff + nudg + cor + vol. \quad (2)$$

We integrate these terms in time, such that for instance $\int_0^t dt$ Drag represents the contribution of the bottom drag for the KE at a given time t . Finally, we horizontally integrate the results in the main eddy's contour S (calculated by AMEDA). This allows to follow in detail which physical mechanism is responsible for the evolution of the main eddy's KE.

3. Results

In this section, we describe the results of our study. We first explain qualitatively the course of a simulation representative of the RT, *i.e.*, the mRTD simulation. Then we discuss the impact of the different parameters on the evolution of the main eddy.

3.1. Qualitative evolution of the simulations

In the mRTD simulation, the main eddy is present from $t = 0$ at the center of the bowl topography (see Fig. 5 for the time evolution of the mRTD simulation). Because it is anticyclonic, it is stuck in the center of the bowl to conserve its potential vorticity (Carnevale et al., 1991). Thus, it cannot climb out without external disturbance. During the first year of the simulation, the main eddy does not move from the center of the bowl. Its volume slightly increases because of a azimuthal mode 2 and mode 4 destabilization, similar to the one observed in de Marez et al. (2020a) (a vorticity tripole can be seen at $t = 5$ months in Fig. 5).

Simultaneously, SCVs are generated at the corner of the land mask. As shown in Deremble et al. (2016), such boundary singularities generate dipolar structures. In our case, about 35 dipoles are generated each

year. The anticyclonic pole is attracted by the bowl, while the cyclonic pole tends to step aside. Indeed, on a slope, the topographic β -drift makes anticyclones (resp. cyclones) drift downhill (resp. uphill) (La-Casce, 1998; Lam and Dritschel, 2001). This leads to the separation of about all dipoles in two monopoles of opposite vorticities. Also, in some cases, the positive pole is rolled up around the anticyclone, leading to a shielded anticyclonic SCV. In both cases, this results into anticyclonic SCVs attracted by the bowl. However, they do not all reach the bowl (*i.e.*, the places where the floor is deeper than 2000 m): only about ten anticyclonic SCVs per year manage to reach it. This is mainly due to the fact that just after generation, SCVs merge between each other, and subsequently converge to the center of the bowl.

At the start of the second year of simulation, SCVs start to interact with the main eddy. These SCVs have two effects.

First, the SCVs' velocity field slightly disturb the main eddy, resulting in small displacements of the main eddy in the bowl. From this date, the main eddy can thus be found at tens of kilometers from the center of the bowl, see *e.g.* $t = 15, 25$, or 55 months, in Fig. 5.

Second, SCVs merge with the main eddy. In this simulation – *i.e.*, during about 7 years and a half – 41 merging events between SCVs and the main eddy are observed. Two kinds of merger occur. On the one hand, small SCVs that have experienced a few merging with other SCVs before reaching the bowl, are attracted by the main eddy and steered around it. They are finally absorbed by the main eddy which eventually grows by aggregating vorticity and azimuthal velocity outside of its core (Sutyryn and Radko, 2019; Sutyryn, 2019). This mechanism is referred to as *Vortex Thinning* in the literature. A vortex thinning event results in a small increase of the eddy volume; examples can be seen at $t = 15$ or 70 months in Fig. 5. On the other hand, the main eddy can merge with SCVs that have grown in size due to successive merging with other SCVs. This results in situations where the main eddy is either of the same size of the vortex it merges with, or smaller than it. In both cases, the merging is roughly symmetric, and it results in an abrupt increase of volume of the main eddy. An example can be seen between $t = 30$ and 35 months in Fig. 5.

These mergers can also be called alignment, because the main eddy's core density is not necessarily the same than its companion's one (see *e.g.* Nof and Dewar (1994), and sections 7.1.3 and 7.2.4 of Lilly et al. (2003) that discuss cases of vortex alignment in the Labrador Sea). It can be mentioned that, in a stratified fluid, mergers must manifest as alignment because there will always be small differences in the core density of the two eddies. The impact of this three-dimensional view is discussed in the next sections. Also, we detail in the following the physical mechanism that occur in the simulations, and lead to changes of volume for the main eddy.

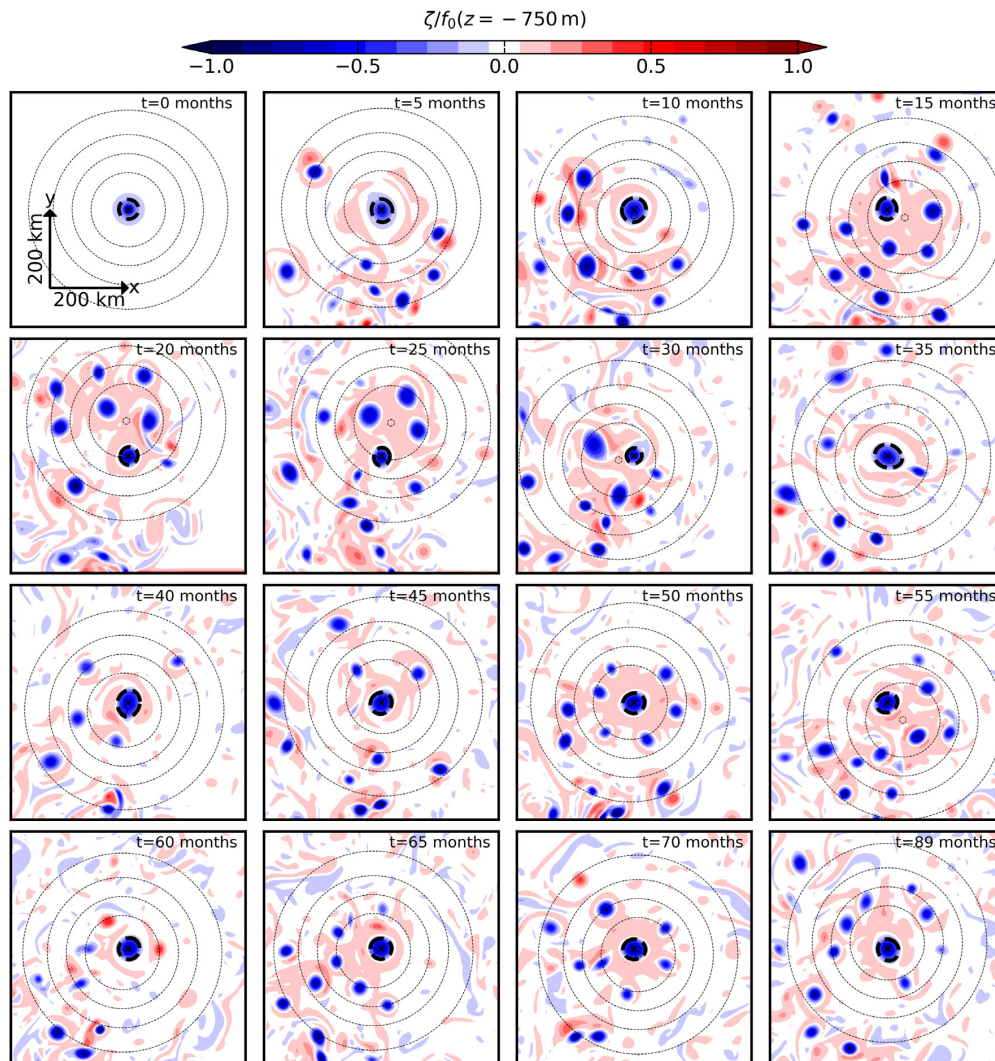


Fig. 5. Snapshots of normalized relative vorticity at 750 m depth, in the mRTD simulation. Each panel is 600 km large, and is centered around the main eddy. Bold dashed contours indicate the contour of maximum velocity of the main eddy. Thin dashed contours show isobath from 2500 to 2000 m depth with a 100 m interval.

3.2. Mechanisms of eddy growth

In all simulations, as in *e.g.*, mRTD (see Fig. 5), the main eddy growth is intermittent and occurs at specific moments of the simulation. As discussed in the introduction, this eddy growth can be attributed to two mechanisms: merging with vortex companions, and convection. We detail in this section these physical mechanisms.

3.2.1. Merging with SCVs

To discuss the impact of merger on the main eddy, we analyze the time evolution of R_{\max} in different simulations, see Fig. 6. Both kinds of merging events discussed in the previous section for mRTD simulation – vortex thinning and symmetric merger – can be seen in Fig. 6(a). They appear as steps in the time evolution of R_{\max} , at *e.g.*, $t = 35$ or 75 months (in the mRTD simulation, see arrows in Fig. 6(a)). In all simulations, symmetric mergers have a greater impact on R_{\max} , as it can double the radius of the main eddy in a few days.

In all simulations with the RT composite at initialization (Fig. 6(a)), the radius of the main eddy oscillates around about 30 km. After

periods of radius decrease, the merging efficiently increases the radius. The horizontal extension of the main eddy is thus similar to its initial one after 7 years of simulation. It can be noticed that in the sRTD simulation, the main eddy appears to have a larger radius than in other simulations. Even with this difference, the purely horizontal view described by the time evolution of R_{\max} is qualitatively similar in dRTD, mDRTD, mRTD, msRTD, and sRTD.

The main difference between the simulations is the final vertical shape of the main eddy, *e.g.*, after 66 months (Fig. 7). In the dRTD simulation, the main eddy has a 3D shape similar to the initial RT composite. This is due to the fact that SCVs have difficulty to merge with the main eddy. Oppositely, in the sRTD and msRTD simulations, SCVs easily merge with the main eddy, and thus drastically modify its 3D shape. The final shape of the main eddy differs from the RT composite because it is intensified at the surface, with a larger horizontal extension due to the numerous mergers it experienced. In the mRTD and mDRTD simulations, the merging events lead to an important intensification of the eddy intensity at depth. In the mDRTD simulation, the final shape

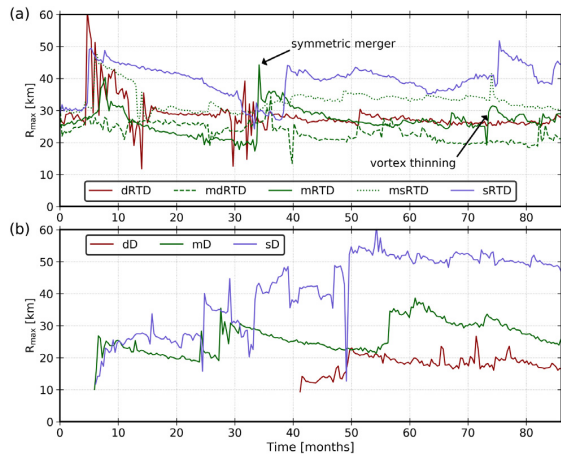


Fig. 6. Evolution of R_{max} during simulations, for different initialization depth of the SCV shotgun (a) with and (b) without the RT composite at the center of the bowl. All simulations include bottom drag parameterization.

of the main eddy is a double-core eddy, with two vorticity maxima, at ~ 500 m depth and ~ 1300 m depth.

The merging efficiency is not the same in all simulations because of (1) the background stratification, and (2) the vertical structures of the main eddy and the SCVs it merges with. Indeed, Verron et al. (1990), Verron and Valcke (1994), Corréard and Carton (1999) altogether showed, using 2-layer numerical simulations, that the merger (or alignment) of two like-signed vortices depends on their shape before the merging. Vortices can be separated into two kinds: PVI (potential vorticity initialization) vortices and RVI (relative vorticity initialization) vortices. PVI vortices are represented by a patch of constant potential vorticity in a single layer – and in some cases a vertical dipole of potential vorticity –, associated with nearly barotropic

relative vorticity. RVI vortices have a constant relative vorticity in a single layer. Corréard and Carton (1999) showed that PVI vortices easily align together while RVI vortices do not. Verron et al. (1990), Verron and Valcke (1994) showed that the ambient stratification plays a different role in the merging depending on the vortex shape: RVI vortex merger strongly depends on the stratification while PVI vortex merger does not. If the stratification is weak, RVI vortices form a pair of heton-like structures, that repel each other. If the stratification is stronger, the ambient flow is more barotropic, and merger is easier. In a configuration more realistic than the 2-layer quasi-geostrophic model, like in our study, the distinction between RVI or PVI vortices can be tricky because of the Gaussian vertical shape that eddies often take (McWilliams, 1985).

In our simulations, the categorization of eddies is difficult because the main eddy and its companion eddies can be categorized as PVI-like vortices (they appear as – roughly constant – PV patches confined in a single layer, see Fig. 8), but also RVI-like vortices (the maximum of relative vorticity is confined in ~ 1000 m deep layers, around which the relative vorticity either changes sign or is close to zero). Merging vortices are thus PVI/RVI hybrids. The background stratification should thus play a role in the merger efficiency. Our background stratification is similar to the RT case (Fig. 1(d)) and it has Brunt–Väisälä frequency maxima at the surface and near 750 m depth. Thus for RVI vortices, the merger is facilitated at these particular depths, while it is harder to merge for deeper eddies. This could explain in part why SCVs have more difficulties to merge with the main eddy in the dRTD simulation than in the other simulations.

One can observe a critical depth for the SCV shotgun, between 1000 and 750 m depth, for which the merging/alignment of eddies do not lead to the intensification of the main eddy's core. If SCVs are close enough (in both vertical and horizontal directions), they eventually align with the main eddy, but this only results in a deepening of the eddy and/or a double-core eddy, with no influence on the original eddy core. Because of the complicated form of eddies and ambient stratification, it is here difficult to be more quantitative about the key parameters that influence the merging. A more extensive study in the parameter space would be necessary to discuss in details the alignment of vortices in a 3D primitive equation framework.

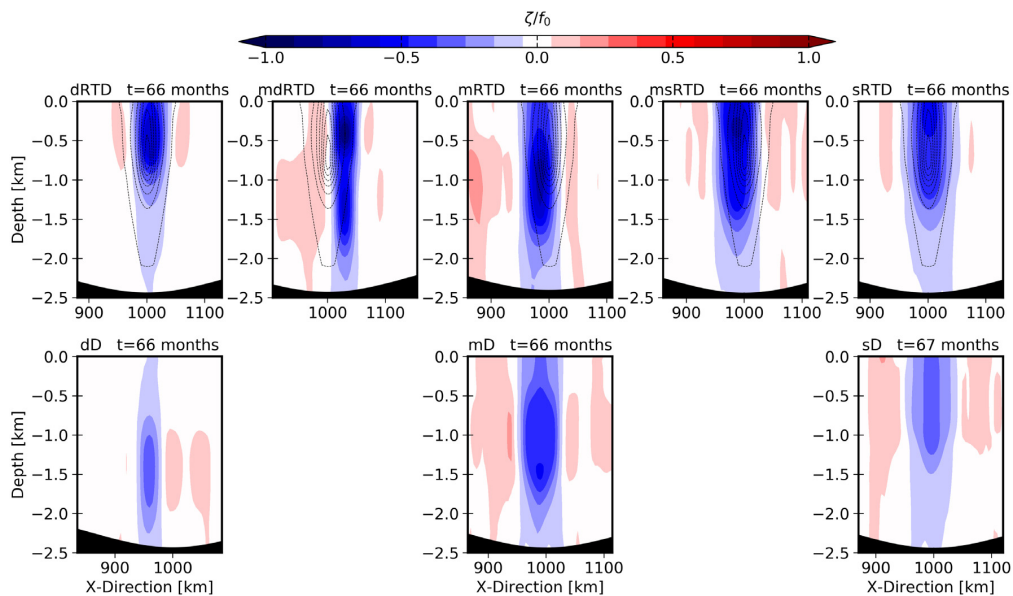


Fig. 7. Vertical sections of normalized relative vorticity passing through the center of the main eddy after ~ 5 and a half years of simulation, for simulations shown in Fig. 6. Thin contours in the top row show the contours of normalized vorticity through the center of the RT composite at initialization; note that line and color contours are shown for the same vorticity values.

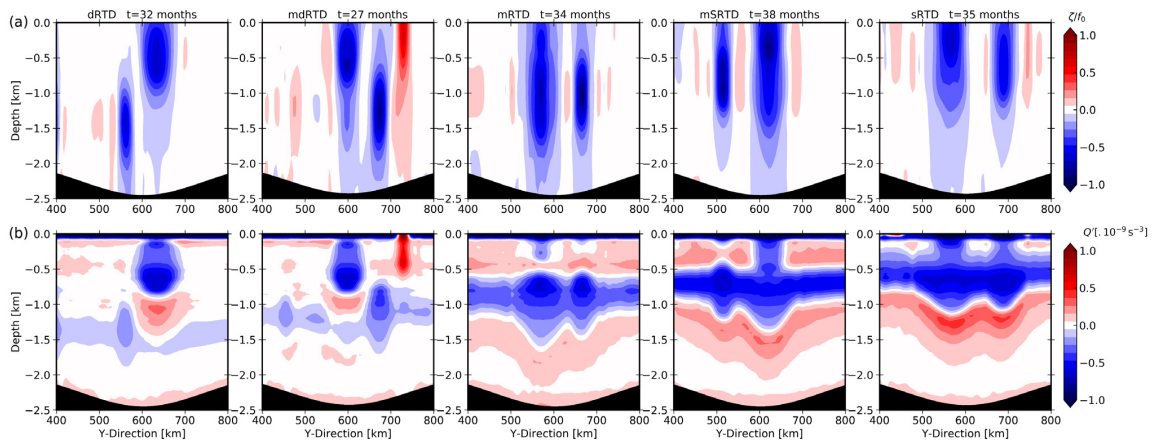


Fig. 8. Vertical section of (a) normalized relative vorticity and (b) associated PV anomaly, at times just before a merger of the main eddy with a companion eddy, in dRTD, mdRTD, mRTD, mSRTD, and sRTD simulations. All sections pass through the center of both eddies.

If no initial RT composite is present, the time evolution of R_{\max} (Fig. 6(b)) is roughly similar to cases described above. However, the main eddy vertical structure near the end of the simulation is strongly influenced by the SCVs generation depth (Fig. 7). In the dD simulation, SCVs hardly merge, because of the weak stratification below 1000 m depth, leading to a weak resulting eddy, intensified at depth. In the sD simulation, SCVs are not very intense, but they easily merge, leading to a weak surface-intensified anticyclone, that does not resemble the RT eddy either. In the mD simulation, the final shape of the main eddy is roughly similar to the mRTD simulation's one. This shows that the merging of SCVs between each other produces an eddy similar to the RT eddy only if SCVs are generated at a realistic depth, where merger is easier because of the strong stratification. This supports the view of Smilenova et al. (2020), that from an ocean at rest, the RT eddy results from a succession of merging events between SCVs generated at ~ 750 m depth.

3.3. On the importance of convection

If we add a negative heat flux at the surface (as in RTDC, mRTDC, dRTDC or DC simulations), convection appears. As a result, isopycnals deepen during about 6 months each year, following the imposed seasonal cycle (Fig. 4). The Ertel potential vorticity Q defined as

$$Q = (f_0 + \zeta)\partial_z b - (\partial_z v)(\partial_x b) + (\partial_z u)(\partial_y b), \quad (3)$$

with f_0 the Coriolis frequency, b the buoyancy, and ζ the relative vorticity, undergoes a seasonal increase in the main eddy's core (see Fig. 9(b)). The shallower the SCV shotgun is, the larger this intensification. This mechanism of intensification by wintertime convection is rather multifaceted. The deepening of the core intensifies radial density gradients and subsequently increases the azimuthal velocity of the eddy. During these convective periods the main eddy is thus intensified, and its radius increases (see Fig. 9(a)). On the other hand, when density gradients are increased the eddy is no longer in thermal wind balance, and therefore an adjustment mediated by a secondary circulation is required. We refer the reader to Legg et al. (1998), Legg and McWilliams (2001) for a full explanation of this process.

If we compare the RTD and the RTDC simulations, one can see that even if no SCV shotgun is present, the evolution of the main eddy's radius experiences sharp increases in the presence of convection. This is due to the fact that during convective periods, the surface mixed-layer deepens in the whole domain, and SCVs are spontaneously generated by mixed-layer baroclinic instabilities (Callies et al., 2015). This leads

to vortex thinning events between convectively-generated SCVs and the main eddy, that subsequently increase the main eddy's radius (Schubert et al., 2020). These events appear throughout the whole simulation involving convection, and they are difficult to characterize because they can be generated above the main eddy and merge with it within a few days. However, it can be noticed that in the simulation with both a SCV shotgun at mid-depth and convection (mRTDC), we observe that the main eddy's radius continuously oscillates between a mean value of about 30 km. In this simulation, the SCVs are more numerous than in the mRTD simulation. The number of merging events of small SCVs with the main eddy is larger when convection is present. This leads to a lot of small increases of radius rather than decrease periods followed by a large increase.

Convection and merging events with convectively-generated SCVs act together to increase the horizontal shape of the main eddy, but also its intensity at depth. Indeed, with convection, the main eddy is more intensified at depth than in simulation without convection, see e.g., Fig. 9(c) for the dRTDC simulation. The main eddy is intensified at a depth where no merging with neither the convectively-generated SCVs in the mixed-layer nor the SCV shotgun SCVs occurs. This reflects the importance of the direct convectively driven mode. As mentioned in the previous section, if the SCVs are generated below a critical depth (e.g. in dRTD simulation), little merging events are observed. If we add the convection (dRTDC simulation), the main eddy's core deepens. Subsequently, the vertical distance between the main eddy's core and SCVs decreases, and merger/alignment is eased. This leads to a deep intensification of the main eddy, see Fig. 9(c). Convection thus allows to intensify the main eddy's core by (1) deepening the core during wintertime, (2) generating small SCVs – by mixed-layer instabilities – that can eventually merge with the main eddy, and (3) helping alignment by reducing the distance between the main eddy's core and deeply-generated SCVs. It should be noticed however that from our analysis, the relative importance of these three mechanisms cannot be precisely gauged. This quantification should be the aim of further investigations.

As a sensitivity test, we also ran a simulation with only convection (DC simulation, not shown). In this simulation, anticyclonic convectively-generated SCVs are attracted by the bowl-shaped topography. They subsequently merge between each other, and eventually form a ~ 50 km radius anticyclone in the bowl, i.e., a main eddy. This eddy appears after about 33 months of simulation and is intensified between 1000 and 1500 m depth. This test further shows that the convection by

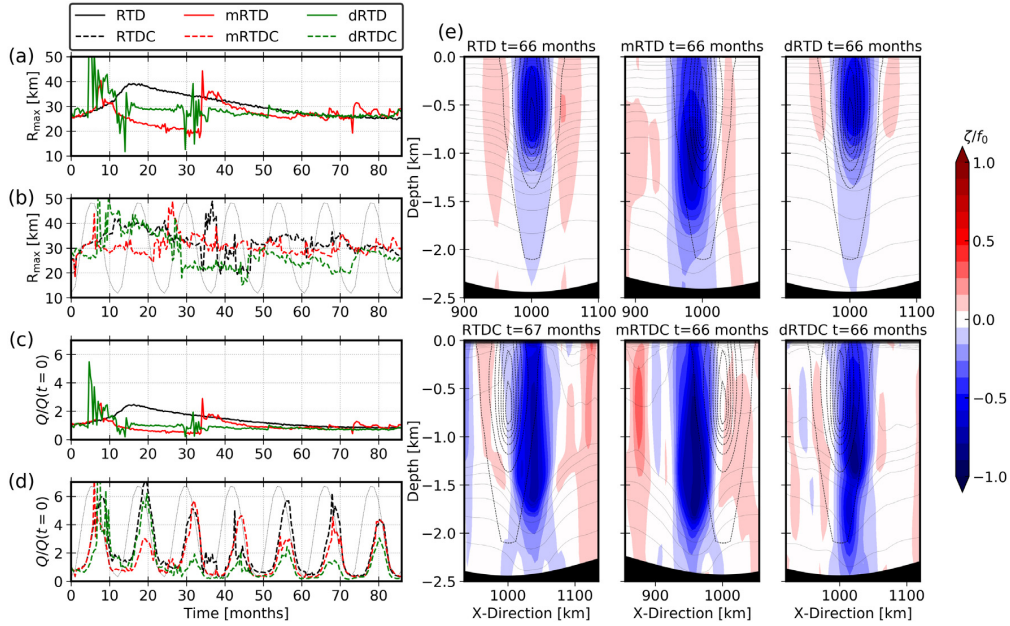


Fig. 9. (a,b) (resp. c,d) Time evolution of R_{max} (resp. ratio between PV and initial PV integrated over the main eddy) for some simulations without (a,c, solid line) or with (b,d, dashed lines) convection; the thin gray line shows the time evolution of the SNHF applied at the surface in the simulations with convection (see Fig. 4 for the values it reaches). (e) Same as Fig. 7 for the 6 simulations shown in (a,b).

itself is sufficient to lead to a single long-lived anticyclonic eddy in a bowl topography.

3.4. Mechanisms of eddy decay

As can be seen in the time evolution of R_{max} (see e.g., Fig. 6), after the main eddy's radius increases due to either merging or convection, periods of decay that can last for several years are observed. During these periods, little merging occur, and some physical mechanisms lead to the erosion of the eddy. We describe those in the following section.

3.4.1. Bottom drag

The principal mechanism responsible for the eddy decay in our simulations is the bottom drag. We observe that no radius decay period are seen in simulations without bottom drag parameterization (Fig. 10(a)). This leads to a main eddy being too intense, and too large in comparison with the RT eddy. Also, without drag, the main eddy becomes anomalously barotropic (see for instance Fig. 11(c)). It thus has a 3D shape very different from the RT eddy.

The bottom drag seems to be the major limiting factor for the eddy growth due to merging with SCVs. In the KE equation budget (Fig. 10(b)) the pressure gradient, the advection and the Coriolis terms dominate the main eddy's KE gain (C in Fig. 10(b)). They are the result of merging with other coherent structures (SCVs), and conversion from potential to kinetic energy (not shown). The horizontal diffusion and mixing, as well as volume change and nudging have a neglectable contribution to the KE budget (B). The bottom drag (A_2), included in the vertical mixing (A_1), appears to dominate the main eddy's KE loss. It compensates the other terms, and increases in amplitude each time the eddy gains KE by merging with other vortices. The bottom drag contribution is intensified when the main eddy drifts away from the center of the bowl, because the water depth is smaller. It is thus greater just before symmetric merger events, and subsequently drifts away from the center of the bowl. This can be seen in Fig. 10(b), with Drag KE term peaking just before merging related steps (see at e.g. $t = 35$ months).

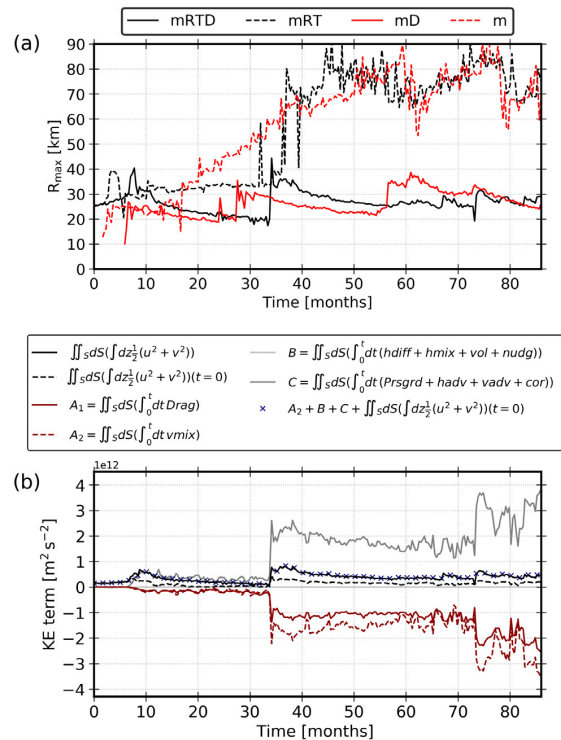


Fig. 10. (a) Evolution of R_{max} during simulations, with (solid) and without (dashed) bottom drag parameterization. (b) Evolution of kinetic energy terms in the mRTD simulation. Each term is integrated in time and in the contour of the main eddy. Note that the superposition of blue crosses with the black solid lines shows that the KE energy budget is closed, with respect to Eq. (2).

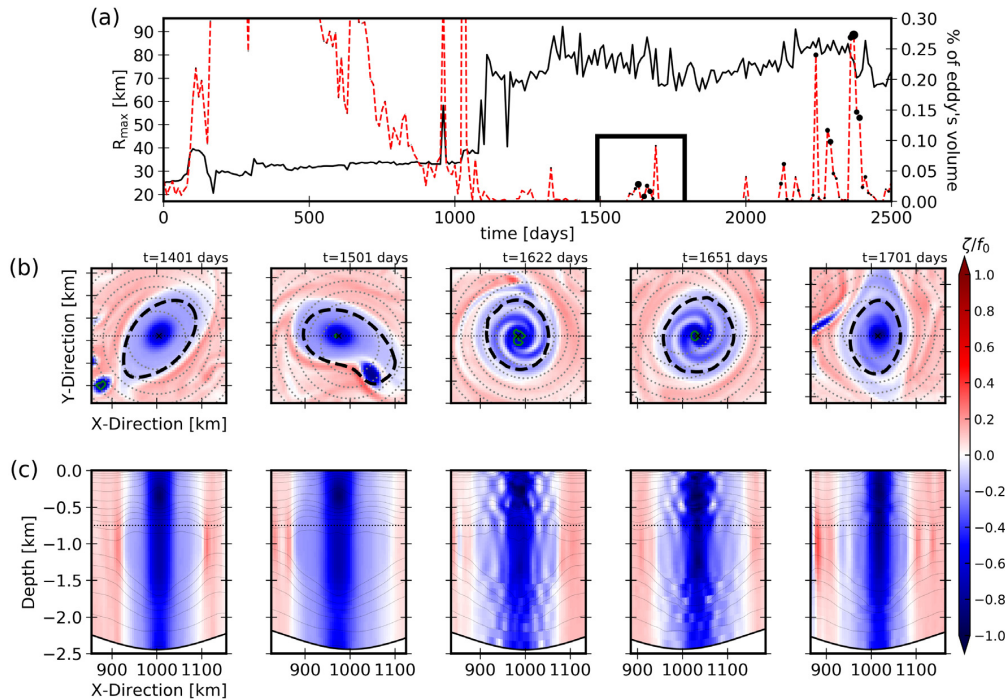


Fig. 11. (a) Time evolution of R_{\max} (black line) and % of eddy's volume with negative PV (dashed red) for the mRT simulation. The size of black dots indicates the amplitude (in absolute value) of the minimum PV in the eddy's contour. (b) Horizontal sections of normalized relative vorticity at 750 m depth; green contours indicate the places where the PV is negative. (c) Vertical sections of normalized relative vorticity passing through the center of the main eddy; the thin dashed lines indicate the depth of horizontal sections shown in (b).

3.4.2. Centrifugal instability

In cases without drag, it can be seen that the main eddy still experiences abrupt radius decrease events, see *e.g.*, between $t = 1500$ and 1700 days in mRT simulation (Fig. 11(a)). At this time, a rapid radius decrease is seen just after a vortex thinning event with a small SCV. Horizontal sections of relative vorticity (Fig. 11(b)) show that after the main eddy absorbs the SCV, a spiral-like pattern appears in the eddy's core. This pattern is seen in the whole water column. There, the normalized relative vorticity reaches $\zeta/f_0 \sim -1$.

This pattern is typical of centrifugal instability (Cushman-Roisin and Beckers, 2011). This diagnostic is confirmed by the following facts. (1) The PV in the eddy's core is negative near its center (green contours in Fig. 11(b)), which is the necessary condition ($fQ < 0$) for centrifugal instability. (2) The horizontal shear terms are responsible for the extreme decrease of PV in the eddy's core (not shown).

Negative PV patches are strongly unstable, and the nearly materially conserved nature of PV implies that negative PV does not occur spontaneously inside the fluid. Thus, the generation of negative PV in the fluid must be forced, for instance by appropriate frictional interactions with nearby boundaries or interactions with the wind. Here, no such mechanism is present. The decrease of PV is due to the abrupt change of horizontal velocity gradients resulting from the vortex thinning of a small SCV around the main eddy (Fig. 11(b)). The change of PV occurs where density fronts are sharp and parameterized diapycnal mixing occurs (see Appendix C in de Marez et al. (2020a)). The centrifugal instability is thus triggered by the interaction of the main eddy with the SCV, and eventually leads to an abrupt erosion of the eddy. About five major centrifugal instability events occur at $t > 1000$ days, see the peaks of red dashed curve in Fig. 11(a), that show times when negative PV is seen in the eddy's core. Note that before $t = 1000$ days, negative PV is found in the eddy's core, but with values very close to zero. The eddy is thus at this moment not intense enough to be subject to the instability.

Such centrifugal instabilities are preferably seen in simulations without drag. In those, the main eddy is more intense, and it reaches very low PV values that are suitable for instabilities. Nevertheless, such instabilities can still be seen in *e.g.*, mRTD simulation, with a smaller signature than in mRT (not shown).

4. Summary and discussion

We studied the lifecycle of an anticyclonic eddy trapped in a bowl-like topography, which is subject to the interaction with like-signed SCVs and/or convection. From the analysis of 16 simulations with varying parameters, we show that the balance between merger and bottom drag allows the eddy to have a roughly constant 3D shape throughout several years. On the one hand the vortex merger with small SCVs allows the eddy to grow in size, and intensify at depth. As merger events occur at the SCV generation depth, the final main eddy is intensified at this particular depth. These mergers are enhanced when SCVs are generated at a depth where the stratification is large, and when convection is at work. Indeed, the convection (1) deepens the main eddy and increases the merger efficiency at depth, and (2) generates other SCVs in the mixed-layer that eventually merge with the main eddy. On the other hand the bottom drag erodes the eddy. The bottom drag is the main contribution to the eddy's KE loss. When it is not included in simulation, the eddy becomes barotropic, and centrifugal instabilities triggered by the merger with SCVs erode the eddy over the whole water column.

Merging and convection both contribute to the maintaining of anticyclonic eddies trapped in bowl-shaped topographies. Our study thus shows that it is difficult to disentangle the two mechanisms, in particular if we replace this in a more realistic context. However, the final shape of the main eddy can give keys about the mechanisms responsible for the long lifetime of such eddies. If the main eddy is intensified at

multiple depth (it has *e.g.*, a double-core eddy), the eddy has certainly experienced one or several merging with other vortices. Also, if the depth of intensification of the main eddy is correlated with the depth of a SCV generation site nearby, merger between these vortices probably happened. One can therefore state that in these cases, merging played a major role in the maintaining of the eddy.

In the real ocean, other processes can affect the shape of such an eddy. For instance, internal waves and fine-scale ($\mathcal{O}(1)$ m) processes can lead to the dissipation of long-lived mesoscale eddies. In the LV case, [Fer et al. \(2018\)](#) showed through high-resolution turbulence measurements that the background shear as well as near-inertial waves trapped by the negative vorticity of the LV are the dominant sources of kinetic energy loss. More generally, internal waves are suspected to drain a significant part of the energy of such mesoscale eddies ([Barkan et al., 2021](#)). These mechanisms are hardly resolved in the simulations discussed in the present paper, and are mainly controlled by the numerical parameterization (*i.e.*, the vertical mixing induced by the KPP scheme). Furthermore, the simulation lacks realistic levels of internal waves. Simulations with higher resolution and fully realistic atmospheric and tidal forcings should thus be required in order to determine the relative importance of these other processes compared to the bottom drag. At larger scales opposite-signed mesoscale coherent structures can travel to the eddy's location. This could modify the behavior of the eddy by dipolar effect, and affect the merging efficiency with SCVs ([Rodríguez-Marroyo et al., 2011](#)). Furthermore, the presence of a mean current due to large-scale circulation or local coastal current can erode the eddy because of the presence of an ambient horizontal shear ([Perrot and Carton, 2010](#)). If the eddy moves toward the coast, the interaction with coastal Kelvin waves can also affect its trajectory and shape ([Dewar and Hogg, 2010](#); [Gula and Zeitlin, 2010](#); [Hogg et al., 2011](#); [de Marez et al., 2020b](#)).

Despite this, in the Rockall Trough (as well as in *e.g.*, the Lofoten Basin) the semi-permanent anticyclonic eddies are rather isolated from the coast and other currents. Our study can thus support the view of [Smilenova et al. \(2020\)](#) or [Trodahl et al. \(2020\)](#) that such semi-permanent anticyclonic eddies are mainly maintained by the merger (or alignment) with smaller-scale vortices. In this high latitude regions, convection is large, and indeed deepens isopycnal and subsequently increases the eddy's core potential vorticity, as discussed in *e.g.*, [Bosse et al. \(2019\)](#). However, we show here that convection principally enhances the number of merger with small eddies, either at the surface or at depth with SCVs. The merging/alignment with SCVs is thus likely to be the more important mechanism to sustain mesoscale anticyclones trapped in a bowl, as stated in the LV case by [Trodahl et al. \(2020\)](#) and by [Smilenova et al. \(2020\)](#) in the RT eddy case.

CRedit authorship contribution statement

Charly de Marez: Conceptualization, Methodology, Software, Writing – original draft. **Mathieu Le Corre:** Software, Writing – review & editing. **Jonathan Gula:** Writing – review & editing, Supervision, Funding acquisition.

Declaration of competing interest

The authors declare that they have no known competing financial interests or personal relationships that could have appeared to influence the work reported in this paper.

Acknowledgments

This work was funded by the Direction Générale de l'Armement (DGA), France via a full grant for Charly de Marez's Ph.D. J.G. gratefully acknowledges support from the French National Agency for Research (ANR) through the project DEEPER (ANR-19-CE01-0002-01). Simulations were performed using the HPC facilities DATARMOR of 'Pôle de Calcul Intensif pour la Mer' at Ifremer, Brest, France. The authors thank X. Carton for helpful discussions.

References

- Barkan, R., Srinivasan, K., Yang, L., McWilliams, J.C., Gula, J., Vic, C., 2021. Oceanic mesoscale eddy depletion catalyzed by internal waves. *Earth Space Sci Open Archive* 14. <http://dx.doi.org/10.1002/essoar.10507068.1>.
- Bosse, A., Fer, I., Lilly, J.M., Soiland, H., 2019. Dynamical controls on the longevity of a non-linear vortex : The case of the Lofoten Basin Eddy. *Sci. Rep.* 9, <http://dx.doi.org/10.1038/s41598-019-49599-8>.
- Bosse, A., Testor, P., Houpert, L.C., Damien, P., Prieur, L., Hayes, D., Taillandier, V., Durrieu de Madron, X., d'Ortenzio, F., Coppola, L., Karstensen, J., Mortier, L., 2016. Scales and dynamics of submesoscale coherent vortices formed by deep convection in the northwestern Mediterranean Sea: Vortices in the NW Mediterranean Sea. *J. Geophys. Res. Oceans* 121, 7716–7742. <http://dx.doi.org/10.1002/2016JC012144>.
- Callies, J., Ferrari, R., Klymak, J.M., Gula, J., 2015. Seasonality in submesoscale turbulence. *Nature Commun.* 6, <http://dx.doi.org/10.1038/ncomms7862>.
- Carnevale, G., Kloosterziel, R., Van Heijst, G., 1991. Propagation of barotropic vortices over topography in a rotating tank. *J. Fluid Mech.* 233, 119–139. <http://dx.doi.org/10.1017/S0022112091000411>.
- Carton, J.A., Chepurin, G.A., Chen, L., Grodsky, S.A., 2018. Improved global net surface heat flux. *J. Geophys. Res. Oceans* 123, 3144–3163. <http://dx.doi.org/10.1002/2017JC013137>.
- Chelton, D., Gaube, P., Schlax, M., Early, J., Samelson, R., 2011. The influence of nonlinear mesoscale eddies on near-surface oceanic chlorophyll. *Science* 334, 6054. <http://dx.doi.org/10.1126/science.1208897>.
- Corréard, S.M., Carton, X., 1999. Vertical alignment of geostrophic vortices. In: *IUTAM Symposium on Simulation and Identification of Organized Structures in Flows*. Springer, pp. 191–200.
- Cushman-Roisin, B., Beckers, J.-M., 2011. *Introduction To Geophysical Fluid Dynamics: Physical and Numerical Aspects*. Academic Press.
- de Marez, C., Carton, X., L'Hégaret, P., Meunier, T., Stegner, A., Le Vu, B., Morvan, M., 2020. Oceanic vortex mergers are not isolated but influenced by the β -effect and surrounding eddies. *Sci. Rep.* 10, <http://dx.doi.org/10.1038/s41598-020-59800-y>.
- Dereemble, B., Dewar, W.K., Chassignet, E.P., 2016. Vorticity dynamics near sharp topographic features. *J. Mar. Res.* 74, 249–276. <http://dx.doi.org/10.1357/002224016821744142>.
- Dewar, W.K., Hogg, A.M., 2010. Topographic inviscid dissipation of balanced flow. *Ocean Modell.* 32, 1–13. <http://dx.doi.org/10.1016/j.ocemod.2009.03.007>.
- Dong, C., McWilliams, J.C., Liu, Y., Chen, D., 2014. Global heat and salt transports by eddy movement. *Nature Commun.* 5, 3294. <http://dx.doi.org/10.1038/ncomms4294>.
- Fer, I., Bosse, A., Ferron, B., Bouruet-Aubertot, P., 2018. The dissipation of kinetic energy in the lofoten basin Eddy. *J. Phys. Oceanogr.* 48, 1299–1316. <http://dx.doi.org/10.1175/JPO-D-17-0244.1>.
- Garreau, P., Dumas, F., Louazel, S., Stegner, A., Le Vu, B., 2018. High-resolution observations and tracking of a dual-core anticyclonic Eddy in the Algerian basin. *J. Geophys. Res. Oceans* 123, 9320–9339. <http://dx.doi.org/10.1029/2017JC013667>, <http://doi.wiley.com/10.1029/2017JC013667>.
- Gelderloos, R., Katsman, C.A., Drijfhout, S.S., 2011. Assessing the roles of three Eddy types in restratifying the Labrador Sea after deep convection. *J. Phys. Oceanogr.* 41, 2102–2119. <http://dx.doi.org/10.1175/JPO-D-11-054.1>.
- Gula, J., Molemaker, J., McWilliams, J., 2015. Gulf stream dynamics along the Southeastern U.S seaboard. *J. Phys. Oceanogr.* 45, 690–715. <http://dx.doi.org/10.1175/JPO-D-14-0154.1>.
- Gula, J., Molemaker, M.J., McWilliams, J.C., 2016. Topographic generation of sub-mesoscale centrifugal instability and energy dissipation. *Nature Commun.* 7, <http://dx.doi.org/10.1038/ncomms12811>.
- Gula, J., Zeitlin, V., 2010. Instabilities of buoyancy-driven coastal currents and their nonlinear evolution in the two-layer rotating shallow-water model. Part 1. Passive lower layer. *J. Fluid Mech.* 659, 69–93. <http://dx.doi.org/10.1017/S0022112010002405>.
- Heywood, K.J., McDonagh, E.L., White, M.A., 1994. Eddy kinetic energy of the North Atlantic subpolar gyre from satellite altimetry. *J. Geophys. Res.* 99, 22525. <http://dx.doi.org/10.1029/94JC01740>.
- Hogg, A.M., Dewar, W.K., Berloff, P., Ward, M.L., 2011. Kelvin wave hydraulic control induced by interactions between vortices and topography. *J. Fluid Mech.* 687, 194–208. <http://dx.doi.org/10.1017/jfm.2011.344>.
- Ioannou, A., Stegner, A., Le Vu, B., Taupier-Letage, I., Speich, S., 2017. Dynamical evolution of intense ierapetra Eddies on a 22 year long period. *J. Geophys. Res. Oceans* 122, 9276–9298. <http://dx.doi.org/10.1002/2017JC013158>, <http://doi.wiley.com/10.1002/2017JC013158>.
- Ivanov, Y., Korabev, A., 1995. Formation and regeneration of the pycnocline lens in the Norwegian Sea. *Russ. Meteorol. Hydrol.* 62–69.
- Klein, P., Hua, B.L., Lapeyre, G., Capet, X., Le Gentil, S., Sasaki, H., 2008. Upper ocean turbulence from high-resolution 3D simulations. *J. Phys. Oceanogr.* 38, 1748–1763.
- Köhl, A., 2007. Generation and stability of a Quasi-permanent vortex in the Lofoten basin. *J. Phys. Oceanogr.* 37, 2637–2651. <http://dx.doi.org/10.1175/2007JPO3694.1>.
- LaCasce, J.H., 1998. A geostrophic vortex over a slope. *J. Phys. Oceanogr.* 28, 2362–2381.
- Lam, J., Dritschel, D.G., 2001. On the beta-drift of an initially circular vortex patch. *J. Fluid Mech.* 436, 107–129. <http://dx.doi.org/10.1017/S0022112001003974>.

- Large, W., McWilliams, J., Doney, S., 1994. Oceanic vertical mixing: A review and a model with a nonlocal boundary layer parameterization. *Rev. Geophys.* 32, 363–403. <http://dx.doi.org/10.1029/94RG01872>.
- Le Corre, M., Gula, J., Smilenova, A., Houpert, L., 2019. On the dynamics of a deep quasi-permanent anticyclonic eddy in the rockall trough. Association Française de Mécanique, Brest, France 12.
- Le Corre, M., Gula, J., Tréguier, A.-M., 2020. Barotropic vorticity balance of the North Atlantic subpolar gyre in an eddy-resolving model. *Ocean Sci.* 16, 451–468. <http://dx.doi.org/10.5194/os-16-451-2020>.
- Le Vu, B., Stegner, A., Arsouze, T., 2018. Angular momentum Eddy detection and tracking algorithm (AMEDA) and its application to coastal Eddy formation. *J. Atmos. Ocean. Technol.* 35, 739–762. <http://dx.doi.org/10.1175/JTECH-D-17-0010.1>.
- Legg, S., McWilliams, J.C., 2001. Convective modifications of a geostrophic eddy field. *J. Phys. Oceanogr.* 31, 874–891.
- Legg, S., McWilliams, J., Gao, J., 1998. Localization of deep ocean convection by a mesoscale eddy. *J. Phys. Oceanogr.* 28, 944–970.
- Lilly, J.M., Rhines, P.B., Schott, F., Lavender, K., Lazier, J., Send, U., D'Asaro, E., 2003. Observations of the Labrador Sea eddy field. *Prog. Oceanogr.* 59, 75–176. <http://dx.doi.org/10.1016/j.pocan.2003.08.013>.
- de Marez, C., L'Hégaret, P., Morvan, M., Carton, X., 2019. On the 3D structure of eddies in the Arabian Sea. *Deep-Sea Res. I* <http://dx.doi.org/10.1016/j.dsr.2019.06.003>, <https://linkinghub.elsevier.com/retrieve/pii/S0967063718303650>.
- de Marez, C., Meunier, T., Morvan, M., L'Hégaret, P., Carton, X., 2020a. Study of the stability of a large realistic cyclonic eddy. *Ocean Model.* 146, 101540. <http://dx.doi.org/10.1016/j.ocemod.2019.101540>.
- de Marez, C., Meunier, T., Tedesco, P., L'Hégaret, P., Carton, X., 2020b. Vortex–wall interaction on the β -plane and the generation of deep submesoscale cyclones by internal Kelvin Waves–current interactions. *Geophys. Astrophys. Fluid Dyn.* 114, 588–606. <http://dx.doi.org/10.1080/03091929.2020.1772779>.
- McWilliams, J.C., 1985. Submesoscale, coherent vortices in the ocean. *Rev. Geophys.* 23, 165. <http://dx.doi.org/10.1029/RG023i002p00165>.
- Ménesguen, C., Le Gentil, S., Marchesiello, P., Ducousso, N., 2018. Destabilization of an oceanic meddy-like vortex: energy transfers and significance of numerical settings. *J. Phys. Oceanogr.* 48, 1151–1168. <http://dx.doi.org/10.1175/jpo-d-17-0126.1>.
- Mkhinini, N., Coimbra, A.L.S., Stegner, A., Arsouze, T., Taupier-Letage, I., Béranger, K., 2014. Long-lived mesoscale eddies in the eastern mediterranean sea: Analysis of 20 years of AVISO geostrophic velocities. *J. Geophys. Res. Oceans* 119, 8603–8626. <http://dx.doi.org/10.1002/2014JC010176>, <http://doi.wiley.com/10.1002/2014JC010176>.
- Nof, D., Dewar, W., 1994. Alignment of lenses: laboratory and numerical experiments. *Deep-Sea Res. I* 41, 1207–1229. [http://dx.doi.org/10.1016/0967-0637\(94\)90041-8](http://dx.doi.org/10.1016/0967-0637(94)90041-8).
- Perrot, X., Carton, X., 2010. 2D vortex interaction in a non-uniform flow. *Theor. Comput. Fluid Dyn.* 24, 95–100. <http://dx.doi.org/10.1007/s00162-009-0127-4>.
- Rodríguez-Marroyo, R., Viúdez, A., Ruiz, S., 2011. Vortex merger in oceanic tripoles. *J. Phys. Oceanogr.* 41, 1239–1251. <http://dx.doi.org/10.1175/2011JPO4582.1>.
- Roullet, G., Capet, X., Maze, G., 2014. Global interior eddy available potential energy diagnosed from Argo floats. *Geophys. Res. Lett.* 41, 1651–1656. <http://dx.doi.org/10.1002/2013GL059004>.
- Schubert, R., Gula, J., Greatbatch, R.J., Baschek, B., Biastoch, A., 2020. The submesoscale kinetic energy cascade: Mesoscale absorption of submesoscale mixed layer eddies and frontal downscale fluxes. *J. Phys. Oceanogr.* 50, 2573–2589. <http://dx.doi.org/10.1175/JPO-D-19-0311.1>, [arXiv:https://journals.ametsoc.org/jpo/article-pdf/50/9/2573/4992078/jpod190311.pdf](https://journals.ametsoc.org/jpo/article-pdf/50/9/2573/4992078/jpod190311.pdf).
- Shchepetkin, A.F., McWilliams, J.C., 2005. The regional oceanic modeling system (ROMS): a split-explicit, free-surface, topography-following-coordinate oceanic model. *Ocean Modell.* 9, 347–404.
- Shchepetkin, A.F., McWilliams, J.C., 2011. Accurate Boussinesq oceanic modeling with a practical, “stiffened” equation of state. *Ocean Modell.* 38, 41–70. <http://dx.doi.org/10.1016/j.ocemod.2011.01.010>.
- Smilenova, A., Gula, J., Le Corre, M., Houpert, L.C., Reecht, Y., 2020. A persistent deep anticyclonic vortex in the rockall trough sustained by anticyclonic vortices shed from the slope current and wintertime convection. *J. Geophys. Res. Oceans* 125, <http://dx.doi.org/10.1029/2019JC015905>.
- Solodoch, A., Stewart, A.L., McWilliams, J.C., 2021. Formation of anticyclones above topographic depressions. *J. Phys. Oceanogr.* 51, 207–228. <http://dx.doi.org/10.1175/JPO-D-20-0150.1>.
- Sutyrin, G., 2019. On vortex intensification due to stretching out of weak satellites. *Phys. Fluids* 31, 075103. <http://dx.doi.org/10.1063/1.5098068>.
- Sutyrin, G., Radko, T., 2019. On the peripheral intensification of two-dimensional vortices in smaller-scale randomly forcing flow. *Phys. Fluids* 31, 101701. <http://dx.doi.org/10.1063/1.5118752>.
- Trodahl, M., Isachsen, P.E., Lilly, J.M., Nilsson, J., Kristensen, N.M., 2020. The regeneration of the lofoten vortex through vertical alignment. *J. Phys. Oceanogr.* 50, 2689–2711. <http://dx.doi.org/10.1175/JPO-D-20-0029.1>, URL: <https://journals.ametsoc.org/view/journals/phoc/50/9/jpoD200029.xml>.
- Verron, J., Hopfinger, E., McWilliams, J., 1990. Sensitivity to initial conditions in the merging of two-layer baroclinic vortices. *Phys. Fluids A* 2, 886–889. <http://dx.doi.org/10.1063/1.857647>.
- Verron, J., Valcke, S., 1994. Scale-dependent merging of baroclinic vortices. *J. Fluid Mech.* 264, 81–106. <http://dx.doi.org/10.1017/S0022112094000595>.
- Volkov, D.L., 2005. Interannual variability of the altimetry-derived eddy field and surface circulation in the extratropical north atlantic ocean in 1993–2001. *J. Phys. Oceanogr.* 35, 405–426. <http://dx.doi.org/10.1175/JPO2683.1>.
- White, M.A., Heywood, K.J., 1995. Seasonal and interannual changes in the north atlantic subpolar gyre from Geosat and TOPEX/POSEIDON altimetry. *J. Geophys. Res.* 100, 24931. <http://dx.doi.org/10.1029/95JC02123>.
- Xu, W., Miller, P.L., Quartly, G.D., Pingree, R.D., 2015. Seasonality and interannual variability of the European slope current from 20years of altimeter data compared with in situ measurements. *Remote Sens. Environ.* 162, 196–207. <http://dx.doi.org/10.1016/j.rse.2015.02.008>.
- Yu, L., Bosse, A., Fer, I., Orvik, K.A., Bruvik, E.M., Hessevik, I., Kvalsund, K., 2017. The lofoten basin eddy: Three years of evolution as observed by seagliders: THE LOFOTEN BASIN EDDY. *J. Geophys. Res. Oceans* 122, 6814–6834. <http://dx.doi.org/10.1002/2017JC012982>.
- Zhang, Z., Wang, W., Qiu, B., 2014. Oceanic mass transport by mesoscale eddies. *Science* 345, 322–324. <http://dx.doi.org/10.1126/science.1252418>.

ONDES DE SILLAGE DANS LE GULF STREAM

Nous présentons ici une étude commencée avant la thèse, durant un stage de M2, et finalisé en parallèle des études présentées dans ce manuscrit, puis publié dans le journal *Scientific Reports*. Nous utilisons une simulation réaliste de l'Atlantique Nord pour étudier la génération d'ondes de sillage par le Gulf Stream, le long de la côte Nord-Américaine. Cette partie permet une illustration de l'importance de la bathymétrie sur la dynamique océanique, mais également de l'importance de la stratification pour la génération d'ondes internes, comme présenté dans les sections 1.2.2 et 1.2.3.

OPEN **Interaction of the Gulf Stream with small scale topography: a focus on lee waves**Charly de Marez ^{*}, Noé J. Lahaye & Jonathan Gula 

The generation of lee waves in the Gulf Stream along the U.S. seaboard is investigated using high resolution realistic simulations. The model reproduces the surface signature of the waves, which compares favourably with observations from satellite sun glitter images in the region. In particular, a large number of internal waves are observed above the Charleston Bump. These waves match well with the linear theory describing topographically-generated internal waves, which can be used to estimate the associated vertical transport of momentum and energy extracted from the mean flow. Finally, small scale topographic features are shown to have a significant impact on the mean flow in this region of the Gulf Stream, and the specific role of lee waves in this context is outlined.

Large-scale currents impinging on the topography can generate numerous physical processes, including internal waves –so-called lee waves–, which extract energy from the current and radiate it away from the bottom. For instance, in the Drake Passage, the energy transport due to a lee wave has been estimated locally at a peak rate of $O(1) \text{ W m}^{-2}$ ¹. The impact in the global ocean is significant as lee waves are thought to extract about 20% of the global wind power input to the geostrophic circulation². Half of this energy is dissipated in the water column, within a kilometer of the topography², when waves break and induce turbulent mixing³. Hence, lee waves provide a significant mechanism for the transfer of energy from large-scale flows to turbulent length scales⁴. Lee waves also redistribute momentum from the mean flow and can affect the large-scale circulation through the generation of a drag^{5,6}. Numerical models have thus to take into account the redistribution of momentum and energy, by using parameterizations of the wave drag and energy dissipation⁷.

The Gulf Stream flows northward along the U.S. continental shelf from the Strait of Florida to Cape Hatteras, see Fig. 1(a,b). Its path is mainly controlled by the bottom topography and boundary shape⁸. The current is strong, with a maximum at the surface of about 2.5 m s^{-1} ⁹. Near 31.5° N , 79° W , a prominent topographic feature is present off the coasts of South Carolina and Georgia: the Charleston Bump. Above it, the flow is shallow ($O(500) \text{ m}$) and intense ($O(1) \text{ m s}^{-1}$) even at the bottom, thus providing a context of strong current-topography interaction¹⁰ and conditions that are favorable for the generation of lee waves¹¹.

Internal waves can be observed using synthetic aperture radars (SAR) or sun glitter images through their surface roughness signature. Over the Charleston Bump, quasi-stationary wavefront-like patterns in the surface roughness have been attributed to lee waves generated through the interaction of the Gulf Stream with seamounts¹². Similar signals have also been observed in this area through their impact on patchiness in seabird distribution¹³. More recently, measurements using sea-gliders have confirmed the presence of lee waves along the path of the Gulf Stream near the Charleston Bump¹¹.

In this paper, we investigate the dynamics of lee waves and, more generally, the role of small-scale topography on the mean current, with a focus on the Charleston Bump region. Our results rely on regional realistic simulations of the Gulf Stream using very high horizontal and vertical resolution (see section 2.2) that allows us to resolve small-scale topographic features ($O(1) \text{ km}$) as well as vertical motions in the range 10–100 m. We address the following questions: (1) Are lee waves generated in the high resolution simulations of the Gulf Stream? (2) What are their structure and their properties? (3) How the small scale topographic features impact the mean flow of the Gulf Stream? In a first part we present some elements of theory considered for the study of lee waves and the numerical setup of the simulation we used. Then we analyze the lee wave generation in the path of the Gulf Stream using the simulation and theory. Finally we discuss the impact of the small topographic features on the mean current.

Université de Bretagne Occidentale, CNRS, IRD, Ifremer, Laboratoire d'Océanographie Physique et Spatiale (LOPS), IUEM, Brest, France. *email: charly.demarez@univ-brest.fr

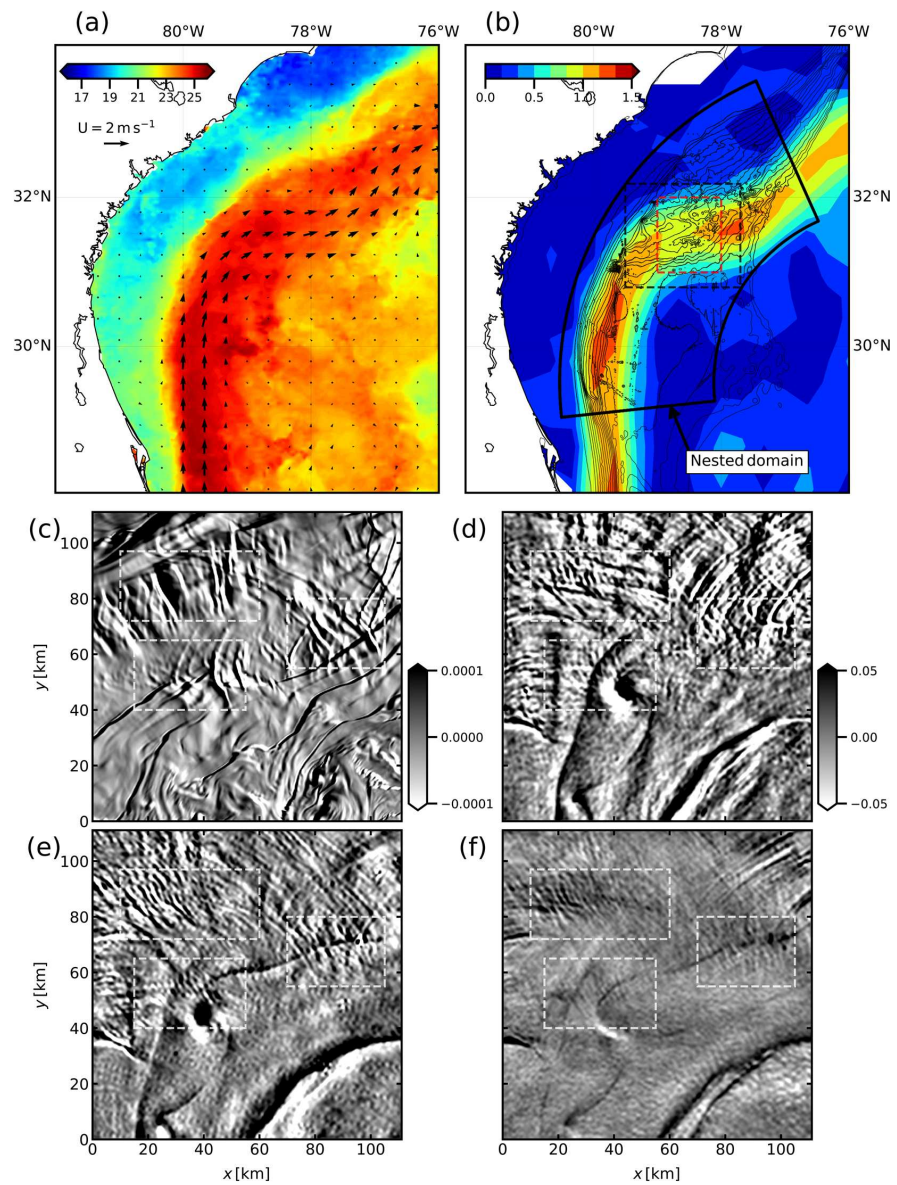


Figure 1. (a) Sea Surface Temperature [in °C] over the Gulf Stream region on 2010/04/01²⁷ and surface currents from AVISO on 2010/03/31. (b) Geostrophic surface currents norm from AVISO on 2010/03/31 [in m s^{-1}], black contours are isobaths from the surface to 1000 m depth every 50 m. The red dashed rectangle indicates the area of the zoom presented in panels (c-f); the black dashed rectangle indicates the area where we then show the lee waves related quantities. (c) Estimation of the surface roughness [in s^{-1}] in the LEEWA simulation. The coordinate (0, 0) corresponds to 79°W 31°N. (d-f) Surface roughness [in arbitrary units] from Sun-glitter measured on 2010/04/01 by 3 different satellites (TERRA, AQUA, and Envisat) with (MODIS, MODIS, and MERIS) instruments in the same area than (c). White dashed rectangles indicate places where qualitatively similar roughness patterns appear in both the simulation and the satellite observations. The rightmost rectangle corresponds to the position of Hoyt Hills, where the same kind of wavefront-like pattern has already been observed¹².

Methods

Linear theory of lee waves. The equation for the propagation of lee waves can be obtained by linearizing the incompressible primitive equations around a steady state. Following ref. 5, we first neglect the background rotation to keep the equations simple. This assumption is reasonable for monochromatic topography of horizontal lengthscale $O(<10)$ km (a criterion which is satisfied where we compare the solution with the model outputs). Seeking steady solutions ($\partial_t \rightarrow 0$), the vertical displacement of a streamline η is defined such that $w = U\partial_x\eta$, where w is the vertical velocity within the fluid and $U(z)$ is the mean horizontal current, oriented along the x -axis. The lee wave problem in the horizontal Fourier space (k, m) thus reads:

$$\partial_{zz}\tilde{\eta}(k, m, z) + n^2\tilde{\eta}(k, m, z) = 0, \tag{1}$$

supplemented by a radiation condition at the top of the domain and a Dirichlet condition at the bottom:

$$\tilde{\eta}(k, m, z = 0) = \tilde{h}(k, m). \tag{2}$$

Here, \tilde{h} (resp. $\tilde{\eta}$) is the Fourier transform of the topography h (resp. the streamline η), and $n(k, m, z)$ can be interpreted as a local vertical wavenumber of the solution.

In the case of lee waves, the condition for a hydrostatic flow is:

$$\varepsilon = \frac{2\pi U}{NL} \ll 1 \rightarrow \text{Hydrostatic} \tag{3}$$

where L is the typical length of the topographic features (equal to the horizontal wavelength of the waves). Under this regime, the dispersion relation for a hydrostatic lee wave is⁵:

$$n^2(k, m, z) = \frac{k^2 + m^2}{k^2} \left(\frac{N^2}{U^2} + \frac{\partial_{zz}U}{U} \right), \tag{4}$$

where $N(z)$ is the Brunt-Väisälä frequency. In specific regions of the ocean such as the Charleston Bump area, the vertical shear of the mean current is large, with variations of current up to 2 m s^{-1} over 500 m depth. In these conditions, $\frac{\partial_{zz}U}{U} \sim \frac{N^2}{U^2}$, and the shear of the mean flow must be taken into account in the dispersion relation. In the following, the 3D theoretical prediction of hydrostatic lee waves is obtained by numerically solving Eq. (1) using the WKBJ approximation¹⁴, with the bottom condition (2) and the dispersion relation (4).

Finally, we briefly recall the criteria for the linear propagation of lee waves in the ocean. The rotation of the Earth imposes a lower bound to the range of horizontal wavenumbers k for which waves can propagate. In terms of the non-dimensional number ε , the radiation condition in a rotating and stratified fluid is²:

$$\text{Pr} < \varepsilon \tag{5}$$

where $\text{Pr} = f/N$ is the Prandtl number and f is the Coriolis frequency. Without the hydrostatic approximation, an additional upper bound $\varepsilon < 1$ is present.

The importance of nonlinear effects associated with lee waves can be estimated using a “lee wave Froude number”¹⁵ (or “steepness parameter”¹⁶). It is given by:

$$\text{Fr}_{\text{lee}} = \frac{NH}{U} = \frac{\text{vertical velocity within the lee wave}}{\text{group velocity of the lee wave}}, \tag{6}$$

where H is the scale of the bathymetry height. It follows that:

$$\begin{aligned} \text{Fr}_{\text{lee}} < 1 &\rightarrow \text{linear propagation of the waves} \\ \text{Fr}_{\text{lee}} \gtrsim 1 &\rightarrow \text{non-linearity of the waves.} \end{aligned} \tag{7}$$

Model setup. To study the generation of lee waves, we performed realistic simulations in the Gulf Stream region using the Coastal and Regional Ocean COmmunity model (CROCO¹⁷). It solves the hydrostatic primitive equations for the velocity \mathbf{u} , the temperature T and the salinity S , using a full equation of state for seawater¹⁸. A one-way nesting approach is used, with successive horizontal grid resolutions of $\Delta x \sim 750$ m for the parent, and $300 \text{ m} > \Delta x > 150$ m for the child simulations. The parent simulation has been shown to accurately represent the Gulf Stream Dynamics and the hydrography along the U.S. seaboard⁸. In this paper we study outputs of the child simulations. The nested domain, shown in Fig. 1(b), consists of a grid of 2050×1026 points. The time step is chosen so that it respects the Courant–Friedrichs–Lewy condition, $dt = 30$ s. Sub-grid parameterizations are identical than in the parent simulation; see section 2 in ref. 8 for further details. In particular, vertical mixing of tracers and momentum is done using a K-profile parametrization (KPP), and the effect of bottom friction is parameterized through a logarithmic law of the wall. Simulations have 128 terrain-following vertical levels, which are stretched such that the resolution increases near the surface and the bottom; for instance, over the Charleston Bump, $\Delta z \sim 2$ m at the surface, $\Delta z \sim 8$ m at 500 m and $\Delta z \sim 6$ m at the bottom. The simulations are initialized by interpolating a snapshot of the parent simulation on the child grid (on 2016/03/20). They are forced at the lateral boundaries by the parent simulation, and at the surface by a monthly varying wind, which limits the generation of near-inertial waves. There is no tidal forcing (and hence no internal tides). Two simulations have been run, hereafter named LEEWA and SMOOTH, with two different bathymetries. The latter are constructed from the

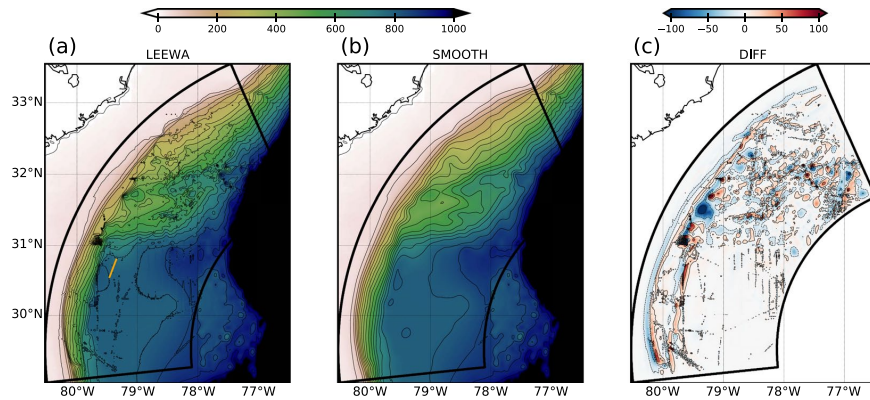


Figure 2. Bathymetry [in m] from the SRTM30_PLUS dataset used in (a) the LEEWA simulation and (b) the SMOOTH simulation; the orange straight line in (a) indicates the position where we then compare the model with the linear theory. The difference [in m] between the two bathymetries is displayed in (c).

SRTM30_PLUS dataset and are smoothed using a Gaussian kernel, with a width of 4 grid points for LEEWA and 50 grid points for SMOOTH. This avoids aliasing, and retains small scale topographic features only in the LEEWA simulation. The bathymetries used for the two simulations are shown in Fig. 2. For both simulations, we considered a 4-days spin-up period. All diagnostics shown, including time-averages over the whole simulation, are performed after this spin-up, during a one-month long period (the time of the simulations), which is long enough for studying lee waves because they adjust rapidly to the flow.

Lee Waves in the Gulf Stream

In this section, we show that our numerical simulations produces lee waves and describe their dynamics. We first provide a qualitative comparison of their surface signature against SAR images, then we present more quantitative results on the lee wave dynamics and their impact on the flow based on diagnostics of the simulations and linear theory.

Surface signature. Streak-like patterns of the surface roughness have been observed by synthetic aperture radars (SAR) in the path of the Gulf Stream and interpreted as the surface signature of lee waves by ref.¹². Similar surface roughness patterns can be seen in more recent sun glitter images collected on 2010/04/01 by three different satellites over the Gulf Stream region, as shown in Fig. 1(d–f) and Fig. 1(a) of Supporting Information. The data have a resolution of 250 m and are band-passed between 2 and 25 km. They show roughness streak-like patterns upstream and over the Charleston Bump, where the intense current flows over rough topography (see Fig. 1(a,b)). Patterns typical of lee waves and similar to the ones described in ref.¹² are visible over Hoyt Hills, see Fig. 1(d–f). The signal also includes the signature of submesoscale fronts and filaments advected by the Gulf Stream, which can be identified in the SST field. An unstable filament breaking up into submesoscale cyclonic vortices (described in ref.¹⁹) is visible between the bottom left and the right side of the satellite images.

Here, we compare the observed surface roughness patterns to the outputs of a simulation, showing that the latter qualitatively reproduces the signature of lee waves observed at the surface by sun glitter images. To this aim, we compute the quantity $(\partial_x + \partial_y)(u + v)$ at the surface in the LEEWA simulation (Fig. 1(c) and Fig. 1(b) of Supporting Information). Indeed, the surface roughness observed in sun glitter images can be interpreted as²⁰:

$$\text{roughness} \sim \alpha \partial_x u + \beta \partial_y u + \gamma \partial_x v + \delta \partial_y v,$$

where the coefficients α , β , γ and δ are functions of the wind direction and the position of the measuring device with respect to the position of the sun. Setting the coefficients to 1 gives a first approximation of the surface roughness in the simulation. As in the satellite observations, fronts related to mesoscale and submesoscale turbulence within the simulation are visible throughout the domain.

Roughness patterns can be seen upstream and over the Charleston Bump in the simulation, similarly as in the satellite observations, see Fig. 1(b) of Supporting Information. More precisely, wavefront-like patterns are visible over the Charleston Bump and over Hoyt Hills (Fig. 1(c)). More quantitative comparisons between model outputs and observations are made difficult by the fact that (1) the details (including the wavelength) of topographic features may differ between the bathymetry used in the simulation and the real one, and (2) the apparent wavelength of the wavelike patterns in the sun glitter images may be misleading due to the unknown transfer function of the measurement device – see the discrepancies between the images from three different satellites in Fig. 1. However, this comparison shows that the simulation produces wavefront-like patterns at locations that are consistent with the satellite images. We should stress that these patterns are persistent in time (the three satellite images were taken at 6 h intervals), which is consistent with topographically-generated disturbances. These wave patterns are

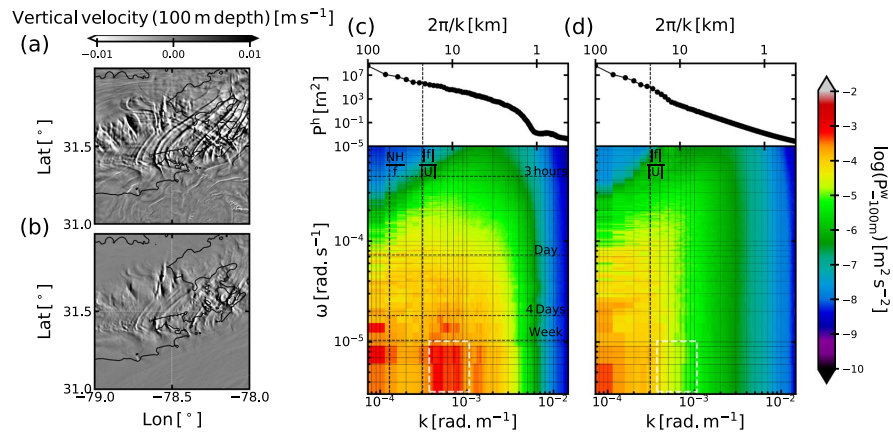


Figure 3. (a) (resp. (b)): Snapshot of vertical velocity (resp. time-lowpass-filtered vertical velocity) at 100 m depth in the LEEWA simulation on 2016/04/10 (after 22 days of simulation). Black contours are the isobath at 600 m. (c) (resp (d)): (k, ω) Power Spectral Density of the vertical velocity at 100 m depth in the (k, ω) space (bottom panels) in the LEEWA (resp SMOOTH) simulation. The power spectrum of the bathymetry used in the simulation are represented in the top panels. Vertical dashed lines indicate $|NH|/|f|$ and $|f|/|U|$, which are estimated using spatial averages of the stratification, height, bottom velocity and Coriolis frequency. $|NH|/|f|$ is the first Rossby radius of deformation indicating the typical horizontal extension of mesoscale eddies. White dashed rectangles indicate the area of the spectrum where we expect to spot the signature of lee waves.

also visible in the vertical velocity field at 100 m depth (Fig. 3(a)), *i.e.* below the thermocline (which is about $O(50)$ m depth in the Gulf Stream). This reinforces the hypothesis that these patterns in the simulations are most likely induced by lee waves, which is further confirmed in the following.

Properties of the lee waves. Dispersion diagrams $((k, \omega)$ spectra) of the variance of vertical velocity at 100 m depth are calculated in both simulations above the Charleston Bump and shown in Fig. 3(c,d) (see Supporting Information for more details on the calculation). Azimuthally averaged power spectra of bathymetry for the two simulations are also shown in Fig. 3(c,d). An energetic region in the (k, ω) space is clearly visible in the LEEWA simulation spectrum (dashed white rectangle in Fig. 3(c,d)) at spatial scales of $O(10)$ km and temporal scales of $O(>1)$ weeks. This is a signature typical of lee waves, which are expected to be quasi-stationary and associated with spatial scales lower than $|f|/|U|$, as follows from the condition (5). The slow temporal variations of the lee waves are due to the oscillation of the Gulf Stream between a deflected and a weakly deflected position over the Charleston Bump⁶. Looking at the SMOOTH bathymetry spectrum, one can see that topographic features of length scale lower than $|f|/|U|$ have been cut-off. According to the theory (see section 2.1), lee waves can not propagate under these conditions. Hence, there should not be such waves in the SMOOTH simulation, which is confirmed by the absence of the corresponding energetic patch in the (k, ω) spectrum.

The shape of the lee waves within the LEEWA simulation is compared with the 3D linear solution (see section 2.1). To do so, we first isolate lee waves in the simulation: quasi-stationary dynamical features are extracted using a fourth-order low-pass Butterworth filter. The cutting period is chosen at 4 days to retain the slow variations of the current ($O(1)$ week) while removing all rapid ($O(<1)$ day) motions; this period is justified by the fact that lee waves have a temporal scale lower than 4 days (see Fig. 3(c)). In particular, low-pass filtered vertical velocity, density and horizontal velocities are used to compute the vertical energy and momentum fluxes (shown in Figs. 4(c) and 5(c–e)). An example of such filtering can be seen in Fig. 3(a,b). The comparison is shown in Fig. 4 along a typical section (indicated by a bold orange line in Fig. 2(a)). The section is centered around an isolated seamount and tangential to the flow. Along the section, $U \sim 10^2 \times N$, the topography has a magnitude H of order $O(<50)$ m, and a typical lengthscale of about 2 km, such that the dynamics is hydrostatic and linear, and the rotation can be neglected. The theoretical prediction is computed using smoothed profiles of U and N from the simulation (shown in Fig. 4(b)) and a de-trended and windowed topography.

The horizontal structure of the lee wave generated by the seamount at $(x, y) \sim (5, 4)$ km in the model (Fig. 4(a)) is very similar to the theoretical prediction. The vertical structure also matches well with the theoretical prediction (Fig. 4(b)) in the lower half of the domain. In particular the orientation of the phase lines and the intensity of the vertical velocity at the bottom (Fig. 4(c)) are in good agreement. The shape and intensity of the pressure anomaly p' calculated from the simulation outputs (see Supporting Information) are also very similar to the theoretical predictions (Fig. 4(c)), with a positive pressure anomaly upstream and a negative one downstream. The vertical energy flux $Fe^z = p'w^z$ is found positive with a peak value of $Fe^z = O(0.1)$ W m^{-2} (Fig. 4(c)), which agrees with the theoretical prediction and confirms the *a priori* expectation that energy is radiated upward.

While the horizontal structure and amplitude of the waves match well with the theory near the bottom, the patterns near the surface are different. This is likely due to the reflection of the waves at the free surface and the

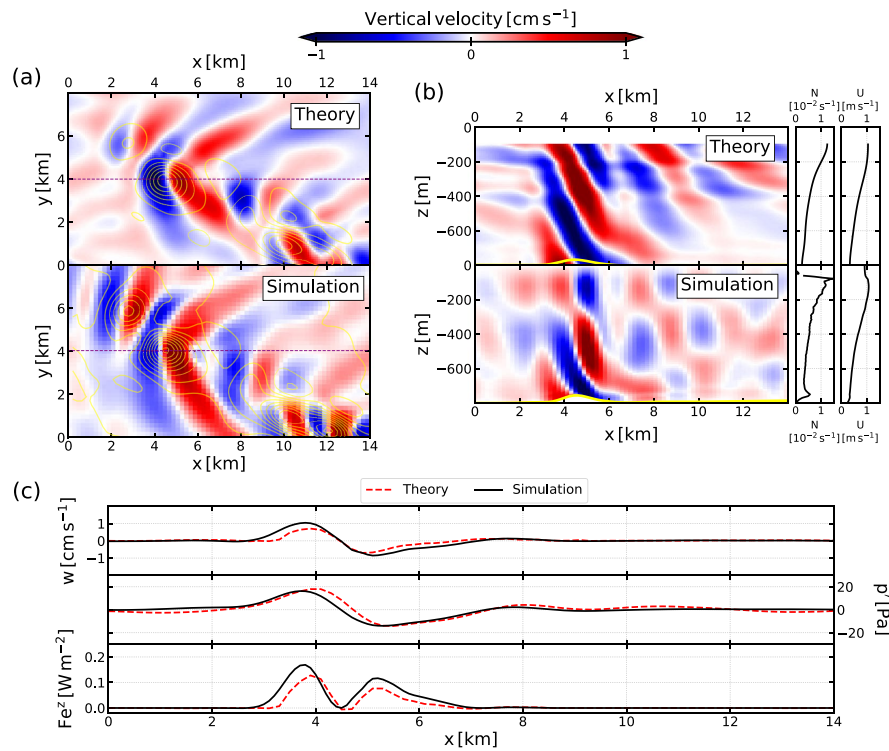


Figure 4. Comparison between the 3D hydrostatic linear theory and time-lowpass outputs from the LEEWA simulation (around the location presented by the orange line in Fig. 2(a)). (a) Horizontal sections at 500 m depth of vertical velocity. Yellow contours indicate 5 m-separated isobaths. (b) Vertical sections taken above an isolated seamount (see purple line in (a)) and profiles of stratification N and along-section velocity U . Bold yellow line indicates the bathymetry. (c) Values of vertical velocity w , pressure anomaly p' and vertical energy flux Fe^z at the bottom of sections (b).

associated modal structure of the waves, which are not taken into account in our 3D linear solution. These modes are clearly visible here because the thickness of the fluid layer is very close to $2\pi U/N$ (the theoretical vertical wavelength of hydrostatic lee waves). The fact that the bottom still presents the characteristics of upward propagating waves may be because the waves lose energy near the surface, thus reducing the amount of energy propagating downward in the deeper part of the water column. A possible cause is that wave energy is redistributed to the mean current through *e.g.*, imbalanced processes near the surface, where the vertical shear of the current is large²¹.

The generation process and the amplitude of the lee waves within the simulation can be reasonably well described by linear hydrostatic theory along the section of Fig. 4. Comparisons with theory along other vertical sections show the same overall agreement. In particular, the depth-averaged “lee wave Froude number” (defined in Eq. (6)) is lower than unity over most of the Charleston Bump (Fig. 5(b)). Moreover, the “radiation parameter” ε (defined in Eq. (3) and shown in Fig. 5(a)) satisfies both the radiation condition and the hydrostatic condition ($Pr \ll \varepsilon \ll 1$) above most of the important topographic features over the Charleston Bump. Note that the smoothing of the topography (see section 2.2) implies that the typical length of the seamounts is always greater than 1 km, which is the main reason why the later inequality is mostly satisfied.

In some (limited) locations where the current is intense and the fluid is weakly stratified, we observe $\varepsilon = O(1)$, thus implying that the hydrostatic assumption does not stand there and that the numerical model reaches its limits. Also, some regions of the Charleston Bump have topographic features with a typical horizontal lengthscale too large to enable the generation of propagating lee waves, thus showing the impact of the scale of topographic features on the amount of energy radiated into lee waves. This is the case in the small area 1 shown in Fig. 5, where the fluxes of energy and momentum are close to zero, in opposition to the small area 2 where lee waves propagate, see Fig. 5(e).

Hence, we have shown above that lee waves can propagate and are hydrostatic and linear in most of the domain. The above conclusion allows us using linear hydrostatic theory to draw more quantitative conclusions on the lee waves dynamics in this region. The total energy converted into lee waves over the Charleston Bump area

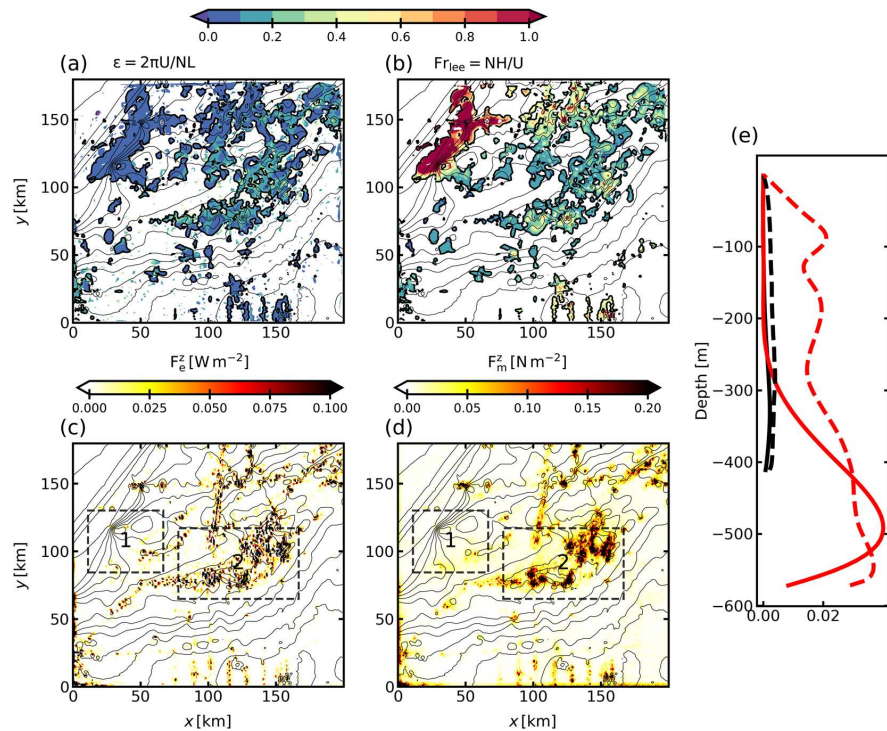


Figure 5. Maps of (a) radiation parameter ε , (b) lee wave Froude number Fr_{lee} , (c) vertical flux of energy F_e^z , and (d) vertical flux of momentum F_m^z , associated with the generation of lee waves over the Charleston Bump in the LEEWA simulation. (a and b) are computed between the surface mixed-layer and the bottom mixed-layer, while (c and d) are mean values at the bottom (in the first 200 m); (a–d) are time-averaged over the whole simulation. The coordinate (0, 0) corresponds to 79.5°W 30.8°N. Integrating F_e^z and F_m^z over the domain shown gives respectively a net flux of energy of 0.3 GW and a net flux of momentum (equivalent to the form drag induced by waves) of 0.6 GN. (e) Timely and horizontally averaged profiles of F_e^z [in $W m^{-2}$] (solid), and F_m^z [in $N m^{-2}$] (dashed) in area 1 (black) and 2 (red) shown in (c,e).

(computed in the LEEWA simulation) is 0.3 GW (corresponding to a mean value of $F_e^z = 8 \cdot 10^{-3} W m^{-2}$ in the bottom 200 m, see Fig. 5(c)), which is again in good agreement with a linear estimate using ref. 2's method, which yields a total conversion of $O(0.3)$ GW (not shown). Finally, we estimate the form drag exerted by lee waves on the mean flow following¹⁴:

$$F_D = \rho_0 \sqrt{(u'w)^2 + (v'w)^2},$$

where u' and v' are estimated by keeping only the small-scale variations (similarly to the pressure anomaly p' , see Supporting Information). F_D is equivalent to the vertical flux of momentum radiated by lee waves F_m^z , shown in Fig. 5(d). Integrated over the Charleston Bump, this gives a drag of $O(1)$ GN. It represents about 10% of the form drag exerted by the whole Charleston Bump ($O(10)$ GN, from ref. 8) or 30% of the viscous drag exerted by the whole Charleston Bump ($O(3)$ GN, from ref. 8). Note that calculation of the form drag over non-isolated bathymetry is quite sensitive to the subdomain chosen for evaluating the bottom pressure anomaly. Personal calculations (not shown) show that the corresponding value could be lower than the estimate by ref. 8, meaning that the fraction attributed to lee waves can be taken as a lower bound. This shows anyway that lee waves have a significant impact on the Gulf Stream's mean flow, over the Charleston Bump.

Hydrodynamical Impact of Small Scale Topographic Features

The diagnostics discussed in the previous section show that lee waves with physically-consistent properties are generated in the LEEWA simulation. Although probably dominant in this region of strong current, lee waves are not the only physical mechanism through which small scale topographic features impact the mean current (other processes include e.g. the generation of larger scales evanescent waves and small-scale turbulence). In this section, we discuss this aspect more generally by comparing the two simulations (LEEWA and SMOOTH) with different (resp. rough and smooth) topography.

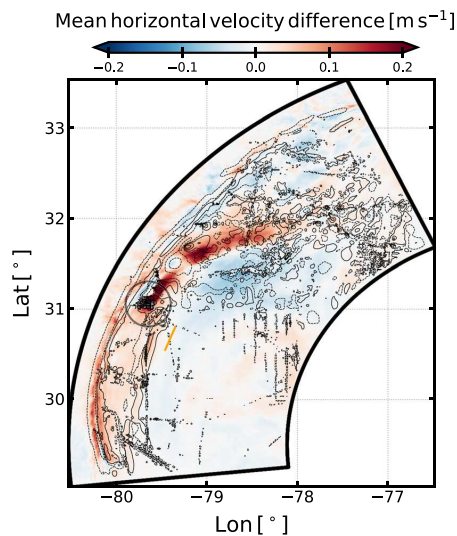


Figure 6. Timely and vertically averaged difference of the horizontal velocity magnitude between the SMOOTH and the LEEWA simulations (a positive pattern means that the velocity in the SMOOTH simulation is larger than in LEEWA). Black contours are differences between the bathymetry used in the two simulations, at values [± 10 , ± 50 , ± 100] m, orange straight line indicates the position of the section discussed in Fig. 4.

The mean horizontal flow is significantly different between the two simulations. The timely and vertically averaged difference between horizontal velocity amplitudes in the SMOOTH and the LEEWA simulations is shown in Fig. 6. The difference reaches up to 0.2 m s^{-1} in the areas where the largest seamounts have been smoothed. The dipolar structure of the difference indicates that it corresponds to a modification of the path of the Gulf Stream. The mean current is shifted northward in the SMOOTH simulation and forms a less pronounced meander. Mean velocity profiles over the Charleston Bump show that the velocity difference reaches up to 1 m s^{-1} near the surface (not shown). This difference is most likely due to hydrodynamical control of the flow by the shape of the seafloor, since topography is the only difference between the simulations. Therefore, the mean current of the Gulf Stream, over a one-month period, is strongly impacted by small scale seamounts with horizontal size of $O(<20)$ km and vertical extent of $O(<100)$ m.

It would be speculative to attribute the difference in the mean flow between the two simulations to the impact of lee waves only, as other processes – e.g. evanescent lee waves^{16,22} and nonlinear motions – may play a role as well, in places such as area 1 in Fig. 5. Nonetheless, it has been shown in the previous section that lee waves exert a significant drag on the current in that region (more than 10% of the total drag). Lee waves impact the vertical structure of the flow by extracting kinetic energy at depth (cf. Fig. 5), and subsequently redistributing (and partially dissipating it) through wave-mean flow interactions²¹ or nonlinear processes (including breaking). The less pronounced meander in the SMOOTH simulation is consistent with the behavior observed in lower resolution simulations using the same model, which tend to underestimate the amplitude of the semi permanent meander over the Bump⁸. The lower resolution simulations have topographies comparable to the topography of the SMOOTH simulation and are missing the drag induced by the lee waves as well. This wave drag might play a role in modifying the large-scale form drag and subsequently the path of the Gulf Stream over the Bump. Further diagnostics and a longer integration would be useful to understand more thoroughly the processes at stake and confirming the effects on the mean flow.

Summary and Discussion

We observe in a realistic simulation the generation of lee waves that are in qualitative agreement with observations from satellite observations. These waves are mostly in hydrostatic and linear regime according to typical dimensionless numbers. Hence, linear theory is able to reproduce and thereby quantify the essential properties of observed lee waves, at least as far as their amplitude, wavelength of generation, and associated vertical energy flux are concerned. Furthermore, we have shown that small scale topographic features strongly impact the structure of the Gulf Stream, and that lee waves may play an active role in this topographic control. This is particularly important since these areas are most of the time omitted in global studies of lee waves.

As is well known, lee waves are a significant energy sink for the ocean circulation. Approximately 0.2 TW is converted into lee waves in the global ocean and about half of this energy is dissipated within a kilometer above the bottom². Quantifying the actual amount of energy dissipated in energetic regions such as the Gulf Stream path is thus essential to understand the cascade of energy towards small scale. Further work is needed to fully quantify the impacts of lee waves generated in extreme/shallow regions, and our paper shows that high resolution

numerical simulations are a valuable tool for such studies. However, these results are strongly dependent on the representation of the bathymetry in the simulations. First, small scale seamounts strongly impact the amount of lee waves radiated upward, by setting the horizontal wavelength of the waves. Second, the direction and the intensity of the mean current is modified by the smaller scales of the topography. This implies that the energy transferred through physical processes other than lee waves could be misevaluated. Third, localized overturning events (hydraulic jumps, although these cannot be well resolved in a hydrostatic simulation) can occur in the wake of seamounts (not shown in this paper), which are strongly impacted by the shape of the bathymetry. These findings can be linked with other recent studies, which also put forth the impact of small scale topography in affecting oceanic processes, such as water exchange dynamics between the Red Sea and the Gulf of Aden²³, the evolution of internal solitary waves over the continental shelf of the South China Sea²⁴, or the bi-modality of the path of the Kuroshio south of Japan²⁵. These results all together therefore emphasize that an accurate representation of the bathymetry is essential to understand the ocean dynamics.

This task is all the more arduous that available high-resolution bathymetry often show suspicious patterns on the seafloor. As an example, a row of large seamounts can be seen near 31°N, 79.7°W (see gray circle in Fig. 6). In our (LEEWA) simulation, these seamounts slow down the Gulf Stream, and generate large amplitude lee waves. Moreover, small seamounts (see near 30.5°N, 78.3°W) appear suspiciously well aligned, which may result from mismatching observational data being inaccurately processed by the interpolation schemes used for bathymetry production. Such artifacts in the bathymetry would obviously result in spurious generation of lee waves and other small-scale topography-related motions. On the other hand, some real seamounts are missing in the available bathymetry datasets. For example the Stetson Mesa (30°20'N, 79°25'W), which is highlighted in ref.¹³ as a source of internal waves, is not present in the SRTM30_PLUS dataset used in this study. Thus, as discussed in ref.²⁶, it is essential to have a better representation of the bathymetry, at a resolution down to a few hundred meters, in order to further understand the fine-scale dynamics of the ocean using high resolution numerical simulations.

Received: 4 November 2019; Accepted: 22 January 2020;

Published online: 11 February 2020

References

- Cusack, J., Garabato, A. N., Smeed, D. & Girton, J. Observation of a large lee wave in the Drake passage. *Journal of Physical Oceanography* **10**, 793–811, <https://doi.org/10.1175/JPO-D-16-0153.1> (2017).
- Nikurashin, M. & Ferrari, R. Global energy conversion rate from geostrophic flows into internal lee waves in the deep ocean. *Geophysical Research Letters* **38**, L08610, <https://doi.org/10.1029/2011GL046576> (2011).
- Dossmann, Y. *et al.* Experiments with mixing in stratified flow over a topographic ridge. *Journal of Geophysical Research* **121**, 6961–6977, <https://doi.org/10.1002/2016JC011990> (2016).
- Ferrari, R. & Wunsch, C. Ocean circulation kinetic energy: reservoirs, sources, and sinks. *Annu. Rev. Fluid. Mech* **41**, 253–282, <https://doi.org/10.1146/annurev.fluid.40.111406.102139> (2009).
- Baines, P. G. *Topographic effects in stratified flows* (Cambridge University Press, 1995).
- Klymak, J. M. Nonpropagating form drag and turbulence due to stratified flow over large-scale abyssal hill topography. *Journal of Physical Oceanography* **48**, 2383–2395, <https://doi.org/10.1175/JPO-D-17-0225.1> (2018).
- Trossman, D. *et al.* Impact of parameterized lee wave drag on the energy budget of an eddying global ocean model. *Ocean Modelling* **72**, 119–142, <https://doi.org/10.1016/j.ocemod.2013.08.006> (2013).
- Gula, J., Molemaker, J. & McWilliams, J. Gulf Stream dynamics along the southeastern u.s. seaboard. *Journal of Physical Oceanography* **45**, 690–715, <https://doi.org/10.1175/JPO-D-14-0154.1> (2015).
- Stommel, H. *The Gulf Stream* (Univ. of Calif. Press, 1976).
- Gula, J., Blacic, T. M. & Todd, R. E. Submesoscale coherent vortices in the Gulf Stream. *Geophysical Research Letters* **46**, 2704–2714, <https://doi.org/10.1029/2019GL081919> (2019).
- Todd, R. High-frequency internal waves and thick bottom mixed layers observed by gliders in the Gulf Stream. *Geophysical Research Letters* **44**, 6316–6325, <https://doi.org/10.1002/2017GL072580> (2017).
- Zheng, Q. *et al.* Deep-water seamount wakes on SEASAT SAR image in the Gulf Stream region. *Geophysical Research Letters* **39**, L16604, <https://doi.org/10.1029/2012GL052661> (2012).
- Haney, J. Internal waves as sources of small-scale patchiness in seabird distribution on the Blake Plateau. *The American Ornithologists' Union* **104**, 129–133, <https://doi.org/10.2307/4087244> (1987).
- Gill, A. E. *Atmosphere-Ocean Dynamics* (Academic Press, 1982).
- Mayer, F. & Fringer, O. An unambiguous definition of the Froude number for lee waves in the deep ocean. *Journal of Fluid Mechanics* **831**, R3–1, <https://doi.org/10.1017/jfm.2017.701> (2017).
- Nikurashin, M., Ferrari, R., Grisouard, N. & Polzin, K. The impact of finite-amplitude bottom topography on internal wave generation in the southern ocean. *Journal of Physical Oceanography* **44**, 2938–2950, <https://doi.org/10.1175/JPO-D-13-0201.1> (2014).
- Shchepetkin, A. & McWilliams, J. The regional oceanic modeling system: A split-explicit, free-surface, topography-following-coordinate ocean model. *Ocean Modelling* **9**, 347–404, <https://doi.org/10.1016/j.ocemod.2004.08.002> (2005).
- Shchepetkin, A. & McWilliams, J. Accurate Boussinesq modeling with a practical, “stiffened” equation of state. *Ocean Modelling* **38**, 41–70, <https://doi.org/10.1016/j.ocemod.2011.01.010> (2011).
- Gula, J., Molemaker, M. & McWilliams, J. C. Submesoscale cold filaments in the Gulf Stream. *J. Phys. Oceanogr.* **44**, 2617–2643, <https://doi.org/10.1175/JPO-D-14-0029.1> (2014).
- Raschle, N., Chapron, B., Ponte, A., Arduin, F. & Klein, P. Surface roughness imaging of currents shows divergence and strain in the wind direction. *Journal of Physical Oceanography* **44**, 2153–2163, <https://doi.org/10.1175/JPO-D-13-0278.1> (2014).
- Kunze, E. & Lien, R.-C. Energy sinks for lee waves in shear flow. *Journal of Physical Oceanography*, <https://doi.org/10.1175/JPO-D-19-0052.1> (2019).
- MacCready, P. & Pawlak, G. Stratified flow along a corrugated slope: Separation drag and wave drag. *J. Phys. Oceanogr.* **31**, 2824–2839, [https://doi.org/10.1175/1520-0485\(2001\)031<2824:SFAACS>2.0.CO;2](https://doi.org/10.1175/1520-0485(2001)031<2824:SFAACS>2.0.CO;2) (2001).
- Xie, J., Krokos, G., Sofianos, S. & Hoteit, I. Interannual variability of the exchange flow through the Strait of Bab-al-Mandeb. *Journal of Geophysical Research: Oceans* **124**, 1988–2009, <https://doi.org/10.1029/2018JC014478> (2019).
- Xie, J., He, Y. & Cai, S. Bumpy Topographic Effects on the Transbasin Evolution of Large-Amplitude Internal Solitary Wave in the Northern South China Sea. *Journal of Geophysical Research: Oceans*, <https://doi.org/10.1029/2018JC014837> (2019).
- Tanaka, Y. & Hibiya, T. Effects of Koshu Seamount on the Development of Baroclinic Instability Leading to the Kuroshio Large Meander. *Journal of Physical Oceanography* **47**, 2563–2576, <https://doi.org/10.1175/JPO-D-17-0050.1> (2017).

26. Wöfl, A.-C. *et al.* Seafloor Mapping – The Challenge of a Truly Global Ocean Bathymetry. *Frontiers in Marine Science* **6**, <https://doi.org/10.3389/fmars.2019.00283> (2019).
27. NASA Ocean Biology Processing Group. SeaWiFS Level 2 Ocean Color Data Version 2014, https://doi.org/10.5067/ORBVIEW-2/SEAWIFS_OC.2014.0 (2015).

Acknowledgements

We gratefully acknowledge support from Conseil Général du Finistère, Région Bretagne, ANR project LuckyScales (ANR-14-CE02-0008) and LEFE/IMAGO (Project AO2017-994457-RADII). The research leading to these results has received funding from the People Programme (Marie Curie Actions) of the European Union's Seventh Framework Programme (FP7/2007–2013) under REA grant agreement n. PCOFUND-GA-2013-609102, through the PRESTIGE programme coordinated by Campus France. Simulations were performed using HPC resources from GENCI-TGCC (Grant 2017-A0010107638) and using the HPC facilities DATARMOR of “Pôle de Calcul Intensif pour la Mer” at Ifremer, Brest, France. We also thank N. Rasle for providing surface roughness data and helpful discussions; and M. Le Corre for his help on some diagnostics calculation. Scripts used in this analysis, together with processed data and additional source files, can be obtained on the author's github (<https://github.com/demarez/LeeWaves>).

Author contributions

C.d.M. conducted the experiment, led the analysis of the simulation outputs and the theoretical analysis. C.d.M., N.L. and J.G. analysed the output of the simulation. J.G. conceived the experiment. All authors participated in the writing and editing of the article.

Competing interests

The authors declare no competing interests.

Additional information

Supplementary information is available for this paper at <https://doi.org/10.1038/s41598-020-59297-5>.

Correspondence and requests for materials should be addressed to C.d.M.

Reprints and permissions information is available at www.nature.com/reprints.

Publisher's note Springer Nature remains neutral with regard to jurisdictional claims in published maps and institutional affiliations.



Open Access This article is licensed under a Creative Commons Attribution 4.0 International License, which permits use, sharing, adaptation, distribution and reproduction in any medium or format, as long as you give appropriate credit to the original author(s) and the source, provide a link to the Creative Commons license, and indicate if changes were made. The images or other third party material in this article are included in the article's Creative Commons license, unless indicated otherwise in a credit line to the material. If material is not included in the article's Creative Commons license and your intended use is not permitted by statutory regulation or exceeds the permitted use, you will need to obtain permission directly from the copyright holder. To view a copy of this license, visit <http://creativecommons.org/licenses/by/4.0/>.

© The Author(s) 2020

BIBLIOGRAPHIE

- Al Saafani, M. A., Shenoi, S. S. C., Shankar, D., Aparna, M., Kurian, J., Durand, F., & Vinayachandran, P. N. (2007). Westward movement of eddies into the Gulf of Aden from the Arabian Sea. *Journal of Geophysical Research*, *112*. doi :10.1029/2006JC004020.
- Amores, A., Monserrat, S., Melnichenko, O., & Maximenko, N. (2017). On the shape of sea level anomaly signal on periphery of mesoscale ocean eddies. *Geophysical Research Letters*, *44*, 6926–6932. doi :10.1002/2017GL073978.
- Arakawa, A., & Lamb, V. R. (1977). Computational design of the basic dynamical processes of the ucla general circulation model. *General circulation models of the atmosphere*, *17*, 173–265.
- Argo (2019). Argo float data and metadata from Global Data Assembly Centre (Argo GDAC). URL : <https://www.seanoe.org/data/00311/42182/>. doi :10.17882/42182 type : dataset.
- Armi, L., Hebert, D., Oakey, N., Price, J. F., Richardson, P. L., Rossby, H. T., & Ruddick, B. (1989). Two Years in the Life of a Mediterranean Salt Lens. *Journal of Physical Oceanography*, *19*, 354–370. doi :10.1175/1520-0485(1989)019<0354:TYITL0>2.0.CO;2.
- Beal, L. M., & Donohue, K. A. (2013). The Great Whirl : Observations of its seasonal development and interannual variability. *Journal of Geophysical Research : Oceans*, *118*, 1–13. doi :10.1029/2012JC008198.
- Bertrand, C., & Carton, X. (1993). Vortex merger on the β -plane. *Comptes rendus de l'Académie des sciences. Série 2, Mécanique, Physique, Chimie, Sciences de l'univers, Sciences de la Terre*, *316*, 1201–1206.
- Boccaletti, G., Ferrari, R., & Fox-Kemper, B. (2007). Mixed Layer Instabilities and Restratification. *Journal of Physical Oceanography*, *37*, 2228–2250. doi :10.1175/JP03101.1.
- Bosse, A., Testor, P., Houpert, L., Damien, P., Prieur, L., Hayes, D., Taillandier, V., Durrieu de Madron, X., d'Ortenzio, F., Coppola, L., Karstensen, J., & Mortier, L. (2016). Scales and dynamics of Submesoscale Coherent Vortices formed by deep convection in the northwestern Mediterranean Sea. *Journal of Geophysical Research : Oceans*, *121*, 7716–7742. doi :10.1002/2016JC012144.

- Bosse, A., Testor, P., Mayot, N., Prieur, L., D'Ortenzio, F., Mortier, L., Le Goff, H., Gourcuff, C., Coppola, L., Lavigne, H., & Raimbault, P. (2017). A submesoscale coherent vortex in the Ligurian Sea : From dynamical barriers to biological implications. *Journal of Geophysical Research : Oceans*, *122*, 6196–6217. doi :10 . 1002/2016JC012634.
- Bower, A. S. (2002). Gulf of Aden eddies and their impact on Red Sea Water. *Geophysical Research Letters*, *29*. doi :10 . 1029/2002GL015342.
- Bower, A. S., & Furey, H. H. (2012). Mesoscale eddies in the Gulf of Aden and their impact on the spreading of Red Sea Outflow Water. *Progress in Oceanography*, *96*, 14–39. doi :10 . 1016/j . pocean . 2011 . 09 . 003.
- Bower, A. S., Hunt, H. D., & Price, J. F. (2000). Character and dynamics of the Red Sea and Persian Gulf outflows. *Journal of Geophysical Research : Oceans*, *105*, 6387–6414. doi :10 . 1029/1999JC900297.
- Brannigan, L., Marshall, D. P., Naveira Garabato, A. C., Nurser, A. J. G., & Kaiser, J. (2017). Submesoscale Instabilities in Mesoscale Eddies. *Journal of Physical Oceanography*, *47*, 3061–3085. doi :10 . 1175/JP0-D-16-0178 . 1.
- Bretherton, F. P. (1966). Critical layer instability in baroclinic flows. *Quarterly Journal of the Royal Meteorological Society*, *92*, 325–334. doi :10 . 1002/qj . 49709239302.
- Bryden, H. L., & Hall, M. M. (1980). Heat Transport by Currents Across 25 N Latitude in the Atlantic Ocean. *Science*, *207*, 884–886. doi :10 . 1126/science . 207 . 4433 . 884.
- Buckingham, C. E., Khaleel, Z., Lazar, A., Martin, A. P., Allen, J. T., Naveira Garabato, A. C., Thompson, A. F., & Vic, C. (2017). Testing Munk's hypothesis for submesoscale eddy generation using observations in the North Atlantic. *Journal of Geophysical Research : Oceans*, *122*, 6725–6745. doi :10 . 1002/2017JC012910.
- Burgess, B. H., Dritschel, D. G., & Scott, R. K. (2017). Vortex scaling ranges in two-dimensional turbulence. *Physics of Fluids*, *29*, 11104. doi :10 . 1063/1 . 4993144.
- Callies, J., Ferrari, R., Klymak, J. M., & Gula, J. (2015). Seasonality in submesoscale turbulence. *Nature Communications*, *6*. doi :10 . 1038/ncomms7862.
- Carnevale, G. F., McWilliams, J. C., Pomeau, Y., Weiss, J. B., & Young, W. R. (1991). Evolution of vortex statistics in two-dimensional turbulence. *Physical Review Letters*, *66*, 2735–2737. doi :10 . 1103/PhysRevLett . 66 . 2735.

- Carton, X. (2001). Hydrodynamical modeling of Oceanic Vortices. *Surveys in Geophysics*, 22, 179–263. doi :10.1023/A:1013779219578.
- Carton, X. (2009). Instability of Surface Quasigeostrophic Vortices. *Journal of the Atmospheric Sciences*, 66, 1051–1062. doi :10.1175/2008JAS2872.1.
- Carton, X., Ciani, D., Verron, J., Reinaud, J., & Sokolovskiy, M. (2016). Vortex merger in surface quasi-geostrophy. *Geophysical & Astrophysical Fluid Dynamics*, 110, 1–22. doi :10.1080/03091929.2015.1120865.
- Carton, X., Daniault, N., Alves, J., Cherubin, L., & Ambar, I. (2010). Meddy dynamics and interaction with neighboring eddies southwest of Portugal : Observations and modeling. *Journal of Geophysical Research*, 115, C06017. doi :10.1029/2009JC005646.
- Carton, X., L'Hégaret, P., & Baraille, R. (2012). Mesoscale variability of water masses in the Arabian Sea as revealed by Argo floats. *Ocean Science*, 8, 227–248. URL : <https://www.ocean-sci.net/8/227/2012/>. doi :10.5194/os-8-227-2012.
- Carton, X., & McWilliams, J. (1989). Barotropic and Baroclinic Instabilities of Axisymmetric Vortices in a Quasigeostrophic Model, . 50, 225–244. doi :10.1016/S0422-9894(08)70188-0.
- Carton, X. J., Flierl, G. R., & Polvani, L. M. (1989). The Generation of Tripoles from Unstable Axisymmetric Isolated Vortex Structures. *Europhysics Letters (EPL)*, 9, 339–344.
- Carton, X. J., & McWilliams, J. C. (1996). Nonlinear oscillatory evolution of a baroclinically unstable geostrophic vortex. *Dynamics of Atmospheres and Oceans*, 24, 207–214. doi :10.1016/0377-0265(95)00452-1.
- Chaigneau, A., Le Texier, M., Eldin, G., Grados, C., & Pizarro, O. (2011). Vertical structure of mesoscale eddies in the eastern South Pacific Ocean : A composite analysis from altimetry and Argo profiling floats. *Journal of Geophysical Research*, 116. doi :10.1029/2011JC007134.
- Chassignet, E., & Marshall, D. (2008). Gulf stream separation in numerical ocean models. *Geophysical Monograph Series*, 177, 39–61.
- Chavanne, C. P., & Klein, P. (2010). Can oceanic submesoscale processes be observed with satellite altimetry? : OCEANIC SUBMESOSCALE PROCESSES FROM ALTIMETRY? *Geophysical Research Letters*, 37. doi :10.1029/2010GL045057.

- Chelton, D. (2001). *Report of the high-resolution ocean topography science working group meeting*. Oregon State University, College of Oceanic and Atmospheric Sciences.
- Chelton, D. B., deSzoeke, R. A., Schlax, M. G., El Naggar, K., & Siwertz, N. (1998). Geographical Variability of the First Baroclinic Rossby Radius of Deformation. *Journal of Physical Oceanography*, 28, 433–460. doi :10 . 1175/1520-0485 (1998)028<0433 :GVOTFB>2 . 0 . CO ; 2.
- Chelton, D. B., Gaube, P., Schlax, M. G., Early, J. J., & Samelson, R. M. (2011a). The Influence of Nonlinear Mesoscale Eddies on Near-Surface Oceanic Chlorophyll. *Science*, 334, 328–332. doi :10 . 1126/science . 1208897.
- Chelton, D. B., & Schlax, M. G. (1996). Global Observations of Oceanic Rossby Waves. *Science*, 272, 234–238. doi :10 . 1126/science . 272 . 5259 . 234.
- Chelton, D. B., Schlax, M. G., & Samelson, R. M. (2011b). Global observations of nonlinear mesoscale eddies. *Progress in Oceanography*, 91, 167–216. doi :10 . 1016/j . pocean . 2011 . 01 . 002.
- Chelton, D. B., Schlax, M. G., Samelson, R. M., & de Szoeke, R. A. (2007). Global observations of large oceanic eddies. *Geophysical Research Letters*, 34. doi :10 . 1029/2007GL030812.
- Ciani, D., Carton, X., Bashmachnikov, I., & Chapron, B. (2015). Influence of deep vortices on the ocean surface. In *EGU General Assembly Conference Abstracts*. volume 17.
- Ciani, D., Carton, X., & Verron, J. (2016). On the merger of subsurface isolated vortices. *Geophysical & Astrophysical Fluid Dynamics*, 110, 23–49. doi :10 . 1080/03091929 . 2015 . 1135430.
- Cresswell, G. R. (1982). The Coalescence of Two East Australian Current Warm-Core Eddies. *Science*, 215, 161–164. doi :10 . 1126/science . 215 . 4529 . 161.
- Cui, W., Wang, W., Zhang, J., & Yang, J. (2019). Multicore structures and the splitting and merging of eddies in global oceans from satellite altimeter data. *Ocean Science*, 15, 413–430. doi :10 . 5194/os-15-413-2019.
- Cummings, J. A. (2005). Operational multivariate ocean data assimilation. *Quarterly Journal of the Royal Meteorological Society*, 131, 3583–3604. doi :10 . 1256/qj . 05 . 105.
- Cummings, J. A., & Smedstad, O. M. (2013). Variational Data Assimilation for the Global Ocean. In *Data Assimilation for Atmospheric, Oceanic and Hydrologic Applications (Vol. II)* (pp. 303–343). Springer Berlin Heidelberg. doi :10 . 1007/978-3-642-35088-7_13.

- Cusack, J., Garabato, A. N., Smeed, D., & Girton, J. (2017). Observation of a large lee wave in the Drake passage. *Journal of Physical Oceanography*, *10*, 793–811. doi :10.1175/JPO-D-16-0153.1.
- Cushman-Roisin, B. (1989). On the Role of Filamentation in the Merging of Anticyclonic Lenses. *Journal of Physical Oceanography*, *19*, 253–258. doi :10.1175/1520-0485(1989)019<0253:OTROFI>2.0.CO;2.
- Cushman-Roisin, B., Tang, B., & Chassignet, E. P. (1990). Westward motion of mesoscale eddies. *Journal of Physical Oceanography*, *20*, 758–768.
- D'Asaro, E. A. (1988). Generation of submesoscale vortices : A new mechanism. *Journal of Geophysical Research*, *93*, 6685. URL : <http://doi.wiley.com/10.1029/JC093iC06p06685>. doi :10.1029/JC093iC06p06685.
- Debreu, L., Marchesiello, P., Penven, P., & Cambon, G. (2012). Two-way nesting in split-explicit ocean models : Algorithms, implementation and validation. *Ocean Modelling*, *49-50*, 1–21. doi :10.1016/j.ocemod.2012.03.003.
- Deem, G. S., & Zabusky, N. J. (1978). Vortex Waves : Stationary " V States," Interactions, Recurrence, and Breaking. *Physical Review Letters*, *40*, 859–862. doi :10.1103/PhysRevLett.40.859.
- Deremble, B., Dewar, W. K., & Chassignet, E. P. (2016). Vorticity dynamics near sharp topographic features. *Journal of Marine Research*, *74*, 249–276. doi :10.1357/002224016821744142.
- Deremble, B., Johnson, E., & Dewar, W. (2017). A coupled model of interior balanced and boundary flow. *Ocean Modelling*, *119*, 1–12. doi :10.1016/j.ocemod.2017.09.003.
- Dewar, W. K., & Hogg, A. M. (2010). Topographic inviscid dissipation of balanced flow. *Ocean Modelling*, *32*, 1–13. doi :10.1016/j.ocemod.2009.03.007.
- Dickey, T. D. (1991). The emergence of concurrent high-resolution physical and bio-optical measurements in the upper ocean and their applications. *Reviews of Geophysics*, *29*, 383. doi :10.1029/91RG00578.
- do Rosario Gomes, H., Goes, J. I., Matondkar, S. G. P., Buskey, E. J., Basu, S., Parab, S., & Thoppil, P. (2014). Massive outbreaks of *Noctiluca scintillans* blooms in the Arabian Sea due to spread of hypoxia. *Nature Communications*, *5*. doi :10.1038/ncomms5862.

- Doblar, R. A., & Cheney, R. E. (1977). Observed Formation of a Gulf Stream Cold Core Ring. *Journal of Physical Oceanography*, 7, 944–946. doi :10.1175/1520-0485(1977)007<0944:0F0AGS>2.0.CO;2.
- Dong, C., McWilliams, J. C., Liu, Y., & Chen, D. (2014). Global heat and salt transports by eddy movement. *Nature Communications*, 5, 3294. doi :10.1038/ncomms4294.
- Dritschel, D. G. (2002). Vortex merger in rotating stratified flows. *Journal of Fluid Mechanics*, 455, 83–101. doi :10.1017/S0022112001007364.
- Dugan, J. P., Mied, R. P., Mignerey, P. C., & Schuetz, A. F. (1982). Compact, intrathermocline eddies in the Sargasso Sea. *Journal of Geophysical Research*, 87, 385. doi :10.1029/JC087iC01p00385.
- Etter, P. C. (2018). *Underwater acoustic modeling and simulation*. CRC press.
- Ferrari, R., & Wunsch, C. (2009). Ocean Circulation Kinetic Energy : Reservoirs, Sources, and Sinks. *Annual Review of Fluid Mechanics*, 41, 253–282. doi :10.1146/annurev.fluid.40.111406.102139.
- Findlater, J. (1969). A major low-level air current near the Indian Ocean during the northern summer. *Quarterly Journal of the Royal Meteorological Society*, 95, 362–380. doi :10.1002/qj.49709540409.
- Fischer, A. S., Weller, R. A., Rudnick, D. L., Eriksen, C. C., Lee, C. M., Brink, K. H., Fox, C. A., & Leben, R. R. (2002). Mesoscale eddies, coastal upwelling, and the upper-ocean heat budget in the Arabian Sea. *Deep Sea Research Part II : Topical Studies in Oceanography*, 49, 2231–2264. doi :10.1016/S0967-0645(02)00036-X.
- Flagg, C. N., & Kim, H.-S. (1998). Upper ocean currents in the northern Arabian Sea from shipboard ADCP measurements collected during the 1994–1996 U.S. JGOFS and ONR programs. *Deep Sea Research Part II : Topical Studies in Oceanography*, 45, 1917–1959. doi :10.1016/S0967-0645(98)00059-9.
- Flierl, G. R. (1978). Models of vertical structure and the calibration of two-layer models. *Dynamics of Atmospheres and Oceans*, 2, 341–381. doi :10.1016/0377-0265(78)90002-7.
- Flierl, G. R. (1988). On the instability of geostrophic vortices. *Journal of fluid mechanics*, 197, 349–388. doi :10.1017/S0022112088003283.

- Fratantoni, D. M., Bower, A. S., Johns, W. E., & Peters, H. (2006). Somali Current rings in the eastern Gulf of Aden. *Journal of Geophysical Research*, *111*. doi :10.1029/2005JC003338.
- Frolov, S. A., Sutyrin, G. G., Rowe, G. D., & Rothstein, L. M. (2004). Loop Current Eddy Interaction with the Western Boundary in the Gulf of Mexico. *Journal of Physical Oceanography*, *34*, 2223–2237. doi :10.1175/1520-0485(2004)034<2223:LCEIWT>2.0.CO;2.
- Fuglister, F. C., & Worthington, L. V. (1951). Some Results of a Multiple Ship Survey of the Gulf Stream. *Tellus*, *3*, 1–14. doi :10.3402/tellusa.v3i1.8614.
- Garrett, C., & Munk, W. (1979). Internal Waves in the Ocean. *Annual Review of Fluid Mechanics*, *11*, 339–369. doi :10.1146/annurev.fl.11.010179.002011.
- Gent, P. R., & McWilliams, J. C. (1986). The instability of barotropic circular vortices. *Geophysical & Astrophysical Fluid Dynamics*, *35*, 209–233. doi :10.1080/03091928608245893.
- Gill, A., & Griffiths, R. (1981). Why should two anticyclonic eddies merge. *Ocean Modelling*, *41*, 501–518.
- Gula, J., Blacic, T. M., & Todd, R. E. (2019). Submesoscale Coherent Vortices in the Gulf Stream. *Geophysical Research Letters*, *46*, 2704–2714. doi :10.1029/2019GL081919.
- Gula, J., Molemaker, M. J., & McWilliams, J. C. (2015). Topographic vorticity generation, submesoscale instability and vortex street formation in the Gulf Stream. *Geophysical Research Letters*, *42*, 4054–4062. doi :10.1002/2015GL063731.
- Gula, J., & Zeitlin, V. (2010). Instabilities of buoyancy-driven coastal currents and their nonlinear evolution in the two-layer rotating shallow-water model. Part 1. Passive lower layer. *Journal of Fluid Mechanics*, *659*, 69–93. doi :10.1017/S0022112010002405.
- Gula, J., Zeitlin, V., & Bouchut, F. (2010). Instabilities of buoyancy-driven coastal currents and their nonlinear evolution in the two-layer rotating shallow water model. Part 2. Active lower layer. *Journal of Fluid Mechanics*, *665*, 209–237. doi :10.1017/S0022112010003903.
- Guyon, E., Petit, L., & Hulin, J.-P. (1991). *Hydrodynamique physique*. interéditions.
- Halo, I., Backeberg, B., Penven, P., Ansorge, I., Reason, C., & Ullgren, J. (2014). Eddy properties in the Mozambique Channel : A comparison between observations and two numerical ocean circulation models. *Deep Sea Research Part II : Topical Studies in Oceanography*, *100*, 38–53. doi :10.1016/j.dsr2.2013.10.015.

- Helber, R., Carnes, M., Townsend, T., Barron, C., & Dastugue, J. (2012). Validation test report for the improved synthetic ocean profile (ISOP) system, part I : Synthetic profile methods and algorithm, .
- Hogg, A. M., Dewar, W. K., Berloff, P., & Ward, M. L. (2011). Kelvin wave hydraulic control induced by interactions between vortices and topography. *Journal of Fluid Mechanics*, *687*, 194–208. doi :10.1017/jfm.2011.344.
- Hoskins, B. J. (1974). The role of potential vorticity in symmetric stability and instability. *Quarterly Journal of the Royal Meteorological Society*, *100*, 480–482. doi :10.1002/qj.49710042520.
- Hoskins, B. J., McIntyre, M. E., & Robertson, A. (1985). On the use and significance of isentropic potential vorticity maps. *Quarterly Journal of the Royal Meteorological Society*, *111*, 877–946. doi :10.1002/qj.49711147002.
- Hua, B. L. (1988). The Internal Barotropic Instability of Surface-Intensified Eddies. Part I : Generalized Theory of Isolated Eddies. *Journal of Physical Oceanography*, *18*, 40–55. doi :10.1175/1520-0485(1988)018<0040:TIBIOS>2.0.CO;2.
- Hua, B. L., Ménesguen, C., Le Gentil, S., Schopp, R., Marsset, B., & Aiki, H. (2013). Layering and turbulence surrounding an anticyclonic oceanic vortex : in situ observations and quasi-geostrophic numerical simulations. *Journal of Fluid Mechanics*, *731*, 418–442. doi :10.1017/jfm.2013.369.
- Ikeda, M. (1981). Instability and Splitting of Mesoscale Rings using a Two-Layer Quasi-Geostrophic Model on an f -Plane. *Journal of Physical Oceanography*, *11*, 987–998. doi :10.1175/1520-0485(1981)011<0987:IASOMR>2.0.CO;2.
- Ilicak, M., Özgökmen, T. M., & Johns, W. E. (2011). How does the Red Sea outflow water interact with Gulf of Aden Eddies? *Ocean Modelling*, *36*, 133–148. doi :10.1016/j.ocemod.2010.10.006.
- Jiménez, J., Moffatt, H. K., & Vasco, C. (1996). The structure of the vortices in freely decaying two-dimensional turbulence. *Journal of Fluid Mechanics*, *313*, 209–222. doi :10.1017/S0022112096002182.
- Kemp, M. (2019). Leonardo da Vinci's laboratory : studies in flow. *Nature*, *571*, 322–323. URL : <http://www.nature.com/articles/d41586-019-02144-z>. doi :10.1038/d41586-019-02144-z.

- Keppeler, L., Cravatte, S., Chaigneau, A., Pegliasco, C., Gourdeau, L., & Singh, A. (2018). Observed Characteristics and Vertical Structure of Mesoscale Eddies in the Southwest Tropical Pacific. *Journal of Geophysical Research : Oceans*, 123, 2731–2756. doi :10.1002/2017JC013712.
- Kostianoy, A., & Belkin, I. (1989). A Survey of Observations on Intrathermocline Eddies in the World Ocean. In *Elsevier Oceanography Series* (pp. 821–841). Elsevier volume 50. doi :10.1016/S0422-9894(08)70223-X.
- Kraichnan, R. H., & Montgomery, D. (1980). Two-dimensional turbulence. *Reports on Progress in Physics*, 43, 547. doi :10.1088/0034-4885/43/2/001.
- Kumar, P. H., & Mathew, B. (1997). Salinity distribution in the Arabian Sea. *Indian Journal of Marine Sciences*, (pp. 271–277).
- Lahaye, N., & Zeitlin, V. (2015). Centrifugal, barotropic and baroclinic instabilities of isolated ageostrophic anticyclones in the two-layer rotating shallow water model and their nonlinear saturation. *Journal of Fluid Mechanics*, 762, 5–34. doi :10.1017/jfm.2014.631.
- Large, W. G., McWilliams, J. C., & Doney, S. C. (1994). Oceanic vertical mixing : A review and a model with a nonlocal boundary layer parameterization. *Reviews of Geophysics*, 32, 363. doi :10.1029/94RG01872.
- Laurindo, L. C., Mariano, A. J., & Lumpkin, R. (2017). An improved near-surface velocity climatology for the global ocean from drifter observations. *Deep Sea Research Part I : Oceanographic Research Papers*, 124, 73–92. doi :10.1016/j.dsr.2017.04.009.
- Lazar, A., Stegner, A., Caldeira, R., Dong, C., Didelle, H., & Viboud, S. (2013a). Inertial instability of intense stratified anticyclones. Part 2. Laboratory experiments. *Journal of Fluid Mechanics*, 732, 485–509. doi :10.1017/jfm.2013.413.
- Lazar, A., Stegner, A., & Heifetz, E. (2013b). Inertial instability of intense stratified anticyclones. Part 1. Generalized stability criterion. *Journal of Fluid Mechanics*, 732, 457–484. doi :10.1017/jfm.2013.412.
- Le Groupe Tourbillon (1983). The Tourbillon experiment : a study of a mesoscale eddy in the eastern North Atlantic. *Deep Sea Research Part A. Oceanographic Research Papers*, 30, 475–511. doi :10.1016/0198-0149(83)90086-9.

- Le Traon, P. Y., Nadal, F., & Ducet, N. (1998). An Improved Mapping Method of Multisatellite Altimeter Data. *Journal of Atmospheric and Oceanic Technology*, *15*, 522–534. doi :10.1175/1520-0426(1998)015<0522:AIMMOM>2.0.CO;2.
- Le Vu, B., Stegner, A., & Arsouze, T. (2018). Angular Momentum Eddy Detection and Tracking Algorithm (AMEDA) and Its Application to Coastal Eddy Formation. *Journal of Atmospheric and Oceanic Technology*, *35*, 739–762. doi :10.1175/JTECH-D-17-0010.1.
- Lee, C. M., Jones, B. H., Brink, K. H., & Fischer, A. S. (2000). The upper-ocean response to monsoonal forcing in the Arabian Sea : seasonal and spatial variability. *Deep Sea Research Part II : Topical Studies in Oceanography*, *47*, 1177–1226. doi :10.1016/S0967-0645(99)00141-1.
- Leweke, T., Le Dizès, S., & Williamson, C. H. (2016). Dynamics and Instabilities of Vortex Pairs. *Annual Review of Fluid Mechanics*, *48*, 507–541. doi :10.1146/annurev-fluid-122414-034558.
- L'Hégaret, P., Beal, L. M., Elipot, S., & Laurindo, L. (2018). Shallow Cross-Equatorial Gyres of the Indian Ocean Driven by Seasonally Reversing Monsoon Winds. *Journal of Geophysical Research : Oceans*, . doi :10.1029/2018JC014553.
- L'Hégaret, P., Carton, X., Louazel, S., & Boutin, G. (2016). Mesoscale eddies and submesoscale structures of Persian Gulf Water off the Omani coast in spring 2011. *Ocean Science*, *12*, 687–701. doi :10.5194/os-12-687-2016.
- L'Hégaret, P., Duarte, R., Carton, X., Vic, C., Ciani, D., Baraille, R., & Corréard, S. (2015). Mesoscale variability in the Arabian Sea from HYCOM model results and observations : impact on the Persian Gulf Water path. *Ocean Science*, *11*, 667–693. doi :10.5194/os-11-667-2015.
- Li, L., Nowlin, W. D., & Jilan, S. (1998). Anticyclonic rings from the Kuroshio in the South China Sea. *Deep Sea Research Part I : Oceanographic Research Papers*, *45*, 1469–1482. doi :10.1016/S0967-0637(98)00026-0.
- Lukas, R., & Santiago-Mandujano, F. (2001). Extreme water mass anomaly observed in the Hawaii ocean time-series. *Geophysical Research Letters*, *28*, 2931–2934. doi :10.1029/2001GL013099.
- Lumpkin, R., & Pazos, M. (2007). Lagrangian Analysis and Prediction of Coastal and Ocean Dynamics. (pp. 39–67). Cambridge University Press.
- Lévy, M., Ferrari, R., Franks, P. J. S., Martin, A. P., & Rivière, P. (2012). Bringing physics to life at the submesoscale : FRONTIER. *Geophysical Research Letters*, *39*. doi :10.1029/2012GL052756.

- Lévy, M., Franks, P. J. S., & Smith, K. S. (2018). The role of submesoscale currents in structuring marine ecosystems. *Nature Communications*, 9. doi:10.1038/s41467-018-07059-3.
- Mahdinia, M., Hassanzadeh, P., Marcus, P. S., & Jiang, C.-H. (2017). Stability of three-dimensional Gaussian vortices in an unbounded, rotating, vertically stratified, Boussinesq flow : linear analysis. *Journal of Fluid Mechanics*, 824, 97–134. doi:10.1017/jfm.2017.303.
- McDougall, T. J., & Barker, P. M. (2011). *Getting started with TEOS-10 and the Gibbs Seawater (GSW), Oceanographic Toolbox*.
- McWilliams, J. C. (1984). The emergence of isolated coherent vortices in turbulent flow. *Journal of Fluid Mechanics*, 146, 21–43. doi:10.1017/S0022112084001750.
- McWilliams, J. C. (1985). Submesoscale, coherent vortices in the ocean. *Reviews of Geophysics*, 23, 165–182. doi:10.1029/RG023i002p00165.
- McWilliams, J. C., Gent, P. R., & Norton, N. J. (1986). The Evolution of Balanced, Low-Mode Vortices on the β -Plane. *Journal of Physical Oceanography*, 16, 838–855. doi:https://doi.org/10.1175/1520-0485(1986)016<0838:TEOBLM>2.0.CO;2.
- McWilliams, J. C., Weiss, J. B., & Yavneh, I. (1999). The vortices of homogeneous geostrophic turbulence. *Journal of Fluid Mechanics*, 401, 1–26. doi:10.1017/S0022112099006382.
- Ménesguen, C., Le Gentil, S., Marchesiello, P., & Ducoussou, N. (2018). Destabilization of an Oceanic Meddy-Like Vortex : Energy Transfers and Significance of Numerical Settings. *Journal of Physical Oceanography*, 48, 1151–1168. doi:10.1175/jpo-d-17-0126.1.
- Meschanov, S., & Shapiro, G. (1998). A young lens of Red Sea Water in the Arabian Sea. *Deep Sea Research Part I: Oceanographic Research Papers*, 45, 1–13. doi:10.1016/S0967-0637(97)00018-6.
- Metzger, E., Helber, R. W., Hogan, P. J., Posey, P. G., Thoppil, P. G., Townsend, T. L., Wallcraft, A. J., Smedstad, O. M., Franklin, D. S., Zamudo-Lopez, L. et al. (2017). *Global ocean forecast system 3.1 validation test*. Technical Report NAVAL RESEARCH LAB STENNIS DETACHMENT STENNIS SPACE CENTER MS STENNIS SPACE CENTER United States.
- Metzger, E. J., Smedstad, O. M., Thoppil, P., Hurlburt, H., Cummings, J., Walcraft, A., Zamudio, L., Franklin, D., Posey, P., Phelps, M., Hogan, P., Bub, F., & DeHaan, C. (2014). US Navy Operational Global Ocean and Arctic Ice Prediction Systems. *Oceanography*, 27, 32–43. doi:10.5670/oceanog.2014.66.

BIBLIOGRAPHIE

- Meunier, T., Pallas-Sanz, E., Tenreiro, M., Portela, E., Ochoa, J., Ruiz-Angulo, A., & Cusí, S. (2018a). The Vertical Structure of a Loop Current Eddy. *Journal of Geophysical Research : Oceans*, *123*, 6070–6090. doi :10.1029/2018JC013801.
- Meunier, T., Tenreiro, M., Pallàs-Sanz, E., Ochoa, J., Ruiz-Angulo, A., Portela, E., Cusí, S., Damien, P., & Carton, X. (2018b). Intrathermocline Eddies Embedded Within an Anticyclonic Vortex Ring. *Geophysical Research Letters*, *45*, 7624–7633. doi :10.1029/2018GL077527.
- Mkhinini, N., Coimbra, A. L. S., Stegner, A., Arsouze, T., Taupier-Letage, I., & Béranger, K. (2014). Long-lived mesoscale eddies in the eastern Mediterranean Sea : Analysis of 20 years of AVISO geostrophic velocities. *Journal of Geophysical Research : Oceans*, *119*, 8603–8626. doi :10.1002/2014JC010176.
- Morel, Y., & McWilliams, J. (1997). Evolution of Isolated Interior Vortices in the Ocean. *Journal of Physical Oceanography*, *27*, 727–748. doi :10.1175/1520-0485(1997)027<0727:EOIIVI>2.0.CO;2.
- Morel, Y. G., Darr, D. S., & Talandier, C. (2006). Possible Sources Driving the Potential Vorticity Structure and Long-Wave Instability of Coastal Upwelling and Downwelling Currents. *Journal of Physical Oceanography*, *36*, 875–896. doi :10.1175/JP02899.1.
- Morrow, R. (2004). Divergent pathways of cyclonic and anti-cyclonic ocean eddies. *Geophysical Research Letters*, *31*. doi :10.1029/2004GL020974.
- Morvan, M., L'Hégaret, P., de Marez, C., Carton, X., Corréard, S., & Baraille, R. (2020). Life cycle of mesoscale eddies in the Gulf of Aden. *Geophysical & Astrophysical Fluid Dynamics*, (pp. 1–19). doi :10.1080/03091929.2019.1708348.
- Nguyen, H. Y., Hua, B. L., Schopp, R., & Carton, X. (2012). Slow quasigeostrophic unstable modes of a lens vortex in a continuously stratified flow. *Geophysical & Astrophysical Fluid Dynamics*, *106*, 305–319. doi :10.1080/03091929.2011.620568.
- Nof, D. (1988). The Fusion of Isolated Nonlinear Eddies. *Journal of Physical Oceanography*, *18*, 887–905. doi :10.1175/1520-0485(1988)018<0887:TFOINE>2.0.CO;2.
- Nof, D. (1999). Strange encounters of eddies with walls. *Journal of Marine Research*, *57*, 739–761. doi :10.1357/002224099321560555.

- Ollitrault, M., & Rannou, J.-P. (2013). ANDRO : An Argo-Based Deep Displacement Dataset. *Journal of Atmospheric and Oceanic Technology*, 30, 759–788. doi :10.1175/JTECH-D-12-00073.1.
- Olson, D. B., & Evans, R. H. (1986). Rings of the Agulhas current. *Deep Sea Research Part A. Oceanographic Research Papers*, 33, 27–42. doi :10.1016/0198-0149(86)90106-8.
- Overman, E. A. (1982). Evolution and merger of isolated vortex structures. *Physics of Fluids*, 25, 1297. doi :10.1063/1.863907.
- Penven, P., Debreu, L., Marchesiello, P., & McWilliams, J. C. (2006). Evaluation and application of the ROMS 1-way embedding procedure to the central california upwelling system. *Ocean Modelling*, 12, 157–187. doi :10.1016/j.ocemod.2005.05.002.
- Penven, P., Halo, I., Pous, S., & Marié, L. (2014). Cyclogeostrophic balance in the Mozambique Channel. *Journal of Geophysical Research : Oceans*, 119, 1054–1067. doi :10.1002/2013JC009528.
- Perrot, X., & Carton, X. (2010). 2d vortex interaction in a non-uniform flow. *Theoretical and Computational Fluid Dynamics*, 24, 95–100. doi :10.1007/s00162-009-0127-4.
- Polvani, L. M., Zabusky, N. J., & Flierl, G. R. (1989). Two-layer geostrophic vortex dynamics. Part 1. Upper-layer V-states and merger. *Journal of Fluid Mechanics*, 205, 215. doi :10.1017/S0022112089002016.
- Pous, S., Lazure, P., & Carton, X. (2015). A model of the general circulation in the Persian Gulf and in the Strait of Hormuz : Intraseasonal to interannual variability. *Continental Shelf Research*, 94, 55–70. doi :10.1016/j.csr.2014.12.008.
- Prasad, T. G., Ikeda, M., & Kumar, S. P. (2001). Seasonal spreading of the Persian Gulf Water mass in the Arabian Sea. *Journal of Geophysical Research : Oceans*, 106, 17059–17071. doi :10.1029/2000JC000480.
- Quadfasel, D. R., & Schott, F. (1982). Water-Mass Distributions at Intermediate Layers off the Somali Coast during the Onset of the Southwest Monsoon, 1979. *Journal of Physical Oceanography*, 12, 1358–1372. doi :10.1175/1520-0485(1982)012<1358:WMDAIL>2.0.CO;2.
- Queste, B. Y., Vic, C., Heywood, K. J., & Piontkovski, S. A. (2018). Physical Controls on Oxygen Distribution and Denitrification Potential in the North West Arabian Sea. *Geophysical Research Letters*, 45, 4143–4152. doi :10.1029/2017GL076666.

- Reinaud, J. N., & Dritschel, D. G. (2005). The critical merger distance between two co-rotating quasi-geostrophic vortices. *Journal of Fluid Mechanics*, 522, 357–381. doi :10.1017/S0022112004002022.
- Richardson, P. L. (1983). Gulf Stream Rings. In A. R. Robinson (Ed.), *Eddies in Marine Science* (pp. 19–45). Berlin, Heidelberg : Springer Berlin Heidelberg. doi :10.1007/978-3-642-69003-7_2.
- Richardson, P. L., Strong, A. E., & Knauss, J. A. (1973). Gulf Stream Eddies : Recent Observations in the Western Sargasso Sea. *Journal of Physical Oceanography*, 3, 297–301. doi :10.1175/1520-0485(1973)003<0297:GSEROI>2.0.CO;2.
- Rodríguez-Marroyo, R., Viúdez, A., & Ruiz, S. (2011). Vortex Merger in Oceanic Tripoles. *Journal of Physical Oceanography*, 41, 1239–1251. doi :10.1175/2011JP04582.1.
- Sansón, L. Z., Graef, F., & Pavía, E. G. (1998). Collision of anticyclonic, lens-like eddies with a meridional western boundary. *Journal of Geophysical Research : Oceans*, 103, 24881–24890. doi :10.1029/98JC02547.
- Scharffenberg, M. G., & Stammer, D. (2010). Seasonal variations of the large-scale geostrophic flow field and eddy kinetic energy inferred from the TOPEX/Poseidon and Jason-1 tandem mission data. *Journal of Geophysical Research*, 115. doi :10.1029/2008JC005242.
- Shapiro, G., & Meschanov, S. (1991). Distribution and spreading of Red Sea Water and salt lens formation in the northwest Indian Ocean. *Deep Sea Research Part A. Oceanographic Research Papers*, 38, 21–34. doi :10.1016/0198-0149(91)90052-H.
- Shchepetkin, A. F., & McWilliams, J. C. (1998). Quasi-Monotone Advection Schemes Based on Explicit Locally Adaptive Dissipation. *Monthly Weather Review*, 126, 1541–1580. doi :10.1175/1520-0493(1998)126<1541:QMASBO>2.0.CO;2.
- Shchepetkin, A. F., & McWilliams, J. C. (2005). The regional oceanic modeling system (ROMS) : a split-explicit, free-surface, topography-following-coordinate oceanic model. *Ocean Modelling*, 9, 347–404. doi :10.1016/j.ocemod.2004.08.002.
- Shchepetkin, A. F., & McWilliams, J. C. (2011). Accurate Boussinesq oceanic modeling with a practical, “Stiffened” Equation of State. *Ocean Modelling*, 38, 41–70. doi :10.1016/j.ocemod.2011.01.010.

- Shi, C., & Nof, D. (1993). The splitting of eddies along boundaries. *Journal of marine research*, 51, 771–795.
- Shi, C., & Nof, D. (1994). The Destruction of Lenses and Generation of Wodons. *Journal of Physical Oceanography*, 24, 1120–1136. doi :10.1175/1520-0485(1994)024<1120:TDOLAG>2.0.CO;2.
- Shinoda, T., Zamudio, L., Guo, Y., Metzger, E. J., & Fairall, C. W. (2019). Ocean variability and air-sea fluxes produced by atmospheric rivers. *Scientific Reports*, 9. doi :10.1038/s41598-019-38562-2.
- Simmons, R. C., Luther, M. E., O'Brien, J. J., & Legler, D. M. (1988). Verification of a numerical ocean model of the Arabian Sea. *Journal of Geophysical Research*, 93, 15437. doi :10.1029/JC093iC12p15437.
- Smith, D. C. (1986). A Numerical Study of Loop Current Eddy Interaction with Topography in the Western Gulf of Mexico. *Journal of Physical Oceanography*, 16, 1260–1272. doi :10.1175/1520-0485(1986)016<1260:ANSOLC>2.0.CO;2.
- Sofianos, S. S., & Johns, W. E. (2003). An Oceanic General Circulation Model (OGCM) investigation of the Red Sea circulation, 1. Exchange between the Red Sea and the Indian Ocean. *Journal of Geophysical Research*, 107. doi :10.1029/2001JC001184.
- Soufflet, Y., Marchesiello, P., Lemarié, F., Jouanno, J., Capet, X., Debreu, L., & Benshila, R. (2016). On effective resolution in ocean models. *Ocean Modelling*, 98, 36–50. doi :10.1016/j.ocemod.2015.12.004.
- Spence, T. W., & Legeckis, R. (1981). Satellite and hydrographic observations of low-frequency wave motions associated with a cold core Gulf Stream ring. *Journal of Geophysical Research : Oceans*, 86, 1945–1953. doi :10.1029/JC086iC03p01945.
- Stegner, A., & Dritschel, D. G. (2000). A Numerical Investigation of the Stability of Isolated Shallow Water Vortices. *Journal of Physical Oceanography*, 30, 2562–2573. doi :10.1175/1520-0485(2000)030<2562:ANIOTS>2.0.CO;2.
- Stommel, H. (1948). The westward intensification of wind-driven ocean currents. *Transactions, American Geophysical Union*, 29, 202. doi :10.1029/TR029i002p00202.
- Stommel, H. (1963). Varieties of oceanographic experience. *Science*, 139, 572–576.

- Stumpf, H. G., & Rao, P. K. (1975). Evolution of Gulf Stream Eddies as Seen in Satellite Infrared Imagery. *Journal of Physical Oceanography*, *5*, 388–393. doi :10.1175/1520-0485(1975)005<0388:EOGSEA>2.0.CO;2.
- Sun, B., Liu, C., & Wang, F. (2019). Global meridional eddy heat transport inferred from Argo and altimetry observations. *Scientific Reports*, *9*. doi :10.1038/s41598-018-38069-2.
- Sutyrin, G. G., Hesthaven, J. S., Lynov, J. P., & Rasmussen, J. J. (1994). Dynamical properties of vortical structures on the beta-plane. *Journal of Fluid Mechanics*, *268*, 103–131. doi :10.1017/S002211209400128X.
- Sutyrin, G. G., Rowe, G. D., Rothstein, L. M., & Ginis, I. (2003). Baroclinic Eddy Interactions with Continental Slopes and Shelves. *Journal of Physical Oceanography*, *33*, 283–291. doi :10.1175/1520-0485(2003)033<0283:BEIWCS>2.0.CO;2.
- Talley, L. D. (2011). *Descriptive physical oceanography : an introduction*. Academic press.
- Thoppil, P. G., Metzger, E. J., Hurlburt, H. E., Smedstad, O. M., & Ichikawa, H. (2016). The current system east of the Ryukyu Islands as revealed by a global ocean reanalysis. *Progress in Oceanography*, *141*, 239–258. doi :10.1016/j.pocean.2015.12.013.
- Tollefson, J. (2018). Ocean scientists work to forecast huge plankton blooms in Arabian Sea. *Nature*, *555*, 569–570. doi :10.1038/d41586-018-03698-0.
- Trott, C. B., Subrahmanyam, B., Chaigneau, A., & Delcroix, T. (2018). Eddy Tracking in the Northwestern Indian Ocean During Southwest Monsoon Regimes. *Geophysical Research Letters*, *45*, 6594–6603. URL : <http://doi.wiley.com/10.1029/2018GL078381>. doi :10.1029/2018GL078381.
- Vallis, G. K. (2017). *Atmospheric and oceanic fluid dynamics*. Cambridge University Press.
- Vic, C. (2015). *Western Boundary Dynamics in the Arabian Sea*. Ph.D. thesis Université de Bretagne occidentale-Brest.
- Vic, C., Capet, X., Rouillet, G., & Carton, X. (2017). Western boundary upwelling dynamics off Oman. *Ocean Dynamics*, *67*, 585–595. doi :10.1007/s10236-017-1044-5.
- Vic, C., Rouillet, G., Capet, X., Carton, X., Molemaker, M. J., & Gula, J. (2015). Eddy-topography interactions and the fate of the Persian Gulf Outflow. *Journal of Geophysical Research : Oceans*, *120*, 6700–6717. doi :10.1002/2015JC011033.

- Vic, C., Rouillet, G., Carton, X., & Capet, X. (2014). Mesoscale dynamics in the Arabian Sea and a focus on the Great Whirl life cycle : A numerical investigation using ROMS. *Journal of Geophysical Research : Oceans*, *119*, 6422–6443. doi :10.1002/2014JC009857.
- von Hardenberg, J., McWilliams, J. C., Provenzale, A., Shchepetkin, A., & Weiss, J. B. (2000). Vortex merging in quasi-geostrophic flows. *Journal of Fluid Mechanics*, *412*, 331–353. doi :10.1017/S0022112000008442.
- Warren, B., Stommel, H., & Swallow, J. (1966). Water masses and patterns of flow in the Somali Basin during the southwest monsoon of 1964. *Deep Sea Research and Oceanographic Abstracts*, *13*, 825–860. doi :10.1016/0011-7471(76)90907-4.
- Weiss, J. B., & McWilliams, J. C. (1993). Temporal scaling behavior of decaying two-dimensional turbulence. *Physics of Fluids A : Fluid Dynamics*, *5*, 608–621. doi :10.1063/1.858647.
- Yim, E., & Billant, P. (2015). On the mechanism of the Gent–McWilliams instability of a columnar vortex in stratified rotating fluids. *Journal of Fluid Mechanics*, *780*, 5–44. doi :10.1017/jfm.2015.426.
- Yim, E., & Billant, P. (2016). Analogies and differences between the stability of an isolated pancake vortex and a columnar vortex in stratified fluid. *Journal of Fluid Mechanics*, *796*, 732–766. doi :10.1017/jfm.2016.248.
- Yim, E., Billant, P., & Ménesguen, C. (2016). Stability of an isolated pancake vortex in continuously stratified-rotating fluids. *Journal of Fluid Mechanics*, *801*, 508–553. doi :10.1017/jfm.2016.402.
- Young, W. R., & Chen, L. (1995). Baroclinic Instability and Thermohaline Gradient Alignment in the Mixed Layer. *Journal of Physical Oceanography*, *25*, 3172–3185. doi :10.1175/1520-0485(1995)025<3172:BIATGA>2.0.CO;2.
- Yu, Z., Metzger, E. J., Thoppil, P., Hurlburt, H. E., Zamudio, L., Smedstad, O. M., Na, H., Nakamura, H., & Park, J.-H. (2015). Seasonal cycle of volume transport through Kerama Gap revealed by a 20-year global HYbrid Coordinate Ocean Model reanalysis. *Ocean Modelling*, *96*, 203–213. doi :10.1016/j.ocemod.2015.10.012.
- Zhang, Z., Tian, J., Qiu, B., Zhao, W., Chang, P., Wu, D., & Wan, X. (2016). Observed 3D Structure, Generation, and Dissipation of Oceanic Mesoscale Eddies in the South China Sea. *Scientific Reports*, *6*. doi :10.1038/srep24349.

BIBLIOGRAPHIE

Zhang, Z., Wang, W., & Qiu, B. (2014). Oceanic mass transport by mesoscale eddies. *Science*, 345, 322–324. doi:10.1126/science.1252418.

Titre : Dynamique des structures cohérentes de méso et sousméso-échelle en Mer d'Arabie

Mots clés : tourbillon, méso-échelle, sousméso-échelle, instabilité, mer d'Arabie.

Résumé : Dans des régions particulières du globe, les tourbillons ont un impact sur la circulation plus grand que la circulation grande échelle elle-même. C'est le cas en mer d'Arabie où le transport des propriétés de la colonne d'eau est dominé par le transport induit par les tourbillons.

Dans ce manuscrit de thèse, nous présentons tout d'abord la structure tridimensionnelle des tourbillons de méso-échelle en mer d'Arabie, grâce à l'utilisation conjointe de mesures altimétriques et de mesures *in situ*. Nous décrivons ensuite le cycle de vie de ces tourbillons à l'aide de simulations numériques, sous l'hypothèse qu'ils sont isolés du reste de la dynamique. Pour ces simulations, un tourbillon composite extrait des données *in situ* est utilisé comme condition initiale. Cela permet de réaliser des simulations très idéalisées, mais pour la première fois pertinentes et représentatives de la dynamique tourbillonnaire d'une région particulière.

Nous discutons de l'impact de la stabilité des tourbillons sur leur durée de vie et sur la génération de structures de sousméso-échelle à la surface. Nous discutons également l'interaction entre les tourbillons et les frontières ouest des bassins océaniques, et mettons en relation ces résultats avec la mesure d'un tourbillon cyclonique de sousméso-échelle effectuée durant la campagne PHYSINDIEN 2019.

Comme les tourbillons de méso-échelle ne sont en réalité pas isolés du champ tourbillonnaire ambiant, nous discutons finalement d'une partie des interactions entre tourbillons qui se produisent en mer d'Arabie : les fusions. Un des résultats principaux de cette étude est que la comparaison entre la distance pour laquelle deux tourbillons dans l'océan fusionnent, et la distance critique de fusion obtenue à partir d'études idéalisées de fusion de deux tourbillons isolés sur un plan f omet les paramètres principaux impliqués dans la fusion : le champ turbulent ambiant et l'effet β .

Title: Dynamics of meso and submesoscale structures in the Arabian Sea

Keywords: vortex, mesoscale, submesoscale, instability, Arabian Sea.

Abstract: In the Arabian Sea, eddies have a greater impact on the circulation than the large-scale circulation.

In this manuscript, we present the three-dimensional structure of mesoscale eddies in the Arabian Sea, through the joint use of altimetry and *in situ* measurements. We then describe the lifecycle of these eddies using numerical simulations, under the assumption that they are isolated from the rest of the dynamics. For these simulations, a composite vortex extracted from *in situ* data is used as an initial condition. We discuss the impact of vortex stability on the vortex lifetime and the generation of submesoscale structures at the surface.

We also discuss the interaction between eddies and the western boundaries of ocean basins, and relate these results to the measurement of a cyclonic submesoscale vortex performed during the PHYSINDIEN 2019 experiment.

Because mesoscale eddies are actually not isolated from the ambient eddy field, we finally discuss one part of the eddy interactions that occur in the Arabian Sea: mergers. One of the main results of this study is that the comparison between the distance for which two eddies in the ocean merge, and the critical merging distance obtained from idealized studies of two eddies isolated on an f -plane omits the main parameters involved in merging: the ambient turbulent field and the β -effect.